IN STRICT CONFIDENCE

CRANFIELD UNIVERSITY

KISORTHMAN VIMALAKANTHAN

PASSIVE FLOW CONTROL DEVICES FOR A MULTI MEGAWATT HORIZONTAL AXIS WIND TURBINE

SCHOOL OF ENGINEERING
Department Of Power And Propulsion

PhD
Academic Year: 2010 - 2014

Supervisor: Dr. David G MacManus
03 2014

IN STRICT CONFIDENCE

CRANFIELD UNIVERSITY

SCHOOL OF ENGINEERING
Department Of Power And Propulsion

PhD

Academic Year 2010 - 2014

KISORTHMAN VIMALAKANTHAN

PASSIVE FLOW CONTROL DEVICES FOR A MULTI MEGAWATT HORIZONTAL AXIS WIND TURBINE

Supervisor: Dr. David G MacManus
03 2014

Executive summary

Renewable energy is an environmentally friendly alternative to the use of fossil fuels. In response to reducing the dependency on fossil fuels, the European Wind Energy Association (EWEA) has made a policy to increase the overall renewable energy consumption by three times the current amount by the year 2020. Critical to achieving this target will be the use of wind turbines. There is a scope to increase the performance of wind turbines by utilising the existing techniques from the aeronautical industry. One of these techniques is the use of passive flow control which involves no moving parts that has a reduced complexity compared to active flow control techniques.

Initially eleven flow control devices applicable for a wind turbine were identified. Out of the eleven devices four possible flow control devices were selected for this research project (vortex generator, vortex trapping, passive ventilation and sinusoidal leading edge wing). These four concepts have been evaluated for their applicability for a wind turbine. A novel CFD work was conducted for a wedge type vortex generator for wind turbine blade. A number of different configurations as well as its performance over different operating conditions were assessed. The wedge type vortex generator (VG) showed the most benefit for a wind turbine blade and it is recommended for wind turbine application, specifically for the root part of the blade. It was found that up to 0.2% increase in AEP is possible with integration of this VG at the blade root, which corresponds to about €30,000 worth of additional energy production of a 5MW turbine per annum.

A series of theoretical studies using Blade Element Momentum (BEM) theory was conducted to establish the requirements for an optimum wind turbine blade. Based on this investigation it was found that the current root geometry is unable to attain the optimum lift force and in fact it produces negative torque.

One of the interests of this project was to identify ways to reduce the blade loads. This simple BEM based investigation was conducted to quantify potential the chord reduction available with the use of conventional vane and passive air-jet vortex generators (PAJVG). Findings from this exercise showed that large chord reductions are possible with the use of these devices. Only the PAJVGs were able to attain chord reduction up to 10% while allowing the blade to operate within a safe stall margin.

Extensive number of 2D CFD simulations was conducted to validate the current 2D CFD methods. Baseline 2D CFD methods have been successfully validated for the pre-stall angle of attack. The effect of modelling transition for a 2D and 3D wind turbine simulation has been established using the Menter's SST γ-θ transition model.

Acknowledgements

I would like to take the time to thank everyone who has immensely supported me throughout this PhD research.

Firstly I will forever be thankful to my supervisor Dr David G MacManus for his unstinting support within the past three years. He has helped me immensely to develop my skills in critical thinking, technical assessments and report writing. He was able to provide me with limitless number of guidance throughout this research. I'm very glad that he was willing to provide help even at a time that may not be suitable for him. I'm also thankful for his sustained commitment to our shared ambitions towards this research. I'm very grateful for his scientific advice, knowledge and many insightful discussion and suggestions.

Secondly I would like to thank and acknowledge the financial support from the RETC and specifically Senvion SE (formally known as REpower Systems) for their contribution towards this PhD. I'm honoured to have obtained valuable industrial experience from the two separate placements that they offered me. Many of the CAD and CFD skills developed for this study would not been possible without this placements. Many thanks to Dr Sascha Erbslöh for his enormous support on organising the placements, conferences and also for all the interesting and technical discussion we had together. I would also like to thank Bert Gollnick for training me on the CFD modelling for a large scale wind turbine, which was essential for conducting this research. Finally I thank all the colleagues I meet in the Aerodynamics team at Senvion SE for all the knowledge they've shared with me regarding wind turbine aerodynamics.

I would also like to thank Gillian Hargreaves and Nicola Datt for providing me with all the administrative support within the Cranfield University. They made all the admin related tasks during my study at Cranfield seem effortless.

Finally I would like to thank all my friends (too many to list here but you know who you are) for their constant support throughout this research study. Special thanks to my best PhD buddies: Tom Elson, Robert Christie and Nnamdi Ben Anosike for all their support and for all those invaluable arguments/discussions on aerodynamics and general engineering.

Last but not least I would like to especially thank my mum, dad and sister. My hard working parents have sacrificed their lives for my sister and myself and provided unconditional love and care. I would not have made it this far without them. I know I always have my friends and family to count on when the times were rough.

I dedicate this thesis to four special people in my life,
my farther Vairamuthu V., my mother Siyamalathevi V., my sister Yasmicca V.
and
my late aunty Kousalya R., who passed away at the time of writing this thesis (18/11/2013).
May she rest in peace…

Table of Contents

Table of Figures

Table of Tables

Nomenclature

a	Axial induction factor
A	Amplitude of the tubercles
a’	Tangential induction factor
B	Number of blades
c	Airfoil or blade chord (m)
C_d	Coefficient of drag
C_l	Coefficient of lift
C_m	Coefficient of moment
C_P	Coefficient of pressure or power
C_Q	Coefficient of torque
C_T	Coefficient of thrust
C_μ	Blowing coefficient
D	Drag
d	Duct diameter (mm)
d( )	Incremental value
$( )_{(opt)}$	Optimum value
$( )_{(oper)}$	Operational value
F	Prandtl’s loss parameter
h	Vortex device height
H	Shape factor
L	Lift (N)
M	Mach number
PPD	O-ring lateral spacing parameter
Q	Torque (Nm)
q	Dynamic head ($0.5\rho V^2$)
r	Local radius
R	Blade radius
S	Planform area (m2)
S^+	Reynolds number relative to riblets width
T	Thrust (N)
t	Airfoil thickness
TM	Turbulence model
U_∞, Ws	Wind speed (m/s)
V	Velocity (m/s)
W	Local incident velocity (m/s)
w	Lateral spacing between wedges
$\dot{m}$	Mass flow rate (kg/s)
R_{hub}	Hub/spinner radius

Greek symbols

α, AoA	Angle of attack (^{o})
Ω, Omega	Rotational speed of the rotor (RPM)
Γ	Circulation (m^2/s)
δ	Boundary layer thickness
δ*	Displacement thickness
θ	Momentum thickness
θ_r	Sectional twist angle (^{o})
λ	Wavelength (m)
ϕ	Relative flow angle (^{o})
β	Blade pitch angle (^{o})
γ	Turbulence intermittency
Ψ	Precone angle (^{o})
ρ	Density (kg/m^3)
μ	Dynamic viscosity (m^2/s)
μ_t	Turbulence eddy viscosity
τ	Shear stress
σ	Blade solidity
κ	Turbulent kinetic energy
ω	Turbulence frequency or
ω_r	Tangential velocity at the rotor plane

Abbreviations

AEP	Annualised Energy Production
ASM	Algebraic stress model
BEM	Blade element momentum
BLF	Boundary layer fence
BSL	Baseline κ-ω turbulence model
CFD	Computational fluid dynamics
EWEA	European Wind Energy Association
EOG	Extreme operating gust (wind model)
HAWT	Horizontal axis wind turbine
LE	Leading edge
MVG	Miniature vortex generator
NREL	National renewable energy laboratory
PAJVG	Passive air jet vortex generator
PFC	Passive flow control
RNG	Re-Normalisation Group
Re	Reynolds number
RSM	Reynolds stress model
RMS	Root mean square
SST	Shear Stress Transport
SSG	Speziale, Sarker and Gatski's Reynolds stress model
DI	Step depth
TSR	Tip speed ratio
TE	Trailing edge
VVG	Vane vortex generator
VG	Vortex generator

1 Introduction

Climate change is one of the greatest threats facing the planet. Currently most of the world energy demands are met by burning fossil fuels, which is causing more detrimental effects to the planet's climate. Wind energy as a form of renewable energy can help to reduce the dependencies on fossil fuels for energy.

Increasing demand for wind energy can be achieved with different ways. The simple approach is to have as many wind turbines as possible, however this requires higher capital cost. Another approach will be to have bigger wind turbines to generate the large amount of power. Greater energy demands can be also satisfied with a smaller number of highly efficient turbines. The efficiency of the turbine depends on many aspects. This includes the structural and aerodynamic efficiency. The increase in structural efficiency will reduce the maintenance and material costs. The aerodynamic efficiency helps to gain the necessary power demand, with a smaller number of efficient wind turbines. One of the several ways of improving these efficiencies is the use of innovative technologies such as passive flow control devices which does not require an additional energy input avoiding the implementation of a complex system.

This project aims to determine the potential benefits for a horizontal axis wind turbine (HAWT) by the use of passive flow control devices. The improvements are mainly focused on the aerodynamic flow characteristics of a wind turbine. Notable improvement to the power output of the turbine without any compromise at all on the structural integrity is the desired outcome.

There are many ways to alter the flow on a wind turbine to attain the best performance. One of the methods is to use flow control devices to achieve the desired flow topology. Passive flow control (PFC) can also be used in addition to airfoil redesign to give possible additional benefits. There are two types of flow control techniques: passive and active. PFC techniques can be described as a system without the need for additional energy input i.e. small geometrical change that take advantage of the local flow characteristics to modify the flow in a way that beneficial results can be obtained. Active flow control techniques are not desirable due to their need for external energy input and regular maintenance (additional cost).

The rationale behind this project is that PFC devices have been successful in the aeronautical sector and there is currently a small amount of research on integrating PFC devices to a wind turbine available on the open literature. This project aims to fill this gap in research by identifying a suitable PFC device for wind turbine application. The objective of this project is to use computational fluid dynamics (CFD) analysis to assess the applicability of the PFC devices that could improve the performance of wind turbine. Theoretical studies based on blade element momentum method (BEM) will also be conducted to assess the baseline rotor as well as some aspects of the structural benefits offered by the PFC device.

The novel aspect in the project lies in the fact that most of the PFC technologies studied in this project have not been applied to a wind turbine. Thus this project will enable the

understanding of the device's behaviour in a wind turbine flow environment and discuss the potential benefits offer to the rotor.

This research started with a broad scope of identifying the aerodynamic improvements that a PFC can offer for a wind turbine. Then various PFC devices were reviewed and numerous refinements were conducted to finally select two devices that are the most appropriate for wind turbine application. Based on this research strategy the thesis is structured in the following way.

This thesis is split in to six separate parts, a brief summary of the chapters are outlined below.

Chapter 2: This part of the report addresses the available technologies for improving the performance of a wind turbine. Eleven PFC devices which could be applicable to a large scale wind turbines are documented in this section. Four potential flow control devices were then selected for further analysis in this research project.

Chapter 3: This chapter will discuss the wind turbine aerodynamics using a theoretical approach (BEM). The aerodynamic requirements for an ideal wind turbine are presented. The difficulty in achieving these requirements will be discussed and the use of PFC devices to address these problems will be presented.

Chapter 4: This part of the document will outline the 2D and 3D CFD methodology used for this research. The objective of this study is to determine the most suited CFD procedure and methods for a wind turbine. This includes the mesh density, domain size and right choice of turbulence model. The results from the initial study will be compared to experimental or CFD data in order to have confidence in the CFD results.

Chapter 5: This chapter will present the results from the CFD simulations of the investigated PFC devices. The performances of the individual PFCs are discussed and its applicability to the baseline rotor is presented. Finally the overall performance of the devices in terms of power at the design point and annualised output is established.

Chapter 6: This chapter will summarise and conclude the research with the main finding and novel aspects from this study.

1.1 Road map

The project is split into several work packages (Figure 1-1). In the initial stages of the project, eleven passive flow control (PFC) devices applicable for wind turbine implementation were reviewed. National Renewable Energy Laboratory (NREL) has defined a conceptual turbine [1] for the purpose of academic research (NREL 5MW). This turbine has been used on numerous studies around the world [1], such as the EU UpWind research program, the IEA Wind Task 23 OC3 project, and the IEA Wind Task 30 OC4 project. This NREL 5MW (see Appendix 8.3) rotor was selected as the baseline rotor for this project. Its geometrical definitions and specifications are presented in the document published NREL [2]. It is a three bladed upwind rotor with a rotor diameter of 126m.

In the second phase of the project the 2D and 3D CFD models were generated and its results were compared against measurements and data from open literature. Theoretical assessments using BEM were also carried out to determine the aerodynamic requirements for an ideal turbine. It also showed the effect of aerodynamic forces on the axial induction factor. Some aero-elastic assessments of the baseline rotor were conducted to quantify the structural impact due to blade chord reduction by using passive flow control devices.

Finally in the third phase, the chosen PFC devices were installed on the baseline rotor and its performances were determined using 3D CFD methods. The devices effect on the local flow field were analysed and work was done to establish an initial design space for the chosen device.

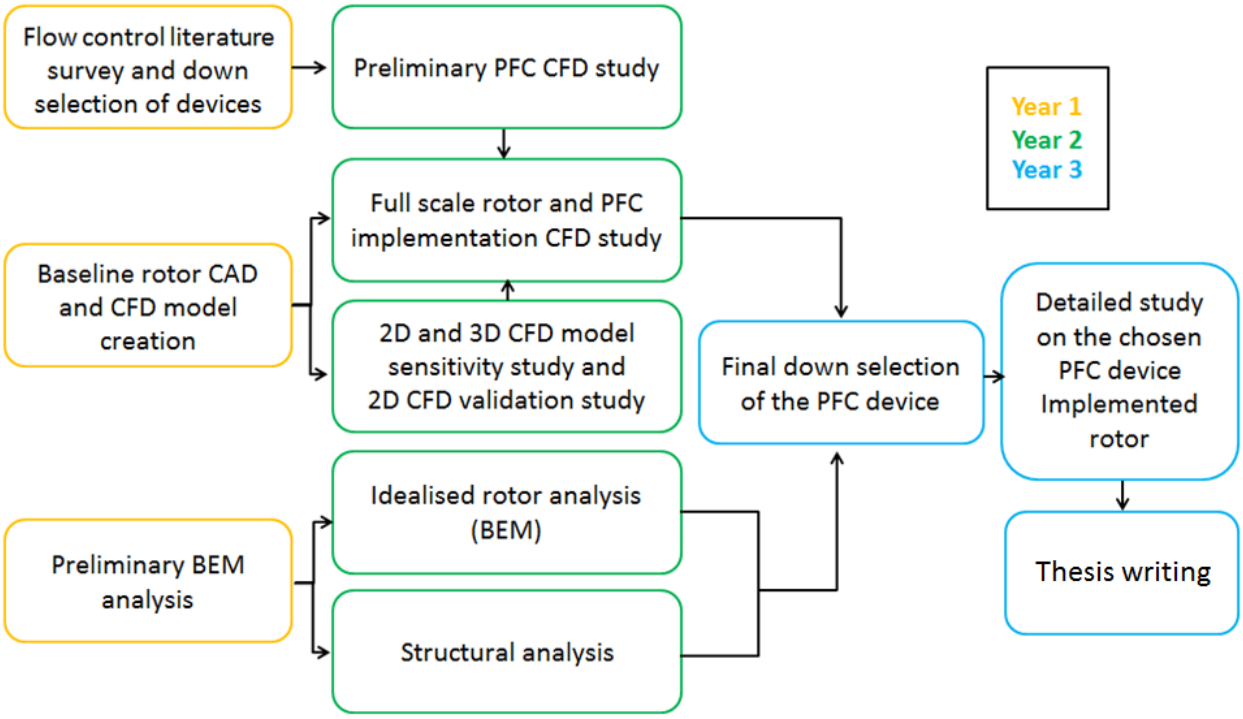

Figure 1-1 Road map for this project

2 Literature review and state of the art

2.1 Introduction

The objective of this part of the thesis is to present a review of passive flow control devices that could be considered for use on a large-scale horizontal axis wind turbine. Flow control methods are usually classified in two categories: passive and active. These methods can improve the flow characteristics to "achieve transition delay, separation postponement, lift increase, skin-friction and pressure drag reduction, turbulence augmentation, heat transfer enhancement, or noise suppression" [3]. This current research mainly focuses on passive methods of flow control which do not rely on an external energy source. As the flow control methods or the technique itself are presented, its applicability to a wind turbine rotor is also briefly considered.

Flow control devices have been applied in the aeronautical industry and this research assesses its potential benefits for a wind turbine blade. At the root of the blade, the structural demands require the airfoils to have a high thickness to chord ratio up to 40%. These thick airfoil sections are prone to early flow separation and therefore an effective method for reducing separation is of interest at this part of the blade [4]. The intermediate sections of the blade (e.g. r/R from 0.3 to 0.6) typically correspond to the power generation portion of the blade and usually the airfoil profiles in this region are traditionally streamlined designs. A flow control method to provide high aerodynamic efficiency (lift to drag ratio) is desirable to gain the best power to thrust ratios at this part of the blade. Finally, the tip of the blade has the highest potential to generate torque. Usually the tip of the blade is composed of smaller (thickness and chord) airfoil section, this is mainly to reduce the thrust production and to minimise deflection. Load alleviation techniques may also be required to relieve the blade from structural fatigue [5].

In summary, the objectives of this review are to identify and initially evaluate flow control devices that could potentially:

1. Mitigate flow separation and increase lift, in particular at the blade root
2. Increase lift to drag ratio for the outer half of the blade
3. Alleviate structural loads

A range of potential passive flow control devices have been reviewed for this research, which include:

- Vortex generators
- Vortex trapping airfoil
- Passive aspiration
- Spanwise flow modifier (fences and O-ring)
- Leading edge tubercles
- Direct transition to turbulence (roughness)
- Riblets
- Trailing edge effectors (T-strip, Micro tabs and Miniature trailing edge effectors)
- Flat trailing edge airfoils and base drag reduction
- Porous airfoil
- Winglets

The integration of PFC devices with a large scale wind turbine blade is briefly introduced. Preliminary conclusions were then drawn for each method and an initial selection of methods has been proposed for more extensive research.

2.2 Vortex generators

Vane vortex generators (VVG) are becoming more commonly used in flow control applications. They are simple solid tabs mounted on the surface of the blade and this device promotes flow mixing and delays flow separation [5]. By delaying flow separation the maximum lift coefficient can be increased. There are many types of vortex generators and some of these are shown in Figure 2-1. They are usually mounted near the root of the blade to mitigate inboard flow separation. However for attached flow conditions the vortex generator causes an undesirable increase in drag.

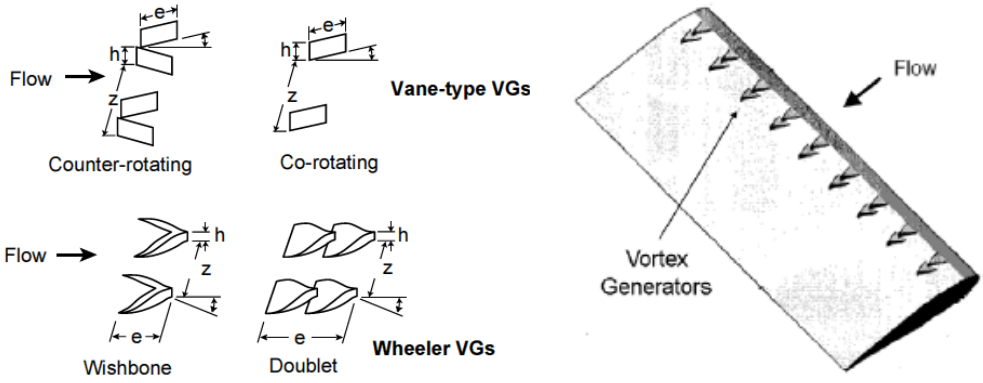

Figure 2-1 Vortex generator [6]

This device works by passively changing the momentum distribution in the flow. One way is to turn the mean flow using embedded stream wise vortices generated by fixed lifting surfaces [7]. The embedded vortices cause overturning of the near-wall flow, which in turn causes the fluid particles with high streamwise momentum to be swept along a helical path towards the surface and thereby to mix and entrain the flows. To an extent, this high momentum flow then replaces the retarded near-wall flow [7]. Vortex generators help to keep the flow attached to the airfoil surface and in return reducing the form drag. By delaying flow separation, higher maximum lift is achieved. Hence overall higher lift to drag ratio (L/D) is obtained. Lin et al [25] have published a summary of vortex generators.

There are two types of vortices which can originate from VGs, these are counter rotating and co-rotating vortices (Figure 2-2). Counter rotating vortices usually generate a large region of vorticity to rise above the surface and hence are not as efficient as the co-rotating types. However co-rotating vortices will cancel other vortices if the optimum spacing is not used, for the co-rotating VGs, the spanwise spacing should be greater than three device heights to avoid cancellation of the vortices. [7].

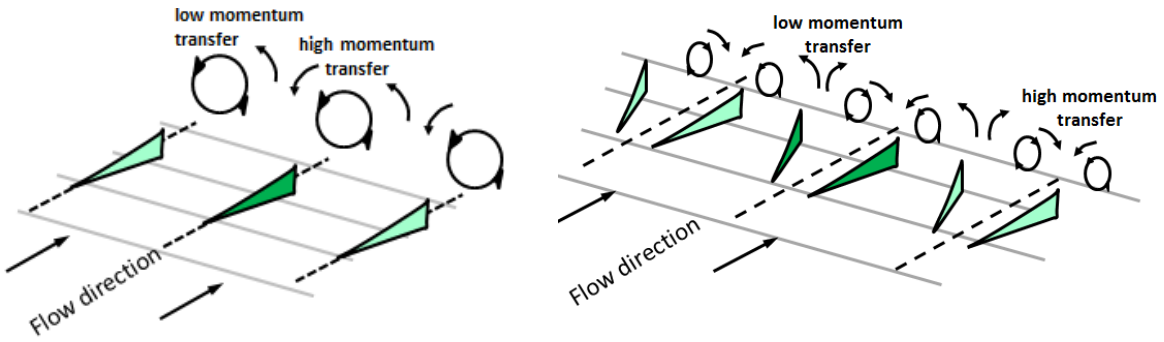

(a) (b)

Figure 2-2 Co-rotating (a) and counter-rotating (b) vane vortex generators adapted from [8]

Barrett et all [6] conducted experiments on a conventional passive vortex generator and compared it with an optimised vortex generator (Figure 2-3). This active or smart technology is optimised for the gain of best lift to drag ratios using shear-flow separation as an input [6]. The author concluded that large lift to drag ratios (up to 62) are only achieved using active smart vortex generators.

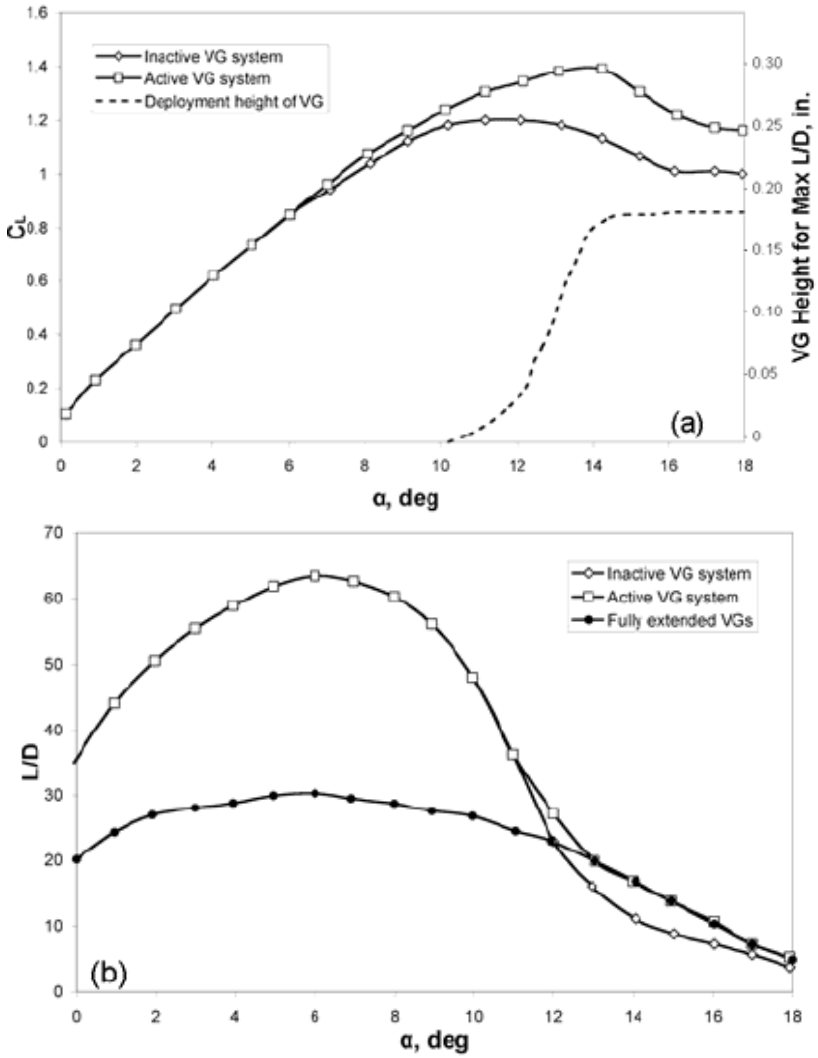

Figure 2-3 Lift (a) and lift to drag ratio (b) as a function of drag for passive (fully extended), inactive (no shape memory alloy activate, only deployment in time), active (memory shape memory alloy) systems, results from [6] **presented in** [5]

There are also smaller geometric versions of vortex generators which are called miniature vortex generators (MVG) or sub boundary layer VGs. Properly designed micro vortex generators (MVG) can perform as efficiently as the traditional vortex generators at low speeds [9]. MVG are defined as having a height of 10-50% of boundary layer thickness [9]. This type of vortex generator can achieve a significant reduction of drag in the attached flow regime, due to its small geometric size [9].

The work done by Lin [10] also showed that, even though MVGs produce weaker vortices, a well-designed MVG produces sufficiently strong vortices to inhibit flow separation and therefore tend to be more efficient. Vortex generators have been applied to mitigate flow separation, but the drag associated with them (when they are inactive) still poses a problem. Therefore for the root section of the blade, vortex generators may be used to achieve an attached flow and the drag penalty associated with vortex generators can be compromised at this section of the blade. A load alleviation technique based on the use of a vane vortex generator was also suggested by Corten [11]. This is discussed in section 3.2

Currently, conventional vane vortex generators are in service for a large scale wind turbine to delay flow separation [12]. Due to the thin physical nature of the vane VGs it lacks structural robustness. They are known to break off during maintenance activity of the turbine, as there is a gap in knowledge in terms of a VG design that addresses the structural integrity of a vane VG that is applicable for a wind turbine. This was one of the main interests of this research study, to find a structurally robust VG design that can perform effectively as a vane VG but with an increased structural robustness.

In 1954 McCullough et al, investigated the wedge type VGs for the delay of flow separation [13]. This wedge type VGs encloses a larger volume of material than the conventional vane VGs consequently achieving a greater structural resistance to bending or breaking. It also has a greater area of contact with the surface i.e. increased gluing area compared to a vane VG. The authors argued that the forward wedges have more potential to re-energise the boundary layer than small aspect ratio wings. The generated vortices from the wedges have a greater circulation (three fold) compared to the tip vortices generated by a small aspect ratio wing. The mechanism of how the wedges generate the vortices is described as the wedges discharge the oncoming boundary layer following up the ramp as a sheet of vorticity over the oblique edge where the discharged vortex sheet rolls up into a trailing vortex [13].

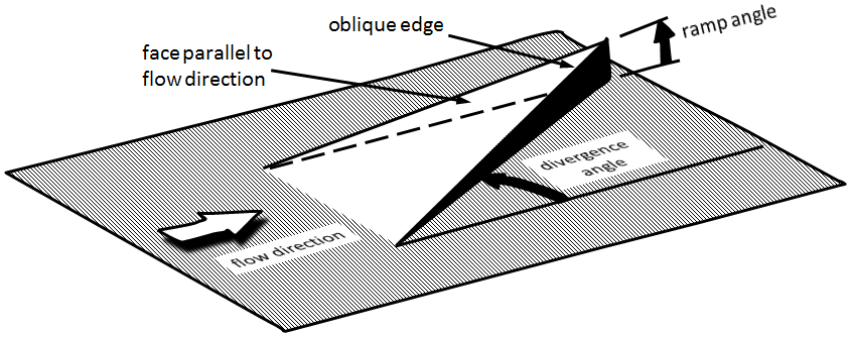

Figure 2-4 Forward facing half wedge investigated by McCullough et al adapted from [13]

McCullough's investigation was conducted experimentally at the Reynolds number of 5.8 million, which within the Reynolds number range found on a large scale wind turbine (1-10

million). The result from this study suggested the wedge type VGs are able to generate vortices that are sufficient to control the boundary layer. It was found that as the angle of divergence was increased beyond 50° the vortices break away from the oblique edge and passed downstream, and the vortices remain visible within the 15-50° range of divergence angle. Reduction in ramp and divergence angle reduces the circulation and the drag coefficient (Table 2.2-1). It is reported that the absolute circulation (Γ) is only considered to be accurate within +/- 5% however the relative changes are quantitatively correct at least.

Wedge		$\frac{\Gamma}{V}$ (m)	Pressure-drag coefficient
Ramp angle (deg)	Divergence angle (deg)		
7	30	0.26	0.29
4	30	0.14	0.18
6	15	0.10	0.12

Table 2.2-1 Performance of forward facing half wedge investigated by McCullough et al [13]**, drag and circulation measurements of three wedges**

Generally it was found that the wedges placed further away from the leading edge of the NACA 633018 wing generate a smaller maximum lift coefficient (Figure 2-5). The results suggest that the wedges should be placed within 0.1<x/c<0.4 to gain beneficial increase in maximum lift coefficient. Larger wedge height of about 2 inches (51mm) showed better increase in maximum lift coefficient than smaller 1inch height wedges. Up to a 40% increase in maximum lift coefficient is possible with the wedge placed at x/c =0.25. McCullough et al's results showed that full wedges (flagged symbol) placed closer together (lateral spacing = 0) are not as efficient as the half wedges in terms of gain in maximum lift coefficient.

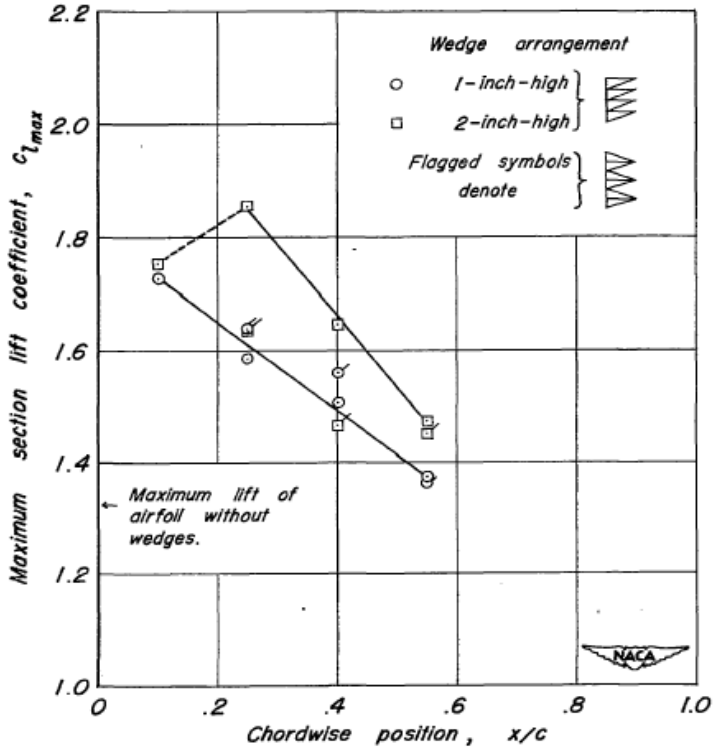

Figure 2-5 Changes in maximum lift coefficient for different chord placement [13]

The lateral wedge spacing of one wedge width was seen to generate the maximum lift coefficient of 1.93 for the 2-inch-high (51mm) half wedges with their leading edge at x/c = 0.10. The drag data from this investigation (Figure 2-6) suggests that wedges placed closer to the trailing edge generate less incremental drag than the ones placed closer to the leading edge. As anticipated the larger wedges generate larger incremental drag. It was reported that doubling the height more than tripled the incremental drag and removing every other wedge reduced the incremental drag of the model by half.

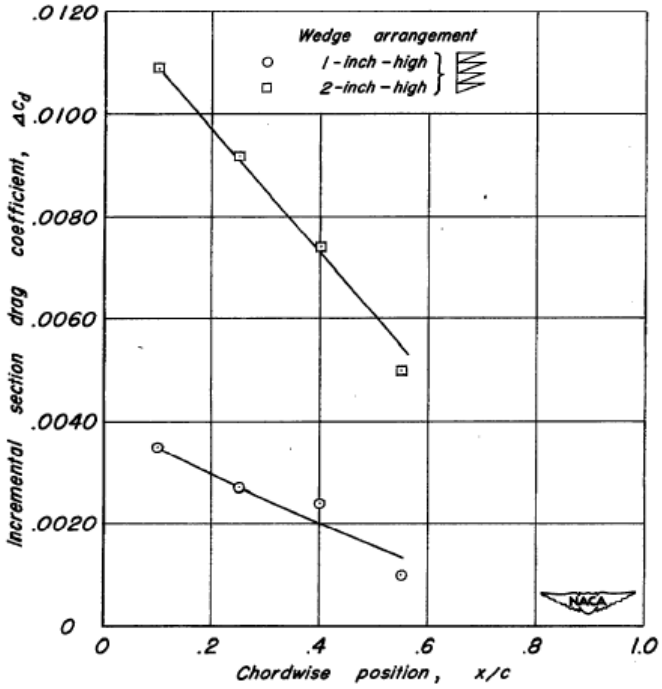

Figure 2-6 Variation of incremental drag at zero lift with chordwise position of leading edges of the adjoin wedges [13]

Based on these results it was decided that wedge type VGs are viable for further research and a detail assessment of this device was recommended to assess its potential for the wind turbine blade root. This is considered in section 5.7.

2.2.1 Using VGs to reduce blade chord

For a device to mitigate high structural loading on the blade, it should reduce the thrust force. At the extreme load case for a wind turbine the wind turbine enters a parked state, where a 90° blade pitch is applied. Therefore due to the increased projected area a considerable amount of thrust is encountered by the blade. These thrust forces can be reduced by reducing the blade chord using VGs without compromising torque at the operating condition.

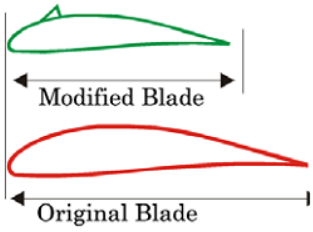

Figure 2-7 Schematic of delay stall technology showing modified blade with shorter chord comparison with original blade with same performance [5]

Stall delay devices increase lift at high angles of attack. Corten [11] proposed an idea to use delay stall devices to mitigate extreme loading on the wind turbine blades. The argument is to keep the lift forces the same as the original unmodified airfoil, while operating at a larger C_l and at a larger AoA, where the stall delay device allows for a safe stall margin. For example, the modified airfoil with the vortex generator will be designed in a way to achieve the same lift force as the unmodified airfoil. This is achieved by designing the modified blade with a smaller chord (Figure 2-7). The lift curve slope ($dL/d\alpha$) is reduced. The AoA of the C_{Lmax} is increased by delaying the stall onset. Hence the same lift is achieved at a higher incidence.

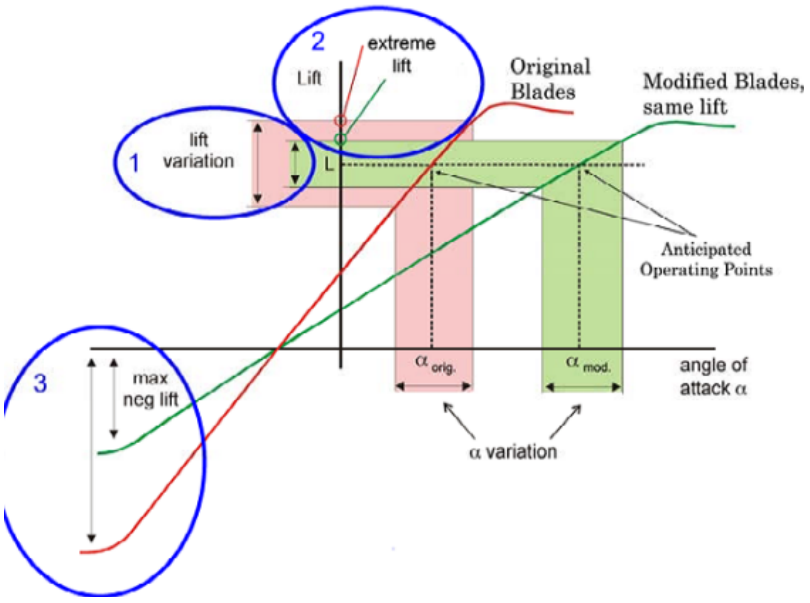

Figure 2-8 Modified and unmodified airfoil's lift curve slopes [11]

There are three main aspects that reduce loading on the blade (Figure 2-8). Firstly, the variation of lift with AoA is smaller for the modified blade than the unmodified blade and this result in the reduction of the oscillating loads. Secondly, the maximum lift for a given change in angle of attack is reduced and finally the reduced lift curve slope helps to reduce loads on the blade by reducing the maximum lift at negative incidence This reduction in negative lift is desirable for pitch-to-feather machines (reducing the angle of attack), as they experience high blade loading when a reduction in incidence is relatively rapid [5]. Corten's research indicates a potential reduction of 20-40% in lift variation with AoA, a potential reduction of 6-12% in extreme lift and a potential reduction of 20-40% for maximum negative lift for a blade chord reduction of 20-50% [11].

The major gain from this method is to keep the performance the same while reducing the chord. This ideally reduces the moment arm for the sectional pitching moment. Therefore this provides a reduction in high torsional blade loading. However this method is purely dependent upon other separation control devices, I.e. vortex generator. Therefore an efficient flow separation control device has to be found first, before Corten's idea [11] can be implemented on the wind turbine blades. This method seems viable for alleviating blade loads at extreme conditions, and an effective separation control device is vital for this device. Using VGs as an effective delay stall device to reduce blade chord and in return reduce the blade load was investigated. The results from this study were used to rectify

Corten's claims and conclusion. An assessment was also done in terms of its applicability to a wind turbine. The analysis is reported in section 3.2.

2.3 Vortex trapping airfoil

Most of the traditional devices associated with lift increase also produce considerable amounts of drag increments i.e. slats and flaps. Typically this simultaneous increase in lift and drag does not increase the aerodynamic efficiency (lift/drag ratio). Hence these devices are generally used in applications where an increase in drag is not overly penalising [3] or indeed may even be beneficial e.g. aircraft landing. One method of increasing lift is to consider a steady separated vortex above a wing at high angle of incidence [3]. In this arrangement, a trapped vortex can arise where the use of a vortex cell helps to keep it trapped. One of the main difficulties in adapting the vortex trapping techniques is to keep a stable captured vortex close to the airfoil surface having sufficient energy left for the main flow to reattach [3]. Stability of the vortex is achieved when the vortex core is maintained at a constant location.

Initially, Kasper developed a wing capable of capturing a vortex (Figure 2-9) [14]. However the experimental results from Kruppa in 1977 [14] showed that it was not possible to capture a stable vortex and consequently, the adverse effect of vortex shedding was observed (Figure 2-10). Kruppa investigated different configurations of this wing to observe its characteristics. Unfortunately he reported a loss of performance whereby there was a reduction in lift and the onset of vortex shedding. He did not succeed in demonstrating the use of passive vortex capturing techniques.

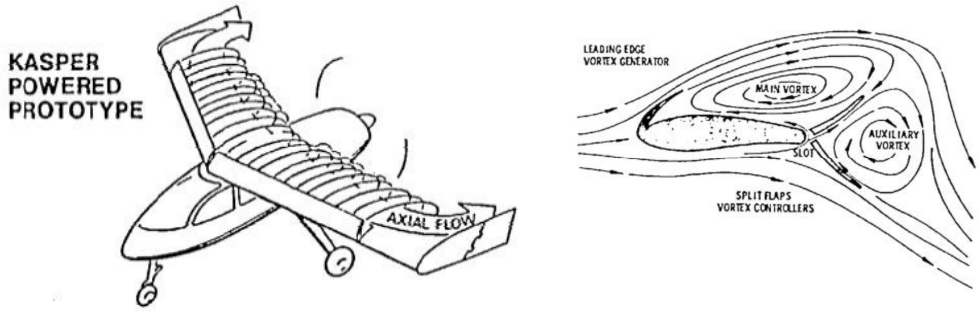

Figure 2-9 Kasper wing concept [14]

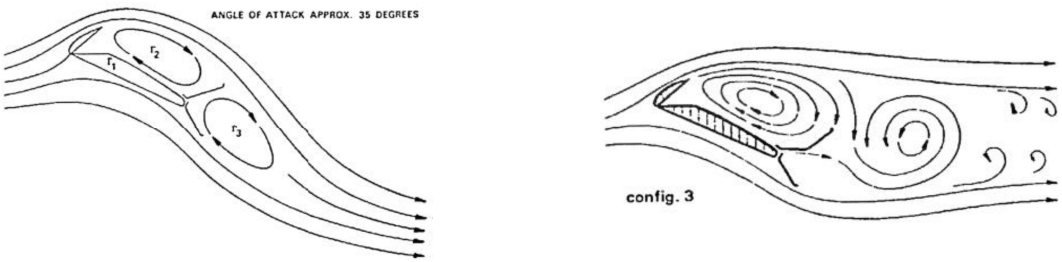

Figure 2-10 Flow visualisation of Kasper wing (Left: Ideal vortex lift flow, Right: Kruppa's experiment) [14]

In the same paper [14] the author also presented some desirable results using a vortex capturing airfoil combined with spanwise blowing (Figure 2-11). This shows that the lift coefficient of this airfoil can be improved with lateral blowing.

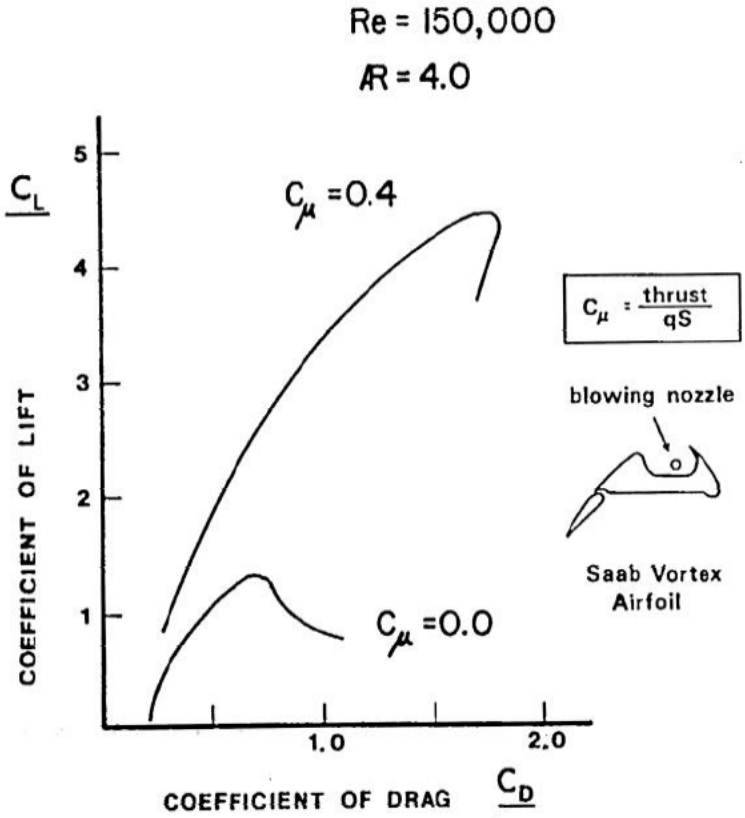

Figure 2-11 Saab vortex airfoil with and without blowing [14]

Finally, Kruppa concludes with the statement that there was no promising vortex lift performance at the flow Reynolds number below 250,000 without the use of lateral blowing [14]. Hence the author suggests that the Reynolds number effects cannot be ignored for the vortex lift concept and studies should be performed for specific operational conditions. The operating Reynolds number for a large scale (5MW) wind turbine is > 3million, therefore at these different flow characteristics where large inertial forces dominates the flow the lateral blowing may not be necessary for vortex lift performance.

Following Krupp's research, Rossow studied the vortex lift wing using potential flow theory [15]. His analysis included the flow field mapping from a cylinder to a flapped airfoil using conformal transformation [15]. This mapping enables the idealised flow analysis on an airfoil section. This research study was conducted using a single frontal flap, where using potential flow theory a relationship between frontal fence length and C_L was established (Figure 2-12, left). This work also computed the location of equilibrium points (vortex centre) for each configuration in the 2D flow field. A sample one of these configurations is shown in Figure 2-12 (right).

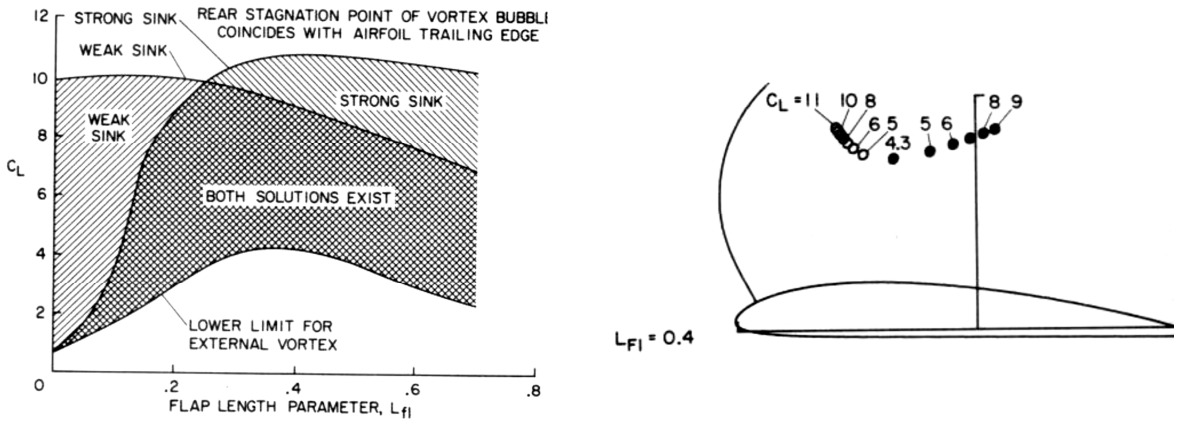

Figure 2-12 V.J Rossow findings for the flap length as a function of lift coefficient (left) and their corresponding vortex centers (right) , left: lift coefficient as a function of frontal flap length, right: equilibrium points (vortex centre) for the investigated cases [15]

Rossow discusses the stability of trapped vortex using potential flow analysis. Stability of a vortex is achieved when the focal point (vortex centre) of the vortex is maintained at a stationary point. Unfortunately the results from this study found only some of the starting locations of the vortex that were able to return back to its equilibrium points, such as point A in Figure 2-13. Rossow also states that stability of the vortex is a delicate study and should be studied more carefully in detail [15].

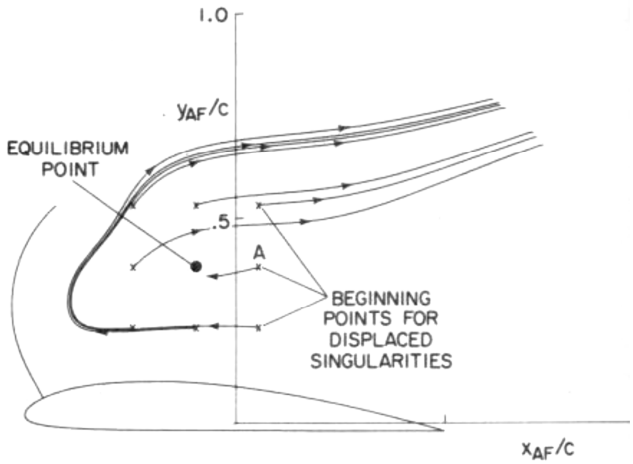

Figure 2-13 Displacement of the equilibrium points [15]

Later, Rossow investigated the case of trapping a vortex using two fences [16] (Figure 2-14). His idea was to use suction to control the vortex bursting. Initially a separation bubble is generated by the frontal fence. The vorticity in the bubble is concentrated into a vortex by suction through the orifices (Figure 2-14) [15]. With time, the vortex dominates the shear layer and inhibits the vortex shedding from the frontal fence. When this happens the vortex archives its maximum strength, where the velocity contribution at the focal (centre) point of the vortex adds to zero.

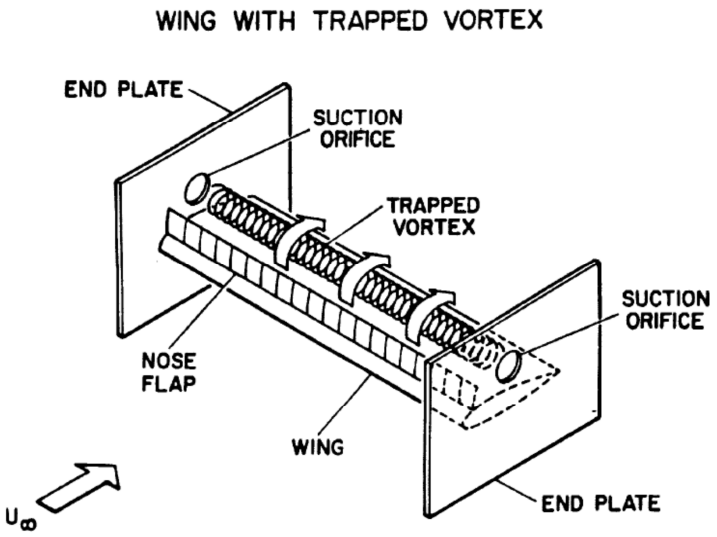

Figure 2-14 Rossow's experimental setup for a vortex lift system using fences and suction applied at the end plates [16]

An idealised vortex trapping method was also presented by Rossow (Figure 2-15), where the vortex is arranged to cover the whole surface of the airfoil. The author states that at this condition it is possible to attain a C_L value of 6 [15]. This value was calculated using potential flow theory from his earlier study [15] using a single frontal fence.

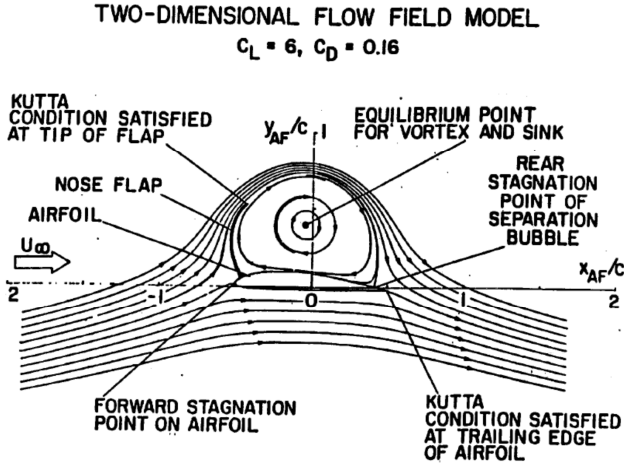

Figure 2-15 Idealised vortex capturing using frontal fence with suction [15]

From the experiment by Rossow [15], it was found that mass removal was not only required to form the vortex but also to sustain the vortex in its equilibrium position. He states that the sink flow in the core of the vortex produces drag [15]. It was also found that, if the mass flow at the core of the vortex was strong enough, the mass flowing through the vortex can disrupt the formation of the vortex. This can then occupy the whole trapped vortex and spill the flow into the free stream. Hence, in order to eliminate the mass flow at the core of the vortex, the author found that the additional fence at the trailing edge was compulsory [16]. Rossow has presented a relationship of length of rear fence required to create this zero mass flow at the vortex core (Figure 2-16).

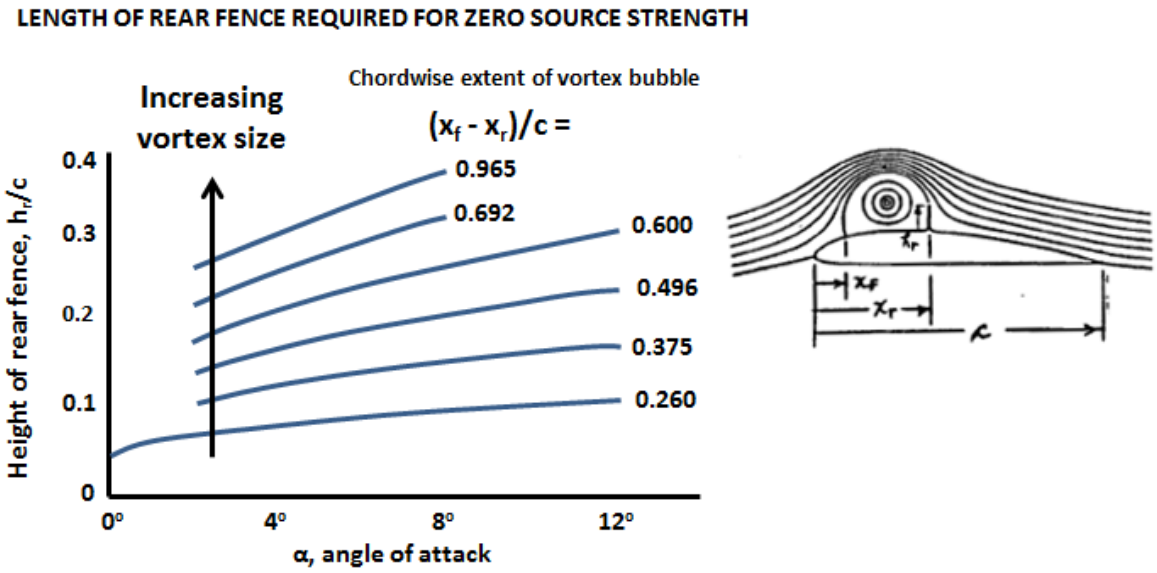

Figure 2-16 Rossow's fence height as a function of AoA, adapted from [16]

Rossow [16] demonstrated that it is possible to trap a vortex and keep it stable in order to obtain beneficial results (Figure 2-17), using two fences with suction. Also from the results it is clear that the size of the vortex has a significant effect on the increase in lift, where the largest vortex showed to achieve lift coefficient up to 7. The location of the vortex also acts as another parameter to enhance the performance of the airfoil. From the relationship between the pitching moment and the vortex size (Figure 2-17, right), it can be seen that an increase in vortex size increases the pitching moment, this is directly due to the increase in lift by the increased vortex size (Figure 2-18). The disadvantage of this increase in pitching moment is the increase in torsional load on the airfoil section. Overall Rossow's work has shown that vortex lift is possible using two fences and has also established initial guidelines to attain vortex lift using fences. However it is expected that large drag forces may arise from these lateral fences and it is not recommended for a wind turbine application. Consequently the vortex lift using lateral fences was not studied in this thesis.

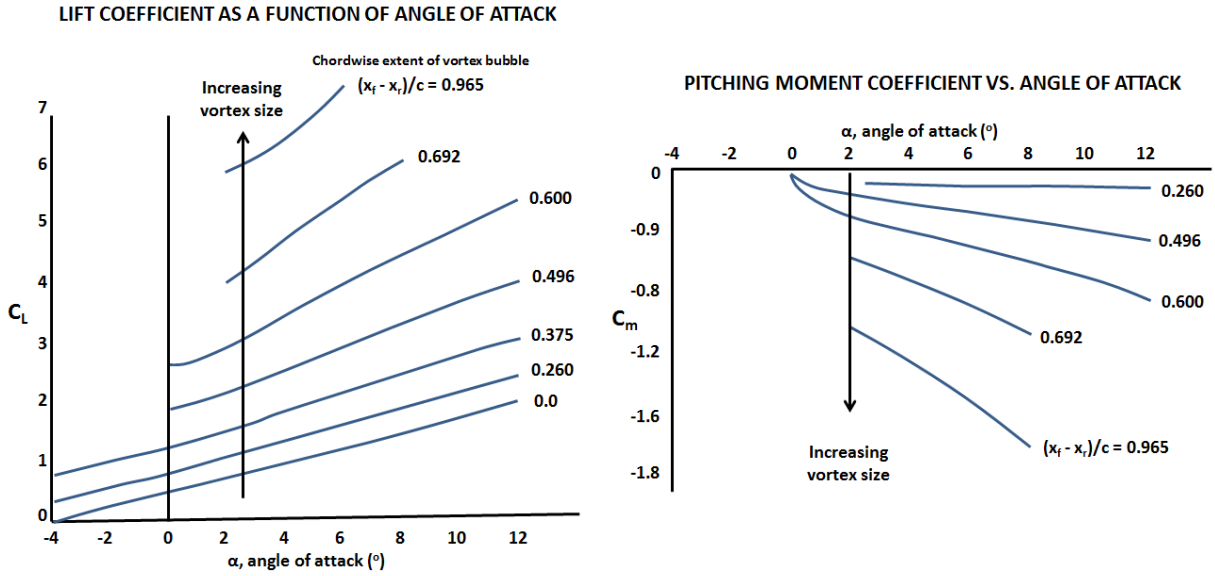

Figure 2-17 Lift (left) and pitching moment (right) coefficient as a function of AoA for different vortex sizes, adapted from [16]

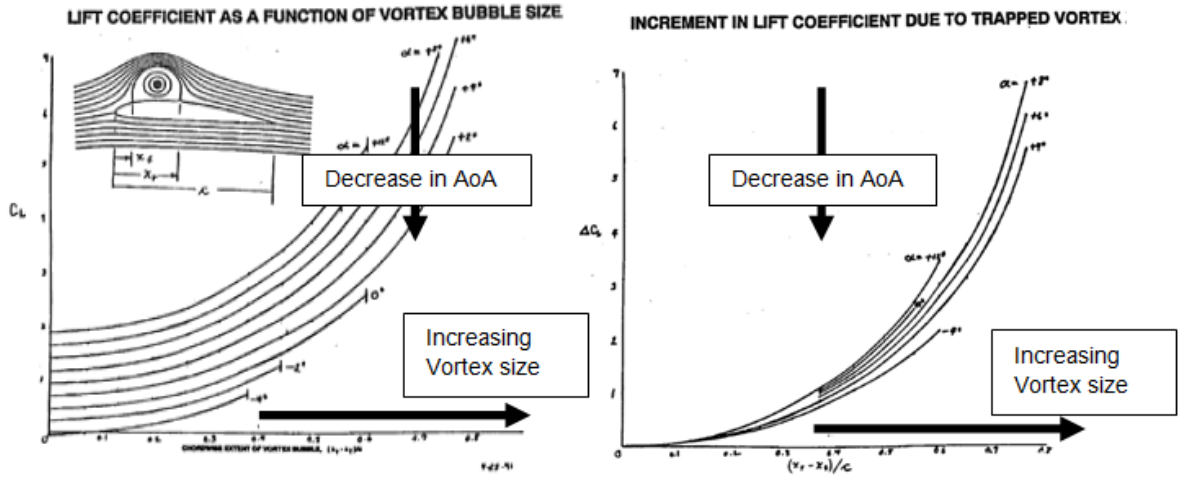

Figure 2-18 Lift coefficient (left) and increment (right) in lift as a function of vortex size [16]

Fertis published a promising paper [17] regarding the vortex trapping airfoil. He has claimed that a new airfoil shape can increase the aerodynamic efficiency (lift to drag ratio). Fertis' proposed airfoil consisted of a simple geometric alteration to the conventional airfoil (Figure 2-19). It was reported that this step modification on a conventional airfoil produces an improvements in the aerodynamic characteristics of the existing airfoil in terms of lift, drag, and lift-to-drag ratio [17]. In addition, Fertis also mentions that the turbulence induced by the discontinuity will either "eliminate stall for angles of attack up to at least 40 degrees or provide a much smoother stall" [17].

Figure 2-19 Fertis's new airfoil concept [17]

The experiments were performed in the Reynolds number range of $1x10^5$ to $5.5x10^5$ [17]. This Reynolds number is one order of magnitude less than of a large scale (5MW) wind turbine blade. Consequently these results cannot be used directly for a wind turbine study. Nevertheless, they may form a pertinent starting point for future research.

The NACA 23012 airfoil was used in the experiment. The studies were conducted to observe the effect of depth and the location of the step on the airfoil. The studies were performed for step locations of 40%, 50% and 60% chord. A step depth ranging from 0 – 50% of the airfoil thickness were studied to analyse the effect of step depth. The measurements were reported within the angle of attack range of 0^0 to 30^0 [17]. Based on the results (Figure 2-20), it is evident that there is an increase in lift coefficient and an extended smoother stall characteristic for this step modification. A 15° increase in stall angle was also observed (Figure 2-20).

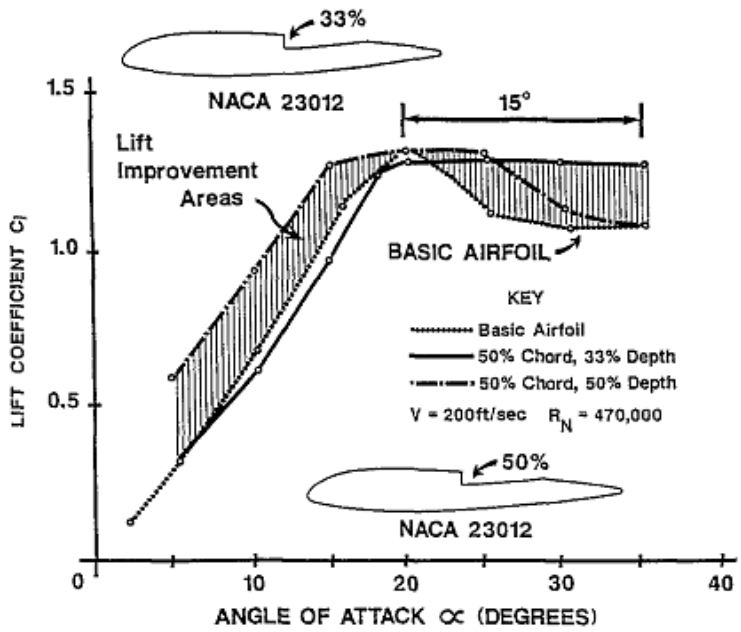

Figure 2-20 Lift results of Fertis's research [17]

The increment in the aerodynamic efficiency (L/D) is the most desirable attribute of this device (Figure 2-21). At the angle of attack of 20° there is a 50% increase in aerodynamic efficiency compared with the conventional airfoil. Two different configurations of the step extension were studied. One with the step extension from 50% x/c to 75% x/c and the other is from 50% x/c to the trailing edge (100%).

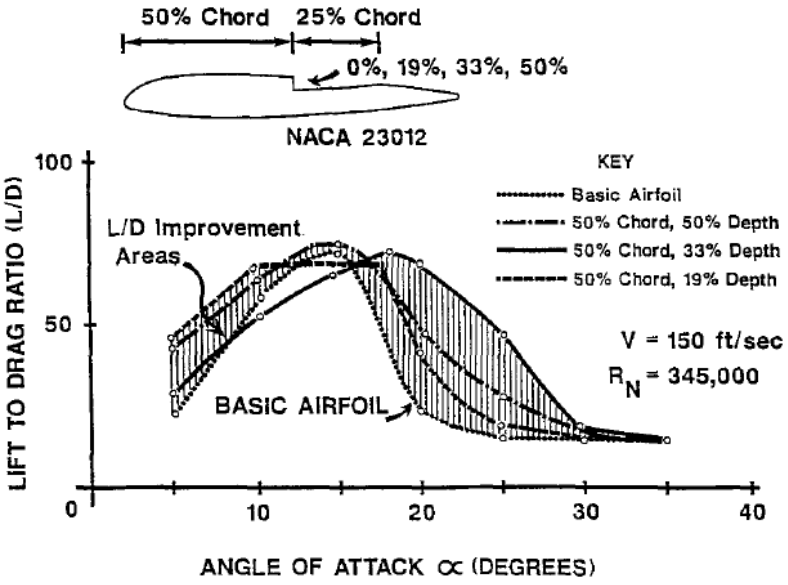

Figure 2-21 Lift/drag ratio results of Fertis's research [17]

Fertis also noticed a further improvement to the increase in lift when the step discontinuity was extended from 50% chord to the trailing edge (Figure 2-22). However, this effect is reduced for higher flow speeds (>60m/s) i.e. both, the step extension of 75% chord and the airfoil step extended to trailing edge achieves the similar lift increments at higher speeds (Figure 2-22). The increase in lift to drag ratio was also observed for both step extensions.

The results (Figure 2-23) show that only in the incidence range of 20-30^0 the step extended to the trailing edge increases the aerodynamic efficiency. Also at higher speeds, the airfoil with the step extended to the trailing edge seems to operate in a slightly opposite way i.e. lower L/D ratio than a step extension to 70% chord. The step extension to 75% chord airfoil increases the aerodynamic efficiency at all tested incidences. In summary, the step extension from 50% chord to trailing edge is best suited for achieving higher maximum lift and the step extension from 50% to 75% chord is desirable for increasing the aerodynamic efficiency.

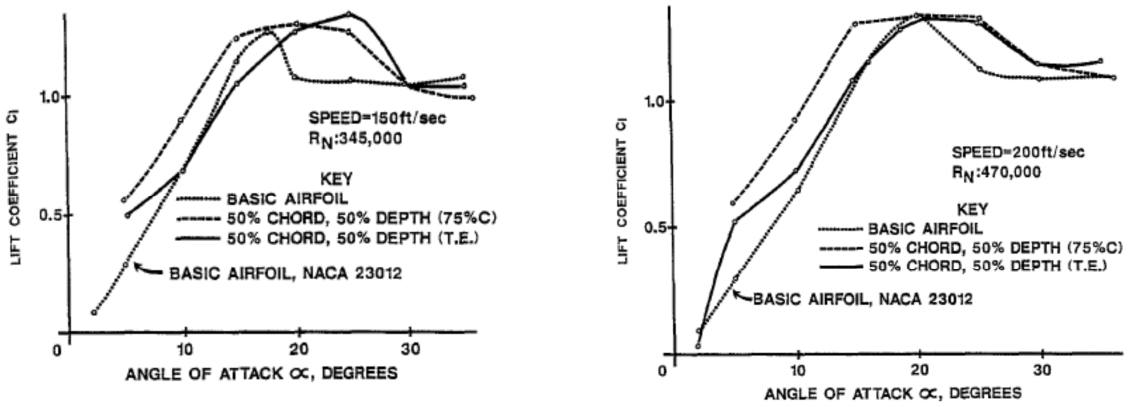

Figure 2-22 Lift coefficient for step extensions [17]

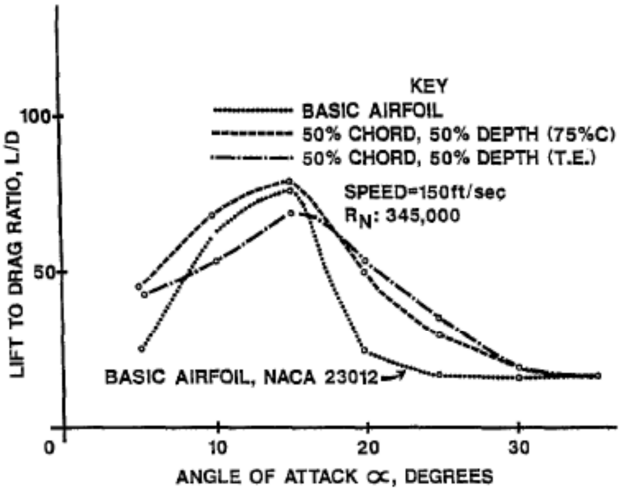

Figure 2-23 Lift/drag ratio for step extensions [17]

The study on the effect of step depth reveals that a smaller depth (19% and 33% airfoil thickness) is desirable to make beneficial changes to the pitching moment at all the angles of attack analysed (Figure 2-24). Therefore, the depth size could be used to affect the torsional load on the turbine blade. In conclusion, Fertis suggests that due to the increment in lift and L/D ratios, the cut-in speed of a horizontal axis turbine could be reduced by adapting this device. The advantage of using this device is greater power generation of the rotor or reduced rotor diameter for a same power requirement. It is noted that the step modification means a risk to the structural integrity of the blade and may also arise considerably difficulties in the manufacturing process of this modified blade, nevertheless a

purely aerodynamic assessment was conducted to evaluate the benefits that the step modification offers for a wind turbine.

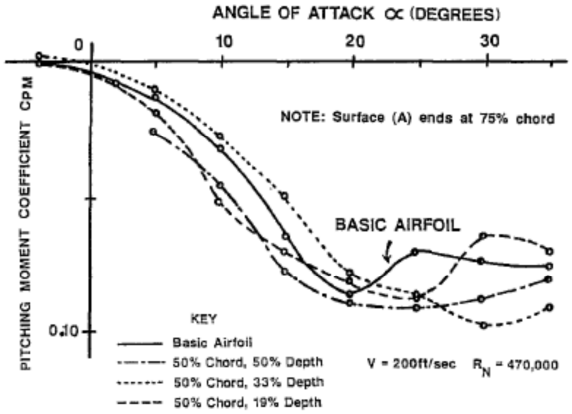

Figure 2-24 Changes in moment coefficient due to step depth [17]

In the same year of this Fertis' report [17], a closure document [18] was also published. This closure document has raised some reliability questions regarding Fertis's results. Luzauskas and Kirke [18] have analysed the application of this modified airfoil on a vertical axis turbine, and have found that the performance is degraded with this modification. However they also state that this is may be due to an interaction between the vertical rotor blades. This issue may not be the case for a horizontal axis wind turbine.

These authors [18] have also identified that the stall AoA reported by Fertis' is questionable. Luzauskas and Kirke [18] stated that "a 20^{o} stall angle is remarkable for any airfoil at the Reynolds number 345,000 and a 30^{o} stall angle is amazing, but a 10^{o} apparent discrepancy leads us to question the data presented in the paper [17]". Overall they have indicated some disagreement over the results from Fertis [17]. Due to these uncertainties regarding Fertis's result and the difference in Reynolds numbers between a large-scale horizontal turbine and those of his experiment, a more detailed study of this concept at the appropriate conditions is an important consideration for this current work.

In 2005, a European research project called VortexCell2050 was launched to investigate the possibility of controlling flow separation using trapped vortex cavities and active control [3]. Later in 2008, Fabrizio and Fraioli [3] published a document on the recent experimental studies on a vortex lift airfoil. This experiment was conducted for a model equipped with a spanwise oriented circular cavity. This study includes the effects of both with and without blowing and suction. The experimental setup is shown in Figure 2-25.

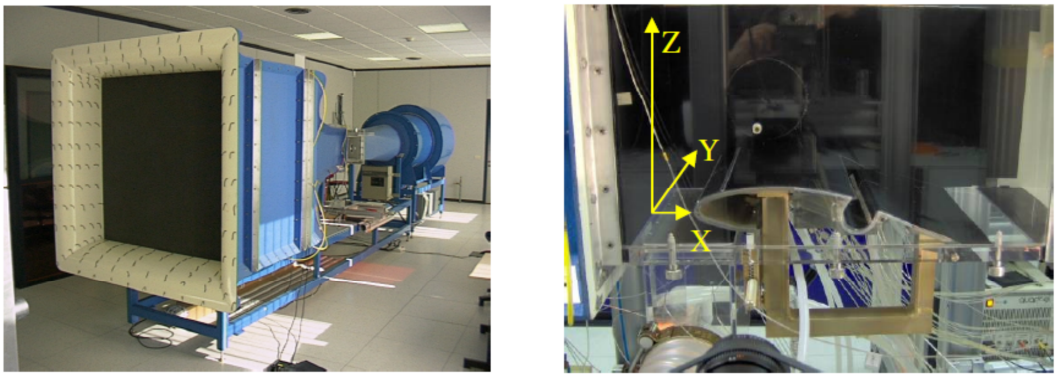

Figure 2-25 Experimental set up of the cavity type vortex capture device [3]

The vortex cavity was fitted with numerous suction pumps and they are referred to as CAV 1, 2, 3 [3]. The mass injection pump is referenced as CAV 4. This is presented in Figure 2-26. Test have been performed for various wind speeds (15 m/s to 30 m/s) and a range of mass flow suction (from 3 m^3/h to 25 m^3/h) and blowing (from 3 m^3/h to 50 m^3/h) as well as simultaneous suction and blowing was considered. The effect of incidence was also investigated and the experiment was conducted at a Reynolds number of 1 million [3].

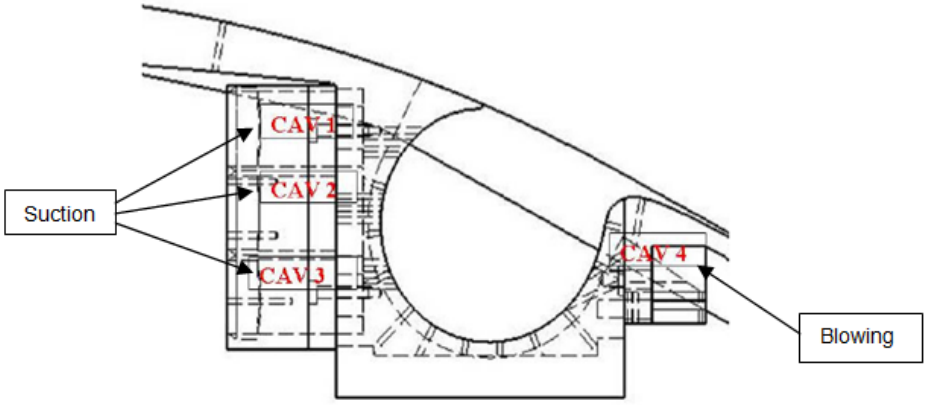

Figure 2-26 Locations of the pumps used in the cavity type vortex capture device [3]

The pressure measurements were recorded using pressure tappings connected to an electronic pressure scanner, which has an accuracy value of ±0.15% [3]. The flow field measurements are recorded using the means of particle image velocimetry (PIV) techniques. The pressure tapping location is shown in Figure 2-27.

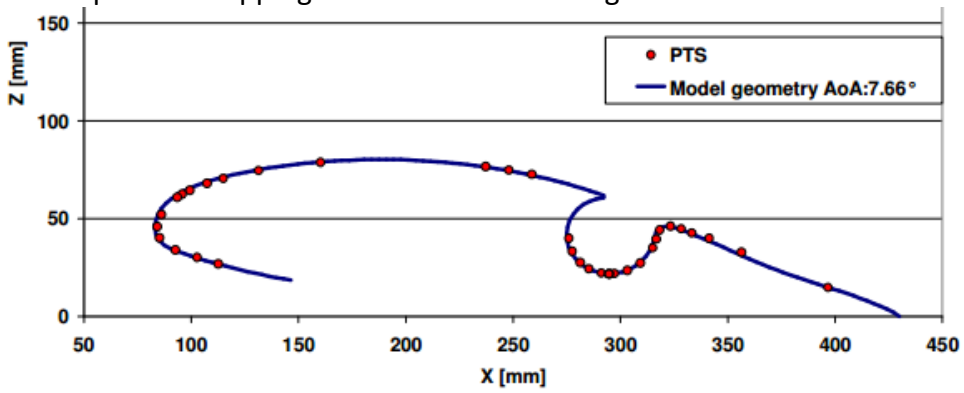

Figure 2-27 Pressure tapping locations used in the vortex trapping study [3]

The authors [3] stated that the investigation of the vortex trapping without mass transfer was initially conducted for a range of different free stream velocities and angles of attack (AoA). However based on an initial passive method study, it was reported that the flow separated from the cavity tip and did not reattach downstream of the cavity. This effect was found to be more pronounced as the wind speed or the angle of attack increased [3]. Hence, the authors decided to analyse the passive model without mass transfer only at low speeds (<15m/s) for numerous angle of incidences [3].

The results from the passive (no mass transfer) vortex trapping study are shown in Figure 2-28. Based on these results, it is apparent that the flow does not reattach to the airfoil surface and separates with an increase in angle of attack. The strength of the vortex is not sufficient to force reattachment [3]. At higher angles of attack the vortex core is sucked into the shear layer and the downstream separated flow is drawn into the cavity [3]. When the core of the vortex is drawn towards the shear layer it gets further drawn outside the cavity and induces additional vortex shedding. Hence for a higher angle of attack this passive vortex capturing method will have a larger separation and will cause an increase in drag compared to an unmodified airfoil. [3]

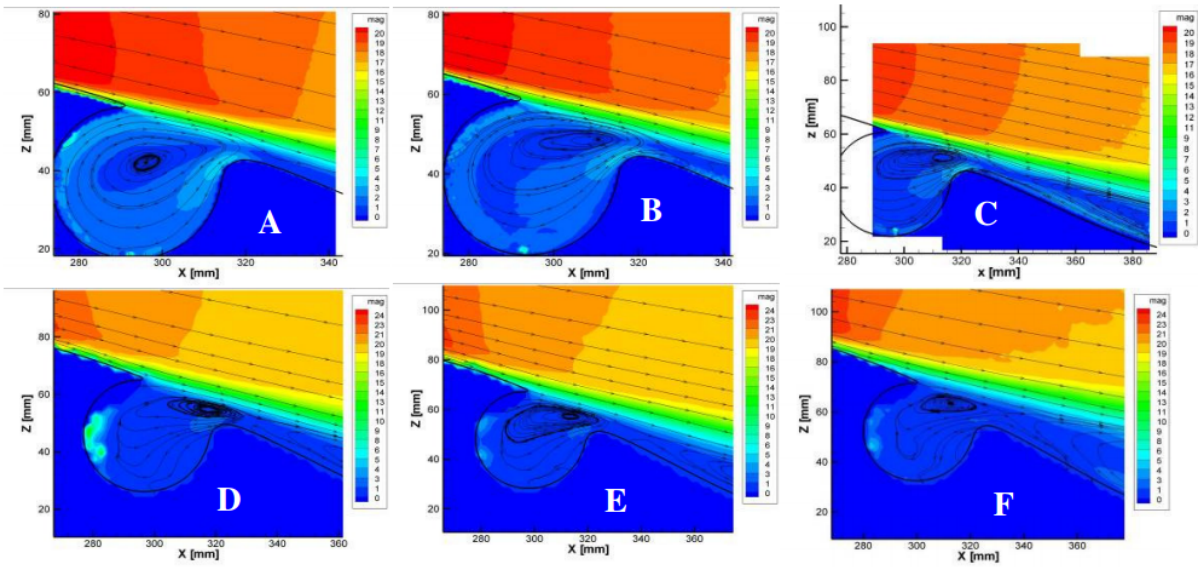

Figure 2-28 Measured flow velocity inside the cavity for six different angle of attack in ° (A=5.660, B=6.660, C=7.660, D=9.660, E=10.660, F= 12.660) freestream velocity: 15m/s, without suction or blowing mass flow [3]

The plateau pressure distribution from the cavity (Figure 2-29, left) suggest that the flow in the cavity is mainly separated [3]. Also the suction surface pressure values continue to remain constant downstream of the cavity which suggests a separated flow. The existence of a vortex is determined with strong gradients in tangential velocities inside the cavity. Only at lower incidence a small difference in tangential velocity is observed within the cavity (Figure 2-29, right). With increase in incidence, the gradient of tangential velocity reduces, again suggesting a separated flow regime within the cavity [3]. These results suggest that passive control of a cavity trapped vortex is not possible.

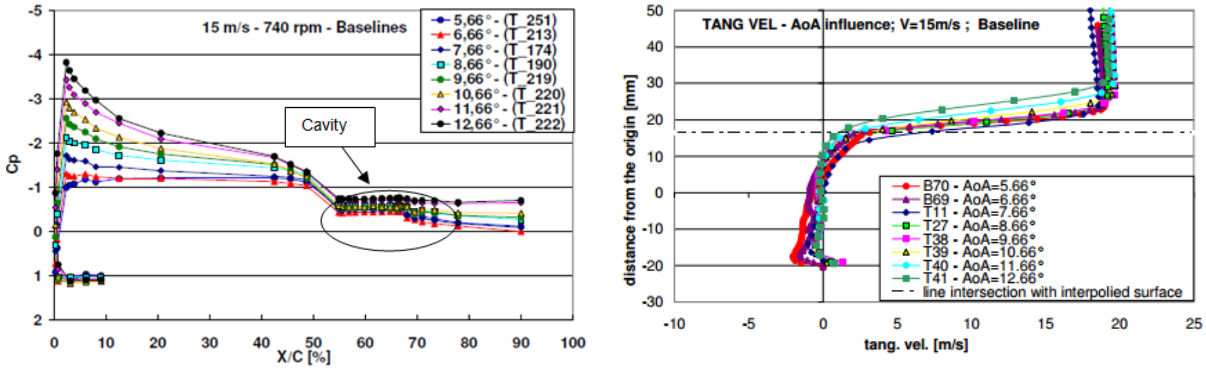

Figure 2-29 Coefficient of pressure (Cp) for different angle of attack (left) and tangential velocity of the vortex in the cavity (right), without suction or blowing mass flow [3]

Based on the results from the active vortex trapping study using both suction and blowing, the stability of the vortex is greatly improved by application of the mass transport. The blowing coefficient is defined as $C_\mu = \dot{m}V/qS$ where $\dot{m}$ is the mass flow suction/blowing in the cavity, V is the flow velocity through the cavity pore, S is the models planform area and $q = 0.5\rho V_\infty^2$ is the dynamic pressure. It is clear that the lowest mass flow (C_μ=0.000189) improves the vortex trapping, but it still inhibits the flow reattachment to the airfoil. The minimum suction massflow required for reattachment was found to be C_μ=0.000756. With an increase in massflow the reattachment is achieved with stronger vortices (Figure 2-30, right).

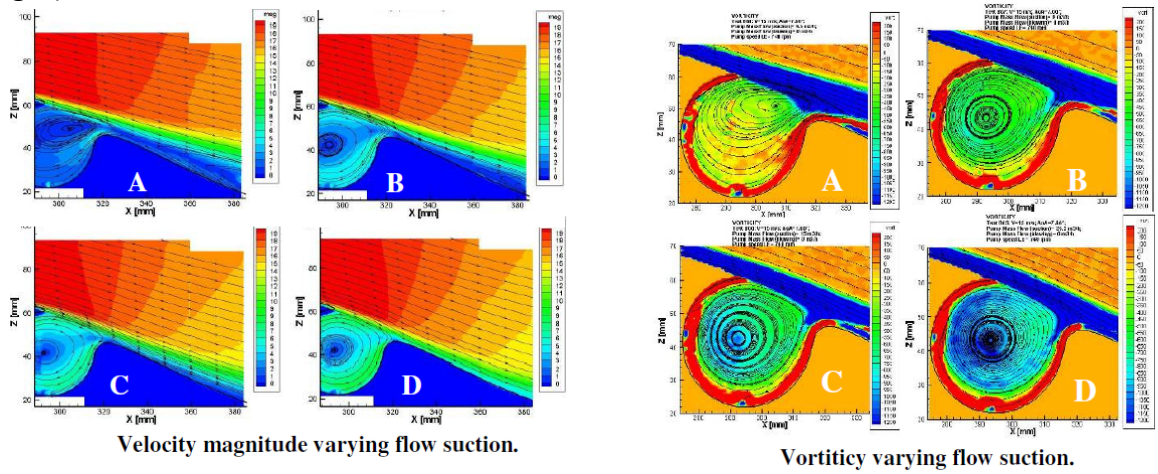

Figure 2-30 Results for active vortex trapping for various suction, velocity magnitude (left) and vorticity magnitude (right) in the cavity (A -$\dot{m}$=4.5 m3/h and Cμ=0.000189, B- $\dot{m}$=9 m3/h and Cμ=0.000756, C- $\dot{m}$=15 m3/h and Cμ=0.0021, D - $\dot{m}$=25.4 m3/h and Cμ=0.0059) [3]

The pressure distribution in the cavity was not found to be as flat as the pressure distribution obtained for a passive system. This suggests a better flow attachment with the active control. A sudden increase in pressure is observed downstream of the cavity (Figure 2-30, left). This is due to the deceleration of the flow after the vortex, and it is not due to the adverse pressure gradient associated with airfoil shape [3]. This deceleration of the velocity is also observed in the velocity magnitude plot (Figure 2-31, top).

The author states that this behaviour is due to the downstream flow deceleration due to the presence of the vortex [3]. This increase in pressure after the trapped vortex is also shown theoretically in the publication by Yeung (Figure 2-32) [19]. The tangential velocity

distribution for the active case shows much familiar velocity profile of the vortex. It also shows that with increase in suction the vortex strength becomes greater (Figure 2-31, bottom).

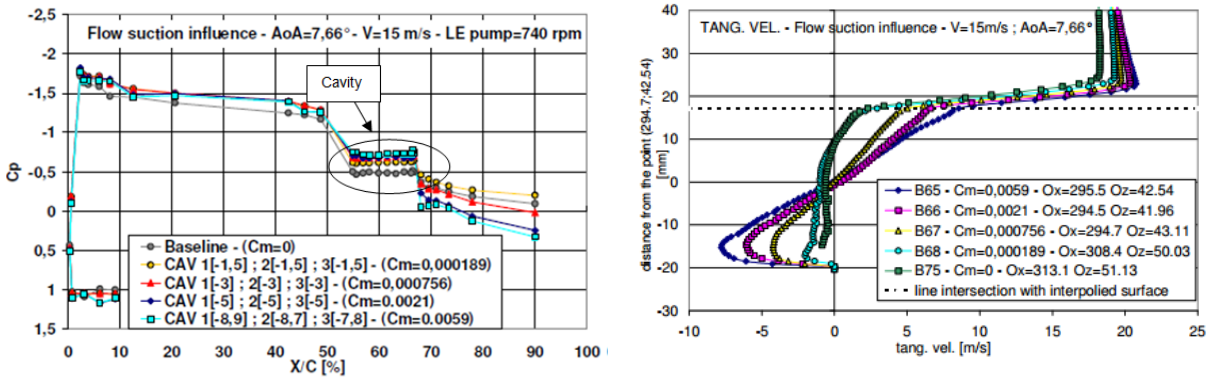

Figure 2-31 Cp distribution (left) and tangential velocity of the vortex (right) inside the cavity for varying mass flow suction

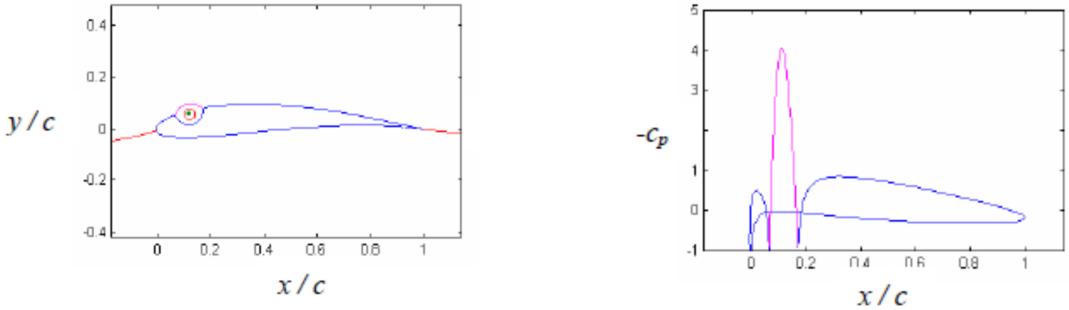

Figure 2-32 Theoretical vortex trapping results from Yeung (left: airfoil profile with trapped vortex, right: coefficient of pressure distribution across the airfoil) [19]

The author [3] states that, it is not possible to give a final conclusion regarding the application of the vortex trapping method from the comparison, However, it is also reported that all model configurations had the same maximum coefficient of pressure and that the flow separation of the vortex trapping model which occurs earlier (x/c=0.54) in comparison with the clean airfoil (x/c=0.70) is due to the existence of the cavity for passive vortex trapping. The active vortex trapping device was found to have fully attached flow with a noticeable decrease in pressure drag [3].

Based on the review of the literature for a trapped vortex airfoil design, the stability of the vortex is the key to achieving useful flow control. At the moment, previous work indicates that passive vortex capturing using a cavity is not feasible. However, passively trapping vortex using a step wise discontinuity may be possible based on Fertis' work. Fertis showed that a 14% increase in lift and 13% increase in lift to drag ratios are possible, but uncertainties have been identified with regards to these results. Therefore, a detailed study on this stepped airfoil was conducted to investigate the applicability of this technology for a large scale wind turbine. Also the understanding of the effects of rotation and spanwise pressure gradients on this airfoil is vital for a wind turbine implementation. At the moment, the literature on passive vortex capturing devices using a cavity fails to provide the increment in lift, but they have proved that it is possible to obtain a stable vortex using massflow transfer. The rotational effects of the turbine may provide a passive mass flow

through the trapped vortex core and allow for a beneficial vortex lift performance using cavity.

The high lift associated with this device is well suited for the root part of the wind turbine blade. The intermediate part of the blade can also benefit with its high lift to drag ratios. The understanding of this device suggests that this technology is not quite mature yet but there is a potential for a high lift capability. This device requires further study and may be viable for wind turbine flow control applications. An assessment of these aspects for a modern large scale turbine is presented in Section 5.3.

2.4 Passive Aspiration

In this section, the PFC method of using the natural pressure difference generated on the airfoil surfaces to increase the performance of the blade is presented. One of the ways of using the passive blowing is to implement it as a vortex generator jets. Vortex generator jets are generated by air exiting through the surface to create a dominant vortex in the streamwise direction [5]. This is similar to the vane vortex generator but excludes the drag associated with them. The schematic of the vortex generator jet is shown in Figure 2-33.

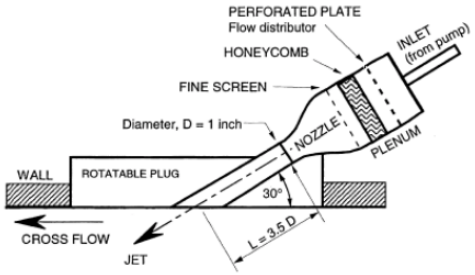

Figure 2-33 Vortex generating jet [20]

Tensi et al's [21] research on a NACA 0015 airfoil with VG jets at the Reynolds number of 0.93 million showed that with a small amount of steady blowing coefficient (C_μ=0.09) and for a jet located at the 30% of chord and jet skew angle of 30°, the maximum lift was increased by 5-10% and a 50% reduction in drag was achieved. The results for this study are shown in Figure 2-34. If these blowing coefficients are achieved via a passive system, these promising results make this technology a potentially attractive concept for wind turbine flow control implementation.

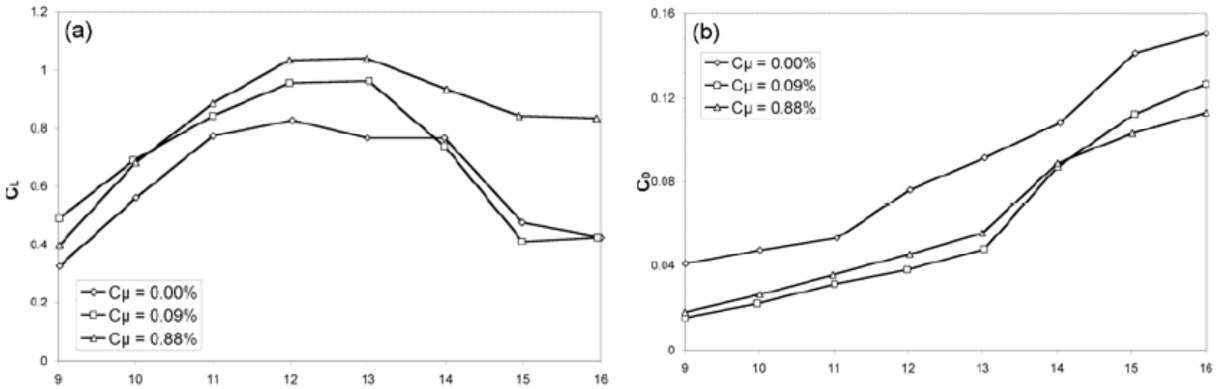

Figure 2-34 Effect of VG jets on lift (a) and drag (b) coefficient of the NACA 0015 airfoil using steady blowing, results from [21] **presented in** [5]

Very little has been researched on the passive aspiration technology and the only pertinent research that was found on this technology was by Prince et al [22]. Experimental and computational analysis of a passive aspiration system was conducted. The schematic of the design is shown in Figure 2-35. The study also involved the analysis of active blowing. The study was conducted at the Reynolds number of 1.1 million [22]. The cut-away three dimensional image (Figure 2-36, left) shows the 30 degree skewed air vortex generator ducts.

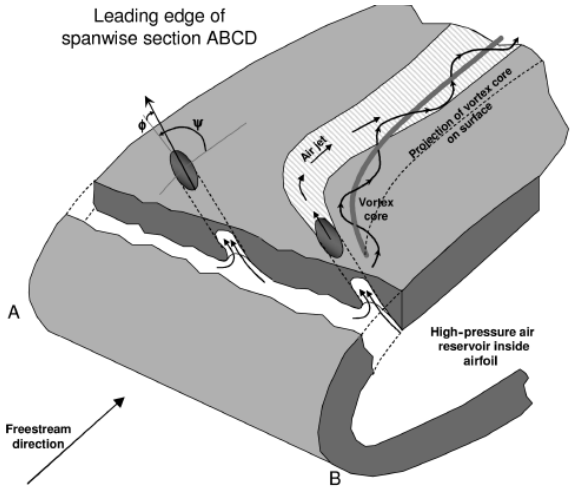

Figure 2-35 Passive vortex generator jet design [22]

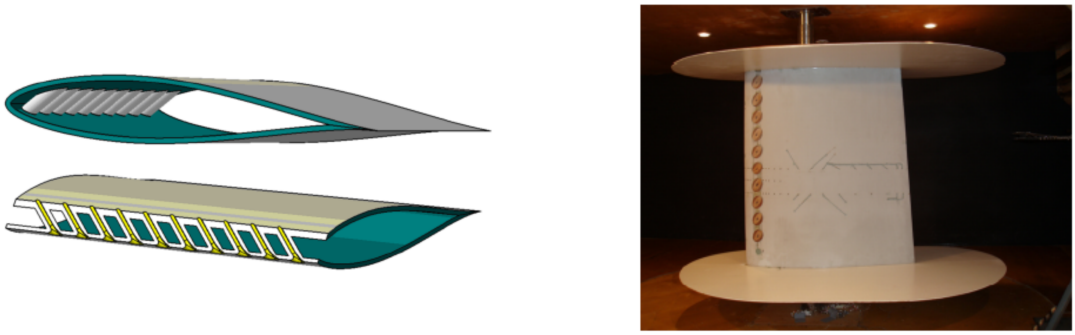

Figure 2-36 Passive vortex generator jet cut away (left), experimental model in wind tunnel (right) [22]

The research was conducted using 10 vortex generator jets located at 12% chord on the suction surface. A duct with 4.88mm in diameter (d/c: 0.01) was directly connected to the pressure surface at 4% of axial chord. NACA 23012C and NACA 63_2-217 airfoils were used for this investigation [22]. The experimental conditions were replicated in the numerical analysis (CFD). The computational grid is shown in Figure 2-37.

The measured lift coefficients (Figure 2-38, left) show a better performance for the wing with the passive air jet vortex generator (black line) than the reference unmodified wing (blue). End effects were ignored and only the two dimensional pressure distributions were obtained using pressure tapings on the wing surface. The maximum lift coefficient was increased by 13% with a significant increase in the stall angle of attack by up to 3^o.

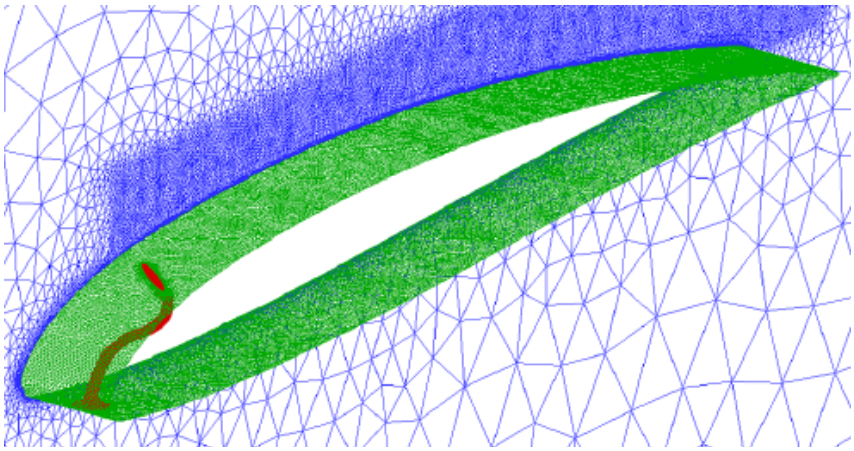

Figure 2-37 Computational grid for passive vortex generator jet [22]

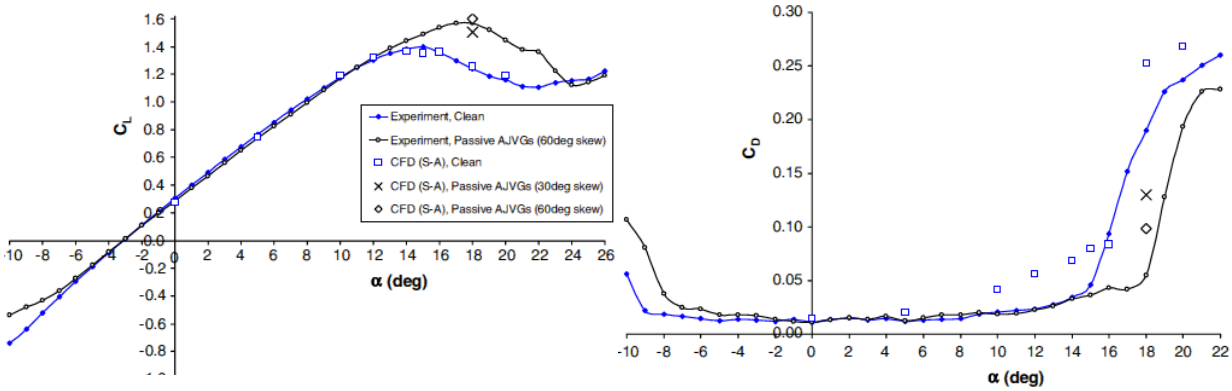

Figure 2-38 Effect of passive VG jets on lift (a) and drag (b) coefficient of the NACA 23012C airfoil [22]

A comparison of the active and passive air jet vortex generator (PAJVG) showed that the active PAJVGs were able to double the increase in performance (ΔC_N) compared to the passive VGs (Table 2.4-1). The author conclusively states that passive vortex generator jets are found to be effective at delaying separation and in return increasing lift and lift to drag ratio. This research has shown that the "passive air jet vortex generator making use of a purely natural process, can achieve worthwhile aerodynamic performance improvements for airfoil-sectioned elements, such as aircraft wings and helicopter or wind turbine rotor blades, without the need for any active energy input and without significant drag penalty" [22].

Air-jet blowing	Active	Passive	Passive
Skew angle, deg	60	30	60
Velocity ratio	2.50	1.25	1.27
C_μ	0.0100	0.0024	0.0025
ΔC_N, %	28	9	14
$\Delta\alpha_{stall}$, deg	5	3	3

Table 2.4-1 Comparison of active and passive vortex generator jet results [22]

Prince et al has clearly shown that PAJVGs are able to perform effectively and increases maximum lift coefficients by 13% with a significant increase in the stall angle of attack,

based on this conclusive evident from Prince et al's research it was decided that PAJVGs will be further analysed and evaluated for a wind turbine application.

2.5 Spanwise flow modifiers

In this section the devices that will help to modify the secondary flow will be discussed. Strong spanwise pressure gradients exist on a wind turbine blade were found for the NREL 5MW rotor based on CFD simulation conducted in this work (section 4.3). The control of this flow is crucial for improved performance. One of the main undesirable effects of this strong radial flow is the possibility of flow separations found at the blade hub (Figure 2-39).

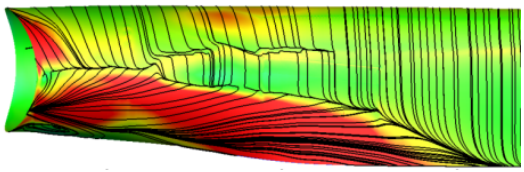

Figure 2-39 Flow separation found at the suction side of the NREL 5MW blade hub, Ws: 9m/s, displayed span range: r/R=0.05 – 0.30

2.5.1 Fences

Chow and van Dam investigated the effects of the ring fence on a wind turbine blade [4]. Their study involved the use of the ring fence in the inboard section (root, 3-40% of the span) of a blade to mitigate flow separation caused by the span wise velocity components. The NREL 5MW baseline blade was used for the analysis. The study was conducted using computational fluid dynamics (CFD).

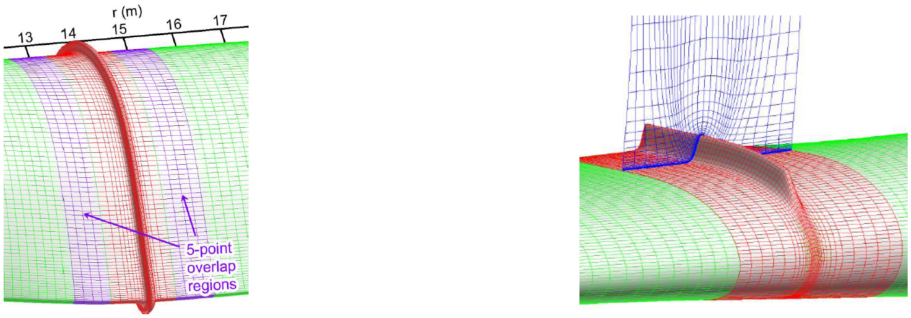

Figure 2-40 Ring fence implementation on the wind turbine blade [4]

Two configurations were studied. One with a full ring fence surrounding the airfoil (Figure 2-40, left) and the second configuration was tested using the fence only at the suction side (Figure 2-40, right). The second configuration was chosen due to the flow separation generally occurs at the suction side of the blade as seen for the clean blade (without modification) in Figure 2-41. Studies on the effects of the fence position in the spanwise direction and the height of the fences were also performed.

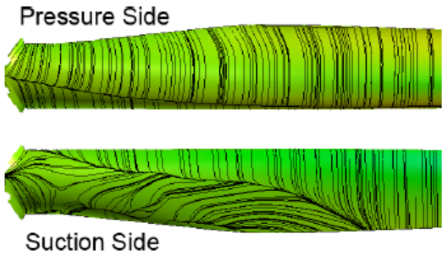

Figure 2-41 Hub separation computed for the NREL 5MW rotor, Ws: 11m/s [4]

The authors report that this device reduces the radial extent of the hub separation [4] and therefore it inhibits the flow separation propagation towards the outboard section of the blade (Figure 2-42). The author also states that the fence has a tendency to increase the blade loading in the inboard side of the fence and to reduce the loading in the outboard of the fence [4]. These are a result of reduced flow separation at the blade hub, as the drag forces are reduced.

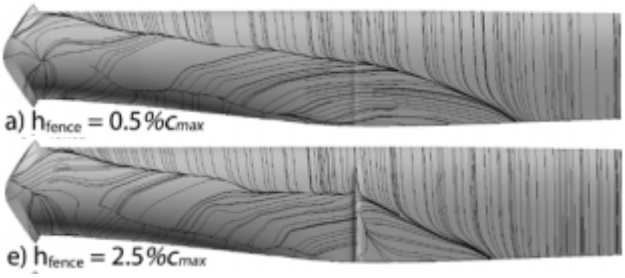

Figure 2-42 Fence's effect on hub seperation computed for the NREL 5MW rotor, Ws: 11m/s [4]**, fence span location: r/R = 22%, (a): fence height of 0.5% Cmax, (b): fence height of 2.5% Cmax**

It was found that the full fence is able to increase the power output of the blade by 0.9% (Figure 2-43) with the total thrust increase of 0.65% for 8m/s flow speed [4]. The thrust increase is not only gained at the location of the fence but experienced by the whole span of the blade. An increase in thrust can correspond to an increase in the structural blade loading and it is clearly desirable to keep this under control. The torque on the other hand is the power generating moment for the turbine. Based on Figure 2-43 it was found that at the location of the fence the thrust coefficient was increased by 10% without any benefit in torque. Overall the full fence showed an increase in thrust as well as torque, however the increase in thrust seems to outweigh the benefit in torque, therefore we can deduce that a full ring fence is not adequate at increasing the overall performance of the blade.

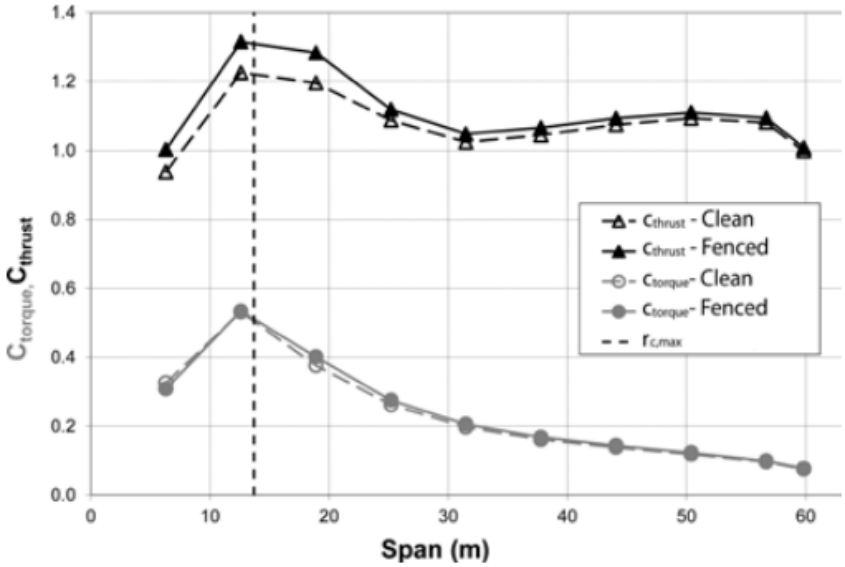

Figure 2-43 Calculated effect of a full ring fence on the spanwise distribution of torque (Ctorque) and thrust (Cthrust) coefficients. NREL 5MW turbine Ws: 8m/s, R= 63m [4]

Due to the separation that was found on the suction side, the subsequent fence studies were conducted using the suction side fence and the results for a change of fence height are presented in Figure 2-44. The fence was held at a constant location of about r/R =0.22 and the height was varied across the 0.5 – 15% c, where c is the maximum chord [4].

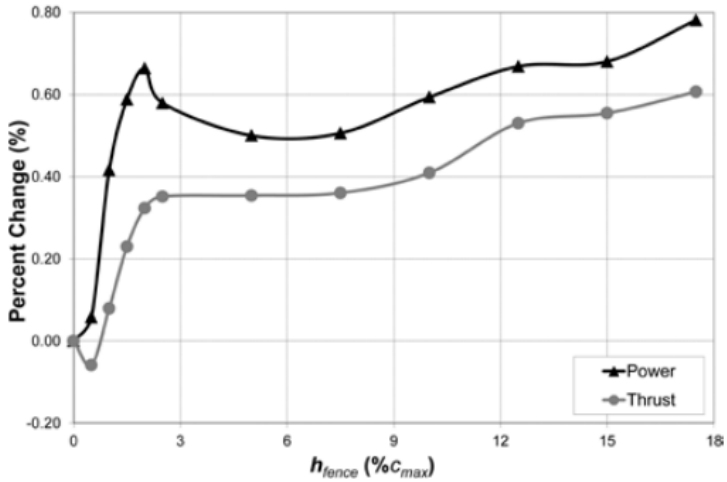

Figure 2-44 Calculated effect of the height of fence on the rotor power and thrust. NREL 5MW turbine Ws: 8m/s , h_{fence} = 10% $_{cmax}$ [4]

The author reports that when the fence is placed only on the suction side, the thrust is beneficially reduced by approximately by 30% relative to the full ring fence configuration. The increase in power was nearly the same as the full ring fence. Based on results (Figure 2-44), the achieved power to thrust ratio for a rotor with small height boundary layer fences ($[power/thrust]_{max}$=1.85, h_{fence}/c_{max}= 0.01 to 0.025) is greater than that for taller fences ($[power/thrust]_{max}$= 1.42, h_{fence}/c_{max} >0.05) [4]. The increase in thrust seems to drop off when the fence height is less than 2%c_{max} and the optimal height for the fence can be determined from Figure 2-44 to be 2%c_{max}. This is where a power improvement of 0.67% and thrust increase of 0.34% is attained.

The result of the fence location study is shown in Figure 2-45, this study was conducted with a fence h_{fence}/c_{max}= 0.10. This shows that the power to thrust ratio is constant regardless of the location of the fence. However the effectiveness of the fence reduces with an increased distance from the root, i.e. the furthest location about r/R= 0.25 has the lowest performance values.

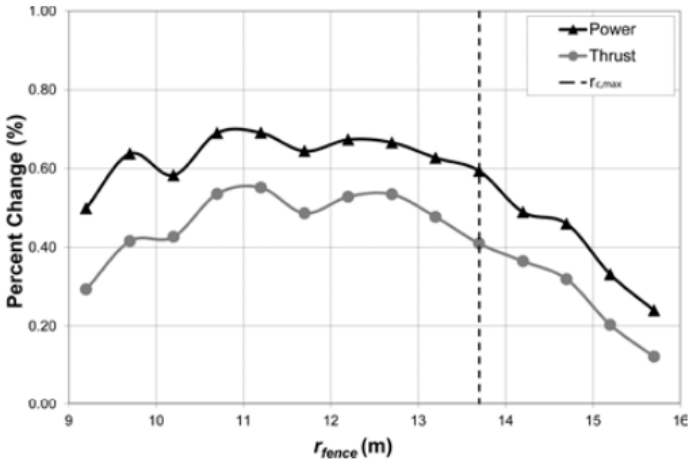

Figure 2-45 Calculated effect of the radial location of the fence on the rotor power and thrust. NREL 5MW turbine Ws: 11m/s [4]

The final investigation was to look at how the inboard rotor twist angles affects the flow separation and the results are presented in Figure 2-46. The flow separation is directly linked to the adverse pressure gradient generated by the local twist angles [4]. Increased twist means decreasing local flow angle of attack and vice versa for decreasing incidence [4]. With an increase in twist angle, the power generation drops significantly, this is generally due to the decrease in lift because of the reduced local angle of attack. However the power seems to be constant for a reduction in twist angle. This is where the inboard section of the blade experiences a stall because of the increased local incidence and therefore the drag increases [4]. Likewise thrust increases due to an increase in drag. The author suggests that this separation is impossible to avoid and additional devices should be used to mitigate this flow separation.

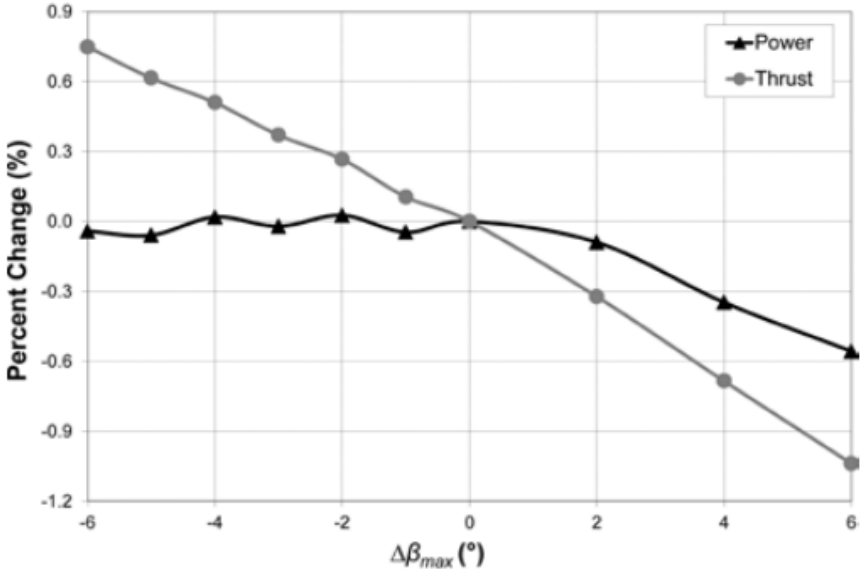

Figure 2-46 Calculated performance for change in inboard blade twist angle [4]

From these results we can clearly see that fences can significantly improve the performance of the blade. Fences are also currently in operation for large scale wind turbines (Figure 2-47). The spanwise separation control achieved by this device makes it well suited for the three dimensional flow control required at the wind turbine blade root. This is a relatively mature technology and it is difficult to see a clear research requirement for it in relation to a large-scale wind turbine.

Figure 2-47 Fence implemented turbine blade, fence location: r/R= 17% and 22% [23]

2.5.2 O-rings

This device is adapted by adding ring shape vanes along the chord of the airfoil. The studies were initially conducted using a cylinder (Figure 2-48) and therefore pertain to largely separated flows. The work by Lim and Lee [24], shows that for a cylinder at flow Reynolds number of $1.2x10^5$, it is possible to obtain a 9% drag reduction. Their studies were performed to minimise the spanwise flow and to suppress vortex shedding. The experimental setup is shown in the Figure 2-49. The authors also state that, for higher Reynolds numbers ($>1.2x10^5$), O-rings mitigate the vortex shedding [24]. This suppression of the vortex shedding is desirable for reducing the mean base drag. Studies were conducted on the effect of varying thickness of the O-rings and the spacing between them (PPD).

Figure 2-48 O rings on a cylinder (D= diameter of the cylinder) [24]

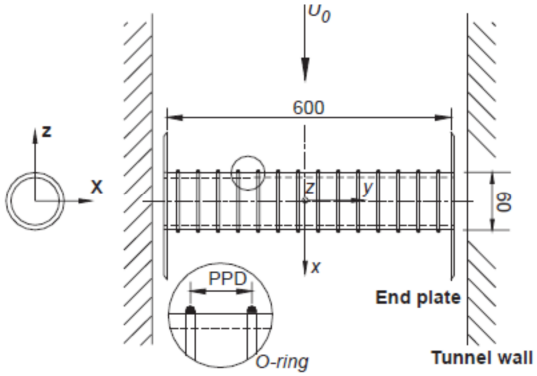

Figure 2-49 Experimental setup of Lim et all's study [24]

The drag coefficient measured for the d/D=0.0167 case is present in Figure 2-50. The variable 'd' corresponds to the diameter of the O-ring(thickness). Overall a linear drag reduction is observed from the drag variation plot, especially for high Reynolds number flows. The Reynolds numbers for these results is not appropriate to directly implement this design for a wind turbine, where a higher Reynolds number of 3 million and above operates. However based on these results at higher Reynolds number greater benefits are found, this technology can be used on the circular sections at a wind turbine blade root to reduce base drag.

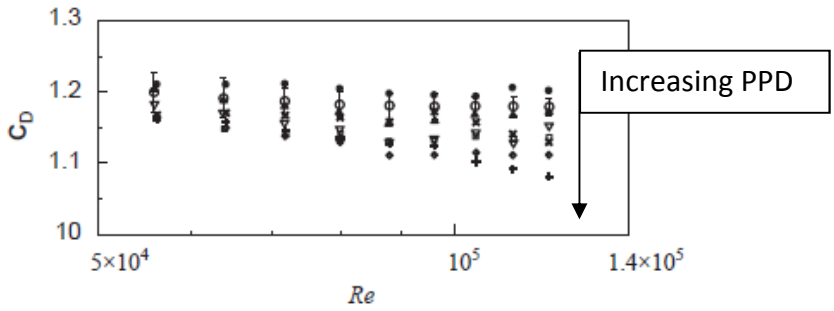

Figure 2-50 Drag coefficient of the test configuration d/D=0.0167, O, smooth cylinder; ∇, PPD=2D; Δ, PPD=1D; -, PPD=0:5D; ♦, PPD=0:25D; +; PPD=0:165D;×; PPD=0:083D; •, PPD = 0:0167D.

In conclusion it is clear that fences are more effective at reducing axial flow separation and O-rings mitigate vortex shedding. However, based on the studies by Chow and van Dam [4] a negative performance was noted when an O-ring type configuration was tested for a wind turbine blade, hence it is not suitable to further study the effect of O-rings on a wind turbine blades within the context of this project. Fences on the other hand may require further study for its benefits for a large scale wind turbine blade, but it is not studied in this thesis as it is known to be implemented in the wind turbine industry.

2.6 Leading edge tubercles

Leading edge control devices are not readily used for flow control applications. Altering the natural flow at the leading edge affects the entire flow over the wing and creates downstream turbulence and increases the frictional drag. Nevertheless, Wu [25] has stated that "leading edge modifications of streamlined bodies apparently offer cost-effective performance enhancements" [25].

The leading edge tubercles originated from the flippers of a sea whale seems potentially promising for flow control application on the wind turbine blade. The leading edge of the blade is made in a way to resemble the sinusoidal distribution seen on whale flippers (Figure 2-51). There are various experimental and numerical analysis for this flow control technique. However, the current literature does not clearly state the mechanism by which this device improves the aerodynamics, but some work has been done regarding hydrodynamics, as the sea water is the mother fluid which the flippers move forward.

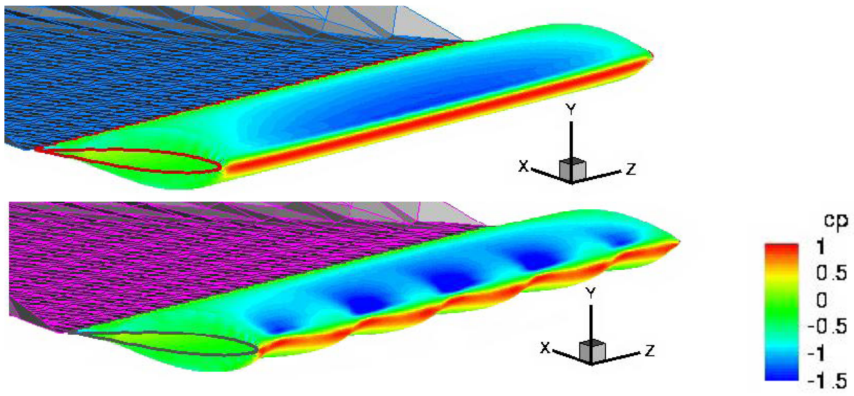

Figure 2-51 Calculated coefficient of pressure distribution for clean and modified (leading edge tubercles) NACA 634-021 wing, Re: not reported [25]

A numerical study on the leading edge tubercles was conducted by Fish et al [25]. For the reference airfoil NACA 634-021, the suction surface pressure distribution shows the conventional reduction in static pressure towards the wing tip and trailing edge (Figure 2-51) However, for the modified wing a broader low pressure distribution region is achieved between the tubercles. The stagnation pressures (indicated by red in Figure 2-51) show that the modified wing seems to have a noticeable reduction in the stagnation pressure on the side of the tubercles which is associated with the leading edge local sweep angle. The mechanism by which these modifications affect the airfoil performance is not understood and the authors do not propose a coherent argument. This aspect requires more careful consideration. Nevertheless, this control technique generates a 4.8% lift increase with 10.9% induced drag reduction [25]. Overall, a 17% increase in lift to drag ratio is reported [25].

The author [25] reports that the increment in lift is associated with the change to the stagnation line along the leading edge. However this aspect is not developed in detail. The author has stated that very little variation was found in the shear stress distributions (frictional drag) between the modified and unmodified blade. However, the boundary layer thickness is considerably reduced compared to an unmodified wing. The author also reports that a coefficient of pressure value of -0.5 is achieved at the trailing edge of the modified

wing. This is the primary reason for the favourable pressure gradient, unlike the unmodified blade with a coefficient of pressure value of +0.5 (adverse pressure gradient) [25]. The flow Reynolds number is not reported in this work and it is therefore not possible to comment on the appropriateness of this research to a wind turbine.

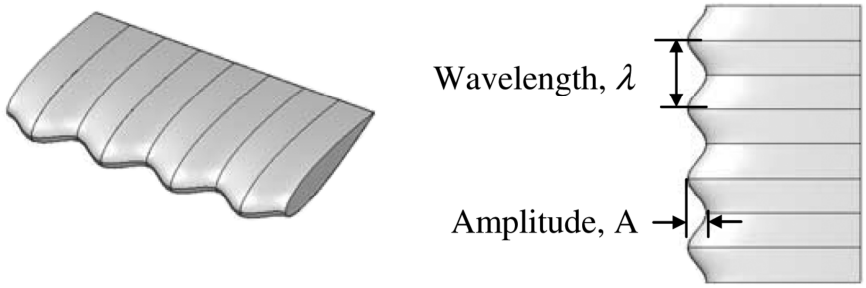

Figure 2-52 Schematic of the experimental model (leading edge tubercles) wing [26]

An experimental study was conducted for the sinusoidal leading edge (tubercles) airfoils by Hansen et al [26]. The authors studied the effect of sinusoidal amplitude and wavelength on the aerodynamic performance (Figure 2-52). They used two different airfoil sections to observe the effect of different profiles. These airfoil sections are a NACA 65-021 and a NACA 0021.

It was reported that delayed stall and higher maximum lift coefficients are achievable with the use of this passive wing modification [26]. Experiments were conducted at the Reynolds number of 1.2×10^5. A boundary layer trip was used during these experiments to generate a fully turbulent flow regime over the airfoil. The results are shown in Figure 2-53.

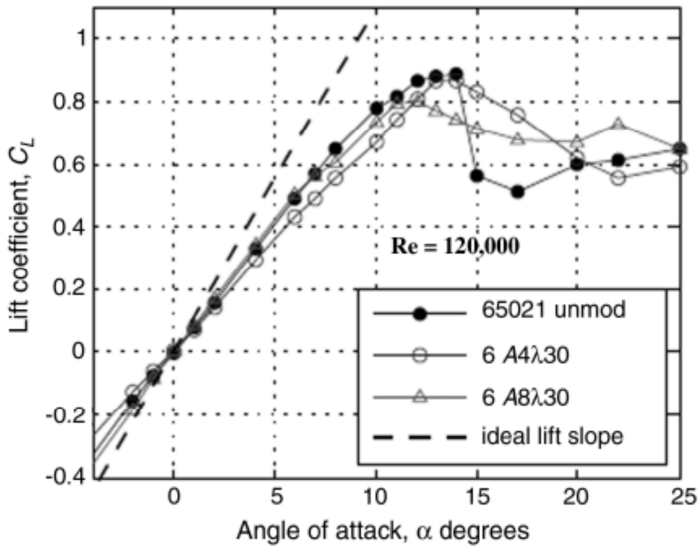

Figure 2-53 Measured lift coefficients of clean and modified NACA 65-021 airfoil for varying amplitude, A4= amplitude of 6%chord, A8= amplitude of 11%chord, λ30 =wavelength of 43% chord [26]

The result for NACA 65-021 (Figure 2-53) suggests that the modified airfoil provides significant improvements to the performance, such as an increase in the post stall lift, up to 27% (AoA =15^o). In addition, a much smoother stall regime is achieved for both airfoils with leading edge tubercles (Figure 2-53 and Figure 2-54).

The gains in lift forces were found to be better for a NACA 0021 (dCl = 35%, AoA= 15^{o}) than a NACA 65-021 at the post-stall conditions (Figure 2-54). The effect of varying the amplitude for the NACA 0021 suggests that the increase in sinusoidal amplitude decreases the maximum lift coefficient. However, a much smoother stall is achieved with larger amplitude. Drag data (Figure 2-55) shows that, approximately the same amount of drag is achieved between the modified and unmodified wing (Figure 2-55) within 0-5^{o} AoA. This result is not affected by the airfoil profiles. The drag forces were found to be reduced by 30% due to the corrugated leading edge within 6-7^{o} AoA, however it was found to increase the drag forces by up to 45% within 10-15o AoA, which is contrary to the report [25]. The greater the A the greater the drag force induced (Figure 2-55).

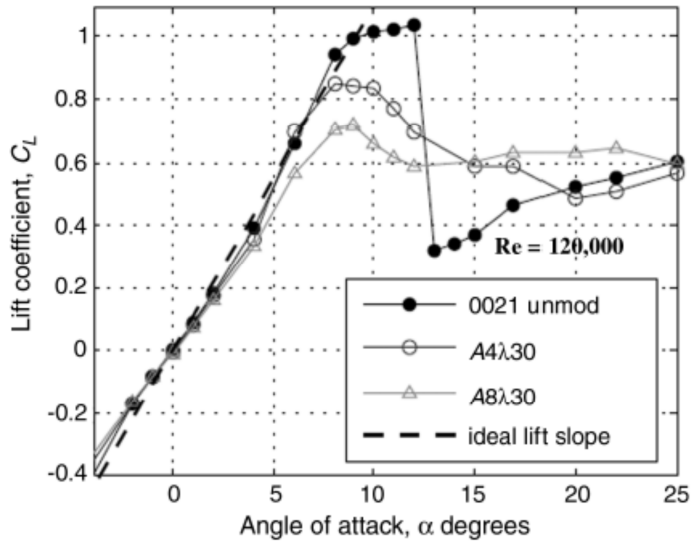

Figure 2-54 Lift coefficient results of clean and modified NACA 0021 airfoil for varying amplitude, A4= amplitude of 6%chord, A8= amplitude of 11%chord, λ30 =wavelength of 43%chord [26]

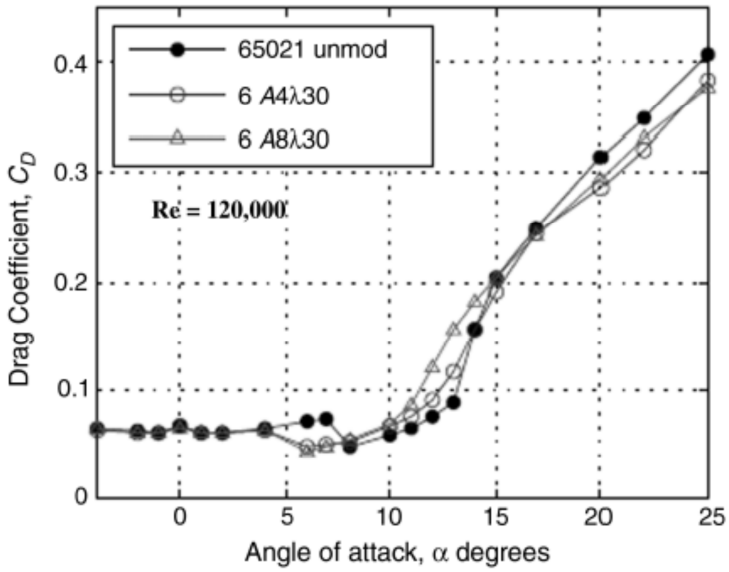

Figure 2-55 Drag coefficient results of clean and modified NACA 65-021 airfoil for varying amplitude, A4= amplitude of 6%chord, A8= amplitude of 11%chord, λ30 =wavelength of 43%chord [26]

The investigation of varying wavelength was only carried out for a NACA 0021 airfoil [26], which also showed poor performance in lift within the pre-stall AoA (Figure 2-56). It is similar to the results from NACA 65-021 airfoil, the benefit of the corrugated leading edge on the NACA 0021 airfoil was seen in the post-stall lift. However, it was reported that for a given amplitude, there is a limitation on the wavelength where this increased performance is achieved. Hence, an optimised wavelength to amplitude was found to be 3% chord amplitude and 11% chord wavelength [26]. This is the smallest amplitude and wavelengths used in the investigation. In summary, a small amplitude and wavelength have to be adapted to obtain the best performance, which is surprising as it is closer to the unmodified airfoil.

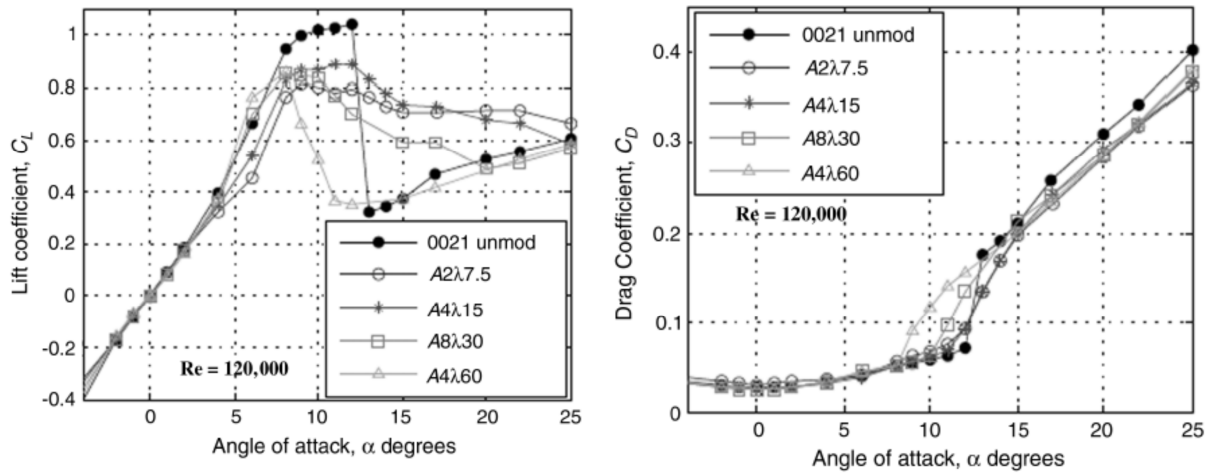

Figure 2-56 Lift and drag coefficient results of clean and modified NACA 0021 airfoil for varying wavelength, A2= amplitude of 3%chord, A4= amplitude of 6%chord, A8= amplitude of 11%chord, λ7.5 =wavelength of 11%chord, λ15 =wavelength of 21%, λ30 =wavelength of 43%chord, λ60 =wavelength of 86%chord [26]

This experimental study on the corrugated leading edge modification shows promising results for flow control application in the post stall AoA. This device will be well suited for increased lift and smoother stall condition in the post stall AoA. However the improvement in lift to drag ratios seen in the numerical study [25] seems attractive for this device to be adapted for the intermediate and outboard section of the blade. In conclusion this device could be further investigated for wind turbine airfoils with these optimised amplitude to wavelength parameters and thereby evaluate the benefits and applicability to the wind turbine blade. However, the major caveat with these previous investigations is that the work was performed at relatively low Reynolds numbers and that there is very little understanding of the flow control mechanism. This is because these pattern comes from animal evolution, applied to low Re and inside water. The benefits only lie in the post stall AoA, which is not applicable for a wind turbine. Nevertheless, given the potential benefits and the simplicity of the design, it is worth considering further study of this technology and is assessed in more detail in section 5.5.

2.7 Direct transition to turbulence (roughness)

This method of control is achieved by tripping the laminar boundary layer to a turbulent boundary layer. If the Reynolds numbers are high enough, it is possible to trigger boundary

layer instabilities which in return give a strong near-wall momentum to the flow [27]. Strong near wall momentum is desirable due to its resistance to adverse pressure gradient and the onset of flow separation. This aspect limits the viability of this control technique to regimes where there is a subcritical Reynolds number ($Re \leq 2x10^5$) [28].

Surface roughness can be taken as an example of this control. Drag reduction by surface roughness can be possible within a limited range of Reynolds numbers. The results from the studies performed by Achenbach in 1971 [28] show that the drag coefficient sharply decreases and then increases rapidly with increasing Reynolds number (Figure 2-57). The critical Reynolds number ($2x10^5 < Re \leq 3.7\ x10^5$) decreases when increasing roughness.

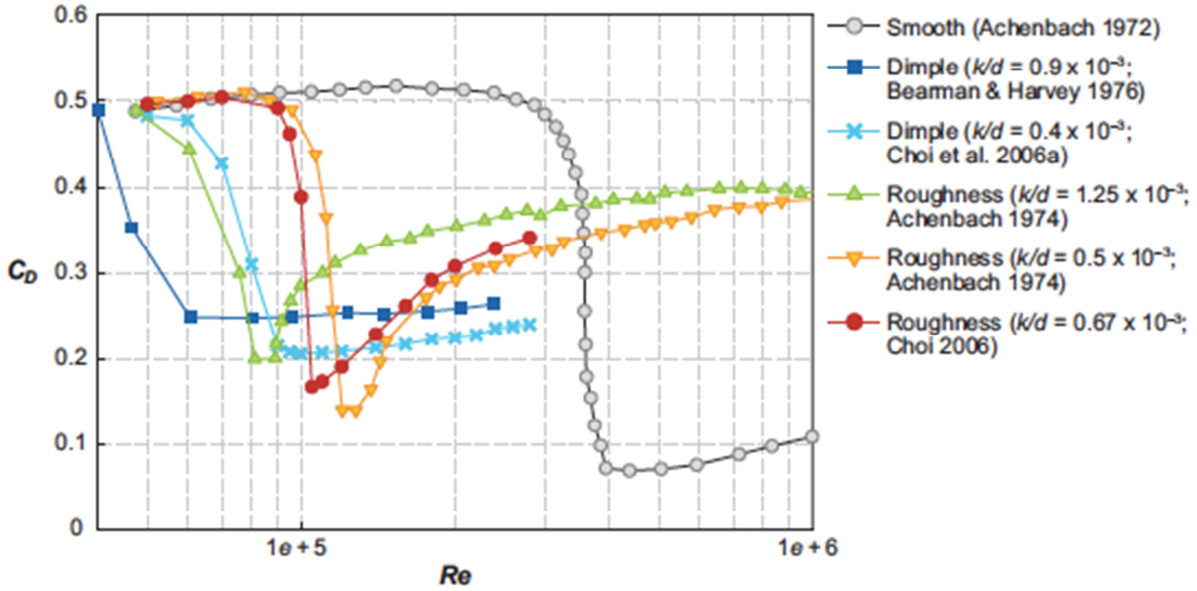

Figure 2-57 Measured variation of drag coefficient for different surface roughness, from [28] **presented in** [27]

In summary, the large Reynolds number (>3 million) flows present on a multi-megawatt wind turbine blade is inappropriate for the use of direct transition to turbulence, due to the large increase in drag forces. This limits the viability of roughness on a large scale turbine blade and it is not considered further in this research.

2.7.1 Riblets

Riblets are groves on the surface which are aligned in the mean streamwise flow direction. They are also considered as a modification to the surface texture of the wall [29]. The ribbed surface reduces the turbulent skin friction [30] which provides a reduction in overall drag. Based on the experimental study undertaken by Bechert et al. [30], it was found that a reduction in drag of 5% is gained by implementing the riblets. Based on another study by Pollard [29], up to 10% reduction in frictional drag was found to be possible by implementing riblets. An experimental study on a C-block type (Figure 2-58) riblet is presented by Dean [31] and the results of the study shown in Figure 2-59.

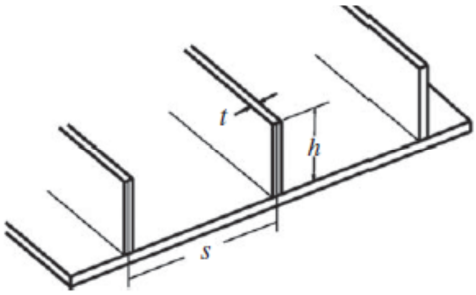

Figure 2-58 Schematic of a C-block type riblet [31]

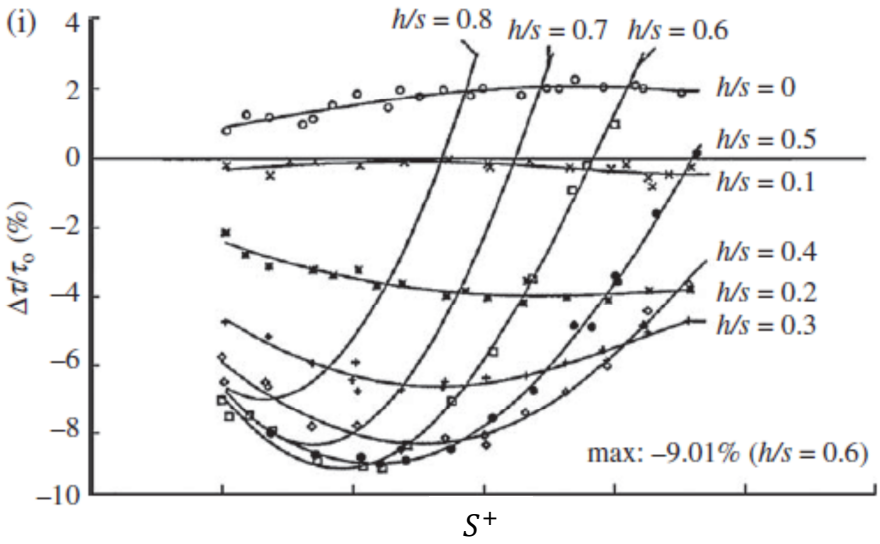

Figure 2-59 Result for a C-block type riblet [31] **(h and s are the geometric dimensions of the riblet (Figure 2-58), $\Delta\tau/\tau_0$: frictional drag, S^+ : Reynolds number in terms of riblets width (s).**

Usually the increased wetted area associated with riblets should result in a drag increase. During the operation of riblets, vortices are formed above the riblet (Figure 2-60) surface and they only expose the tip of the riblets to the turbulent shear flow [29]. Hence the reduction in frictional drag is achieved [31]. The shark adopts this flow control techniques on its surface to gain a reduction in frictional drag (Figure 2-61). The riblets are most effective at reducing turbulent skin friction associated with large wetted area.

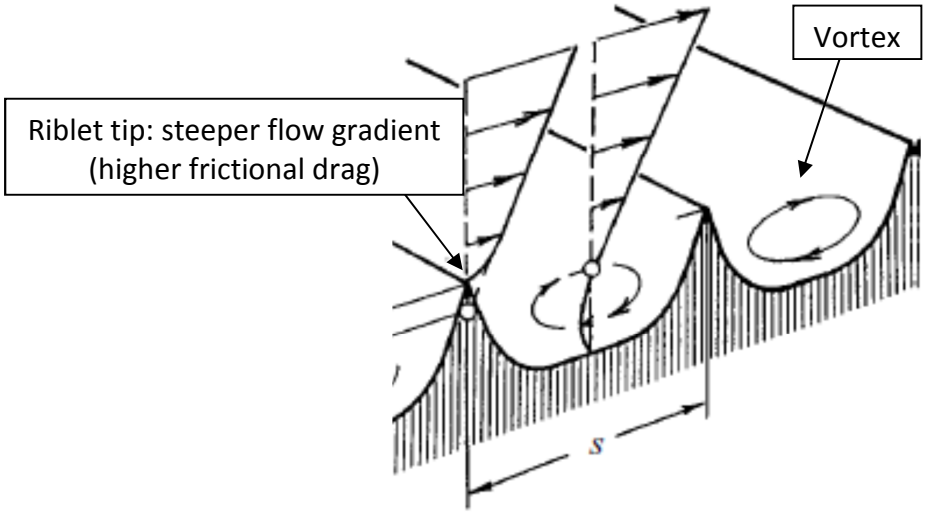

Figure 2-60 Flow schematic of a riblet [30]

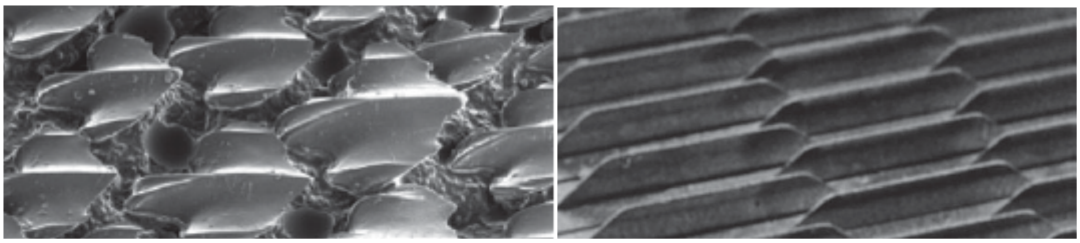

Figure 2-61 Shark surface denticles or spicules (left) and manmade riblets (right) [31]

Dean reports that "where pressure drag or flow separation is the dominant form of drag, application of riblets would have minimal effect" [31]. In the fully attached flow regime on a wind turbine blade, riblets will help to reduce turbulent drag. However this method of control is ineffective due to its lack of robustness and sensitivity to dirt. Overall riblets possess an attractive feature in reducing turbulent drag but with some performance uncertainties at off design conditions and maintenance issues. It is expected that the dominant form of drag on a wind turbine blade will be due to flow separation especially at the blade where the riblets will offer negligible benefit compared to the difficulty that presents in the physical implementation of this device. Therefore this concept is not chosen for investigation in this thesis.

2.8 Trailing edge effectors

Trailing edge devices helps to modify the flow beneficially at the trailing edge to increase performance. One of these improved performances is greater lift due to the increased airfoil camber. Gurney flaps are one of the well-known trailing edge effectors, and already in operation on large scale wind turbines. Cavanaugh [32] showed significant lift increase up to 46% is possible with Gurney flaps. These tests were performed at the Reynolds number range of 0.5-1.95 million. This Reynolds number is closer to that of a large scale wind turbine blade. The change in lift coefficient as a function of incidence for a Gurney flap is shown in Figure 2-62. In the following sections some of the devices derived from the Gurney flaps will be presented.

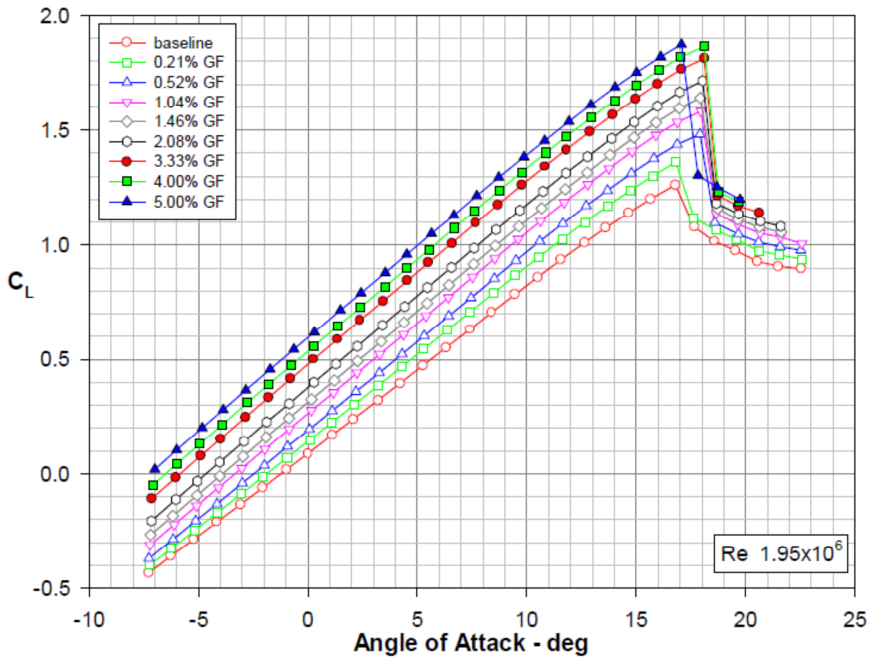

Figure 2-62 Gurney flap implemented airfoil lift curve slopes (GF: Gurney flap height in percentage of chord) [32]

2.8.1 T-Strip

Cavanaugh [32] also describes another trailing edge effector. A T-Strip configuration (Figure 2-63) was also tested at the same Reynolds number as the tests performed for Gurney flaps. These results suggest that T-Strip configuration of the Gurney flap is better at increasing the lift curve slope (Figure 2-64). Johansen et al [5] have stated that an increase in lift curve slope increases the structural blade loading, which is usually avoided. However lower maximum lift coefficient is achieved with a T-Strip than with a Gurney flap. The change in maximum lift coefficient is shown in Figure 2-65.

T-Strips produced no change in sectional pitching moment for varying flap height, unlike the Gurney flap (Figure 2-66). This enables the T-Strips to achieve a lift increment of 28% with reduced torsional blade loading compared to a Gurney flap. However it was found that T-Strip generates larger drag forces than Gurney flaps (Figure 2-67). Overall this adaptation of a Gurney flap is unlikely to give the flow control that is required for a large-scale wind turbine and hence is not considered for further study.

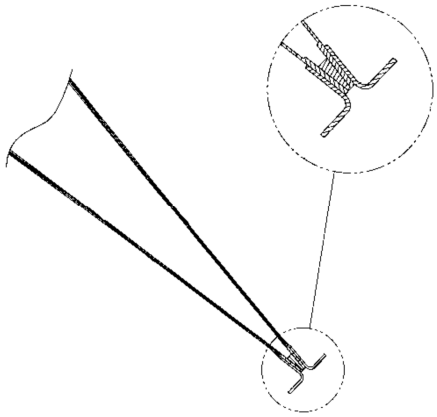

Figure 2-63 T-strip adapted trailing edge [32]

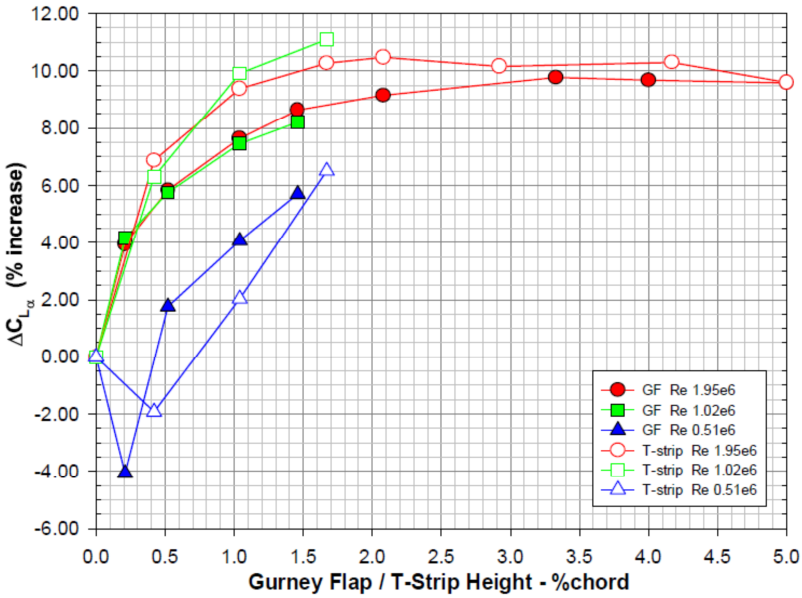

Figure 2-64 Gurney flap/T-strip implemented airfoil lift curve slopes [32]

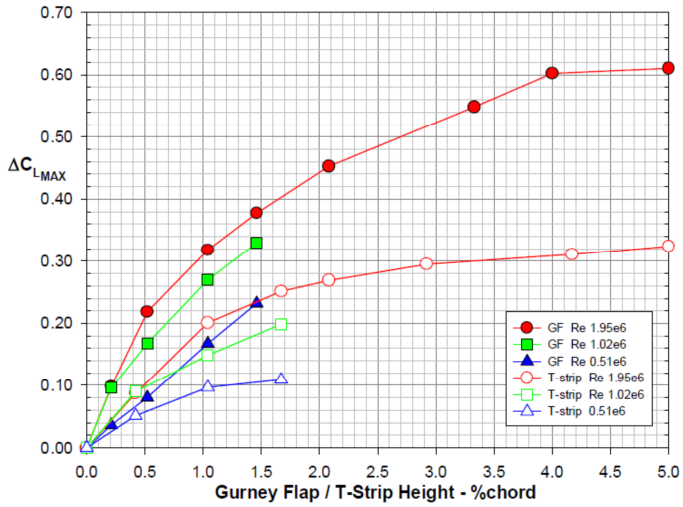

Figure 2-65 Gurney flap/T-strip implemented airfoil maximum lift increments as a function of flap height [32]

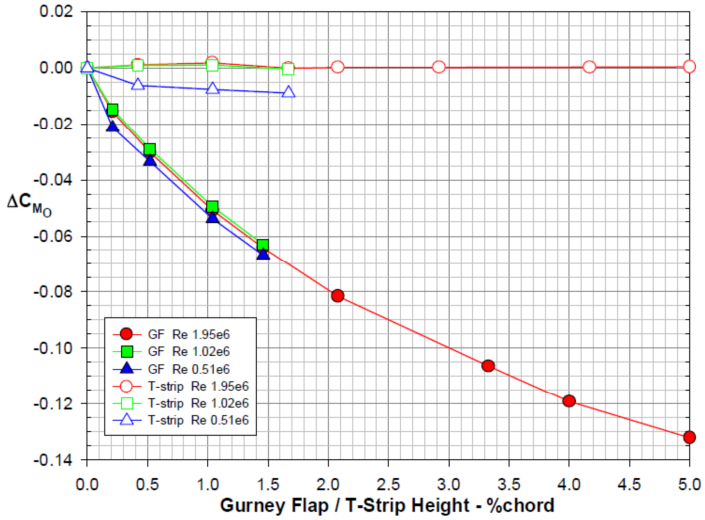

Figure 2-66 Gurney flap/T-strip implemented airfoil's change in pitching moment as a function of flap height [32]

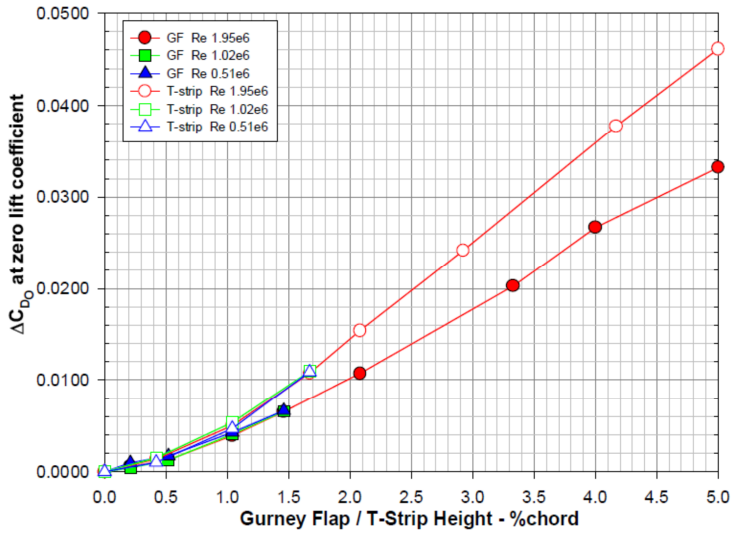

Figure 2-67 Gurney flap/T-strip implemented airfoil's change in drag as a function of flap height [32]

2.9 Flat trailing edge airfoils

There are two types of methods which exist when adapting a flat trailing edge for flow control purposes. Simple truncation of the traditional airfoil is known as a cut-back airfoil (Figure 2-68). Flat-back airfoils have a blunt trailing edge of equal thickness on either side of the camber line (Figure 2-68). Initially from Horner and Borst studies [33], it was believed that a cut-back airfoil causes lift argumentation for all airfoils. However, Standish and van Dam [34] have shown that this is not true for non-symmetrical airfoil and states that cambered cutback airfoils tend to reduce lift for a given range of angle of attack when compared with its baseline airfoil. This disadvantage of the cutback airfoil can be exploited for the use of load alleviation of the rotor blade as a lift dumping device.

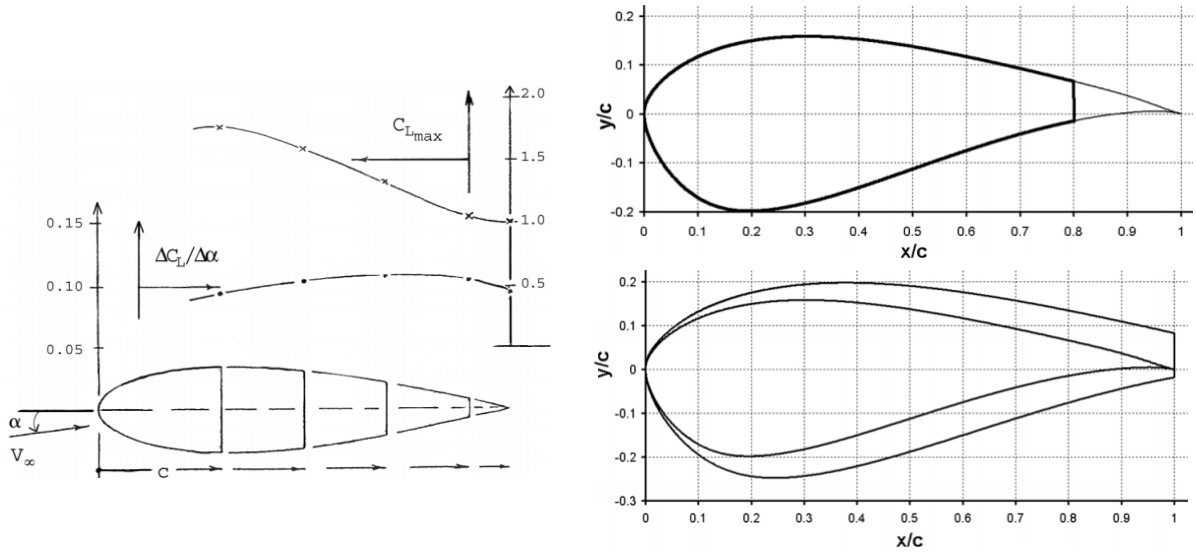

Figure 2-68 Cut back airfoil performance, Left: top: truncated airfoil at 80% chord, bottom: comparison of cutback and unmodified airfoil. [34]

The overall increase in lift is caused by the aft camber (large curvature at the trailing edge). This aft camber lift causes large pitching moments (Figure 2-69) which is undesirable. The root sections can accommodate large torsional loads because of its large cross sectional area. Hence, generally only the root section of the wind turbine blade could be applicable for this flow control method. The base pressure drag and the vortex shedding are associated with blunt trailing edge airfoils. Unsteady behaviour of the flow becomes a problem for this control technique due to vortex shedding and load fluctuation [7]. Flat trailing edge airfoils are known to be in operation on wind turbines at the blade root, hence further study on these airfoil sections are not required and are therefore unlikely to be considered for more detailed studies in themselves as part of this research.

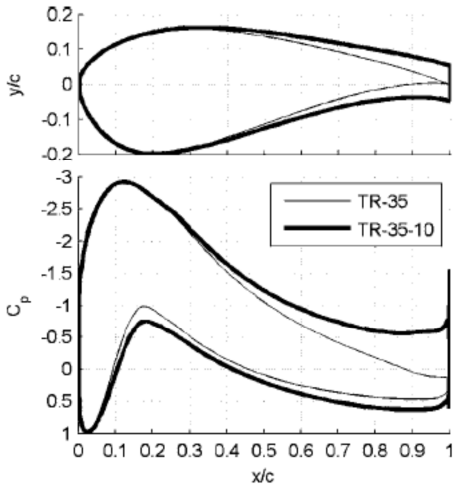

Figure 2-69 Cp distribution of a flat back airfoil [35]

2.9.1 Base drag reduction

Following the discussion on flat-back and cut-back airfoils, this section presents the ways of reducing the base drag associated with blunt trailing edge airfoils. It is well known that vortex shedding increases the mean drag and the lift fluctuations when compared to the designs which inhibit vortex shedding. For example, a trailing edge tab that is optimised for low drag is known to provide a 33% increase in base pressure and to inhibit vortex shedding [36]. Lift fluctuations will excite the aeroelastic vibrations experienced by the wind turbine blades and this may poses a danger to the structural integrity of the blade. Thus, it is generally desirable to have a flow without vortex shedding to minimise drag and lift fluctuations.

The studies carried out by Barker and van Dam [35] shows that it is possible to reduce the base drag and mitigate vortex shedding by adding an offset cavity at the base region. Approximately 50% drag reduction was achieved using this modification (Figure 2-70). C.P van Dam [23] has also shown that by adding a segregated splitter plate it is possible to reduce the base drag and inhibit the vortex shedding (Figure 2-71). This drag reduction technique should be adapted for both cut-back and flat-back airfoils to gain an improvement in their corresponding aerodynamic characteristics.

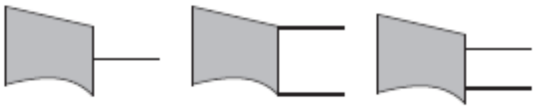

Figure 2-70 Drag reduction devices implemented at the trailing edge of a flat back airfoils (splitter plate, cavity, offset cavity) [35]

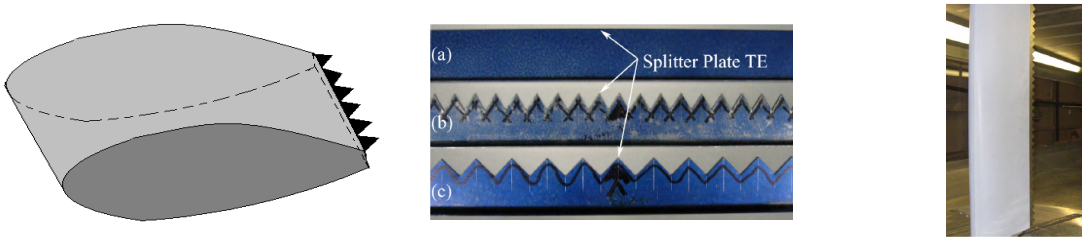

Figure 2-71 Left: Sketch of the splitter plate adapted for flat back airfoils, Right: Segregated splitter plate for flat back airfoil [35]

Park et al [36] proposed a small-size tab, mounted on part of the upper and lower trailing edges of a bluff body (Figure 2-72) to effectively attenuate vortex shedding and reduce drag. The optimal configuration of tabs produced an approximately 33% increase in the base pressure and a reduction in pressure drag. Due to the tabs, the vortices shed from the upper and lower trailing edges lose their 2D nature and the trailing edge vortex position was also changed. The Von Karman vortex shedding completely disappeared right behind the bluff body but re-occurred weakly at locations further downstream [36].

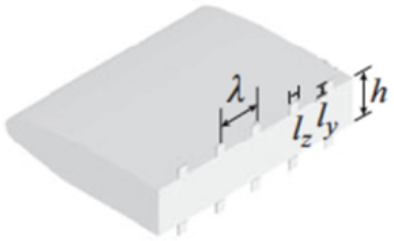

Figure 2-72 Trailing edge tabs [36]

There are several other devices that reduce the base drag. One such technique uses a control cylinder to be placed in the proximity of the trailing edge in the wake (Figure 2-73). Thiria [37] reports that, the "drag reduction is directly linked to the base pressure coefficient". The author reports that 17.5% drag reduction can be achieved by adapting a control cylinder in the base region to increase the base pressure coefficient [37]. This method of drag reduction also mitigates vortex shedding.

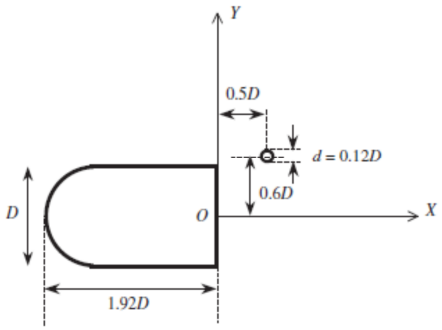

Figure 2-73 Base drag reduction method [37]

It is proposed that the control cylinder delays the von Karman instabilities, which is the main cause for the vortex shedding. Due to this modification of the instabilities, the closure of the vortex bubble is delayed and during this time delay the base pressure increases within the flow which results in the reduced drag [37]. The experimental flow visualization is shown in Figure 2-74.

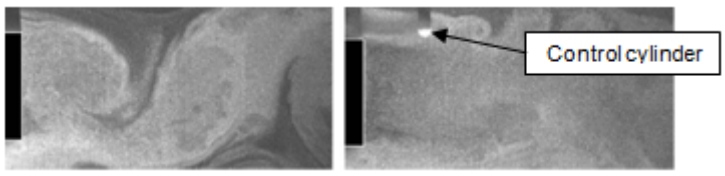

Figure 2-74 drag reduction using control cylinder (left: clean/no control cylinder, right: with control cylinder) [37]

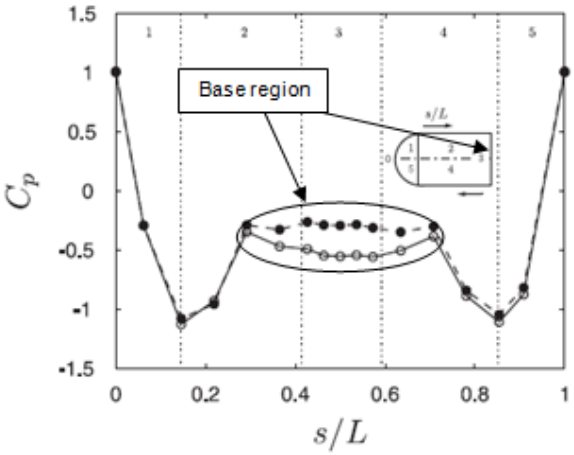

Figure 2-75 Surface pressure distribution of the model (open circle: clean blunt body, closed circle: blunt body with control cylinder) [37]

The base pressure modification using the control cylinder is clear from the surface pressure distribution (Figure 2-75). There is a significant increase in the base pressure due to the control cylinder, but the main advantage of this device is the mitigation of vortex shedding phenomenon. The implementation of this device on a wind turbine blade creates a difficulty, because the control cylinder has to be placed in the wake of the blade. Therefore, an external link is required between the blade and the control cylinder. This may negatively affect the structural and the aerodynamic performance of the wind turbine blade. Nevertheless these simple adaptations of base drag reduction devices at the trailing edge could provide a better performance of the wind turbine. Base drag reduction could be studied in detail especially for the reduction in drag of the flat back airfoil implemented root section of the blade, or specifically at the base region of the nacelle. However this technology is not studied in this work.

2.10 Porous airfoil

This flow control method is implemented by using a porous surface to reduce the drag and to increase lift. In 1991 Peter [38] proposed the porous airfoil and patented the design. The patent describes an airfoil surface covered with holes (Figure 2-76). Theoretical results of the airfoil show promising performance improvements. Euler equations were employed to obtain the lift (Figure 2-77, 'a' and 'b') and lift to drag (Figure 2-77, 'c') values for transonic Mach numbers. The patent describes how this airfoil achieves these improvements in performance. Permeability is defined as total hole area over the whole surface area of the airfoil [38].

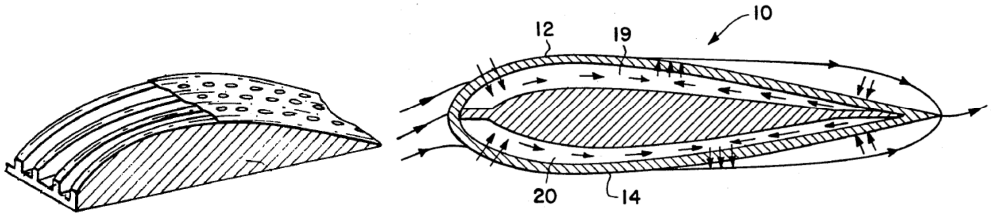

Figure 2-76 Porous airfoil invention (left: close up of the suction surface, right: flow visualisation of the airfoil), recreated from [38]

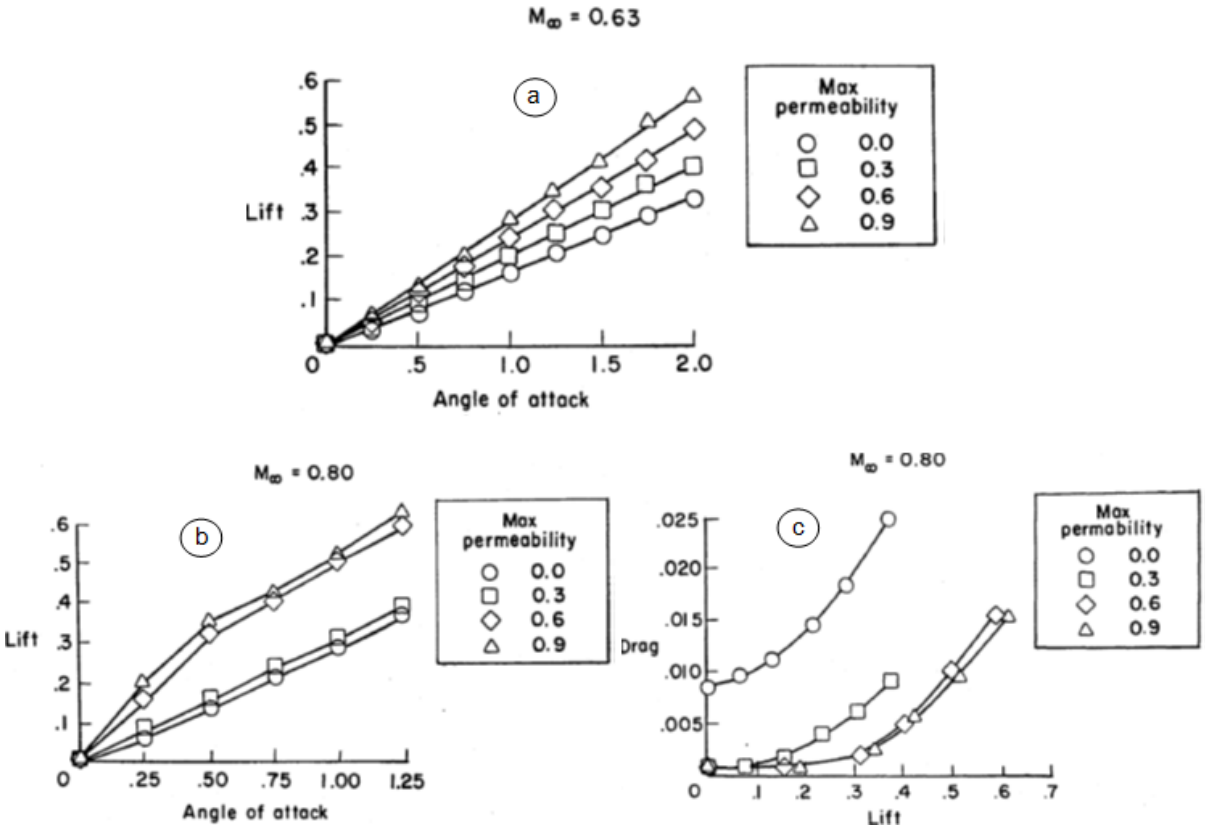

Figure 2-77 Theoretical lift and drag values of porous airfoil for different Mach number (M) (a: lift, M=0.63, b: lift, M=0.8, ct: L/D, M=0.8) [38]

Firstly, the airfoil produces high pressure regions at the leading and trailing edge and therefore the flow is vented towards the low pressure region in the mid-section of the airfoil. This venting leads to an inflow in the nose region, effectively reducing the nose radius. At the trailing edge the flow is allowed to recirculate and this changes the location of maximum thickness and its magnitude. This gives rise to the increase in lift. However the inventor fails to report how the airfoil modifies the drag.

The results presented in the patent (Figure 2-76) were computed using theoretical calculations and have been performed for transonic Mach numbers. Wind turbine blades operate in the subsonic flow regime and hence a preliminary study is required before this technology could be considered for a wind turbine blade. This technology seems to show a desirable effect on increasing the lift to drag ratio. Increased lift and lift to drag ratio could be exploited at the root and outboard sections respectively. However, the potential pressure ratios available at low sub-sonic conditions probably means that this technology is unrealistic for a wind turbine application and therefore further investigation is probably unwarranted.

2.11 Winglets

These control devices are added on the blade tip (Figure 2-78) to minimize tip flow between the suction and the pressure sides of the blade and to minimise the induced drag. The generated vortical flow leaves the blade tip as trailing vortices. Winglets have been known to be readily used in aircraft wings. The vortex from the winglet helps to effectively reduce the downwash and thereby reduce the induced drag. However for a wind turbine, due to

the tower clearance, the winglet is usually deflected towards the pressure side (upstream of the flow)[9].

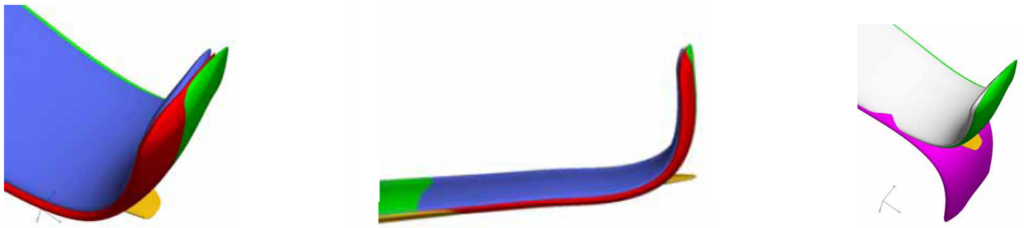

Figure 2-78 Winglet implemented on wind turbine blade (orange: original blade, green: winglet1, red: winglet2, blue: winglet3, white: winglet4, purple: winglet5) [9]

Johansen et all from DTU [9] have analysed winglets on wind turbines. Five configurations of winglets were considered (Table 2.11-1). A reference rectangular blade tip without a winglet was tested as the datum case. The analysis on these winglets was carried out using CFD methods for a range of freestream velocities.

Name	Airfoil	Defected towards	Twist angle (^{o}) towards nacelle
Winglet1	NACA 64-018 (symmetrical)	Pressure side	0
Winglet2	NACA 64-518 (cambered)	Pressure side	-2
Winglet3	NACA 64-518 (cambered)	Pressure side	-5
Winglet4	NACA 64-518 (cambered)	Pressure side	+5
Winglet5	NACA 64-518 (cambered)	Suction side	-2

Table 2.11-1 Assessed winglet configuration in the Johansen et all work [9]

The increase in rotor power and thrust is shown in Figure 2-79 left and right respectively. Power is the beneficial component of the winglets performance while the thrust on the winglet is usually the undesired component as thrust produces the structural fatigue on the blade.

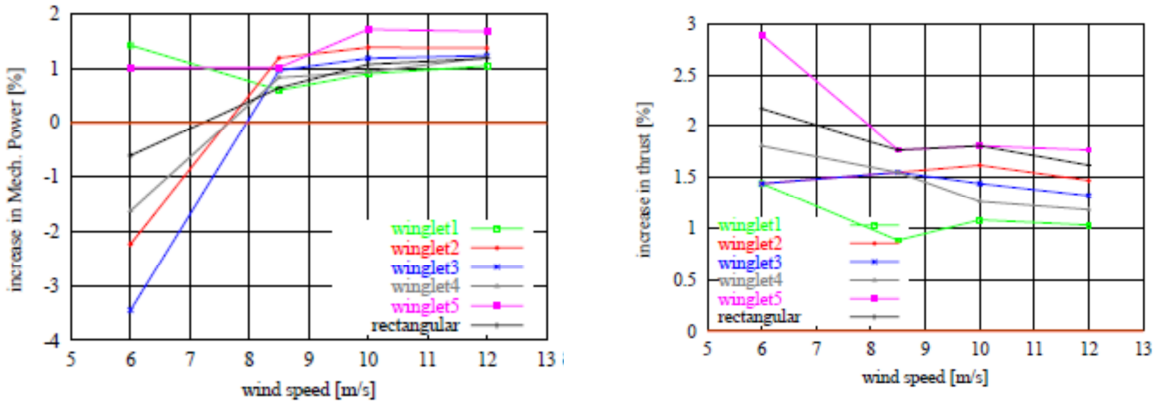

Figure 2-79 Mechanical power (left), Thrust (right) increase for different winglet designs [9]

From the results (Figure 2-79), it is observed that the suction side facing winglet (Winglet5) seems to have a positive impact on the power output of the rotor. However, the same winglet also has a negative increase in thrust production. This is a logical finding whereby the greater lift production also contributes to the thrust increase and results in a high blade

structural loading. Likewise, Winglet 1 has the best performance for load alleviation, due to its low thrust production. From further analysis it was proven that winglets pointed towards the suction side produces more driving force (power) but also increases the blade loading [9].

As a conclusive statement the author has reported that, “There is no doubt that adding a winglet to the existing blade can change the downwash distribution leading to increased produced power, but a load analysis must be made whether the additional thrust can be afforded.” [9]. They have also stated that it is possible to obtain a power increase of 1.3% with a thrust increase of 1.6% for a freestream velocity of 6m/s with the best performing winglet (winglet2). Therefore a compromise between the lift and thrust production has to be made, when implementing a winglet on a wind turbine blade. The author finally states that the effect of sweep and cant (lateral deflection) is not analysed in this publication and that it should be studied for better understanding of the behaviour of winglets on wind turbine blades.

The conclusions regarding the winglets are that they can produce a considerable amount of thrust. The tip location of winglets imposes heavy blade loading, where the structural integrity is relatively low compared to the inboard part of the blade. At the present moment, there is insufficient evidence to indicate that there is a significant benefit to implementing this technology for a wind turbine, therefore it was decided that winglet will not be selected for further study.

2.12 Initial down selection of the PFC devices

A range of flow control methods has been reviewed with an emphasis on techniques which could be considered for a large-scale wind turbine application. Within this remit, the focus has been on techniques which could provide improvements in lift, lift to drag ratio as well as structural load alleviation. The summary of the review and the selection for further research within this study is presented in Table 2.12-1

Device	Benefits	Issues	Selected	Comments
Vortex generators	• Reduces flow separation • Up to 40% increase in maximum lift coefficient • Can be used to reduce blade chord and reduce blade loads	• Increase drag in the attached flow conditions • Vane VGs have low structural robustness • Easily breaks off from the surface	• Yes	• The wedge VGs **selected** for this research due to its structural robustness and the increased gluing area • A viable device to reduce hub separation where drag penalties are not as important
Vortex trapping airfoil	• Up to 14% increase in lift coefficient • Up to 50% increase in lift to drag ratios	• Uncertainty with the measurements • Require lateral mass flow within trapped vortex to keep it stable	• Yes	• Step modification is **selected** for this research due to its large increments in lift
Passive aspiration	• Reduces flow separation • Up to 5-10% increase in maximum lift coefficient • Up to 50% reduction in drag • Can be used to reduce blade chord and reduce blade loads	• May not perform well on a wind turbine blade • Benefit lie in post stall AoA • Difficult to implement	• Yes	• PAJVG is **selected** for this research due to its beneficial effect on lift and drag ratios
Fence	• Reported increased wind turbine rotor power by 0.9%	• Can increase total blade thrust by 0.65%	• No	• This device is **not-selected** • Mature technology
Leading edge tubercles	• 4.8% lift augmentation • 10.9% induced drag reduction • Easy to implement	• Benefit lie in post stall AoA • Measured data only exists at very low Re	• Yes	• Leading edge tubercles is **selected** for this research beneficial effect on lift and drag ratios

Direct transition to turbulence (roughness and Riblets)	• Large drag reduction up to 70% by roughness below critical Re • 10% reduction in frictional drag by riblets	• Roughness is detrimental at wind turbine Re values • Sensitivity to dirt • Difficult to implement	• No	• This device is **not-selected** • Roughness is detrimental • Riblet only addresses frictional drag where profile drag dominate on a wind turbine • Maintenance issues
Trailing edge effectors	• Lift augmentation up to 46%	• Large drag forces	• No	• This device is **not-selected** • Mature technology
Flat trailing edge airfoils and base drag reduction	• Lift augmentation • Easy to implement	• Not beneficial for cambered airfoils • Vortex shedding • Drag reduction is difficult to implement	• No	• This device is **not-selected** • Control cylinder technology can be used to reduce drag and vortex shedding for a wind turbine nacelle
Porous airfoil	• Lift augmentation	• No measured results • Difficult to implement	• No	• This device is **not-selected** • Due to the issues
Winglets	• Increases rotor power by 1.3%	• increase total blade thrust by 1.6%	• No	• This device is **not-selected** • Large blade tip loads

Table 2.12-1 Summary of the reviewed PFC devices and the selections for further research

Based on these initial findings, the following methods are considered for further study to address the current lack in understanding as well as considering the practical aspects on development into service:

- Vortex trapping airfoil
  - High lift
  - Increase lift/drag
- Passive aspiration
  - Delay stall
  - Increase lift/drag
  - Increased lift
- Leading edge tubercles
  - Increase lift
  - Smooth stall
- Vortex generators (PFC device for blade root)
  - Reduce secondary flow
  - Reduce hub separation
  - Increase lift

Up to this point in the thesis, the literature survey and an initial downselection process is presented. The following chapters will present a theoretical approach to wind turbine design, which helps to understand and establish the aerodynamic requirements for an ideal wind turbine. Then the CFD methodology used to assess the devices will be presented. After establishing the aerodynamic requirements and tools used to evaluate the performance of the individual PFC devices, a second refinement or downselection of the chosen passive flow control devices will be presented using the results from the CFD simulations.

3 Theoretical analysis of a wind turbine

To utilise the PFC device for a wind turbine, the requirements for an ideal wind turbine were determined. A wind turbine blade experiences different flow condition along the span due to the blade speed and therefore different blade profiles with their appropriate angle of attack are stacked along the span to optimise energy extraction. A desirable design will be to enable the local blade portion along the span to achieve the ideal energy extraction from the wind, and this assessment presents the difficulties of achieving an ideal rotor and some discussion on practical rotor design. This theoretical study is conducted using the BEM method. The baseline NREL 5MW rotor (Appendix 8.3) was used to conduct this investigation. This study provides the understanding of the aerodynamic requirements for a wind turbine and the difficulties of achieving them. This assessment will also help to identify these difficulties and the potential benefits of using a PFC to satisfy the aerodynamic requirements. A method of using PFC devices to reduce structural loads is also discussed later in this chapter.

3.1 Ideal wind turbine BEM analysis

Based on a preliminary BEM study, it was found that a change in local sectional aerodynamic forces significantly affects the axial induction factor. There are two different induction factors that are considered for a wind turbine: axial and tangential. These factors accounts for the fractional decrease in axial or tangential wind velocity between the freestream and the rotor plane.

The axial induction factor is defined as:

$$a = \frac{(U_\infty - U_2)}{U_\infty} \qquad \text{Eqn 1}$$

Where U_∞= freestream velocity, U_2 = velocity at the rotor plane.

The tangential induction is defined as:

$$a' = \frac{\omega_r}{2\Omega} \qquad \text{Eqn 2}$$

Where ω_r= tangential velocity at the rotor plane, Ω = rotational velocity of the rotor.

An increase in lift force does not necessarily mean an increase in power output. The increased lift force increases the axial induction factor and thus reduces the torque production. By varying the local twist angles (Figure 3-1) it is possible to attain the optimum lift force that is required for an ideal power production. The main focus of the work is on the aerodynamic aspect of the consideration for the optimum twist distribution. The investigation is only conducted for wind speed range within the sub-rated power region for the NREL 5MW rotor (3m/s to 11 m/s).

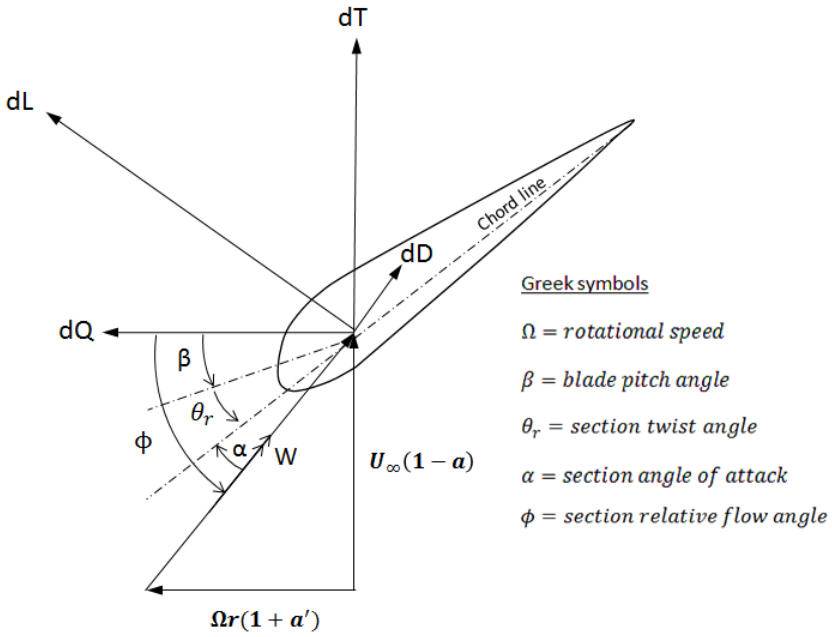

Figure 3-1 Velocity triangle for an airfoil section on a wind turbine

The objective of this study is to progressively investigate the main parameters that affect the turbine aerodynamic performance and to systematically develop and understand the primary sensitivities that impact onto a practical rotor configuration. With this in mind the investigation comprises five main aspects:

1. Variable rotor geometry when the effect of hub and tip losses and the drag forces are neglected
2. Variable geometry when the effect of drag forces are neglected
3. Fixed geometry with the effect of drag forces
4. Fixed geometry with hub and tip losses, and the drag forces
5. Fixed geometry with hub and tip losses, drag forces and with sub-rated pitch regulation

The first two studies were conducted using an impractical rotor that can change its radial twist angles at each span station i.e. is able to attain the optimum twist distribution at each different wind speed and rpm configuration. These studies are conducted only to establish the theoretical maximum power production and to study the effect of hub and tip losses on the power output.

The subsequent studies (3 and 4) are conducted using a more practical fixed twist rotor geometry but with and without the effect of drag force included. This helps to determine the potential maximum of the benefits from a drag reduction PFC device. Finally the 5th study was conducted to assess the effect of pitch regulation in the sub-rated power region.

3.1.1 Maximum power output

This section of the thesis discusses the optimum aerodynamic properties for a wind turbine that is required to achieve the maximum power extraction from the wind. These optimum aerodynamic properties for maximum power can be estimated analytically using the blade element momentum (BEM) theory.

The power in the wind can be determined using the kinetic energy per unit time contained in the flow that follows through the circular area prescribed by the rotor [39] (Eqn 3)

$$\frac{d(KE)}{dt} = \frac{1}{2}\dot{m}|V_\infty|^2 = \frac{1}{2}\rho A|V_\infty|^3 = P_w \qquad \text{Eqn 3}$$

The baseline rotor has a maximum power production of 5.6 MW at 9m/s (sea level conditions), assuming a 100% energy conversion process. This maximum power is not achievable in practice due to the limitation in current energy extraction methods. Modern wind turbines may only extract half of this potential energy because of aerodynamic and mechanical losses [40]. Nevertheless, using BEM theory, a theoretical maximum power can be determined for a conventional wind turbine, which will help to evaluate the difference in power between a theoretical turbine and a practical one.

Considering an incompressible fluid and using the actuator disk (Figure 3-2) theory the air velocity at the rotor disk (U_2) and the downstream of the rotor (U_4) can be expressed using the axial induction factor (a) (Eqn 4 and Eqn 5) [39]. Wind turbine also

$$U_2 = U_\infty(1-a) \qquad \text{Eqn 4}$$
$$U_4 = U_\infty(1-2a) \qquad \text{Eqn 5}$$

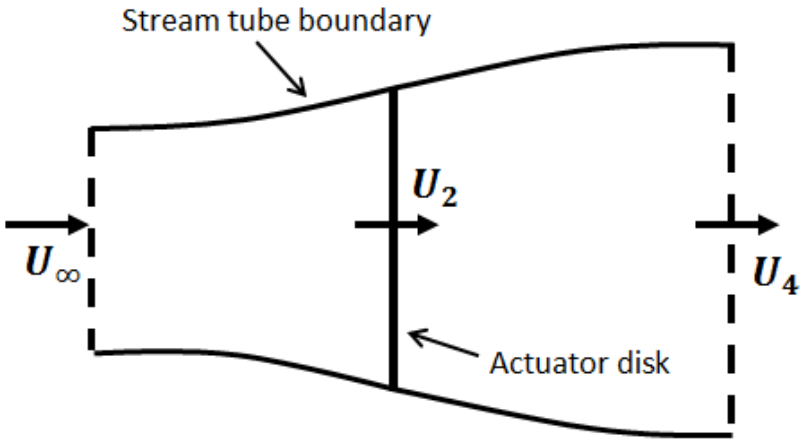

Figure 3-2 Actuator disk

The power extracted by the turbine is equal to the product of the thrust (T) and axial velocity at the disk. The thrust force on the blade disk can be calculated using Eqn 6.

$$T = \frac{1}{2}\rho A(U_\infty^2 - U_4^2) \qquad \text{Eqn 6}$$

Where ρ = density, A = circular area of the actuator disk. The power of the turbine can be determined using:

$$P_w = \frac{1}{2}\rho A(U_\infty^2 - U_4^2)U_2 = \frac{1}{2}\rho A U_2(U_\infty + U_4)(U_\infty - U_4) \qquad \text{Eqn 7}$$

Substituting the expressions for U_2 (Eqn 4) and U_4 (Eqn 5), in to the expression for turbine power (Eqn 7) gives:

$$P_w = \frac{1}{2}\rho A U_\infty^3 4a(1-a)^2 \qquad \text{Eqn 8}$$

Wind turbine rotor performance is usually characterised by its power coefficient, C_P:

$$C_P = \frac{P_w}{\frac{1}{2}\rho U_\infty^3 A} = \frac{Power}{Power\ in\ the\ wind} \qquad \text{Eqn 9}$$

So that the power expression (Eqn 6) reduces to the power coefficient (C_p) as:

$$Cp = 4a(1-a)^2 \qquad \text{Eqn 10}$$

Thus for a maximum power:

$$\frac{dC_P}{da} = 4(1-4a+3a^2) = 0$$

The ideal operating condition for maximum power is at:

$$a = \frac{1}{3}, C_T = \frac{8}{9}\ and\ C_p = \frac{16}{27} = 0.59 \qquad \text{Eqn 11}$$

Where $C_T = \frac{T}{\frac{1}{2}\rho U_\infty^3 A}$ is the coefficient of thrust and C_P coefficient of power.

This operating condition is known as the Betz-Lanchester limit [40]. This condition gives the upper limit for the aerodynamic power that can be extracted by a conventional wind turbine, assuming an incompressible flow without any end effects or viscous losses. In practice it is found that efficient wind turbines are able to achieve C_P values between 0.4 and 0.5 [40]. Therefore even with a PFC application it is noted that only a limited invrease of power extraction is possible with a conventional wind turbine.

3.1.2 Twist optimisation for a wind turbine

This section discusses the process of twist optimisation for a wind turbine. The twist (θ_r) is defined as the angle between the relative wind (ϕ) angle and the local angle of attack (α) minus the pitch angle (β), as shown in Figure 3-1. The rotor twist can be optimised to achieve the ideal operating conditions for maximum power (Eqn 11), which was derived previously using the BEM theory.

The optimum aerodynamic properties described in Eqn 11 can be achieved by optimising the local twist (θ_r) of the local 2D airfoil sections along the blade span. NREL 5MW rotor has a global pitch angle of zero within the sub rated power region. Thus the twist is defined as $\theta_r = \phi - \alpha$ for this region of wind speeds (3 m/s to 11 m/s). Based on the BEM theory, it is reasonable and common to optimise the local blade twist to achieve an axial induction factor (a) of 1/3, where the turbine achieves the maximum power.

Based on the equation of thrust (Eqn 6), the local thrust (dT) for an annulus strip (dr) can be expressed as:

$$dT = \rho U_\infty^2 4a(1-a)\pi r dr \quad \text{Eqn 12}$$

And based on Figure 3-1, the local thrust force can be expressed as:

$$dT = \frac{1}{2}\rho W^2 (C_l \cos\phi + C_d \sin\phi) Bcd \quad \text{Eqn 13}$$

Where c = local chord, B = number of blades.

The relative wind velocity (W) can be expressed as:

$$W = \frac{U_\infty (1-a)}{\sin\phi} \quad \text{Eqn 14}$$

Combining Eqn 12 and Eqn 13 gives:

$$2a(1-a) = \frac{\sigma_L W^2 (C_l \cos\phi + C_d \sin\phi)}{2U_\infty^2} \quad \text{Eqn 15}$$

$\sigma_l = \frac{Bc}{2\pi r}$ is known as the local blade solidity parameter. Substituting the expression for relative wind velocity, W (Eqn 14) into Eqn 15 and after some rearrangements we obtain:

$$\frac{a}{1-a} = \frac{\sigma_L (C_l \cos\phi + C_d \sin\phi)}{4\sin^2\phi} \quad \text{Eqn 16}$$

Using this relationship, the local axial induction factors are determined using an iterative algorithm as a function of local forces (L and D) and wind speed (Ws).

It should be noted that only lift coefficient (C_l) is commonly used in the axial induction calculation due to the reason that the effect of drag is only experienced in close proximity to the blade or downstream - especially in the viscous wake [41]. Wilson and Lissaman [42] has also argued that using the drag term in the axial induction computation will affect the orthogonally of the relative velocity and the induced velocities and suggested that it is better to not included in the axial induction algorithm. Therefore only the local lift coefficients are used to evaluate the local axial induction factors, this result in the following equation:

$$\frac{a}{1-a} = \frac{(\sigma_L C_l)\cos\phi}{4\sin^2\phi} \quad \text{Eqn 17}$$

Based on this equation it is clear that for a fixed radius and blade chord, where the σ_L is constant, the local lift coefficient and the relative flow angles dictates the local axial induction.

3.1.3 Analysis of the NREL 5MW rotor with a fully variable geometry

Initially a study was conducted using the NREL 5MW wind turbine model assuming a fully variable geometry which is not practical. This assessment is only conducted in order to determine the maximum potential power output of the baseline NREL 5MW rotor with the chord distribution and wind speed to rpm ratio defined by NREL [2]. The blade's local 2D

sections are assumed to change its twist angle as a function of radius, wind speed and rpm configuration to achieve an axial induction factor of 1/3.

3.1.3.1 Ideal NREL 5MW rotor - without Prandtl's hub and tip loss

This preliminary assessment of the twist optimisation was conducted without considering Prandtl losses at the hub and tip as it will help to establish the potential maximum power without these lift losses at the hub and tip part of the blade.

The assumptions made for this study are as follows:

I. An idealised fully variable geometry
II. Axial induction factor (a) = 1/3
III. No precone or shaft tilt (blade is perpendicular to the wind)
IV. No Pandtl hub and tip losses
V. Drag forces are neglected ($C_d = 0$)
VI. No swirl effect ($a' = 0$)

Following the assumptions above, Eqn 16 can be rearranged to find the required lift coefficient to achieve the optimum axial induction factor of a=1/3:

$$C_{l(Opt)} = \frac{2\sin^2\phi}{\sigma_l \cos\phi} \quad \text{Eqn 18}$$

Thus the ideal lift force can be found using:

$$\mathrm{L} = \frac{1}{2}\rho W^2 c dr\, C_{l(Opt)} \quad \text{Eqn 19}$$

The local wind flow angle is calculated using:

$$\tan\phi = \frac{1-a}{1+a'}\frac{U_\infty}{r_l\Omega} \quad \text{Eqn 20}$$

Where r_l is the local section's radius. The local wind velocity is found using Eqn 14. The sectional torque (dQ) produced by each element/blade section can also be found by:

$$dQ = \frac{1}{2}\rho W^2 c r dr C_{l(Opt)} \sin\phi \quad \text{Eqn 21}$$

Hence the power produced by the blade can be evaluated using:

$$P_w = B\ \Omega\ \Sigma \mathrm{dQ} \quad \text{Eqn 22}$$

Firstly the baseline rotor blade (R=63m) was discretised with 17 blade section, based on the aero elastic study conducted by the NREL for this baseline rotor [2]. The proposed discretisation by NREL is to better capture the large structural gradients at the blade root and the large aerodynamic gradients at the blade tip, the three inboard and three outboard blade sections are two-thirds the size of the 11 equally spaced mid span blade sections.

Using the discretised blade sections, the ideal lift coefficients were determined for each blade section at different wind speeds with Eqn 18 (Figure 3-3). This ideal lift coefficient distribution is used to determine the optimum lift force distribution using Eqn 19 (Figure 3-4), which is required to achieve the ideal Betz power conditions (Eqn 11). The power output of the turbine (Eqn 22) is then equal to the product of number of blades (B), rotor's rotational speed (Ω) and the total sectional torques (ΣdQ).

The determined ideal lift coefficient ($C_{l(Opt)}$) (Figure 3-3) and lift force (L) (Figure 3-4) distribution play a key role in understanding the requirements for an optimum power production of the NREL 5MW rotor. It is clear that a large coefficient of lift up to 5 is required at the blade root for ideal power production. This is mainly due to the low relative velocities present at this part of the blade. This high lift coefficient requirement at the blade root can be reduced by an increased blade chord at this blade part, thus achieving the required optimum lift force (Figure 3-4) for ideal power production.

For optimum power production, the blade demands a moderate lift force at the blade tip region (Figure 3-4). The local dynamic head at this part of the blade are relatively large, therefore even with a small blade chord, a moderate lift coefficients about $C_l < 2$ are requested to achieve this large optimum lift forces (Figure 3-3). The irregular distribution of lift force found at the tip is mainly due to the combined effect of the chosen blade section discretisation with the blade chord distribution.

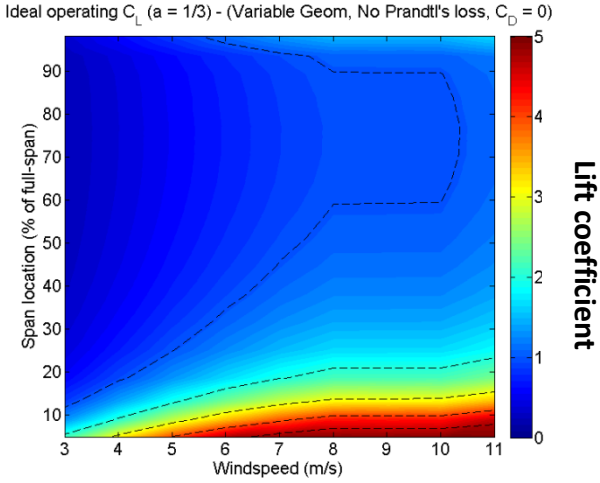

Figure 3-3 Optimum lift coefficient (C_l) distribution for the NREL 5MW

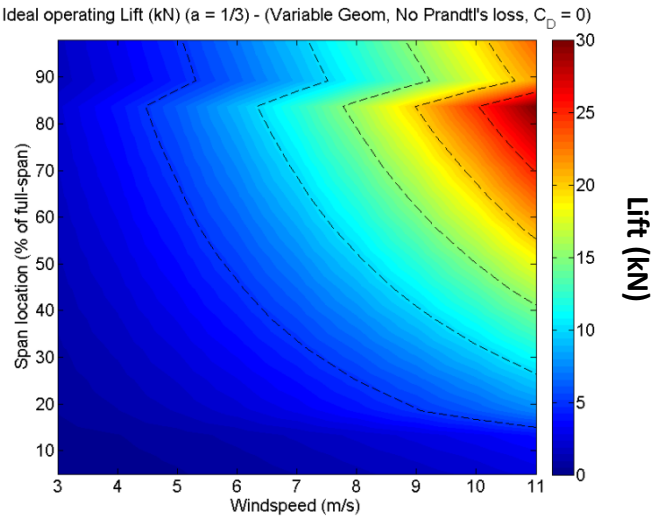

Figure 3-4 Optimum lift (L) distribution NREL 5MW

This idealised geometry has the potential to increase the annual power production by 8.5% relative to the baseline NREL 5MW geometry. Annual power production of a wind turbine can be estimated using a probability density function to model the wind speed occurrence. There are two commonly used probability functions in the wind turbine industry: Weibul and Rayleigh [39]. Weibull distribution requires two parameters to define the probability distribution and Rayleigh uses only one parameter (mean wind speed) to generate the probability distribution. This distribution also accounts for the wind turbines non-operating conditions such that the wind speeds where the wind turbine stops turning. For this

research, based on sponsors recommendations the annual energy production (AEP) was calculated assuming a 10 m/s mean Rayleigh wind speed distribution (Appendix 8.4). According to this probability density function it is assumed that the wind turbine is in operation for 95% of the year and, only 5% where it is assumed to be in the non-rotating state. The predicted power distribution (Figure 3-5) from this study shows the potential maximum (upper bound) power output available for the chosen baseline NREL 5MW rotor.

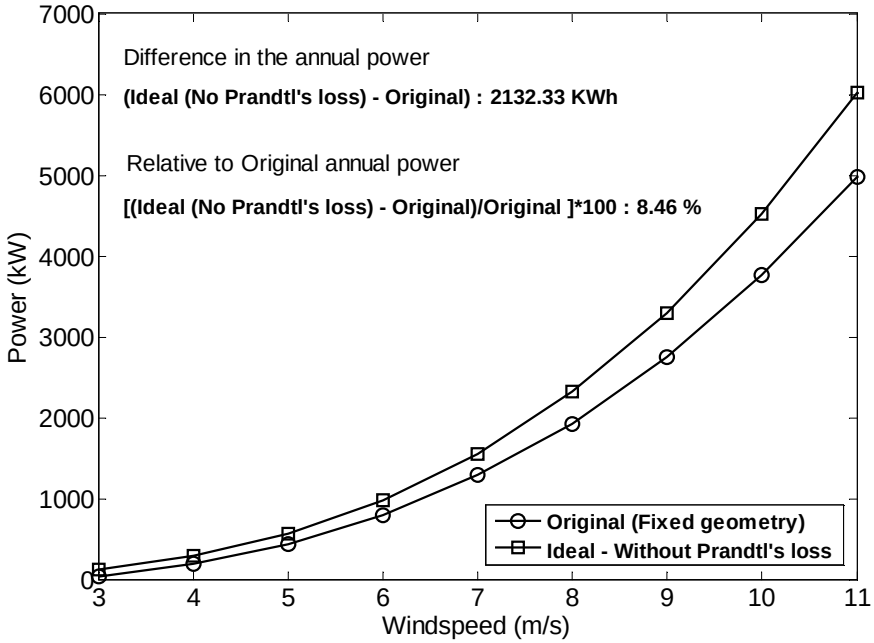

Figure 3-5 Power curve comparison between Original NREL 5MW (Fixed geometry with the original twist defined in [2]**) and Ideal variable NREL 5MW geometry.**

3.1.3.2 Variable geometry with Prandtl's hub and tip losses

One of the major limitations of the original BEM theory is that there is no account of the influence of vortex shedding at the blade tip to the induced velocities [43]. The previous analysis (section 3.1.3.1) did not account for these aerodynamic losses. Modelling the aerodynamic losses associated with a turbine blade will result in a more realistic power estimation of a wind turbine. Similar to the previous assessment, this investigation also assumes a non-realistic rotor geometry, which is able to change its local 2D sections twist angles as a function of radius, wind speed and rpm configuration to optimise for the ideal lift forces. However this study includes the effect of hub and tip loss on the BEM model as well as the power output of the turbine.

In a real flow the trailing vortices found at the blade tip will curl up around the strong tip vortices [44]. This effect significantly reduces the circulation at the blade tip and as a consequence the torque is reduced [39]. The blade element forces at the blade tip contribute greatly to the total torque output by the blade and thus to the overall performance of the rotor. This effect of vortex shedding is also found in the hub region of the blade [43] and therefore incorporating Prandtl tip and hub loss models [45] in to the BEM code is of interest.

Prandtl's tip loss correction factor, F, to the induced velocity field is expressed by the following relationship [43]:

$$F = \frac{2}{\pi}\cos^{-1} e^{-f} \quad \text{Eqn 23}$$

Where f is defined as:

$$f = \frac{B}{2}\frac{R-r}{r\sin\phi}$$

And where R is the maximum blade radius, r is the local element radius and ϕ is the wind flow angle.

Likewise Prandtl's hub correction factor to the induced velocity field is expressed by replacing f with the following:

$$f_{hub} = \frac{B}{2}\frac{r-R_{hub}}{R_{hub}\sin\phi} \quad \text{Eqn 24}$$

Where R_{hub} is the hub radius. Therefore total loss due to the tip and hub can be expressed as:

$$F_{Total} = f_{tip}\, f_{hub} \quad \text{Eqn 25}$$

Thus the equation for the ideal lift coefficient (Eqn 16) after accounting for hub and tip losses yields to:

$$C_l = \frac{a\, F_{Total}\, 4\sin^2\phi}{\sigma_l \cos\phi} \quad \text{Eqn 26}$$

Hence using this loss accounted lift coefficient with the Eqn 21 and Eqn 22 the power production of the loss accounted wind turbine is estimated.

Another limitation of the BEM theory is that, when the axial induction factor reaches above 0.4, the traditional BEM theory becomes invalid [43]. The wind turbine enters a turbulent wake state when local axial induction factors (a) reach 0.5, where the flow in the far wake starts to propagate upstream based on Eqn 5, which is a violation of the basic BEM theory. In practice the flow reversal does not occur instead more flow entrains from the outside and increases the turbulence within the turbine wake, the flow velocity decreases within the wake but the thrust on the blade continue to increase [43].

To compensate for this effect, the Glauert's correction is used to calculate the large axial induction factors (>0.4). This correction is based on experimental measurements and it is applied to the coefficient of thrust (C_T). A modified Glauert's empirical relation (Figure 3-6) based on measurements that incorporates the tip-loss correction (Eqn 27) by Buhl [46] is used to calculate the optimum lift coefficient for a high axial induction factors.

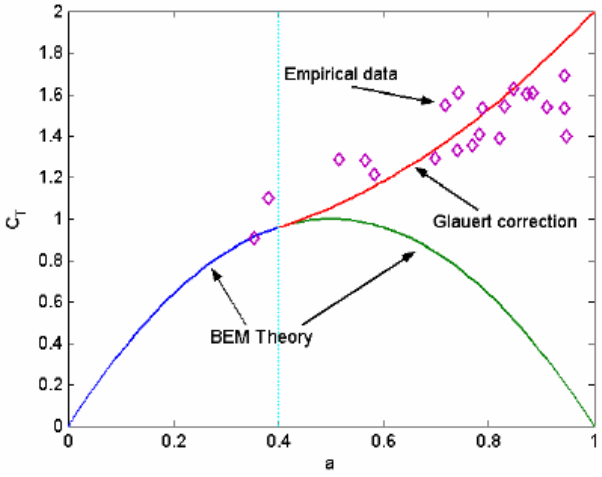

Figure 3-6 Glauert correction for tip-loss factor, F=1.0 [43]

The relationship between the large axial induction and thrust coefficient is defined as follows:

$$C_T = \frac{8}{9} + \left(4F - \frac{40}{9}\right)a + \left(\frac{50}{9} - 4F\right)a^2 \quad for\ a > 0.4 \qquad \text{Eqn 27}$$

Assuming zero drag coefficients (C_d=0), the equation for the optimum lift coefficient for an axial induction factor greater than 0.4 can be calculated using the following [43]:

$$C_L = \frac{\sin^2\phi\ C_T}{\sigma_L(1-a)^2\cos\phi} \quad for\ a > 0.4 \qquad \text{Eqn 28}$$

The optimum conditions previously found for maximum power (Betz conditions - Eqn 11) does not apply when the Prandtl's loss and Glauert's correction are accounted in the BEM model. Therefore the optimum condition for maximum power was determined by assessing the local blade torque productions (C_Q) for varying the axial induction factor (a). The optimum axial induction factors (a) were determined using the maximum local torque coefficient (C_Q) (Figure 3-7) for the Prandtl's loss and Glauert's correction implemented BEM model i.e. $\frac{dC_q}{da} = 0$.

$$C_Q = \frac{dQ}{\frac{1}{2}\rho U_\infty^2 Ar} \qquad \text{Eqn 29}$$

Where A is the area of the annulus ($2\pi r\ dr$) and r is the local radius of the element.

Based on this investigation, the results (Figure 3-7) suggest that, at the blade root (6% span), the optimum axial induction factor was found to be greater than Betz' 1/3. The implemented loss in lift force requires a larger axial induction factor up to 0.64 that is greater than the Betz 1/3 to gain the optimum ratio between local flow angle (ϕ) and the local velocity (W). At this optimum ratio the maximum torque production is estimated.

However, in the mid part of the blade (50% span), where the influence of the hub and tip losses are the minimum ($F_{Total} = 1$), the optimum axial induction factor (Figure 3-7) for maximum power was found to be equal to the optimum axial induction factor found using the basic BEM theory (Eqn 11). But at the blade tip region, larger optimum axial induction factors are required.

This assessment was repeated for all the wind speed to evaluate their specific optimum axial induction factor distribution. This result (Figure 3-8) shows that a non-uniform optimum axial induction factors exist for a BEM model with hub and tip loss models included. This optimum axial induction factor distribution was then used to calculate the optimum lift coefficient (Figure 3-9) and lift forces (Figure 3-10) required for maximum power for the BEM model of the NREL 5MW when the losses at the hub and tip are accounted for.

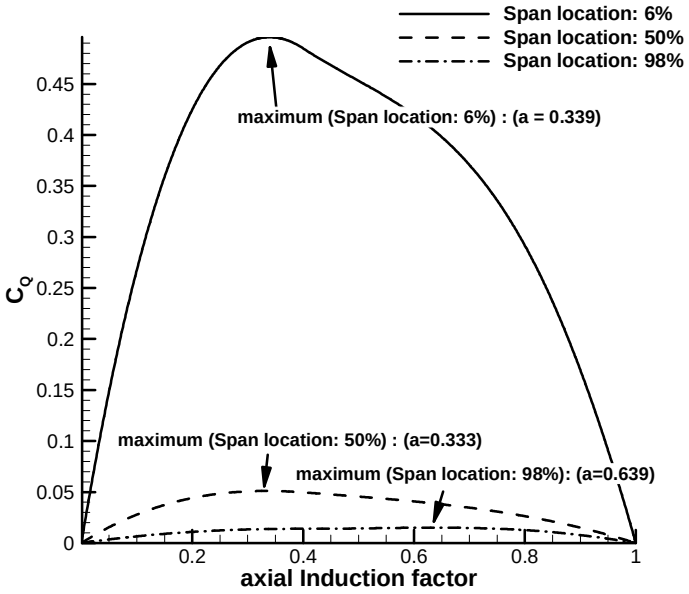

Figure 3-7 Ideal induction factor as a function of local blade torque coefficient for a range of spanwise positions (Ws: 9m/s, Omega: 10.3RPM)

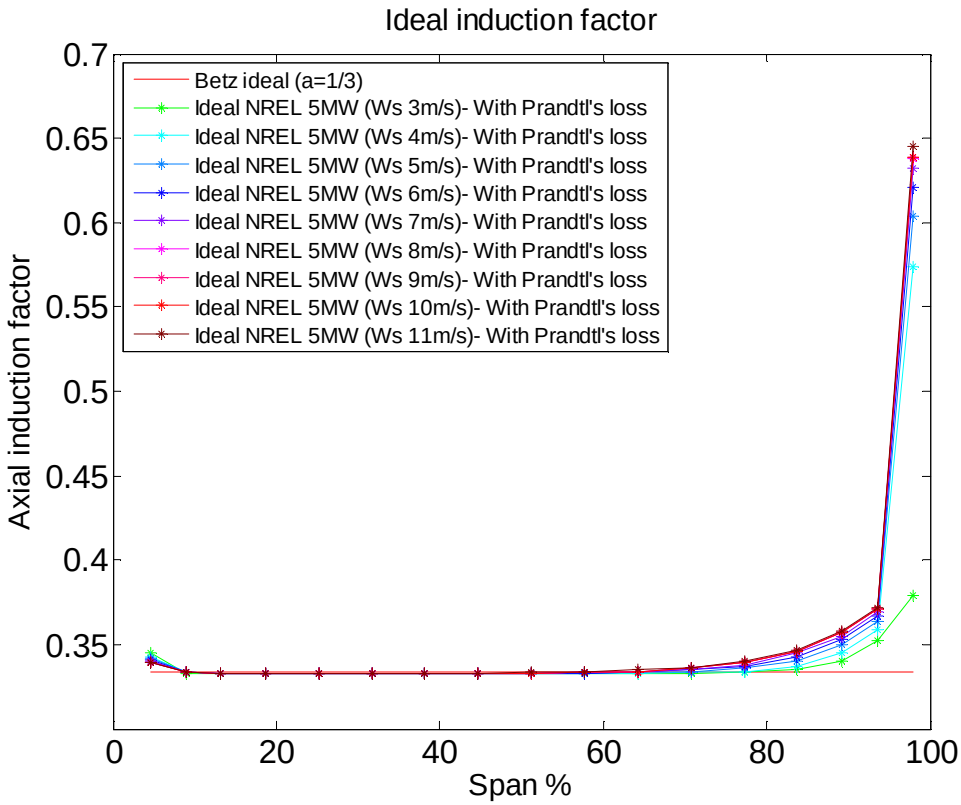

Figure 3-8 Optimum axial induction factor as a function of blade span for varying wind speed

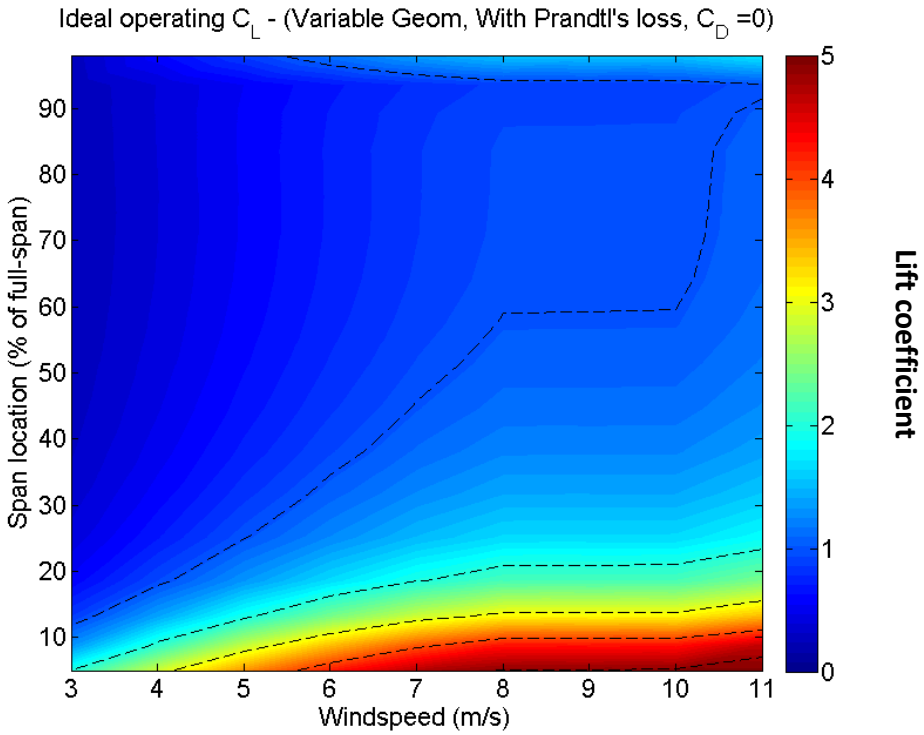

Figure 3-9 Ideal operating lift coefficient distribution for the NREL 5MW (Variable geometry, with Prandtl's loss, $C_D = 0$)

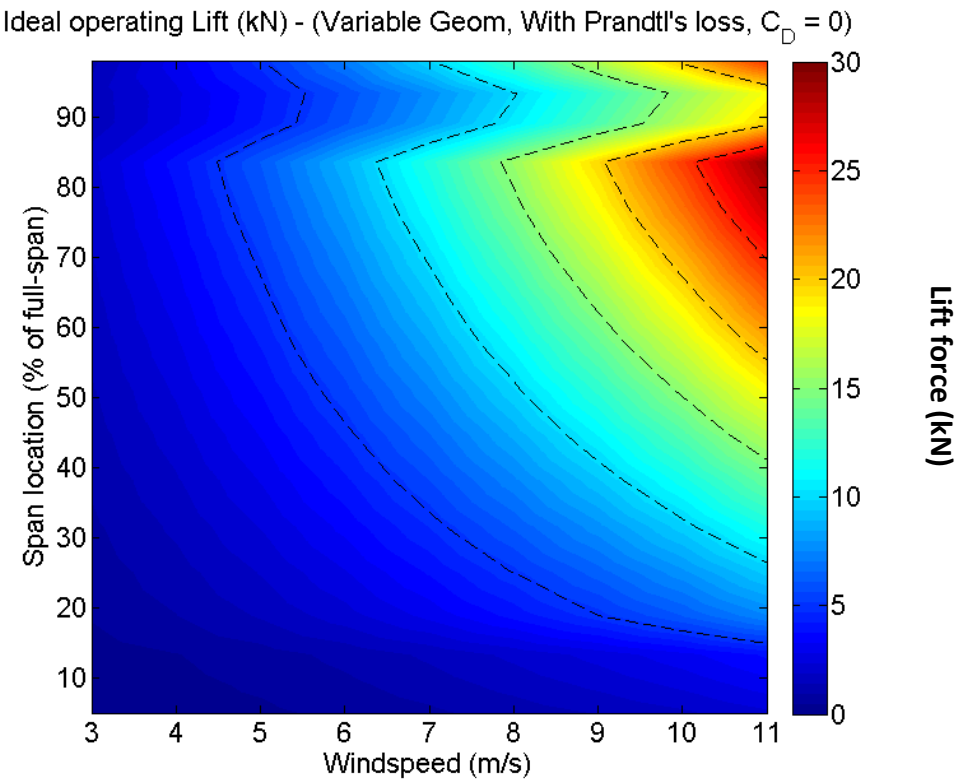

Figure 3-10 Ideal operating lift force distribution for the NREL 5MW (Variable geometry, with Prandtl's loss, C_D = 0)

The power calculation using the BEM method with the Prandtl hub and tip loss suggest an increase of 5.2% in annual power (relative to the NREL geometry) is attainable with a variable geometry NREL 5MW (Figure 3-11).

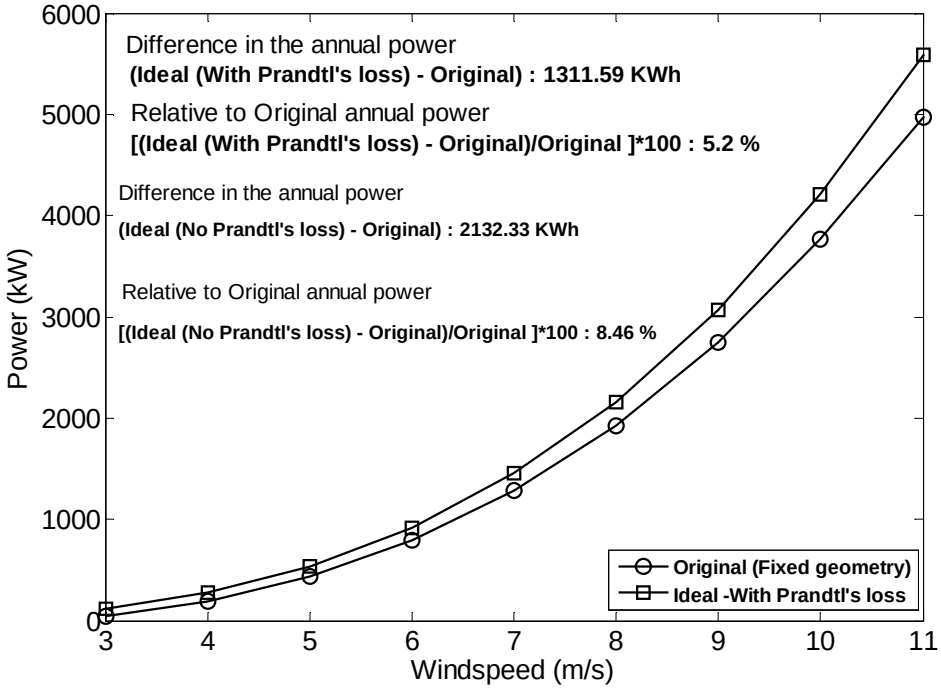

Figure 3-11 Power curve comparison between Original NREL 5MW (Fixed geometry with the original twist defined in [2] **and Ideal variable NREL 5MW geometry with Prandtl's loss.**

Ideally an 8.5% increase in annual power is calculated for a non-realistic fully variable NREL 5MW geometry blade when the drag forces and the effect of hub and tip losses are neglected. Yet a 5.2% increase in annual power is estimated for this unpractical NREL 5MW rotor when the hub and tip losses are accounted.

Some of the assumptions that have been taken to perform this analysis are not practical. The fully variable geometry assumption where the individual rotor section in the blade radius is able to modify its twist angle as a function of wind speed and rpm configuration is not realistic. Clearly, neglecting drag is another assumption that is not realistic. The purpose of these preliminary investigations only serves to determine the potential upper bound power capacity of the NREL 5MW rotor.

3.1.4 Analysis of the NREL 5MW rotor with a fixed geometry

Usually the twist distribution across the span of a wind turbine is optimised for the optimum tip speed ratio (TSR). The optimum tip speed ratio is dictated by the generator i.e. the design point of the wind turbine is chosen at the most efficient rotational speed of the generator. The wind speed, rpm configuration was set by NREL [2]. For the considered baseline rotor (NREL 5MW), the optimum TSR was found to be 7.5 (Figure 3-12).

Three of the wind speed-rpm configurations for the NREL 5MW rotor have been deliberately placed at the optimum tip speed ratio (Figure 3-12) in order for the wind turbine to operate at the ideal design point of the generator. The twist optimisation is conducted for the chosen design point wind speed of 9 m/s. Thus the wind turbine's ideal conditions are achieved at the design point of the power generator to maximise the efficiency of the energy extraction.

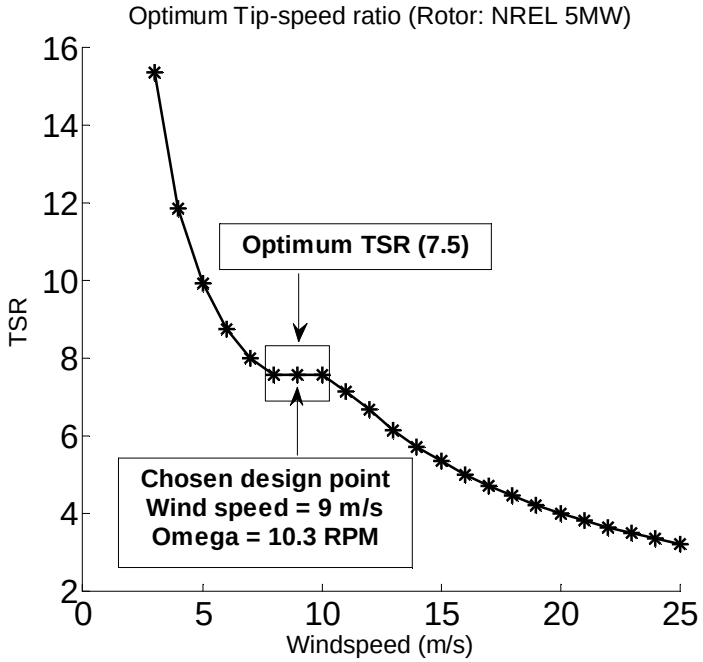

Figure 3-12 Optimum TSR design point

Initially this study was conducted with and without the effect of drag. The non-uniform axial induction factors found using a BEM model in which the effect of hub and tip loss is taken into account (Figure 3-13) will be used for this exercise. However the effect of using the conventional method for twist optimisation, where a uniform Betz ideal induction factor is used will be presented and discussed for the study that assess the effect of drag forces (section 3.1.4). Therefore a direct comparison can be made between this improved method of twist optimisation and the conventional twist optimisation process that is currently implemented in the industry.

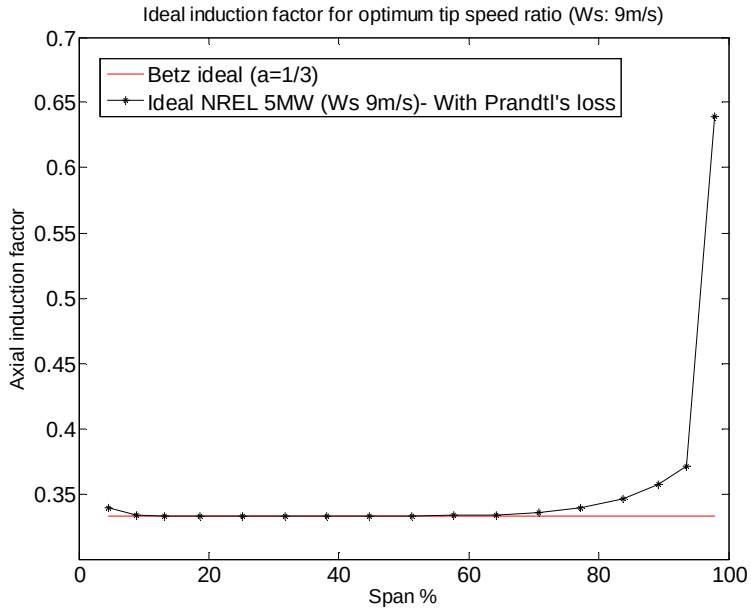

Figure 3-13 Ideal induction factor for the NREL 5MW rotor for the wind speed of 9m/s

Twist optimisation assuming an ideal axial induction was conducted using simple Newton-Raphson integration method with a BEM code developed by NREL (WT_Perf) [47]. WT_Perf uses the BEM theory with an algorithm [48] to find the local axial (a) and tangential induction factors (a'). Numerous changes in twist iterations with their corresponding axial induction were conducted in order to achieve the prescribed ideal axial induction factor (Figure 3-13). Additionally, a BEM code was generated in MATLAB to verify the results from WT_Perf and based on this comparison, a maximum difference of about 5% in axial induction was found between these codes. Based on this result, the WT_Perf code was established for the BEM analysis of this research.

3.1.4.1 Analysis of the NREL 5MW rotor without drag forces (Cd =0)

Firstly, an assessment of the fixed geometry twist optimisation was conducted without the effect of the drag force, but for this assessment the effect of tangential induction were included in the BEM code ($a' \neq 0$). A suitable radial disitrbution of twist based on the ideal induction is determined in an iterative manner (Figure 3-14) to meet the optimum axial induction factor (Figure 3-15). The study was conducted initially with 15 iterations to illustrate the effect of number of iterations and to establish a convergence criterion.

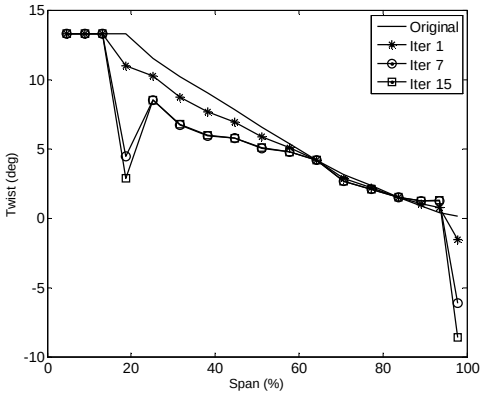

Figure 3-14 Twist (θ_r) convergence with progressive twist changes, Original: NREL 5MW rotor defined in [2]

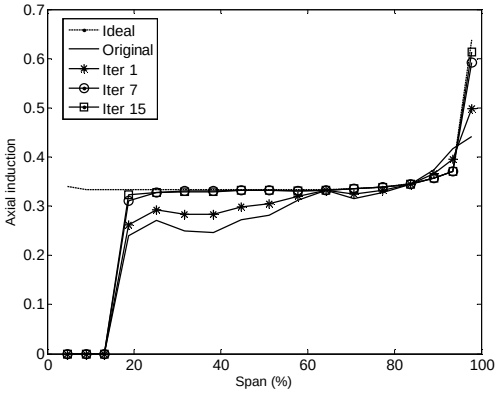

Figure 3-15 Axial induction factor (a) convergence with progressive twist changes, Original: NREL 5MW rotor defined in [2]

For this study no constraints were applied for a smooth twist distribution, hence large gradients in twist are found (Figure 3-14). No constraints were set on the twist in order to achieve the prescribed optimum axial induction factor. Nevertheless the results shows that a reasonable convergence within 4% relative to the ideal axial induction factor was achieved with 15 number of iteration (Figure 3-15).

The zero axial induction factor found for the three sections found at the blade root (5-15% span) of the blade is because in this region the blade is defined with cylinders and they do not contribute any power and their twist angles has no significance.

The result from this study suggest that a forced optimisation for the single design point reduces the efficiency at the off design conditions (Figure 3-16). It was found that the optimised twist found with the 15 iteration increase the coefficient of power (Cp) by 1% at the design point while it negatively reduces the Cp at the off design point by about 20% at the TSR of 15 (Ws: 3m/s). This reduces the benefit attained at the design point and compromises the annualised power production of the ideally twist applied turbine i.e. the maximum annualised power based on the chosen design point (Figure 3-17) is reached before the achievement of the ideal condition for the design point (Figure 3-18).

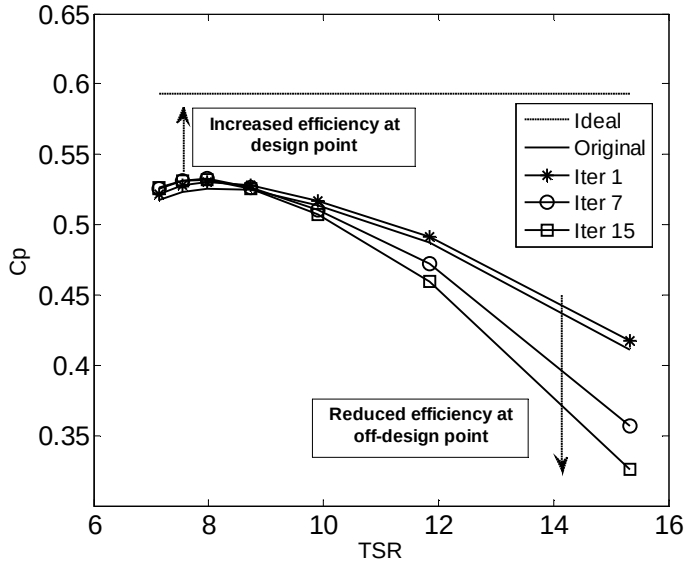

Figure 3-16 Coefficient of power as a function of TSR at different twist iterations

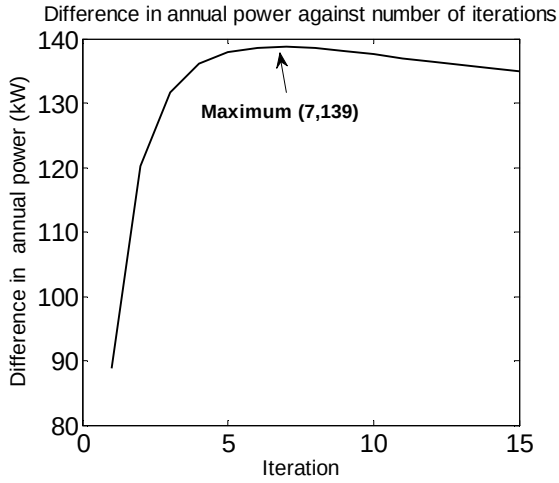

Figure 3-17 Annualised power convergence for the NREL 5MW rotor with progressive twist iterations

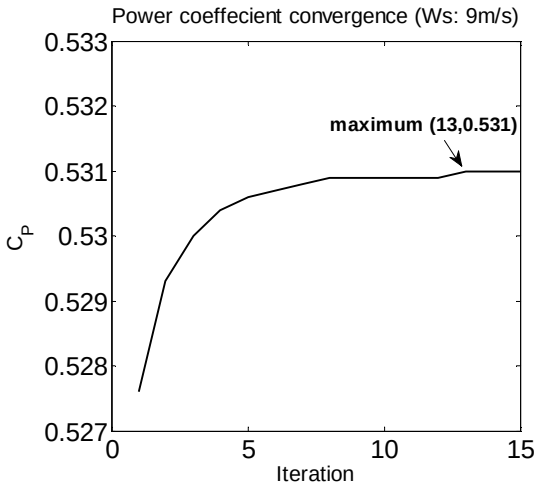

Figure 3-18 Power convergence at the chosen design point for the NREL 5MW rotor with progressive twist iterations

The optimum twist distribution is assumed to be achieved at the maximum gain in annual power (Figure 3-17). It is noticeable that even with the optimum twist for the maximum annualised power the off-design conditions were worse than original twist (Figure 3-16). This is due the wind distribution chosen to estimate the annual power production has higher weighting factor close to the design point (Rayleigh distribution with mean wind speed of 10 m/s) than off-design wind speeds.

The power distribution of the NREL 5MW rotor with an ideal twist and not considering drag forces result in an increase of 0.54% in annual power of the wind turbine. Based on the previous study (section 3.1.3.2) the variable geometry NREL 5MW rotor was able to increase the annualised power by 5.4%. This comparison of the annualised power between the variable geometry and the fixed geometry clearly shows that a large benefit in annualised power is lost when a twist is fixed at one design wind speed.

Most of the lost on beneficial torque is due to fact that the blade tip region fails to achieve the required lift distribution at the off design condition (Figure 3-19). It is also clear that the optimum lift forces required for maximum power production is not achieved at the blade root, this is more profound when it is compared with the ideal lift coefficient (Figure 3-20). The required lift coefficients for ideal power production at the blade root are unrealistic ($C_L > 3$) due to the current blade chord at this location.

It is clear that the current root geometry of the NREL 5MW rotor requires a redesign. Effectively the current root geometry acts as a larger hub area with neutral torque contribution. The cylindrical root is necessary for structural needs, however if the cylinders are able to generate lift forces, the efficiency will increase significantly i.e. a rotating cylinder.

Another method to improve the root is to design the root sections with a larger chord, thus the required optimum lift forces can be achieved with realistic low lift coefficients. This approach is commonly implemented for the ENERCON [49] wind turbines such as the ENERCON E-70 E4 (Figure 3-21).

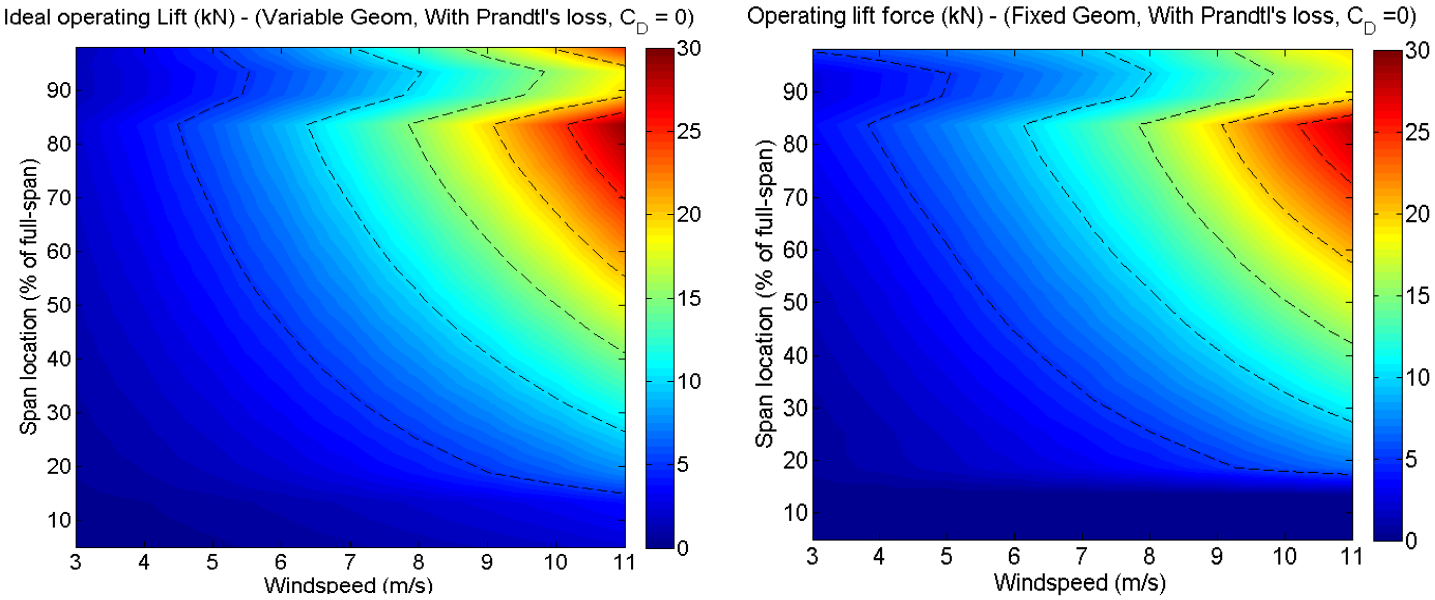

Figure 3-19: Lift force comparison between ideal variable NREL 5MW rotor (left) and the fixed geometry NREL 5MW rotor (right)

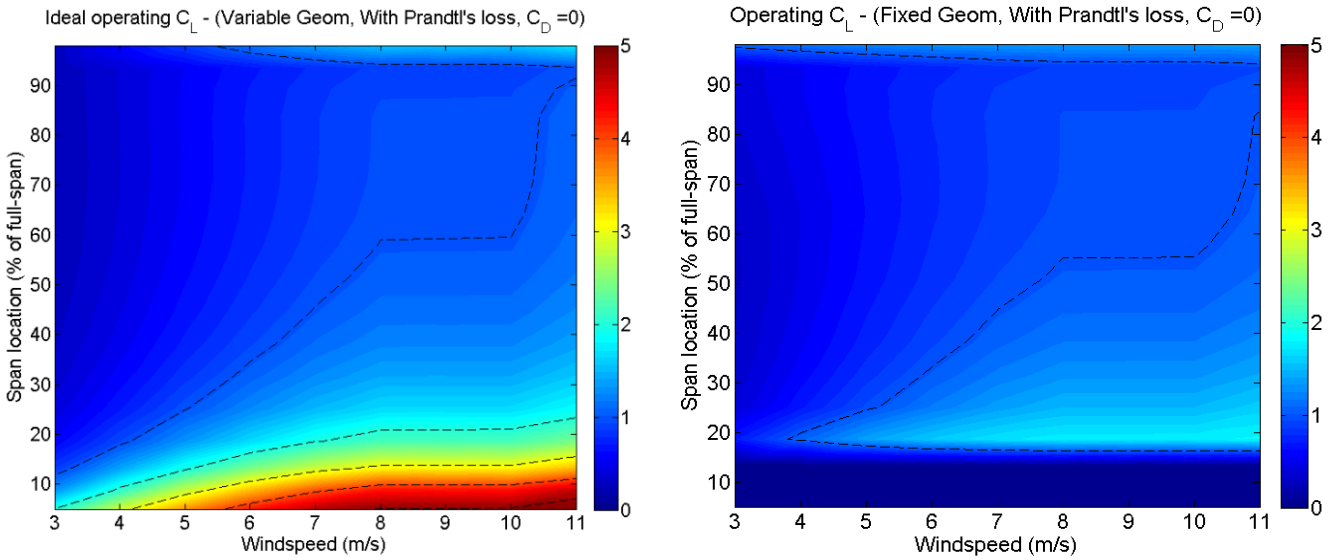

Figure 3-20: Lift coefficient comparison between ideal variable NREL 5MW rotor (left) and the fixed geometry NREL 5MW rotor (right)

Figure 3-21 Airfoil shaped root section adapted for ENERCON E-70 E4 rotor [49]

3.1.4.2 Analysis of the NREL 5MW rotor with drag forces

The previous analysis was conducted without the effect of drag forces to evaluate the ideal power output, which is not practical in the real world. This part of the report will present the work done to optimise the twist for a fixed geometry NREL 5MW. By accounting for the drag force generated at the point of optimum lift force a realistic potential torque production is determined. Comparison between the previous study and this study will help to determine the effect of drag in the twist optimisation method as well as the impact on the power production.

The twist optimisation algorithm, changes the local angle of attack to achieve the lift coefficients that corresponds to the optimum axial induction. When the drag forces are considered in the twist optimisation process, the increase in angle of attack to obtain a higher lift coefficient that satisfies the optimum lift force can also increases the drag coefficient. Therefore a forced twist optimisation for the optimum axial induction factor reduces the annual power i.e. the aerodynamic efficiency (L/D) is lower at the angle of attack where the optimum lift coefficient or optimum induction factor is achieved.

Ideal twist for a wind turbine is achieved at the angle of attack when the optimum local lift coefficients are attained at the lowest drag angle of attack: $\alpha\left(C_{L\,(Opt)}\right) = \alpha(\min C_D)$. It is also beneficial for effective power production, if the airfoil section is able to achieve the optimum lift coefficient at the point of its maximum aerodynamic efficiency or lower: $(\alpha\left(C_{L\,(Opt)}\right) \leq \alpha\ (\max(L/D))$.

The baseline optimisation algorithm forces the calculation to achieve the maximum power output at the design point using the prescribed ideal axial induction factor without considering the drag effect on the annual power production. For this reason, each radial segment of the blade is individually optimised for its maximum torque production using the prescribed optimum axial induction factor as the basis. Then the optimum twist distribution of the blade is determined at the rotor's maximum annual power production (Figure 3-22). This method significantly restricts the ability to achieve the ideal induction factor for the design point. However it finds a twist distribution that achieves the maximum annual output of the turbine. This method of twist optimisation also address the off design power degradation when the blade twist is strictly optimised for a single design point wind speed.

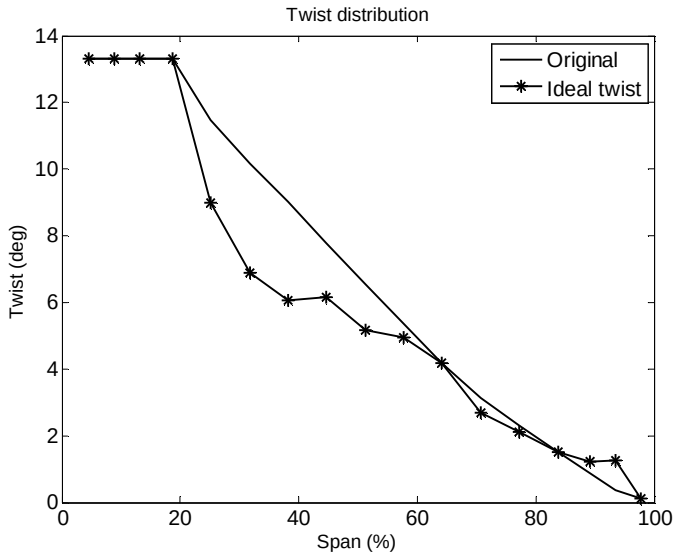

Figure 3-22 Ideal twist distribution based on annualised power for the NREL 5MW rotor when the drag forces are included, Original: NREL 5MW rotor defined in [2]

With this optimised ideal twist distribution (Figure 3-22) the NREL 5MW rotor is able to increase its annual power output by 0.37% (93 kWh) relative to the baseline geometry with the original twist set by NREL [2]. Therefore based on this investigation it is found that including the drag forces reduces the gain in annual output of 0.54% to 0.37%. As expected this ideal twist distribution is able to increase the efficiency of the turbine for all sub-rated wind speeds (Figure 3-23).

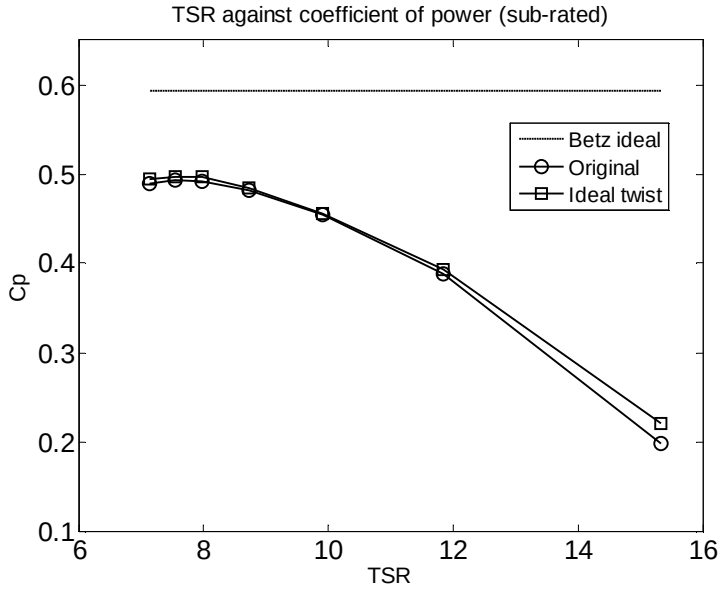

Figure 3-23 Efficiency of the NREL 5MW rotor when drag forces are considered

3.1.5 Twist optimisation methods for a wind turbine

Currently in industry, the twist optimisation is typically carried out using a uniform Betz ideal induction factor of 1/3 for a drag accounted wind turbine that has a fixed twist distribution. This method does not include the effect of non-uniform axial induction factors, off-design power degradation or the effect of drag at the optimum lift conditions.

This part of the thesis presents the comparison between the results from the conventional twist optimisation method and the improved twist optimisation method that has been discussed in this thesis. The improved twist optimisation method takes into account all the effects discussed earlier, which are, the conventional twist optimisation method forces the twist optimisation to achieve a uniform Betz ideal induction factor (a=1/3) without considering these effects. The conventional method optimises the twist for the design point wind speed of 9 m/s, while the improved method optimises twist for the maximum annualised output. By achieving the optimum twist distribution it is possible to attain a better understanding of the different aerodynamics where the PFC device application is fully utilised.

Twist constraints were applied to the section at 20% span, where in was constrained to achieve same twist gradient found for the subsequent sections between the 25-30% span (Figure 3-24, a). Without this twist constraint the conventional twist optimisation method predicted twist gradients that were not practical for the blade's surface. Smooth gradients in twist are required to make it possible for the blade manufacture and to ensure smooth radial curvature distributions.

It is clear that most of the differences in the predicted twist distributions lie on the root and tip part of the blade (Figure 3-24). The improved twist optimisation method's uses a non-uniform ideal induction factor distribution (Figure 3-25) that is based on the inclusion of the effect of blade tip and hub losses, while the conventional method used the uniform Betz optimum axial induction of 1/3, which does not account for the effect of hub and tip losses. This is the reason for the different twist distributions found at these parts of the blade (tip and hub) between the conventional and the improved twist optimisation methods.

The twist convergence for the conventional twist optimisation method used in the industry was assumed to be achieved when the mean residual in the axial induction factor reaches below 1e-04. Due to the applied twist constraint the prescribed optimum axial induction factors are achieved at all point except at the 20% span. The first three elements (span range 5-15%) of the NREL 5MW is defined with non-lifting circular sections and is of no significance to the twist distribution.

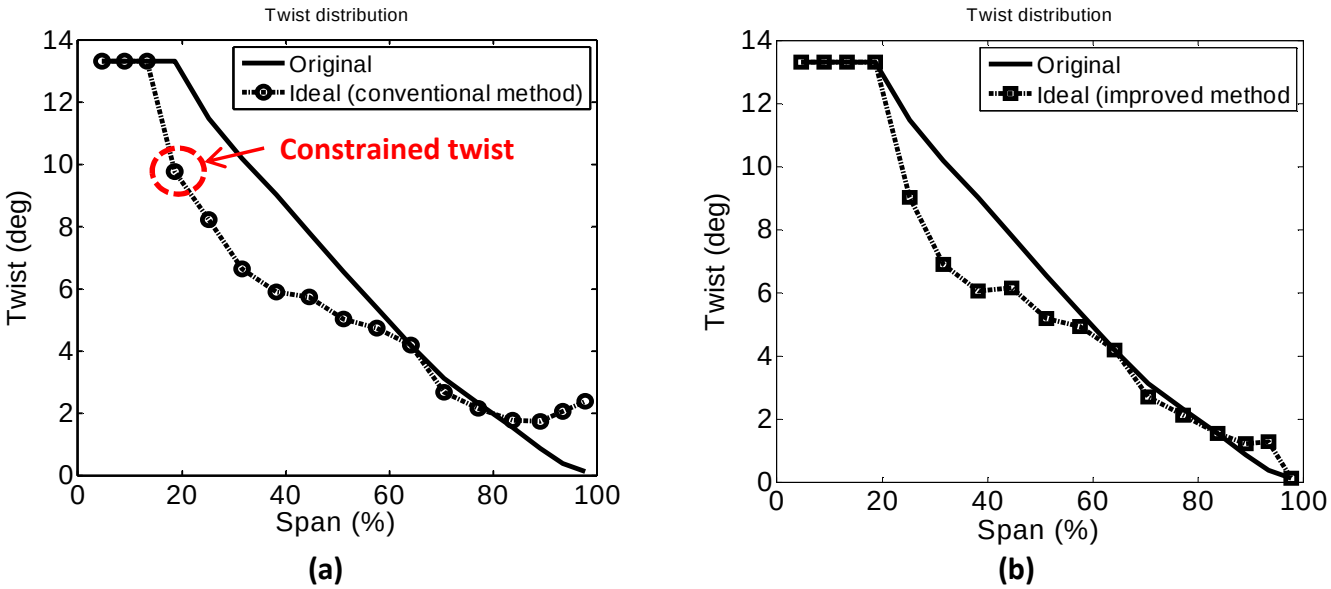

Figure 3-24 Twist distribution comparison between the conventional and the improved twist optimisation methods

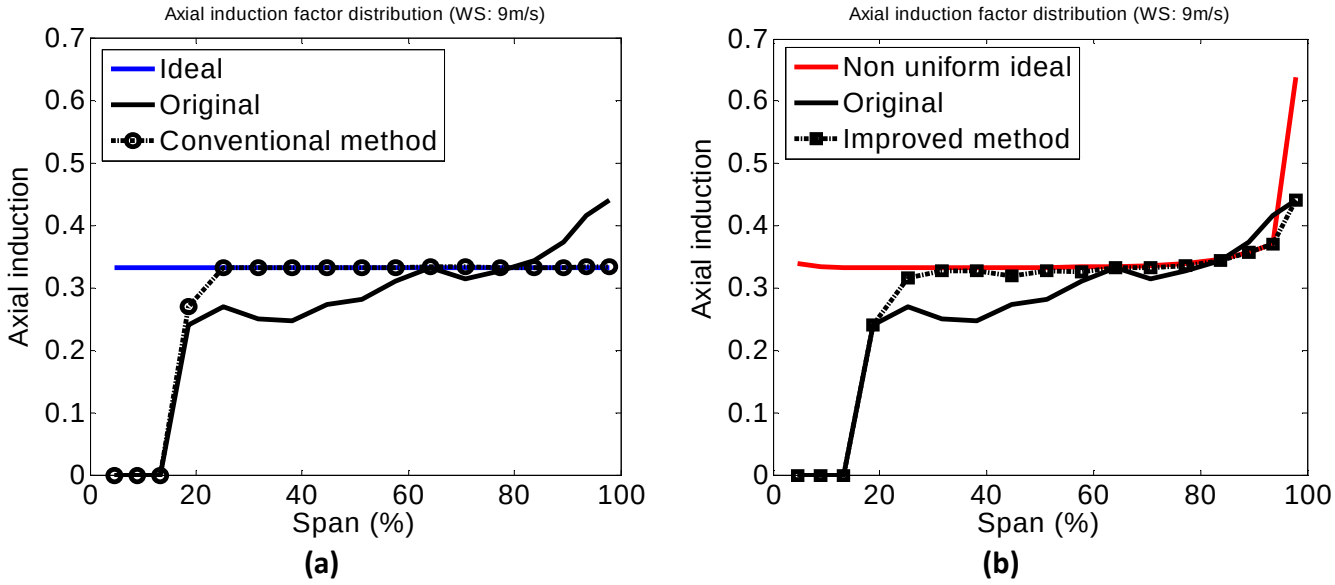

Figure 3-25 Axial induction factor convergence comparison between the conventional and the improved twist optimisation methods, Original: NREL 5MW rotor defined in [2], Ideal: uniform Betz (1/3) induction used in the conventional twist optimisation method, Non uniform ideal: Ideal induction found with the inclusion of hub and tip losses

The results from this study suggest that, by re-twisting the NREL 5MW rotor blades to the twist distribution found using the conventional method, the turbine is able to increase its annual power output by 0.20% (52 kWh). This is slightly lower than the increase in annual power calculated using the improved twist optimisation method (0.37% or 93 kWh).

In conclusion, the improved twist optimisation method is recommended for the twist optimisation process of a wind turbine, specifically when the effects of tip and hub losses are included in the BEM model. This improved optimisation method takes account for the non-uniform axial induction factor distribution that exists for a BEM model with the inclusion of hub and tip losses, the effect of drag, the effect of off-design power degradation

and the maximum annual power output. Whereas the conventional method of optimising the twist for a uniform Betz ideal induction factor without considering these effects, therefore it will not resolve the best twist distribution for maximum power output as shown in this investigation.

3.1.6 Fixed geometry with sub rated pitch regulation

Annual power production of the fixed geometry NREL 5MW with drag forces can be increased by 0.37% when the twist is optimised at the design wind speed. The fixed geometry currently underperforms at the off design wind speeds in comparison with the ideal Cp = 0.59. Pitch regulations at the off design points will increase the efficiency of the turbine at these conditions.

Various pitch angles were tested for each off design wind speeds for maximum power output. The optimum pitch angles found from this study are presented in Table 3-1. The result (Figure 3-26) suggest that the sub-rated pitch regulation increases the efficiency of the turbine at high TSR i.e. the off design conditions.

As expected sub-rated pitch regulation clearly shows improvements to the power production at off design conditions and suggest that by optimising the NREL 5MW rotor blade and regulating the pitch in the sub rated power region the NREL 5MW rotor is able to increase its annual power production of the optimally twisted blades 0.37% to 0.52% relative to the rotor defined by NREL [2].

Wind speed (m/s)	RPM	Original Pitch (^{o})	Optimum Pitch (^{o})
3	6.972	0	2.20
4	7.183	0	2.13
5	7.506	0	1.57
6	7.942	0	0.94
7	8.469	0	0.39
8	9.156	0	0
9	10.296	0	0
10	11.431	0	0
11	11.89	0	0

Table 3-1 Optimum sub-rated pitch angles for the NREL 5MW rotor

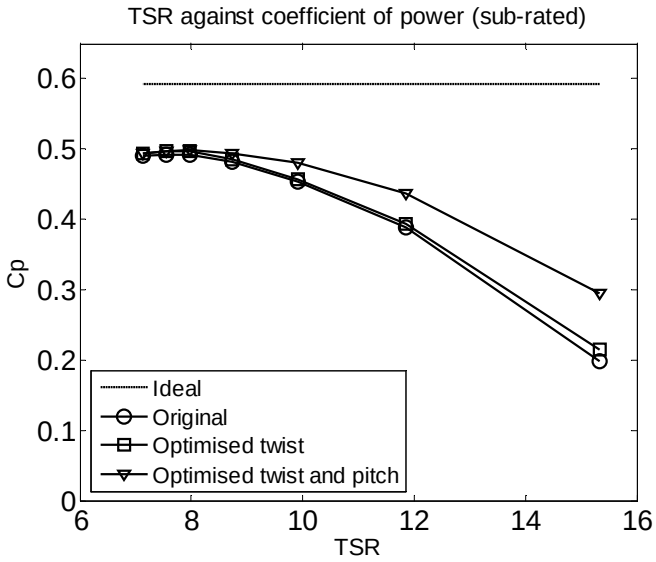

Figure 3-26 Sub-rated pitch regulated NREL 5MW

3.1.7 Conclusion from the ideal NREL 5MW theoretical study

In summary, a small improvement to the NREL 5MW rotor's annual power is practically achievable by re-twisting of the blade due to the need for a fixed geometry. The effect of drag reduces the annual power output, however if sub rated pitch regulation is adapted then additional improvement to the potential power output can be gained. The summary of the improvements and the effect of loss, drag and sub-rated pitch regulation are presented in Table 3-2.

Investigated cases	Practicality	Increase in annual power relative to the original NREL 5MW rotor
Ideal geometry (variable, loss and drag less rotor)	Non realistic	8.46%
Variable, drag less rotor (Cd =0)	Non realistic	5.20%
Fixed , drag less rotor (Cd =0)	Non realistic	0.54%
Fixed rotor	Realistic	0.37%
Fixed rotor with sub-rated pitch regulation	Realistic	0.52%

Table 3-2 Potential benefits by blade re-twisting

This investigation has also revealed that a non-uniform ideal induction factor distribution exists for a BEM model a wind turbine when hub and tip losses are considered. Therefore it is not recommendable using the traditional approach to optimise the blade twist through an uniform Betz axial induction factor.

Factors to be considered when optimising ideal twist of a wind turbine are as follows:

- Non uniform axial induction factor distribution exists for a wind turbine, when the losses at the hub and tip of the turbine are considered.
- The power production at off-design wind speeds deteriorates when optimised for one design wind speed.
- When the blade twist is optimised for a large lift force the drag forces also increases, which reduces the power output.

In summary, a simple method to optimise twist assuming a uniform Betz limit is invalid as the factors mentioned above also play a part in the power production of a wind turbine and should be considered in the twist optimisation algorithm.

It was noticed that due to this change in blade twist, the stall margins for the optimum rotor was reduced by up to 2^{o}, at the highest wind speed of 11m/s within the sub rated power region the stall margin was reduced from the baseline rotor value of 6.34^{o} to 4.64^{o} for the section at 40% of the blade. The stall margin is the difference between the operating angle of attack and the stall angle of attack of the airfoil. Therefore the optimally twisted blade has greater chance of stall than the baseline blade at large wind speeds, nevertheless due to the pitch regulation at 12m/s it is reasonable to assume that the optimally twisted blade will be pitched to a lower AoA before it begins to stall. However this may not be the case for another turbine and it is suggested that the stall margins at the highest wind speed within the sub-rated region should be assessed to gain a practical decision.

With an optimally twisted blade without the drag forces, the current fixed geometry is able to achieve only 0.54% increase in annual power, which then reduces to 0.37% when drag forces are considered. The major reduction in power is due to having a fixed geometry blade, hence the optimum lift forces are not achieved at off-design wind speeds. Thus by using a more complicated pitch control system, at off-design wind speed some of the optimum conditions are attained, which is able to increase the annual power production by 0.52%.

Note, however, that the presented data were obtained without any consideration of the structural aspect of the turbine. It is advisable to evaluate the aero elastic properties of the turbine when the twist is optimised with this non uniform induction factors in order to make a practical judgements.

Based on this BEM study, the possible improvement to the current NREL 5MW blade geometry lies heavily in the root section of the blade. The current non-lifting root geometry does not allow for this part of the blade to achieve the required lift forces for an ideal power production. Adding to the absence of lift forces, it also generates drag forces which reduces the power output for the whole blade.

In summary this investigation has shown that using BEM theory it is possible to arrive at a preliminary design of a wind turbine and assess its aerodynamics. The following part of the thesis will present a case study using this low fidelity method to assess the use of a PFC device.

3.2 Analysis for the potential reduction in rotor chord

Based on the ideal wind turbine analysis (section 3.1.4), the integration of a PFC device can help to attain the optimum lift forces at a smaller angle of attack or helps to reduce the local blade chord, where aerodynamic benefits due to the PFC devices are used to alleviate blade structural loads (chord reduction). Thus, an initial study was conducted to assess the benefits of using a vane vortex generator (VG) and passive air jet vortex generator (PAJVG) for a wind turbine and will form a basis for future comparisons with other flow control methods. This study is based on blade element momentum (BEM) theory. Aero elastic

simulations using the NREL FAST method were performed to gain an initial understanding of the structural benefit these reductions in blade chord offers.

Corten claimed that a 20% chord reductions are possible by using vortex generators. It was estimated that this could contributes to a 2.6% reduction in the cost of the turbine [11]. It is also claimed there are many benefits due to the integration of VGs with the rotor. These benefits include increase of yield, less sensitivity to blade contamination, potential load reduction up to 5% and higher cut out speed. Although Corten proposed these benefits, a systematic analysis to support these points was not presented or proposed. Consequently, this initial study was conducted to evaluate these claims.

Initially the changes in lift and drag coefficients due to vortex generator were determined from an experimental database [12]. These changes in lift and drag from the measurements were used to systematically modify the NREL baseline rotor airfoil polar, which results in the modified aerodynamic polars which accounts for the VG integration. The changes in lift and drag coefficients from the measurements were mapped to the airfoils present on the baseline rotor using the angle of attack of the maximum lift coefficient, $C_{l(\max)}$ as the reference point (Figure 3-27).

It should be noted that this is an initial assessment to quantify the benefits that VG installation delivers for a wind turbine. Thus many assumptions are applied to this study such as the VG performance (changes in lift and drag) is the same for every airfoil present on the baseline rotor regardless of the Reynolds number or geometry change. In general, where there was some uncertainty, optimistic assumptions were made to ensure that the outcome would be identifying an upper limit of the possible benefits. This investigation was conducted for the design wind speed of 9 m/s and the effect of chord reduction on the off design condition has not been analysed.

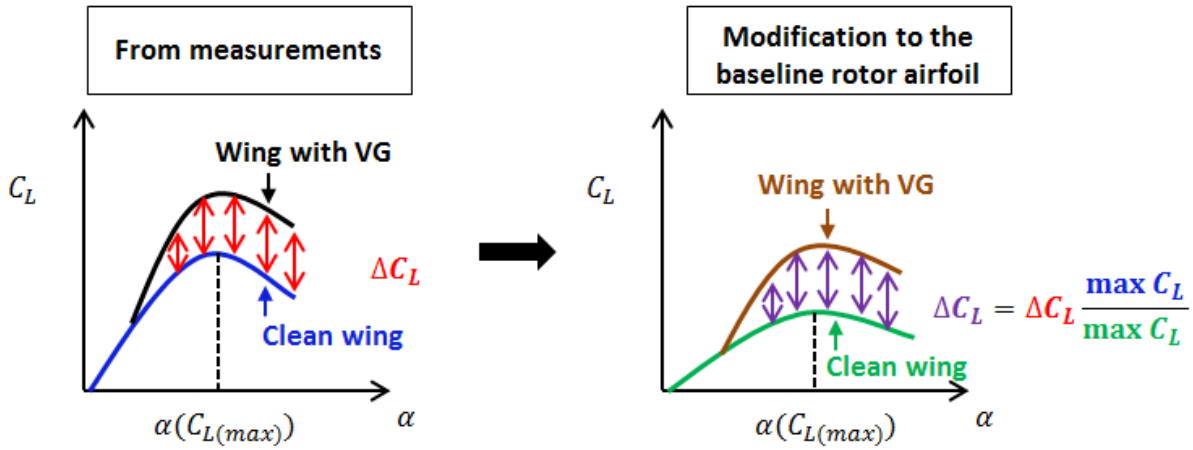

Figure 3-27 Systematic mapping of the changes in lift due to a VG, left: data from measurements, right: modification made to the rotor airfoil

As discussed in section 3.1, an ideal operation of a wind turbine is attained by the achievement of the optimum lift and drag forces. If the wing is able to generate more than the required lift forces by means of a passive flow control device such as a vortex generator (VG) and passive air jet vortex generators (PAJVG), the excess lift can be used to reduce the

blade chord i.e. the required lift forces are achieved with higher lift coefficient and smaller chord. The ratio between the excess lift forces to the ideal lift (Figure 3-28) is the potential available reduction in blade chord (ChordR). After the achievement of the ideal lift forces, any benefits in the lift forces are converted to chord reduction benefits. Thus the power production after the achievement of the ideal lift forces is dominated only by the changes in drag forces.

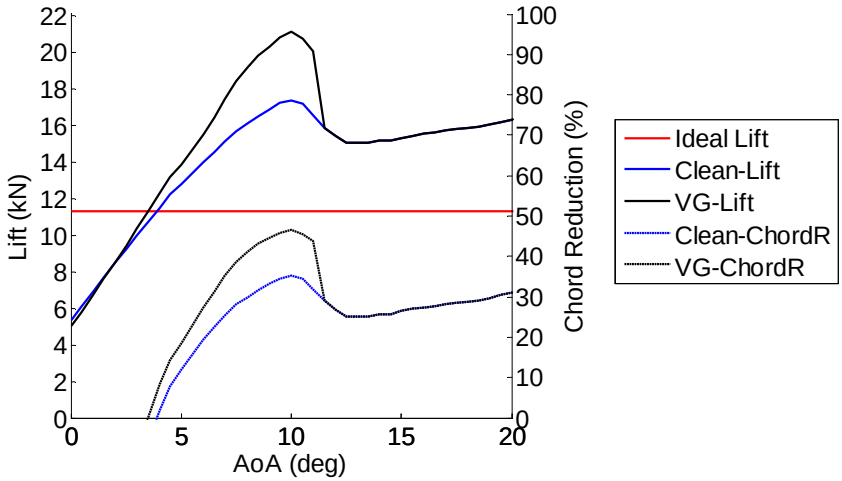

Figure 3-28 Potential chord reduction (ChordR) at 40% span location

Large drag coefficients exist at higher angles of attack, which is required to achieve a large lift coefficient for the optimum lift forces to be used with the reduced chord. Due to the lack of drag data, only the lift and drag changes within the AoA range of 0 – 15^{o} are used for this investigation (Figure 3-29 and Figure 3-30). The benefits of VGs are that they are able to increase the lift coefficients without changing the angle of attack where the maximum C_L is achieved. Therefore a large lift coefficient is achieved with low drag forces compared to a clean wing at the maximum lift condition. It is also able to reduce drag close to the pre-stall condition, this reduction in drag at these excess lift conditions increases the power output (torque) of the turbine relative to the clean blade (Figure 3-31), where large chord reduction up to 40% are possible.

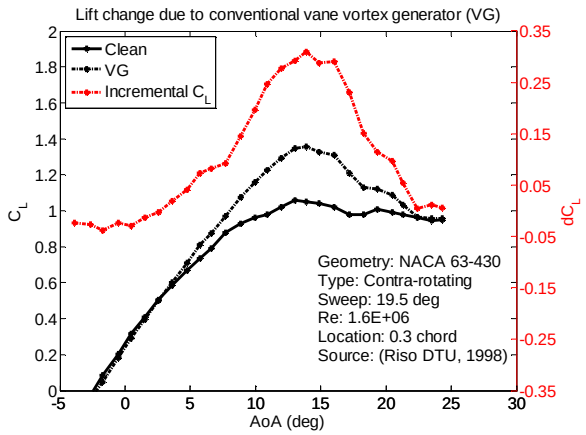

Figure 3-29 Changes in lift due to VG implementation

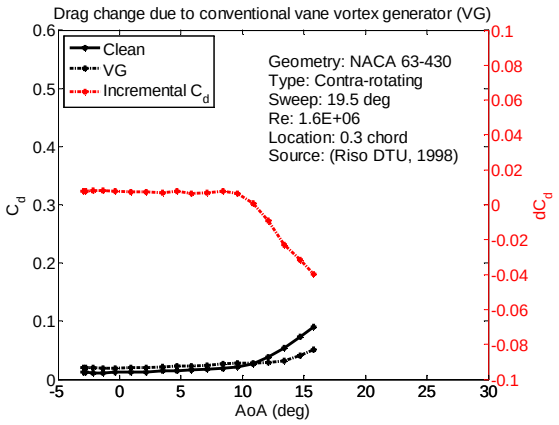

Figure 3-30 Changes in drag due to VG implementation

Large reductions in the blade chord without compromising the power production are only possible when the section is made to operate at large angle of attack (Figure 3-31, red line). This increase in angle of attack increases the chance of blade stall for the wind turbine rotor i.e. the section with a small stall margin is more likely to stall at larger wind speeds. When VGs are used to reduce the chord, the stall margin for the section at 40% span is significantly reduced from the baseline stall margin of 13^{o} to 3^{o}. Therefore it was decided that a reasonable 5^{o} stall margin was to be maintained for all the section at the design wind speed operation. When this is applied (Figure 3-31, green line), it is clear that it is not possible to reduce chord with VGs without comprising the power output (reduced torque relative to current blade).

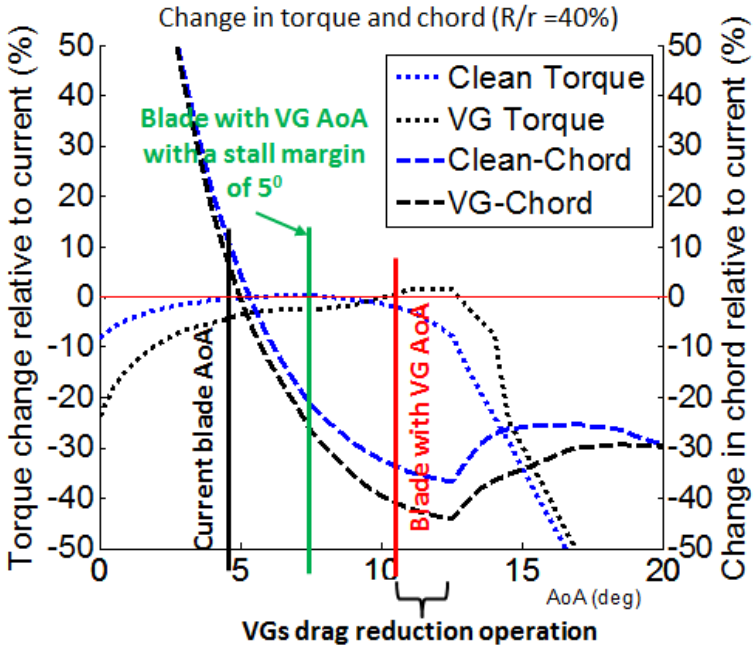

Figure 3-31 Change in torque, thrust and chord at 40% blade span for the NREL 5MW rotor with (VG) and without (Clean) VG

To simplify the aero elastic calculation it was decided to maintain the same the thickness (t) of the blade as the baseline rotor, while the chord (c) is reduced. This increases the relative thickness (t/c) of the profile, which subsequently creates additional drag. This drag force is modelled using a simple equation found from the work done on NACA airfoils [50]. The relative change to the minimum drag coefficient was determined from this relationship (Eqn 30) and added to the modified polars. This added drag reduces the torque production of the VG installed blade (Figure 3-32).

$$C_{d0} = 0.007 + 0.025\ (\mathrm{t/c}) \quad 0.06 < (\mathrm{t/c}) < 0.24 \qquad \text{Eqn 30}$$

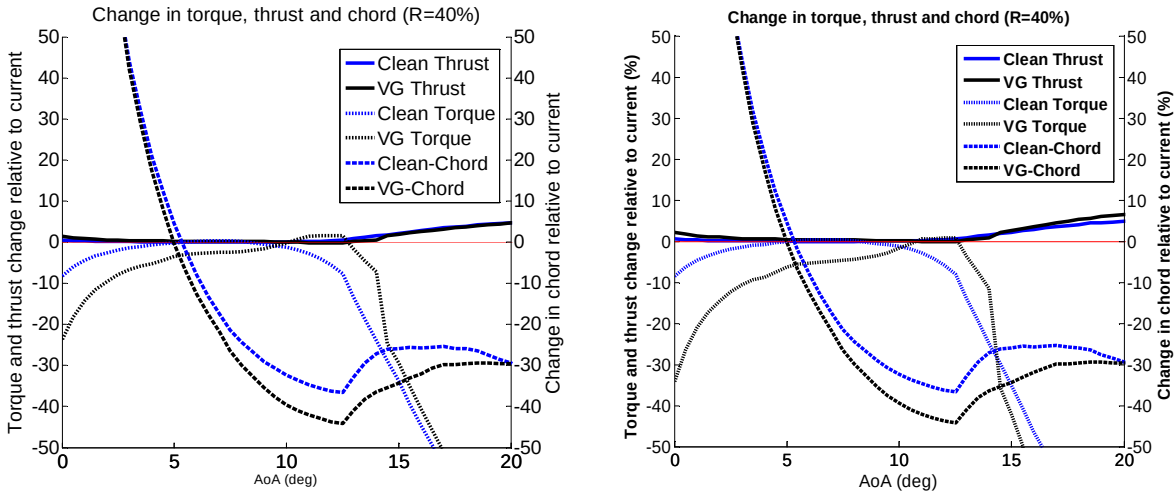

Figure 3-32 Change in torque, thrust and chord at 40% blade span, with (left) and without (right) the increase in drag due to the increased (t/c)

The passive air jet VGs poses a greater advantage when used to reduce blade chord. The benefits of PAJVGs are that they have low drag penalty (dCd = 0.01) at the pre stall condition and that they increase the stall angle of attack by up to 10^{o} (Figure 3-33, Figure 3-34) and therefore they have wider range of operation while providing modest level of chord reduction due (20%) to their modest level of lift increment (20%).

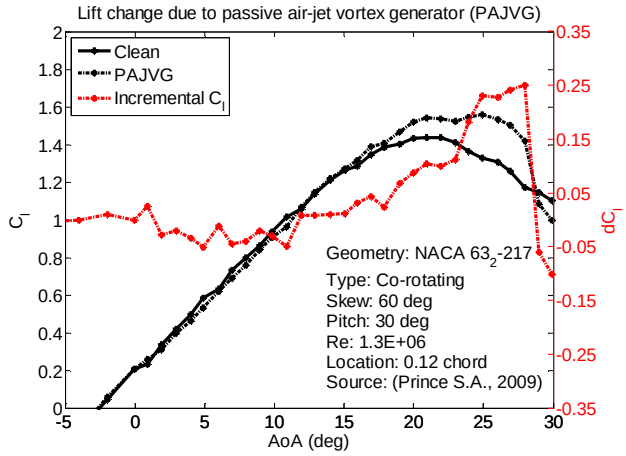

Figure 3-33 Changes in lift due to PAJVG implementation

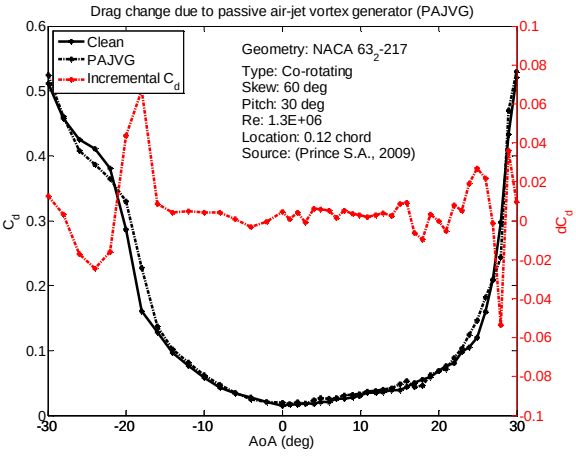

Figure 3-34 Changes in drag due to PAJVG implementation

The benefit of using PAJVGs for chord reduction is seen especially for the section at 58% span, where the drag penalty due to the vane VG does not allow it to generate the baseline torque production even at large angle of attack. The PAJVG is able to achieve a considerable amount of chord reduction up to 20% while satisfying the 5^{o} stall margin.

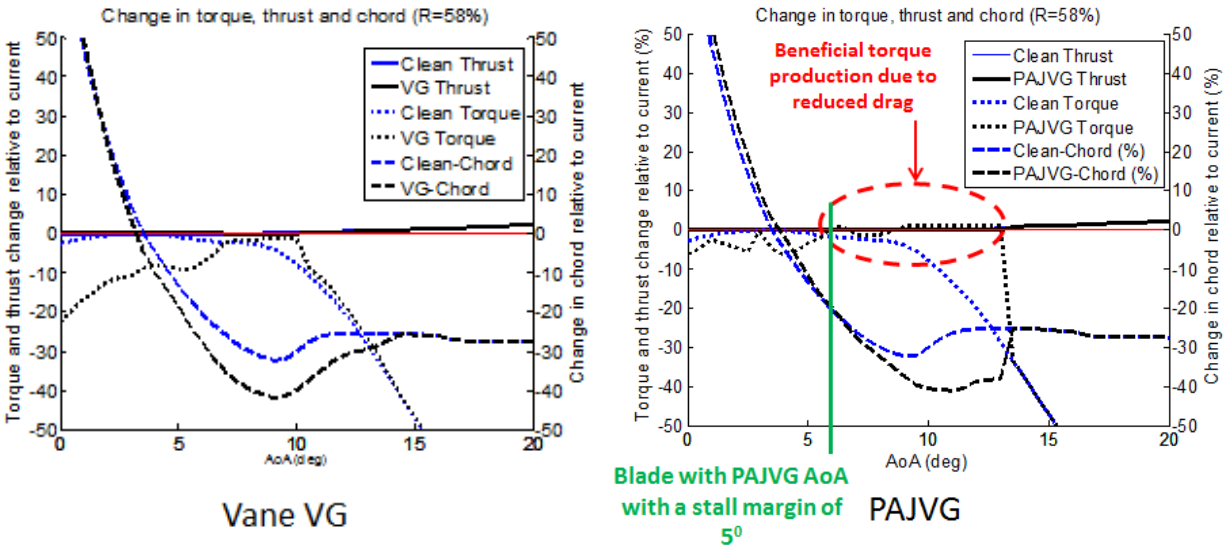

Figure 3-35 Change in torque, thrust and chord at 58% blade span, with vane VG(left) and with PAJVG (right)

The result (Table 3-3) from this analysis suggests the large chord reductions offered by the vane VGs cannot be utilised due to the drag penalty (reduced torque) and the inability to increase the stall AoA. For this example, the vane VGs are only applicable at 19% span with a chord reduction of 1.4%. The PAJVGs provide a moderate chord reduction without the compromise on the power output. It was found that the PAJVGs are beneficial within the span range of 25-30% and 60-65% with a chord reduction up to 20%.

		Δ Torque (%)		Δ Chord (%)		α_{oper} (°)		$\alpha_{Cl_{max}} - \alpha_{oper}$ [°]	
	Span (%)	**PAJVG**	**VG**	**PAJVG**	**VG**	**PAJVG**	**VG**	**PAJVG**	**VG**
Vane VG	**19**	0.00	0.00	1.55	-1.37	13.03	12.91	26.97	22.08
	25	0.00	-2.61	-2.20	-5.79	9.00	8.50	7.00	5.00
	32	0.00	-3.38	-15.18	-21.59	8.41	8.50	7.59	5.00
PAJVG	**38**	-0.71	-4.76	-20.95	-26.38	7.50	7.50	5.00	5.00
	45	-1.94	-7.68	-15.57	-13.53	6.00	5.00	5.00	5.00
	51	-2.31	-9.05	-18.85	-16.89	6.00	5.00	5.00	5.00
	58	0.00	-12.22	-19.09	-9.99	5.90	4.00	5.10	5.00
	64	0.00	-14.01	-18.61	-9.45	5.91	4.00	5.09	5.00
	71	-1.14	-16.43	-30.72	-34.67	9.00	8.50	7.50	5.00
	77	-1.26	-18.23	-29.89	-33.88	9.00	8.50	7.50	5.00
	84	-1.39	-20.25	-28.72	-32.78	9.00	8.50	7.50	5.00
	89	-1.55	-22.66	-28.20	-32.29	9.00	8.50	7.50	5.00
	93	-1.78	-25.88	-29.02	-33.07	9.00	8.50	7.50	5.00
	98	-1.98	-28.74	-30.18	-34.16	9.00	8.50	7.50	5.00

Detrimental

Beneficial

Table 3-3 Chord reduction results using vane VGs and PAJVG for the NREL 5MW rotor, red dashed box indicate the vane VGs applicable location and the red dashed box indicate the vane PAJVGs applicable location

3.2.1 Aero-elastic load analysis for the reduction in blade chord using PAJVGs

Using this chord reduction found using the PAJVGs an aero elastic simulation was performed for the extreme load case 1.6 (Table 3-4). The relative change in maximum a flap wise root moments was selected to assess the benefits of blade chord reduction.

DLC 1.6: Power production, extreme fifty year operating gust	
Analysis	Extreme
Wind model	EOG_{50} (50year extreme operating gust)
Wind speed [m/s]	11.5, 13, 15.5, 25
Yaw misalignment [^{o}]	-8, 0, 8
Variation of the azimuth [^{o}]	0, 30, 60, 90

Table 3-4 Extreme load case DLC 1.6, conditions

Based on this calculation it was found that a maximum reduction of 2.5% in the max flap-wise moment is achieved at a large wind speed of 25m/s. The overall results suggests that the PAJVG implementation helps to reduce chord, however for the NREL 5MW rotor the effective changes in cost and structural impact seems to be insignificant compared to the challenges in integrating the PAJVGs to the blade. It is also noted that the implemented changes in twist and chord for this load evaluation study (Figure 3-36) are not realistic in terms of surface fitting and the manufacturing process. However it is noted that better benefits may be achieved for another rotor, using PFC to reduce blade chord.

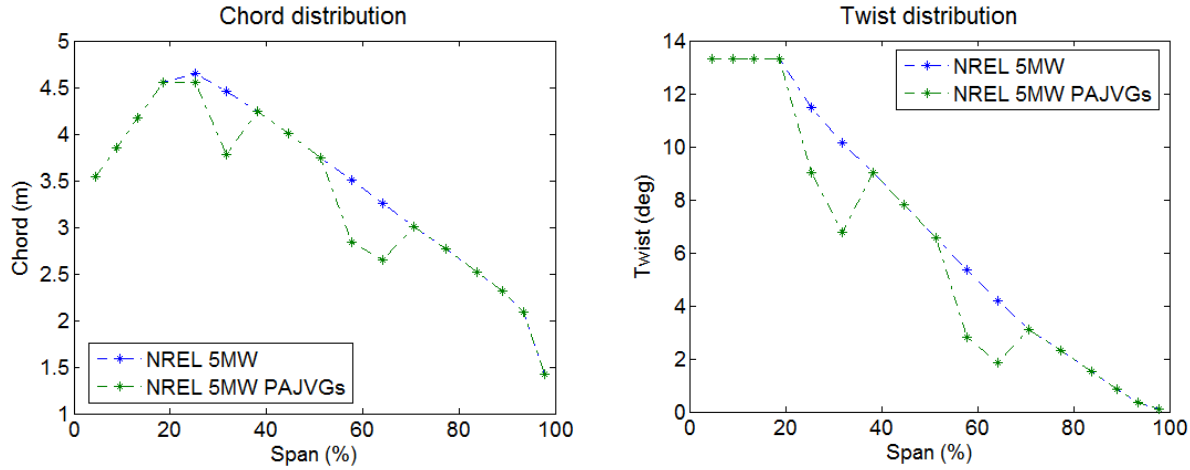

Figure 3-36 Change in chord (left) and twist (right) distribution due to the VG integration

3.2.2 Summary and conclusion of the chord reduction analysis

An initial study was conducted to assess the benefits of using vane or passive air-jet vortex generator (PAJVG) for wind turbines. The changes in lift and drag coefficients due to vane and passive air-jet vortex generator (PAJVG) were determined from Riso DTU [12] and Prince et al's experimental work [22] respectively. These changes were systematically used to modify the NREL baseline rotor airfoils lift-drag polar.

The vane VGs were found to offer larger a reduction in blade chord reduction than PAJVGs, due to their large lift increments. However it also has a higher drag penalty relative to PAJVGs which doesn't allow for a reduction in chord without the reduction in torque (power). The benefits in L/D ratio due to the use of vane VGs are achieved at a higher angle

of attack, which means the blade can operate at higher angle of attack and thereby reduce chord. However, this reduces the stall margin required for safe blade operation. In contrast the PAJVGs not only offer lower drag operation but it seems to increase the stall angle of attack of the airfoil. Therefore it is possible to operate at a higher angle of attack and achieve chord reduction without any compromise on power or stall the margin using PAJVGs. Even so it is recommended that further investigation should be conducted before considering blade chord reductions using PAJVGs.

3.3 Summary of the theoretical analysis of a wind turbine

Using blade element momentum (BEM) theory the aerodynamic requirements for an ideal wind turbine has been determined. Numerous studies were conducted to evaluate the effect of ideal geometry, drag forces and twist optimisation for a wind turbine. An improvement to the conventional twist optimisation method used in the industry has been identified and its benefits are quantified.

Overall, based on this investigation it was found that outboard section of the blades can be optimally twisted to attain the ideal condition for optimum rotor power, however the major inefficiency in rotor power was identified due to the root design of the NREL 5MW rotor. The current root design is not able to achieve the ideal power production conditions due to its lack of lift production. This is where a PFC device can help to improve or attain the lift production of the blade root.

A separate BEM study conducted to assess the use of PFC devices to reduce blade chord which in return reduces structural loads. Based on this investigation it was found that PAJVGs offer notable reduction in chord up to 20% while able to maintain a safe stall margin. However for the NREL 5MW rotor, it has been identified that the reduction in loads due to the reduction is chord is insignificant. Nevertheless it has been established that a positive benefit exists for PAJVGs to be used as a chord reduction device to reduce blade loads at the extreme conditions.

4 CFD methodology

4.1 Introduction

There are various steps that have to be undertaken to establish the confidence level of the results from a CFD simulation. This chapter will present and discuss the methodology developed for the CFD analyses used within this study. Initially the description of the flow solver is presented then after that, the turbulence modelling will be discussed. Next the gridding approaches for the 2D and 3D CFD methods are presented. It is vital to attain a CFD model that calculates a credible result. Various studies were performed to assess the credibility of the results from the CFD model, which are also presented in their corresponding subsections in the 2D and 3D CFD sections of this chapter. These studies are presented as most comprehensive open source testing of CFD for a wind turbine.

4.1.1 Flow solver

For all the simulations conducted for this research project the implicit CFD flow solver Ansys CFX was used. Based on Ansys' recommendations [51] to reduce numerical diffusion, all the simulations conducted in this research were performed using the 'High Resolution' advection scheme. This setting varies the blend factor for the variable gradient throughout the domain i.e. for the flow regions with low variable gradient it assumes a blend factor of 1.0 and where there is a large gradient in the flow variable it assumes a blend factor of 0.0 in order to prevent overshoots and undershoots and to maintain robustness of the calculation [51]. Simulations were conducted in an incompressible adiabatic environment. In this work it is assumed that the solid geometry immersed in the fluid is a rigid body and has no effect of structural impact due to the fluid.

4.1.2 Turbulence and transitional modelling

Turbulence modelling is one of the important steps taken to achieve a credible CFD solution that agrees well with the experimental measurements. This section describes the different approaches and methods to computationally model the turbulent flow characteristics. A closed form solution to the fully turbulent Navier Stokes equations does not exist and computing directly for all scales is computationally expensive. Therefore Reynolds decomposition (RANS) is applied to model the turbulence with a finite degree of freedom [52].

Due to the nature of the decomposition, additional parameters (Reynolds stresses) have to be modelled for the computation of the turbulent flow. There are two types of models to resolve these additional parameters [53]. These are known as first- and second-order models. First order models or eddy viscosity models uses the Boussinesq hypothesis to resolve the Reynolds stresses and fluxes, which models only the isotropic turbulence. The first order model includes one and two equation models, i.e. the number of transport equation used to model the Reynolds stresses [53].

Second-order models compute the Reynolds stresses and fluxes directly from the governing equations. This model does not assume the eddy viscosity hypothesis, which means that it has better resolution when solving the anisotropic behaviour of the turbulent flow. This

uses individual transport equations for each Reynolds stresses, hence a large number (7) of partial differential equations are used to resolve the flow. Examples of the second order models include the Algebraic Stress Model (ASM) and Reynolds Stress Model (RSM).

Ansys CFX used in this study offers a variety of turbulence models. The models chosen for this study are:

- First order models
    - Two equation models
        - RNG κ-ε [54]
        - κ -ω (Wilcox model) [55]
        - BSL (Baseline κ -ω model) [56]
        - κ -ω SST (Menter's model) [57]
        - κ -ω SST Transitional
            - Gamma, γ [58]
            - Gamma theta, γ-θ [58]
- Second order model
    - Speziale, Sarker and Gatski's (SSG) Reynolds stress model [59]

In total, seven turbulence models were tested for their ability to calculate a solution that agrees well with the measurements. A brief description of the chosen turbulence model will be presented in the following part of this section. This will also discuss some of the use for these turbulence models.

4.1.2.1 RNG K-Epsilon (κ-ε)

This model is derived from the standard κ-ε model, using the Re-Normalisation Group (RNG) method which was proposed by Yakhot et al [54]. This statistical mechanical approach in conjunction with a limited assumption regarding the statistics of the small-scale turbulence, provide a rigorous basis for the extension of eddy viscosity models. This helps to represents the small scale turbulence by means of a random forcing function in the Navier-stokes equation, in other words it removes the small scales of motion from the governing equations and modifies the effect in terms of large scale motions and modified viscosity. Versteeg [52] reports that this model out performs the standard κ-ε model for expanding flow, however it performs worse for a contracting duct with the same area ratio.

4.1.2.2 K-ω (Wilcox model)

The k- ω model was proposed by Wilcox [55], where the kinematic viscosity is expressed as the product of a velocity scale and a length scale. This model uses the turbulence frequency ($\omega = \varepsilon/\kappa$) as a second variable. The main advantage of this model is that it does not require a wall damping functions in low Reynolds number flows. This model sets the turbulent kinetic energy (κ) to be zero at the walls and models the infinite frequency with a hyperbolic function. The disadvantage of this model is observed when the turbulence frequency approaches zero (in free stream), where the eddy viscosity term ($\mu_t = \rho\kappa/\omega$) results in infinity. Therefore a non-zero ω is specified in the free-stream, unfortunately the model tends to depend on these assumed values of ω, which poses a problem for an

external aerodynamic calculation [52]. Free stream boundary conditions are used as a matter of routine for external aerodynamic computations.

4.1.2.3 Baseline κ -ω model (BSL)

The BSL model in CFX addresses the problem with the original Wilcox's κ-ω, where the model highly depends on the assumed ω in the free stream. To resolve this issue, Menter proposed a transformation from κ-ε to κ- ω [60] using a blending function to model a κ-ω flow close to the wall and switching to κ-ε in the free stream. In other words, the κ-ω formulation will be used to model the boundary layer κ-ε to model the flows outside the boundary layer. This method uses the best features of two models and combines them into a one turbulence model. However this model fails to properly predict the onset and amount of separation from smooth surface. [60]

4.1.2.4 Menter's κ -ω shear stress transport model SST

The SST model was developed by Menter based on the BSL model described in section 4.1.2.3 [57]. This turbulence model accounts for the transport of the turbulent shear stress and gives a better prediction of the onset and the amount of flow separation under adverse pressure gradients [57]. The shear stress modelling modifies the eddy viscosity by bounding the turbulent shear stress by a constant turbulent kinetic energy inside the boundary layer [60]. This model combines advantages of the κ-ε and κ- ω models and corrects for onset and flow separation. Overall, the SST turbulence model seems well suited for a strong adverse pressure gradient flow, that generally exist for a high Reynolds number flow at the trailing edge (suction side) of an airfoil [60].

4.1.2.5 Transition modelling with Menter's κ -ω SST (SST γ-θ)

The κ- ω SST γ-θ model is based on two transport equations, one for the turbulent intermittency (γ) and the momentum thickness Reynolds number (θ). This model uses an empirical correlation between the γ and θ by Langtry and Menter [58], which covers the standard bypass transition as well as flows in free stream turbulence environment [60]. Two transitional turbulence models were considered for this research. These are the gamma theta (γ-θ) model and gamma model (γ). The γ-θ model computes the onset intermittency and the transitional momentum thickness Reynolds number using two separate equations, while the γ model requires the onset momentum thickness Reynolds number. It is suggested that the grid must have a y+ value of 1, in order to resolve the laminar and transitional boundary layers correctly [51].

4.1.2.6 Speziale, Sarker and Gatski's (SSG) Reynolds stress model

This is a second order model, where the eddy viscosity hypothesis is not used for the computation. This model is based on transport equation for all components of the Reynolds stress tensors and the dissipation rate (seven equations), i.e. the transport equations are solved for the individual stress components [60]. This model was developed by Speziale, Sarker and Gatski [59], which uses a quadratic relation for the pressure-strain correlation. This is one of the most important terms in the Reynolds stress model, which acts to drive the turbulence towards an isotropic state by redistributing the Reynolds stresses. The exact production terms and inherent modelling of stress anisotropies theoretically makes the Reynolds stress models more suited to complex flows.

4.1.3 Iterative convergence

The convergence of the CFD result was assessed using the RMS residuals of mass, momentum and the integrated forces for the 2D CFD configurations. For the 3D cases the power output of the turbine is monitored to assess convergence. It is assumed that adequate convergence is achieved when all residuals of the continuity equation such as the mass, U, V and W momentum reaches below 1e-04 and the integrated parameters are converged within ±0.5% of the reported values (2D: Figure 4-1, 3D: Figure 4-2). However for the 2D CFD simulation of the post stall characteristics i.e. separated flow conditions at large angle of attack, these convergence criteria was not possible to satisfy hence it was assumed that an acceptable level of convergence was achieved when the residuals reach below 1e-03 and a periodic behaviour is seen within the intergraded force history (Figure 4-3). The final value of the interested parameter is averaged over the last 500 values which achieved within ±0.5% of the reported values for all the simulations conducted.

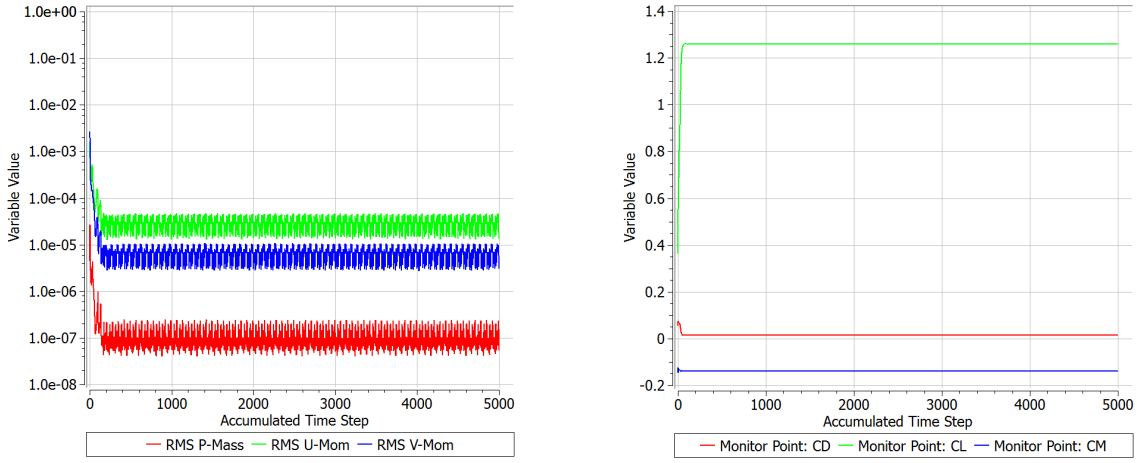

Figure 4-1 Iterative convergence results for 2D CFD, left: residuals convergence, right: integrated force and moment convergence, Airfoil: DU93W210, AoA: 6.7°, Re: 3million, TM: SST γ-θ, CD: coefficient of drag, CL: coefficient of lift, CM: coefficient of pitching moment at 0.25c

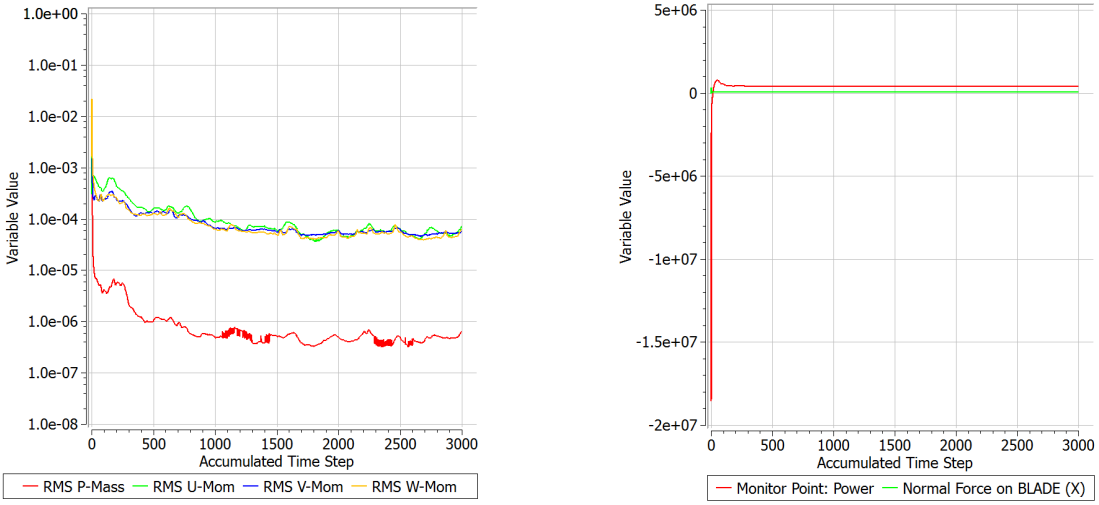

Figure 4-2 Iterative convergence results for 3D CFD, left: residuals convergence, right: rotor power (red line) and thrust (green line), rotor : NREL 5MW, Ws: 5m/s, Omega: , Re: 3million, TM: SST γ-θ

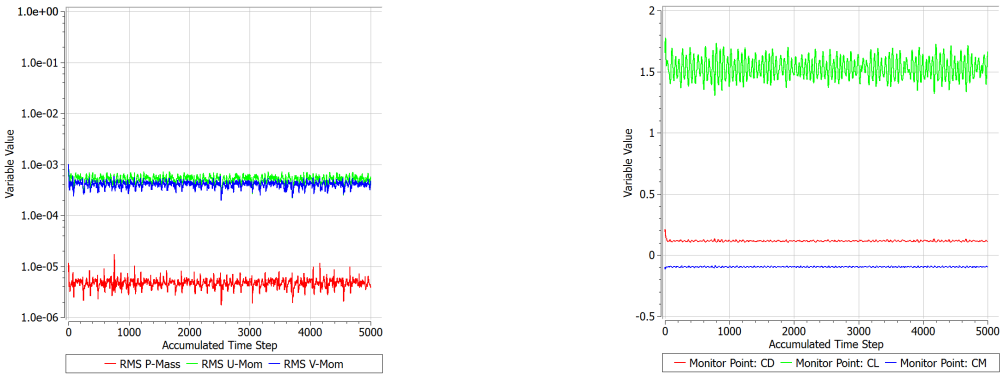

Figure 4-3 Iterative convergence results for 2D CFD, left: residuals convergence, right: integrated force and moment convergence, Airfoil: DU93W210, AoA: 20°, Re: 3million, TM: SST γ-θ, CD: coefficient of drag, CL: coefficient of lift, CM: coefficient of pitching moment at 0.25c

4.2 2D CFD

4.2.1 Introduction

The initial part of the development of the CFD methods for this project is focused on the validation of the prediction tools for the basic 2D airfoil sections that are representative of the airfoils on a wind turbine. This part of the chapter presents the findings and the methods for validating the 2D CFD approach.

The main purpose of this study is to compare the computational results with the experimental findings and to assess the ability of the CFD method to calculate the airfoil flow fields. Validating the computational results against the experimental results determines the uncertainties in the computational model and provides a measure of the confidence on the computational results.

Numerous 2D CFD studies were conducted to assess the quality of the CFD results. The main considerations were:

1. Mesh requirements
2. Turbulence model
3. Domain size

Two separate studies were conducted to establish confidence with the 2D CFD methods. An initial validation study was conducted with the well-known wind turbine airfoil, S809 [61]. This study was vital to gain experience on CFD methods for 2D simulations. Using the knowledge gained from the S809 study, a validation study was also performed using a set of airfoils which are more closely related to the profiles used in the baseline rotor. These airfoils are the DU97W300, DU93W210 and DU91W2250 from the TU Delft University [62].

4.2.2 NREL S809 airfoil study

4.2.2.1 Geometry and available data

The S809 is a sharp trailing edge, 21% thick laminar-flow airfoil (Figure 4-4) design by Somers in the 1989 specifically for wind turbine application [61]. Somers has conducted an experimental study on the S809 airfoil and presented the results in [61]. These experimental results were obtained with a natural transition. These results will be used for this validation

study. Later in 1997 Wolfe has conducted CFD simulations on this geometry [63], which are also used to compare with the CFD results from the current study. Wolfe also validated his CFD results using the measurements from Somers [61]. This will help to determine and compare the improvements in CFD in the past 10 years.

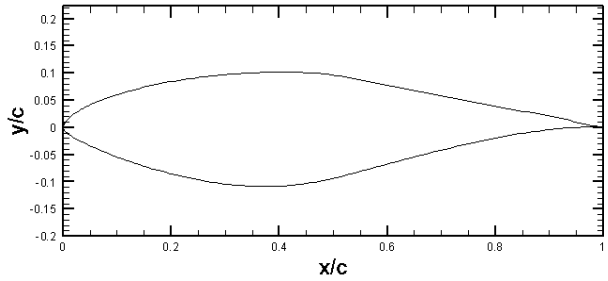

Figure 4-4 S809 geometry

4.2.2.2 Boundary conditions

In order to validate the CFD results, the simulation were conducted at the same flow conditions of the experiments. A quasi 2D simulation is adapted for this study, where the 2D domain is extruded to provide a volume of one cell thickness. For this study, the effect of the mesh resolution was first studied for an initially estimated domain. Following the evaluation of the spatial discretisation requirements, the effect of the domain size was then evaluated. For the initial mesh sensitivity study, the domain extent of ten chord lengths is used to model the boundaries based on Wolfe's CFD study on this airfoil [63]. The schematic of the flow domain and the corresponding boundary conditions are shown in Figure 4-5.

The CFD simulations were conducted to match the chord Reynolds number (Re_c) of the experiment, which is defined as $2x10^6$ [63]. Air at 298 Kelvin was used for the simulation and heat transfer effects were not taken into account (adiabatic). The boundary conditions for the simulation are outlined in Table 4.2-1.

Parameter name	Value
Chord	1m
U_∞ (inlet)	30.9 m/s
Static pressure	101.3 kPa
Static temperature	298K
Density	1.185 kg/m^3
Molecular viscosity	$1.831x10^{-5}$ kg/ms
Reynolds number	$2x10^6$
Mach number	0.09

Table 4.2-1 Boundary conditions

From Somers' test report [61], the hydraulic diameter of the low intensity wind tunnel was 2m, which was used to estimate the turbulence length scale for the current simulations ($l = 0.07d_h$). The length scale was calculated to be 0.14m. Somers also reported that the turbulence intensity varies from 0.02% at 10m/s to 0.04% at 60 m/s, therefore an interpolated value of 0.0284% was for the used free stream flow velocity of 30.9 m/s.

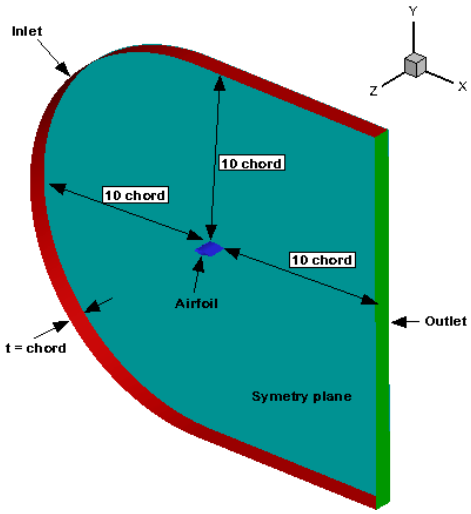

Figure 4-5 Domain schematic showing the quasi 2D C-grid with the boundaries and their extents, Airfoil: S809

4.2.2.3 Domain sensitivity study

The purpose of this study was to determine an appropriate domain size that minimises the influence of the extent of the domain boundaries. Similar to the mesh independence assessment this study was also conducted with three different meshes. The first mesh is identical to the medium mesh (108,800 elements) mentioned in the section 4.2.2.3, where the domain extends 10 chord lengths in all perpendicular directions. The second mesh was constructed using the medium mesh and then the boundaries extended to 20 chord lengths, which results in a total element of 128,708. Likewise the third mesh was generated using the second mesh and extending the boundaries to a 40 chord lengths, which results in a total elements of 171,586. The extensions are shown in different colours (Figure 4-6), i.e. from 10c to 20c in yellow and from 20c to 40c in orange. This study was conducted at an AoA of 1.02° and using the κ- ω SST turbulence model to perform the simulations.

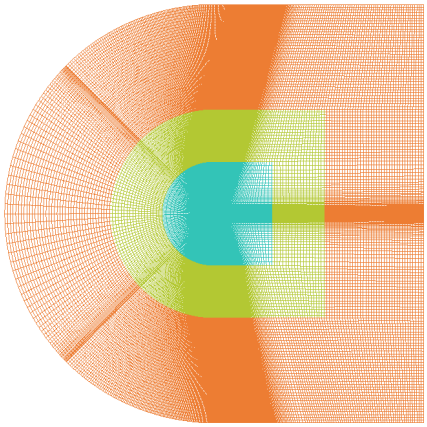

Figure 4-6 Computational domains of 10c (blue), 20c (green) and 40c (orange) for the S809 study

Similar to the mesh refinement study, the surface pressure coefficient distribution from the three simulated grids (10C, 20C and 40C) and the experimental results were compared against each other (Figure 4-7). From this comparison it is noticeable that the size of the domain has very little effect on the surface pressure distribution. The comparison of the integrated forces (Cl, Cd) and pitching moment (Cm) shows in Table 4.2-2 shows that the

domain size has little effect on the interested variables. A maximum difference of 1.2% was found in the drag coefficient between the 40c and the 10c domain extent.

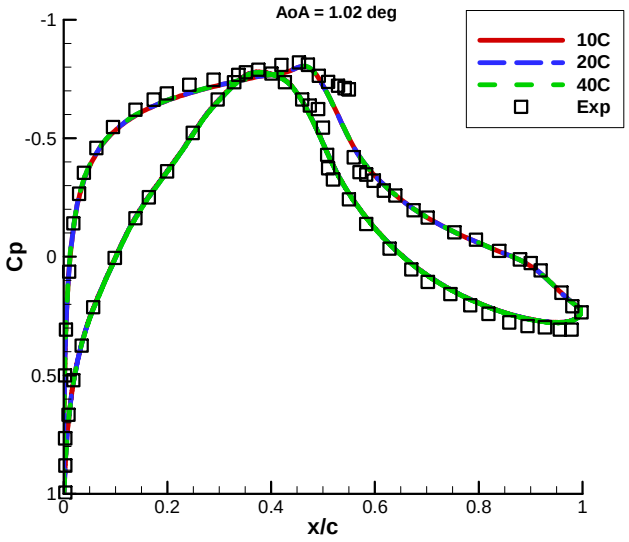

Figure 4-7 Surface distribution for three boundary extended meshes Re: 2million, Geometry: S809, TM: SST γ-θ, Quasi 2D simulation

Domain size (c)	C_L	Difference relative to 40c (%)	C_D	Difference relative to 40c (%)	C_m	Difference relative to 40c (%)
10	0.240025	0.76	0.011968	1.20	-0.03987	0.28
20	0.241854	0.64	0.011824	1.00	-0.03998	0.42
40	0.243419	-	0.011706	-	-0.04014	-

Table 4.2-2 Coefficients of lift, drag and pitching moment for boundary extended meshes

In conclusion, a mesh with a domain boundary extended using 10 chord lengths is adequate for this preliminary 2D CFD study. Therefore the medium mesh with domain boundary extended to 10 chord lengths will be carried forward for the 2D CFD validation study of the S809 airfoil.

4.2.2.4 Mesh refinement study

The mesh refinement will assess if the computational solution is independent of the spatial discretisation. ICEM CFD was used to construct the computational domain and a C-type mesh topology was decided for this 2D CFD study. Three meshes with different mesh density were constructed, which are named coarse (Figure 4-8), medium (Figure 4-10) and fine (Figure 4-11) respectively. The node distribution was concentrated at the leading and trailing edge of the airfoil (Figure 4-9), where large velocity gradients exist. All three meshes were designed to achieve a y+ value of 1. The coarse mesh contained 53,910 elements, the medium mesh contained 108,800 elements and lastly the fine mesh was constructed with 215,640 elements. One element contains two nodes i.e. one node at either side of the extruded volume.

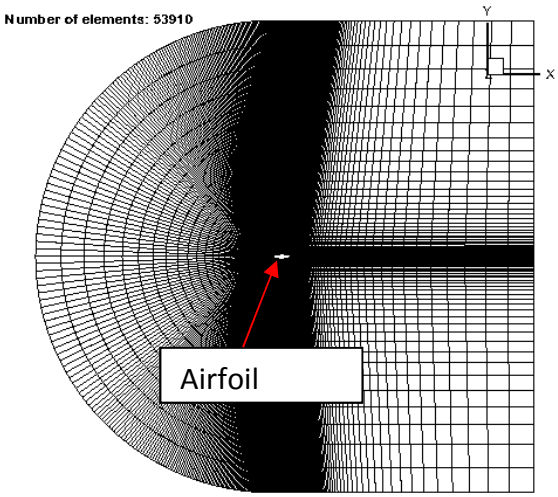

Figure 4-8 Coarse mesh, airfoil: S809, designed for y+ = 1

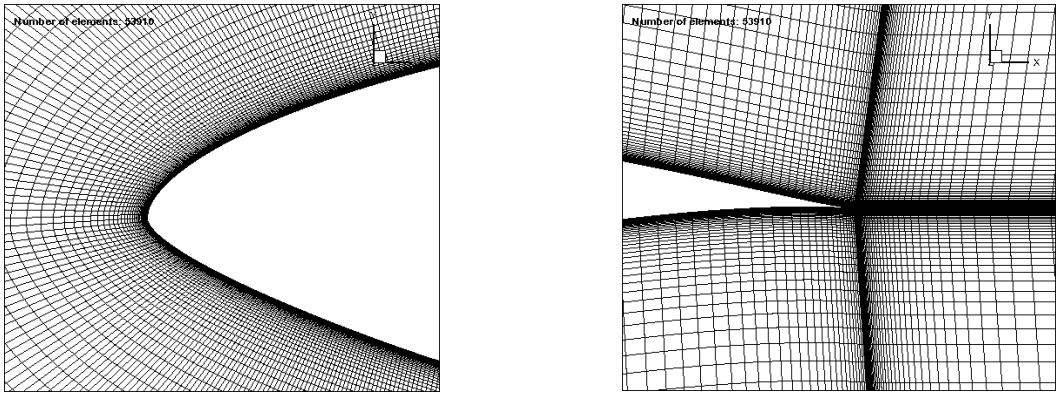

Figure 4-9 Coarse mesh (Left: mesh at the LE, Right: mesh at the TE), airfoil: S809, designed for y+ = 1

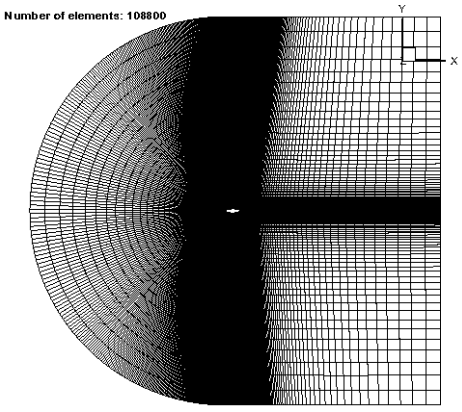

Figure 4-10 Medium mesh Airfoil: airfoil: S809, designed for y+ = 1

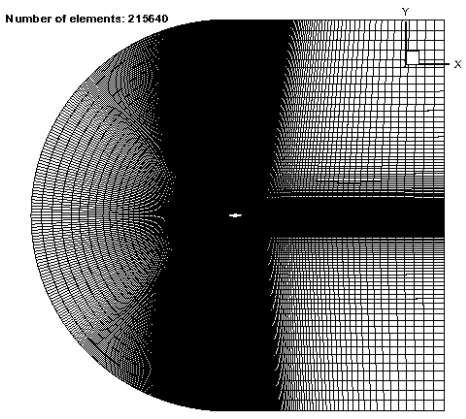

Figure 4-11 Fine mesh, airfoil: S809, designed for y+ = 1

Richardson's extrapolation method [64] (Appendix 8.1) was employed to analyse the effect of the number of elements on the computed solution. The flow simulations were conducted at the 1.02^{o} and 14.24^{o} angle of incidences. The large AoA of 14.24 degree was chosen to study if the different density meshes capture the different flow features which arise at this large angle of attack, such as stall and flow separations. The κ- ω SST turbulence model was used to perform the simulations.

The Cp distribution plot (Figure 4-12 and Figure 4-13) shows that there are only small differences in the distribution for the three meshes. It shows that the calculated Cp distribution is independent of the mesh density. Based on the Richardson's extrapolation method, the results for two different AoA (Table 4.2-3 and Table 4.2-4) using the three meshes results lie in the asymptotic range. The residual discretisation error between the medium and fine mesh for the Cl, Cd and Cm are -1, 2 and -2% respectively, for the large 14.24^{o} AoA. Therefore it is found that a mesh with 100,000 elements is required to provide a solution that achieves an adequate level of mesh independence.

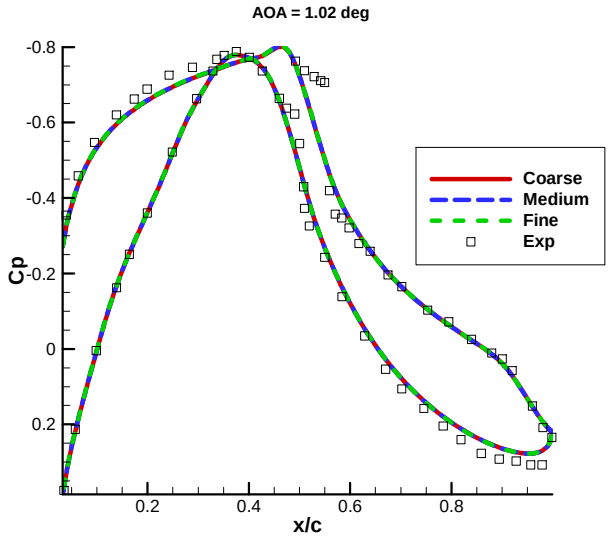

Figure 4-12 Cp distribution at AOA = 1.02 deg, Re: 2million, Geometry: S809, TM: SST γ-θ, Quasi 2D simulation

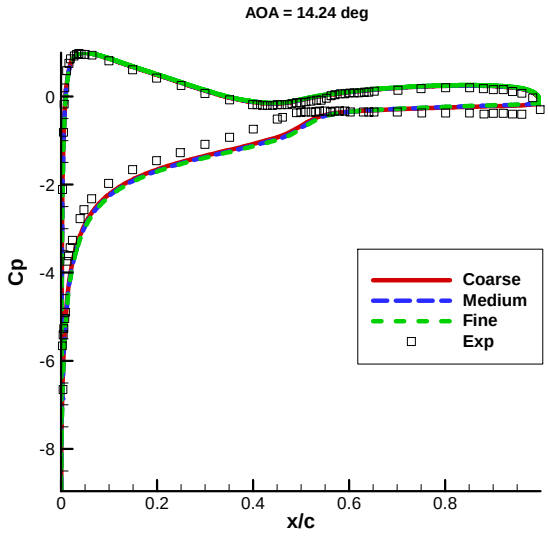

Figure 4-13 Cp distribution at AOA = 14.24 deg Re: 2million, Geometry: S809, TM: SST γ-θ, Quasi 2D simulation

S809 Richardson's extrapolation AoA: 1.02^{o}					
	Coarse	Medium	Fine	Extrapolated	Asymptotic range
No of elements	53910	108800	215640		
C_L	0.2402	0.2405	0.2408	0.24203	**1.0016**
C_d	0.0119	0.0119	0.0118	0.01190	**0.9985**
C_m	-0.0399	-0.0400	-0.0400	-0.04046	**1.0018**

Table 4.2-3 Richardson's extrapolation for S809 airfoil at AoA = 1.02^{o}

S809 Richardson's extrapolation AoA: 14.24^{o}					
	Coarse	Medium	Fine	Extrapolated	Asymptotic range
No of elements	53910	108800	215640		
C_L	1.2808	1.3077	1.3203	1.33135	**1.0210**
C_d	0.0487	0.0460	0.0452	0.04488	**0.9447**
C_m	-0.0426	-0.0430	-0.0438	-0.04215	**1.0095**

Table 4.2-4 Richardson's extrapolation for S809 airfoil at AoA = 14.24^{o}

4.2.2.5 Turbulence model selection

This part of the thesis outlines the methodology undertaken to determine the best suited turbulence model for a CFD studies of a wind turbine. The seven turbulence model described in the section 4.1.2 were used to perform this exercise. The mesh containing 108,800 elements and a domain of 10c was used for this initial study.

Based on the surface pressure distribution for the difference turbulence models (Figure 4-14), it is clear that all the turbulence models capture the flow similar to measurement. The SST γ-θ model seems to perform the best and agrees well with the measured pressure distribution. Somers experiment [61] reported a laminar bubble at about 50% of the chord on the suction and has identified and pointed out its corresponding effect on the experimental surface pressure distribution (Figure 4-14). This effect in pressure distribution is only captured by the SST transitional model.

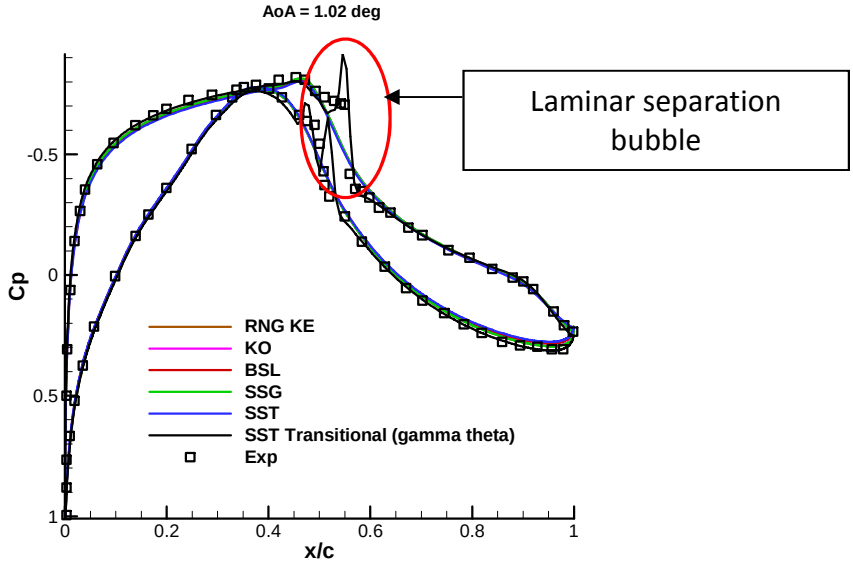

Figure 4-14 : Surface pressure distribution for different turbulence models, airfoil: S809, AoA: 1.02°

For quantifying the differences associated with each model compared with the experimental measurements, a comparison of the coefficient of lift, drag and pitching moment was made (Figure 4-15). The difference was calculated using the Equation (1.5.8.1).

$$Difference = \left(\frac{Experiment - CFD}{Experiment}\right) \times 100 \qquad \text{Equation (1.5.8.1)}$$

The tested turbulence models compute the lift coefficient within an accuracy of 10% (Figure 4-15). The smallest difference of 2% was calculated with the SST γ-θ model. However the drag prediction is poor for all the fully turbulent models with some models reaching a difference of up to 75%. However, there is a notable improvement with the k-w SST transition model where Cd is calculated within 0.6% of the measured value. This result clearly suggests that the SST γ-θ model calculate a solution that agrees well with the experiment. This highlights the importance of modeling transition and its corresponding location for a wind turbine airfoil simulation. In conclusion, these results suggest that the transition modeling is important for an accurate computation of the lift drag and pitching moment, and it is significant in this S809 case.

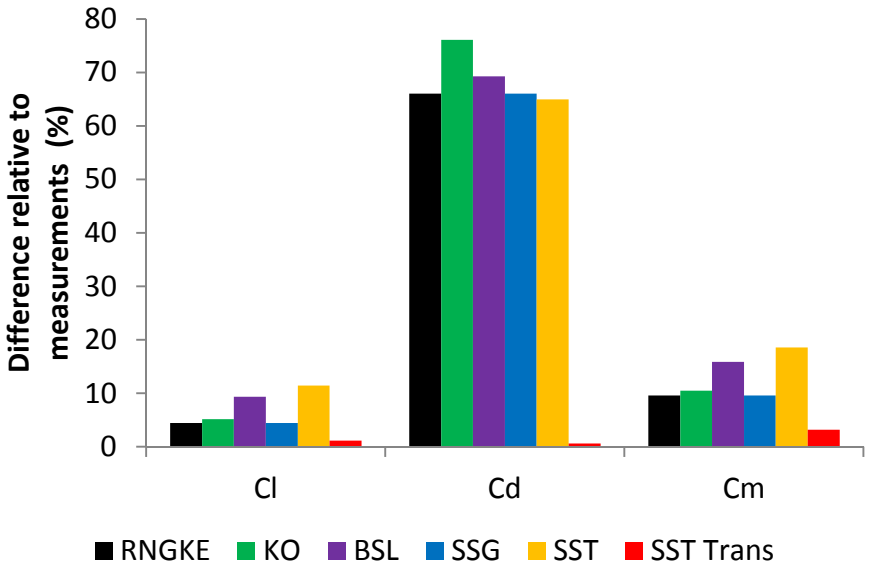

Figure 4-15: Turbulence model selection, Geometry: S809, α: 1.02°, Re: 2x10^6. Key- RNGKE : Renormalisation group analysis K-ε model, KO: Wilcox's K-ω model, BSL: Baseline K-ω model, SST: Menter's K-ω model, SST Trans: Menter's K-ω model with γ-θ transition model.

4.2.2.6 Curvature correction

The two equation eddy viscosity models are known to be insensitive to streamline curvature and system rotation [60]. CFX includes a production limiter to the turbulence kinetic energy to correct for this weakness. The formulation is based on the correlation proposed by Spalart and Shur [65]. This correction sensitises the standard two-equation model to these effects. A default scaling coefficient of 1 was used to study the effect of this correction i.e. the full effect of the production limiter is accounted. This study was conducted using the k-ω SST γ-θ transition turbulence model. Three high angles of incidence were chosen for this investigation (9.12, 14.24, 20.15 degrees) due to the large streamline curvatures expected at these large AoA.

The results (Figure 4-16) show that limitation on the turbulence kinetic energy production can reduce the difference between CFD and measurements by 7% in lift, 5% in drag and 2% pitching moment at the large AoA of 14.24°. The detailed flow field assessment of this feature was not feasible within the time allocated for this project. It was decided that as this short assessment of the curvature correction method is sufficient evident to rectify that the curvature correction helps to calculate a solution that agrees well with the measurements. As the focus of this study was to determine an appropriate CFD model that can replicate the measurements. Hence as a conclusive remark, the k-ω SST γ-θ turbulence model with curvature correction is recommended to be used for this research study.

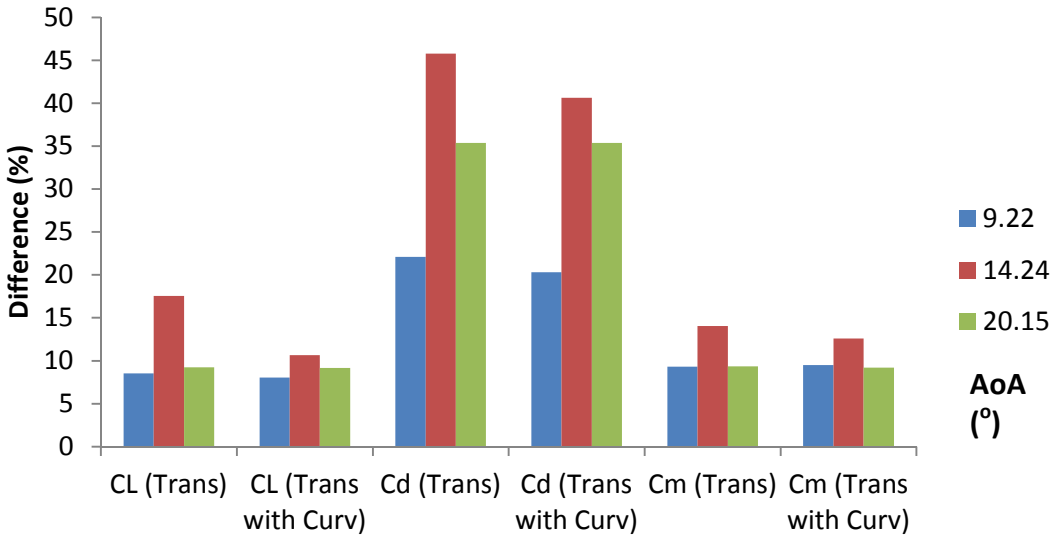

Figure 4-16 Differences relative to measurements with and without curvature (Curv) correction

4.2.2.7 S809 CFD validation study

From the experiences gained with the established simulation set up: 108,800 elements mesh with 10c domain extent and using the k-ω SST γ-θ turbulence model, the validation study was conducted. The lift, drag and pitching moment were compared with the experimental results from the literature published by Sommer [1] and the previous numerical results by Wolfe [63] (Figure 4-17).

The difference in lift coefficient between the CFD (CFX) and the measurements ranged from 1% at AOA= 5.13° to the largest difference of 9% at the AoA of 9.22°. The difference in drag coefficient was found to be -0.00365 (-17%) at the 9.22° AoA and the variation on pitching moment coefficient was found to be 8% at this AoA. It is also noticeable, the results from this investigating performs better than the study conducted by Wolfe et al [63]. CFX simulation seems to account for flow phenomena (flow separation) associated at high angles of attack very well and compute the lift and drag forces that agree well with the measurements while the CFD-ACE simulation conducted by Wolfe et al achieves a reasonable agreement with the measurements. This study also clearly shows the improvements in CFD over the past ten years. A single transitional turbulence model is adequate to compute the interested solutions with a reasonable accuracy.

Based on the result it can be concluded that this CFD model is sufficient to calculate the flow characteristics of the S809 airfoil within the pre-stall AoA. It should be noted that the main purpose of this study was to gain a preliminary understanding of the CFD practices for a wind turbine airfoil simulation, therefore it is expected that the lessons learned from this study will help to achieve a better CFD validation for the TU Delft airfoils.

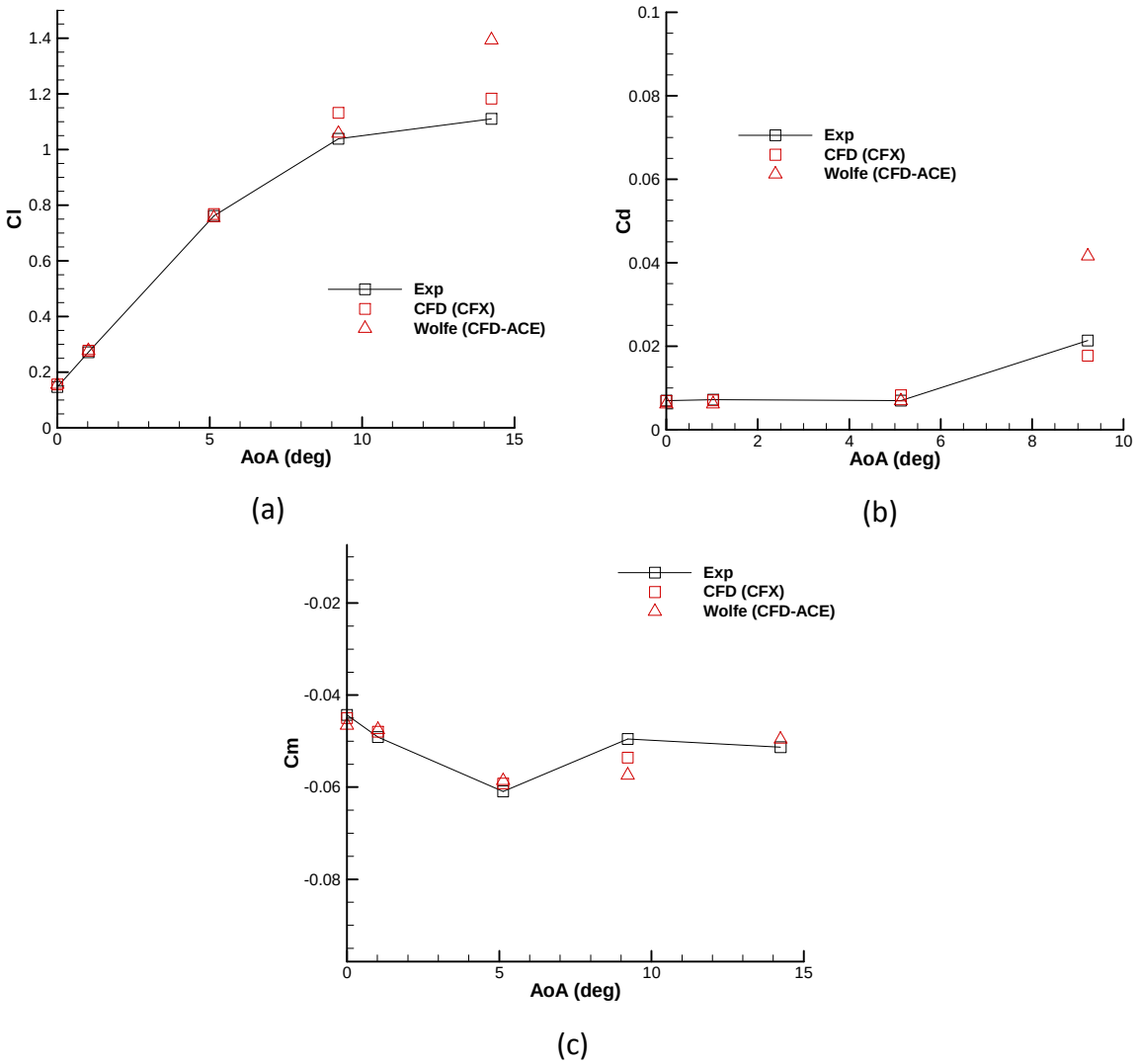

Figure 4-17 CFD results validation using measurements for the S809 airfoil – (a): Lift coefficient comparison, (b): Drag coefficient comparison, (c): Pitching moment comparison

4.2.3 CFD validation for the Delft University airfoils

Validation of the CFD models for the airfoils present in the baseline rotor is vital to gain confidence in the CFD results. With the experience gained from the preliminary S809 CFD study, a final 2D CFD validation study was conducted. For this investigation, various sections closely related to the airfoil sections of the NREL 5MW rotor blade were chosen. The exact airfoil sections present on the NREL 5MW rotor blade were not chosen for this exercise due to the absence of experimental data for these exact profiles.

Three Delft University (DU) airfoil sections were chosen for this investigation (Table 4-5), for which the experimental lift, drag and pitching moment coefficient are available within the angle of attack range of -15 deg to 25 deg [62]. These airfoils are very similar to the airfoils section on the chosen baseline rotor (NREL 5MW) blade, hence the results from this study is a direct interest for this research.

Airfoil designation	NREL 5MW span location (% blade radius)
DU97W300	40
DU92W2250	50
DU93W210	65

Table 4-5: Chosen airfoil section for the 2D CFD validation

A series of studies similar to the S809 case were conducted to assess the sensitivity of the effect of the number of elements, turbulence model and domain extent on the CFD solution. These studies were conducted for section DU97W300 and DU93W210 (Table 4-5). However, only the results for one of the DU97W300 airfoils are presented in this section, as the same conclusions were established for the DU93W210 airfoil (See Appendix 8.2.1 and 8.2.2). The CFD validation study was carried out for all three profiles shown in Table 4-5.

4.2.3.1 Geometry and test conditions

The three TU Delft airfoils studied in this investigation vary in thickness (Figure 4-18) such that the DU97W300 has a thickness to chord ratio (t/c) of 30%, DU92W2250 has a t/c of 25% and the DU93W210 has a t/c of 21%. All three airfoils have a blunt trailing edge with the thickness of 1.74%, 0.66% and 0.50% chord respectively. The chosen validation data for this exercise are from the clean cases where the natural transition is allowed. The measurements were recorded for the Reynolds number of 3 million.

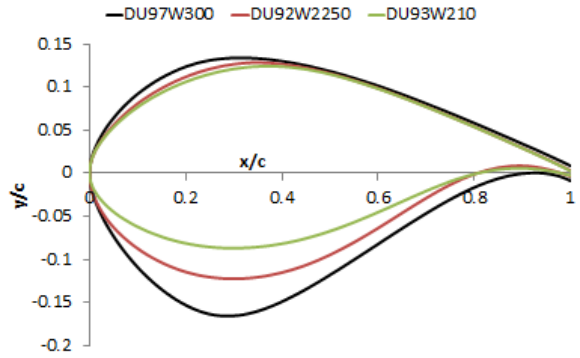

Figure 4-18 TU Delft airfoil geometries

4.2.3.2 Turbulence model selection

The findings from the turbulence model selection study are similar to the conclusions established with the S809 CFD study. SST γ-θ transitional turbulence model produces the smallest difference between the CFD solution and the measurements (Figure 4-19). Therefore SST γ-θ transitional turbulence model was established for the validation study.

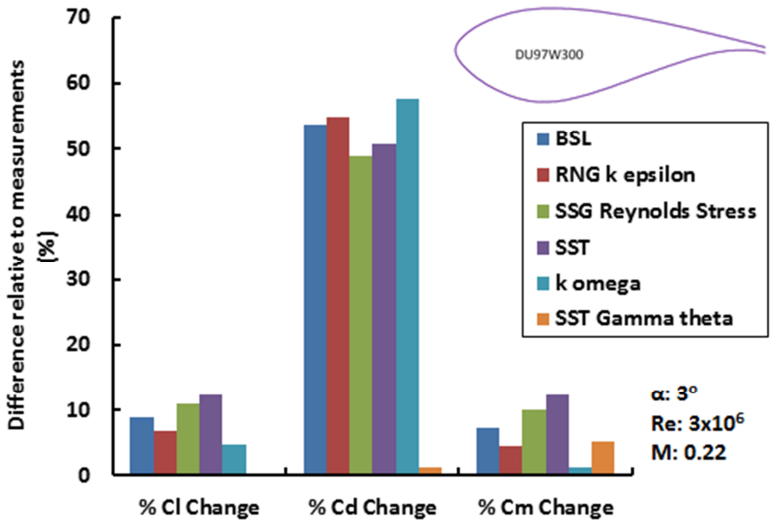

Figure 4-19 Turbulence model selection, Geometry: DU97W300, α: 3°, Re: 3x10^6

4.2.3.3 Domain extent sensitivity study

It is important to establish CFD solutions that is insensitive to the extent on the domain. Three domains with different extents based on the airfoil chord were studied (10c, 20c and 40c) for the domain extent sensitivity study. Two pressure distribution were compared (α: 3° and 12.4°), which showed negligible differences between the three cases (Figure 4-20).

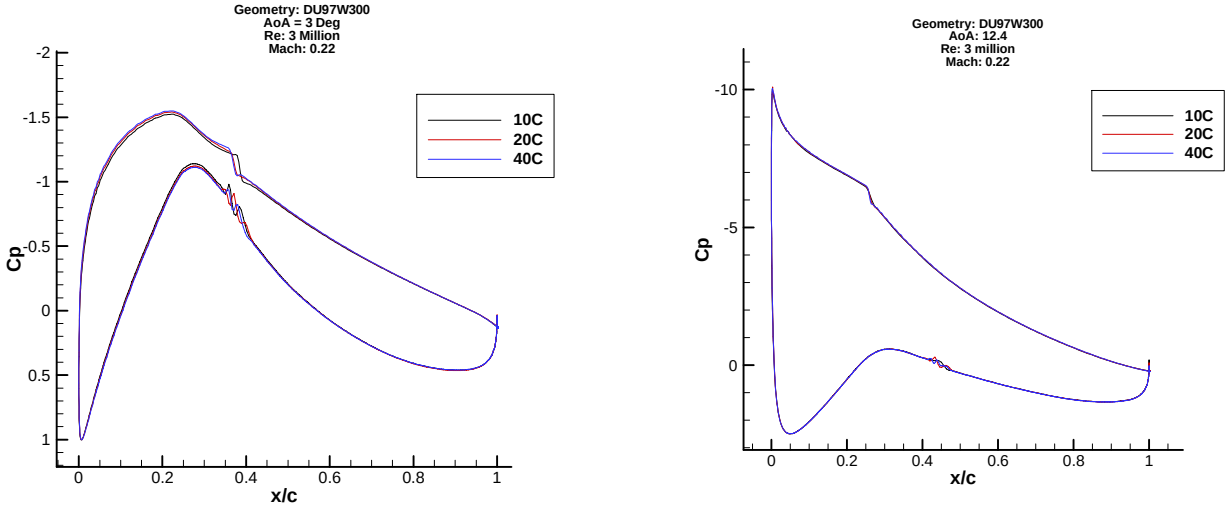

Figure 4-20 Coefficient of pressure distribution as a function of chord, Geometry: DU97W300 (a): α: 3° and (b) α: 12.4°

A maximum difference of 3% in lift and -71% in drag were found for the 10c domain extent relative to the 40c (Table 4-6) at the 12.4° AoA. It is clear that drag calculation is sensitive to the extent of the domain size. The large -71% difference in drag at the 12.4° AoA reduces to -24% for the 20c domain. The results for both AoA cases, suggests that the CFD solutions are becoming asymptotic with the increasing domain extent. The calculated solutions from the 20c and 40c domain extents agree well with the measured coefficients for the small AoA of 3°. A maximum difference of 0.89% in lift, -9% in drag and -6% in pitching moment coefficient was found between the solution calculated by the 20c domain extent and measurements. At the large AoA of 12.4° these differences are increased to -12%, -24%, -

31% for the lift, drag and moment coefficients respectively with the 20c domain extent. It is clear that 40c domain extent should be adapted to achieve a CFD solution that matches the measurements. However the increase in domain extent from 20c to 40c increases the number of elements by 20%, therefore to limit the number of elements without a large compromise on the relative difference between the calculated and measured coefficients, the 20c length domain extent was chosen for subsequent 2D CFD simulations.

Domain size (c)	C_L	C_D	C_m
10	0.651	0.013	-0.119
20	0.669	0.012	-0.120
40	0.678	0.011	-0.120
Measured	0.675	0.011	-0.113

(a)

Domain size (c)	C_L	C_D	C_m
10	1.707	0.036	-0.136
20	1.743	0.026	-0.136
40	1.762	0.021	-0.136
Measured	1.562	0.021	-0.104

(b)

Table 4-6 Integrated force comparison for different domain extents, Geometry: DU97W300 (a): α: 3° and (b) α: 12.4°

4.2.3.4 Grid sensitivity study

Similar to the domain extent sensitivity study the computed CFD solution should be achieved with an adequate level of grid independence. Three meshes with different mesh densities were tested for their effect on the calculated solution. This study was conducted for two of the DU airfoil, but only the results for DU97W300 airfoil are presented here. Two angles of attack were chosen for this investigation: 3° and 12.4°. Similar to the effect of domain extent, negligible differences in pressure distribution was seen between the meshes. These small differences were found to be in the region of flow transition i.e. the change in pressure associated with the transition point is sensitive to the number of elements.

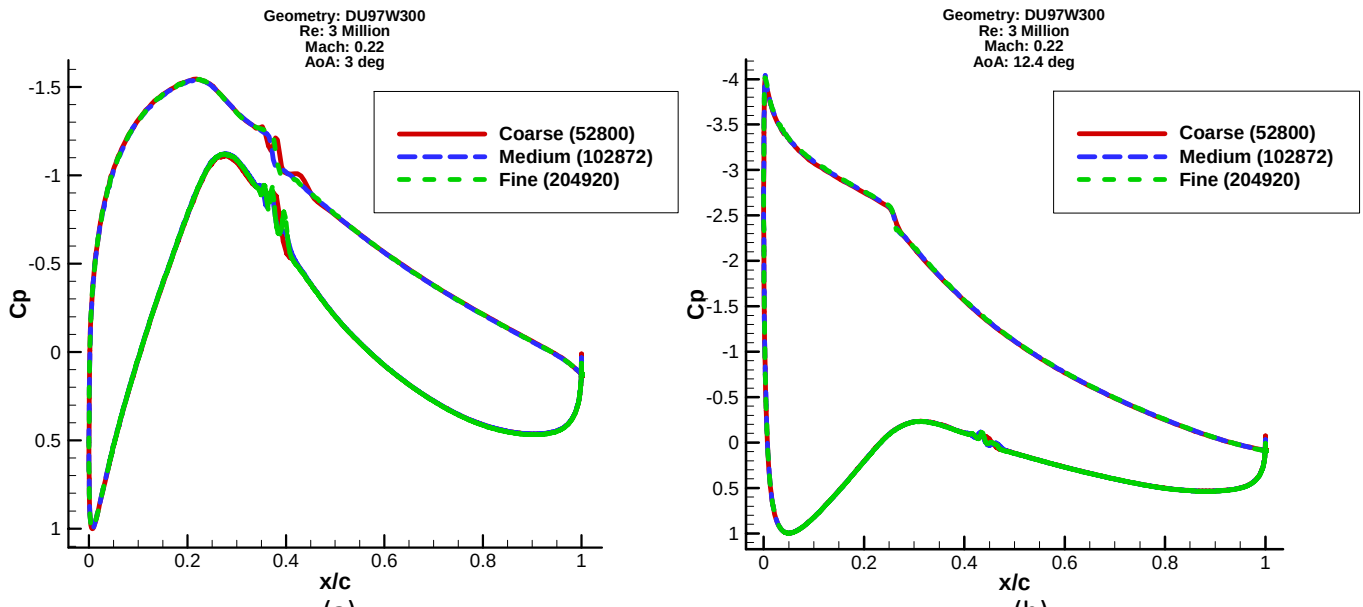

(a) (b)

Figure 4-21 Coefficient of pressure distribution as a function of chord, Geometry: DU97W300 (a): α: 3° and (b) α: 12.4°

For the DU97W300 airfoil, the lift and drag convergence were found to be non-monotonic for the angle of attack case of 3^o and for the DU93W210 airfoil only the drag convergence was found to be non-monotonic at α: 15.2^o. Richadson's extrapolation was carried out for all the monotonically converged cases (Table 4-7). The finding shows that the solution calculated by these grids lie in the asymptotic range of 1, in other words the result from any of these grids is sufficient to produce a solution that achieves an adequate level of grid independence. A largest difference of 2% was seen for the drag calculation between the coarse and fine mesh at the 12.4^o AoA.

	Coarse	Medium	Fine	Experiment	Extrapolated	Asymptotic range
Element size	52,800	102,872	204,920			
C_L (α = 3 ^{o})	0.6726	0.6686	0.6693	0.6750	-	-
C_d (α = 3 ^{o})	0.0113	0.0116	0.0115	0.0109	-	-
C_L (α = 12.4 ^{o})	1.7366	1.7428	1.7458	1.5620	1.7488	1.00
C_d (α = 12.4 ^{o})	0.0267	0.0263	0.0261	0.0213	0.0260	0.98

Table 4-7 Richardson's extrapolation analysis for DU97W300 airfoil

For the non-monotonic cases, the relative difference in the solution was used to assess the grid insensitivities. Small differences below 1% for all three coefficients were found between the results from the medium and fine girds, therefore it is recommended that a grid size of 100,000 elements are adequate to predict a solution that achieves an adequate level of grid independence, which does not require the additional computational resources.

Based on these investigations the suitable methods for the 2D CFD simulations are established.
These are as follows:

- Turbulence model: SST γ-θ with curvature correction
- Domain extent: 20 chord lengths
- Grid size ≈ 100,000 elements

4.2.3.5 Delft airfoil CFD validation results

Using this established settings, the 2D CFD results validation for the DU profiles were conducted. Only the results for the DU97W300 airfoil are presented here (Figure 4-22). Similar results were found from the validation exercise of the the other two profiles DU92W2250 and DU93W210 (see Appendix 8.2.3 and 8.2.4). A low fidelity simulations of the profiles were also conducted using the XFOIL code, to establish the differnce in predictions between low and high fidelity CFD study. The results from this study will also be presented to assess their validity with the measurements for wind turbine airfoils.

Based on the lift calculations, it was found that the CFD model is able to predict lift coefficients that achieve a small difference of 1% and 2% when compared with the measurement at the 3 and 9.13^o AoA respectively. At the post stall AoA of 20^o the CFD model fails to calculate the measured lift coefficient and there is a large difference of 55%. Similar behaviour is seen with the XFOIL calculated results i.e. achieves a reasonable agreement of within 13% difference with the measurements in the pre-stall AoA (0-12^o). The results also shows that the XFOIL over predicts the lift forces by up to 10% in some cases (AoA= 3^o) compared to CFD.

From the drag calculation, it was found that the CFD model calculates drag forces that differ from the measurements by up to 41% (dCd = 0.006) at the 9^{o} AoA, while the XFOIL simulation achieved a small difference of 6%. However for all other drag calculation from the CFD within the pre-stall AoA (0-12^{o}) achieved a difference below 24% (dCd = 0.005). Better drag calculation was found with XFOIL than CFD at the post stall AoA.

The results from the pitching moment computation suggest that the CFD result differs by a large difference of up to 30% at the 12.4^{o} AoA. All other AoA tested showed a difference below 18%. The XFOIL calculations were found to achieve differences of 20% and below when compared with the measurements.

Based on these results it can be stated the CFD model is adequate to achieve a good agreement of below 2% in lift and about 25-40% difference in drag with the measurements within the pre-stall AoA. The XFOIL in the other hand has shown that it is possible to attain reasonable results without the need for high fidelity CFD codes and large computer resources, however it lacks the ability to predict detail flow fields or to model PFC devices integrated blade that is vital for this research.

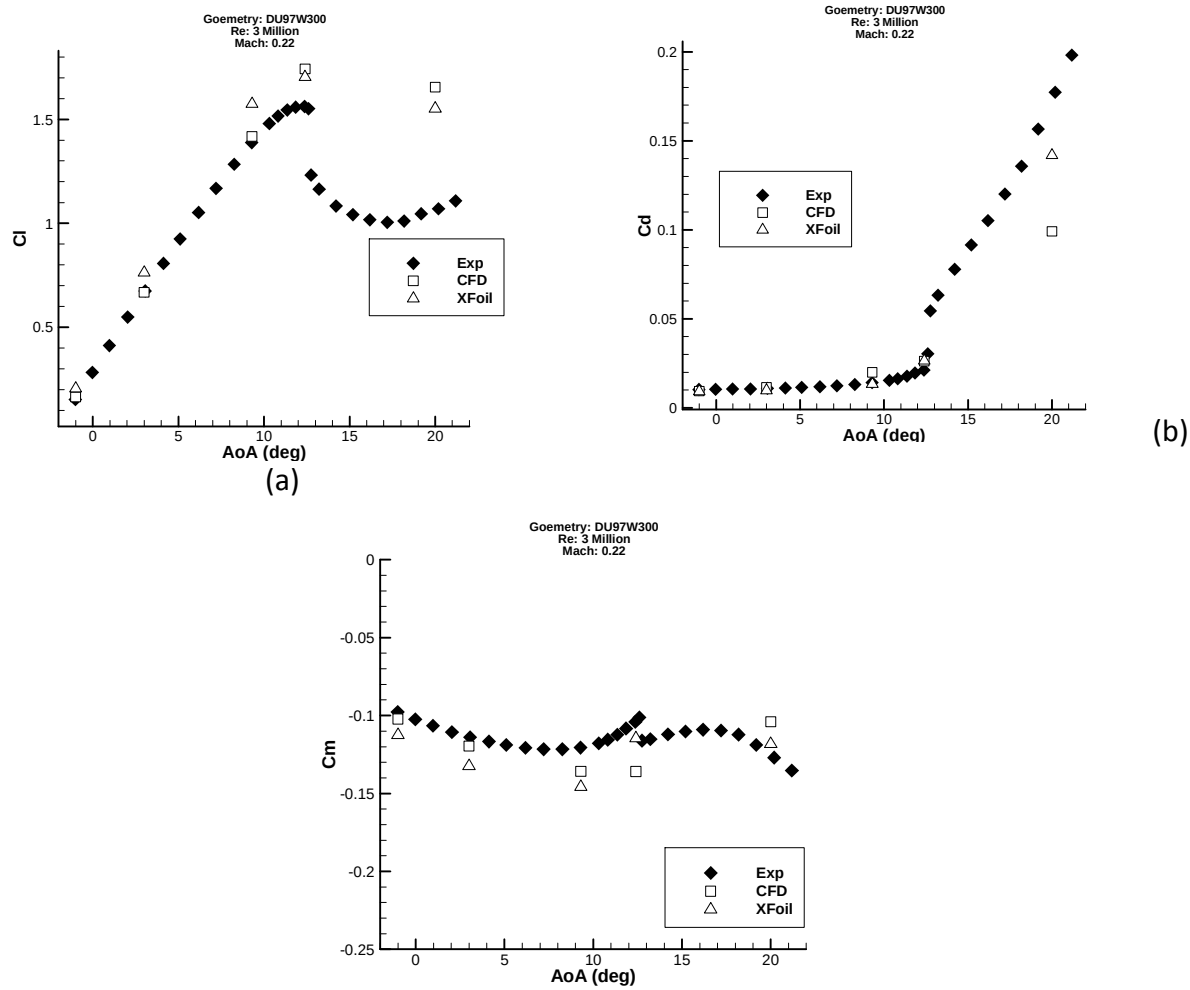

Figure 4-22 CFD results validation using measurements for the DU97W300 airfoil – (a): Lift coefficient comparison, (b): Drag coefficient comparison, (c): Pitching moment comparison

4.2.4 Conclusion

Based on the assessment of a range of typical wind turbine airfoil sections, a suitable CFD method for 2D CFD simulation has been established. With the current method, the 2D CFD approach is validated for the pre-stall angle of attacks.

This project is focused on the wind turbine's performances within the sub-rated power region. Based on the blade element momentum (BEM) theory assessment of the baseline rotor, the operation angle of attack range is within the pre-stall angle of attack of the sections (Figure 4-23). Based on this the validation of the 2D CFD results for the pre-stall angle of attack is adequate for the analysis of the baseline rotor.

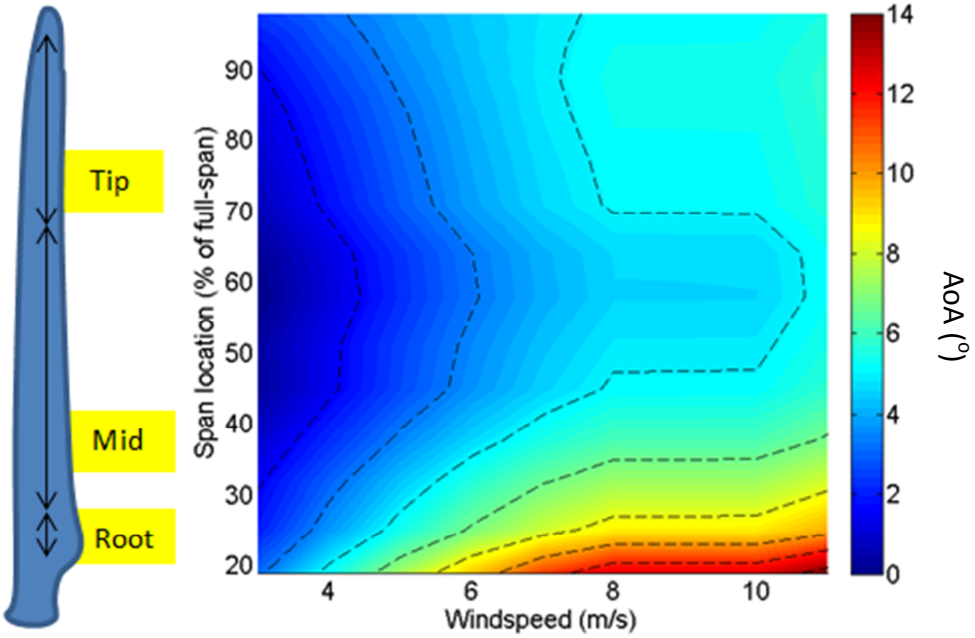

Figure 4-23 Sub-rated operational local angle of attack distribution for the NREL 5MW rotor

The validation of the pre-stall angle of attack is an anticipated result, as the simulations are performed in a steady environment, which is not able to resolve the unsteady flow features that are present at the higher angle of attack such as flow separation. Unsteady simulations were not considered for this project due to the uncertainty in the time required to establish an unsteady 2D and eventually a 3D CFD model and the increase in computational time.

4.3 3D CFD

To study the effectiveness of a PFC device on a full scale rotor, a baseline rotor geometry (NREL 5MW) and its corresponding 3D grid was established. See Appendix 8.3 for details on the NREL 5MW rotor geometry used in this work. This section of the thesis presents the results obtained for the baseline rotor simulation. The objective of this study is to investigate the effectiveness of the 3D CFD method. The NREL 5MW is a conceptual rotor (Figure 4-24) and there is no experimental study of the turbine at this time of the research, therefore a 3D CFD validation was not possible for this rotor. However various studies similar to the 2D CFD were conducted to establish a credible 3D CFD model. This includes the grid and domain size sensitivity analysis. The results from the established 3D CFD model will then be compared against the available CFD data from the open literature.

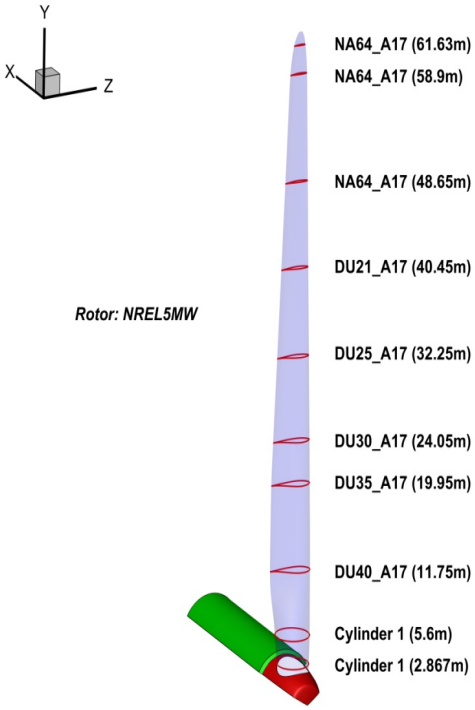

Figure 4-24 NREL 5MW rotor with its constituent airfoil distribution

The initial domain sizing and the grid topology are shown in Figure 4-25 and Figure 4-26. The flowfield is split into two domains comprising rotational inner domain (D1) which is shrouded by a stationary outer domain (D2). The radial extent of the rotational inner domain is 111% of the blade height of 63m. The simulation configuration is presented in Figure 4-27. GGI interfaces were used to model the flow between the stationary and the rotational domains.

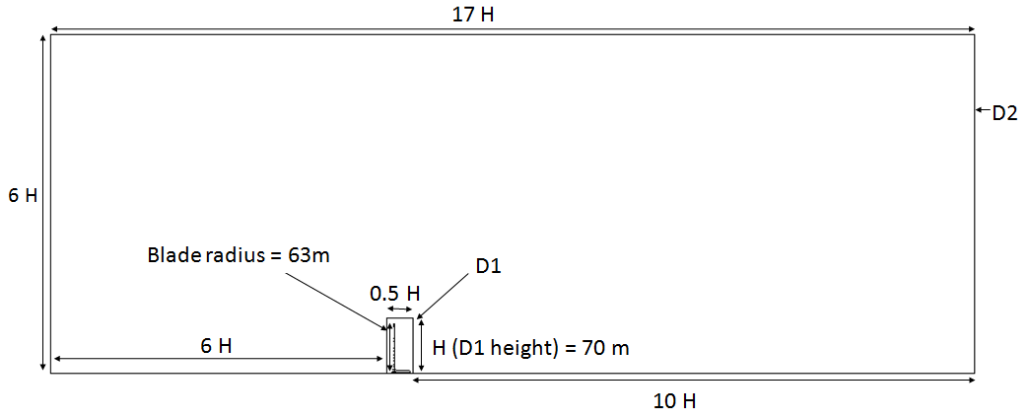

Figure 4-25 Side view of the CFD domain for the NREL 5MW rotor, D1: rotational inner domain, D2: stationary outer domain

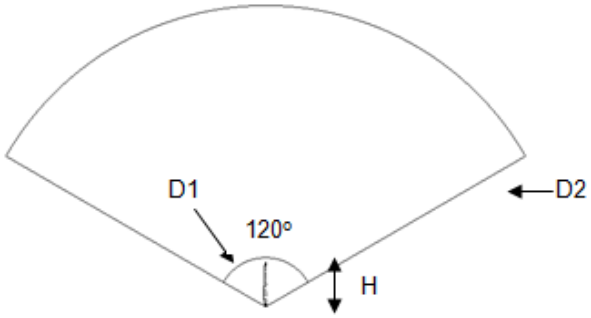

Figure 4-26 Front view of the CFD domain for the NREL 5MW rotor, D1: rotational inner domain, D2: stationary outer domain

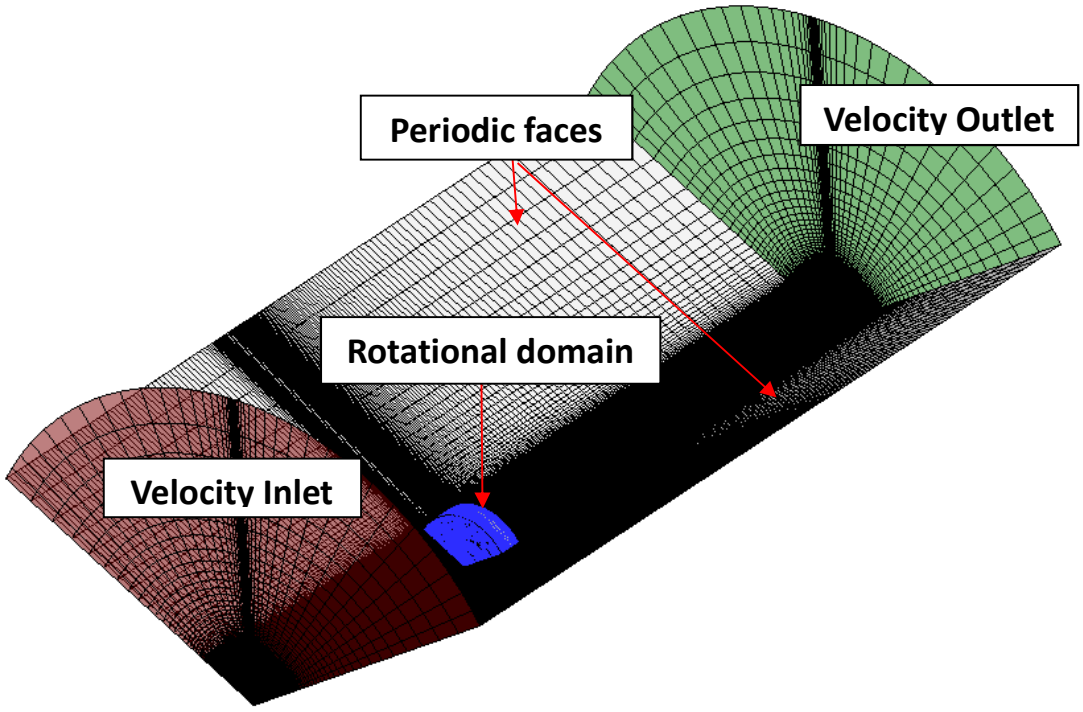

Figure 4-27 3D CFD simulation configuration for the NREL 5MW rotor

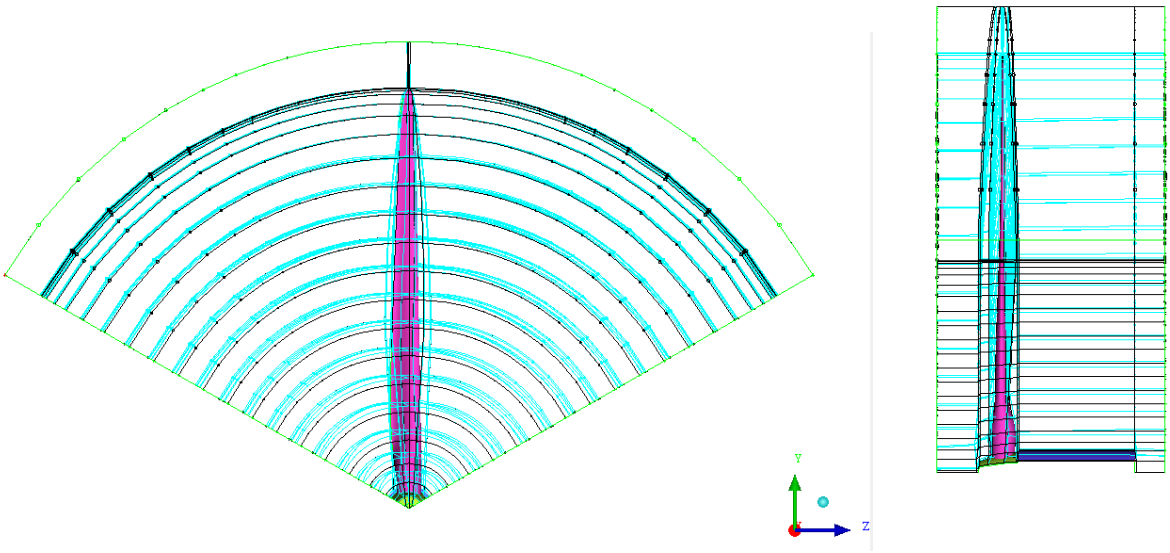

(a) (b)

Figure 4-28 Rotational domain (D1) blocking (a = front view, b = side view)

The blocking strategy for the grid is shown in Figure 4-28 and Figure 4-29. Overall an H-type mesh was adapted for the domains while an O-mesh topology was adapted to resolve the boundary layer on the blade surface. It was designed for a y+ value of 1. A general mesh gradient of 1.2 was maintained throughout the domain. The final mesh contained zero cells with 2x2x2 determinant 0.2 and below, and 99.97% of the total cells do not include mesh angles below 18 degrees. The blade mesh distribution is shown in Figure 4-30. In addition, the transition between the blocks (Figure 4-31) and the local mesh density was increased especially at the spinner blade junction (Figure 4-32) to capture the large flow gradient.

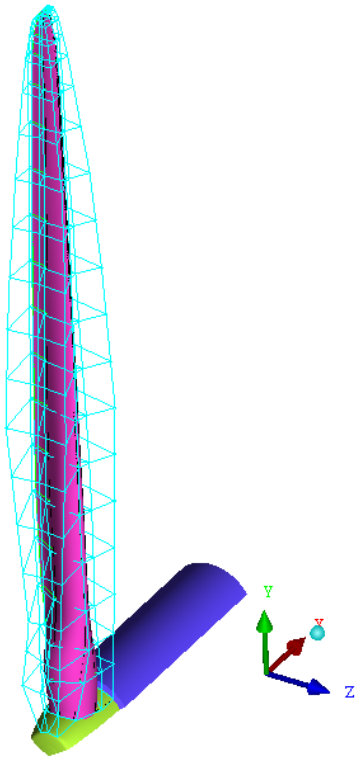

Figure 4-29 O-Block around the NREL 5MW rotor blade

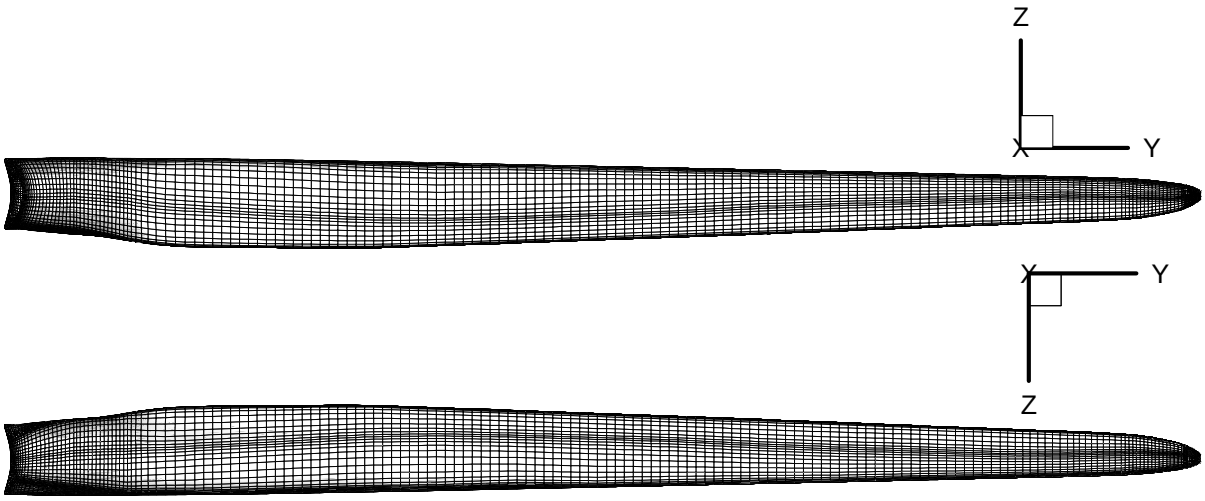

Figure 4-30 Blade mesh (Top: Suction surface, Bottom: Pressure surface)

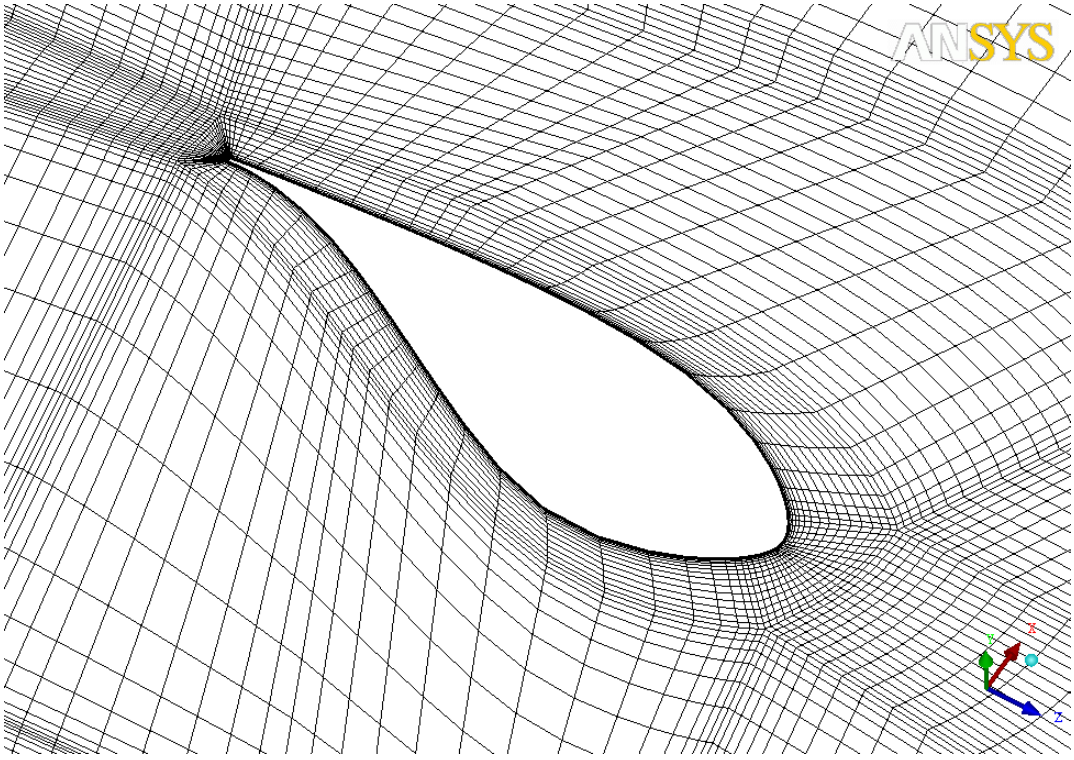

Figure 4-31 Mesh around blade at an intermediate section (30% span)

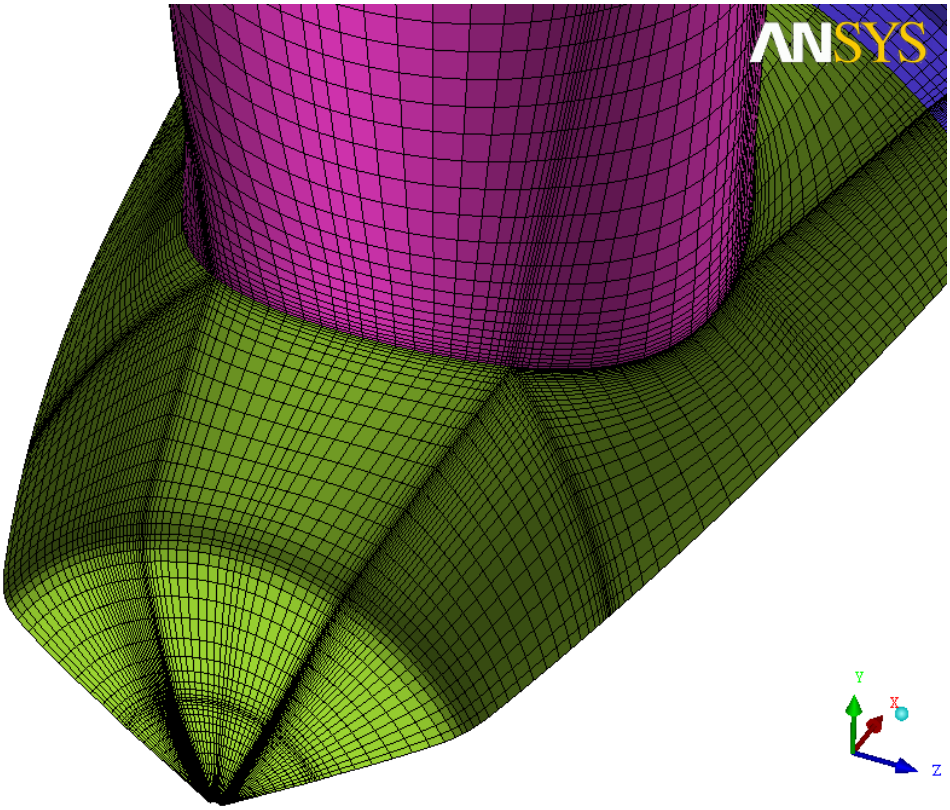

Figure 4-32 Mesh at the spinner blade junction

4.3.1 Simulation configuration

An initial study was conducted to observe the effect of the interface between the D1 and D2 grids. This study investigated how the node matching between the sliding faces of the domains (Figure 4-33) affects the computed solution. To perform this study, the D2 domain blocking was changed from a simple 5 block domain to a more complex 216 block domain (Figure 4-34). SST standard turbulence model was used for this study.

A target estimate for the mesh density (approximately 4million elements) of the rotational domain (D1) with the node matched outer domain (approximately 6 million elements) a total of 10 million elements was used to conduct this investigation node matched case. The non-node matched configuration has a total of 6.5 million mesh elements.

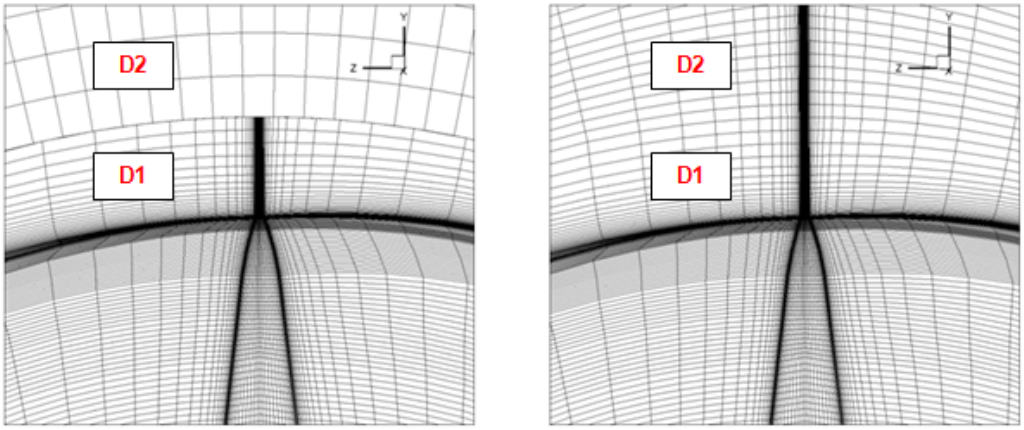

Figure 4-33 Mesh node matching at boundary of D1 and D2 grid domains

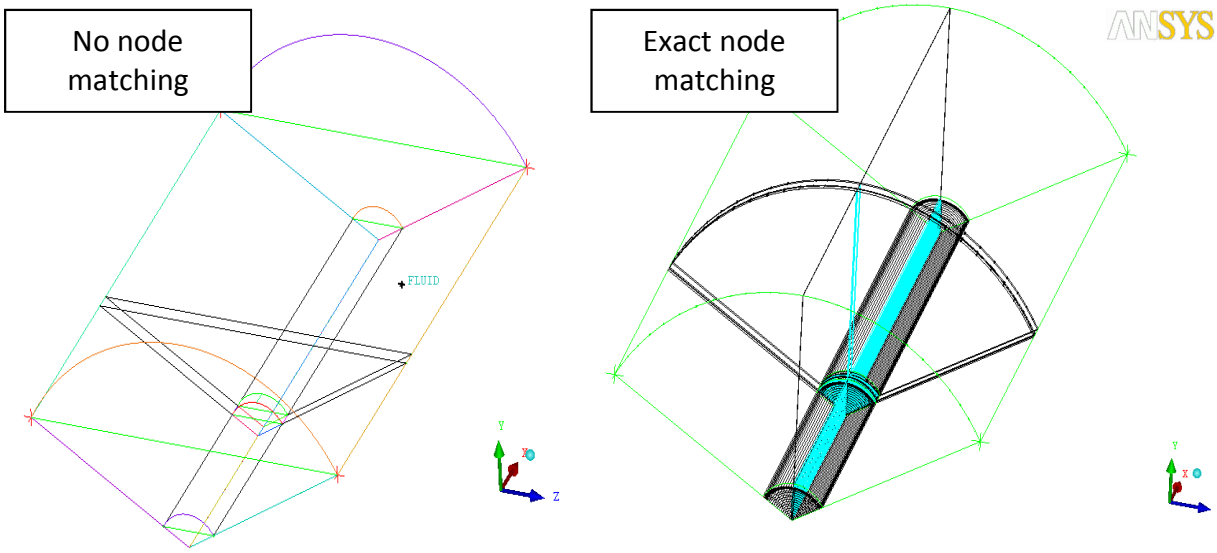

Figure 4-34 D2 domain blocking (Left: No node matching, Right: Exact node matching)

The results from this investigation showed slight differences in the computed pressure at the sliding interface (Figure 4-35). However, the coefficient of pressure at two spanwise location of the blade (20 and 80% span), shows that there is negligible difference in computed pressure values between the exact node matched configuration and the case where the nodes at the interface are not matched (Figure 4-36). A difference in rotor power output of 0.07% was found between the two cases. The calculations also showed that the effect of node matching at the interfaces has small influences (dCq = 0.03 at 5% span) on the blade roots' local torque production and has no influences on the outboard blade above 20% span (Figure 4-37).

Based on the finding, the future 3D CFD investigations will be conducted without node matching to save computational and gridding time. The grid independence study is discussed later in this thesis to ensure that this expected level of spatial resolution is adequate for the baseline rotor. However, it is expected that the grid sizes will increase for configurations which include the selected flow control designs.

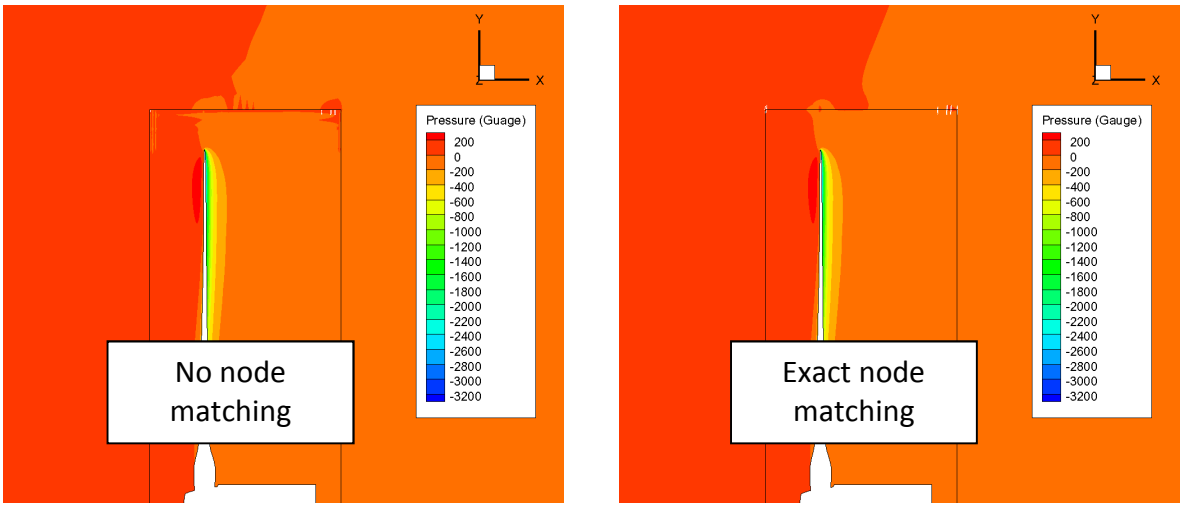

Figure 4-35 Pressure contour comparison of the node matching study (Left: No node matching, Right: Exact node matching), TM: SST, Omega = 10.3 RPM, WS = 9m/s.

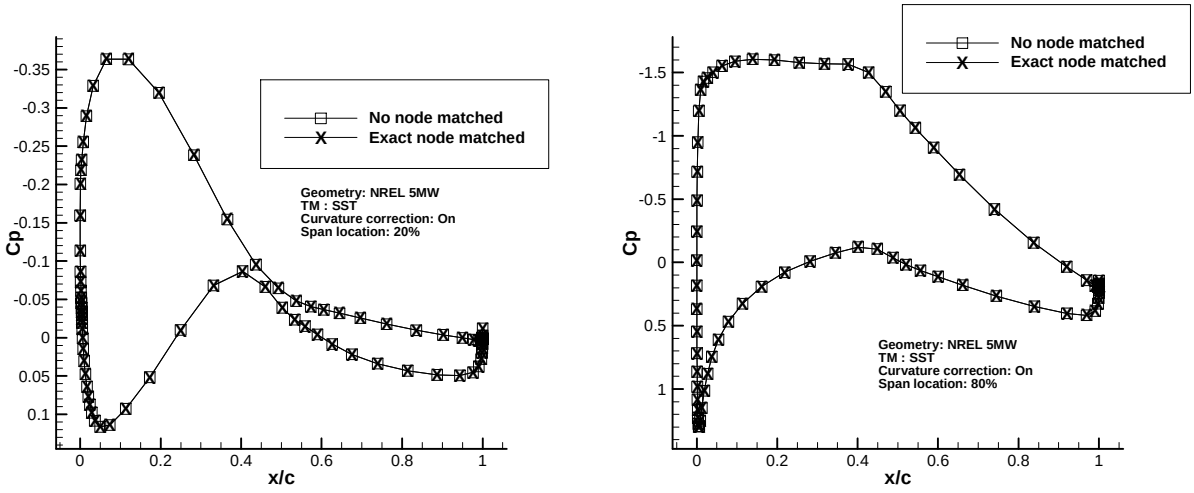

(a) (b)

Figure 4-36 Coefficient of pressure at two different locations in blade span (a: 20% and b: 80%), $C_P = Pressure/\frac{1}{2}\rho W^2$, TM: SST, Omega = 10.3 RPM, WS = 9m/s.

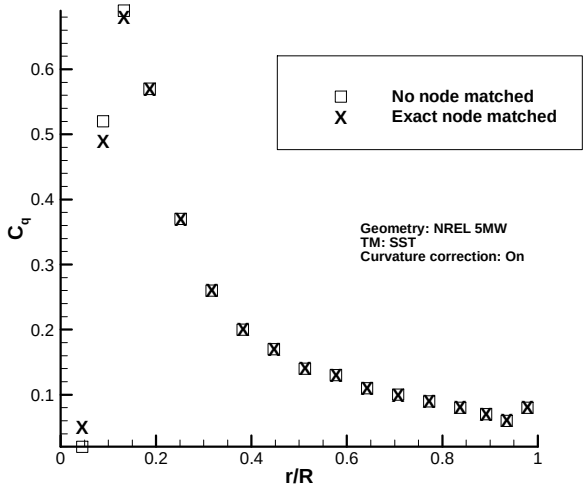

Figure 4-37 Torque coefficient along the blade span ($C_q = dQ/\frac{1}{2}\rho W^2 dA\, r$), TM: SST, Omega = 10.3 RPM, WS= 9m/s.

4.3.2 Grid and domain extent sensitivity study

Similar to the exercise conducted for the 2D CFD study (Section 4.2), a series of investigations was conducted to assess the effect of both the CFD domain and the mesh resolution on the CFD solutions from the 3D CFD model.

The mesh sensitivity study was conducted with three different mesh densities (3.7, 6.7, 11.8 million elements). A monotonic convergence in power was achieved for the three meshes with an increase in the predicted power as the mesh density increased. Based on the Richardson's extrapolation study, all meshes were found to be in the asymptotic range (Table 4-8). The pressure distributions at the 20% span location showed small changes in peak suction due to the changes in number of elements. It was found that the suction pressure found at the x/c =0.1, varied by 8% from the medium mesh to the fine mesh and this variation was reduced to 5% between the fine and superfine mesh. Larger difference up to 21% in pressures between the medium and fine mesh was found at the pressure side of the blade x/c=0.85, which reduces to 14% between the fine and superfine mesh.

The pressure at 80% span, which showed negligible differences between the three cases (Figure 4-38). Maximum difference of 2% in was found between the medium and fine mesh at the x/c =0.18, which reduced to 0.4% between the fine and superfine mesh. Based on these results it can be stated that the baseline 3D CFD model (6.7 million elements) is sufficient to produce a solution that achieves an adequate level of grid independence within the reported discrepancies.

	Medium	**Fine**	Superfine	Extrapolated	Asymptotic range
Elements	3,780,219	**6,691,323**	11,846,917		
Power (W)	2,482,980	**2,680,299**	2,723,482	2,735,580	**1.0795**
% change	-	**7.36**	8.83	-	**-**

Table 4-8 Richardson's extrapolation study for the 3D CFD model

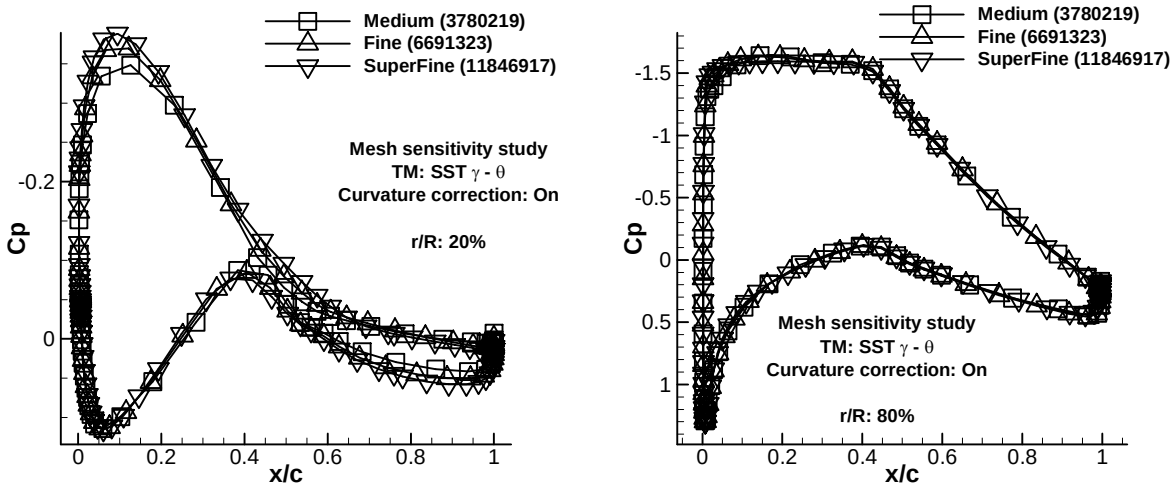

(a) (b)

Figure 4-38 Coefficient of pressure distribution as a function of chord, (a): 20% and (b): 80% span

To study the effect of the domain extents, three domains with different radial extents based on the blade radius (6.8R, 10R and 13R) were studied (Figure 4-39). The local pressure distributions (20% and 80% span), showed very small differences below 1% between the three cases (Figure 4-40). However, with an increase in the radial extent of the domain, a reduction in the predicted power was observed (Table 4-9). The decrease in calculated power between 6.8R and 10R domain was -1.8% with a further decrease of -0.8% when the domain was extended to 13R. This shows that a monotonic convergence of the solutions exists for an increase in domain extent.

The size of the domain extent clearly influences the calculated power of the CFD model (6.8R) and it is recommended to adopt a 10R domain for the future work. This requires an addition of approximately 300,000 elements. In conclusion, it is decided that a mesh containing 7 million elements with a domain extent of 10R is suitable for this project.

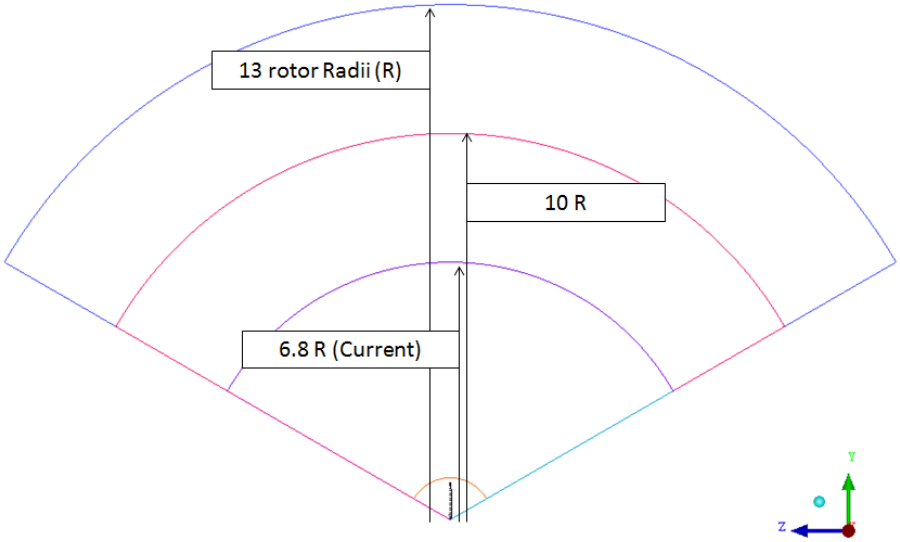

Figure 4-39 The different radial extents chosen for domain extent sensitivity study

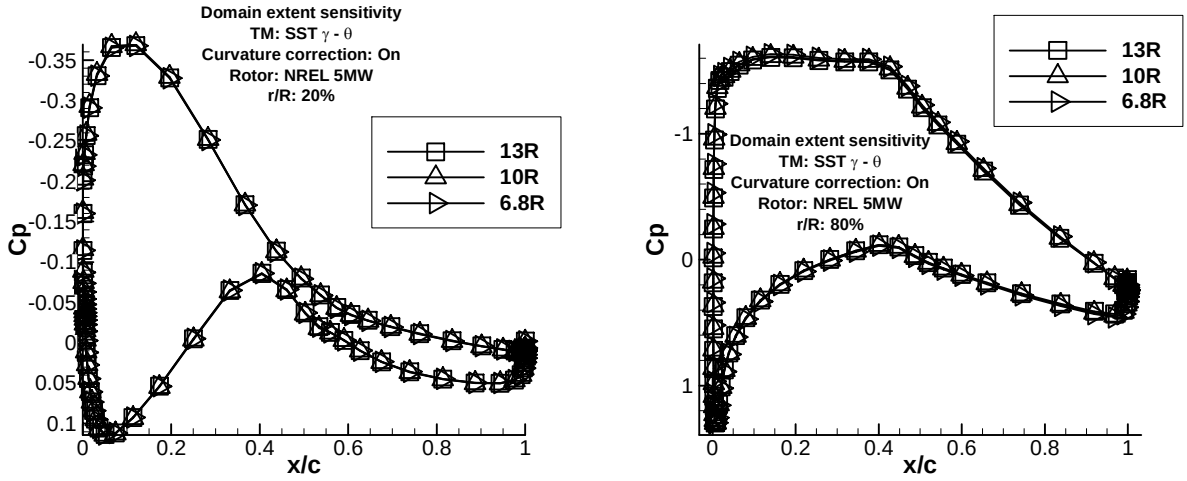

(a) (b)

Figure 4-40 Coefficient of pressure distribution as a function of chord, (a): 20% and (b): 80% span

R	Elements	Power (W)	% change relative to 6.8R
6.8	6.7 x10^6	2,680,299	-
10	7.1 x10^6	2,633,102	-1.76
13	7.4x10^6	2,611,850	-2.55

Table 4-9 Power outputs from the domain extent sensitivity study

4.3.3 Operating conditions

After the determination of the appropriate grid size and the domain extent, a number of preliminary simulations were conducted to assess the performance of the baseline rotor, which is designated with 'CU' for the purpose of comparison with other geometry in the open literature. This study was conducted to gain an indication of the quality of the 3D CFD solution. The aerodynamic boundary conditions and modelling approach are presented in Table 4-10. The simulations were conducted at sea level condition. Four different operating conditions in the sub-rated power region were simulated, which cover the wind speed range of 5m/s to 11m/s. The rpm configurations for the chosen wind speed were specified in the NREL report [2] (Table 4-11). The simulations were conducted with a node-based CFD solver CFX. It should be noted that this study was conducted using the node matched grid and for future studies the non-node matched grid will be used to save computational and gridding time.

Computational flow model	
Solver	Pressure-based
Time	Steady
Advection scheme	High resolution
Turbulence model	SST γ – θ
Static Temperature	15^o C
Static Pressure	101, 325 Pa
Curvature correction	On

Table 4-10 Solver setting

Wind speed (m/s)	**rpm**
5	7.506
7	8.469
9	10.296
11	11.89

Table 4-11 Operating conditions

All the simulations met the iterative convergence criteria of 1e-04 and below and the power output was achieved within 0.5% of the reported values. The results from the simulations were compared against the Blade Element Momentum (BEM) code WT Perf (Section 3.1.4.2), and results from other literature, which investigated the NREL 5MW rotor (UC Davis [4] and Riso DTU [66]). These results are discussed in in the next section 4.3.4.

4.3.4 Baseline rotor performance

The geometry of the baseline NREL 5MW rotor studied in this project does not exactly match the specification of the NREL 5MW rotor as presented in the NREL report [2]. This is due to the crude simplifications for the geometry definition that were made in the NREL report as it was not primarily focused on detailed aerodynamic design.

To ensure a smooth surface definition for the rotor, the rotor geometry was slightly modified in this work (See Appendix 8.3). Specifically, not all of the repeated airfoils in the radial direction were considered for the surface fitting. Consequently not all the cross sections of this CU baseline rotor will be identical to the NREL 5MW rotor as defined in the NREL publication [2]. However, this approach overcomes the simplifications in the initial NREL work and provides an appropriate rotor surface for CFD analysis. This revised rotor geometry will be referred to as CU NREL 5MW.

For all the BEM and CFD calculations, zero pre-cone and shaft tilt angles were adapted, which differs from the angles designated by NREL for this specific rotor (pre-cone: 2.5^{o}, shaft tilt: 5^{o}). The reports from UC Davis[4] and Riso DTU[66] has not provided a clear definition on how they have constructed their NREL 5MW rotor of if they have considered pre-cone or shaft tilt.

The presented results are abbreviated as shown in Table 4-12 i.e. CU (BEM) represents the blade element momentum results for the Cranfield University NREL 5MW rotor.

Abbreviations	Meaning
Original NREL 5MW	Original NREL 5MW rotor geometry defined in [2]
CU / Baseline rotor	Modified NREL 5MW rotor geometry used in this study
UC Davis	Modified NREL 5MW rotor geometry by UC Davis University
Riso DTU	Modified NREL 5MW rotor geometry by Riso DTU University
CU CFD	Results from 3D CFD simulation
CU BEM	Results from the BEM code WT_Perf

Table 4-12 Naming convention used to present the results

4.3.4.1 Comparison with previously published results

Since the experimental result do not exist for this conceptual turbine, it was not possible to conduct a direct validation. Hence similar to the validation work conducted by the UC Davis [4] for their NREL 5MW baseline rotor it was decided that the results from this study will be compared against the UC Davis [4] and their validation case results from Riso DTU [66]. UC Davis has also compared their CFD results with the BEM results using WT_Perf, which is also carried out for the baseline NREL 5MW rotor used for this study. It is noted that UC Davis and Riso DTU have adapted their own modification to the NREL 5MW rotor in order to achieve a geometry that can be used to perform CFD analysis and the exact modifications are not reported. Therefore it is anticipated that slight changes in aerodynamics may be expected based on these individual modifications.

The UC Davis [4] constructed a CFD model of the NREL 5MW rotor (Figure 4-41) using the overset meshing scheme (chimera) and simulated the 3D rotor flow using RANS Overflow2 CFD solver. The standard SST turbulence model was used to compute the solution and hence the boundary layer transition is not modelled. Steady and unsteady simulations were conducted, which showed negligible difference in power in the sub-rated power region. The simulations were conducted using the entire rotor with all three blades but the effect of the spinner and nacelle was neglected.

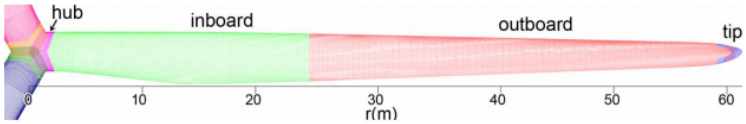

Figure 4-41 Baseline NREL 5MW used in the UC Davis study [4]

Riso DTU [66] also constructed a version of the NREL 5MW rotor (Figure 4-42), which similarly does not model the spinner and the nacelle. They modelled all three blades, and conducted steady and unsteady. Their meshing strategy was to use a conventional O-type mesh, and the standard SST turbulence model was used and the simulations were performed using an in-house CFD solver (EllipSys3D). They have implemented the effect of wind shear in their study, however only the result from 'uniform' (zero wind shear) case was selected for this comparison exercise.

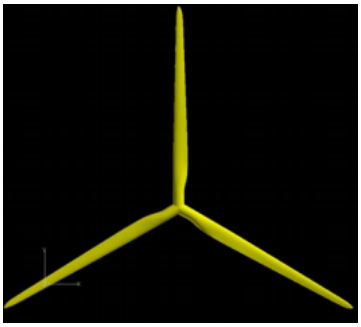

Figure 4-42 Baseline NREL 5MW used in the Riso DTU study [66]

A comparison of the computed power output between the CU baseline rotor and the related studies reported in the open literature (UC Davis [4], Riso DTU [66]) was conducted for the wind speed configuration of 8 and 11m/s (Figure 4-43). In comparison with the Orginal NREL 5MW BEM results, where the measurements used included the effects of transition, the CU baseline rotor has the best agreement. At the 8m/s wind speed the CU CFD computed power that agreed within 2% of the BEM, while the UC Davis and Riso DTU achieved an agreement within 3 and 11% respectively. For the larger wind speed of 11m/s the CU CFD rotor power was found to be within 1% of the computed power using the BEM code WT_Perf (Figure 4-43). The Riso DTU baseline rotor agrees within 2%. Lastly the rotor constructed by UC Davis shows a slightly greater difference in comparison with the original NREL 5MW rotor according to the BEM calculations: 6% difference in power. Better agreement is found with the CU CFD and the BEM is due to the use of transition modelled, where the UC Davis and Riso DTU simulation modelled a fully turbulent flow. The BEM calculations were performed using the measurements where the effect of transition is included.

Overall, all three rotors are in general agreement with the BEM and each other and at worst are within about 11% differences in the power distribution across the speed range designated by NREL [2].

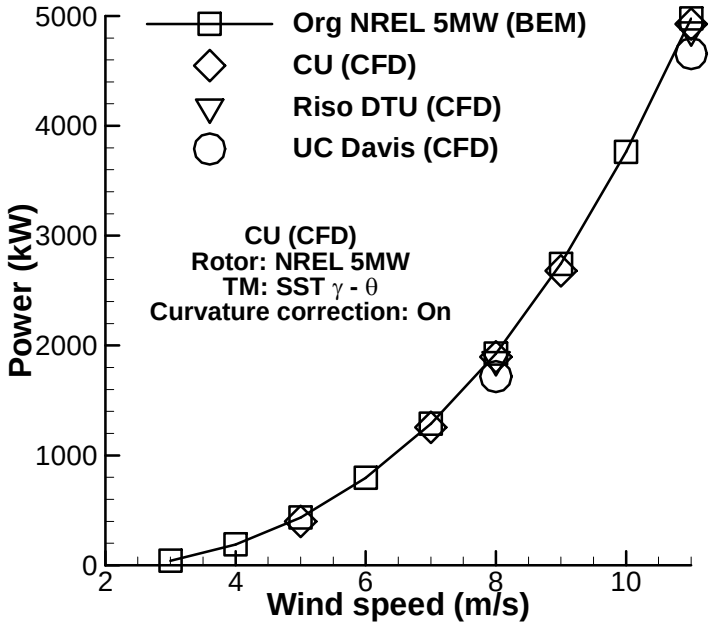

Figure 4-43 Comparison of CU CFD results to other CFD literatures

4.3.4.2 CU and UC Davis NREL 5MW CFD simulations

This section of the thesis presents a more detailed comparison between the CU rotor and the UC Davis NREL 5MW rotor geometry and the corresponding CFD results. Chow has presented a report [4] on the UC Davis 3D CFD simulations and was able to provide the geometry and a dataset from their rotor simulations for a wind speed of 11m/s. Chow focused on the techniques for mitigating inboard stall and separation using fences. Using the provided results, an evaluation of the local flowfield was compared between the CU and UC Davis [4] baseline rotor simulation. The local torque and thrust coefficient were compared in this study.

The aim of this investigation was to assess and evaluate the different flow fields produced by slight changes in the geometry due to the different design approaches that were made by CU and UC Davis. It is noted that this case study was conducted due to the absence of validation test case for conceptual NREL 5MW turbine and this is not a replacement for a CFD validation. It is only a comparison of the results.

The UC Davis rotor does not model the spinner and nacelle and hence they have adapted a wedge shaped root, which forms a connected surface when revolved (Figure 4-44). A small difference in the geometry was also seen at the root part of the blade. UC Davis has also implemented a full tip rotor, whereas the CU baseline rotor has a truncated tip at 99.8% span (Figure 4-45) in order to gain a better grid quality at the blade tip.

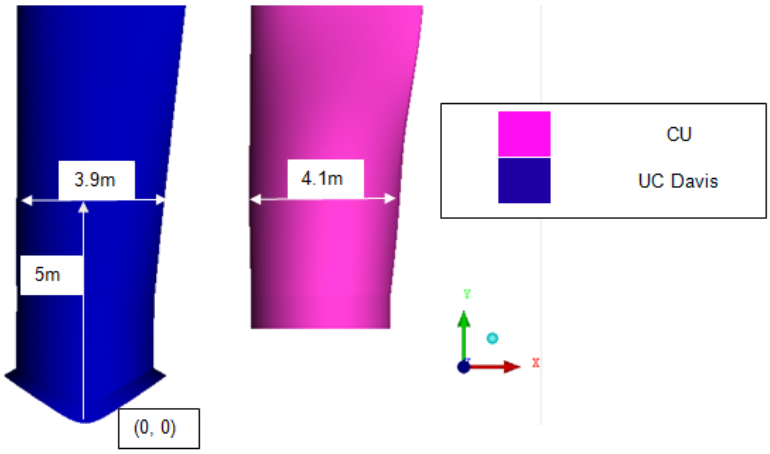

Figure 4-44 Root geometry comparison between UC Davis and CU NREL 5MW rotor (Pressure side view)

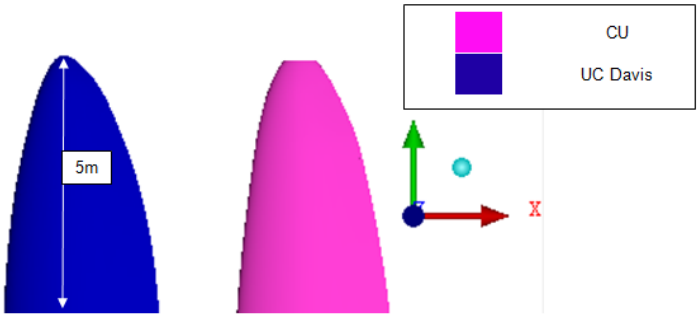

Figure 4-45 Tip geometry comparison between UC Davis and CU NREL 5MW rotor (Pressure side view)

The comparison of the local flow characteristics were compared using local torque and thrust coefficient. The local torque and thrust coefficient were calculated using Eqn 31 and Eqn 32, respectively.

The local torque and thrust coefficients are defined as follows:

$$Cq = \frac{dQ}{qdAr} \qquad \text{Eqn 31}$$

$$Ct = \frac{dT}{qdA} \qquad \text{Eqn 32}$$

Where Cq = local torque coefficient, Ct = local thrust coefficient, q = dynamic head ($0.5\,\rho\,W^2$), dT = local thrust, dQ = local torque, dA = planform area of the local element, r = local spanwise radius and W = local relative velocity ignoring induction ($\sqrt{Uinf^2/(\Omega r)^2}$).

Overall, the distributions and the level of local torque coefficient shows good agreement between the CU and UC Davis CFD solutions over the majority of the rotor from 20% to 90% of span (Figure 4-46). The difference between CU and the UC Davis in this region was found to be less than 6%. Not surprisingly the largest differences were found to be in the root and in the tip section (Figure 4-46). Large difference up to 66% in local torque coefficient was

seen at the blade root (r/R= 0.10), while smaller about 11% difference was noticed at the blade tip (r/R= 0.95).

The results from a fully turbulent simulation using the CU CFD model CU (CFD) – TM: SST was also used in this comparison as the UC Davis simulation was conducted using a fully turbulent SST turbulence model. Based on this comparison it was found that transition modelling had small effect below 5% on the torque coefficient calculation of the CU CFD along most the blade (r/R =0.20-0.90). At the blade root and tip up to 6 and 7% difference in torque coefficient was found between the transition modelled and fully turbulent CU CFD simulation. The fully turbulent result had a better agreement with the UC Davis result at the r/R=95%, where it achieved about 6% difference.

The large changes in torque coefficient at the blade root is due to the inclusion of the spinner and nacelle in the CU geometry where it is neglected in the UC Davis work. The differences in tip region might be due to the truncated tip adapted for the CU NREL 5MW rotor.

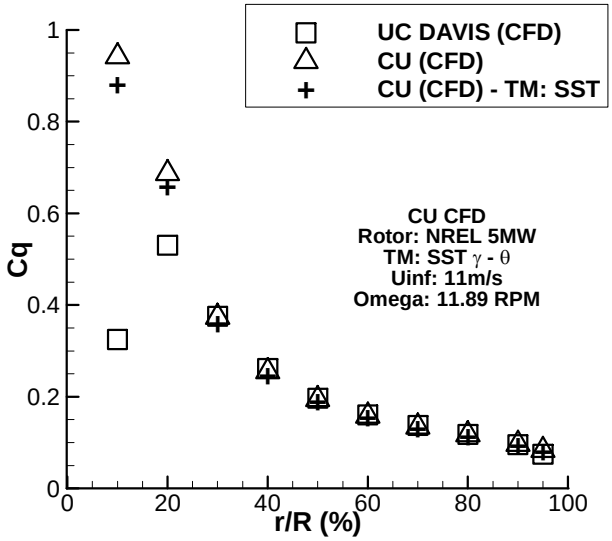

Figure 4-46 Comparison of local torque coefficient between CU CFD, UC Davis CFD for datum condition (U=11m/s, Rpm= 11.89)

A reasonable agreement was found between the CU and UC Davis CFD thrust coefficients (Figure 4-47). Within 30-80% of the blade a good agreement within 4% was achieved between the transition model CU CFD and UC Davis CFD simulation. Surprisingly the fully turbulent CU CFD model showed larger differences up to 8% in comparison with the UC Davis results within this blade span range. About 4% differences in thrust forces were seen between the full turbulent and transition modelled CU CFD simulations. Both modelled showed large differences of thrust about 40% at the blade root in comparison with the UC Davis simulation. Only at the blade tip of r/R=0.95 the fully turbulent CU CFD model achieved a better agreement of 1% with the UC Davis thrust coefficient, where the transition modelled simulation achieved a difference of about 3%.

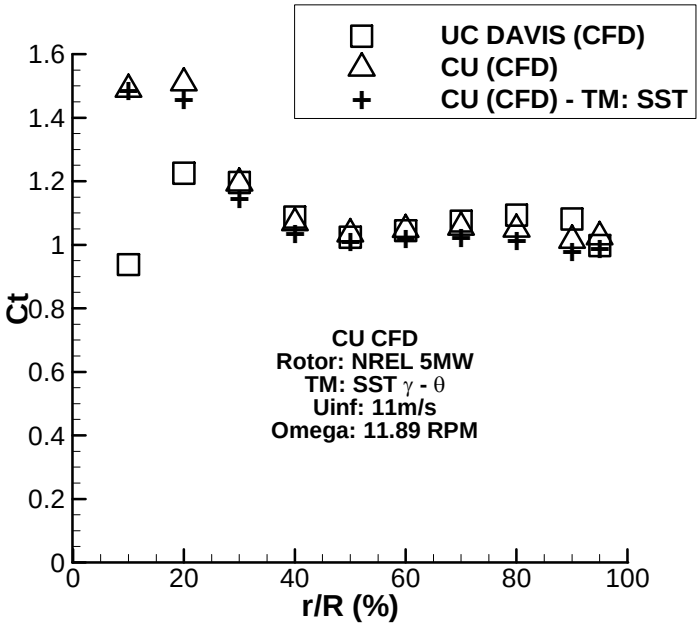

Figure 4-47 Comparison of local thrust coefficient between CU CFD, UC Davis CFD for datum condition (U=11m/s, Rpm= 11.89)

The flow stream traces at the suction side show that the in-board separation is slightly smaller in the CU CFD simulations in comparison with the UC Davis results (Figure 4-48 and Figure 4-49). This may partially explain the larger local torque coefficient in the inboard section for the CU CFD predictions (Figure 4-46). Of course, it is also notable that the CU model includes the hub and spinner which is omitted in the UC Davis results and this is expected to have a notable effect on the local flows in this region.

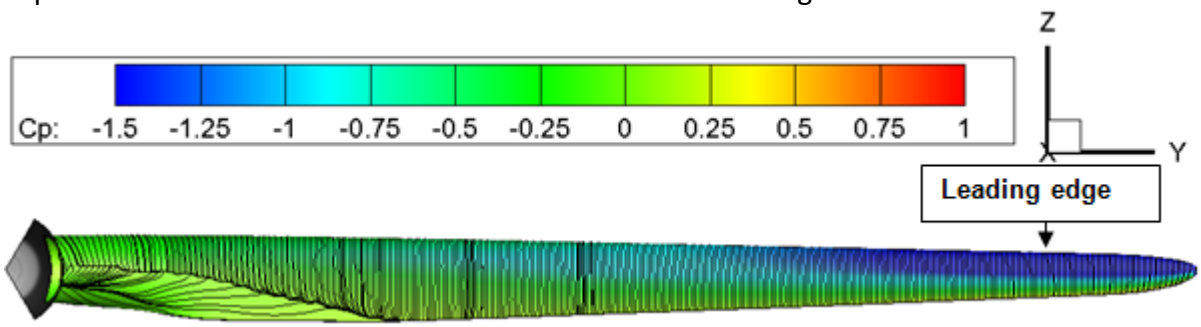

Figure 4-48 Limiting stream traces at suction side of the CU baseline rotor simulation for the wind speed of 11m/s, Omega: 11.89 RPM, TM: SST γ – θ, Curvature correction: On, Re(70% span) : 10 Million, Mach(70% span): 0.16, $C_P = \Delta\text{Pressure}/\frac{1}{2}\rho W_{0.7R}^2$

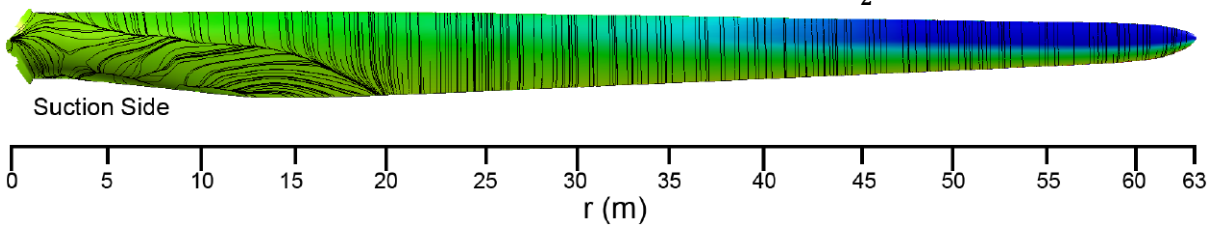

Figure 4-49 Limiting stream traces at suction side of the UC Davis baseline rotor simulation for the wind speed of 11 m/s (Contour levels are not available and not the same as in Figure 4-48) [4]

A more notable difference in flow topology between the CU and UC Davis CFD arises on the pressure side for this same configuration. The CU CFD results indicate that over the inner

portion of the rotor, transition occurs due to a very small laminar separation bubble (Figure 4-50). Clearly this does not arise in the UC Davis case where the flow is assumed to be turbulent from the leading edge (Figure 4-51). Detailed discussion on the separation bubble will be presented in the next section (section 4.3.4.3).

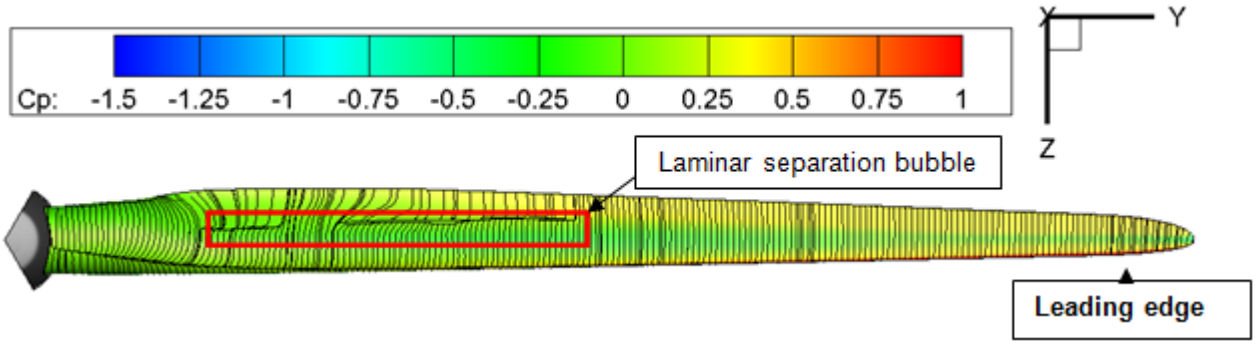

Figure 4-50 Limiting stream traces at pressure side of the CU baseline rotor simulation for the wind speed of 11m/s, Omega: 11.89 RPM, TM: SST γ – θ, Curvature correction: On, Re(70% span): 10 Million, Mach(70% span): 0.16

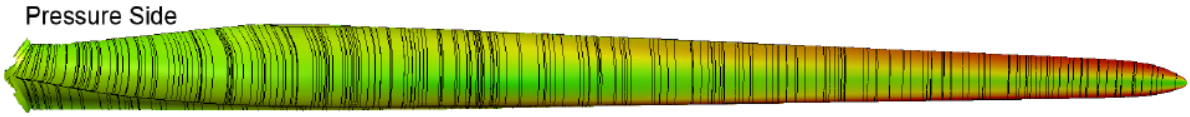

Figure 4-51 Limiting stream traces at pressure side of the UC Davis baseline rotor simulation for the wind speed of 11 m/s (Contour levels are not available and is not the same as in Figure 4-50) [4]

4.3.4.3 CU CFD simulations at different wind speeds

This part of the thesis outlines some of the different flow fields predicted at the off design wind speeds for the CU NREL 5MW rotor. CFD simulations were conducted for four different wind speed configurations within the sub rated range (5 - 11m/s). It is expected that due to the different flow conditions such as local relative velocities and flow angles, different flow topologies are calculated. This work will later allow for the PFC to be assessed over the entire design range and predict its effect on annual yield.

The surface stream-traces on the suction side (Figure 4-52) reveal that the hub separation is present in all the investigated wind speed range. A slight decrease in the extent of the inboard flow separation is seen with reduction in wind speeds (Figure 4-53). However it should be noted that even at a low wind speed of 5 m/s there is still a notable region of separated flow. The likely reasons why this may be possible is due to the increased effective angle of attack, where the flow is more prone to separation (Table 4-13).

On the suction side of the blade hub, a small laminar separation bubble was also observed for the low wind speed (5 and 7m/s), which disappear with increased relative wind speeds (Figure 4-53). This effect is also seen on the pressure surface (Figure 4-54) where the flow field is affected by a laminar separation bubble and induces a flow transition. The analysis of the laminar separation bubble was conducted using an iso-surface where the chordwise velocity is zero shows the position and size of the separation bubble. This iso-surface is not

the dividing stream line separating the separation bubble from the boundary layer i.e. it is only the surface separating the reverse flow fields (Figure 4-55).

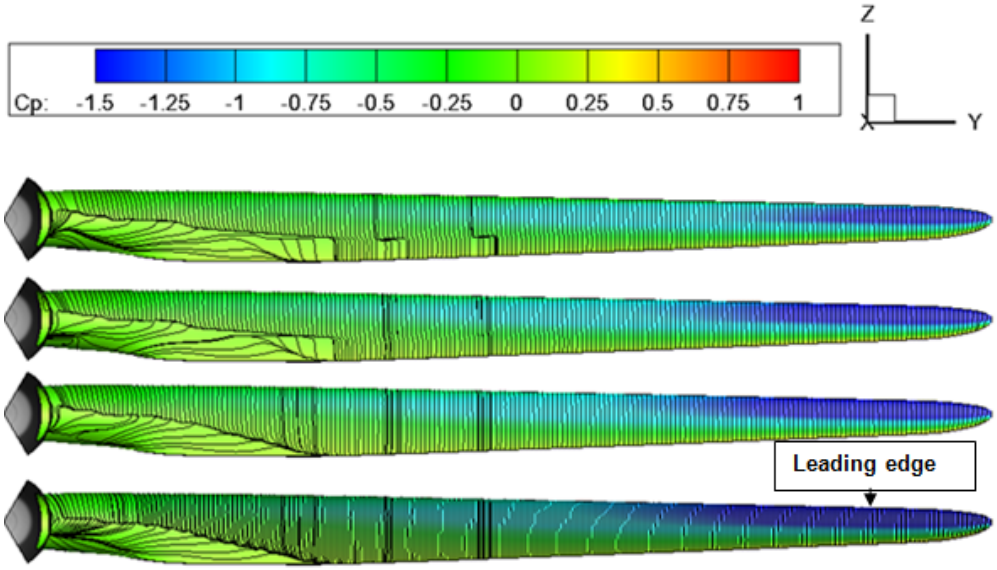

Figure 4-52 Limiting stream lines at the suction surface for all simulated cases (From top – bottom WS: 5 m/s, 7m/s, 9m/s, 11m/s) Time: Steady

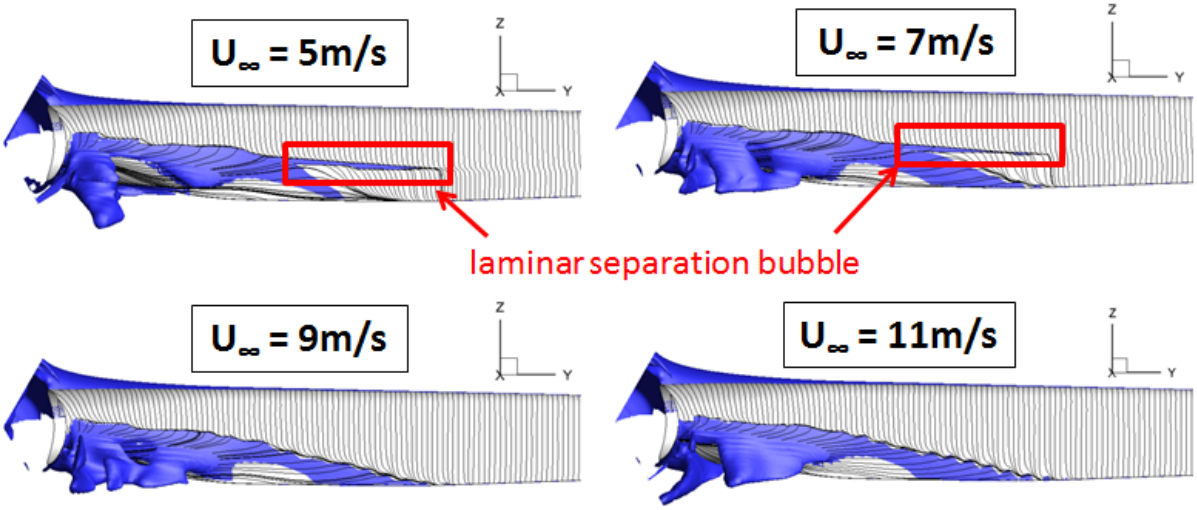

Figure 4-53 Limiting stream lines and iso-surface (blue) showing velocity in the chord wise direction is zero ($V_z = 0\ m/s$). Illustration of the separated region at the hub part of the blade for all the simulated wind speeds (suction side)

Wind speed (m/s)	Omega (RPM)	Inlet relative flow angle $\left[\tan^{-1}\left(\frac{Uinf}{\Omega r}\right)\right]$ at 17% span in degrees
5	7.506	30.75
7	8.469	36.43
9	10.296	37.98
11	11.89	39.56

Table 4-13 Relative flow angle for all the simulated wind speeds

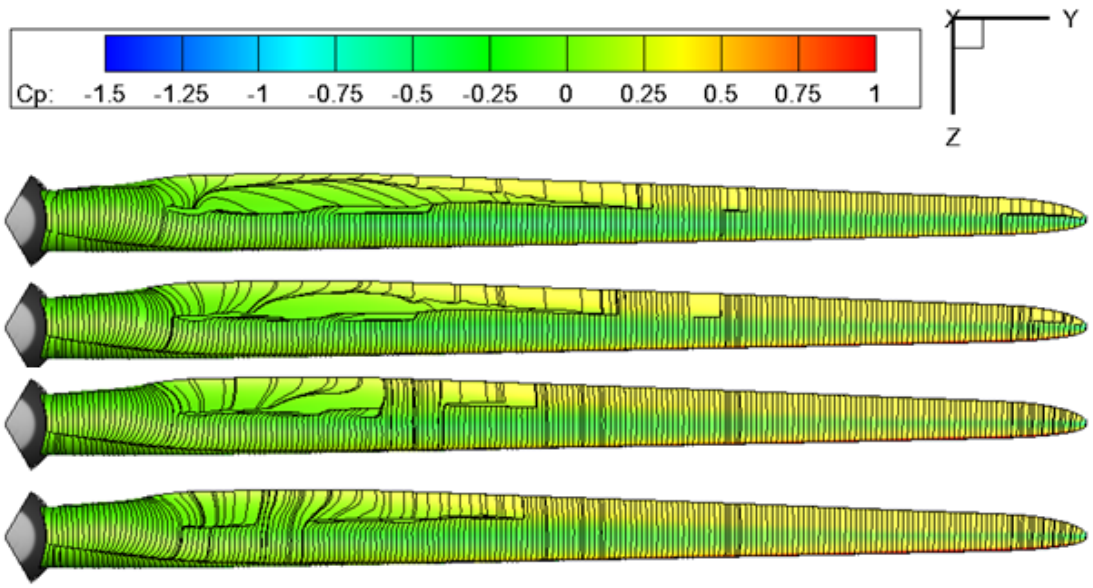

Figure 4-54 Limiting stream lines at the pressure surface for all simulated cases (From top – bottom WS: 5 m/s, 7m/s, 9m/s, 11m/s)

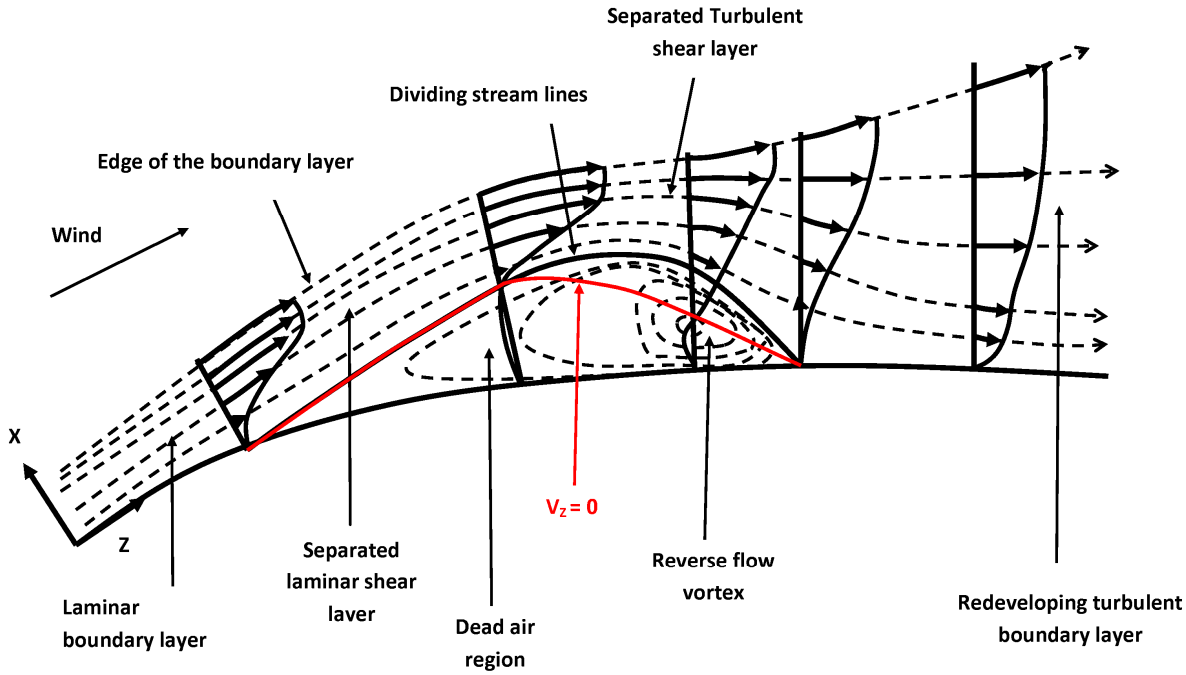

Figure 4-55 Sectional view of a laminar separation bubble, recreated from [67]

Based on this assessment it was clear that the extent of the laminar separation bubble decreases in axial extent with increasing relative freestream velocities (Figure 4-56). The smallest axial extent of the laminar separation bubble was found for the 11m/s wind speed (Table 4-14). For all the simulated cases, the height of the laminar separation bubble is very small relative to the local blade thickness. Even for the bubble with the largest axial extent, which occurs found at U=5m/s, its height from the surface is about 4% of the local blade thickness (Figure 4-57). The contours of turbulence intermittency at a 2D sectional plane of the bubble indicate flow transition is caused by this laminar separation bubble (Figure 4-58).

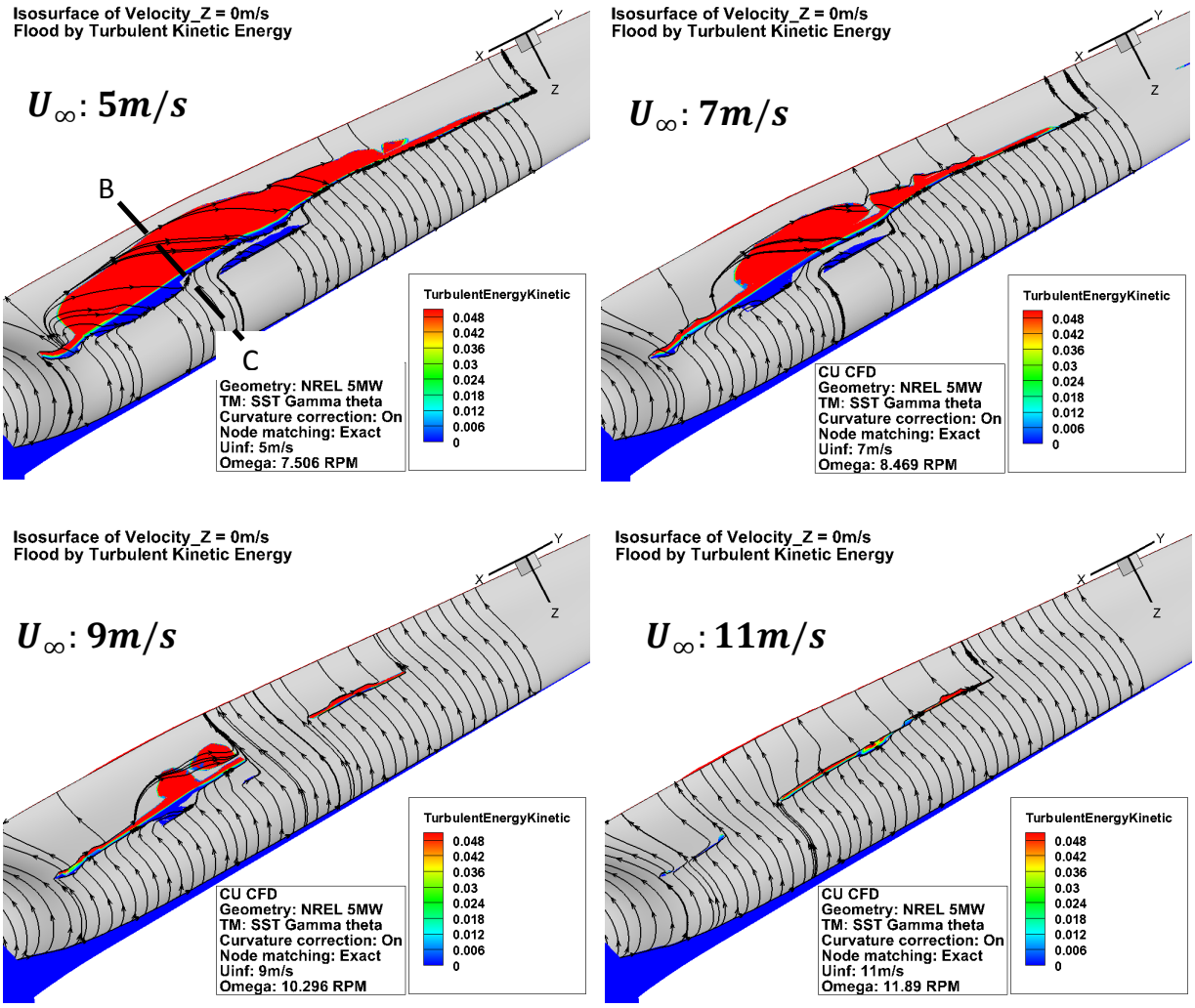

Figure 4-56 Reduction in the axial extent of the laminar separation bubble at the pressure side with wind speed, the 2D plane B –C is presented in Figure 4-57

Wind speed (m/s)	Maximum axial extent of the laminar separation bubble (% local chord)
5	38
7	27
9	22
11	5

Table 4-14 Axial extent of the laminar separation bubble

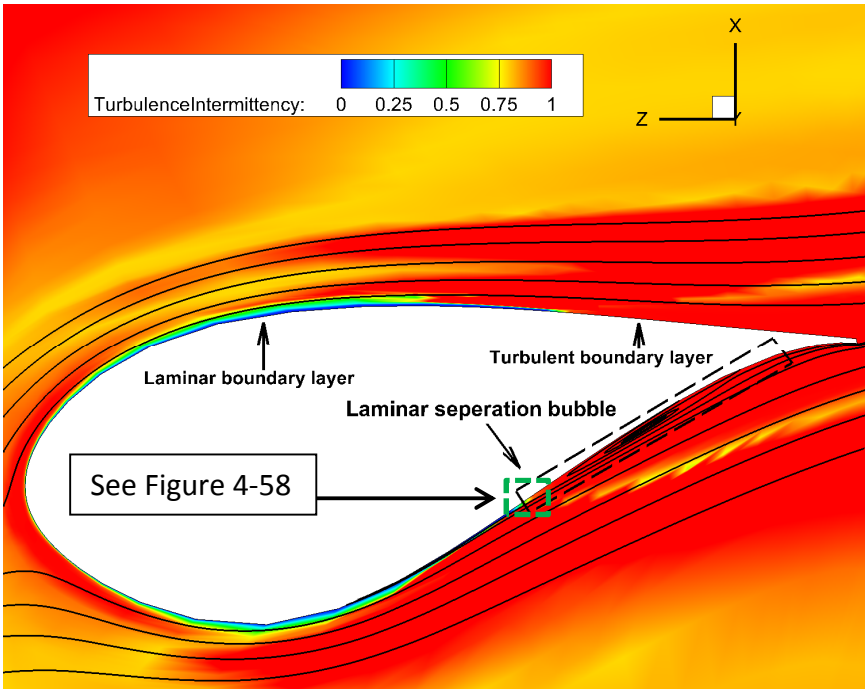

Figure 4-57 Size of the separation bubble at B-C plane, about 30% span (shown in Figure 4-56) for the wind speed of 5m/s

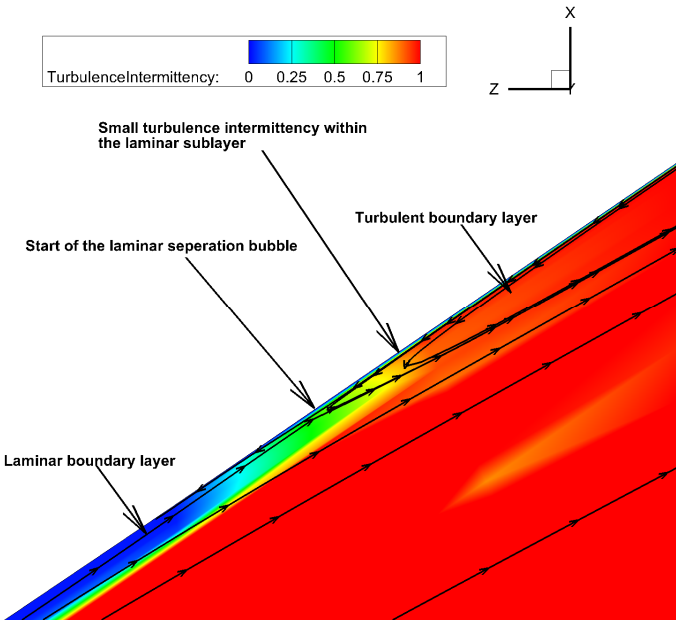

Figure 4-58 Start of the laminar separation bubble on the pressure side and the indication of transition due to the laminar separation bubble at the wind speed of 5m/s

Another flow feature that was identified was the large separated flow found at the blade hub, which seems to be aided by a radial flow towards the blade tip (Figure 4-59). This effect is profound at high wind velocity of 11m/s where the radial flow propagates faster up to 10m/s in the spanwise direction. It is expected that the reduction of these the radial flow at the hub region will reduces the radial extent of the hub separation.

Based on the ideal turbine analysis (Section 2.1), the blade root geometry was unable to obtain the required lift coefficient even with an attached flow regime. The CFD results

suggest that large separated flow exists at this part of the blade which further deteriorates the ability to produce the require lift forces for ideal power production.

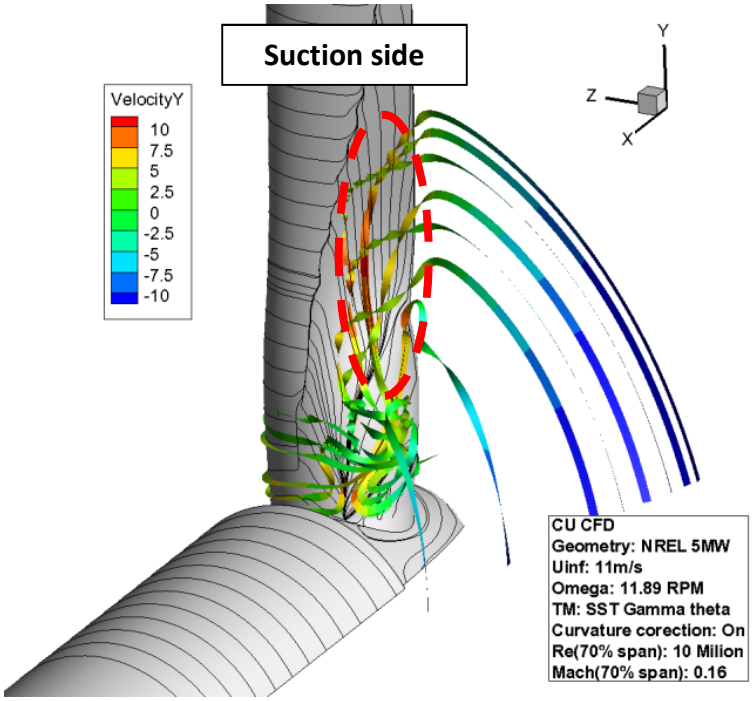

Figure 4-59 Separated flow structure at the blade root at WS: 11m/s, root separation provoke spanwise flow separation (indicated volume ribbons in red)

Finally, an initial assessment of the boundary layer state and the effect of the transition model are considered for the different wind speed and rpm configurations. Turbulence intermittency distribution on the blade was used to determine the transition line on the blade (Figure 4-60 and Figure 4-61). Very low turbulence intermittency were found at the wall as the solver damps out much of the turbulence within the laminar sub boundary layer (Figure 4-58) hence only the rapid change in intermittency is used to predict transition similar to the assessment performed by Menter [68].

Contours of turbulence intermittency on the blade surface reveals that at low wind speeds (5 and 7m/s) most of the blade (>50%) has a laminar flow region (Figure 4-60 and Figure 4-61). The transition line at the suction surface seems to shift towards the leading edge of the blade with increasing wind speed (Figure 4-60); however this shift is not so profound in the pressure side of the blade (Figure 4-61).

There are two transition mechanisms present on the pressure side of the blade. At the intermediate part of the blade (20-60% span) transition is triggered by the laminar separation bubble and for all other parts of the blade, transition occurs without a laminar separation bubble. These flow features would have not been modelled if the flow was simulated using a fully turbulent model. Based on the 2D CFD study (Section 4.2), it was seen that modelling transition improves the drag calculation drastically in terms of the agreement with the measured results. In order to assess the significance of modelling transition for a 3D flow simulation, a detail comparison study was conducted and it is discussed in the next part of the section (Section 4.3.4.4).

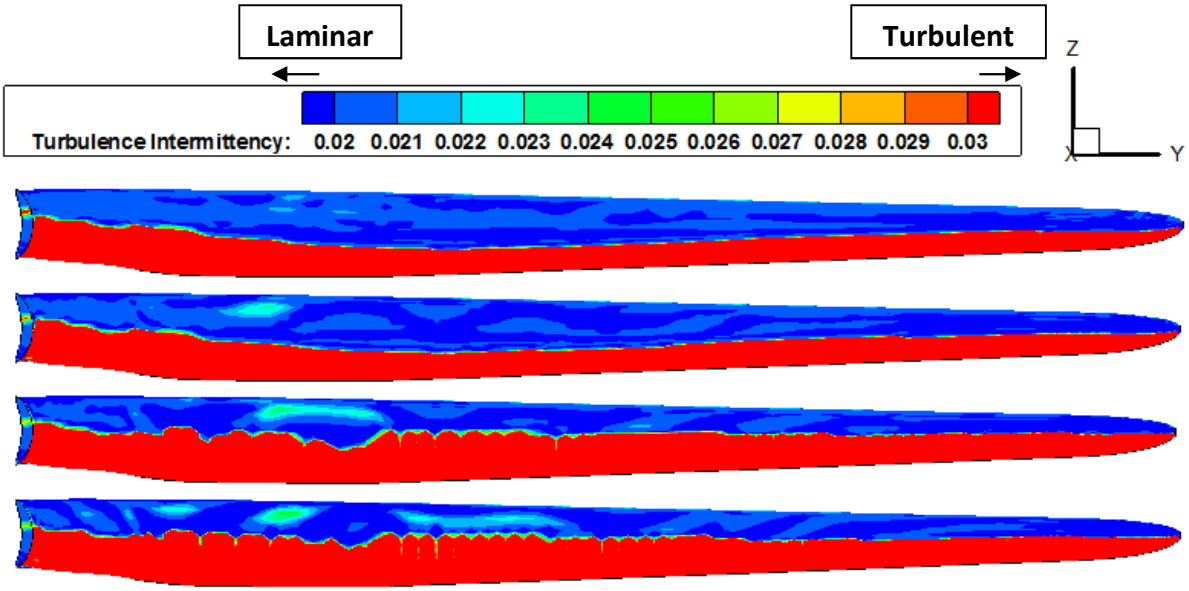

Figure 4-60 Turbulence intermittency contour at the suction surface for all simulated cases (From top – bottom WS: 5 m/s, 7m/s, 9m/s, 11m/s)

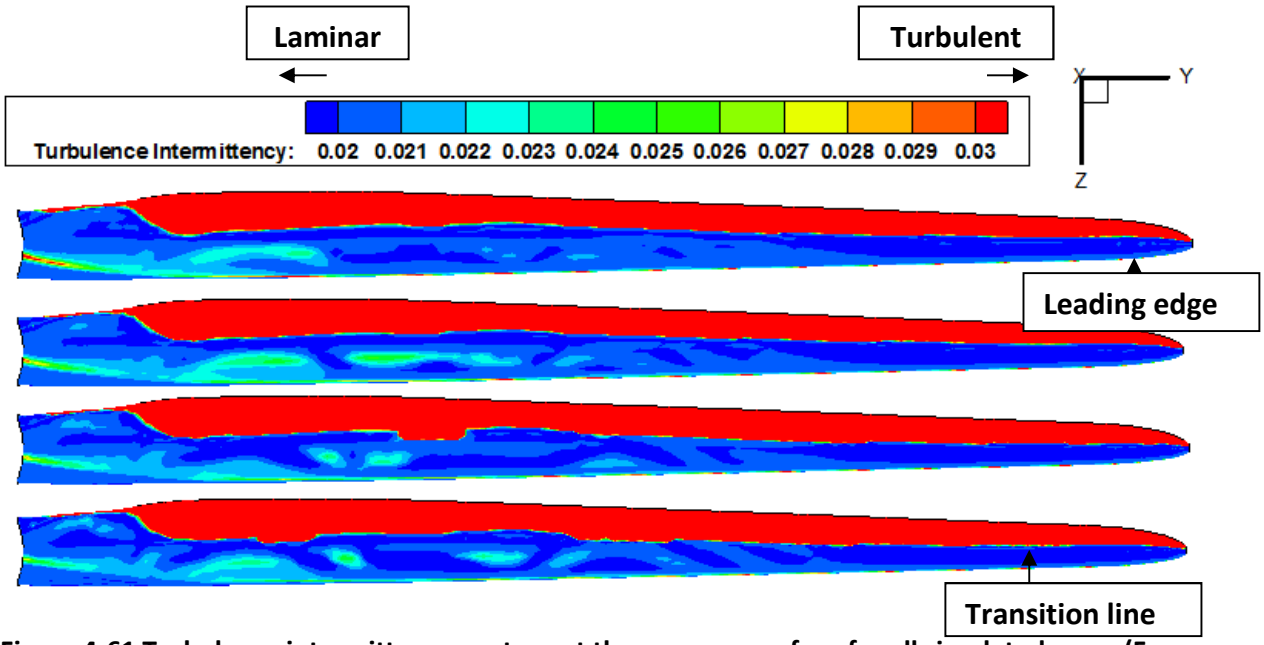

Figure 4-61 Turbulence intermittency contour at the pressure surface for all simulated cases (From top – bottom WS: 5 m/s, 7m/s, 9m/s, 11m/s)

4.3.4.4 Effect of the transition and turbulence models

To evaluate the effects of transition and turbulence model, a fully turbulent turbulence model (SST) was used to calculate the solution for the baseline CU NREL 5MW rotor. The results from this calculation were then compared with the results discussed previously (section 4.3.4.3), where the SST γ-θ transition model is used to compute the solution. The study was conducted for five wind speeds within the sub-rated power region (5, 7, 9 and 11 m/s).

Based on the results (Table 4-15), a notable difference in power was observed between the fully turbulent case and the transition case. This is clearly due to the laminar regions present

on the SST transition case. As discussed in the previous section approximately 50% of the blade is calculated to be in the laminar region, which contributed to a significant amount of drag reduction.

	Power (kW)		
WS	CU NREL (BEM)	Trans (CFD)	Fully Turb (CFD)
5	431	398	367
7	1284	1256	1185
8	1919	1896	1793
9	2732	2680	2563
11	4956	4927	4713

Table 4-15 The effect of transition and turbulence models on power

The results from the SST transition simulation agree well with the power predicted using BEM method. This is expected as the data used for the BEM calculation includes the effect of transition. Largest difference of 7.5% was achieved at the wind speed of 5 m/s. At this wind speed the differences between the fully turbulent case and the BEM computed power was found to be nearly double the difference found for the SST transition case (14.7%).

Notable differences in the hub separation were also found between the fully turbulent calculation and the transitional calculation (Figure 4-62). One of the main differences was that the fully turbulent calculation does not compute the small laminar separation bubble found in the results from the transitional calculation.

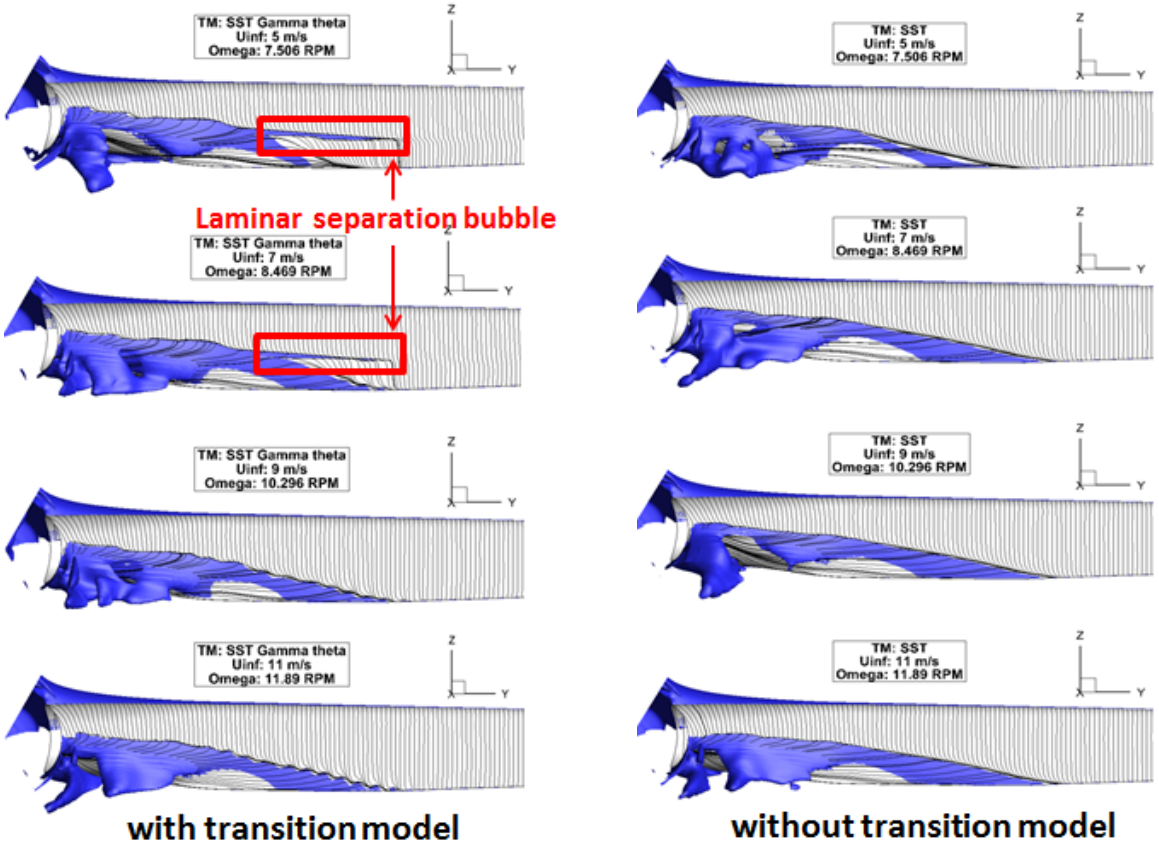

Figure 4-62 Hub separation flow topology with and without transition model (From top – bottom WS: 5 m/s, 7m/s, 9m/s, 11m/s)

4.3.4.5 Summary

Based on this investigation, it is clear that transition modelling changes the integrated blade forces and flow topology at the blade root. The results from the transition model CFD agree well with the BEM computed power. The measurements used for the BEM calculations also include the effect of transition. Similar conclusions were presented by Menter [68], where it was reported that up to 80% difference in torque calculations were seen between the fully turbulent and transition modelled simulations of the NREL Phase VI turbine. The transition model calculation achieved relatively better agreement with the measurements [68]. It is important that correct flow characteristics are calculated and are comparable with the measurement for credible results. The 2D CFD validation study suggested that transition modelling is important for the baseline rotor computation. Due to the absence of measurements for this concept turbine a 3D CFD validation study was not possible. Based on the 2D assessment it is decided that SST γ-θ transition model will be used for this project.

It is also noted that the 2D CFD work recommended a grid size of about 100,000 elements while it was only viable to achieve about 70,000 elements for a single radial location of the 3D blade, which corresponds to about 7 million elements for the entire domain. Therefore it is expected that the level of validation achieved for the 2D CFD model may not be achieved for the 3D CFD model.

4.3.5 Conclusion

A 3D CFD model for the baseline rotor was successfully generated. The simulated results were compared against BEM and other literatures. The results from the simulations suggest that current CFD methods are adequate to resolve the 3D flow physics. Comparison of the CFD results for the baseline rotor with BEM and other literature (UC Davis [4] and Riso DTU [66]) indicate that realistic solutions are attainable with the present CFD methods.

Mesh independence and domain extent studies have been successfully completed for the current 3D CFD grid, where a series of different grid density and different domain extents were investigated for a grid independent solution. It was established that 7 million elements with a domain extent of 10R will be used for this project.

5 Assessment of PFC devices

In the initial stages of the research seventeen passive flow control (PFC) devices which could be applicable for use on wind turbines were reviewed. Based on the initial assessments, three concepts were selected for further research, these are:

1. Vortex trapping
   - Stepped airfoil
     - Fertis' suction side step airfoil [17]
     - Pressure side step airfoil [69]
     - Extruded 3D step implementation
2. Passive ventilation
   - Passive air jet vortex generators [22]
3. Corrugated leading edge wing [70]

The objectives of integrating the PFC devices were to:

- Increase aerodynamic efficiency (L/D) in the outer blade (>20% of R/r)
- Lift augmentation for the inner blade root (<20% of R/r)
  - Requirement based on BEM analysis (Section 2.1)
  - Requirement based on CFD work (Section 4.3.4)
- Reduce span wise flow migration
  - Requirement based on CFD work (Section 4.3.4)

This section summarises the CFD and analytical work conducted to evaluate the effect and performance of the chosen PFC devices. Initially the CFD models used for the study are presented and then the results and finally the conclusions are discussed.

5.1 CFD methods in general

The CFD simulations were conducted following the experience gained through the initial and preliminary assessment (Section 4). All the simulations conducted to evaluate these PFC devices are simulated in steady state conditions. Appropriate grid elements and domain extents were decided based on previous validation experiences during the course of this research (Section 4.2.3). Nearly all of the simulations were conducted with the SST $\gamma - \theta$ transition model. Curvature correction was activated for all the CFD simulations. Further details of the CFD methods for the individual cases will be presented under their corresponding sections.

5.2 Vortex trapping

One method of increasing lift is to consider a steady separated vortex above a wing at high angle of incidence [3]. In this arrangement, a trapped vortex can arise where the use of a step [17] or a cavity helps to keep it in position [3]. Three different configurations were investigated to evaluate their performance for a wind turbine blade (Figure 5-1). The first two devices, the suction side step and pressure side step were investigated using 2D CFD analysis. The third case investigated under the vortex trapping method was the suction side step modification on the full scale rotor wing 3D CFD analysis. The CFD simulations were

conducted to assess the baseline CFD models for their ability to replicate the previously reported experimental or computational work [17] [69].

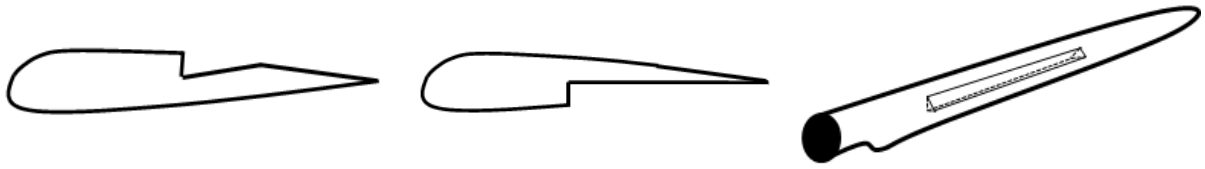

(a) **(b)** **(c)**

Figure 5-1 Investigated modifications for the vortex trapping device, (a): suction side step, (b): pressure side step, (c): suction side step modification on a wind turbine blade

5.2.1 Fertis' suction side step device

It is expected that the suction side step design proposed by Fertis has the potential to increase the lift coefficient by 11% and decrease drag coefficient by 72% at the AoA of 15^{o} [17]. It was reported by Fertis that the device is able to delay stall by 5^{o} AoA.

5.2.1.1 CFD model

The NACA 23012 airfoil was used in Fertis' experimental study, which was conducted at the 470,000 Reynolds number. An O-grid topology due to the airfoil's blunt trailing edge with 20 chords domain extent was selected for the 2D CFD grid (Figure 5-2). The grid generated for the baseline airfoil contained 200,000 hexahedral elements, with 600 elements placed around the airfoil.

Based on Fertis' study a suction side step that begins at the 50% chord (c) and ended at the 75%c with a step depth of 50% thickness (t) showed the best performance within the examined AoA range (Figure 5-3). Up to $\Delta Cl = +0.31$ were reported with this design [17]. Therefore this design was selected for this CFD analysis and the baseline grid was modified to capture the suction side step alteration (Figure 5-4). The node distribution was kept constant from the baseline grid for the NACA 23012 airfoil. To match the experimental conditions, this study was conducted at the Reynolds number of 470,000 within the angle of attack range of $5^{o} – 25^{o}$.

Iterative convergence was assumed to be achieved when the residuals from the momentum and continuity equation reach below 1e-4 and the lift and drag forces on the airfoil is achieved within 0.5% of the reported values.

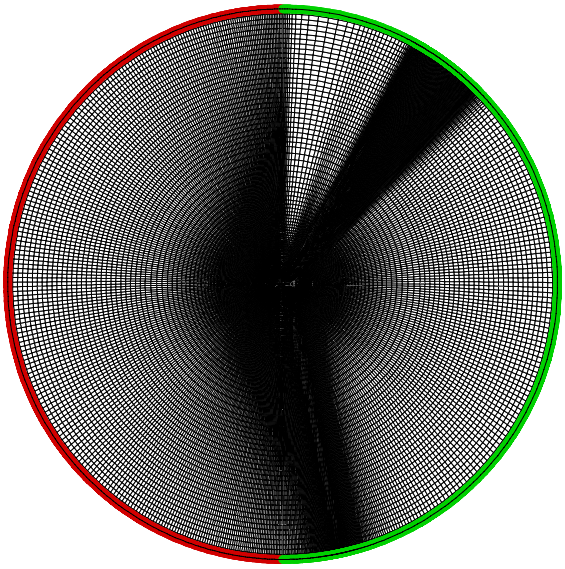

Figure 5-2 O-mesh topology adapted for Fertis' suction side airfoil (Airfoil: NACA23012, Red: Velocity inlet, Green: Pressure outlet)

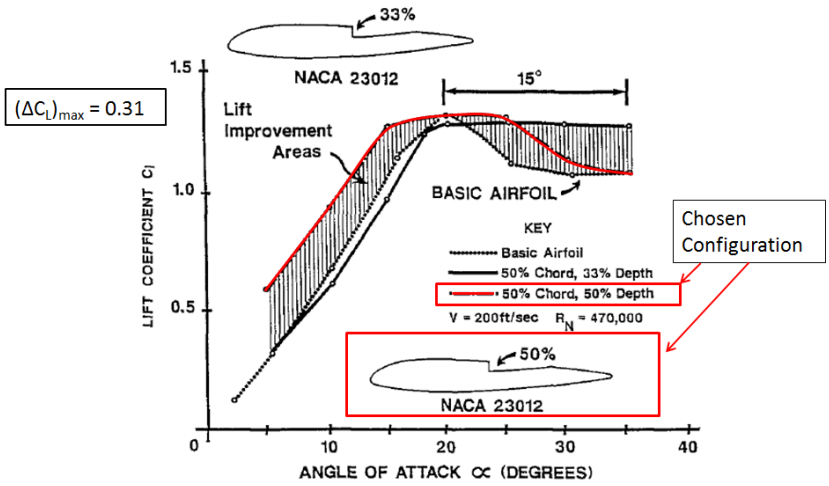

Figure 5-3 Changes in lift coefficient due to suction side step modification, altered from [17]**, chosen design: start-50%c, end-70%c, 50%depth**

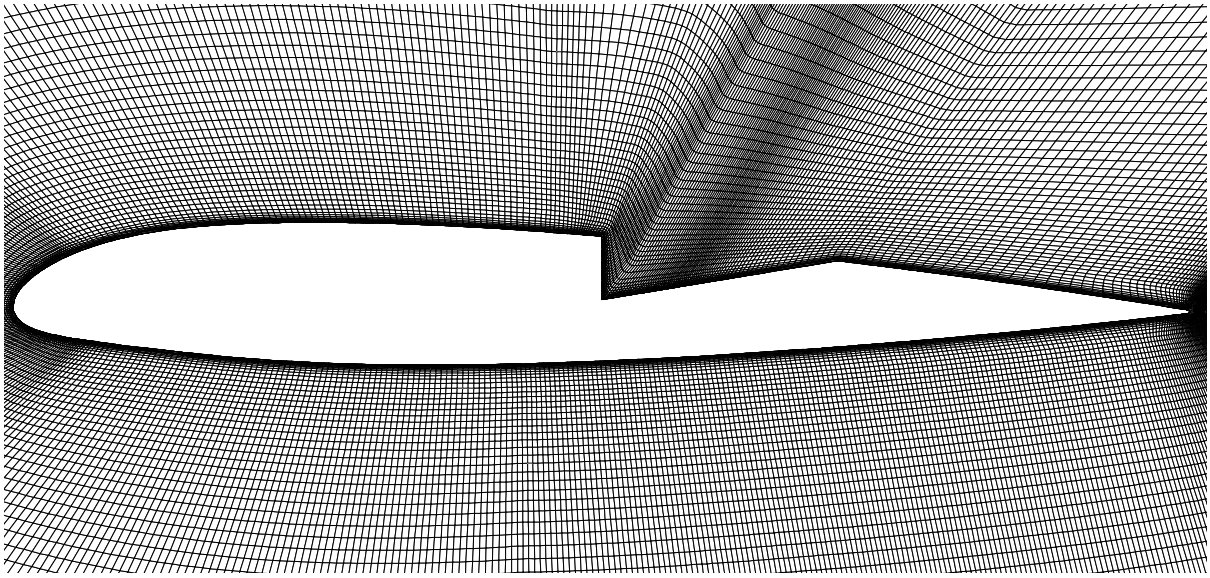

Figure 5-4 Mesh adapted for Fertis' suction side step device, NACA 23012, step: start-50%c end-70%c depth- 50%t, Grid: O-topology, 200,000 hexahedral elements, with 600 elements placed around the airfoil

5.2.1.2 Results

The results from the CFD simulation (Figure 5-5) showed poor agreement with the measurements from Fertis' study [17]. Up to 70% difference in lift coefficient were seen at the AoA of 10^{o} between the CFD and measurements. An XFoil simulation was also conducted for the baseline airfoil to compare with these results, which agreed well with the CFD results. Up to 10% difference in lift coefficient was seen between the XFoil and CFD results at the AoA of 10^{o}.

Fertis' results for the baseline airfoil were also compared against another experimental result at a larger Reynolds number of 3 million [50] (Figure 5-6). This also showed large differences in lift coefficient up to 70% between them, which may be due to the change in Reynolds number. However the measurements from [50] agreed well within 8% of the lift coefficient at the AoA of 10^{o} from the XFoil simulation of the baseline airfoil i.e. the disagreement between XFoil and Fertis' results raises some uncertainty with the measured results from Fertis. Despite this poor validation with Fertis' results, this investigation of the suction side step modification was evaluated using CFD.

The result from the baseline CFD model for the suction side step shows no aerodynamic improvements by this device. Based on the results, the suction side step reduces lift production by up to 8% and increases drag force on the airfoil by 50% at the AoA of 10^{o} (Figure 5-7). This is contrary to the benefits reported by Fertis [17].

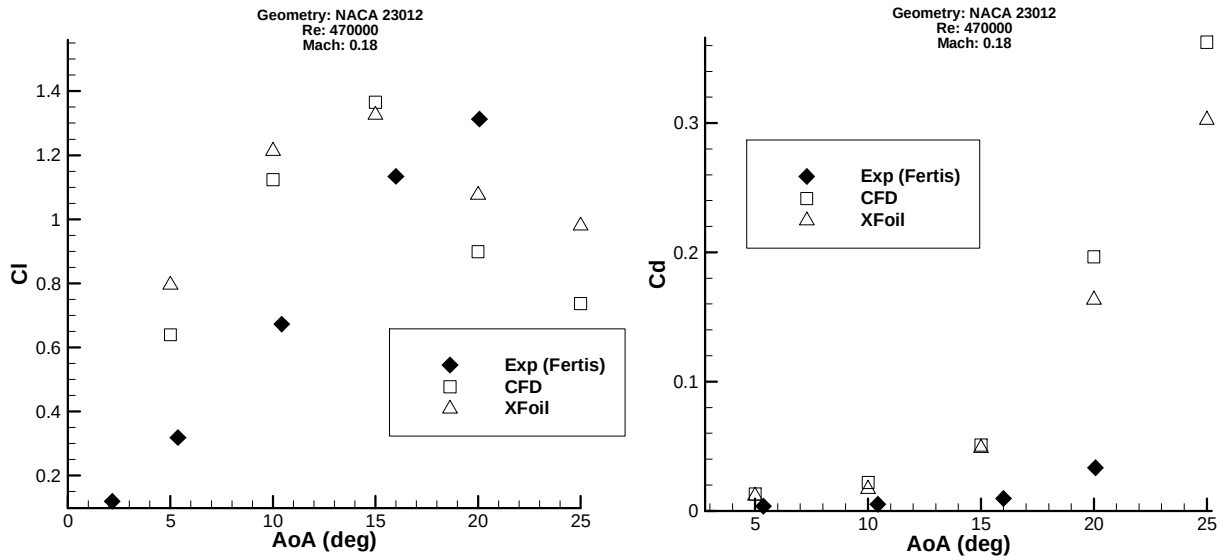

Figure 5-5 Comparison of lift (left) and drag (right) coefficient between CFD, XFoil and experiment (baseline airfoil)

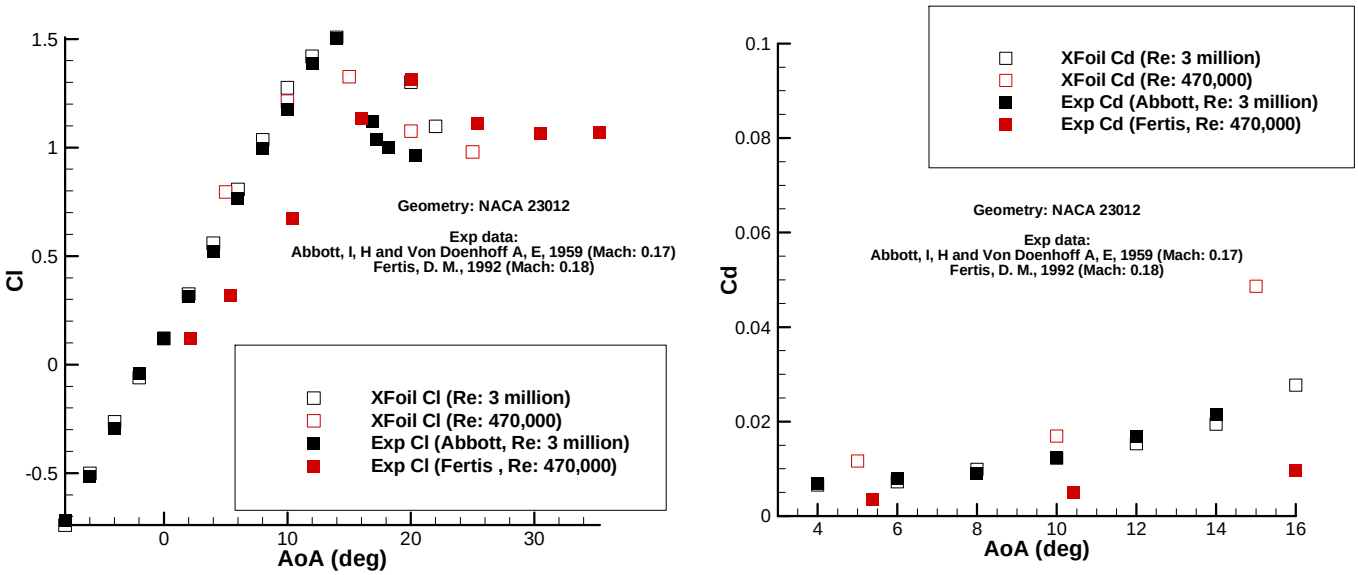

Figure 5-6 XFoil results comparison with another experimental data for NACA 23012 (Exp source: [17] **and** [50]**)**

The results from this 2D CFD simulation of the Fertis' suction side step show that vortex trapping is possible with a suction side step for angle of attack up to 10^{o} (Figure 5-8 and Figure 5-9), therefore this result is of interest for wind turbine application where the local AoA are below 12^{o}. For 15^{o} angle of attack, the Fertis' suction side step results in an increase in the chord wise flow separation (Figure 5-10), and this may not be a concern within the operating regime of a large scale wind turbine.

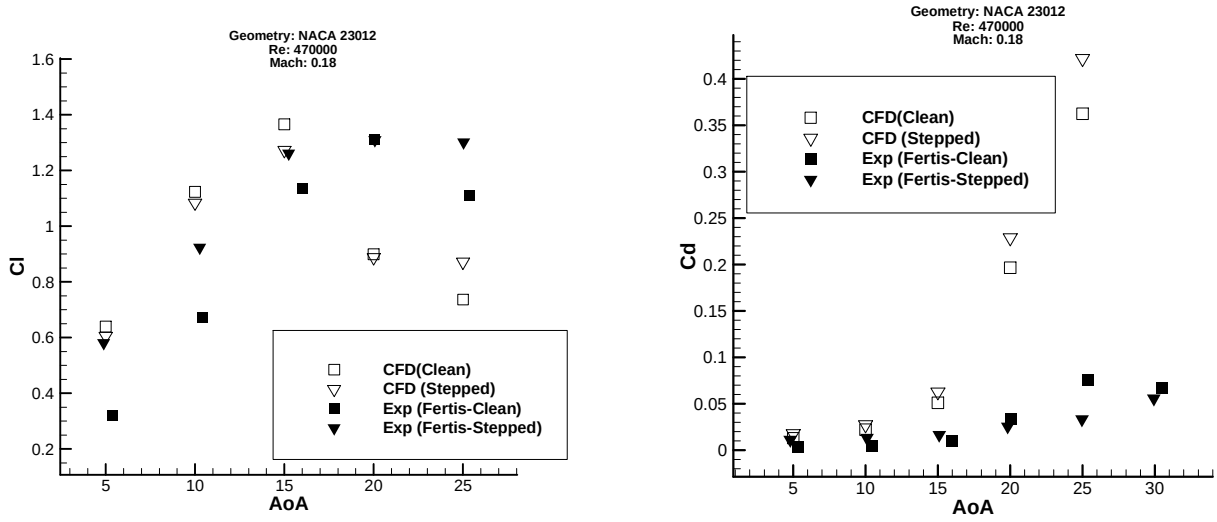

(a) (b)

Figure 5-7 Coefficient of lift (a) and drag (b) as a function of angle of attack for suction side step device

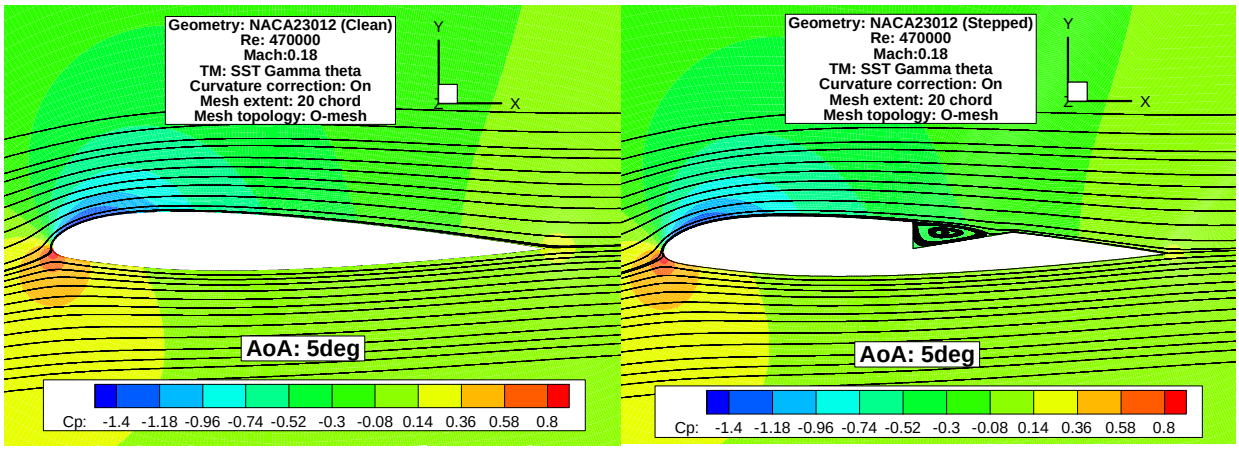

Figure 5-8 Stream line pattern for the Fertis' suction side step airfoil (Geometry= NACA 23012, Re: 470, 000, M: 0.18, AoA: 5°, left: clean airfoil, right: modified airfoil)

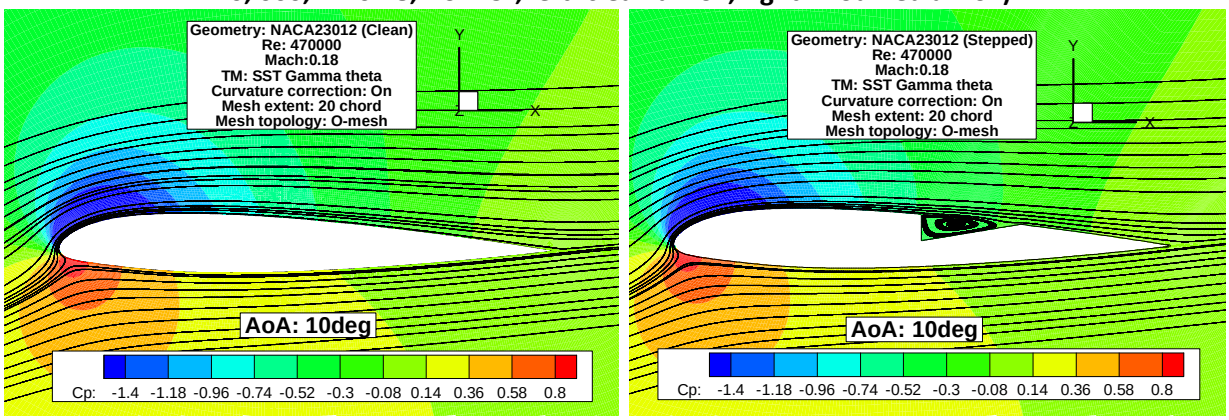

Figure 5-9 Stream line pattern for the Fertis' suction side step airfoil (Geometry= NACA 23012, Re: 470, 000, M: 0.18, AoA: 10°, left: clean airfoil, right: modified airfoil)

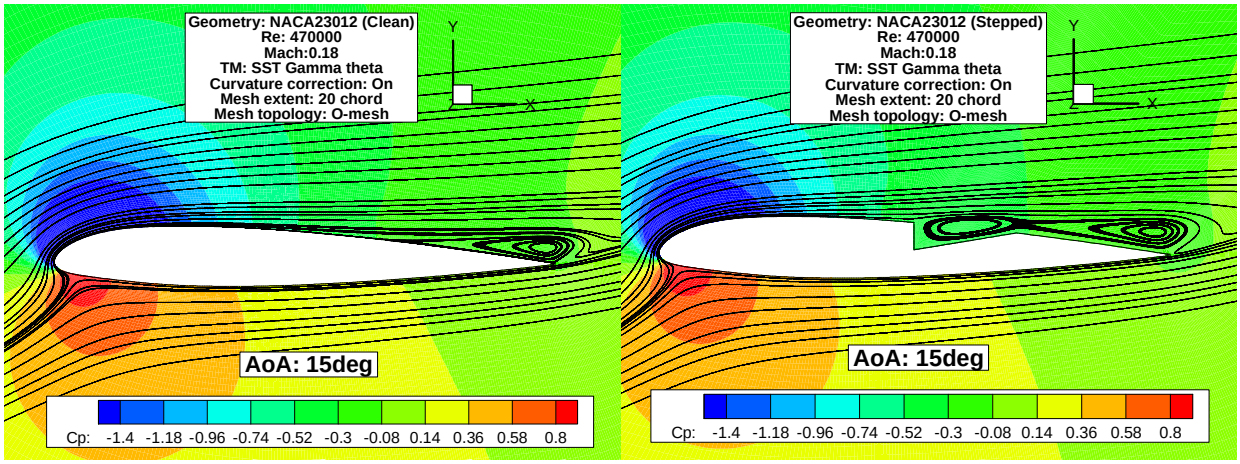

Figure 5-10 Stream line pattern for the Fertis' suction side step airfoil (Geometry= NACA 23012, Re: 470, 000, M: 0.18, AoA: 15°, left: clean airfoil, right: modified airfoil)

Overall, based on the surface static pressure distribution comparison (Figure 5-11) between the clean and modified airfoil, the Fertis' suction side step device contribute to a small beneficial reduction of suction pressure of about 10% within the step at x/c=0.6. Greater reduction up to 15 and 55% in suction pressure was seen at the start and end location of the step, which is greater than the reduction in pressure contributed by the vortex. However a large pressure rise up to 65% found at the aft portion (x/c=0.67) of the step seems to outweigh these small benefits in reduction in pressure.

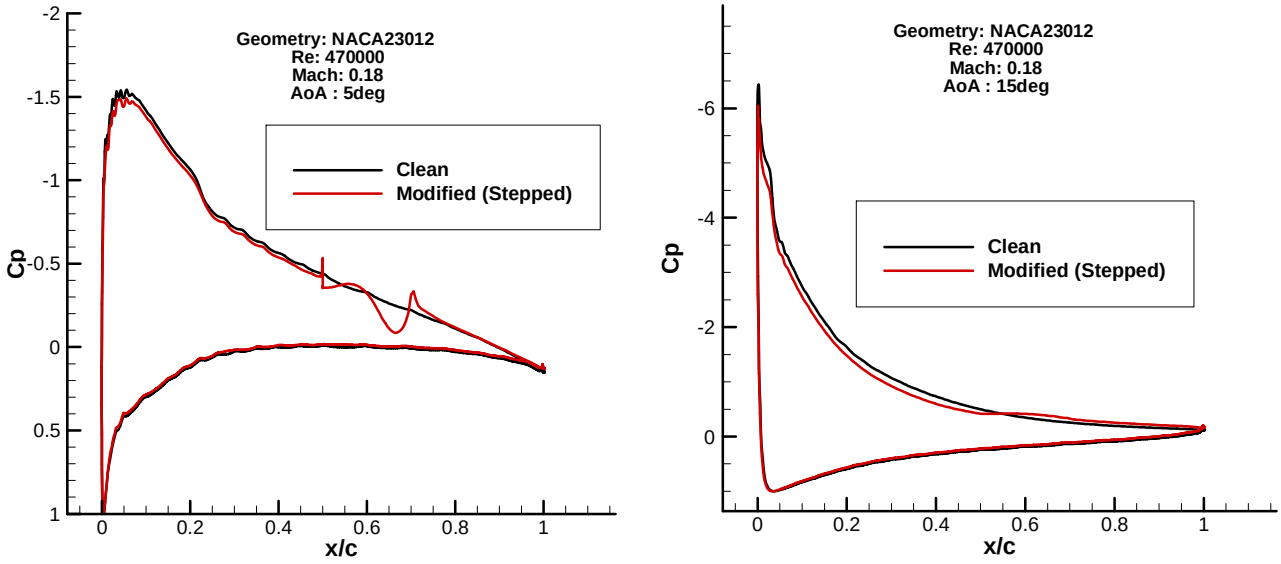

Figure 5-11 Coefficient of pressure distribution (Device: suction side step, left: 5° AoA, right: 15° AoA)

At large angles of attack of 15°, a small beneficial reduction in pressure up to 30% were seen downstream from the step (x/c: 0.6 - 1) due to the suction side step modification (Figure 5-11). The pressure distribution upstream of the step is also found to be negatively affected (decreased suction).

5.2.1.3 Discussion

Currently there is an uncertainty on the credibility of the work by Fertis. The study on a suction side step modification showed no beneficial aerodynamic effects, contrary to the work by Fertis. This current study was conducted in a 2D environment and there might be greater promise for the step modification within a 3D flow environment such as the experiment conducted by Fertis. Fertis' experiment was conducted using a NACA 23012 wing and no end plates were mentioned on his publication [17] i.e. a 3D flow flied. The loss of suction is maybe due to the two dimensional nature of the CFD case.

The 3D version of this step device will enable its performance to be assessed in the environment for a rotor blade, where its performance can be evaluated over the different sectional pressure distribution and geometry. It is also noted that Rossow [16] reported that mass removal at the core of the vortex helps to generate and maintain the vortex in its location and it is expected that the radial flow present on the rotor blade may help to achieve this requirement in the 3D environment. Thus a 3D version of this technology has been studied as part of these preliminary assessments. It is expected that the spanwise flow will help to transport the mass flow at the vortex core and produce a beneficial vortex. The results from this study will be presented later in section 5.3. However the 2D CFD work on the suction side step was not investigated further.

5.2.2 Pressure side step

The pressure side step device originated from the CFD work done by Finash [69]. Finash's study was conducted using a NACA 0012 airfoil, and various step configurations were studied. However only the step modification that originates at the 50% chord with 50% depth on the pressure side extending to the TE of the airfoil was chosen for this investigation (Figure 5-13). Finash reported that at 10^{o} angle of attack, an increase of 0.2 in the lift coefficient is possible with this device (Figure 5-14). This CFD study was conducted to replicate Finash's findings that were obtained at the Reynolds number of 500,000. Simulations were conducted with AoA range of -5 – 20^{o}.

5.2.2.1 CFD model

The grid was constructed based on the mesh described in the work of Finash [69], and from the experiences gained from the validated 2D CFD methods (Section 4.2.3). A domain extent of 40c was chosen for this study which is about ten times larger than the CFD model used by Finash (4c). C-mesh grid topology (Figure 5-12) was selected for this 2D CFD model due to the airfoils sharp trailing edge. The grid was generated with about 50,000 elements.

Iterative convergence was assumed to be achieved when the residuals from the momentum and continuity equation reach below 1e-4 and the lift and drag forces on the airfoil is achieved within 0.5% of the reported values.

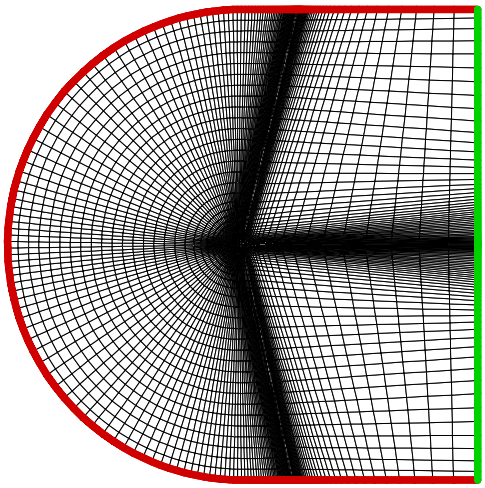

Figure 5-12 C-mesh topology adapted for pressure side step airfoil (Red: Velocity inlet, Green: Pressure outlet), step: originates at 50% chord with 50% depth on the pressure side extending to the TE, mesh size: 50,000 elements, domain extent: 40c

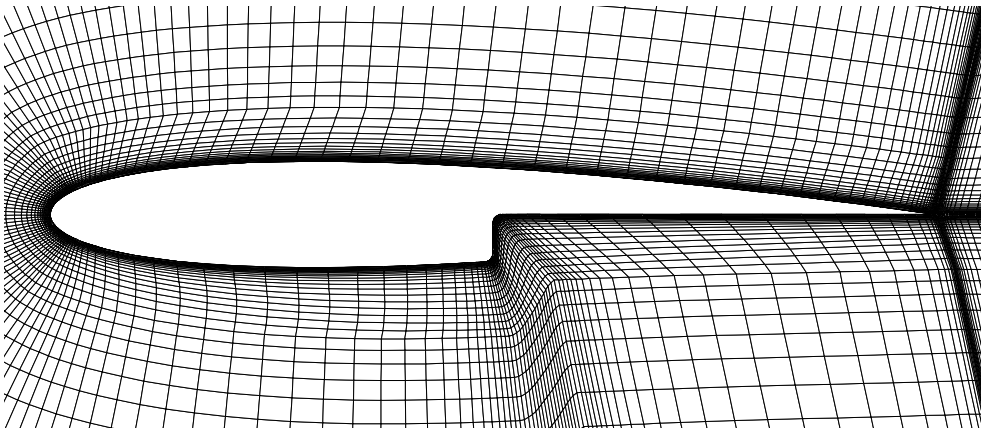

Figure 5-13 Mesh generated for pressure side step device (213 elements around airfoil)

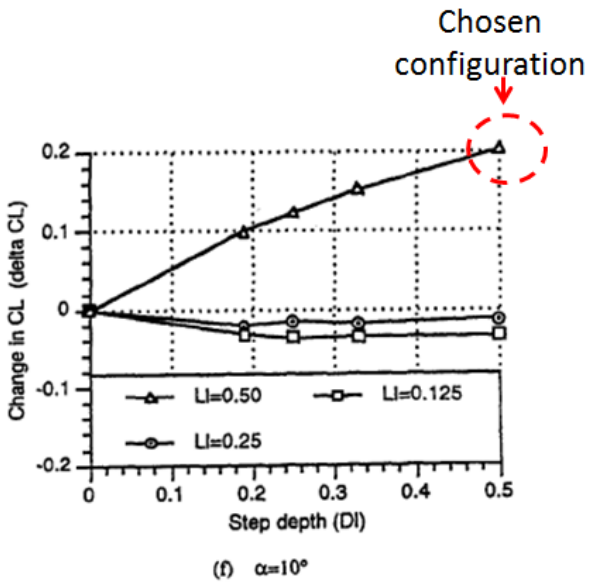

(f) α=10°

Figure 5-14 Selected pressure side step configuration (DI: Step depth in chords, LI: Step location in chords) [69]

5.2.2.2 Results

It was not possible to compare the baseline results for the NACA0012 airfoil with Finash's study as only the relative change in lift due to the step modification was reported in [69]. However a comparison was made between the results from the CFD and measurements for the clean NACA0012 airfoil. The measurements were taken from the work of Jacobs and Sherman [71] at a slightly higher Reynolds number of 660,000, while the CFD simulations were conducted at the 500,000. Therefore it is expected that some variation is the integrated forces may be due to this difference in flow conditions. It was found that the baseline CFD model for the clean NACA0012 was able to calculate the lift forces within 30% this large difference was seen at the large AoA of 15^o. For the pre-stall AoA (0-10^o) the CFD calculates lift forces within 20% of the measurements.

Very large differences were seen between the CFD calculated drag forces and the measurements. Up to an order of magnitude (x10) difference in drag forces were found at the AoA of 15^o. This is expected of 2D steady CFD simulation i.e. the flow is grossly separated 2D steady analysis is not valid. It was only at the lower AoA of 5^o the CFD calculated drag force agreed well with the measurements within 3%. Overall these results show that the current CFD model is insufficient to calculate the baseline aerodynamics of the NACA0012 airfoil above the AoA of 5^o. Despite this poor validation, it was decided to test the step modification to determine the relative change on the aerodynamic forces.

The integrated force distributions show that an increase in lift was achieved by the pressure side step for all the simulated angle of attack (Figure 5-15). Largest lift increment of up to 50% was seen at the AoA of 15^o by this pressure side step modification. While at the lower AoA of 5 and 10^o a lift increment of 10 and 15% was achieved respectively. Only one of the results from this study (AoA: 0^o) agree with the lift increment (0.17 increase in lift coefficient) predicted by the Finaish et al (Figure 5-16).

It was found that this device increases the drag forces for all the tested angle of attack (Figure 5-15). A maximum drag increase of 0.1 in drag coefficient was seen at 15^o AoA. The relative change in drag forces were found to be large at the pre-stall AoA, where the minimum drag coefficient at the AoA of the airfoil (Cd=0.008) was increased by up to 110% (cd = 0.017) by the step modification. The increases in drag forces were found to be about 80 and 40% at the AoA of 5 and 10^o respectively.

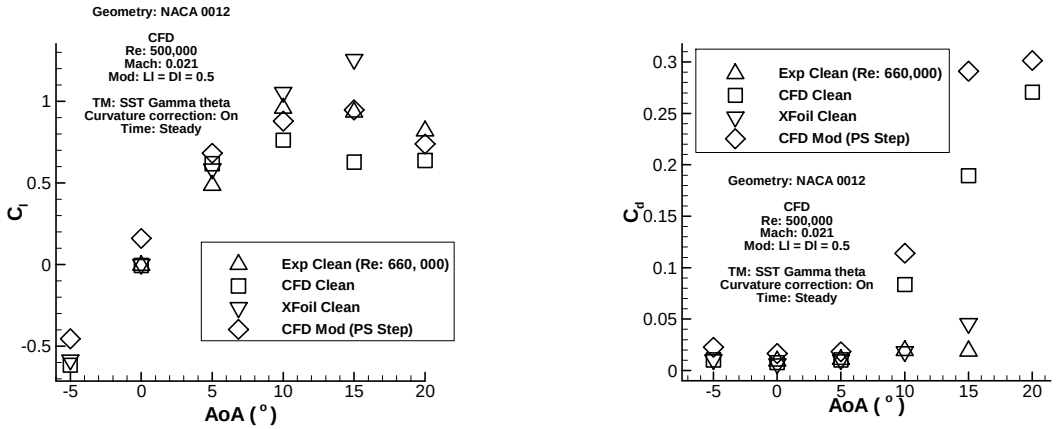

Figure 5-15 Comparison of lift (left) and drag (right) coefficient between CFD, XFoil and experiment (pressure side step)

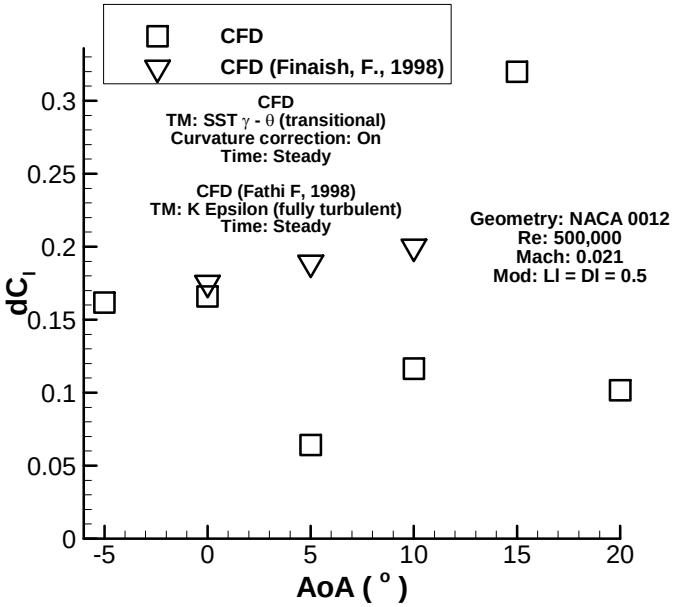

Figure 5-16 Change in lift comparison between CFD and published results [69]

The CFD results for this device, shows that vortex trapping at the pressure side of an airfoil is possible with the tested design at all the simulated angle of attacks. Based on the streamline patterns for the 5° angle of attack (Figure 5-17), it is clear that the downwash angle has been increased due to this step modification. The increase in downwash angle is an indication of the increased circulation.

At a higher angle of attack (AoA: 10°) a large separated flow is present on the suction side of the modified airfoil (Figure 5-18). This may be due to an increase in the upwash angle. Overall the pressure side step design configuration slightly increases the upwash and downwash angles, this result in a higher circulation around the airfoil. These effects are very similar to an airfoil with an increased camber.

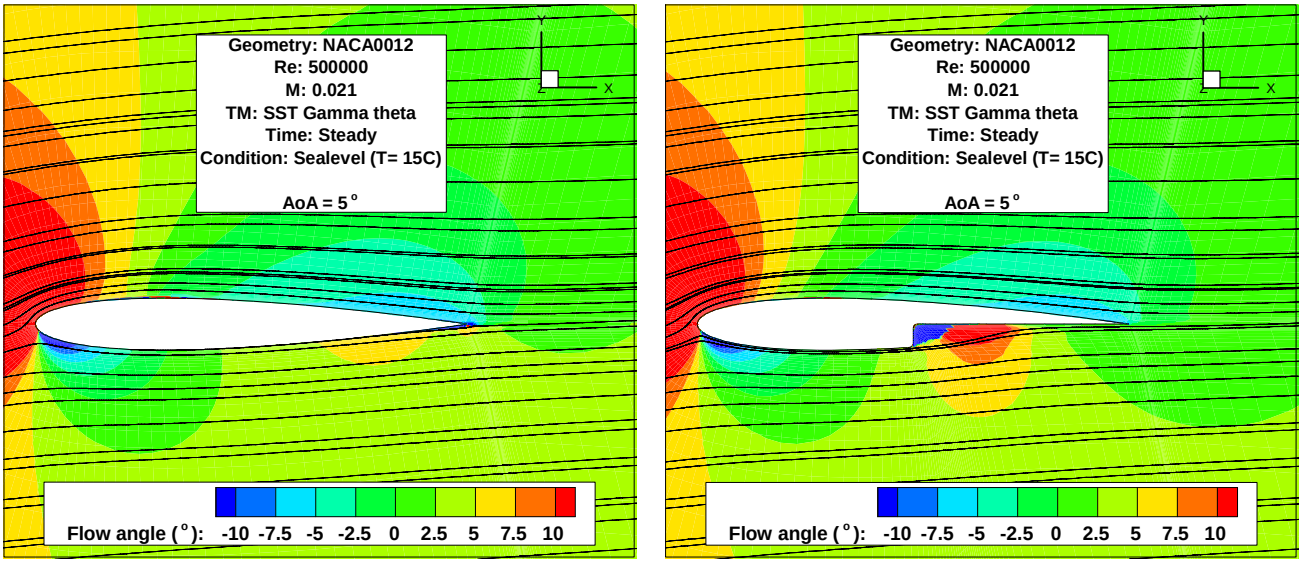

Figure 5-17 Stream line pattern for the pressure side step airfoil (AoA: 5°, left: clean airfoil, right: modified airfoil)

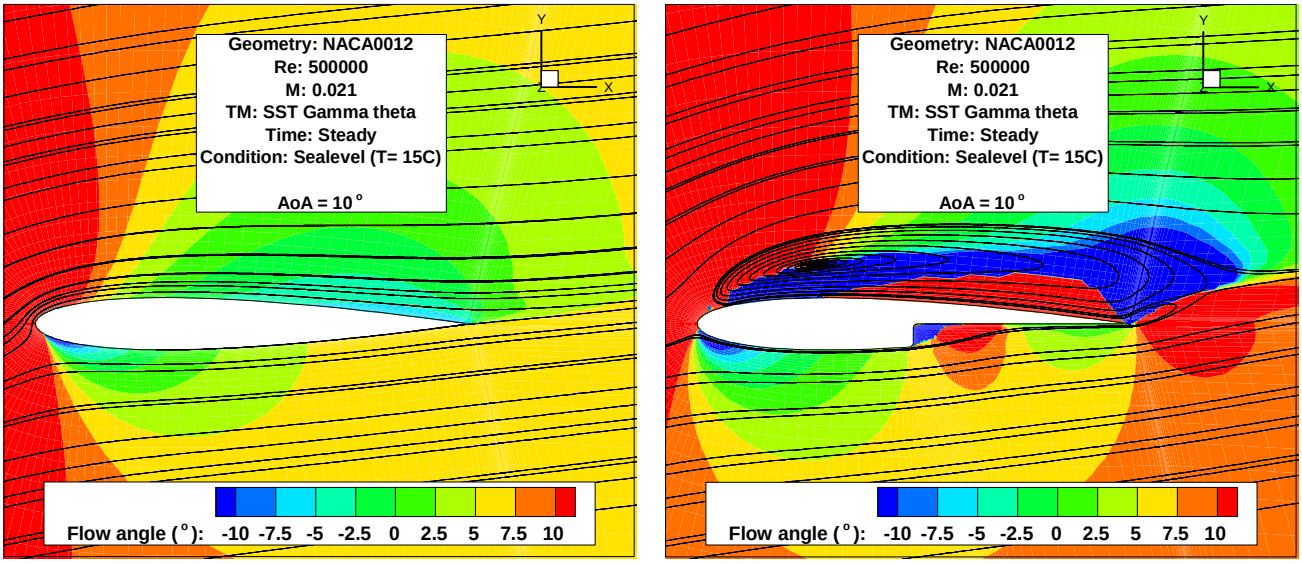

Figure 5-18 Stream line pattern for the pressure side step airfoil (AoA: 10°, left: clean airfoil, right: modified airfoil)

Comparison of the static pressure distribution between the clean and modified airfoils (Figure 5-19) reveals that the pressure side step modification not only increases the lift production after 50% chord but it also modifies the pressure distribution outside the step geometry.

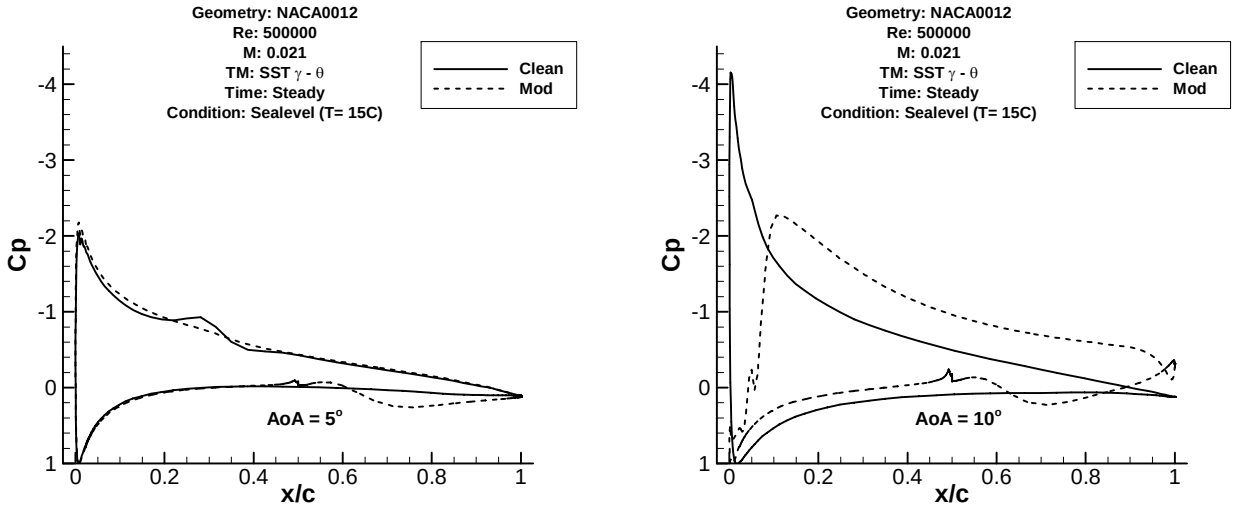

Figure 5-19 Coefficient of pressure distribution (Device: pressure side step, left: 5° AoA, right: 10° AoA)

5.2.2.3 Discussion

The results indicate that the beneficial improvements to the aerodynamic properties due to the pressure side step modification maybe due to the changes in the airfoil's effective camber. To investigate this presumption, a study was conducted to compare the difference in forces produced by changes in camber using XFoil simulations. Three NACA airfoils with different cambers located at 50% chord were chosen for this study: NACA1512 - 1% camber, NACA2512 – 2% camber and NACA1512 with 1.5% camber.

The result from this study suggests that similar or better aerodynamic benefits can be gained by a simple increase in airfoil camber (Figure 5-20). The step modification showed to increase lift and drag forces by up to 10 and 80% respectively at the AoA of 5^{o}, where with a simple increase in camber by 2% (NACA 2512) showed to increase lift forces by 20% and beneficially reduce drag forces by 7%. Therefore no further study was conducted for this device.

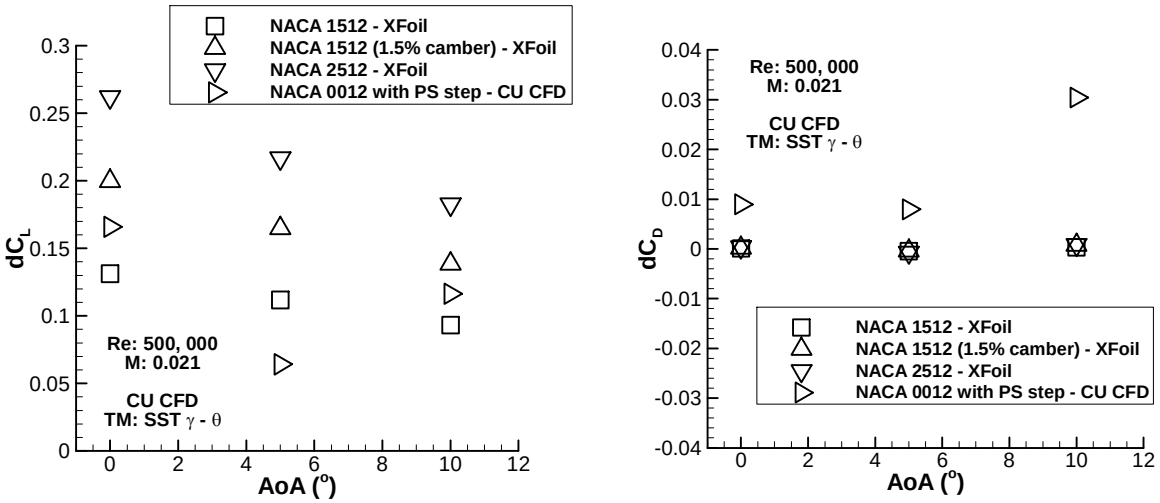

Figure 5-20 Changes in lift (left) and drag (right) compared to unmodified (clean) NACA 0012 – NACA1512: 1% camber at 50% chord, NACA2512: 2% camber at 50% chord and NACA1512 (1.5% camber): 1.5% camber at 50% chord

5.3 3D step rotor design

This concept is based on the idea proposed by Fertis [17], where he claims that a step modification at the suction side is able to increase lift by 17% and decrease drag by 70% due to a trapped vortex – although there is notable uncertainty regarding these published findings (see section 5.2.1). A 3D study was performed to assess the viability of this concept for a 3D large scale wind turbine rotor.

It is also noted that Rossow [16] reported that mass removal at the core of the vortex helps to generate and maintain the vortex in its location and it is expected that the radial flow present on the rotor blade may help to achieve this requirement in the 3D environment.

It is acknowledged that this design is not a realistic configuration from a manufacturing point of view and, of course, the abrupt change in geometry at each radial extent is not desirable. However, the aim of the simulations was to obtain an initial insight into the three dimensional aspects of a stepped vortex. Of particular interest was to understand the effect of the radial pressure gradients and to consider the strength of the radial flow velocities. Thus it is anticipated that poor end effects may arise from the current step design. However, the main aim was to examine the detailed aerodynamics for the mid-sections and to evaluate the impact of the radial flow at the vortex core on the local aerodynamics.

5.3.1 CFD Model

The third device investigated under the vortex trapping devices, was an extruded 3D step configuration. The design is derived from the Fertis' work on suction side step airfoil (see section 5.2.1). Fertis' suction side step was applied at the 25% and 65% blade span airfoils (Figure 5-23). Then the step is extruded from the 25% to 65% blade span to create the 3D derivation of the Fertis' suction side step device. Two different step geometries were studied (Figure 5-23), the first design is based on the Fertis' suction side step geometry (V1) and the second design was based on the cavity type vortex trapping device (V2) presented in [3]. The geometric definition of the V1 and V2 step designs are presented in Figure 5-21 and Figure 5-22 respectively.

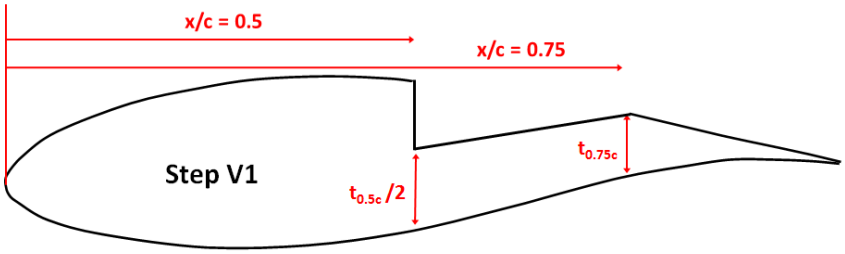

Figure 5-21 Geometry definition of the Fertis' suction side step (Step V1)

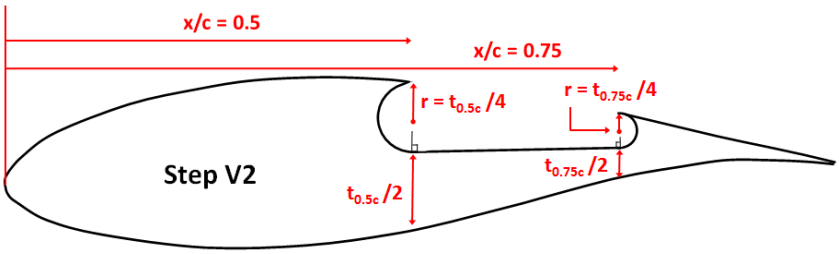

Figure 5-22 Geometry definition of the cavity type suction side step (Step V2)

Different grids were constructed for each step type, which was combined with the established 3D baseline CFD model using interfaces (Figure 5-24). The V1 step geometry was resolved with about 25, 000 elements, while the volume within the step geometry was modelled using about 420, 000 elements. Therefore a total elements of about 4.8 million elements were used simulate the rotational domain which includes the established baseline grid that resolves the blade outside of the step geometry. With the stationary outer domain about 7.6 million elements were used to model the entire computational domain.

For the evaluation of the cavity type step (V2) design, local mesh refinements up to 800,000 additional elements were added to the baseline rotor grid in the vicinity of the step location to increase the resolution at the interface/shear layer. Mesh sensitivity studies were not performed for this work and based on the lessons learned from the 2D CFD work, these grids are assumed to generate a grid independent solution. The V2 step geometry was resolved with about 30, 000 elements, while the volume within the step geometry was modelled using about 800, 000 elements. Increased number of elements were used to satisfy the meshing criteria to contain zero cells with 2x2x2 determinant 0.2 and below, and to minimise the number of cells that has a mesh angles below 18 degrees. A total elements of about 6.5 million elements were used simulate the rotational domain which includes the

step geometry, volume and the established baseline grid. With the stationary outer domain about 9.3 million elements were used to model the entire computational domain.
The extruded step was simulated at 5 different wind speeds range (5 -11m/s) to evaluate its performance at design and off-design wind speeds. The iterative convergence was assumed to be achieved when the residuals from the momentum and continuity equation reach below 1e-4 and the power output from the turbine is achieved within 0.5% of the reported values.

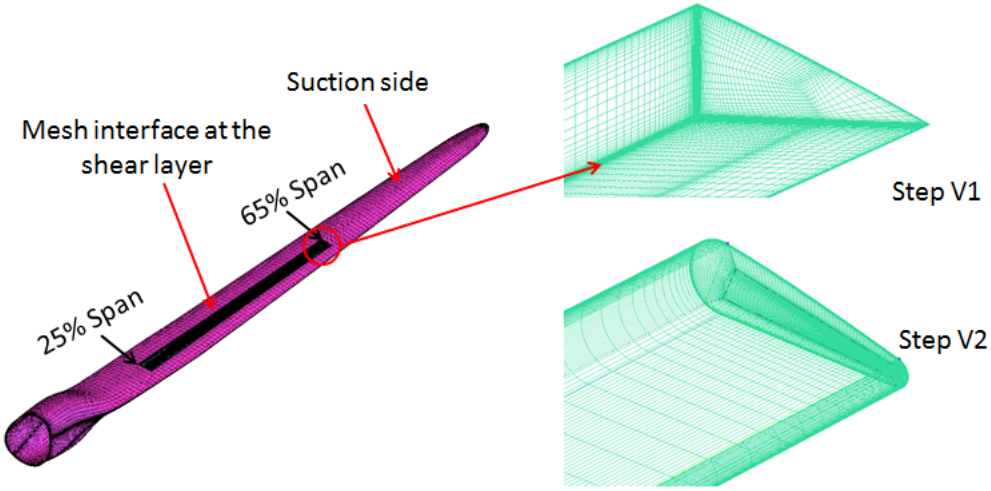

Figure 5-23 Extruded step geometry installed on the baseline rotor

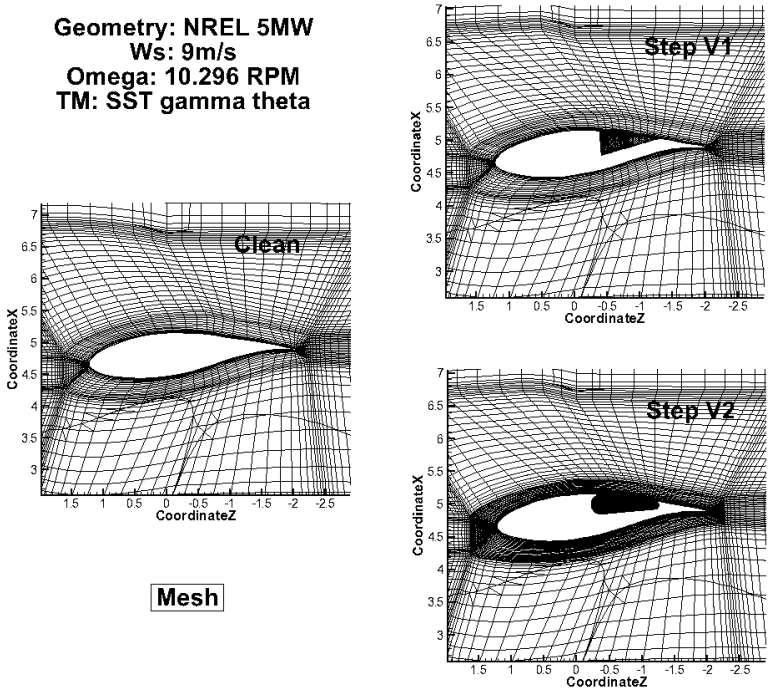

Figure 5-24 Grid generated for the extruded step installed on the baseline rotor, see Figure 5-23. Mesh size (elements) - V1: 7.6million, V2: 9.3 million

5.3.2 Results

The power production comparison between the clean and modified baseline rotor shows that both step designs are detrimental to the power output of the baseline rotor (Figure

5-25), such that at the design point wind speed of 9m/s both step modifications were found to reduce the rotor power by 10%. As the detrimental end effects of the slot are included in these metrics, it is useful to examine the aerodynamics in more detail at different radial positions to see if there are any benefits to the sectional aerodynamics.

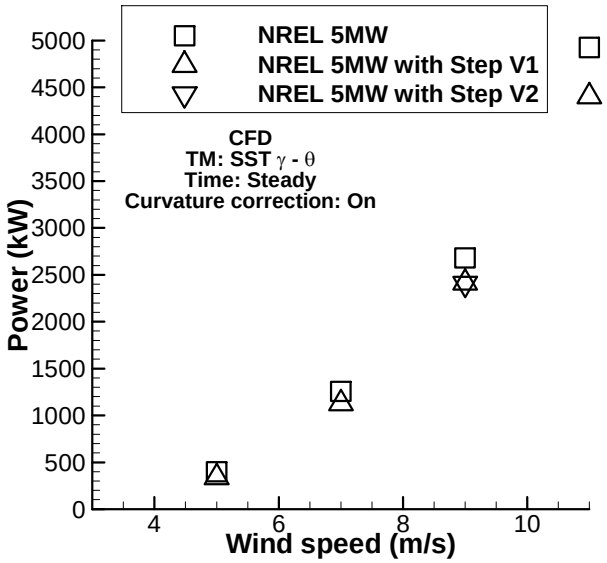

Figure 5-25 Power output using 3D step rotor design

The blade local aerodynamic forces were extracted from the CFD results using the methods presented on [72]. Based on this investigation (Figure 5-26) it was seen that both step modifications reduced the local lift forces by up to 23% within its location on the blade (25-65% r/R). Largest reductions in lift were found at the 65% blade span. This is due to the poor end effect by the step modification. However it was found that both step designs beneficially increased the lift production of the blade root, where the V1 step was able to increase the blade root lift forces by up to 10%, while the V2 step only contributed about 5% increase.

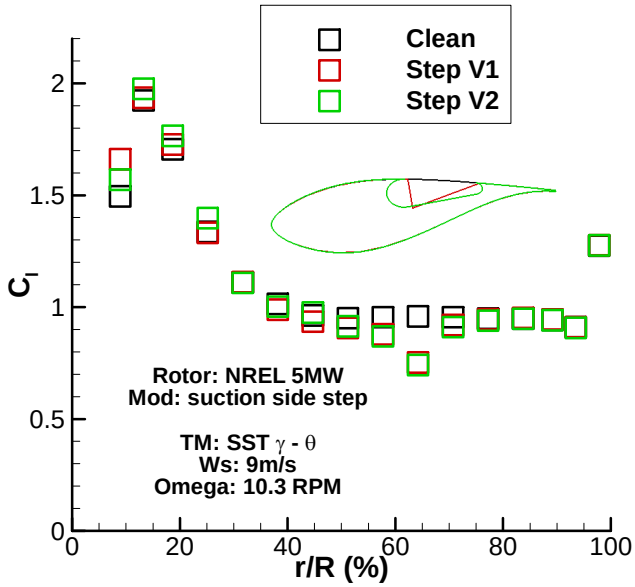

Figure 5-26 Changes in blade local lift coefficient due to the extruded step modification on the suction side of the blade, step location: 25 – 75% r/R

It was found that both step designs significantly increase the local drag forces at its location (Figure 5-27). As the low pressure region generated by the vortex also contributes to the pressure drag on the step similar to a base drag experience on a blunt airfoil. Large increase in local drag forces within the range of 10 -160% were found within 25 – 75% blade span. The largest increase up to 160% in drag force was found with the V2 step design at the span location of about 60%. Slightly better drag penalty was found with the V1 design, where about 150% increase in local drag forces were incurred due to the V1 step at the r/R = 60%.

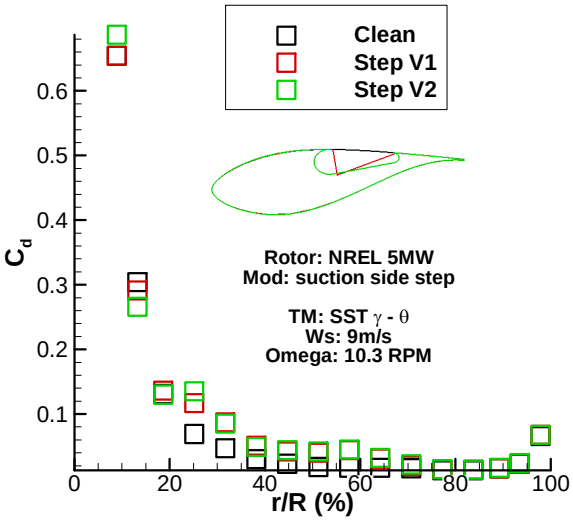

Figure 5-27 Changes in blade local drag coefficient due to the extruded step modification on the suction side of the blade, step location: 25 – 75% r/R

Overall the step modification has shown to negatively affect the local aerodynamics. It reduces the local lift forces and increases the local drag forces. As a result the step modification was found to negatively affect the local lift to drag ratio within the 25-90% blade span (Figure 5-28). Large reductions in local lift to drag ratios by about 30 – 65% were found within the span range of 25 – 70%. The largest reduction in drag forces were seen at the span location of 57%, where the V1 and V2 step reduced the lift to drag ratios by 63 and 65% respectively.

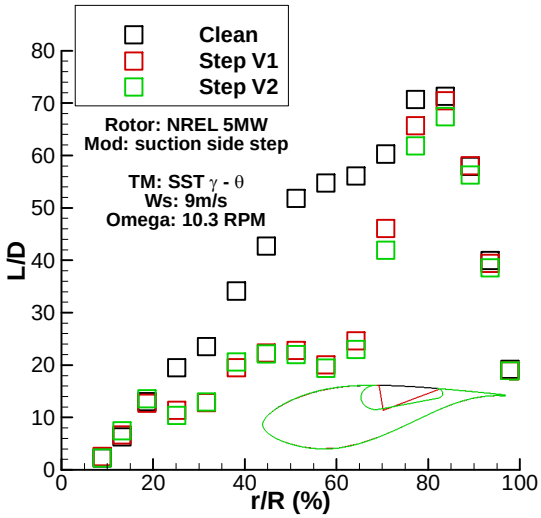

Figure 5-28 Changes in blade local lift to drag ratio due to the extruded step modification on the suction side of the blade, step location: 25 – 75% r/R

The CFD results also showed that step modification negatively affects the local axial induction of the blade (Figure 5-29). It was found that the step modification at the 25-75% span negatively reduced the axial induction from 25-98% of the blade span. Large reduction in axial induction up to 18% were seen at the blade span of 57% blade span with the V2 step design, where the V1 step contributed to a slightly smaller reduction of about 16%.

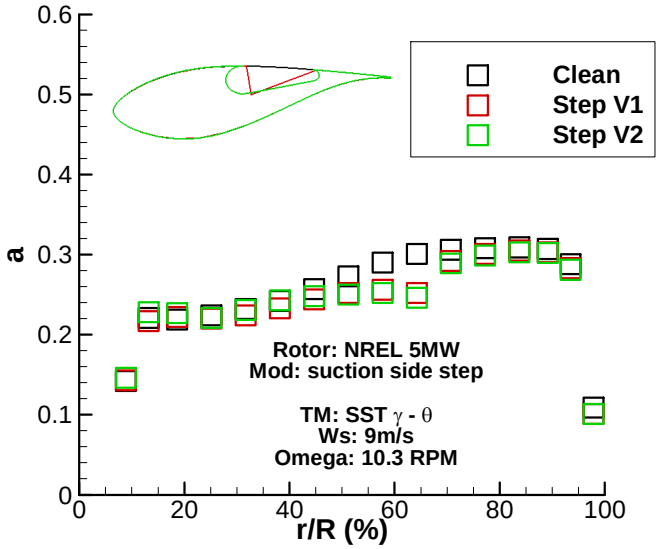

Figure 5-29 Changes in blade local axial induction due to the extruded step modification on the suction side of the blade, step location: 25 – 75% r/R

The detailed flow analyses are only conducted for the design tip speed ratio case (WS: 9m/s). Three different locations (25%, 50% and 75%) relative to the span wise extent of the step were selected for the detailed analysis of the flow field (Figure 5-30).

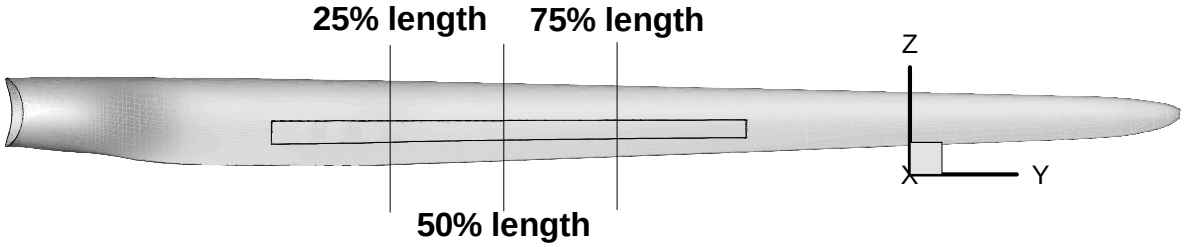

Figure 5-30 Investigated step locations

The vortices generated by the root stake were analysed considering positive circulation, which was determined by finding the vortex core location (peak vorticity) from the vorticity contour plot and integrating the positive spanwise vorticity over a circular area with a radius extending to where the local spanwise vorticity reaches zero. Any negative circulation is neglected within this circular area. The results from this investigation (Figure 5-31) showed that the V2 step design generates a stronger vortex that has 40% more peak circulation than the vortex generated by the V1 step. However it was found that it decays by about 30% of its peak circulation after travelling up to 60% of the step length, and it was also found the vortex generated by the V2 design loses its vortex structure at the 75% step length. Despite the V1 step's low peak circulation, it was found to maintain its peak circulation for a longer radial distance, where even at 75% of the step length it was found to decay only about 5% of its peak circulation. It is also noticeable that V1 step achieves in peak circulation at 50%

step length while the V2 step achieves its peak circulation earlier at 25% step length. Based on this results it can be stated that V1 step design has a slightly better vortex formation.

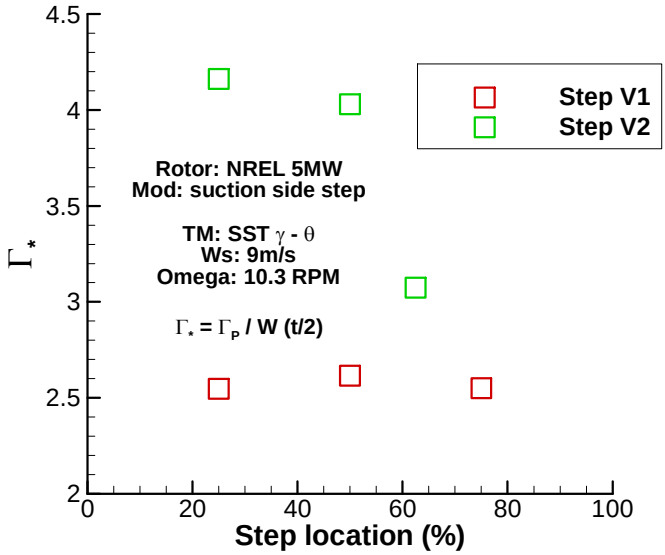

Figure 5-31 Non-dimensional positive circulation along the step length

The vortex from the V2 design was found to be larger than the vortex generated within the V1 step design at the 25% of the step length (Figure 5-32). At 25% step length the vortex from the V2 step was about 10% larger than the vortex from the V1 step. Similar to the circulation distribution the relative radii of the vortex from the cavity type V2 design was also found to reduce in size with increasing blade radius. The cavity type step was found to restrict the vortex size and contain it within its walls while the V1 type step allowed the vortex to gain better growth with increase in blade radius. The vortex from V1 step grows larger by 20% from the 25 – 75% step length, while it was found that the vortex generated by the cavity type design increased it size by 1% within 25-50% step length then reduces it size by about 4% from 50-60% step length.

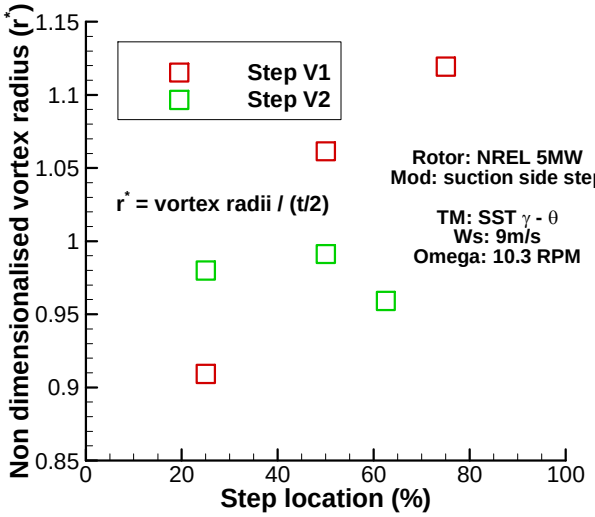

Figure 5-32 Non-dimensional vortex radius (extent of positive vorticity from the peak vorticity to zero) along the step length, t=blade thickness

A vortex was first noticed at 25% of the step extent and the pressure contour clearly shows the relative change in vortex size due to the different type step (Figure 5-33). The cavity

type design (V2) was found to create a larger suction peak than the V1 step (Figure 5-34). This may be due to its larger vortex size, thus the vortex has a larger influence on the blade wall. However the V1 step design based on the Fertis' suction side step performs better in terms of overall reduction in pressure within its modification (Figure 5-34) i.e. the reduction in pressure due to the vortex is influenced over a larger area of the geometry. The pressure recovery outside the step is better with V2 design. This is mainly due to the cavity type step design closely represents the unmodified airfoil shape than Fertis' suction side step modification. Overall at this step location the V1 step preforms well in terms of reduction in pressure within the step, however the negative rise in pressure outside of the step geometry outweighs the benefits and reduces the local lift to drag ratios by up to 40% relative to the clean blade. The V2 design achieves a larger reduction in lift to drag ratios of 43% due to its poor performance within the step geometry.

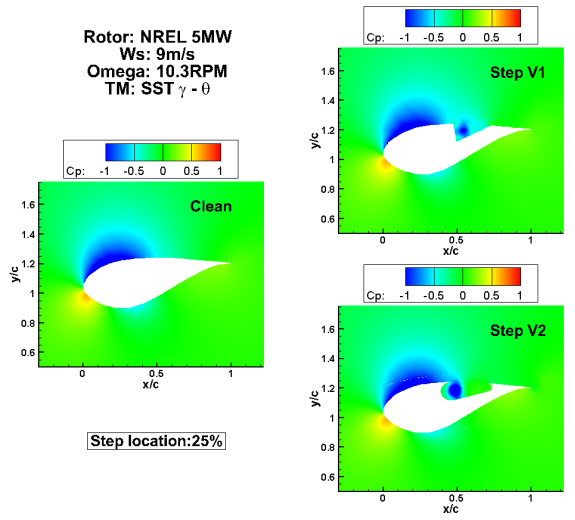

Figure 5-33 Pressure contour at 25% step length

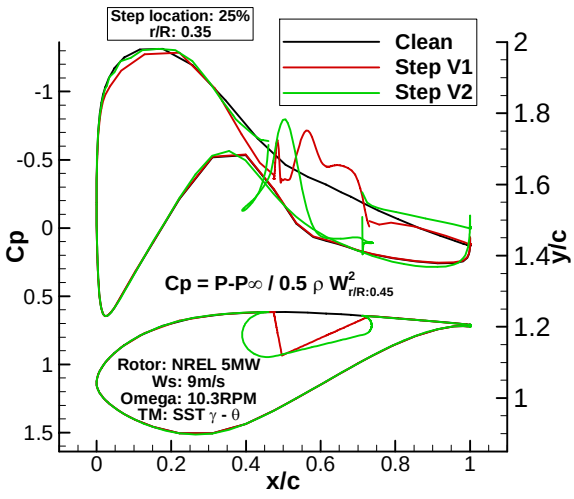

Figure 5-34 Pressure distribution comparison at 25% step length

At 50% step length location (Figure 5-30), the flow features are very similar to that found at the 25% step length. However at this location both vortices produced by the different step designs have grown larger in size (Figure 5-35). This increase in vortex size amplifies the pressure influence on the blade wall (Figure 5-36). Again a larger suction peak was found to be generated by the step V2 design than V1 design and the V2 step design has improved its suction pressure region comparison with its performance found at 25% step length. Similarly, the V2 design produces better pressure recovery outside the step than V1 design and V1 step design achieves an extended suction pressure than cavity type step design (V2). The larger influence on the wall pressure due to the increased vortex size also contributes larger drag increase of the blade. It was found that the V2 design increased the local drag forces by up to 96%, while the V1 design contributed about 86%. However the V2 design was able to increase the local lift production by 1% while the V1 design negatively reduced the lift production by 3%. Overall both designs negatively reduced the lift to drag ratios by 48% relative to the clean blade at this step location.

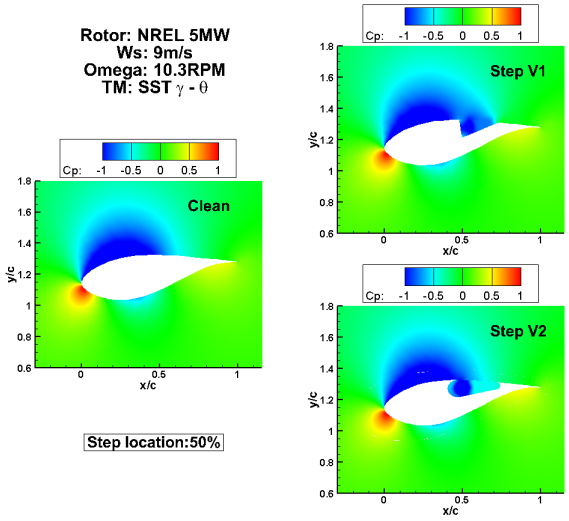

Figure 5-35 Pressure contour at 50% step length

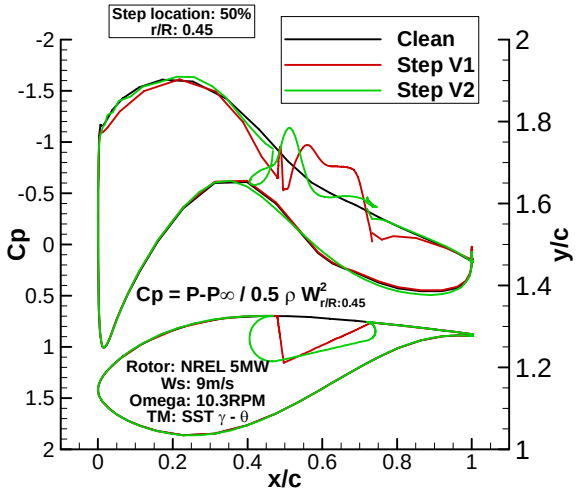

Figure 5-36 Pressure distribution comparison at 50% step length

At 75% of the cavity length, the vortices produced within the two different steps have dispersed considerably (Figure 5-37). This dispersion reduces the effectiveness of the cavity type step at the production of large suction peak as well as the ability to recover suction pressure outside of the step (Figure 5-38). Yet again Fertis' type step design (V1) produces larger extent of the improved suction pressure than cavity type step design. At this location of the blade very large drag contribution were noticed due to the step modification, where the V2 and V1 step design increased the local drag forces by 151 and 157% respectively, where they also reduced the lift production by 8 and 9% respectively. Overall the V2 and V1 step designs negatively reduced the local lift to drag ratios by 65 and 63% respectively.

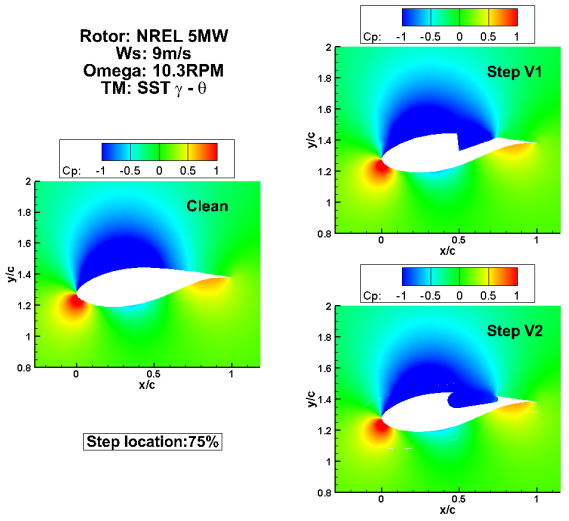

Figure 5-37 Pressure contour at 75% step length

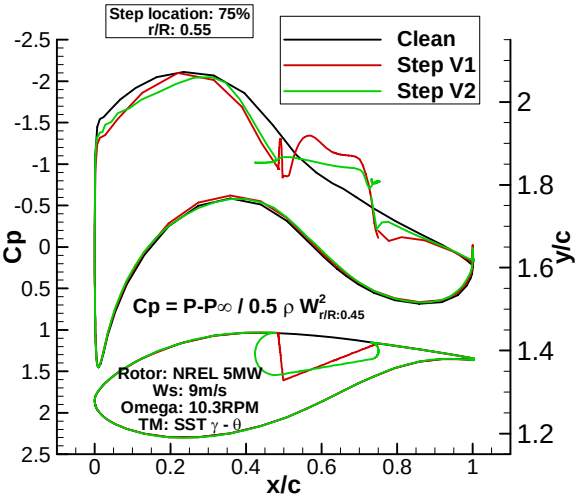

Figure 5-38 Pressure distribution comparison at 75% step length

Based on the sectional aerodynamic assessments of the flow field, the extruded step negatively affects the local blade torque and thrust production (Figure 5-39). The mid part of the step is unaffected by the negative end-effects but it still does not contribute any

improvements to the sectional torque production. Slight improvement to the torque production at the blade root is noticed due to the extruded step, but with an increase of thrust in this part of the blade (Figure 5-40).

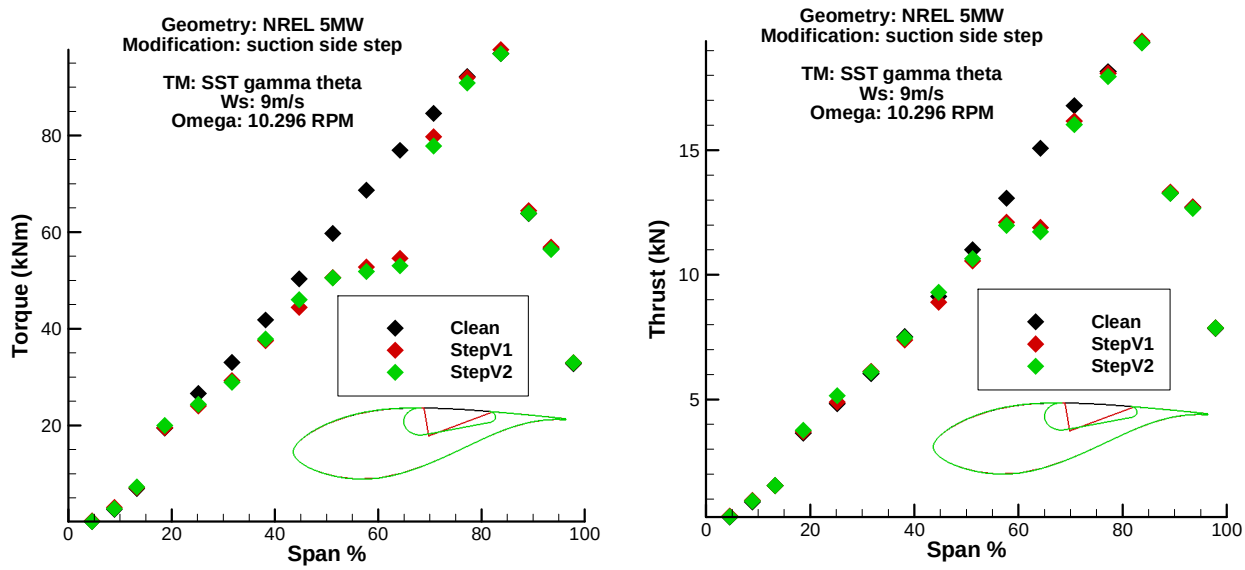

Figure 5-39 local torque (left) and trust (right) distribution as a function of blade span for the NREL 5MW blade with the extruded step designs, Ws: 9m/s, Omega: 10.3 RPM

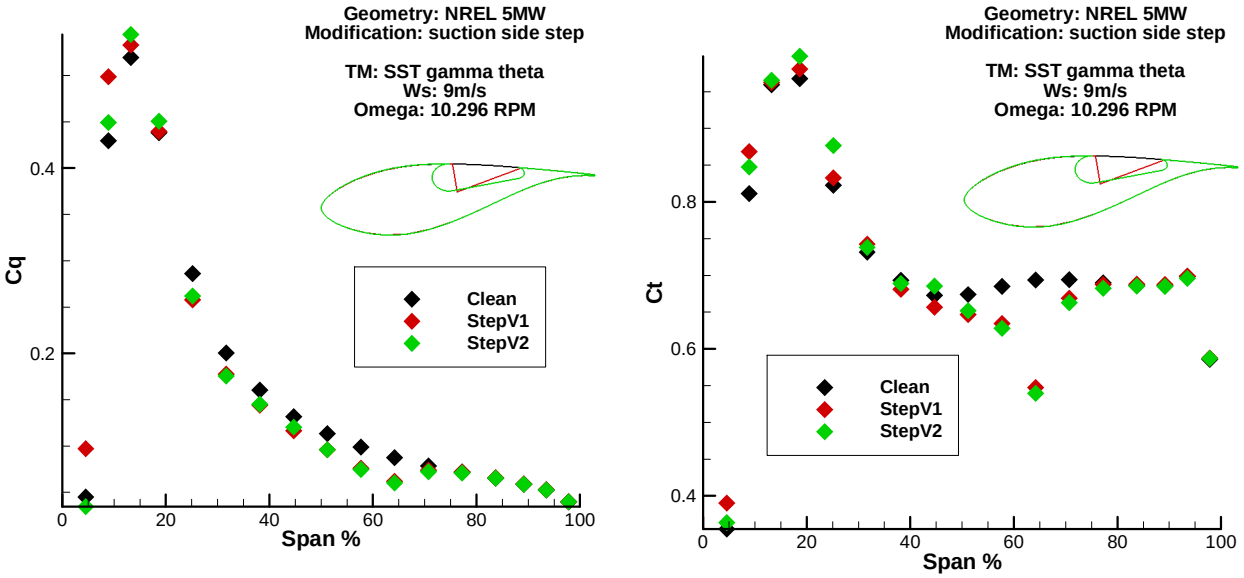

Figure 5-40 local non-dimensional torque (left) and trust (right) distribution as a function of blade span for the NREL 5MW blade with the extruded step designs, Ws: 9m/s, Omega: 10.3 RPM

The limiting steam line pattern reveals that the extruded step may help in the reduction of the extent of the hub separation (Figure 5-41 and Figure 5-42). This reduction in secondary flow may be the reason for the increased torque production at the blade root but the effects are very minor and offset by the notable detrimental aspects in other regions of the blade.

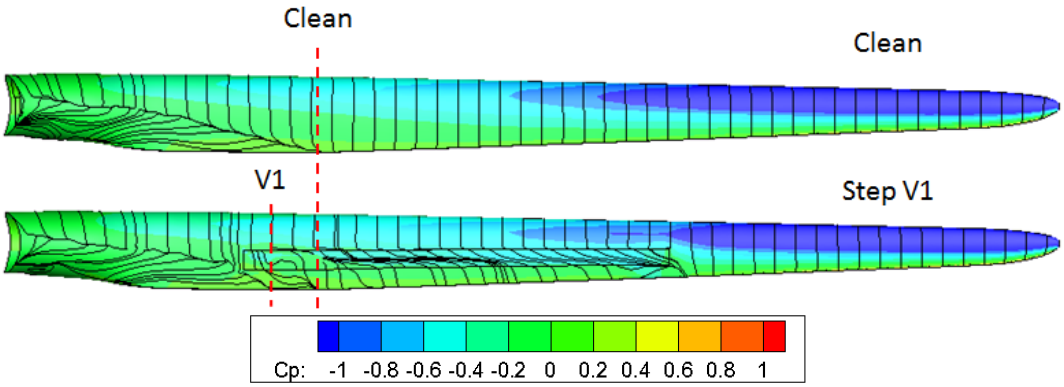

Figure 5-41 Limiting streamline pattern comparison (Step V1), red line indicates the hub separation extent

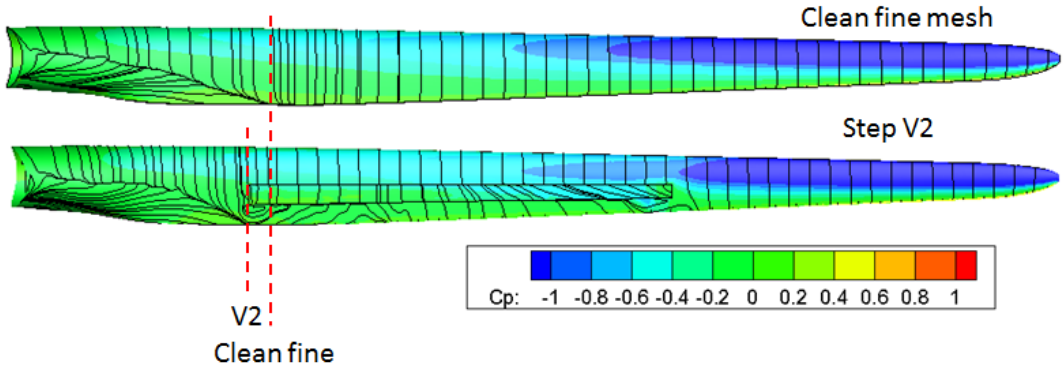

Figure 5-42 Limiting streamline pattern comparison (Step V2), red line indicates the hub separation extent

5.3.3 Discussion

With the current designs, a vortex is captured up to 75% of the cavity length (Figure 5-30) then, as anticipated, the span wise vortical flow leaks out at the end of the step causing a large flow separation from the blade surface. Despite the undesirable end-effects of this step design, it fails to improve the local torque productions even at the intermediate step locations, where an attached flow regime exist. One of the main interests of this investigation was to establish the strength of the radial flow velocity within the step. The results show that strong radial flow up to 40 m/s ($Vy/W_{(r/R):0.7}$ =0.8) is generated for the NREL 5MW rotor with the suction side step (Figure 5-43) at the design point wind speed of 9m/s. This corresponds to a blowing coefficient Cμ = 0.001 and based on the previous study [3], it was reported that a minimum Cμ of 0.000756 is required for beneficial vortex trapping. Therefore it seems that an extruded step geometry installed on wind turbine blade is able to achieve the necessary condition for beneficial vortex trapping without the needs for pumps i.e. the requirements are achieved through passive means.

The blowing coefficient was determined using the definition $C_\mu = \dot{m}V_y/qS$ where $\dot{m}$ is the radial mass flow at the vortex core ($\dot{m} = V_y \rho A$), A is the circular area of the vortex core. V_y is the radial flow velocity at the vortex core, S is the planform area of the blade section with the extruded step (r/R: 25 - 65%) and $q = 0.5\rho W^2_{(r/R):0.7}$ is the dynamic pressure at 70% blade span.

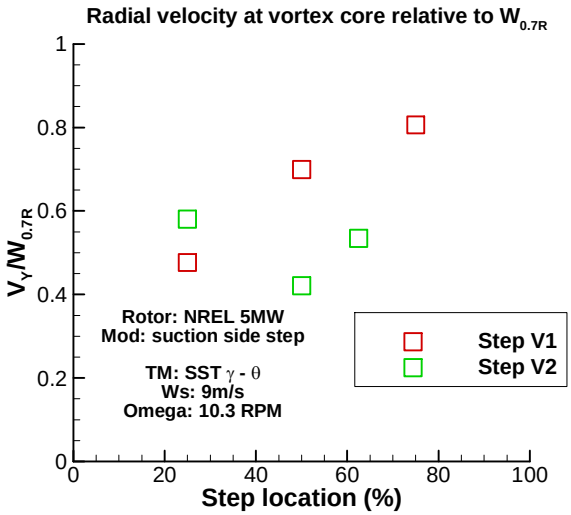

Figure 5-43 Flow through the 3D step (Left: Step V1, Right: Step V2)

Slight improvements to the reduction in secondary flow were also observed due to the extruded step. However due to the overall negative effect that the extruded step impose on the rotor power output no further studies on this device were carried out on this device.

5.4 Passive ventilation

Passive ventilation is a method of using the natural pressure difference generated on the airfoil surfaces to increase the performance of the blade. One of the ways of using the passive blowing method is to exploit it as an air jet vortex generator.

5.4.1 Passive air jet vortex generator

An experimental and CFD work on passive air jet vortex generator (PAJVG) was presented by Prince et al in [22]. The experiment was conducted using two different airfoils: NACA 23012C and NACA 63_2-217. The NACA 63_2-217 airfoil was used to evaluate the PAJVGs effect on a greater thickness to chord ratio airfoil. The cutaway model of the PAJVGs installed on the NACA 63_2-217 is shown in Figure 5-44

The experiment conducted for the NACA 23012C model, had a chord length of 481 mm and a span of 740 mm, fitted with 15 spanwise arrays of air jets of 4.8mm diameter circular orifice, located at 12% chord and spaced equally apart at 45mm between the jet centers. The intake orifice was placed at 4% chord on the pressure side. Prince et al has also performed CFD work on this device [22], the results from this study will be used to validate the results from this research.

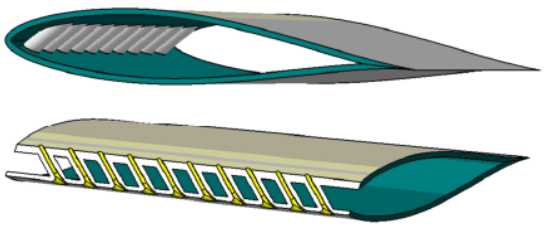

Figure 5-44 General configuration of the PAJVGs integrated NACA 63_2-217 wing [22]

The expected benefits offered by the PAJVGs to a clean NACA 23012C wing include increase maximum lift by 13% and 70% reduction in drag at 18^{o} angle of attack [22]. PAVG increases the stall angle of attack by 5^{o}. A CFD study was conducted to replicate this experimental study conducted for the NACA 23012C to verify that the current CFD method is able to predict the benefits due to PAJVGs. Then based on the results PAJVGs applicability for a wind turbine is discussed.

5.4.1.1 CFD model

CFD studies were conducted for the NACA 23012C airfoil under the same condition of Prince et al work [22] (1.1 million). The entry orifice was placed at 4% chord at the pressure side and the exit orifice was placed at the 12% chord at the suction side (Figure 5-45). Due to the limited space available in the NACA 23012C wing the experiment was conducted with a curve duct in order to achieve the desired positions of the intake and exit duct locations. Due to the absence of clear duct geometry definition, it was simply designed using the side view provided in [22] and it was modelled within the CFD model to resolve the internal flow separation that may have occurred in the experiment due to the considerable swirl. The mesh adapted for the airfoil and duct (Figure 5-46) only contained hexahedral elements unlike the CFD simulations conducted by Prince et al [22] (tetrahedrall elements). O-grid topology was used for this study due to the airfoil's sharp trailing edge.

Based on the experienced gained from the established 2D and 3D CFD methods for this research (Section 4) a grid with 1.5 million was constructed to assess this PAJVG technology. 20,000 mesh elements were placed on the airfoil wall and 3,500 elements on the duct wall. Full 3D grids with four boundary conditions were used to simulate the CFD cases at various angles of attack: velocity inlet, pressure outlet and translational periodicity are used for either side of the wing. SST $\gamma - \theta$ transition model was used to conduct these simulations.

Iterative convergence was assumed to be achieved when the residuals from the continuity and momentum equations reach below 1e-04 and the lift and drag forces are achieved within 0.5% of the reported values.

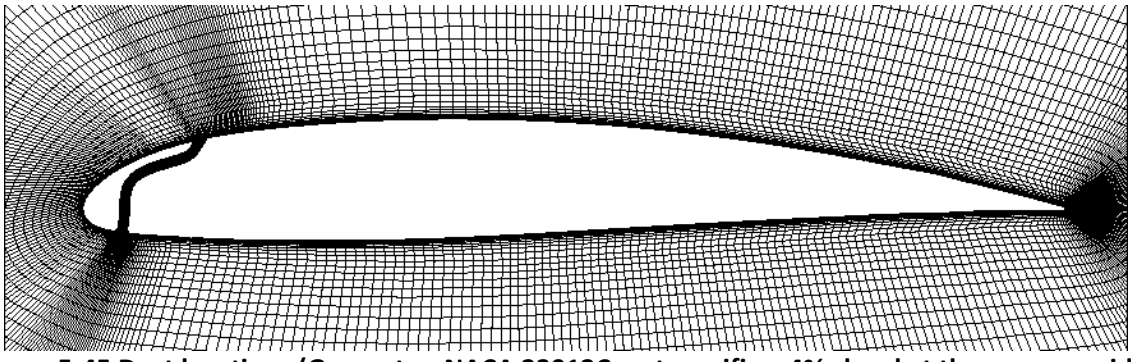

Figure 5-45 Duct locations (Geometry: NACA 23012C, entry orifice: 4% chord at the pressure side, exit orifice: 12% chord at the suction side

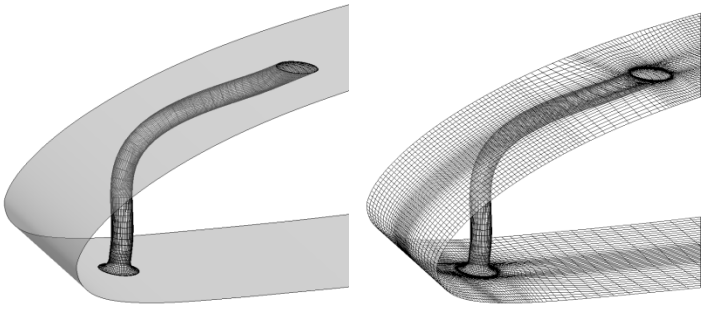

Figure 5-46 Grid made for the internal duct (left: duct mesh only, Right: airfoil and duct mesh)

5.4.1.2 Results

The results from the CFD simulation show poor agreement with the measurements. For the baseline case NACA 23012C airfoil without the PAJVGs the CFD model calculates lift coefficients about 16% larger than the measurements at the AoA of 5^o. Similar difference in lift up to 14% was seen at the larger AoA of 10^o for the clean airfoil. Drag calculation from the CFD showed a difference of 13% at the AoA of 5^o for the baseline airfoil, and a slightly better drag calculation about 9% difference with the measurements was achieved at the larger AoA of 10^o.

Better agreement in lift was found between the CFD and measured lift coefficient for the NACA 23012C airfoil with PAJVGs. The lift coefficient at the AoA of 5^o was calculated within 8% compared to the measurements. Similar or better agreement was achieved for the lift calculation within the AoA range of 5 -18^o. Poor agreement was found between the CFD and the measured drag coefficient for the PAJVG installed wing. Between 80 - 100% differences in drag coefficient were found within the AoA range 5-18^o.

Overall there is a poor agreement between the CFD and measurements, however the CFD model was able to calculate the trend in lift coefficient due to the PAJVGs in comparison with the measurements (Figure 5-47). The CFD model is able to capture the negative reduction in lift due to the PAJVGs below the AoA of 15^o and the positive lift increment at the 18^o AoA. However the relative change in lift is poorly calculated, such that the measurement reported a lift increment of up to 20% at the 18^o by the PAJVGs, where the CFD calculated only up to 6% lift increment due to PAJVGs at this AoA. The CFD model also failed to calculate the reduction in drag due to PAJVGs (Figure 5-47), where the measurements reported that up to 70% reduction in drag coefficient at the AoA of 18^o, while the CFD calculated 8% increase in drag due to PAJVGs at this AoA of 18^o.

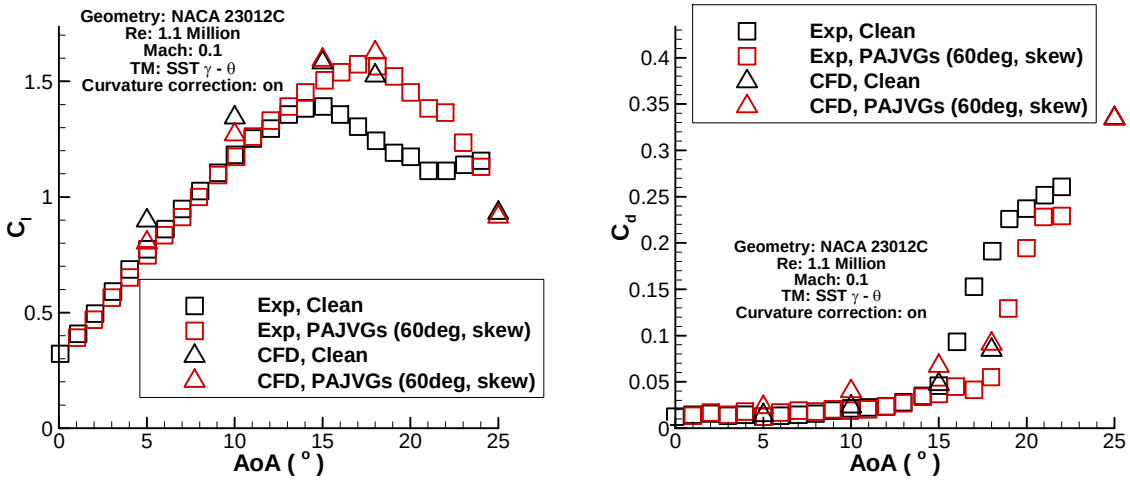

Figure 5-47 Lift (left) and drag (right) coefficient as a function of angle of attack for PAJVG (Exp source: [22]**)**

In order to study the three dimensional flow field, the flow assessments were conducted on two planes which are labelled mid-jet and jet exit planes (Figure 5-48). The flow field at the mid-jet plane is similar to the clean airfoil at small angle of attack (Figure 5-49), however the integrated forces has shown that at this 5° AoA the PAJVG integration reduced the lift and drag coefficient by 11 and 62% respectively. This detrimental effect is also consistent with the static pressure field around the airfoil (Figure 5-50). The reduction in suction pressure is due to streamline divergence from wall due to the air jet.

The velocity ratio measured at the exit orifice (Vr: 1.28) [22] is calculated well with the current CFD model (Figure 5-51). Overall the CFD result suggests that PAJVGs are detrimental at small angle of attack (5°) as found from the measurements.

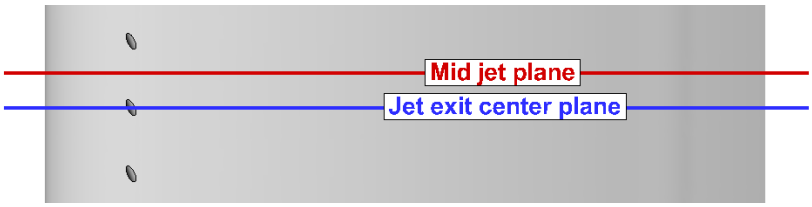

Figure 5-48 Assessment plane for the PAJVGs

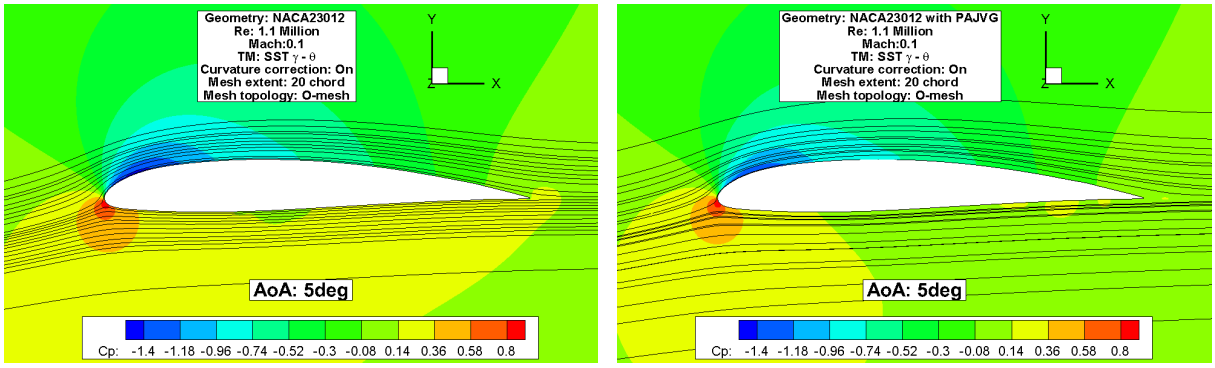

Figure 5-49 Streamline pattern comparison between the clean and PAJVG implemented wing (Left: Clean, Right: PAJVGs – at mid jet plane, AoA: 5deg), Re: 1.1 million

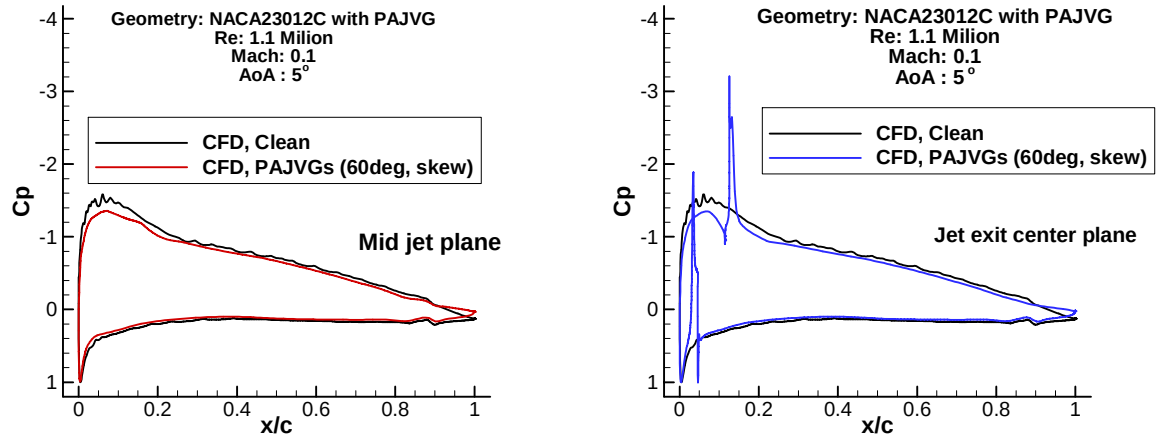

Figure 5-50 Chord wise pressure distribution for PAJVG CFD analysis (AoA: 5°, left: mid-jet, right: jet exit center, Re: 1.1 million)

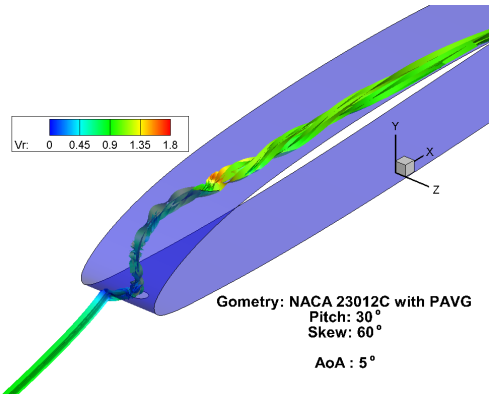

Figure 5-51 Local velocity ratio at the exit orifice, Geometry= NACA23012C with PAJVG, AoA: 5°, Re: 1.1million

The beneficial effects due to PAJVGs were seen at large angle of attack, where significant amount of separated flow exists. The PAJVGs helps to reduce the chord wise extent of the flow separations found at large angles of attack (Figure 5-52). Due to this beneficial effect the lift coefficient was increased by 6% at this AoA of 18°. However CFD also calculates an increase in drag of 9% at this AoA. This is contrary to the measurement, where a drag reduction of up to 70% was reported for this AoA of 18°.

The current CFD model created for the PAJVGs, predict surface pressure distribution that agrees well with the experimental measurements (Figure 5-53). Poor agreement is noticeable between the experimental measurements for the clean airfoil and the results from the 2D CFD model adapted for the clean NACA23012C airfoil, specifically at the suction surface.

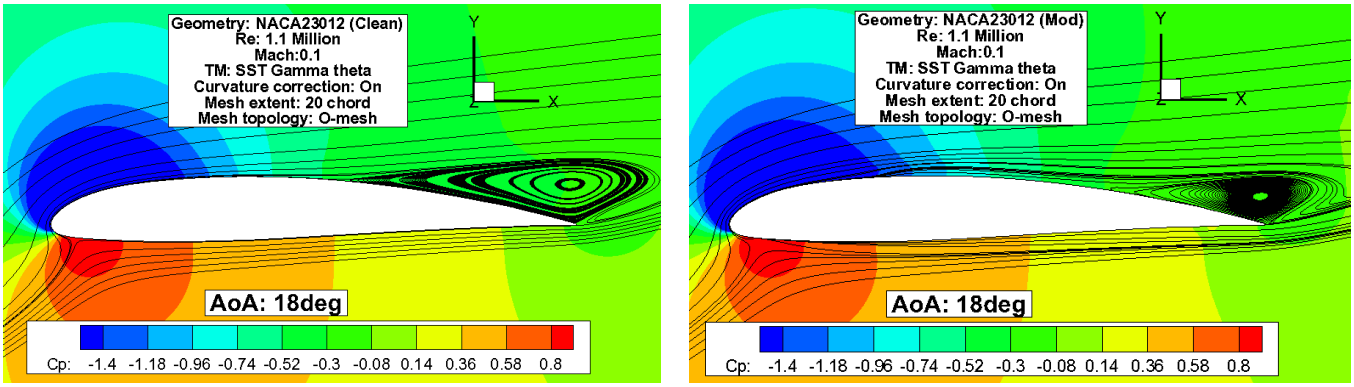

Figure 5-52 Streamline pattern comparison between the clean and PAJVG implemented wing (Left: Clean, Right: PAJVGs – at mid jet plane, AoA: 18 deg), Geometry= NACA23012C with PAJVG, AoA: 18°, Re: 1.1million

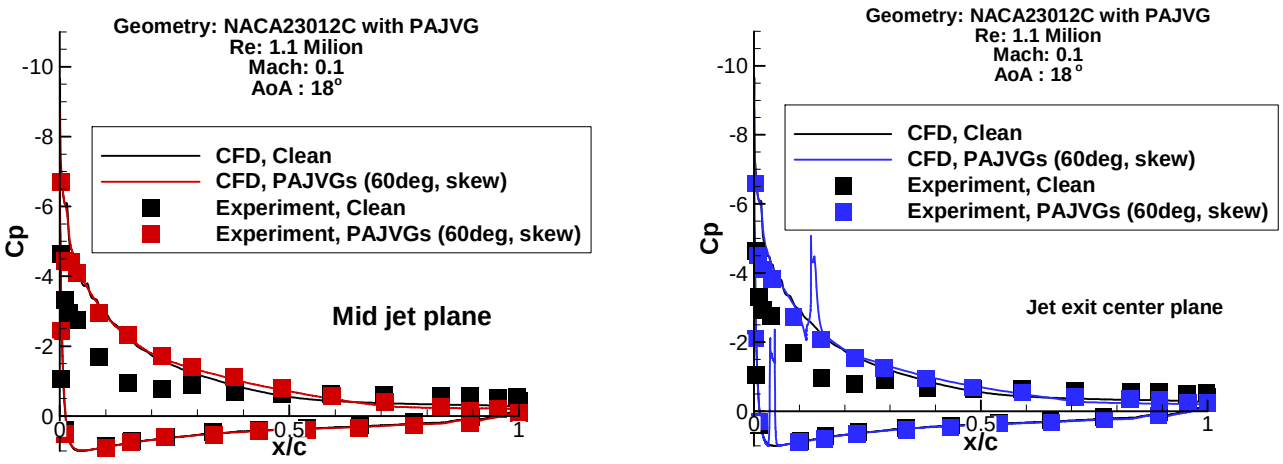

Figure 5-53 Chord wise pressure distribution for PAJVG CFD analysis (AoA: 18°, left: mid-jet, right: jet exit center) [22]

5.4.1.3 Discussion

The CFD study was investigated for five different angles of attack. The baseline CFD model achieved a poor agreement with the measurement however the trends in lift changes due to PAJVG were seen to be calculated, but it fails to predict the reduction in drag due to PAJVGs.

The reported measurements showed promising results for PAJVGs on a NACA23012C airfoil. Initially it was planned to use this increase in aerodynamic efficiency to alleviate blade structural loads by chord reduction. However when PAVGs are applied to an airfoil (NACA 63_2-217) which closely resembles the baseline rotor tip airfoil (NACA 64-618) the reported drag reductions by Prince et al are negligible (Figure 5-54). However the BEM evaluation of chord reduction analysis (Section 3.2) reveals that the increased stall AoA (+5°) reported for the NACA23012C can be used to reduce chord while maintaining a safe stall margin. Nevertheless no further CFD studies were conducted for this device, due to the poor validation achieved with the CFD model.

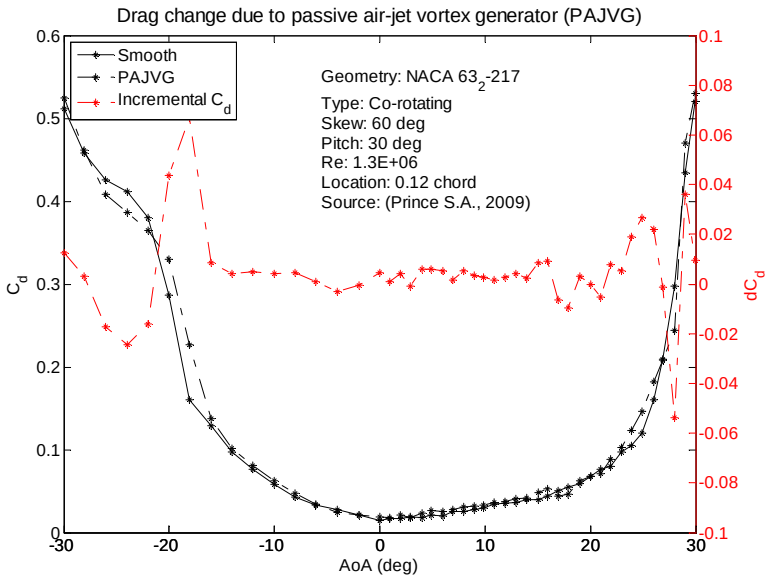

Figure 5-54 Measured changes in drag due to PAJVGs on NACA 63_2-217, calculated from Ca and Cn [22]

5.5 Corrugated leading edge wing

This leading edge modification was initially adapted from the flippers of a sea whale where it has been reported to induce beneficial hydrodynamic effects [70][25][73], and this study assess its potential benefits in terms of flow control application on the wind turbine blade.

The experimental study conducted by Johari et al [70], has shown a 50% increase in lift coefficient at 22^o angle or attack (post stall) is achievable with a corrugated leading edge wing. Better stall characteristics are also reported due to this device implementation [70] [25]. However, many of these studies are conducted at relatively low Reynolds numbers which may affect the pertinence to the much larger Reynolds number regimes encounter in large wind turbines. The Johari et al experimental study [70] conducted at Reynolds number of 183,000 was chosen to be studied using the baseline 3D CFD methods. The main focus of this study is to determine whether the current CFD mode is adequate to replicate or predict the benefits of a corrugated leading edge wing.

5.5.1 CFD model

A NACA 63_4-021 airfoil was used for this investigation. Various configurations were experimentally tested however only one was selected for this CFD evaluation. It comprised a leading edge with corrugations of 0.25c wavelength and 0.025c amplitude (Figure 5-55).

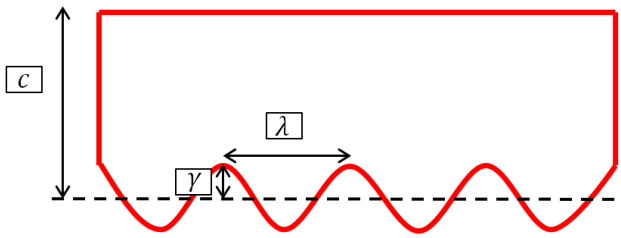

Figure 5-55 Chosen corrugated leading edge design (Wavelength $(\lambda) = 0.25c$, Amplitude $(\gamma) = 0.025c$, based on work from [70]**)**

Based on the experienced gained from the established 2D and 3D CFD methods for this research a 3-D gird with C-grid topology containing 400,000 elements was used to carry out this investigation. The wing wall was modelled with 4,000 mesh elements (Figure 5-56). Four boundary conditions were used to simulate the CFD cases: velocity inlet, pressure outlet and symmetry are used for either sides of the wing. Only half wavelength with symmetric condition was used to simulate the corrugated leading edge wing (Figure 5-57). The simulations were conducted at various angles of attack (0^o - 25^o) at the low Reynolds number of 183,000, with water as fluid to replicate Johari et al experimental work [70]. Fully turbulent calculation (SST) as well as transitional turbulence model (SST $\gamma - \theta$) was used to conduct the simulation.

Iterative convergence was assumed to be achieved when the residuals from the continuity and momentum equations reach below 1e-04 and the lift and drag forces are achieved within 0.5% of the reported values.

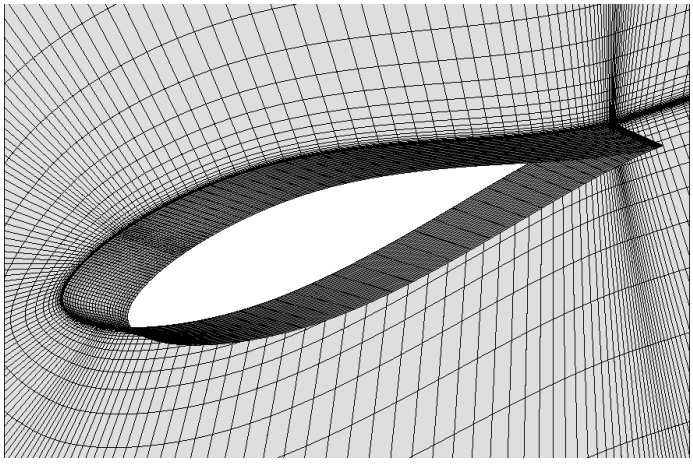

Figure 5-56 Mesh generated for the corrugated leading edge wing, C-grid topology with 400,000 elements (4,000 mesh elements used to model the wing)

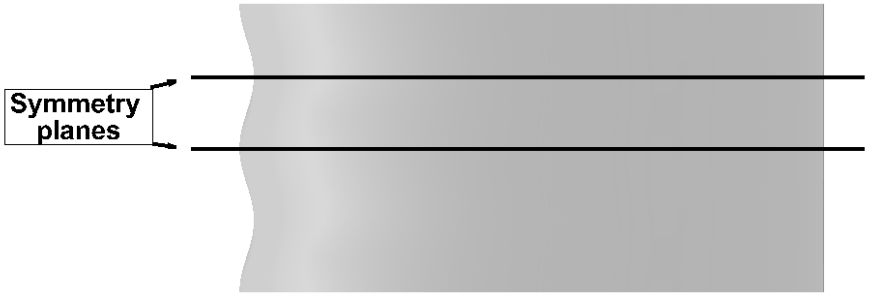

Figure 5-57 Symmetry planes used for the corrugated leading edge wing simulations

5.5.2 Results

Various angles of attack were simulated to assess this devices performance. Based on the CFD calculations, the current CFD model is not able to replicate the measurements even for the baseline NACA 63021 airfoil at the low Reynolds number of 183,000 (Figure 5-58). At the small AoA of 5^o, both transition modelled (CFD-Trans) and fully turbulent model (CFD-Turb) calculated lift coefficients within 10% of the measurements. The transition model under predicts the lift by 10% while the fully turbulent mode over predicts the lift by 7%. For large

AoA of 10° the transition model under predicts the lift by up to 20% while a better agreement of -8% was achieved with fully turbulent model. At the post stall AoA of 20° both turbulent models under predicts the lift by up to 30%. Overall the baseline CFD model is only able to achieve within 20% of the measured lift forces within the pre stall AoA.

The drag calculation from the transition model achieved slightly better agreement with the measurement for the clean NACA63021 airfoil (Figure 5-58). At AoA of 5° it was found that transition model over predicted the drag forces by 17% while the fully turbulent mode under predicted the drag forces by 25% with the measurements. At the 10° AoA transition model over predicted the drag forces by 8% while the fully turbulent model under predicted the drag forces by up to 32%. At the post stall AoA of 20° both turbulent models over predicts the drag forces by up to 30%. These results suggest the transition model performs well with the drag calculation and it is able to predict the drag forces within 8-17% within the pre stall AoA.

The CFD model created for the corrugated leading edge also showed poor agreement with the measurements similar to the evaluation of the CFD model for the baseline airfoil (Figure 5-58). Better agreement with the lift forces from the measurements was found from the fully turbulent CFD model than transition model. Lift forces from the fully turbulent model achieved within 5-13% for the pre stall AoA range, where a larger difference within 15-26% was achieved with the transition model. This may be due to the transitional turbulence model may be deceived by the low Reynolds number flow. However both turbulent models poorly calculated the drag forces of the corrugated wing within the pre stall AoA, where the differences were found up to 25%.

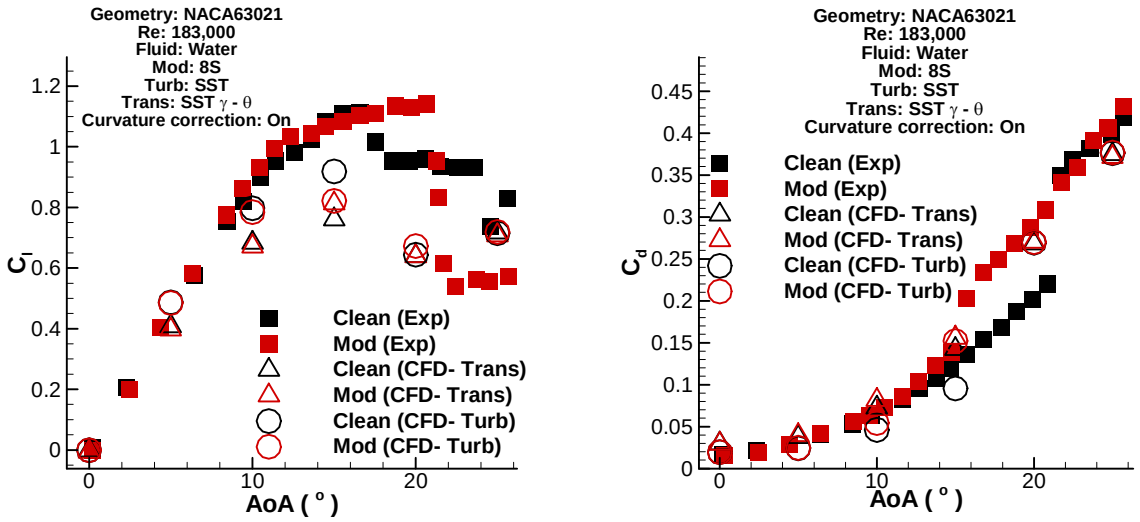

Figure 5-58 Lift (left) and drag (right) coefficient as a function of angle of attack for PAJVG (Exp source: [22]**)**

5.5.3 Discussion

The current CFD model is not adequate to assess this technology and does not calculate the expected benefit from this device. A different turbulence model may be used to recreate this low Reynolds number (183,000) aerodynamics, as the SST or the SST γ – θ transition models fails to even predict the flow characteristics of the baseline wing. This is maybe due to CFD model failing to calculate the low Reynolds number flow of the experiment. It is also

noted that the operational Reynolds numbers of the baseline rotor are large (1 to 10 million) in comparison with this experimental work, i.e. the benefits may not exists for a large Reynolds number flow present on a large scale wind turbine.

The lift increments by the leading edge corrugation lie mainly in the post stall region of angle of attack. Steady state calculations are not suitable to assess the large separated flow regimes present at post stall conditions, where the baseline steady CFD model calculates lift and drag forces that differ by up to 30% from the measurements.

Overall the initial effort to recreate and study the corrugated leading edge wing has shown the difficulty in CFD prediction of the low Reynolds number flows. It was decided that further work on this technology is not suitable for this research as the post stall aerodynamics is not in an interest of this project.

Based on the ideal wind turbine study (Section 3.1.4), it was found that the beneficial increase in lift can be used to reduce local blade chord. However this technology also increases drag at this increased lift condition, which compromises the torque production. Based on the evidence available, this technology does not pose a great benefit for large scale wind turbine. Consequently, no further work was continued with regards to this device.

In summary and as a final refinement conclusion it can be stated that all the technologies reviewed so far in this thesis have either seems to be not applicable for a wind turbine blade or the baseline CFD model fails to calculate the benefits reported. The forthcoming sections will present a more direct approach to tackling the adverse aerodynamic effects found on the baseline rotor using PFC devices, which is one of the main objectives of this investigation. Therefore considerable emphasis is placed on the results and discussion provided on the following sections.

5.6 Passive flow control devices for a wind turbine blade root

Based on the BEM analysis of the ideal baseline rotor (Section 3.1.4), the root region of the blade has a notably reduced lift. The current blade root does not generate the required lift for an optimum operation. The results from the baseline rotor performance study (Section 4.3.4) showed the presence of large separated flow regions at the blade root. One of the main causes of lack of power production at the blade root is due to this hub separation. Based on the CFD study of the baseline rotor (Section 4.3.4), it was identified that the in-board (hub) flow separation was extended in the span wise direction due to the spanwise flow migration. Thus the current underperforming blade root is further degraded by this hub separation.

Vane vortex generators are commonly used in the wind turbine industry to address the hub separation [12]. Only one report [74] seems to present the work on CFD modelling of a VG integrated wind turbine blade. This report outlines the difficulty in modelling VG integrated rotor with a special concern on the demand for computational power. They have used unstructured elements with mesh adaptation focused around the VGs. Consequently they were only able to simulate only one pair of counter rotating vane VGs on a rotor blade (LM

19.1) and have only presented results for the cases without modelling rotation. The rotation modelled cases were reported to be not finalised in time for publication of this report [74].

In this section of the thesis, some technologies similar to vane VGs will be evaluated for a wind turbine blade. These are reported as root strake, root chine and finally a wedged shaped VG for wind turbine. After the presentation of the concept and its results, a parametric study was conducted to establish the initial design space for these devices.

5.6.1 Root strake

An initial effort to reduce the spanwise flow migration was studied using a root strake. The strake design is based on a combined effect of a conventional vane VG and a fence [4] [75] [76]. VGs are commonly used to reduce hub separation however the strake design is expected to produce a significantly larger vortex than the conventional VGs that will oppose the radial flow. Unlike fences, the strake is placed with a toe angle relative to the free stream in order to generate this beneficial vortex. Therefore the root strake is designed to combines the benefits of a VG and a fence.

At 20% blade span, a rectangular strake was installed on the rotor blade with the intention to produce a vortex that opposes the span wise flow migration. The strake dimensions (Figure 5-59) were based on vortex generators and fences adapted for a wind turbine [4] [75] [76]. Work presented in [8] has shown that the optimum toe angle for a counter rotating devise is around 20° and any increase or decrease on the toe angle reduced its performance. Therefore based on [8], a toe angle of 20° and below (relative to free stream) was chosen for this research. Strake height of 2% of the local chord and length of 1/3 local chord was selected as an initial design. The leading edge of the strake was placed at 10% local chord.

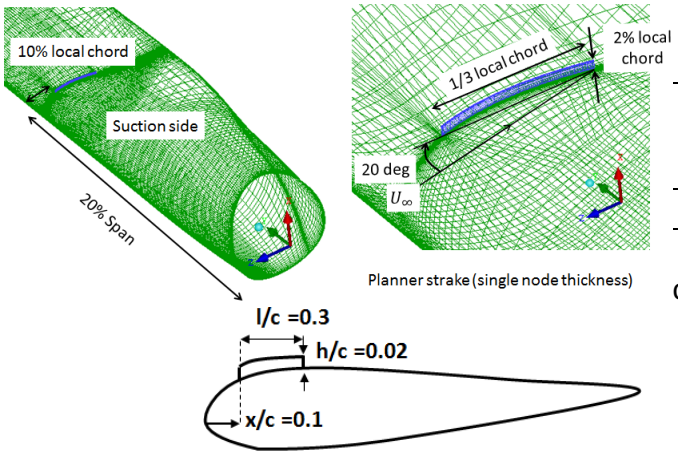

Span Location	Length (l/c)	Height (h/c)	Toe angle
r/R = 0.2	0.3	0.02	20°

c = local chord at 20% span (4.5m)

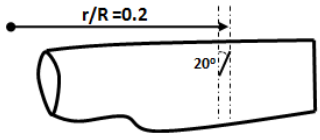

Figure 5-59 Rectangular strake geometry for the 20% blade span of the NREL 5MW rotor

5.6.1.1 CFD model

Initially the strake was designed using the chosen dimensions as a planar surface (infinitesimal thickness). The strake surface was installed to the baseline rotor and then the baseline grid was slightly modified to capture the strake surface. The strake boundary was modelled with single node depth i.e. the effect of strake thickness is not assessed. A non-slip wall boundary condition was applied to the strake. The results for the clean blade were

computed using the same grid but without the wall boundary condition applied to the strake (Figure 5-60). Thus any calculated changes in the flow topology are due to the presence of the strake boundary. Four different wind speeds (Ws = 5, 7, 9 and 11 m/s) where considered and the simulations were performed using the SST γ – θ transition model. The gird convergence study conducted for the baseline rotor was assumed to be adequate for this study as only a small portion around the strake is modified to evaluate its performance. Iterative convergence was assessed similar to the baseline rotor simulations (Section 4.3.4) i.e. RMS residuals below 1e-04 and using the power output changes within +/- 0.5% of the reported value.

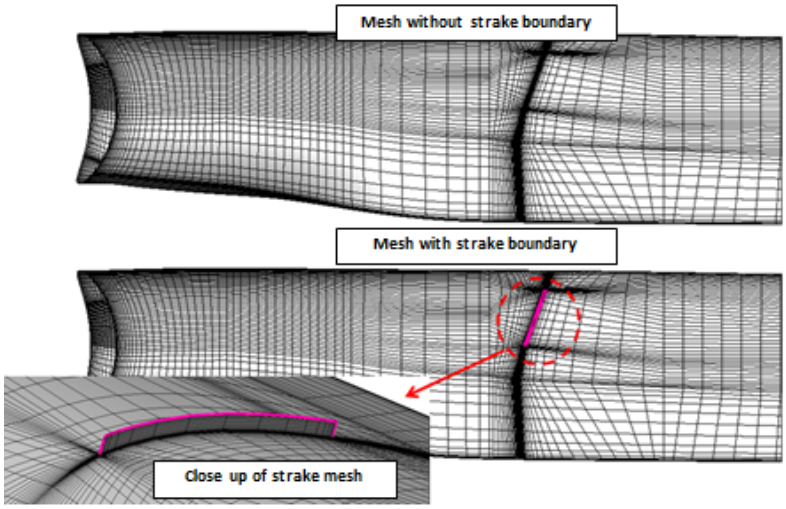

Figure 5-60 Mesh adapted for root strake investigation (plane view of the suction side), displayed span range: r/R=0.05 – 0.30

5.6.1.2 Results for the rectangular root strake

The rectangular strake design is able to increase the power production of the baseline rotor by 0.37% (1.6 kW) at 5m/s wind speed, with an increase of 0.24% to the blade thrust (0.14 kN). The rectangular stake is similar to a fence in terms of its effectiveness to reduce radial flow. Therefore it is reasonable to compare the strake performance with a fence integrated to the wind turbine (Figure 5-61). A previous study on boundary layer fence (BLF) [76] has shown that improvement in rotor power up to 0.6% is possible with an optimised BLF. It should be noted that the effectiveness of a PFC device is also function of the underlying flow, i.e. the BLF can perform better or worse on the same or a different rotor depending on the local flow characteristics.

Figure 5-61 Boundary layer fence implemented to a wind turbine blade [76]

The power production comparison (Table 5.6.1-1) suggests that this strake design is beneficial to power output up to the design wind speed of the baseline rotor (Ws 9m/s). At a higher wind speed the current strake design is detrimental to the power output of the wind turbine. This is due to the adverse effect of the beneficial vortex being elevated away from the blade at higher wind speeds. Based on this study it is clear that PFC designed for a specific design speed may not be suitable for the overall range, and it is recommended that the operational range of a PFC device should be assessed over the entire operating range of the rotor in order to evaluates its performance in terms of annual output.

% Change relative to the clean rotor		
Wind speed (m/s)	Power	Thrust
5	0.37	0.24
7	0.22	0.26
9	**0.13**	**0.12**
11	-0.15	-0.54

Table 5.6.1-1 Power output and blade thrust comparison of the root strake

For low wind speed simulations (5, 7 and 9 m/s) the expected flow features of the strake are predicted with the baseline CFD model. The vortex formed by the strake interacts with the spanwise flow and the expected counter rotating vortex pair is generated (Figure 5-a). At the highest wind speed of 11m/s the vortex structure is significantly changed in comparison with the lower speeds, it is elevated away from the surface and the counter rotating pair is not generated and it's rotation has also is changed to promote radial flow. This may be due to the increase in the inlet flow angle i.e. the $\tan^{-1}\left(\frac{Ws}{\Omega r}\right)$ at r/R =0.2 increases from 33.5^{o} to 35.0^{o} when the wind speed is changed from 9m/s to 11m/s.

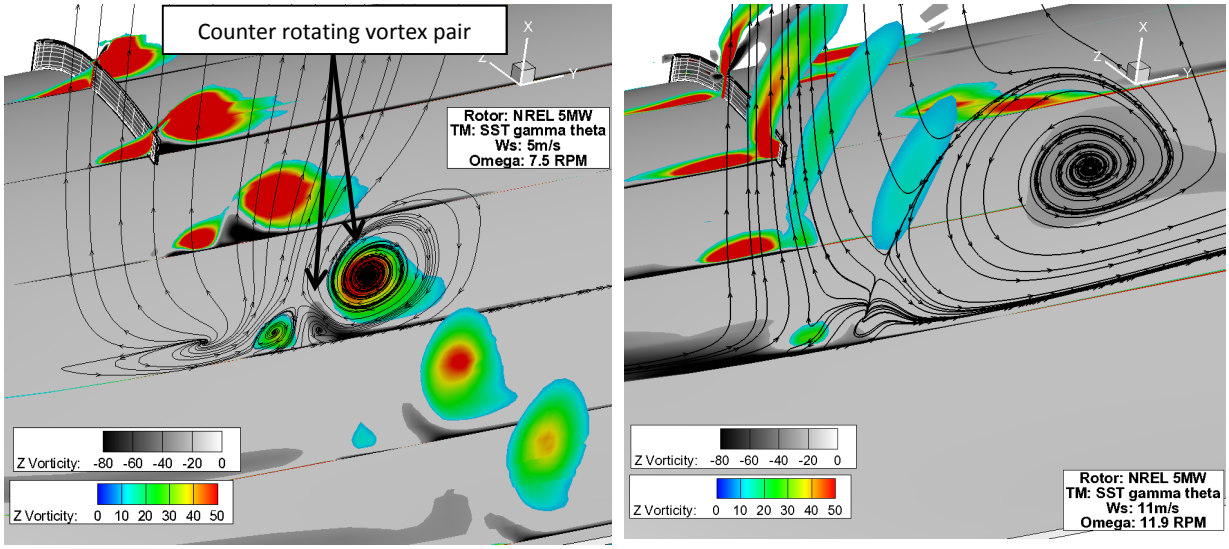

(a) (b)

Figure 5-62 Vortex evolution from the root strake (a - Ws: 5m/s, b – Ws:11m/s), grey scale: counter-rotating vortex, colour scale: co-rotating vortex)

This flow behaviour at the wind speed of 11m/s reduces the effectiveness of the strake to produce a beneficial vortex that opposes the spanwise flow migration. The limiting stream line patterns (Figure 5-63 to Figure 5-66) reveal that the current strake design can successfully prevent spanwise flow migration at low wind speeds (5 - 7 m/s). At higher wind speed of 11 m/s the beneficial vortex is elevated from the blade surface and loses its ability to add momentum to the defected boundary layer downstream or to mitigate radial flow. This lifting of the vortex showed some unsteadiness in the CFD simulation (Figure 5-67), but it was found that the fluctuation in power output was very small about 0.03% from the mean value which was used to assess the effectiveness of this device.

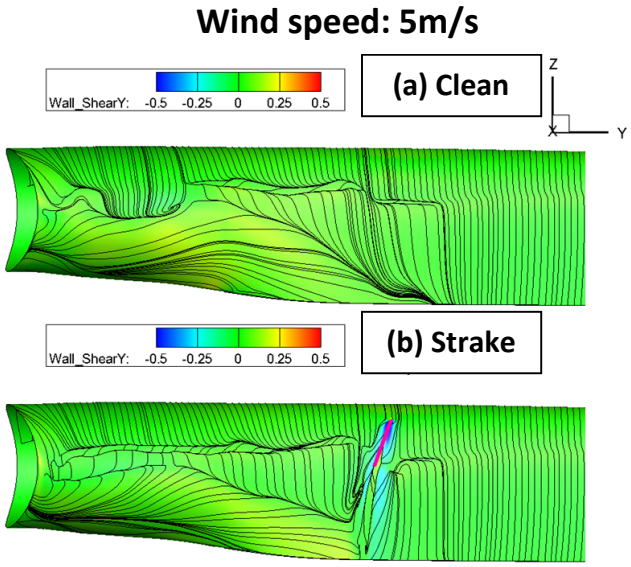

Figure 5-63 Surface streamlines and contours of surface shear stress on rotor suction side for Ws = 5m/s and Omega = 7.6RPM (a) datum geometry (b) with strake, displayed span range: r/R=0.05 – 0.35

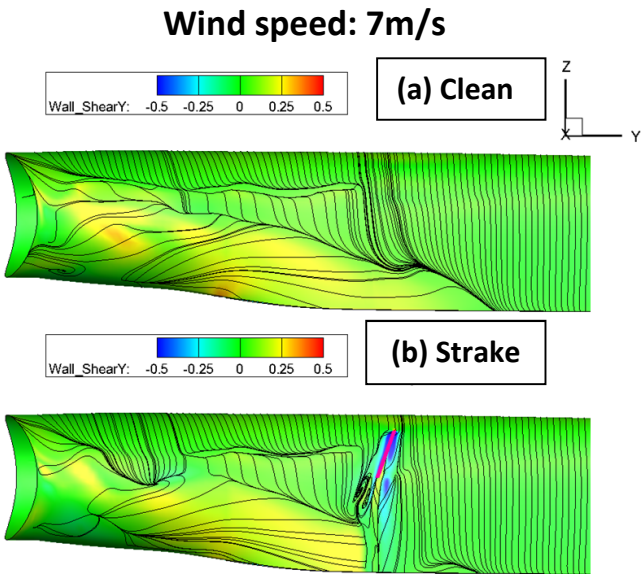

Figure 5-64 Surface streamlines and contours of surface shear stress on rotor suction side for Ws = 7m/s and Omega = 8.5RPM (a) datum geometry (b) with strake, displayed span range: r/R=0.05 – 0.35

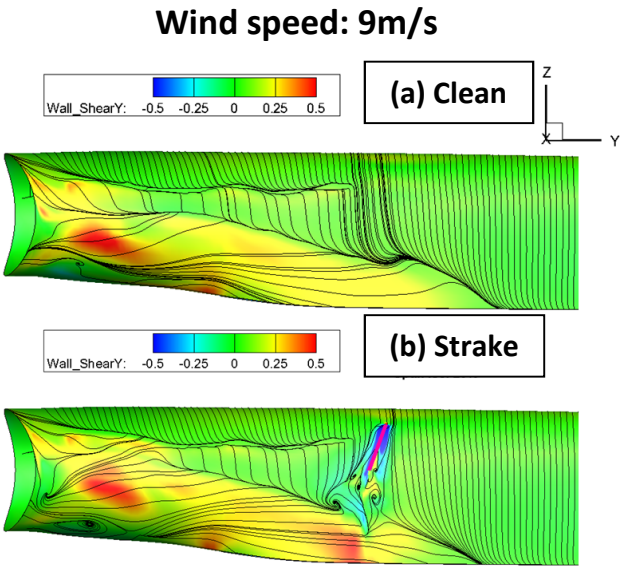

Figure 5-65 Surface streamlines and contours of surface shear stress on rotor suction side for Ws = 9m/s and Omega = 10.3RPM (a) datum geometry (b) with strake, displayed span range: r/R=0.05 – 0.35

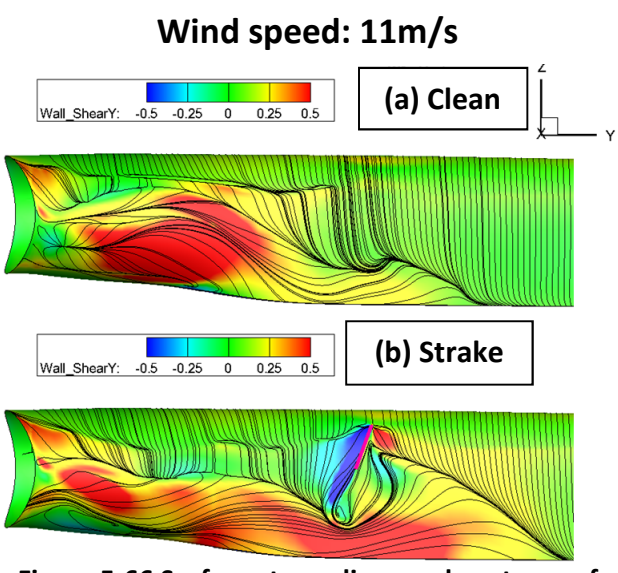

Figure 5-66 Surface streamlines and contours of surface shear stress on rotor suction side for Ws = 11m/s and Omega = 11.9RPM (a) datum geometry (b) with strake, displayed span range: r/R=0.05 – 0.35

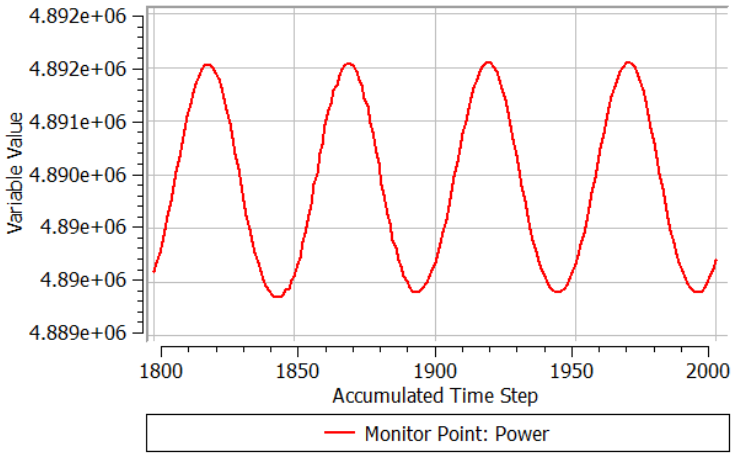

Figure 5-67 Power monitor for rotor with root strake for Ws = 11m/s and Omega = 11.9RPM

The vortices generated by the root strake were analysed considering the positive circulation. This was determined by finding the vortex core location (peak vorticity) from the vorticity contour plot and integrating the positive streamwise vorticity over a circular area with a radius extending to where the local streamwise vorticity reaches zero. The negative circulation is neglected within the integrated circular zone.

The results from this analysis (Figure 5-68) shows that the strake generates the strongest vortex in terms of peak circulation at the wind speed of 7m/s. The peak circulation is reduced significantly with the increase in wind speed, which is maybe due to the increase in incidence. Another factor that influences the strake's effectiveness is the local boundary layer thickness, however only about 0.3% change in boundary layer thickness was noticed within the wind speed range of 5-11m/s, thus the poor performance of the strake at 11m/s could be largely due to the change in inlet flow angle.

At 11m/s the strake is only able to generate a vortex that has 20% strength of the vortex generated at 7m/s. It was also clear that the vortex generated by the root strake decays faster at 9m/s than 7 or 5m/s i.e. the peak circulation is reduced by 50% within 20h downstream from the stake at the wind speed of 9m/s while at 7m/s only 20% of the peak circulation is dissipated within 20h downstream from the stake. This results shows that this strake design is only able to generate efficient vortices at lower wind speeds and fails at higher wind speed of 11m/s, this is may be due to the increase in relative flow angle.

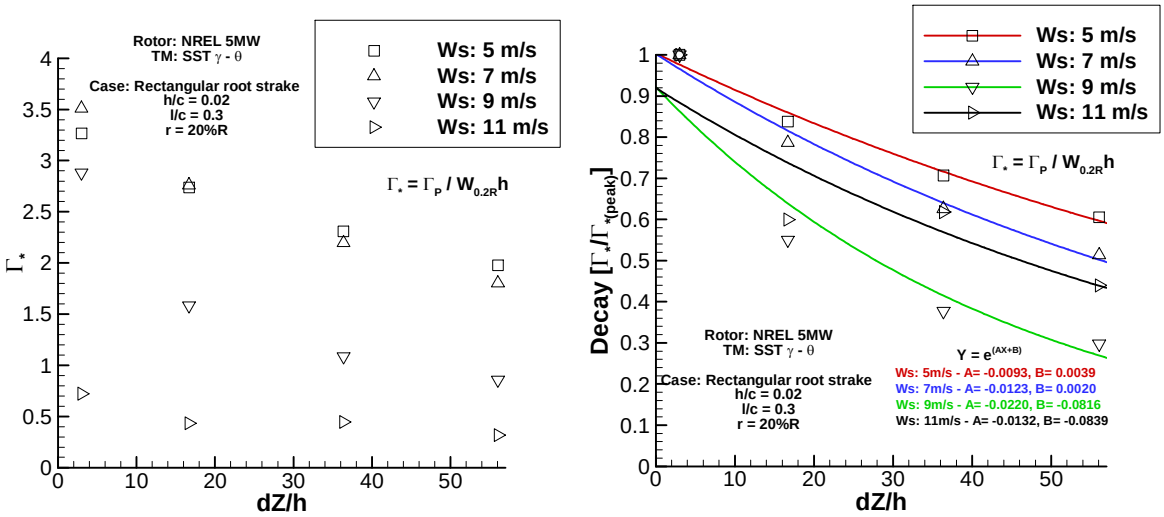

Figure 5-68 Stream wise distribution of vortex circulation (left) and the peak circulation decay rate (right) for the root strake at different wind speeds, dZ originates from the strake TE

The location of the peak vorticity or core of the vortex relative to the blade surface was assessed to evaluate the influence of the vortex to the boundary layer (Figure 5-69). It was found that the vortex generated at lower wind speeds 5, 7 and 9m/s lie closer to the blade surface than the vortex generated at 11m/s, about 4 strake heights within 55h downstream. These vortices generated at low wind speeds were also found to be located within local boundary layer. The vortex placed closer or within the boundary layer will generate a larger momentum transfer to the boundary layer from the flow outside. Therefore it is clear that vortices generated at the lower wind speed have significantly larger influence on the momentum transfer to the boundary layer than the vortex generated at 11m/s. The vortex generated at the higher wind speed of 11m/s was found to be about five times away from the blade surface than the vortices generated at the lower wind speeds. It is clear that the vortex generated at the 11m/s wind speed has the lowest influence on the boundary layer.

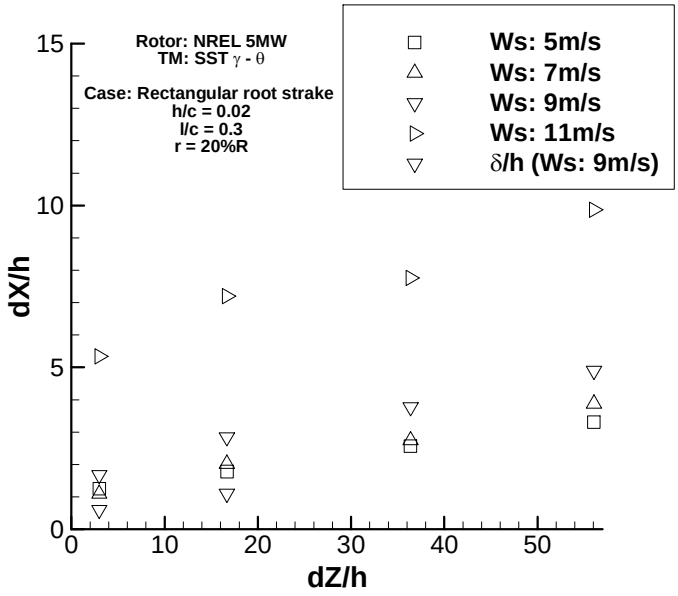

Figure 5-69 Vortex path non-dimensional by the height of the root strake (h) at different wind speeds, the dZ originates from the strake's TE, dX originates from the blade surface

Based on this initial assessment, it was found that the installation of a root strake can be beneficial for a wind turbine. Potential improvement of 0.4% to the power output and 0.13% increase in torque to thrust ratio is possible with this device at the wind speed of 5 m/s. However, a more substantial assessment of the design space and aerodynamic sensitivities is required to understand if this is a viable technology for large scale wind turbine applications.

1.1.1.1. Chine type strake

The initial root strake study was conducted using a simple rectangular strake. Based on chines applied to aircraft nacelles it was decided that a chine type [77] geometry (Figure 5-70) will be used for further studies on the effect of a root strake. This shape is expected to promote an efficient vortex that will be beneficial throughout the sub rated wind speed range. The profile of the chine is defined based on the height and the length of the chine (Figure 5-71). The toe angle is defined in relation to the blade chord wise direction (Figure 5-72).

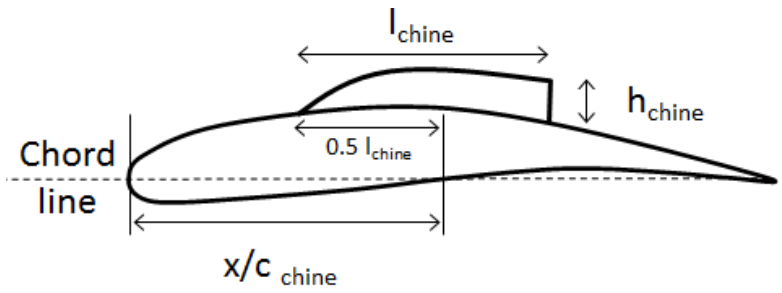

Figure 5-70 Geometry of the chine type root strake

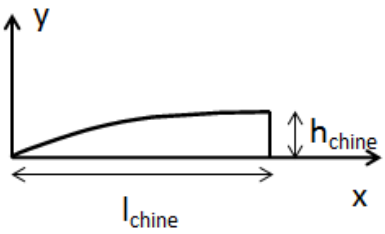

$$y = h_{chine}\left[1 - \frac{(l_{chine} - x)^2}{l_{chine}^{\ 2}}\right]$$

Figure 5-71 Chine profile definition [77]

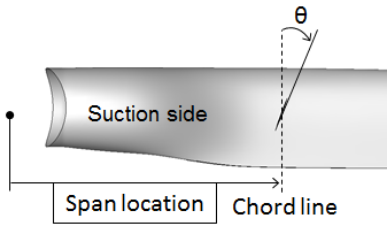

Figure 5-72 Chine toe angle definition

5.6.1.2.1 CFD modelling

It is difficult to generate a pure hexahedral grid for the triangular shaped chine geometry. Initial evaluations showed that it is a notable challenge to establish a gridding method that will both enable a parametric study of a range of chine designs as well as provide credible comparisons with the baseline grid and CFD solutions.

A hexahedral-tetrahedrall conformal hybrid mesh (Figure 5-73) was chosen to model the root chine. Effectively most of the blade is defined with the baseline grid and only a small volume close to the root chine (Figure 5-74) is modelled using tetrahedrall elements with 15 prism layers. The hexahedral and tetrahedrall elements are conformably merged to form a pyramid element at the connections between this small tetra volume and the baseline grid. This type of hybrid mesh does not require the use of non-conformal mesh interfaces for the CFD simulations. Therefore the result from this grid does not experience any interpolation errors at the interface and reduces the meshing complexities when gridding for a root chine that is close to the spinner.

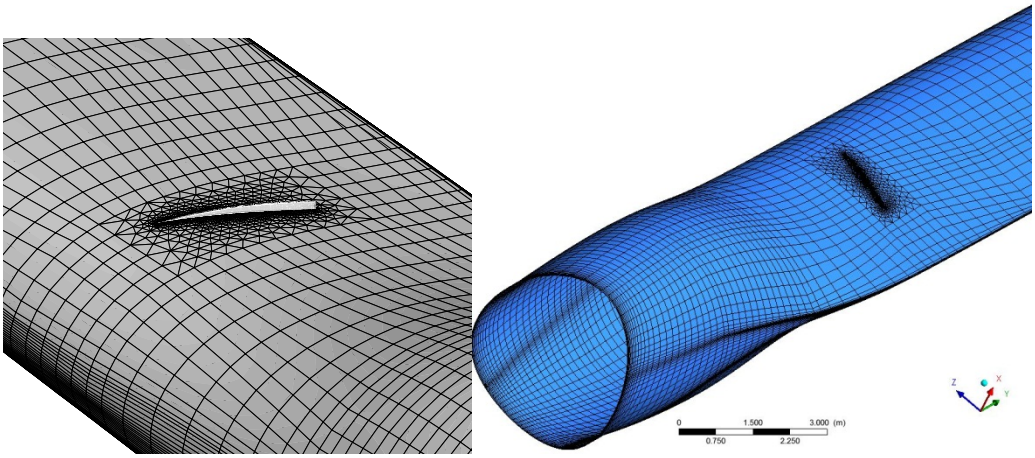

Figure 5-73 Hexahedral-Tetrahedrall conformal hybrid mesh

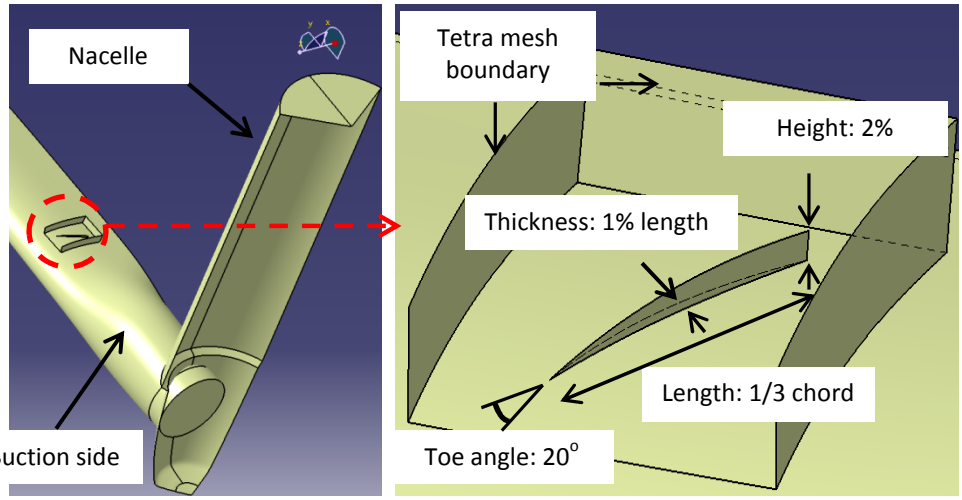

Figure 5-74 Hexahedral-Tetrahedrall conformal hybrid mesh showing the small volume enclosing the tetra elements

There were some differences in flow topology calculated from the established baseline grid and the conformal hybrid grid (Figure 5-75). A difference in rotor power of 0.7% was seen between the baseline grid and the hybrid grid at the wind speed of 5m/s. However the relative changes in performance due to the root chine can be evaluated by using the tetra elements to model the small volume in the vicinity of the chine for clean blade as well as the chine integrated blade. Based on these results the Hexahedral-Tetrahedrall conformal hybrid mesh was decided for the root chine CFD study, as it produces results that achieve a reasonable agreement with the baseline results and it minimises the errors associated with mesh interfaces and reduces the complexities in gridding.

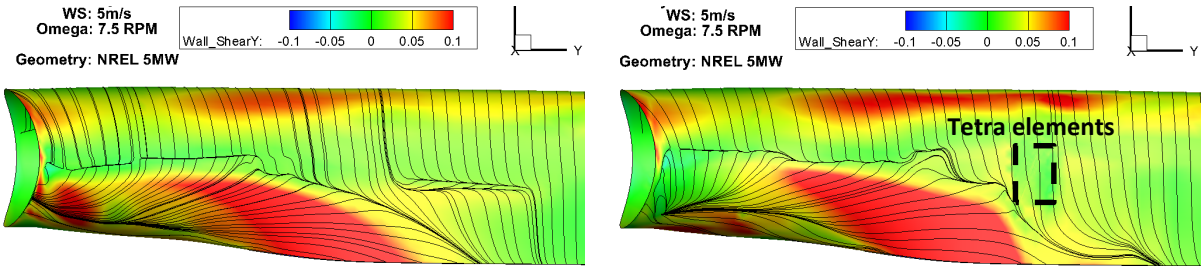

Figure 5-75 Surface streamline patterns on the blade suction surface, left: baseline grid, right: conformal mixed element grid, displayed span range: r/R=0.05 – 0.30

5.6.1.2.2 Root chine parametric design cases

The aerodynamic effects of varying the chine height, length, toe angle, span and chord location were investigated. Various configurations of the chine were used to assess these effects. A case classification was established to record and present the results (Figure 5-76). The evaluation of the chine was conducted for the design wind speed of 9 m/s and the rotational speed of 10.3 rpm. The SST γ – θ turbulence model was used to perform this investigation.

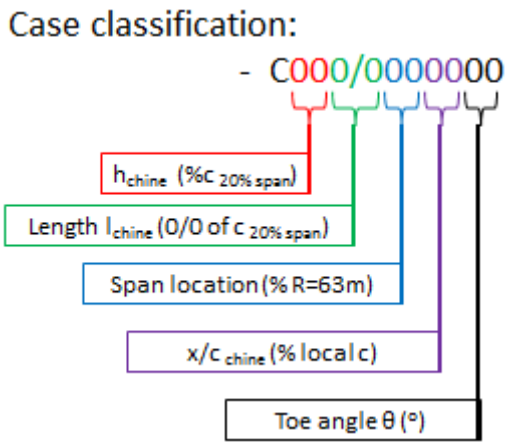

Figure 5-76 Chine's parametric design case classification

5.6.1.2.3 Effect of varying chine's height and span location

The results show (Table 5.6.1-2) that a root chine placed at r/R=0.20 with small height (<0.02c) seems to produce a less effective vortex that is unable to mitigate the radial flow, however if the chine height was increased beyond 0.04c, the beneficial vortex is lofted away from the blade surface and loses its effectiveness to reduce the radial flow.

The effect of the chine on the local aerodynamics was assessed using a blade patch in the vicinity of the chine (Figure 5-77). A method of extracting blade local forces from a 3D CFD simulation is presented in [72]. This method was implemented to determine the local changes in performance.

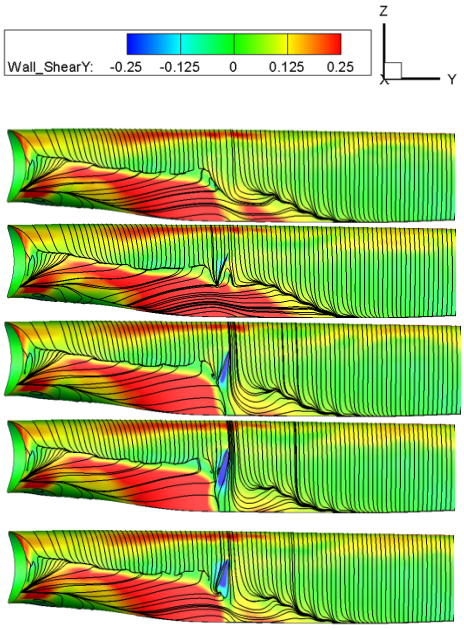

Chine height (C – local chord at 20% blade span)	Power (kW)	Thrust (kN)	% Power	% Thrust
0C - Clean blade	2666.23	161.05	-	-
0.01C	2663.47	160.90	-0.10	-0.09
0.02C	2673.55	161.34	0.274	0.183
0.04C	2668.12	161.21	0.071	0.098
0.06C	2665.33	160.93	-0.034	-0.072

Table 5.6.1-2 Results from the varying chine heights study - span location: 20%, chord location: 50%, toe angle: 20°, length: 0.3C, Ws: 9m/s, Omega: 10.3 RPM, TM: SST γ-θ, curvature correction: on, displayed span range: r/R=0.05 – 0.40

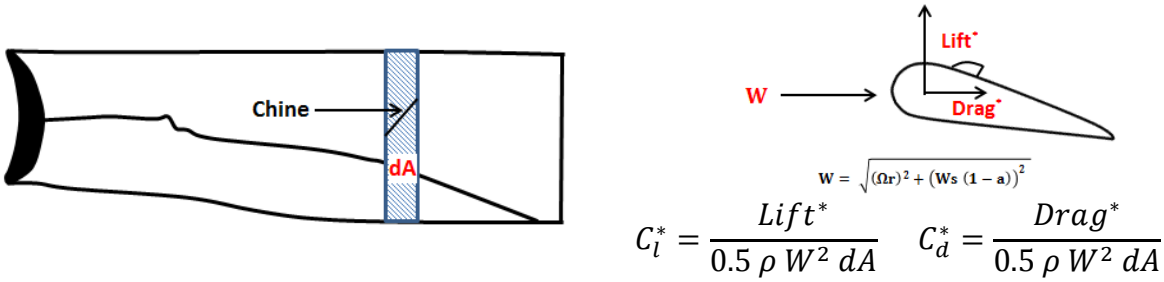

Figure 5-77 blade patch used to assess the local blade performances due to root chine

The results (Figure 5-78) shows that all of the chine heights studied in this exercise have a negative effect on the lift production. Up to 9% reduction in local lift was seen with a chine height of 6% chord. Lowest reduction in local lift of about 8% was seen with a chine height of 2% chord. The benefit of the chine is seen in its drag reduction capability for the chine with h=2%c, where it was able to reduce the local drag forces by about 20%. The 0.04c height chine had negligible effect on the drag (ΔCd = -0.7%). The other two heights (0.01c, 0.06c) investigated showed an increase in drag forces. A maximum drag increase of 10% was seen for the chine height of 6% chord.

The increase in axial induction at this portion of the blade is as important as the increase in lift or reduction in drag (section 2.1). The result showed that only a chine height of 1% chord had a undesirable reduction in axial induction of about 1% while all other heights contributed to a small increase within 0.6% to the local axial induction compared to the clean blade patch. Despite the 8% reduction in lift due to the h=0.02c, the large reduction in drag, increases the relative change in lift to drag ratio by 20%. Overall a chine height of 2% chord shows the positive reduction on drag and an increase in axial induction of 0.43%, it was able to increase the rotor output by 0.3% at the design point wind speed.

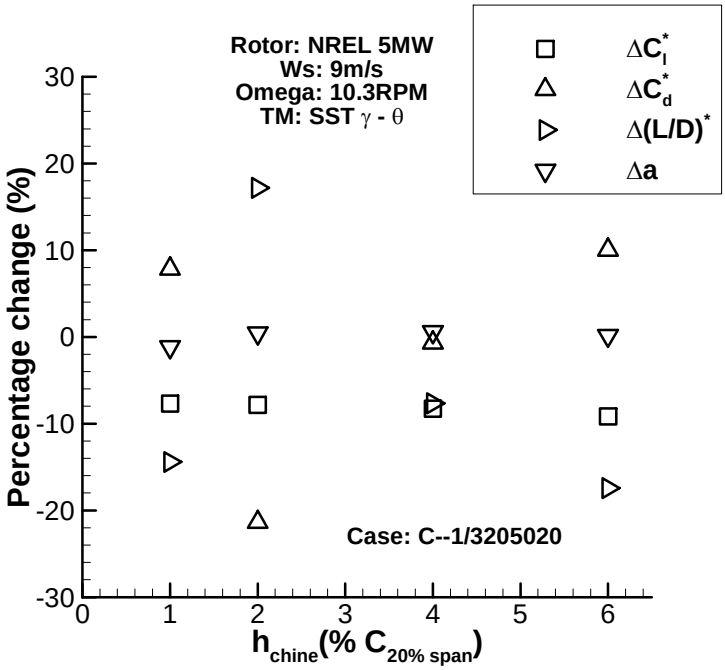

Figure 5-78 Changes in local blade aerodynamics as a function of chine height

The assessment of the radial location of the chine was performed using the chine with h=0.02c, placed at x/c =0.50 with a l/c= 1/3. It was found that, when a chine is placed closer to the hub it loses its ability to generate a beneficial vortex that opposes the radial flow (Table 5.6.1-3), i.e. the chine placed at 10 and 15% blade span is broadly ineffective at its location.

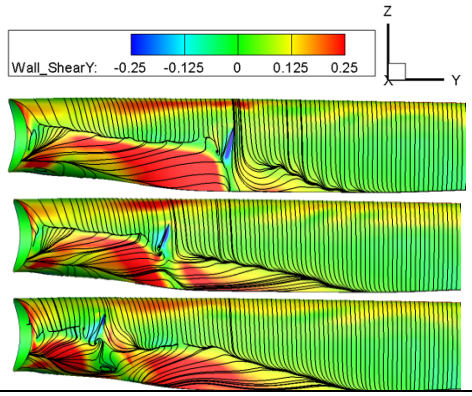

Chine span location	% Power	% Thrust
20%	0.274	0.183
15%	0.07	0.08
10%	-0.17	0.00

Table 5.6.1-3 Results from the varying chine span locations study – height: 2% C, chord location: 50%, toe angle: 20°, length: 0.3C, Ws: 9m/s, Omega: 10.3 RPM, TM: SST γ-θ, curvature correction: on, displayed span range: r/R=0.05 – 0.40

The local aerodynamics (Figure 5-79) shows that a chine placed below 25% span (r/R<0.25) increases the drag forces by up to 24% at the 10% blade span. This is reduced to 21% when the chine is placed at r/R=0.15. However at the span location of r/R=0.10, the root chine was able to increase the lift production by 8% and the axial induction by 3%, but due to the large increase in drag forces the lift to drag ratios are compromised by 13% and as a result the chine reduces the rotor power by 0.17%.

The lift to drag ratios were reduced by 18% relative to the clean blade when the chine is placed at 15% span. For this case with the chine at r/R=0.15, although the local aerodynamics show that the lift and axial induction factor are slightly reduced by 1% and 0.2%, respectively, there is a slight increase in the design point output (ΔP=+0.07%). This is due to the induced changes in the aerodynamic characteristics on the in-board part of the rotor (r/R <0.15) where the lift coefficient is increased by 6%.

It was seen that chine placed at 15% span and below has an influence on the lift and drag production of the blade root below (Figure 5-80, Figure 5-81), while the chine placed at 20% span has negligible or no influences on the lift or drag forces on the root section below i.e. the effects due to the chine is localised when the chine is placed at r/R=0.20.

Overall the results (Figure 5-82) from this study shows that a chine placed at x/c=0.50 and at 20% blade span performs the best with an increase in power output approximately 0.3% relative to a clean blade.

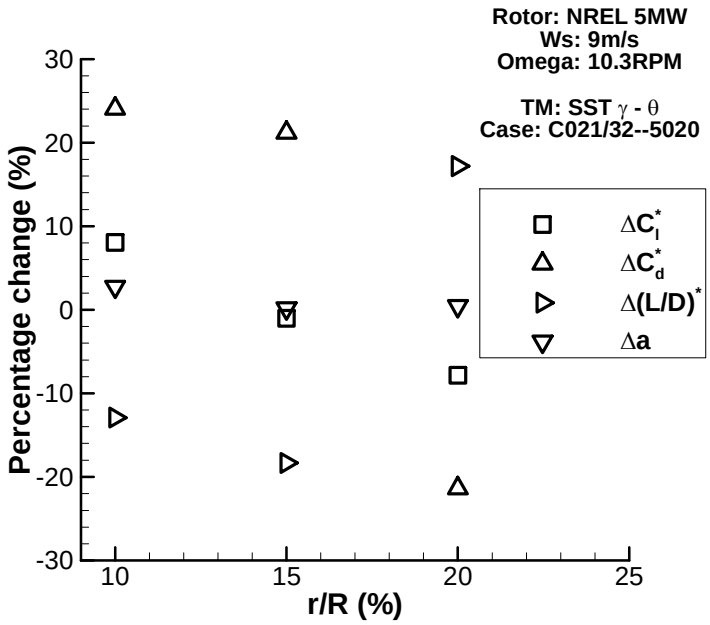

Figure 5-79 Changes in local blade aerodynamics as a function of chine radial locations

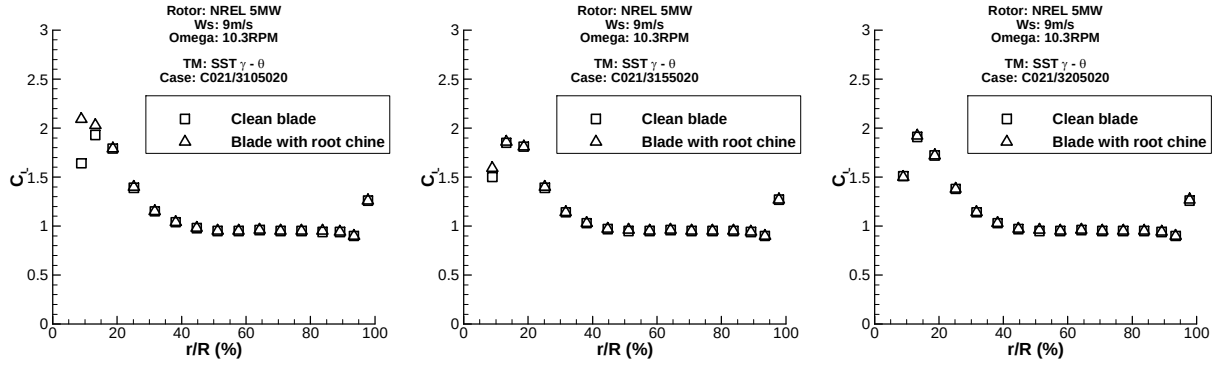

(a) (b) (c)

Figure 5-80 Lift distribution as a function of blade radius for the chine placed at 10% R (a), 15% R (b) and 20% R (c). h=0.02c for all cases.

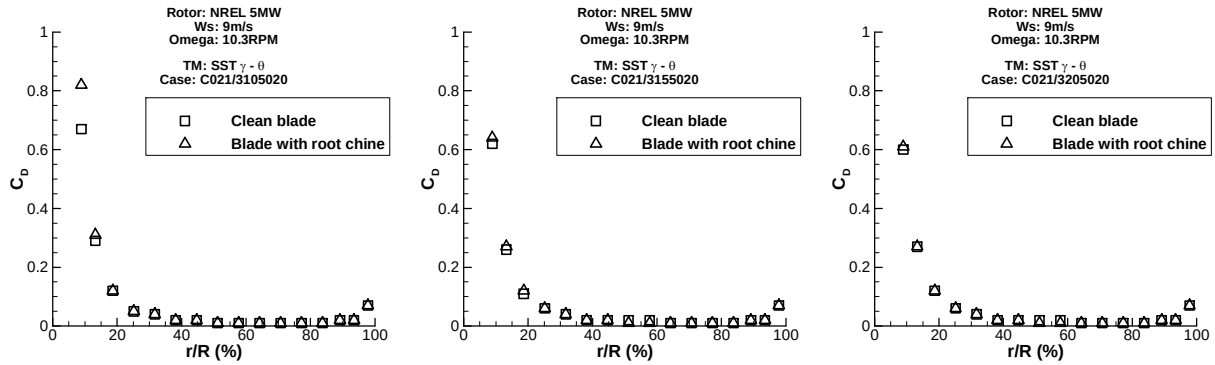

(a) (b) (c)

Figure 5-81 Drag distribution as a function of blade radius for the chine placed at 10% R (a), 15% R (b) and 20% R (c) h=0.02c for all cases.

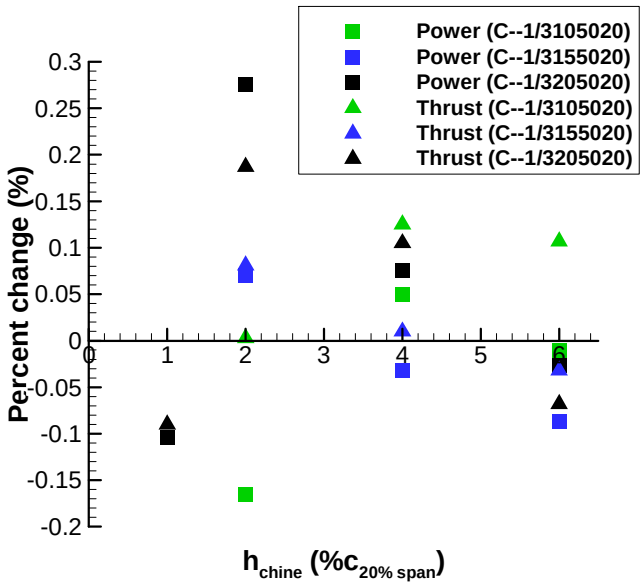

Figure 5-82 Results for the varying chine heights and span locations, Geometry= NREL 5MW, Ws: 9m/s, Omega: 10.3 RPM, TM: SST γ-θ, curvature correction: on.

5.6.1.2.4 Effect of chine chordwise location

When a chine is placed closer to the leading edge (x/c=0.25), it reduces the beneficial flow acceleration and reduces the suction pressure (Figure 5-83). If the chine is placed closer to the TE (75% chord), where nearly 70% of its length is in the separated flow region, it fails to mitigate the radial flow and reduces the power production (Table 5.6.1-4). However if the chine is moved closer to the TE (80% chord), where it is further placed within the separated flow, the power output is slightly improved, as the reduction in radial flow is slightly reduced.

The evaluation of the vortex generated by the chine was studied using the approach conducted for the rectangular strake (section 5.6.1). Based on the results (Figure 5-84), it was found that chine placed closer to the leading edge generates the strongest vortex in terms of non-dimensional peak circulation and it was able to generate double the strength of the vortex produced by the chine placed at 70% chord. The vortex generated by the chine placed at 50% chord was found to have the lowest peak circulation and it was only able to generate about 30% of the peak circulation produced by the chine placed at the 25% chord. This is maybe due to the high momentum flow found at the x/c=0.2 (peak suction) induces a higher vorticity to the generated vortex, while further downstream (x/c=0.5), the flow velocity is reduced considerably (diffusion), thus relatively smaller vorticity is imparted to the vortex.

The vortices generated by the chine placed at x/c=0.25 and 0.5 dissipates its peak circulation by 80% within the first 3 chine heights downstream, while the vortex produced by the chine placed at x/c=0.7 was found to dissipate almost 90% of its peak circulation within the first 3 chine heights downstream. These results show that an efficient vortex is formed only when the chine is placed x/c<0.5.

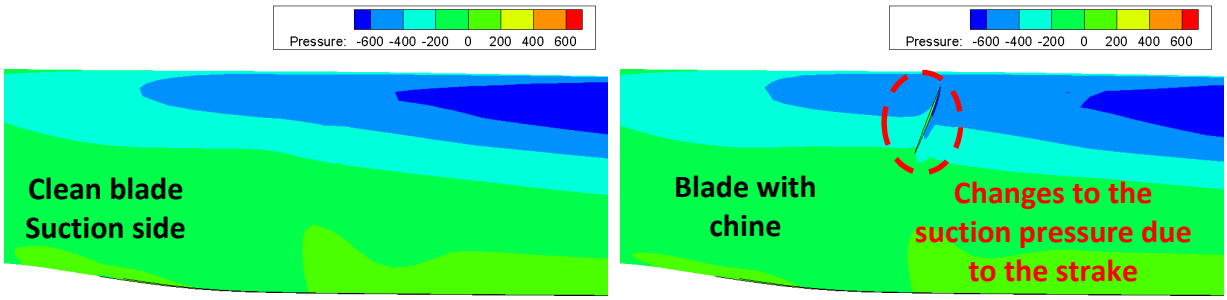

Figure 5-83 Changes in suction side pressure due to chine placed closer to the LE, left: datum case, right: blade with chine placed closer to the leading edge, displayed span range: r/R=0.1 – 0.30

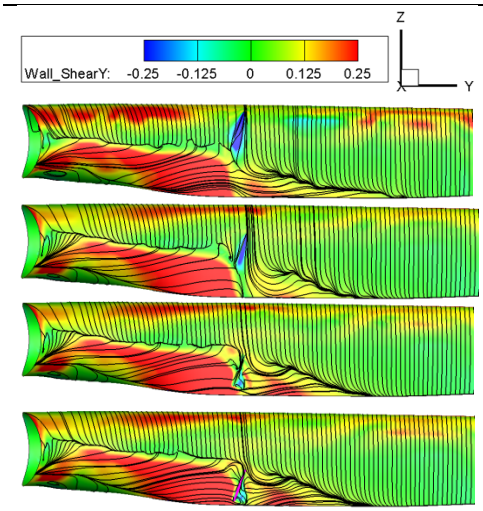

Chord location of l/2	% Power	% Thrust
25%	-4.475	0.021
50%	0.274	0.183
75%	-0.273	0.160
80%	-0.182	0.216

Table 5.6.1-4 Results for the varying chine's chord location study – h/c= 2%, span location: 20%, toe angle: 20°, length: 0.3C, Ws: 9m/s, Omega: 10.3 RPM, TM: SST γ-θ, curvature correction: on, displayed span range: r/R=0.05 – 0.40

Based on the local aerodynamic assessment (Figure 5-85), it was found that chine undesirably reduces the local lift forces. A maximum reduction in lift force of about 12% was calculated for the configuration with the chine placed at x/c=0.25, while a minimum reduction in lift of approximately 8% was found with the chine placed at x/c=0.50. This is consistent with the chine detrimental effect on the blades suction pressure when it is placed at x/c=0.25.

It was found that all chord locations, except the x/c=0.25 showed a beneficial effect on the drag forces. A maximum reduction of 22% in drag was found to be with the chine placed at x/c=0.50. This beneficial change in drag is reduced to 11% when the chine is placed closer to the blades TE (70% chord). Overall a chine placed at x/c=0.50 is able to increase the local lift to drag ratios by 17% while achieving a beneficial improvement in the axial induction of about 0.44%.

In summary, based on these results it is detrimental to place the chine closer to the TE or the LE as it reduces the efficiency of the vortex in terms of circulation decay and reduces the peak suction pressure, respectively. It is only beneficial when the chine is placed at 50% chord (Figure 5-86).

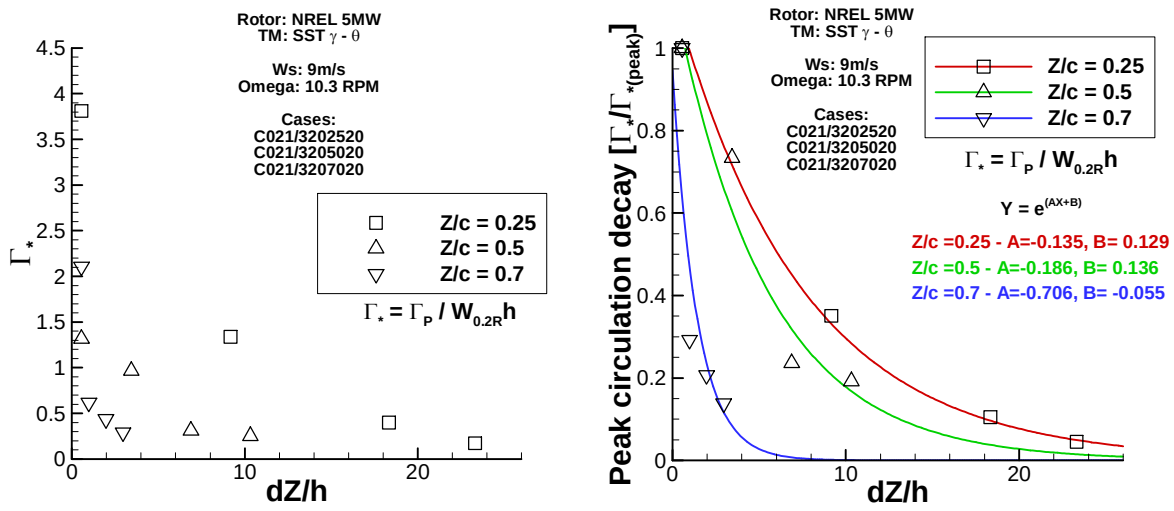

Figure 5-84 Non-dimensional stream wise circulation (left) and peak circulation decay (right) as a function of stream wise distance in terms of chine heights from the chines TE

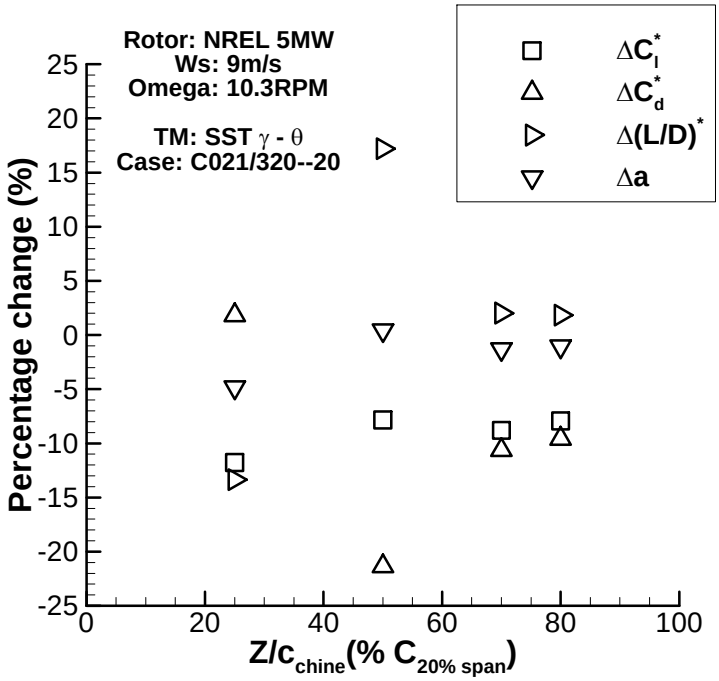

Figure 5-85 Percentage change in local aerodynamics as a function of chine chord location

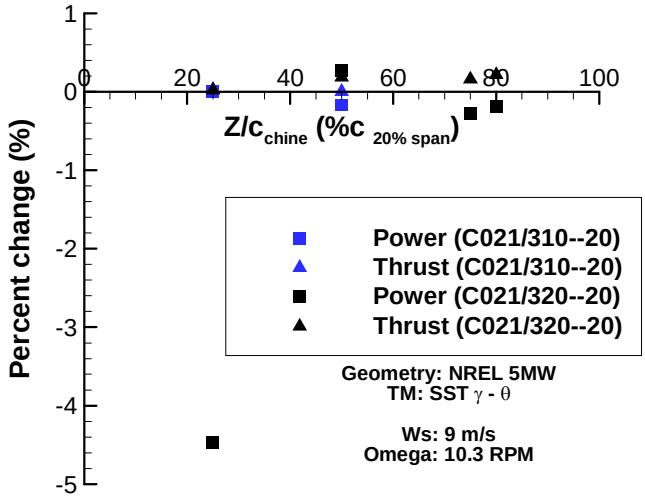

Figure 5-86 Results for varying chines chord location, Geometry= NREL 5MW, Ws: 9m/s, Omega: 10.3 RPM, TM: SST γ-θ, curvature correction: on.

5.6.1.2.5 Effect of chine toe angle and length

Five different toe angles were tested for their effect on the chine performance, as change in toe angle will effect strength, size and location of the generated vortex. The tested toe angles were 0 °, 5 °, 10 °, 15 ° and 20°. The effect of varying toe angle was only tested at the span location of r/R=0.20. The results from this study (Table 5.6.1-5) showed that a root chine with a 10° toe angle achieves the maximum rotor power increment (+0.3% rotor power, +0.24% blade thrust), yet a chine with 20° toe angle produced a better dP/dT (+0.28% rotor power, +0.19% blade thrust).

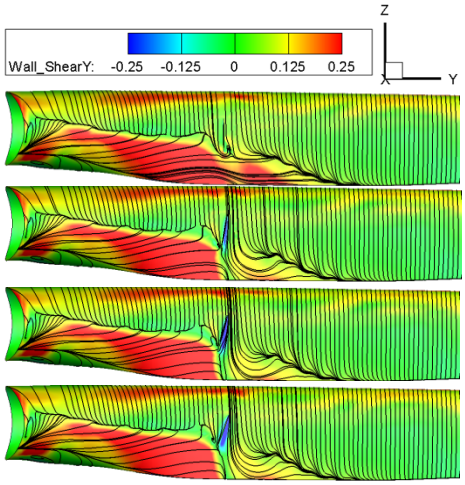

Chine toe angle (θ)	% Power	% Thrust
0	-0.023	-0.015
10	0.30	0.24
15	0.08	0.10
20	0.28	0.19

Table 5.6.1-5 Results for the varying chine toe angle – h/c= 2%, span location: 20%, length: 1/3 C, chord location: 50% C, Ws: 9m/s, Omega: 10.3 RPM, TM: SST γ-θ, curvature correction: on, displayed span range: r/R=0.05 – 0.40

Based on the evaluation of the vortices generated by the chine with different toe angles (Figure 5-87), it was found that a toe angle of 15° generated the strongest vortex in terms of peak circulation and as anticipated the chine with 0° toe angle generated the lowest peak circulation, which was about 13% of the peak circulation generated by the chine with 15° toe angle. It was found that the vortex generated by the chine with 0° decays its peak

circulation by 80% within the first 2h downstream, while it takes 6h for the chine with a toe angle of 10° or 15° to decay its peak circulation by 80% i.e. a robust vortex is generated when a positive toe angle is considered. The chine with 20° toe angle generated the most efficient vortex as it takes about 10h downstream for its vortex to decay its peak circulation by 80%. However it should be noted that the vortex generated by the 15° still has a higher circulation than the vortex produced by the 20° toe angle at 10 heights downstream i.e. 20% of the peak circulation from the 15° is greater than the 20% of the peak circulation from the 20° toe angle i.e.

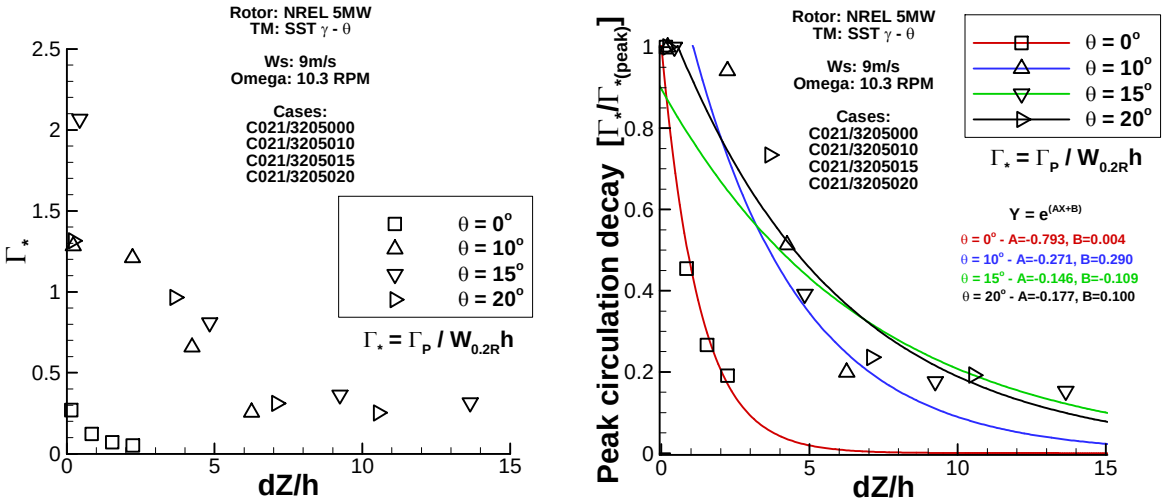

Figure 5-87 Stream wise distribution of vortex circulation (left) and the peak circulation decay rate (right) for the root chine with different toe angles, dZ originates from the chine TE

The location of the vortex core for the chine with 0° toe angle was found to elevate away from the surface faster than for the vortices produced by the other three toe angles (Figure 5-88) i.e. it achieve a distance of 1.8h away from the blade surface within 2h downstream, while it takes nearly three times as much distance downstream for the vortices generated by the chine with the toe angle of 10 and 20° to elevate to 2h. It was found that the vortex generated by 15° toe angle was found to show the best performance in terms of placing the vortex core close to the surface, where it takes 8h downstream for the vortex core to elevate to 1.8h away from the surface. Based on these results it is clear that 15° toe angle of the root chine generates the most beneficial vortex, however this benefit is not reflected on the rotor power.

Contrary to the vortex evaluation study, it was found that 10° and 20° toe angle showed the best performance on the local aerodynamics (Figure 5-89), which is consistent with the increase in rotor power. A chine with 10° toe angle was able to increase the local lift production by 14% and reduce drag forces by 6%, which results in an increase in lift to drag ratio of about 21%. The chine with 20° reduced lift production by 8% however with its large reduction in drag about 20%, it was able to increases the lift to drag ratios by about 20%. This is evident that similar power increment can be achieved with a similar increase in local lift to drag ratios at the 20% span. The 20° toe angle increases lift to drag ratios mainly by a large reduction in drag with a small reduction in lift which accounts for a small increase on thrust unlike a large increase in lift with a small increase in drag by the 10° toe contribute more to the increase in thrust. It was also found that 20° toe angle achieves a slightly better increase in axial induction than the 10° toe angle.

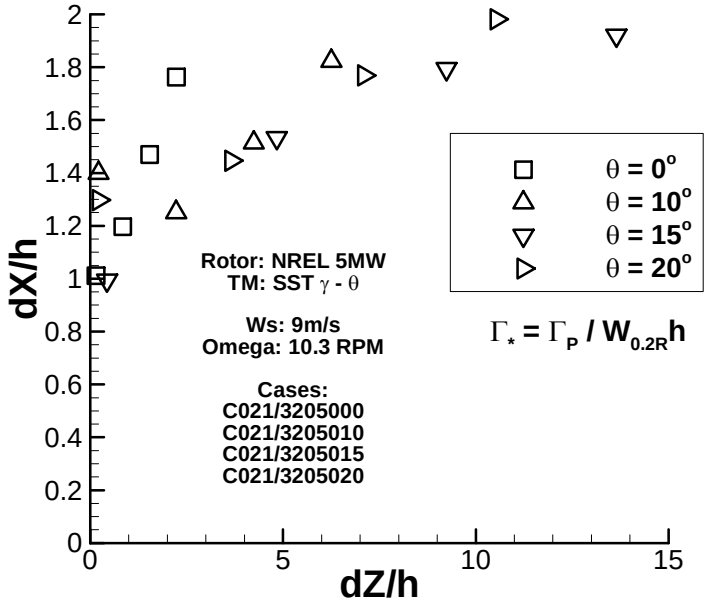

Figure 5-88 Non-dimensional location of the vortex core (peak vorticity) away from the blade surface as a function of stream wise distance from the chine TE

As anticipated it is clear from the results that 0^o toe angle has a negligible effect on the local aerodynamics (Figure 5-89) i.e. it has the lowest influence on the flow field. The 15^o toe angle reduced lift production by a negligible 0.5% while reducing the drag effect by 4%, in return achieving an increase in lift to drag ratio of about 3.4%. With this small increase in lift to drag ratio it achieves the 0.07% increase in rotor power.

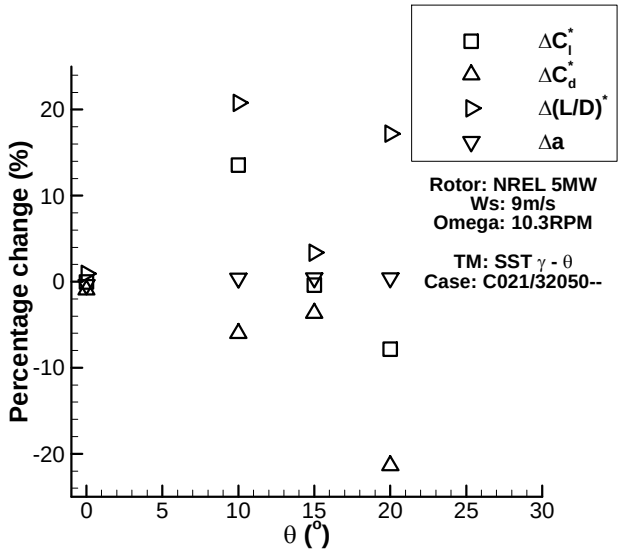

Figure 5-89 Percentage change in local aerodynamics as a function of chines toe angle

Based on this exercise it is recommended that a 20^o toe should be used for a root chine to achieve an efficient vortex and to attain a beneficial increase in rotor power, within out a large increase in thrust forces. This exercise has shown that about 20% increase in lift to drag ratios at the 20% span of the blade contribute to about 0.3% increase in rotor power

and how this is achieved in terms of increase or reduction in lift and drag forces dictates the changes in thrust forces.

Similar to the toe angle investigation, the effect of the chine length was examined for a chine at r/R=0.20 only. Three different lengths of chine were considered: l/c=1/6, 1/3 and 2/3c. The results (Table 5.6.1-6) showed that a chine with small length is less effective at reducing the radial flow migration than a chine with a medium length. A large chine accelerated the radial flow through the passage between the chines TE and blade TE (Figure 5-92), which causes detrimental effect to the rotor power production, as it increases the chord wise extent of the flow separation in the region outboard of the chine .

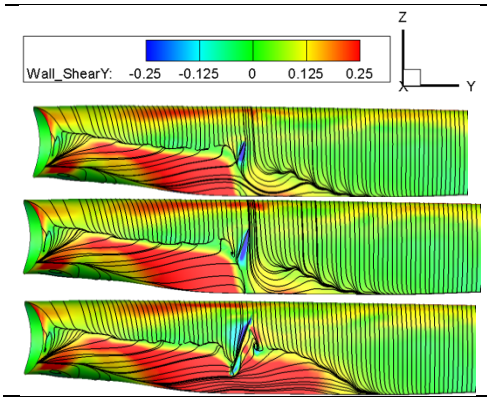

Chine's length (c)	% Power	% Thrust
1/6	0.15	0.14
1/3	0.274	0.183
2/3	-0.47	-0.30

Table 5.6.1-6 Results for the varying chine's length study – height: 2% C, span location: 20%, θ: 20°, chord location: 50% C, Ws: 9m/s, Omega: 10.3 RPM, TM: SST γ-θ, curvature correction: on, displayed span range: r/R=0.05 – 0.40

A chine length of 1/3c was identified to produce beneficial rotor power output of the turbine (Figure 5-92). It was found that the large chine (l/c =2/3) failed to generate a vortex with a coherent structure therefore it was not possible to analyse its characteristics. However the evaluation of the other two chine configurations (l/c=1/3 and 1/6) (Figure 5-90) shows that the smallest chine length of 1/6 chord generates the strongest vortex. It is able to generate a twice as much peak circulation compared to a chine with twice its length. It was found that both vortices had a similar circulation decay characteristics i.e. they both decays about 80% of their peak circulation within 10h downstream. Therefore both lengths have the same its effective range of operation downstream it shows that small chine is sufficient to generate an effective vortex.

The local aerodynamic forces (Figure 5-91) clearly shows the cause of the power reduction due to the large chine length. The large chine with its l/c of 2/3 significantly increased the local drag production by almost 110% and this large gain in drag with a small reduction in lift force of about 2%, reduces the lift to drag ratios by up to 50%. This effect reduces the rotor output at the design point by about 0.5%. The smallest chine on the other hand was found to cause negligible effect on the local lift forces by about -0.26% and to also increase the drag forces by 7%, resulting in a 6.4% reduction in lift to drag ratio. However a positive improvement of about 0.4% on the axial induction was noticed due to the small chine. This positive increase in axial induction seems to outweigh the reduction in lift to drag ratios to increase the power output by 0.15%.

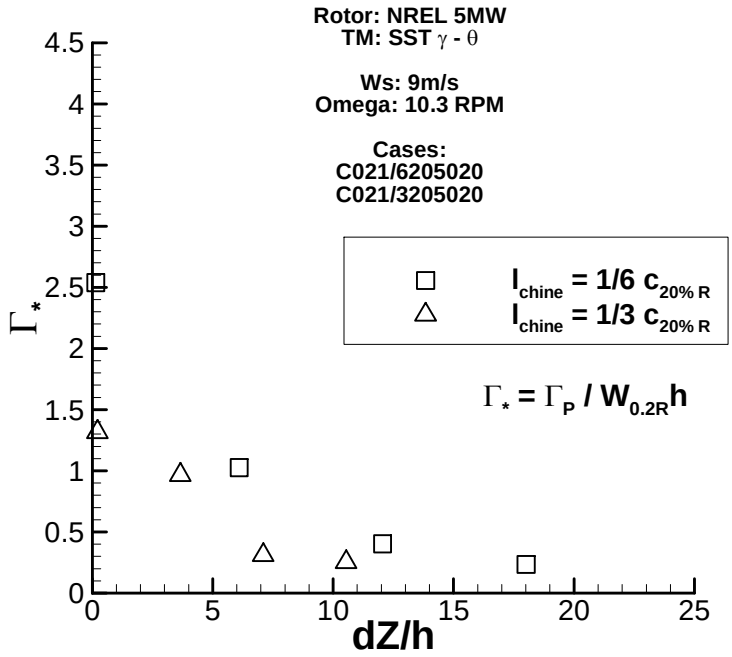

Figure 5-90 Non-dimensional stream wise circulation as a function of stream wise distance in terms of chine heights from the chines TE

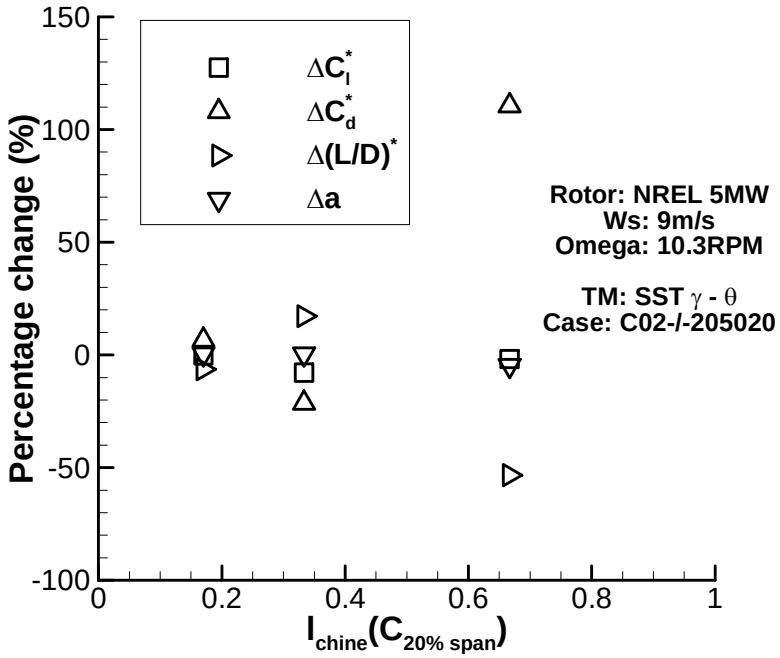

Figure 5-91 Percentage change in local aerodynamics as a function of chines lengths

Based on these results it is suggested that a chine toe angle of 20^{o} and a chine length of 1/3 chord is appropriate to beneficially increase the design point output of a wind turbine such as the NREL 5MW by up to 0.3% (Figure 5-92).

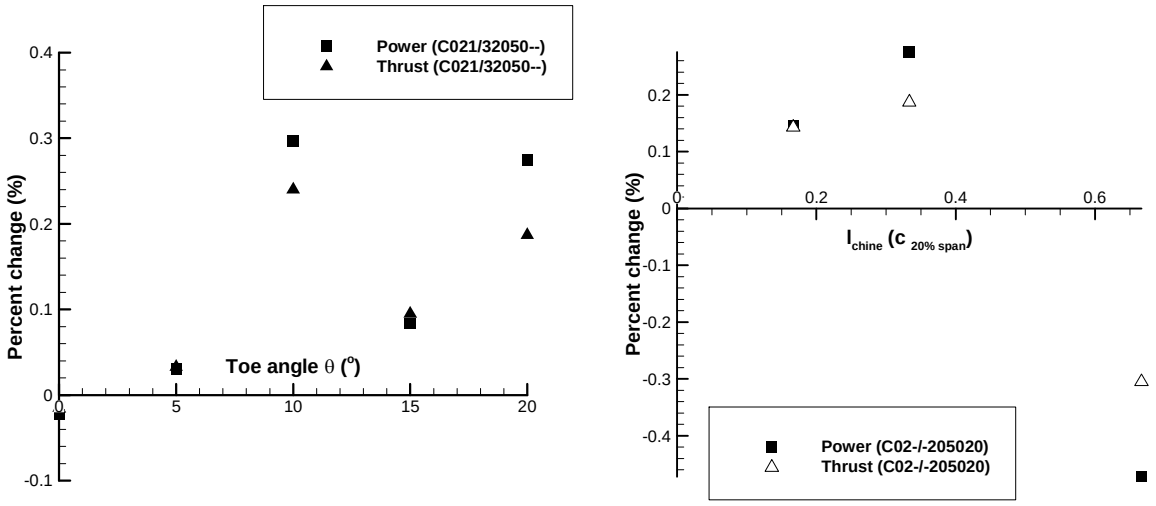

Figure 5-92 Results for varying chines toe angle(left) and varying chines length (right), rotor: NREL 5MW, TM: SST Ws: 9m/s, Omega: 10.3 RPM, TM: SST γ-θ, curvature correction: on

5.6.1.2.6 Discussion

Overall, the effort to establish a design space for the root chine device has been successful. Based on these results a chine with height of 0.02c, length of 30% chord, placed at x/c=0.5, r/R =0.2 with a toe angle of 20° was identified to be the best performing design. This design is able to increase the annual power production (AEP) of the NREL 5MW turbine by 0.05% (Table 5.6.1-7).

Wind speed (m/s)	Power change	AEP change
5	-0.07%	**0.05%**
7	0.17%	
9	0.24%	
11	0.15%	

Table 5.6.1-7: Performance of root chine for the NREL 5MW rotor, TM: SST γ – θ, root chine-[l/c: 30%, h/c= 2%, chord location: 50%, span location: 20%, θ: 20°]

It was found that the chine was able to increase the power production of the NREL 5MW rotor at the wind speeds of >7m/s. At the low wind speed of 5m/s the chine is detrimental for the power output as it reduces the baseline rotor power by 0.07%. However it was found that the chine is able to achieve local flow reattachment downstream from its location for all investigated wind speeds (Figure 5-93).

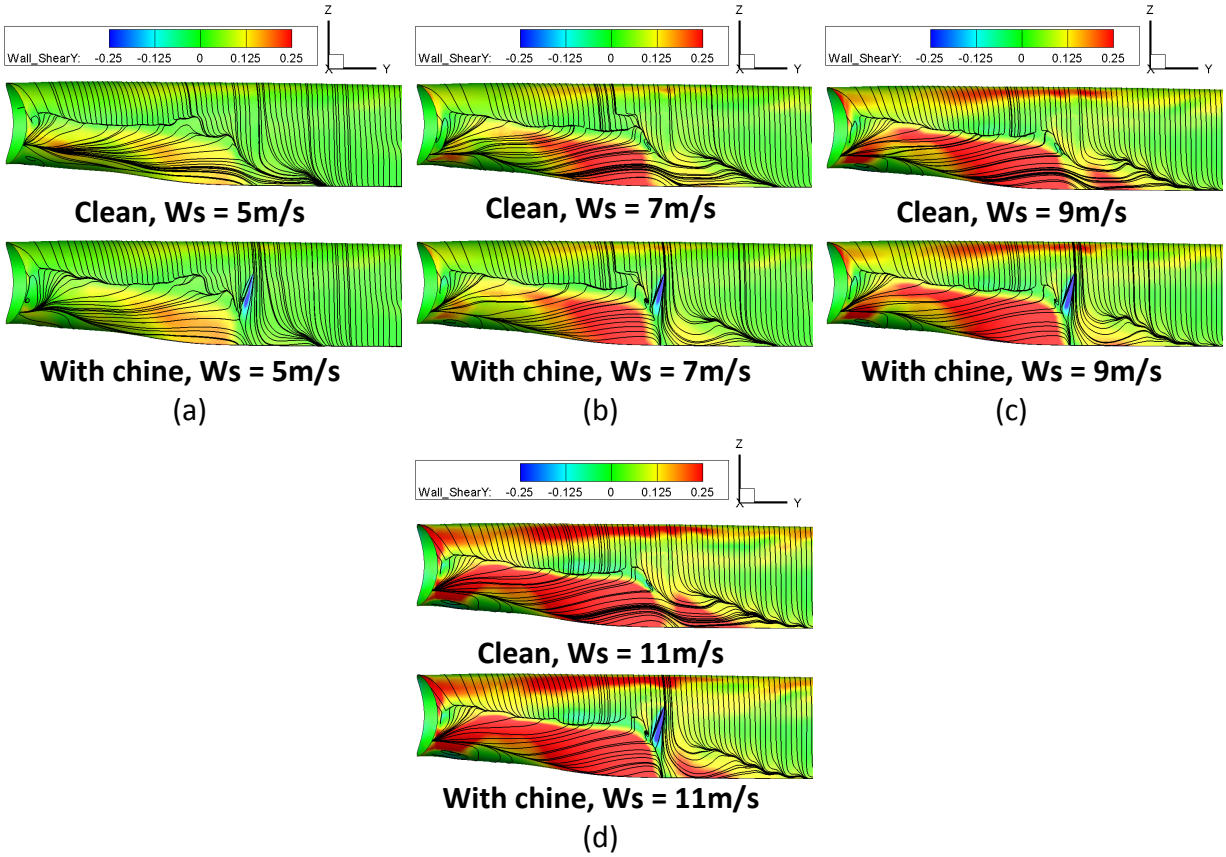

Figure 5-93 Surface streamline patterns for the root chine at different wind speeds, (a)- Ws: 5m/s, Omega: 7.506RPM, (b)- Ws: 7m/s, Omega: 8.469RPM, (c)- Ws: 9m/s, Omega: 10.296RPM, (d)- Ws: 11m/s, Omega: 11.89RPM, , TM: SST γ – θ, root chine-[l/c: 30%, h/c: 2%, chord location: 50%, span location: 20%, θ: 20°], displayed span range: r/R=0.05 – 0.30

The results from the vortex evaluation study (Figure 5-94) suggests that the vortex generated at the 5m/s wind speed has a non-dimensional peak circulation similar to the vortex generated at the 11m/s, i.e. both vortices have a similar influences on the boundary layer. It was also found to have higher relative non-dimensional circulation compared to the vortices generated at the 7 or 9m/s wind speed, about 30% higher than the 7m/s and about 20% higher than the vortex generated at 9 m/s. This suggests that the effect of the vortex generated at 5 and 11m/s should be more pertinent to the flow control application such as the momentum transfer to the boundary layer and reduce flow separation downstream. However the efficiency of the generated vortex is also depends on its ability to sustain its peak circulation downstream and its location relative to the local boundary layer. The vortices generated at the low wind speed of 5 and 7 m/s, were found to decay its peak circulation by 74% within 11h downstream while the vortices generated at the larger wind speed of 9 and 11m/s presented a faster decay. The vortex generated at the 9m/s was found to dissipate 80% of its peak circulation with 11h downstream while at 11m/s, about 90% of the peak circulation is dissipated. Overall these results suggest that vortex found at the 5m/s exhibits the best performance, which is contrary to the detrimental effect seen on the power output at this wind speed.

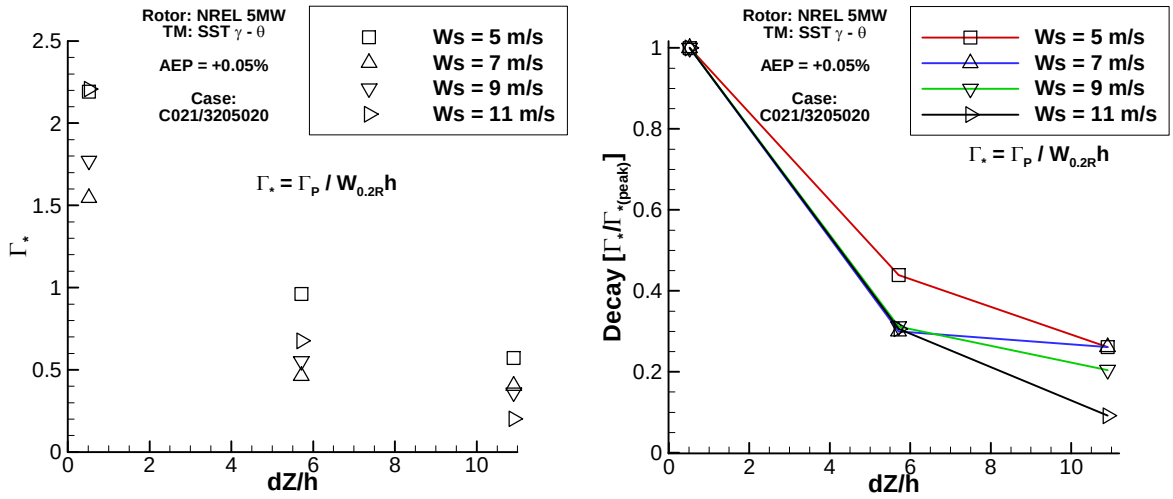

Figure 5-94 Non-dimensional stream wise circulation as a function of stream wise distance (left) and peak circulation decay (right) in terms of chine heights from the chines TE at different wind speeds, TM: SST γ – θ, root chine-[l/c: 30%, h/c: 2% chord, chord location: 50%, span location: 20%, θ: 20°]

Despite the beneficial characteristics shown by the vortex generated at the 5m/s, it was found that the vortex core was placed relatively higher from the blade surface than the vortices generated at 7 and 9m/s (Figure 5-95). At 11m/s the path of the vortex within 6h downstream was found to be similar to the vortices generated at the 7 and 9m/s however it was found to be elevated further away from the blade surface at about 11h downstream. This results suggests the vortices generated at the 7 and 9m/s has greater influence on the momentum transfer to the boundary layer than the vortex generated at the 5 or 11m/s.

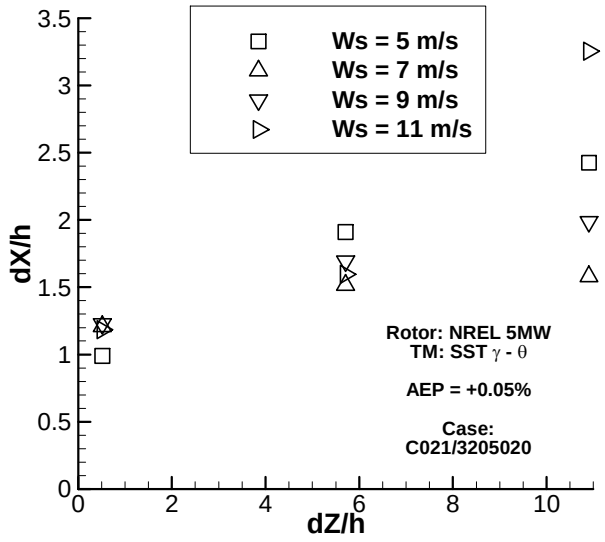

Figure 5-95 Non-dimensional location of the vortex core (peak vorticity) away from the blade surface as a function of stream wise distance from the chines TE at different wind speeds, TM: SST γ – θ, root chine-[l/c: 30%, h/c: 2% chord, chord location: 50%, span location: 20%, θ: 20°]

The chine at 7m/s wind speed showed the lowest influence on the local aerodynamics (Figure 5-96) where it was able to increase the lift to drag ratio by only 0.75%, however it was found to contributed the largest increase in local axial induction of about 0.5%, this

enables the chine to increase the overall power output of the turbine by 0.17%. The chine performs the best at 9m/s wind speed where due to its large drag reduction of about 20% it was able to increase lift to drag ratios by 17%, which results in the beneficial power increment of 0.20% of the baseline rotor. As the wind speed is increased to 11m/s, the chines showed less influence on the local aerodynamics compared to the 9m/s wind speed, where it reduces lift and drag by 1 and 5% respectively, which results in an increase on local lift to drag ratio of about 4% and achieves about 0.15% increase in rotor output.

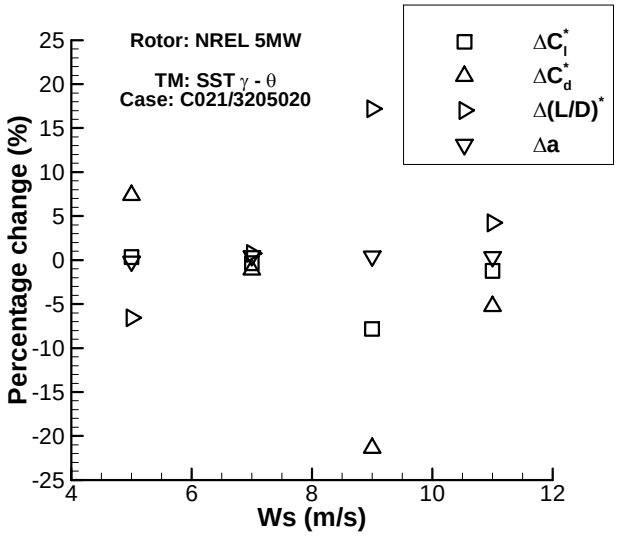

Figure 5-96 Chines localised aerodynamic changes at different wind speeds, TM: SST γ – θ, root chine-[l/c: 30%, h/c: 2% chord, chord location: 50%, span location: 20%, θ: 20°]

Additional to this exercise a CFD study on fences installed at the blade region of r/R: 18-22% of the baseline rotor was also conducted. Based on the ability of the chine to control secondary flows it is reasonable to compare its performance with other devices which are used to reduce or mitigate radial flow migration. Two devices were chosen for this investigation. Two fences based on the work of Heinzelmann et al [76] with a fence height of 3% chord and a single fence with 2% chord was studied using CFD (Figure 5-97). The height of the single fence was based on the investigation by UC Davis [4]. The fences used by Heinzelmann et al were placed at 18 and 22% of blade span.

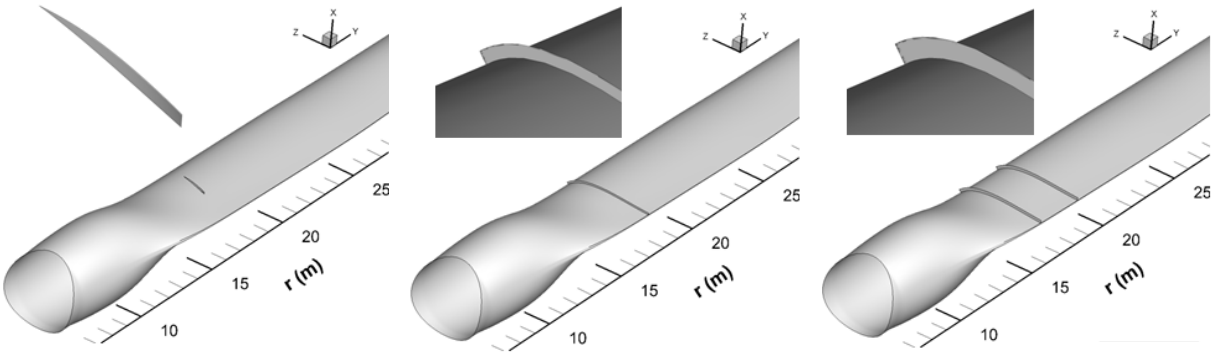

(a) (b) [76] (c) [4]

Figure 5-97 Chine, UCDavis fence and Heinzelmann et al fence geometry, chine-[length: 30% chord, height: 2% chord, chord location: 50%, span location: 20%, toe angle: 20°], Single fence– [fence height: 2% chord, span location: 20%], Heinzelmann et al boundary layer fence– [fence height: 3% chord, span location: 18%, 22%]

The results from the fence study were compared against the outcome from the investigation of the effect of a root chine. Based on the comparison, it was found that the increment in power was better for both types of fences than a root chine at the design wind speed of 9m/s (Table 5.6.1-8). The two fences based on the work by Heinzelmann et al [76] installed at the root part of the blade is able to increase the AEP of the NREL 5MW by 0.3%, where the root chine only achieved about 0.05%. Based on the current results, it seems that a better performance in annual power can be achieved with the fences than a root chine.

Device	Power change	Thrust change
Root Chine	+0.24%	+0.19%
Single fence	+0.44%	+0.33%
Boundary layer fences	+0.58%	+0.45%

Table 5.6.1-8: Performance of PFC devices for the blade root, wind speed: 9m/s, omega: 10.9rpm, TM: SST γ – θ, root chine-[length: 30% chord, height: 2% chord, chord location: 25%, span location: 20%, toe angle: 20o], Single fence– [fence height: 2% chord, span location: 20%], Heinzelmann et al boundary layer fences– [fence height: 2% chord, span location: 18%, 22%]

5.6.2 Robust vortex generator design

Another method to reduce the extent of hub separation is by using vortex generators. The typical thin vane vortex generators used for a wind turbine has a low tendency to break off during maintenance of the rotor. This causes major problems such as the lower output of the turbine, time and cost for repairs in the field. The overall aim of this investigation is to find a structurally sound vortex generator (VG) design that is an alternative to the thin vane VGs which are more commonly used on wind turbines. This investigation was mainly focused on supressing the radial flow and the flow separation found at the root part of the blade. Based on the CFD study of the baseline rotor, it was identified that the in-board (hub) flow separation was extended in the spanwise direction due to the spanwise flow migration. The placements of the VGs are expected to reduce this spanwise flow migration and to reduce the chordwise extent of the flow separation.

The results from the ideal turbine BEM study (Section 3.1.4) showed that the blade root is greatly underperforming due to the lack of lift force. The lift increment at the blade root is more of an interest than the reduction in drag which could accrue from flow reattachment. This is due to the fact that the lift vector is more aligned with the torque component at the blade root than the blade tip (Figure 5-98), which shows that doubling the drag at blade root results in 13% reduction in torque wile doubling the drag force at the blade tip results in 41% reduction in torque production. Therefore the increase in lift force is more effective to the torque production than at the blade tip. It is also noticeable that blade root is less sensitive to drag changes than the blade tip.

Initially as a baseline case, the conventional vane VGs is tested for their performance on the baseline rotor, then a range of wedge type VGs are used to evaluate their corresponding benefits for the baseline rotor. There has been no study to date that has investigated wedge type VGs for a wind turbine, thus this is one of the novelty research from this study.

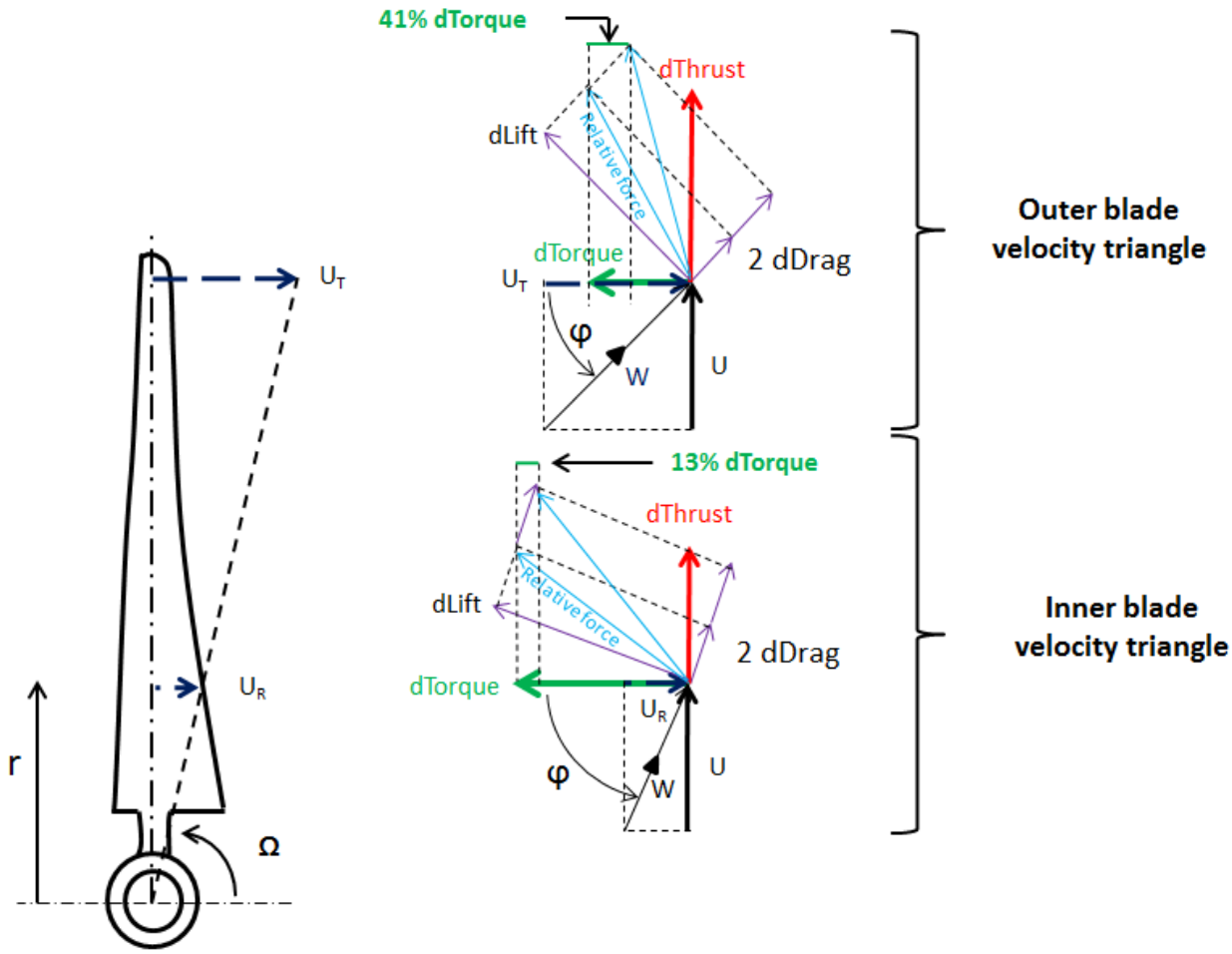

Figure 5-98 Velocity triangles of the inner and outer wind turbine blade

5.6.2.1 CFD model of the vane VG

In order to gain credibility of the CFD result of the conventional vane vortex generators, a validation of the CFD model is required. The work on modern counter rotating VG designs for wind turbines by Riso DTU [12] was chosen as the validation. The experimental results of the VG installed FFA-W3-241 airfoil was selected from the Riso report [12]. The data was chosen for the vane VG height of 0.6% chord (h/c=0.006, h/δ = 2.7) and placed at 10% chord. The experiments were conducted at the Reynolds number of 1.6 million and the available data include the coefficient of lift, drag and moments within the angle of attack (AoA) range of -4.4^o to 25^o. Surface pressure distributions were also available within this AoA range for both clean and the VG installed airfoil. The data for the free boundary layer transition case were selected.

The study was conducted using a prismatic FFA-W3-241 airfoil with a C-grid domain topology (Figure 5-99). A hexahedral-tetrahedrall conformal mixed element meshing strategy was used to model a small volume close to the VG. The external volume outside this small volume enclosing the VG was modelled using a full hexahedral C-grid with a domain extent of 40 chord, to calculate the flow around the airfoil. A quasi 3D simulation with symmetrical boundary conditions applied at either end of the airfoil was used to calculate the results.

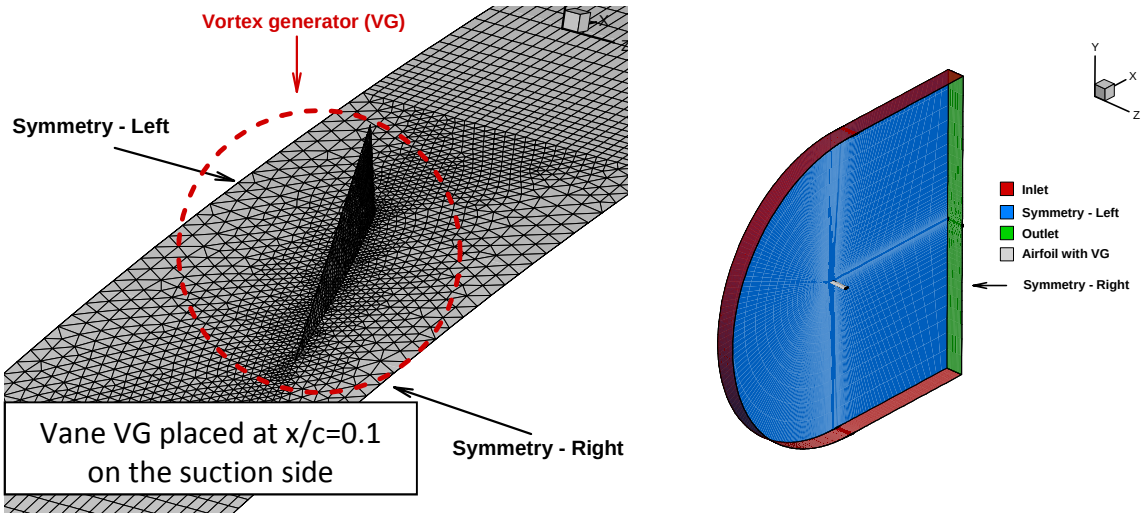

Figure 5-99 left: Gird adapted for the vane VG study, right: boundary conditions

Iterative convergence was assessed in the similar way to the 2D simulations conducted for the wind turbine airfoils simulations. The solution is assumed to achieve convergence when the RMS residuals from the U, V and W momentum as well as from the continuity equation reach below 1e-04 and the lift and drag forces are achieved within 0.5% of the reported values.

Initially a mesh sensitivity study was conducted to establish the number of elements required to calculate a solution for the clean and the VG installed airfoil that reaches an adequate level of grid independence. The mesh independence is assessed using the Richardson's extrapolation method (Appendix 8.1). The results from the Richardson extrapolation analysis (Table 5.6.2-9), shows that the CFD results from all three meshes for the clean case lie in the asymptotic range and that the meshes provide a solution that achieves an adequate level of grid independency. The results from the airfoil with VG case (Table 5.6.2-10) are similar to the clean airfoil case and it also suggests that all three different density meshes provide a solution that achieves an adequate level of mesh independence. Based on these results it was decided that the fine grid with approximately 1,100,000 elements is adequate to calculate a solution that achieves an adequate level of grid independence that does not require additional computational power. This grid is able to achieve an agreement within 15 and 20% with the measure lift and drag coefficient respectively for the clean airfoil. However a poor agreement between the CFD and measurements within 20 and 40% for the lift and drag coefficient was found for the profile with the VG. To further assess the credibility of the CFD model, a comparison of the pressure distribution along the airfoil chord is compared between the CFD calculated results and measurements.

	Medium	**Fine**	Super Fine	Exp	Extrapolated	Asymptotic range
Element size	560,802	1,059,163	2,224,923			
C_L (AoA = 0.9°)	0.3930	0.3942	0.3945	0.4548	0.3946	**1.0**
C_d (AoA = 0.9°)	0.0087	0.0084	0.0083	0.0102	0.0082	**1.0**
C_L (AoA = 9.9°)	1.4313	1.4355	1.4357	1.3328	1.4357	**1.0**
C_d (AoA = 9.9°)	0.0143	0.0139	0.0139	0.0174	0.0138	**1.0**

Table 5.6.2-9 Richardson's extrapolation analysis for the clean FFA-W3-241 airfoil

	Medium	**Fine**	Super Fine	Exp	Extrapolated	Asymptotic range
Element size	575,841	1,102,900	2,432,233			
CL (AoA = 0.9°)	0.3970	0.3996	0.3977	0.4029	-	-
Cd (AoA = 0.9°)	0.0108	0.0106	0.0105	0.0170	-	-
CL (AoA = 9.9°)	1.4725	1.4791	1.4837	1.2132	1.4946	**1.0**
Cd (AoA = 9.9°)	0.0190	0.0183	0.0178	0.0256	0.0168	**1.0**

Table 5.6.2-10 Richardson's extrapolation analysis for the FFA-W3-241 airfoil with VG

The comparison of the chordwise pressure distribution for the clean airfoil from all three meshes (Figure 4-20) shows a good agreement below 9% (AoA: 0.9°, t/c= 0.13) with the measured chordwise pressure distribution. A negligible difference between the three meshes with different density was seen for the tested two AoA = 0.9 and 9.9°. However for the airfoil configuration with VG, the results show that the CFD slightly over predicts the suction side pressure distribution by up to 14% (t/c= 0.24) at the large angle of attack of 9.9°, while the achieving negligible difference between the CFD calculated pressure distribution from all the meshes (Figure 5-101).

At a large AoA of 19.1° the CFD calculated peak suctions does not agree with the measurements (Figure 5-102), this is due to large separated flow regime found at this AoA is not calculated using the 2D steady CFD model. Up to 20% differences were seen between the CFD and the measurements at t/c = 0.15 for the clean case as well as the profiles with VG. However a reasonable agreement was seen between the CFD and the measurements for the trends in the pressure distribution and the magnitude of the change in peak suction due to the VG installation. Based on the measurements it was found that the suction pressure at 0.15% chord is reduced by 42% due to VG while the CFD predicts about 35% reduction in suction pressure at this chord location. Overall, based on this exercise it is noted that the CFD model is able to calculate the effects of vane VGs, and it is established for the assessment of VG designs within 18°.

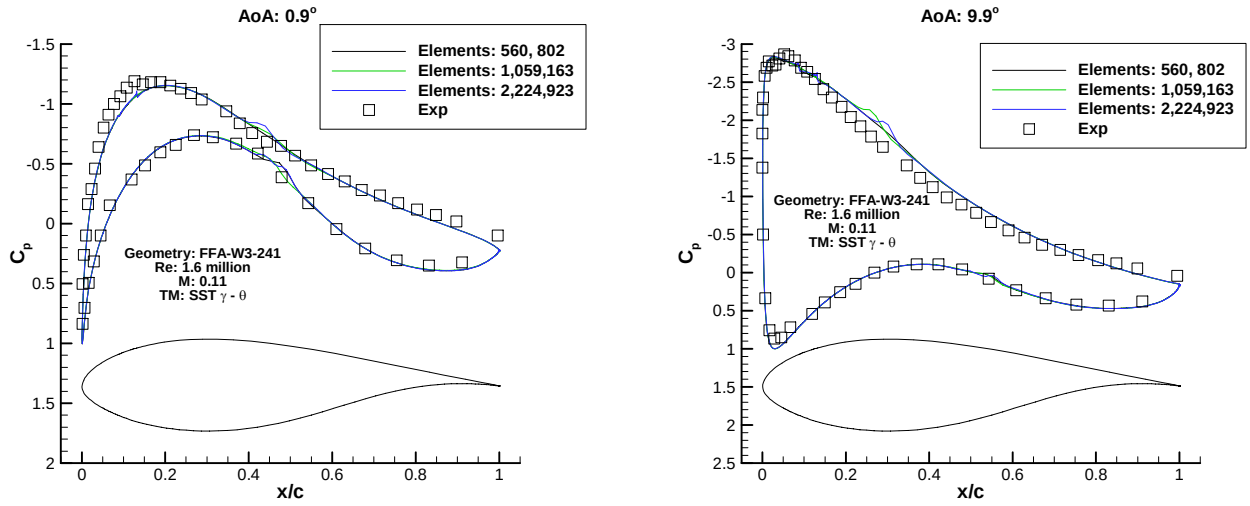

Figure 5-100 Coefficient of pressure distribution as a function of chord, Geometry: Clean FFA-W3-241 (left): α: 0.9° and (right) α: 9.9°, TM: SST γ – θ

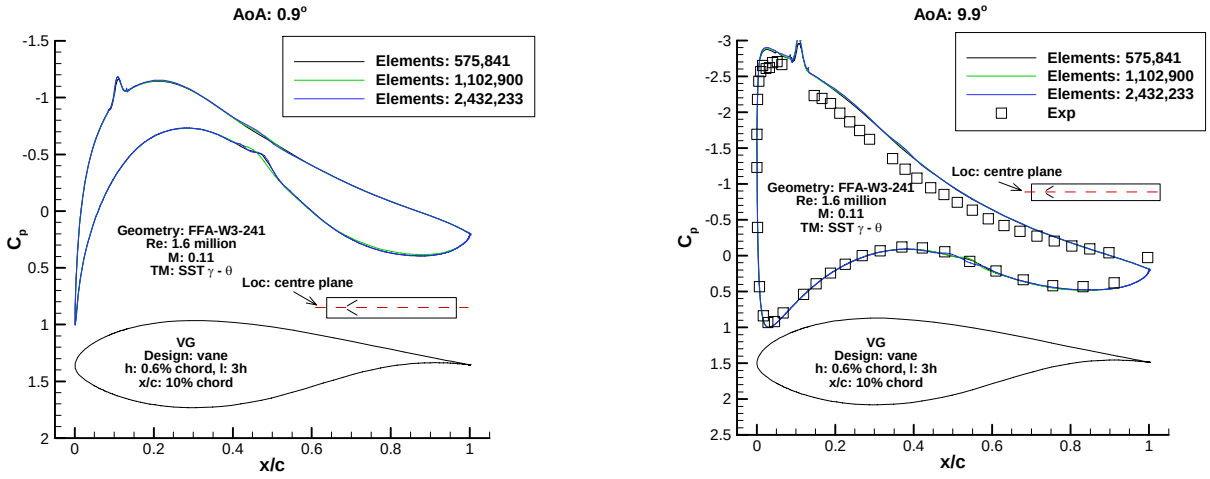

Figure 5-101 Coefficient of pressure distribution as a function of chord, Geometry: FFA-W3-241 with VGs (left): α: 0.9° and (right) α: 9.9°, TM: SST γ – θ

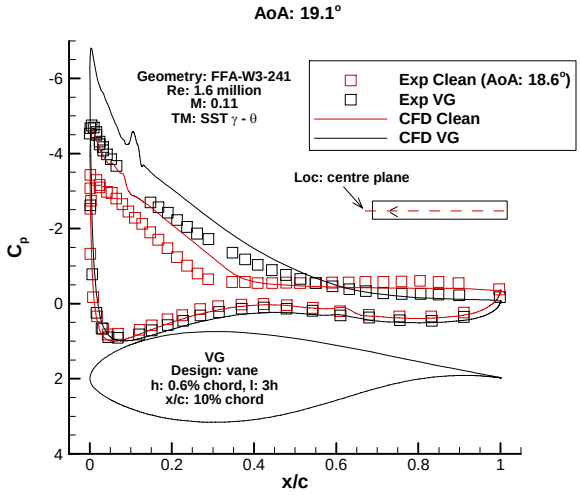

Figure 5-102 Coefficient of pressure distribution as a function of chord, Geometry: FFA-W3-241 with VGs α: 19.1°, TM: SST γ – θ

The CFD model validation study for the clean and VG installed profile was conducted using the established fine grid (1.1M elements), which provides the solution with adequate grid independence. Simulations were conducted within the angle of attack range of -2° to 25°. For the experiments the measurement were performed with natural transition on the airfoil. Consequently, for the computational studies, a fully turbulent SST and transitional SST γ – θ turbulence model was used to understand the effect of the boundary layer transition. The calculations were conducted for the Reynolds number of 1.6 million. The Riso DTU has also conducted their own 2D CFD analysis for this airfoil with and without the VG [74], and they have not modelled transition in their simulations. Their results will be compared against the results from this study (CU CFD).

The results from the validation study (Figure 5-103) suggests that for the clean airfoil, the calculated lift and drag forces for both transition modelled and fully turbulent simulation agree well with the measurements within the linear range (AoA: 0° – 10°) i.e. the flow is generally turbulent. Such that the difference in lift coefficient and drag coefficient relative to the measurement at 7° AoA for the transition modelled case was found to be -1% and -

20% respectively. The lift coefficients from the fully turbulent simulation agree well with measurements at large angle of attack above 10°, such that the CFD calculates lift coefficient within 5% of the measurement at AoA of 20°. A better agreement with the measurement is achieved with the CU CFD than the Riso CFD results, especially for the drag calculations, where the difference in drag coefficient for the fully turbulent CU CFD at 5° AoA is 0.004 while for the Riso DTU results it was 0.03. The difference in drag coefficient from the CU CFD calculation that modelled transition for the 5° AoA was found to be slightly better with 0.0024 in comparison with the measurement.

Similar agreements were seen from the results for the airfoil with the VG, which also shows that the CFD over predicts the lift increments due to the VG installation with a modest level of agreement between the drag calculation and measurements ($\Delta Cl_{AoA:\,7^o}$: 12%, $\Delta Cd_{AoA:\,7^o}$: -35% [-0.0082]). It was decided that the current established mixed element grid with 1,100,000 elements, using the SST γ – θ turbulence model, is an adequate tool to perform initial assessments of the effect of VG configurations.

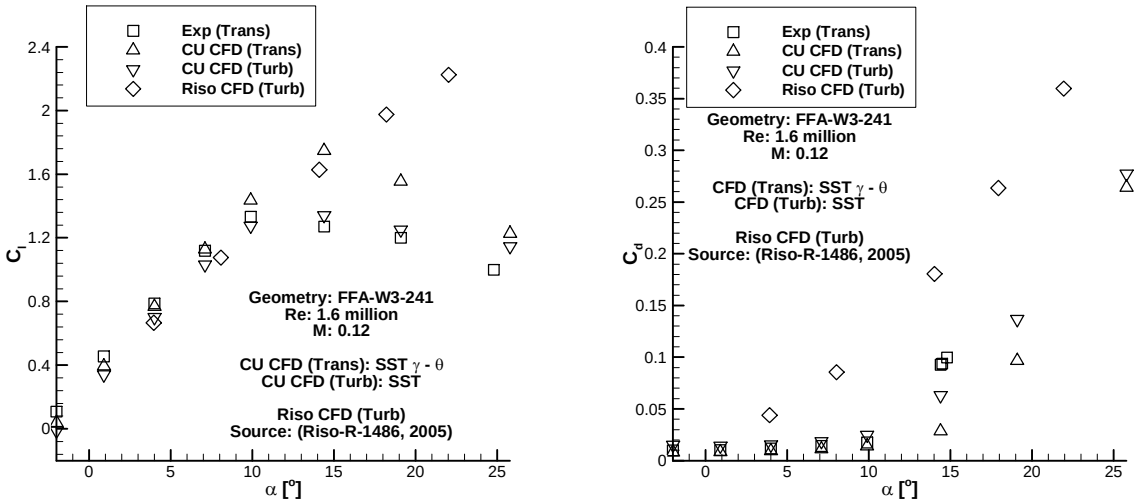

Figure 5-103 Comparison of CFD calculated lift coefficients(left) and drag coefficients(right) with measurements, Geometry: Clean FFA-W3-241, Re: 1.6 million, Riso data; [12]

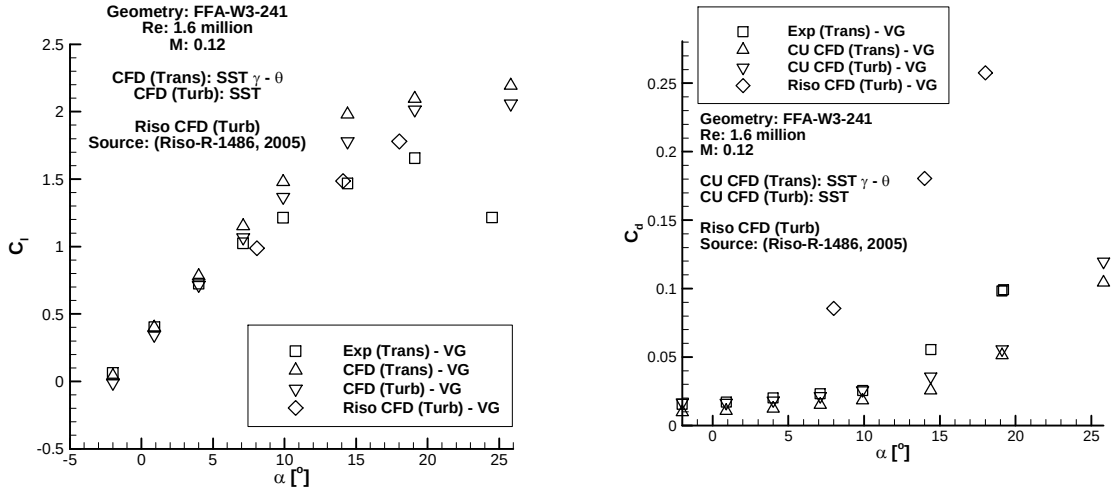

Figure 5-104 Comparison of CFD calculated lift coefficients(left) and drag coefficients(right) with measurements, Geometry: FFA-W3-241 with VG, Re: 1.6 million, Riso data; [12]

5.6.2.2 Isolated vane VG and wedge VG CFD study

The vane VGs used in wind turbine application inherently lacks the structural robustness due to their thin body. The wedge type VGs encloses a larger volume of material than the conventional vane VG, consequently increased structural resistance to bending or breaking away from the surface. An investigation was conducted to determine the best design of a VG for the root part of a wind turbine. Six configurations (Figure 5-105) were tested for their effect on the lift and drag of the FFA-W3-241 airfoil. This includes the conventional vane VG [12], forward wedge [78], half forward wedge [13], backward wedge [78], sub boundary layer vane VG and sub boundary layer forward wedge. Sub boundary layer VG is defined with its height being smaller than the local boundary layer thickness. The simulation was conducted using SST γ – θ model at the Reynolds number of 1.6milion.

The dimensions of the wedges were based on the counter rotating vane VG [12] and the spacing for the vane VGs were based on the Riso study [12]. The spacing for the wedges was chosen to be the one width (w) of the wedge based on the work by McCullough et al [13]. The height of the sub-boundary layer VG was chosen to be 0.5 of the local boundary layer thickness (δ) without the presence of the VG and the length was chosen to be ten heights. The sub boundary layer VGs has shown previously that they can be as good, or better, than conventional VGs [10], for this reason sub boundary layer VGs were included in this initial design assessment study.

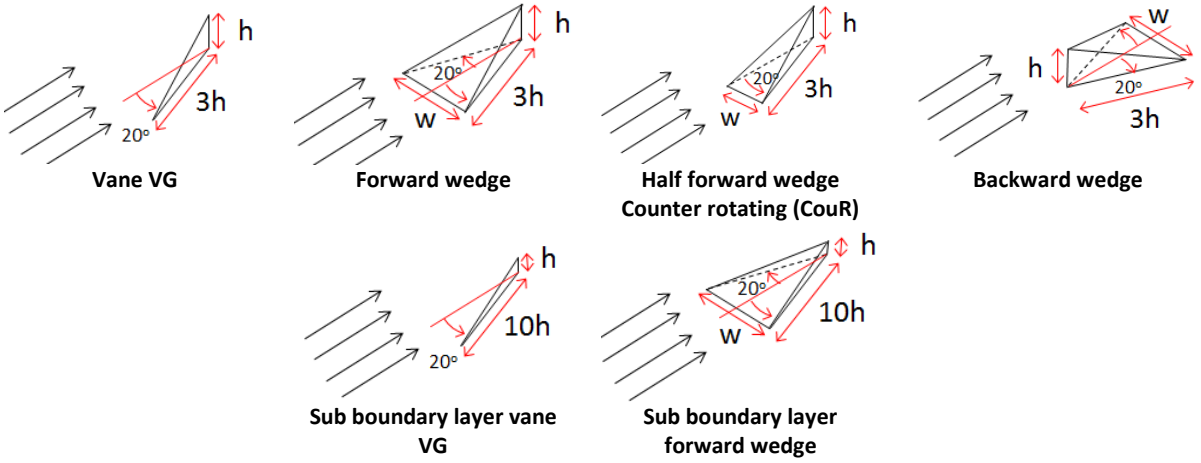

Figure 5-105 Investigated configurations of vortex generators

This CFD study was conducted to replicate the experiment performed by Riso for their vane VG study [12]. The leading edge of the VGs were placed at x/c=0.1. The simulations were conducted at 1.6 million Reynolds number. The local boundary layer parameters at x/c=0.1 were extracted from the CFD simulation of the clean FFA-W3-241 airfoil (Table 5.6.2-11). A separation bubble was calculated at this chord wise location hence the large shape factors (H), generally it is not pertinent to place the VGs at this location however aim of this CFD case study was to replicate Riso DTU work, therefore x/c=0.1 was carried forward for this investigation.

AoA [°]	Ue [m/s]	δ [mm]	δ* [mm]	θ [mm]	H
-2	45.03	0.96	0.15	0.07	2.26
0.9	51.55	1.18	0.17	0.07	2.30
4	58.33	1.19	0.19	0.08	2.38
7.1	64.83	1.28	0.22	0.09	2.50
9.9	70.22	**1.32**	0.27	0.10	2.71

Table 5.6.2-11: Local boundary layer parameters at 10% chord for the FFA-W3-241 airfoil at 1.6 million Re, TM: SST γ – θ

The sub boundary layer VGs was designed based on 50% of the local boundary layer thickness found at the 9.9° AoA (h = 0.7mm). All other VGs were designed with h of 0.6% chord based on the Riso study [12] which corresponds to h = 2.7δ or h = 3.6mm. A C-type grid topology similar to the one used for the VG validation study with a domain with an extent of 40 chords and containing about 1,100,000 elements was used to perform this investigation (section 5.6.2.1).

The results from this investigation (Figure 5-106) shows that the conventional vane VG provide the largest lift increments relative to the clean airfoil with about a ΔCl_{max} of +25% and an increase in the stall AoA by 10°. The backward facing wedge and the half counter rotating forward wedge showed the next best performances with an increment in ΔCl_{max} of 10% and 7% respectively. Both designs were able to increase the stall AoA by 5°. The sub boundary layer VGs on the other hand showed a small or negligible influence on the baseline lift. The increase in lift coefficient due to the full size VGs are mainly due to the VGs ability to reduce the chordwise extent of the flow separation, i.e. vane VGs are the most effective at reducing the flow separation (Figure 5-107).

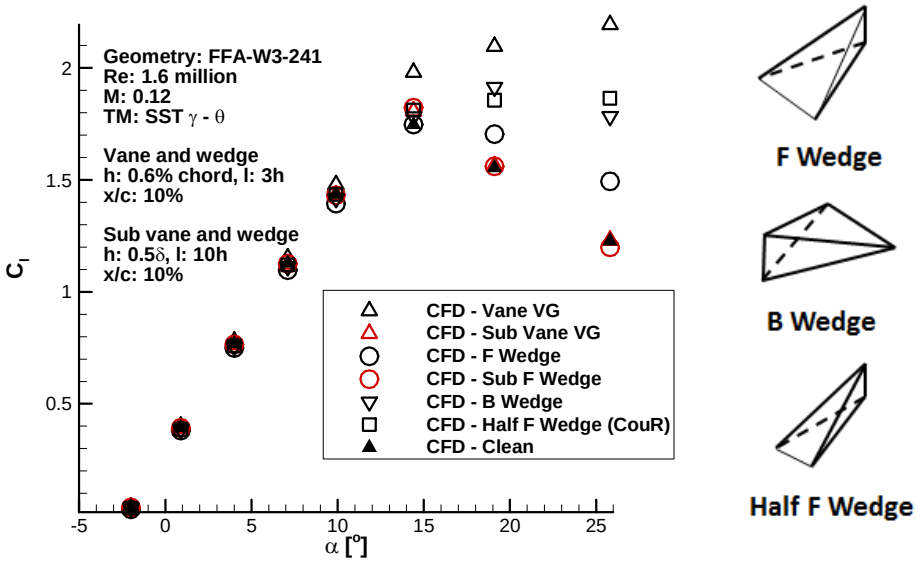

Figure 5-106 Lift polars for the tested vortex generators designs

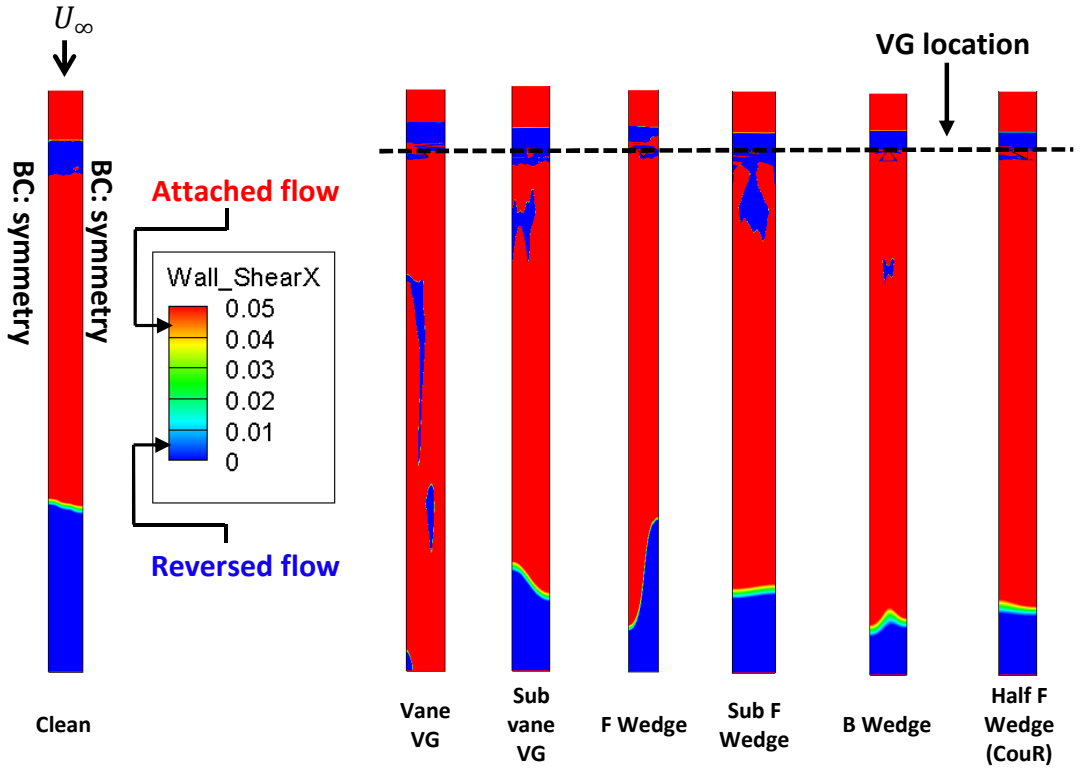

Figure 5-107 Limiting streamline patterns on the suction side wall for the different VG designs, blue indicates separated flow and red indicates attached flow, Geometry: FFA-W3-241, Re: 1.6 million, TM: SST γ – θ, AoA: 14.4°

The results for the drag calculation (Figure 5-108) showed that the airfoil with the conventional vane VGs had the lowest drag relative to the clean airfoil ($\Delta Cd_{AoA:\ 19^o}$: -47% [-0.045]), due to their effectiveness in the reduction of the chord wise extent of the flow separation. Similar to the lift results, the backward wedge ($\Delta Cd_{AoA:\ 19^o}$: -41% [-0.039]) and the counter rotating half forward wedge ($\Delta Cd_{AoA:\ 19^o}$: -34% [-0.033]) performed second best at the reduction in drag forces.

Overall it was found that all the VG designs reduces the lift to drag ratios within the pre stall AoA range of 0 – 10° (Figure 5-109). The largest reduction in lift to drag ratio of up to 36% was seen for the forward wedge design at 10° AoA. The sub boundary layers were seen to have smallest influence on the lift to drag ratio within the pre stall AoA about 0.2% at the AoA of 10°. The benefit of the VGs were mainly found at the post stall AoA, where up to 60% increase in lift to drag ratios were seen with the vane VGs at the AoA of 19°. The full scale wedge type VGs were only able to increase lift to drag ratios beyond 14° AoA. It was found that the backward wedge design was able to increase the lift to drag ratio by 20% at the 19° AoA.

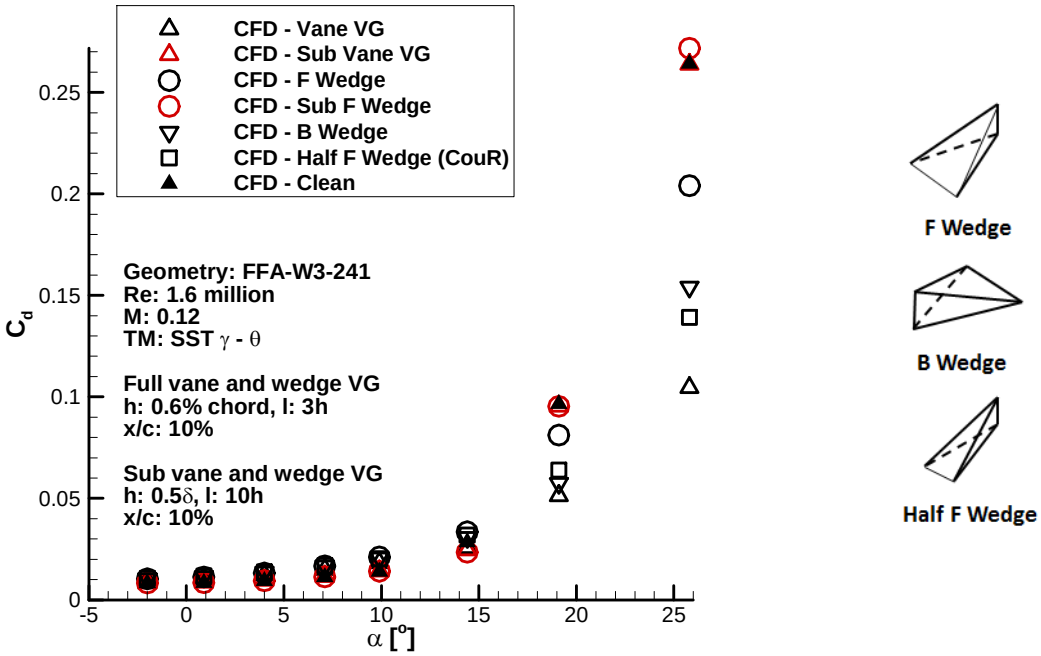

Figure 5-108 Drag polars for the tested vortex generators designs, Geometry: FFA-W3-241, Re: 1.6 million, TM: SST γ – θ

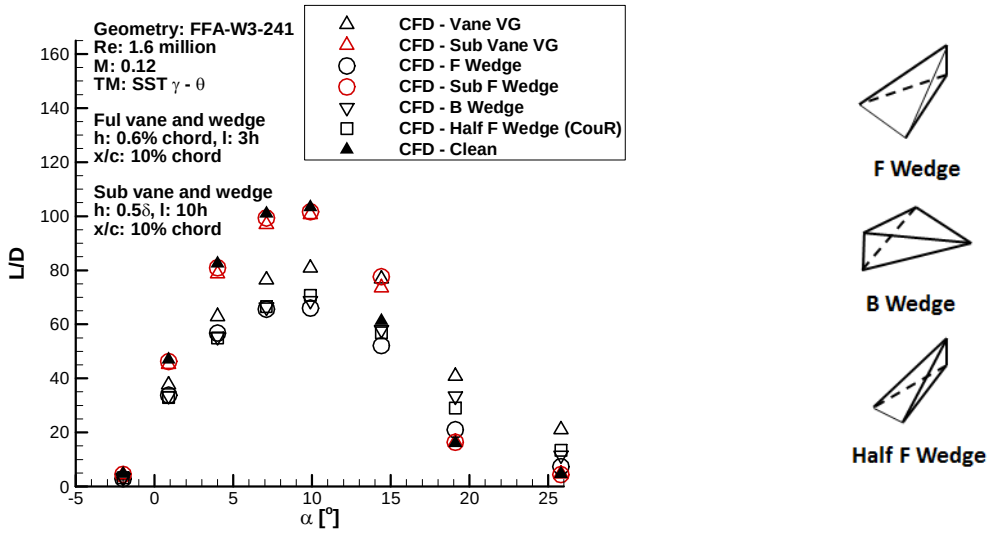

Figure 5-109 Lift to drag ratios for the tested vortex generators designs, Geometry: FFA-W3-241, Re: 1.6 million, TM: SST γ – θ

The evaluation of the vortices generated at the 9.9^{O} AoA by these different types of vortex generators has shown that the full vane VGs generates the strongest vortex in terms of non-dimensional peak circulation compared to all other tested designs (Figure 5-110). The sub boundary layer vane VG was able to generate peak circulation relative to its height closer to the full vane VGs, such that sub vane VG was able to generate a non-dimensional peak circulation about 85% of the full vane VG. However the sub boundary layer vane was only able to generate 30% of the absolute peak circulation generated by the full vane VGs. Nevertheless this has shown that the vane VGs produce similar non-dimensional circulation relative to its height. An experimental circulation distribution from a rectangular vane VG studied on a flat plat was obtained from the work by Yao et al [79]. This study was

conducted at a larger Reynolds number relative to a VG height of $8.6x10^4$ while the corresponding Reynolds number for this study is $1.02x10^4$.

Yao et al has conducted an experimental study on rectangular shaped VGs placed on a flat plate [79]. It should be noted that Yao et al's study was conducted at a larger Reynolds number relative to a VG height of $8.6x10^4$ while the corresponding Reynolds number for this study is $5.2x10^4$. Despite this difference in Reynolds number a comparison of the circulation distribution from this CFD study was made with the measurements from [79] (Figure 5-121). It is also noted that Yao et al's study was conducted with a h/δ =1, where the VGs investigated in this study is are h/δ =2.7 and the rectangular vane VGs used in [79] has a toe angle of 23^o, while the triangular vane used in this study has a toe angle of 19.5^o. And of course Yao et al's study was conducted for a flat plate while this study was performed using the airfoil FFA-W3-241. Despite these differences, a comparison was made between this experimental data with the CFD generated results. Based on this comparison it was found that the vortex generated by the full scale triangular vane VGs installed on an airfoil had about 40% more peak circulation than the rectangular vane on a flat plate. Even the sub vane VGs with the $h//\delta$ =0.5 was seen to generate higher peak circulation than the rectangular vane with $h//\delta$ =1, therefore most of the difference in circulation differences may not be due to the relative height difference and it may be due to the different geometry (rectangular) and flow conditions such as the approaching boundary layer shape factor. However the circulation decay characteristics from [79] seems to lay between the sub boundary layer and the full triangular vane. Nevertheless the comparison between Yao et al's measurements and the results from this study has shown that a reasonable CFD calculation of the vortex is simulated with the baseline CFD model.

The peak circulation decay characteristics shown that the forward and half forward wedge designs were found to generate about 80 and 85% of peak circulation generated by the vane VG, while the backward wedge generates about 40% of the peak circulation from the vane VG. The sub boundary layer forward wedge showed the lowest performance in terms of non-dimensional peak circulation, where it is only able to generate up to 15% of the non-dimensional peak circulation from the full vane VGs and about 18% of the sub boundary layer vane VG.

It was found that the forward wedge design decays its peak circulation by up to 80% within the first 33h downstream, while the backward wedge design dissipates about 50% within this distance from the wedge TE. The full vane and sub vane VGs were able to maintain up to 66 and 50% of its peak circulation within 33h downstream. Only the sub boundary layer forward wedge had the lowest peak circulation decay of about 25% within this distance downstream. In terms of peak circulation and its decay these results show that the vane VGs are able to outperform the wedge type VGs. However it is shown that wedges VGs are able to generate vortices that are comparable with the vane VGs.

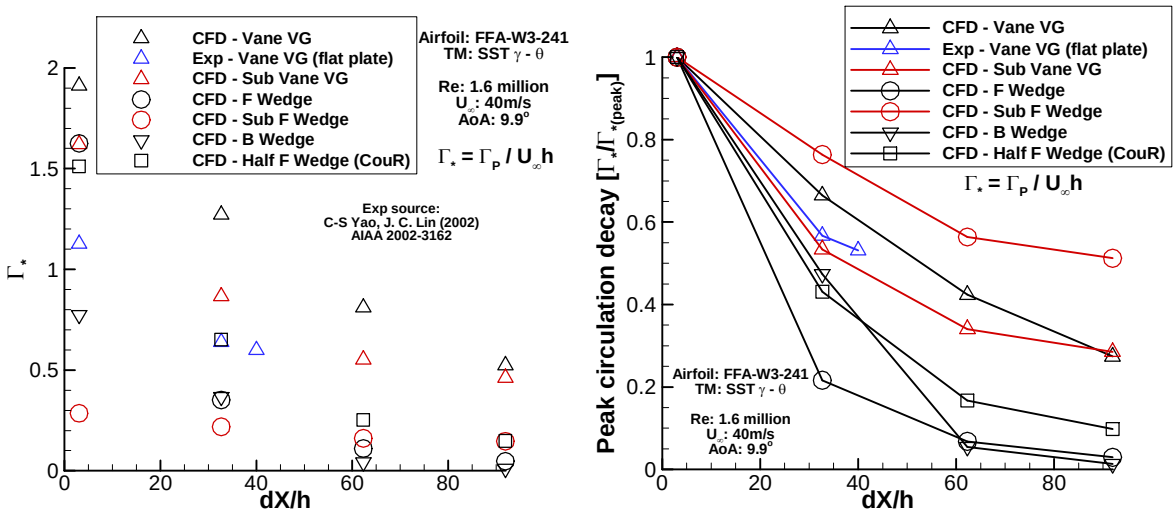

Figure 5-110 Non-dimensional stream wise circulation (left) and peak circulation decay (right) as a function of stream wise distance in terms of VG heights from the VGs TE, TM: SST γ – θ, Re: 1.6 million, Geometry= FFA-W3-241, AoA: 9.9°

The location of the peak vorticity relative to the blade surface is a measure of VGs influence on the boundary layer. The closer the vortex cores to the blade surface greater the momentum entrainment to the boundary layer. As expected the sub boundary layer VGs were found to maintain its vortex core location closest to the blade surface (Figure 5-111), however it should be noted that the absolute circulations were found to be only about 30% of the full scale VGs. The vortex generated by the full scale vane and forward wedge VGs were found to elevate the furthest distance from the blade surface about 8-9h within the first 90h downstream. The backward wedge was found to be the most effective at placing the vortex core close to surface within the full scale VG designs, where it achieves about half the elevated distance of the vane and forward wedge VG within the first 90h downstream.

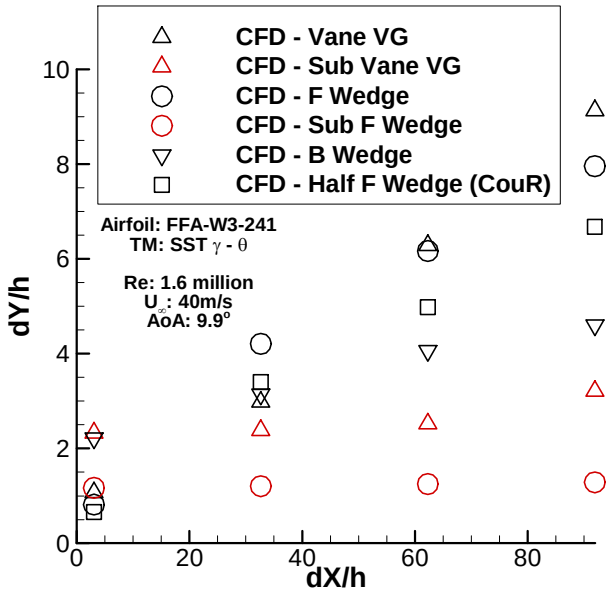

Figure 5-111 Non-dimensional location of the vortex core (peak vorticity) away from the blade surface as a function of stream wise distance from the VGs TE, TM: SST γ – θ, Re: 1.6 million, Geometry= FFA-W3-241, AoA: 9.9°, X originates from VGs TE and Y originates at blade surface

In summary, this investigation showed that a wedge type VG can be almost as effective as the vane VGs. The wedges are able to generate vortices that have similar circulation of the vane VGs and the vortices generated by the backward wedge (B wedge) seems to lie closer to the airfoil surface than vane VG (Figure 5-112). Consequently, the wedges have the potential to be more effective in controlling boundary layer separations. Based on the results it was decided that the structurally robust backward wedge was chosen for the assessment of wedge integrated NREL 5MW rotor.

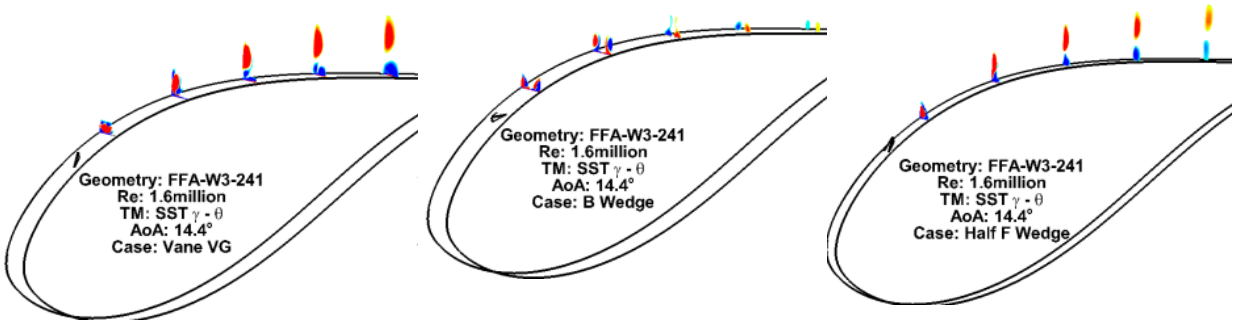

(a) (b) (C)

Figure 5-112 Vortex evolution of the different VG designs, a: vane VG, b: backward wedge, c: half forward wedge, Geometry: FFA-W3-241, Re: 1.6 million, TM: SST γ – θ

5.6.2.3 NREL 5MW rotor with VGs

Based on the CFD study of the baseline rotor (NREL 5MW), a large flow separation extending to 25% of the blade is found at the blade root (Figure 5-113). Based on the idealised rotor BEM study, it was seen that the blade root is greatly underperforming due to a lack of lift force (section 3.1.4) and the poor aerodynamics due to the hub separation adds to the lack of performance at the blade root. The rationale behind this part of the research is that the structurally robust backward wedge VGs can be used to suppress the radial flow and the flow separation found at the root.

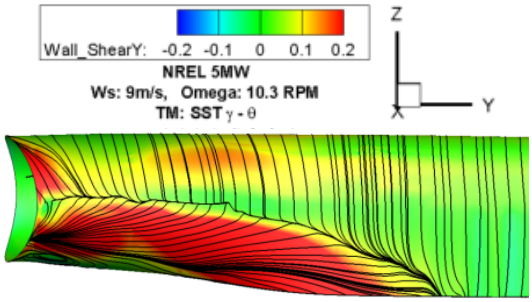

Figure 5-113 Suction side streamline pattern for NREL 5MW blade root, span: 0 – 25%, Ws: 9m/s, Omega: 10.296RPM, TM: SST γ – θ, displayed span range: r/R=0.05 – 0.30

5.6.2.3.1 CFD modelling

Based on the studies presented earlier, a CFD model using a mixed element grid was found to be adequate to predict the flow characteristic of a VG. The backward wedge (B wedge) was selected to be integrated to the baseline rotor for the performance analysis of the VG integrated rotor. Similar to the isolated VG CFD studies, a small volume enclosing the VG

was modelled using tetrahedral and prism elements, while the external volume is modelled using the established baseline rotor grid (Figure 5-114).

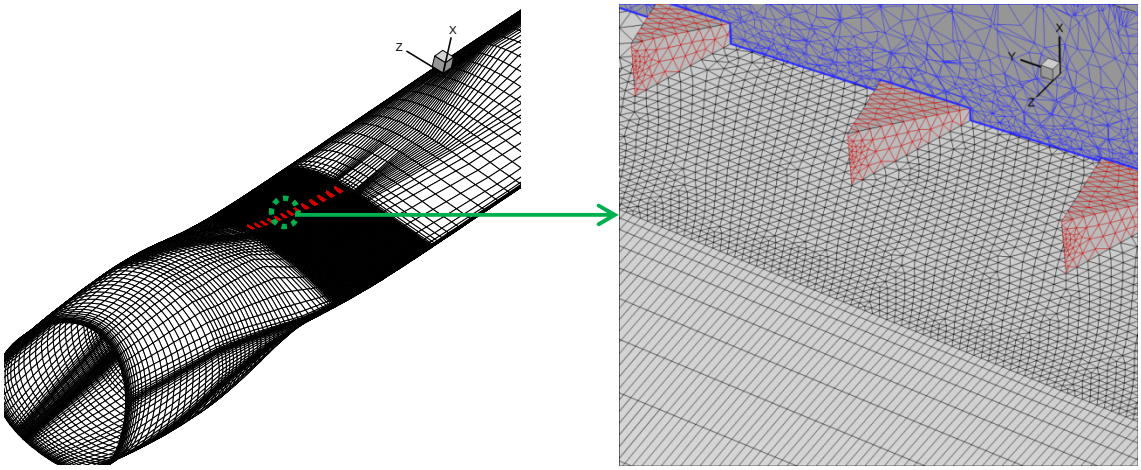

Figure 5-114 Generated mesh for the NREL 5MW rotor blade with wedges

Difficulties arise when attempting to replicate the grid resolution used for the isolated VG design study, as this will drastically increase the total number of elements used to generate the baseline rotor with the wedges, a single wedge would require an additional 1.7 million nodes. This is about a 25% increase in total nodes within the rotational domain. Therefore it was important to establish the minimum number of nodes required in the spanwise direction to resolve the vortices and in the streamwise direction to transports the vortices downstream. It is also important to calculate results that agree well with the validated grid, without the need for additional computational power.

Extensive studies were conducted to determine the minimum required nodes to predict the VG flow. Please see Appendix 8.5 for further detail on this study. Based on this investigation it was found that a single wedge requires 30 spanwise and 30 downstream nodes in the immediate vicinity of the VG to adequately resolve the VG flow characteristics without a large compromise on the differences with the validated grid. This set up achieved below 3% difference in lift and about 10% difference in drag relative to the validated VG grid. This study was vital to enable the full 3D simulation of a VG integrated wind turbine rotor with a range of wedge VGs placed on the suction side.

5.6.2.3.2 NREL 5MW rotor with VGs

A full 3D simulation was conducted for the NREL 5MW rotor with VGs integrated in the root region. The spacing of the vane VGs and the dimensions for vane and wedge VGs are based on the Riso DTU study [12]. The length of the VGs was chosen to be 3h (Figure 5-115) and the toe angle (θ) was chosen to be 20^{o}. Two different studies were conducted, one was performed for VGs with the h of 2δ placed at 10% chord and the other was performed for VGs with the h of 1.3δ placed at 30% chord relative to the leading edge of the VG. Both studies were conducted within the blade span range of 19-20%, this accommodated three pairs of counter rotating vane VGs or four backward wedges.

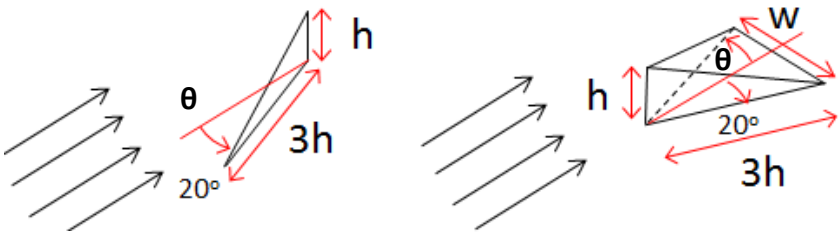

Figure 5-115 Investigated VG designs for the NREL 5MW blade, left: vane, right: backward wedge

This study was conducted with the mixed element grid that was constructed in the similar way to study the root chine integrated blade (see section 5.6.1.2.1). The iterative convergence was assumed to be achieved when the RMS residuals from the continuity and momentum equations reaches below 1e-04 and the power output from the turbine is achieved within 0.5% of the reported values. The domain size was kept constant as the established grid for the baseline rotor (Section 4.3.2).

The results showed that VGs placed at 10% chord were detrimental to the power production of the rotor (Table 5.6.2-12). A small reduction in flow separation and the radial flow was noticed due to the vane VGs, which the wedges fails to achieve (Figure 5-116). This is because the vortices generated by the vane VGs placed at this chord location are able to travel further downstream up to 63% of the chord and oppose the radial flow while the vortices generated by the corresponding wedges (Figure 5-118) travel only up to 44% of the chord. However the VGs placed at 30% chord was found to provide a small increase in power at the design point wind speed of about +0.23%. The vane and wedges placed at 30% chord was able to prevent flow separation and significantly reduce the radial flow which arises in the aft portion of the root sections due to notable separations (Figure 5-117). The vortices generated by both types of VGs placed at 30% chord were found to travel the entire chord downstream (Figure 5-119).

	Design point rotor power relative to clean blade	
Vortex generators	Chord location: 10%	Chord location: 30%
Vane	-0.35%	+0.23%
Backward wedge	-0.45%	+0.20%

Table 5.6.2-12 Performance of NREL 5MW blade with VGs, Ws: 9m/s, omega: 10.3rpm, TM: SST γ – θ, vane-[h/δ: 2, l: 3 h, θ: 20°, span loc: 19-20%, interval spacing based on [12]**], backward wedge - [h/δ: 2, l: 3 h, θ: 20°, span loc: 19-20%, interval spacing: w]**

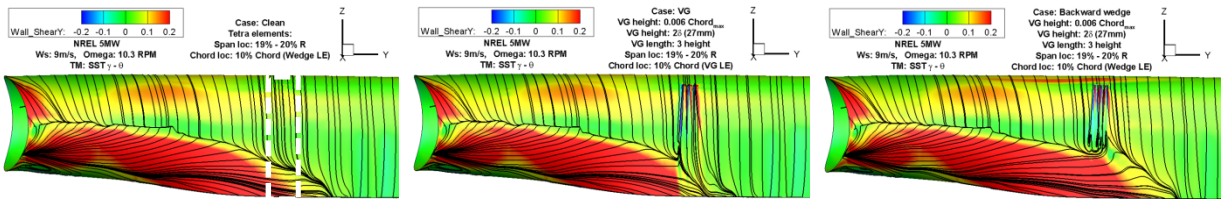

(a) **(b)** **(c)**

Figure 5-116 Vortex generator effectiveness on hub separation, Ws: 9m/s, omega: 10.3rpm, TM: SST γ – θ, (a) clean blade, (b) blade with vanes -[h/δ=2, l=3h, θ= 20°, span loc= 19-20%, chord loc x/c=0.10, spacing based on [12]**], (c) blade with backward wedges - [h/δ: 2, l: 3h, θ: 20°, span loc: 19-20%, chord loc: 10%, spacing: w], displayed span range: r/R=0.05 – 0.30**

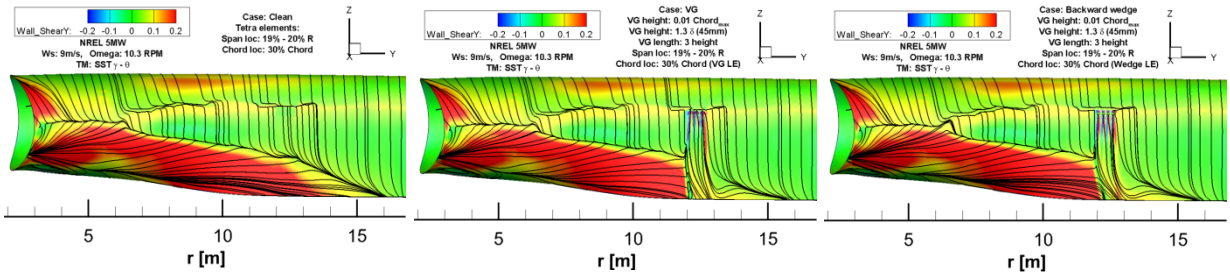

(a) (b) (c)

Figure 5-117 Vortex generator effectiveness on hub separation, wind speed: 9m/s, omega: 10.3rpm, turbulence model: SST γ – θ, (a) clean blade, (b) blade with vanes -[h/δ: 1.3, l: 3h, θ: 20°, span loc: 19-20%, chord loc: 30%, spacing based on [12]], (c) blade with backward wedges - [h/δ: 1.3, l: 3 h, θ: 20°, span loc: 19-20%, chord loc: 30%, spacing: w],

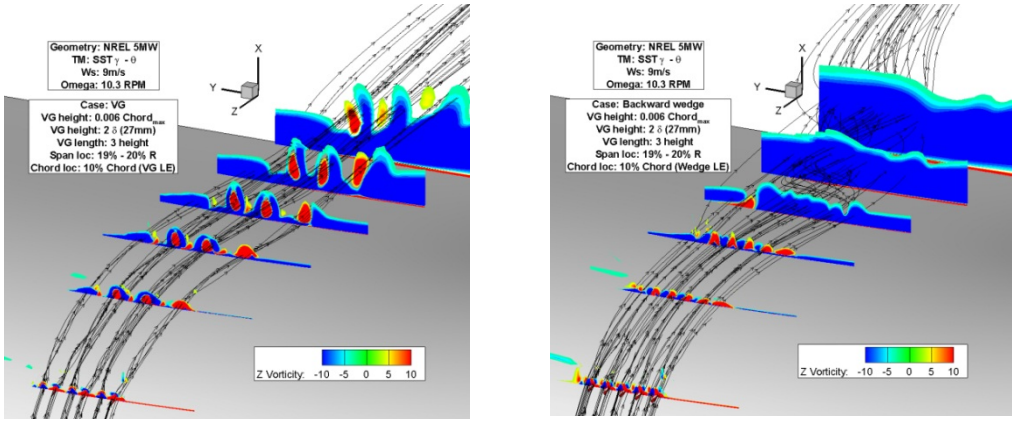

(a) (b)

Figure 5-118 Vorticity distribution along the blade chord at the location of the span location 19-20%, covering the area shown with the white dotted line on Figure 5-116, Ws: 9m/s, omega: 10.3rpm, TM: SST γ – θ, (a) blade with vanes-[h/δ: 2, l: 3h, θ: 20°, r/R: 0.19-0.20, x/c: 0.1, spacing based on [12]], (b) blade with backward wedges - [h/δ: 2, l: 3h, θ: 20°, r/R: 0.19-0.20, x/c: 0.1, w/w_1: 1]

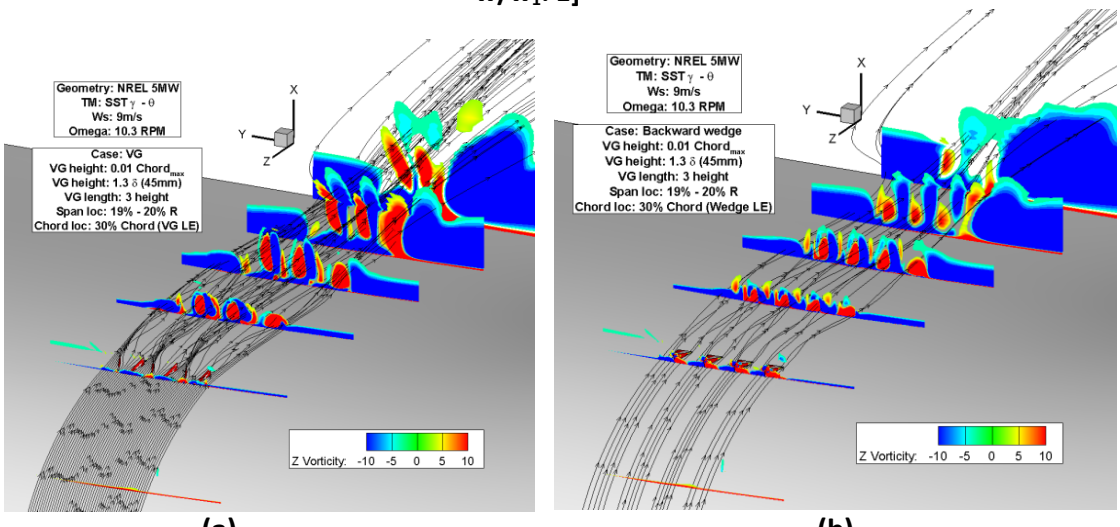

(a) (b)

Figure 5-119 Vorticity distribution along the blade chord at the location of r/R: 0.19-0.20, covering the area shown with the white dotted line on Figure 5-116, wind speed: 9m/s, omega: 10.3rpm, turbulence model: SST γ – θ, (a) blade with vanes-[h/δ: 1.3, l: 3h, θ: 20°, r/R: 0.19-0.20, x/c: 0.3, spacing based on [12]], (b) blade with backward wedges - [h/δ: 1.3, l: 3h, θ: 20°, r/R: 0.19-0.20, x/c: 0.3, w/w_1: 1]

The evaluation of the vortex was conducted using the positive circulation generated by one of the VGs. Based on the results from this exercise (Figure 5-120) it was found that VGs placed at x/c=0.1 generate a higher peak circulation than the VGs placed at x/c=0.3. The largest peak circulation was found for the vortex generated by the vane VG placed at 10% chord, which is reduced by 30% when the vane VG is placed at 30% chord. It was also found that vane VGs generate about 30% more peak circulation than the wedge type VGs, whether it is placed at 10 or 30% chord.

Wedges were also found to decay its peak circulation faster than the vane VGs, where it dissipates up to 90% of its peak circulation within 56h downstream, regardless of its chord wise location. The vane VGs on the other hand only dissipates about 60% of its peak circulation within the first 56h downstream when it is placed at 10% chord. The vane VGs reduces this efficiency to maintain its peak circulation when it is placed at 30% chord, where 75% of its peak circulation is dissipated within 56h downstream.

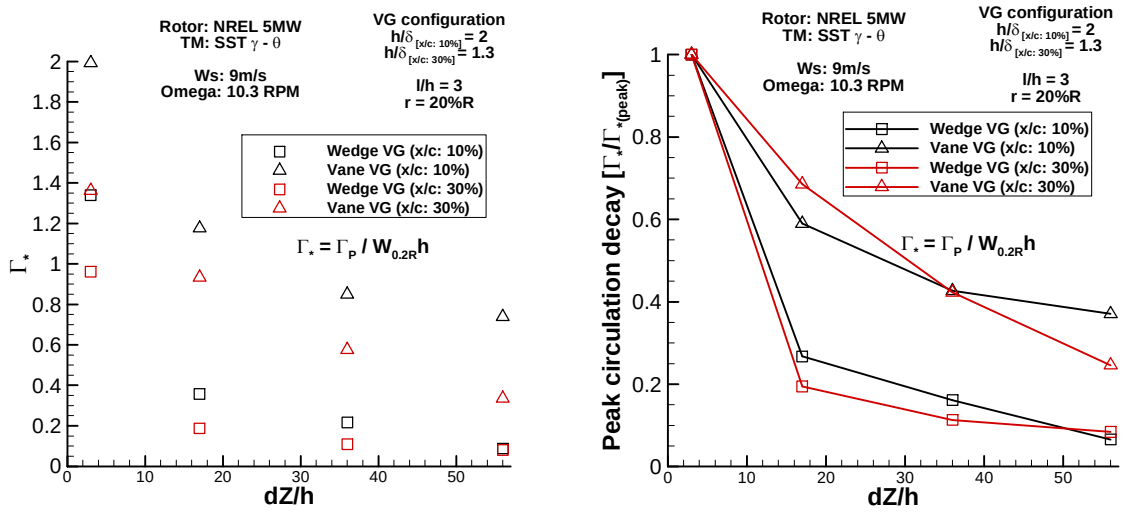

Figure 5-120 Non-dimensional stream wise circulation (left), peak circulation decay (right) per VG as a function of stream wise distance in terms of VG heights from the VGs TE, TM: SST γ – θ, Re: 1.6 million, Geometry= NREL 5MW blade, r = 20% R, Ws: 9m/s, Omega: 10.3RPM

Yao et al [79] has conducted an experimental study on rectangular shaped VGs placed on a flat plate. It should be noted that Yao et al's study was conducted at a larger Reynolds number relative to a VG height of $8.6x10^4$ while the corresponding Reynolds number for this study is $5.2x10^4$. Despite this difference in Reynolds number a comparison of the circulation distribution from this CFD study was made with the measurements from [79] (Figure 5-121). Only the data from the VGs placed at 30% chord was used in this comparison as the h/δ from the Yao et al's study (h/δ =1) are close to the h/δ of the VGs placed at this chord location (h/δ =1.3). It is also noted that the rectangular vane VGs used in [79] has a toe angle of 23^o, while the triangular vane used in this study has a toe angle of 19.5^o.

Based on this comparison it was found that the vane VGs studied in this research are in general agreements with the measurements from Yao et al [79]. It was found that the triangular vane VGs generate about 20% larger peak circulation than the rectangular VGs and the wedges were able to generate up to 85% of the peak circulation from a rectangular

VG, however as seen before the circulation decay for the wedges are found to be poor in comparison with triangular vane or rectangular VGs.

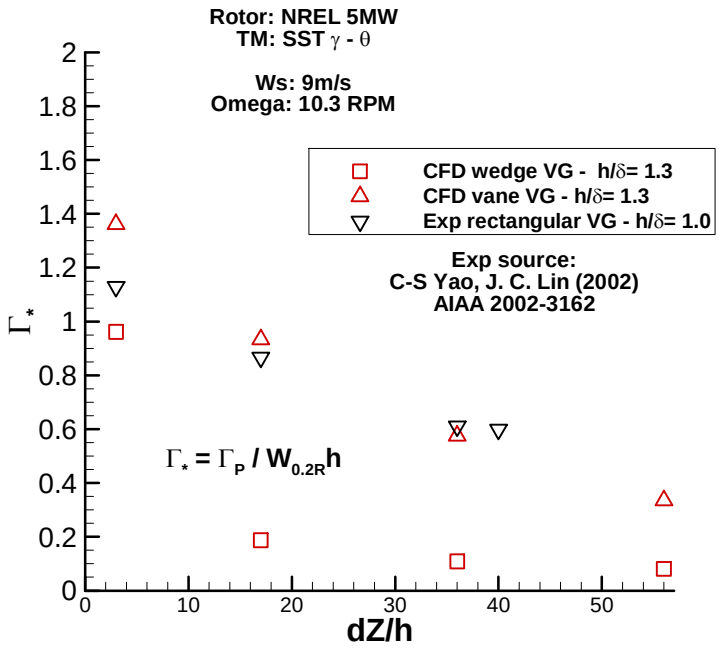

Figure 5-121 Non-dimensional stream wise circulation per VG as a function of stream wise distance in terms of VG heights from the VGs TE, TM: SST γ – θ, Re: 1.6 million, Geometry= NREL 5MW blade, r = 20% R, Ws: 9m/s, Omega: 10.3RPM, Exp source [79]

Is it expected that the effectiveness of the VGs is influenced by the position in the boundary layer at which the vortices are generated and convected. For these cases, the location of the vortex core (peak vorticity) was found to be further way from the blade when the VGs are placed at x/c=0.3 than at x/c=0.1 (Figure 5-122). At 17h downstream, the vortex generated by the vane VG placed at x/c=0.3 was found to be about 2h away from the surface while it was found to be about 0.7h away from the blade when it is placed at x/c=0.1. This places the vortex core closer to the local boundary layer at about 1.4δ away from the blade surface and the vortex core is placed about 2.6δ when the VGs placed at 30% chord, i.e. x/c=0.1 location generates a vortex that induces an efficient momentum transfer to the boundary layer. The beneficial effects of the wedges were seen for the relative location of its vortex core. It was seen that the vane VGs generally places the vortex core further away from the surface than the wedges, therefore the beneficial effect of higher circulation from the vanes are not fully utilised. Based on the results it was found that for the wedges placed at x/c=0.3 places its vortex core within 3h away from the blade surface within 56h downstream, while the vane VG placed at x/c=0.1 was found to be about 7h away from the surface at 56h downstream, i.e. VGs placed at x/c=0.3 has a prolonged influence on the downstream boundary layer.

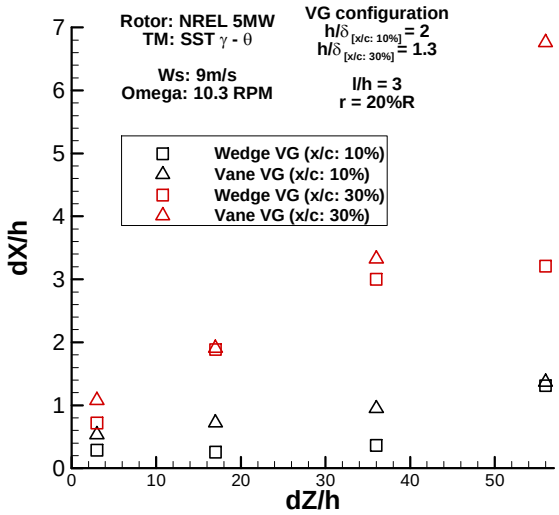

Figure 5-122 Non-dimensional location of the vortex core (peak vorticity) away from the blade surface as a function of stream wise distance from the VGs TE, TM: SST γ – θ, Re: 1.6 million, Geometry= NREL 5MW blade, r = 20% R, Ws: 9m/s, Omega: 10.3RPM

The local chordwise pressure distribution showed that the presence of the vane VG in the peak suction region increases the pressure downstream (Figure 5-123), this is may be due to deficit in the flow velocity caused by the VGs presence is not fully recovered by the vortex inefficient momentum transfer to the downstream boundary layer. Therefore an optimum location is x/c is required to utilise the benefits of VGs, and it is noted that an inappropriate placement of the VGs can be detrimental for the pressure distribution downstream. Only small differences were seen between from the pressure distribution across the vane VG, suggesting a small influences due to the 3D flow (Figure 5-124)

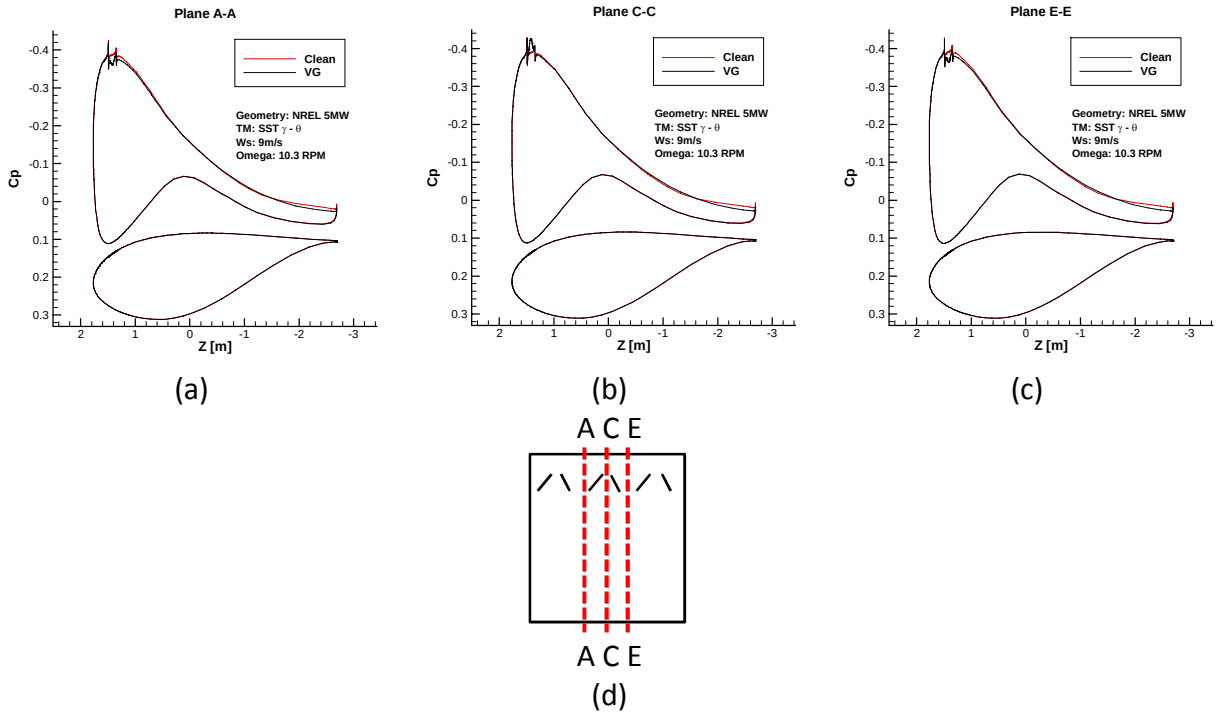

Figure 5-123 Local pressure distribution at various span location around the centre vane VG pair, (a): pressure distribution along plane A-A, (b): pressure distribution along plane C-C, (c): pressure distribution along plane E-E, d: location of the planes

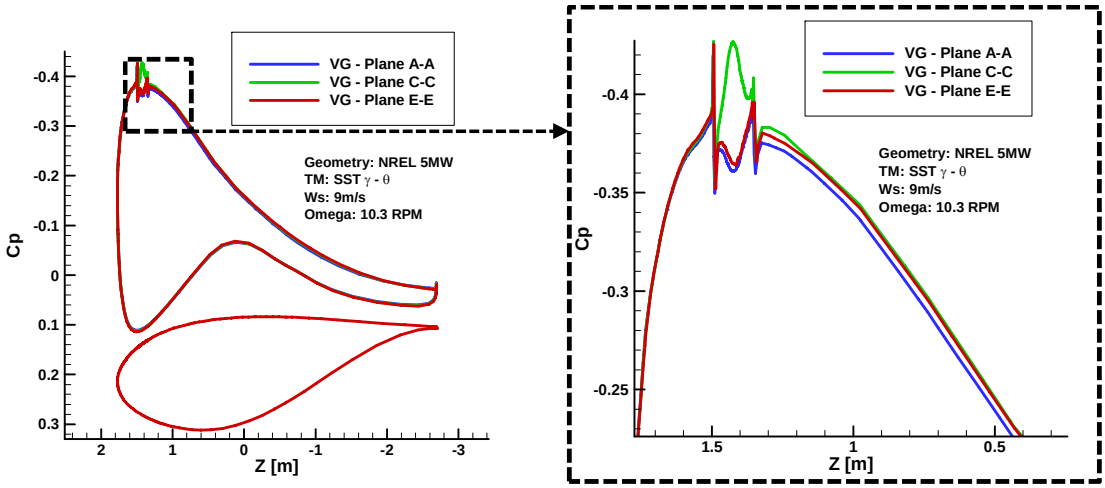

Figure 5-124 Comparison of the local pressure distribution across the vane VG pair, TM: SST γ – θ, Re: 1.6 million, Geometry= NREL 5MW blade, r = 20% R, Ws: 9m/s, Omega: 10.3RPM

This investigation has shown that backward wedges can be almost as effective as vane vortex generators. It was also noticed that the vortices formed from the wedges were of a similar strength but had the added advantage of lying closer to the blade surface than the vane VGs (Figure 5-119), which was also seen in the previous isolated VG design study (section 5.6.2.2). Consequently, wedges have the potential to be more effective in controlling boundary layer separations.

The blade local aerodynamics (Figure 5-125) suggests that both types of VGs have negligible influence (<1%) on the blade's lift production, when the VGs are placed to cover 19-20% span. However it was clear that VGs have an effect on the drag production of the blade. Changes in local blade drag forces within 10% were seen up to 80% of the blade due to the VGs placed over a 1% span at 19-20% of the blade. Based on these results it can be noted that up to 10% reduction in drag within the spanwise region 35-60% R is possible with VG installation at 19-20% span. The wedge VGs were found to have negligible drag penalty at its span location while the vane VG were found to increase local drag forces by 2%, however the vane VGs are more effective at reducing drag up to 10% at the 35-60% span than the wedge type VGs, which was able to achieve drag reductions within 8%.

Based on these results, it was decided to conduct a design study of the wedges installed on the NREL 5MW rotor. This study will involve the assessments of wedge height, placement relative to the clean blade separation line at different span locations.

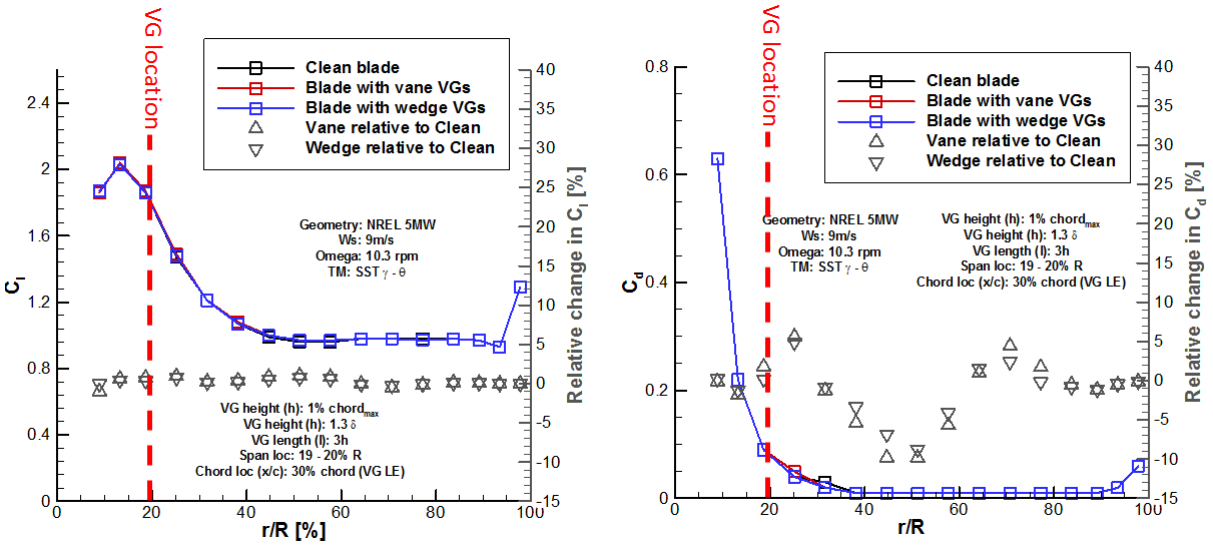

Figure 5-125 blade local force distribution, Ws: 9m/s, omega: 10.3rpm, turbulence model: SST γ – θ, VG location: 19-20%, height: 1.3δ

5.7 Design study of the NREL 5MW blade with wedges

Based on the work presented in the previous sections, it was seen that backward wedges can help to reduce the hub separation found on the baseline rotor and they are evident to suggest that wedges can be as efficient as or better than the vane VGs generally used in the wind turbine industry. They have the added benefit of higher structural integrity which the vane VGs lack therefore it was decided that a parametric design study of the NREL 5MW rotor blade with wedges will be conducted to assess the initial design space for this device. This study involved the assessments of wedge height, length, placement relative to the clean blade separation line at different span locations.

5.7.1 Geometry of the backward wedge

Initial design of the wedges was identified from the work by Rae [78], and the dimension were based on the counter rotating vane VGs from Riso DTUs work on vane VGs for wind turbines. The backward wedge is defined using its height (h), length (l) and the toe angle (θ) (Figure 5-126). The location in the spanwise direction along with the chord wise position will affect the performance of the wedge (Figure 5-127). Conventionally a VGs height is defined based on the local boundary layer height h=f(δ), and it is reasonable to assess the wedge type VGs in the similar manner. The length 'l' of the wedge is defined to be 3h for all the wedges assessed on this investigation. This is based on the Riso DTU work [12]. A constant toe angle of 20^{o} was used for all the cases investigated in this study. The wedges placement in the chordwise position (ΔZ_{VG}) is chosen relative to the baseline separation line in local boundary layer heights (Figure 5-127). The interval spacing (w) is defined by the distance between each wedge in the spanwise direction. The interval or lateral spacing of w/w_1=1, 3 and 5 interval spacing were investigated. Three different span ranges were chosen to be investigated, which are r/R=0.05-0.10, 0.10-0.15 and 0.15-0.20.

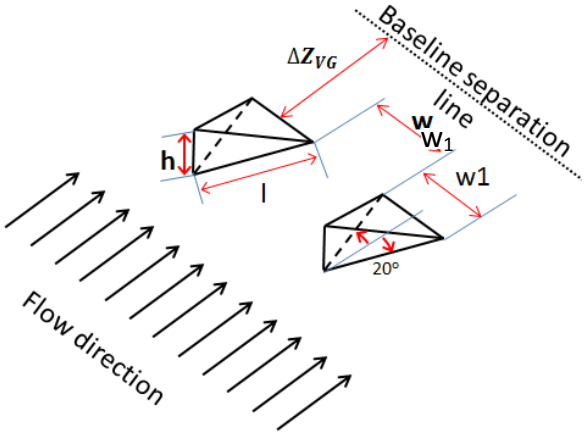

Figure 5-126 Geometric definition of the backward wedge

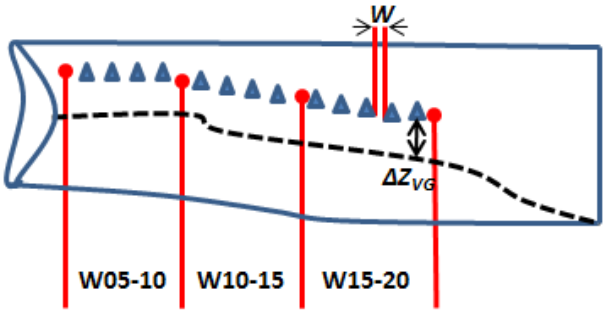

Figure 5-127 Investigated spanwise locations

Various chordwise placement of the vane VGs were identified from the previous literature. Godard et al from his flow over a bump study [8] has shown that an optimum for a counter rotating vane is about 20δ upstream of the baseline separation line. While Lin from a similar study conducted on a bump [10] has recommended that for a conventional vane VG a ΔZ_{VG} of 5δ and for a sub boundary layer VGs a ΔZ_{VG} of 2δ to be used, however this study was conducted at the Reynolds number of 0.6 million. From the earlier study presented here (section 5.6.2.3.2) it was identified that the wedges are beneficial when placed at 30% chord at 20% span, which corresponds to a ΔZ_{VG} of 45δ. Therefore for this parametric study, it was decided that a ΔZ_{VG} of 20δ and 45δ will be used to investigate the effectiveness of the wedges at different chordwise location.

5.7.2 Design matrix

A design matrix containing 15 wedge configurations (Table 5.7.2-13) with their corresponding clean case were tested for each configuration, therefore the relative changes in performance purely due to the wedges are evaluated i.e. any numerical differences due to the introduction of the tetrahedral elements are not reflected in the relative change in performances.

Name	Span location	ΔZ_{VG} (δ)	h (δ)	w/w$_1$	No of VG	Assessment of:
W19-20C45S1.3	19 - 20%	45	1.3	1	4	ΔZ_{VG}
W19-20C20S1.3	19 - 20%	20	1.3	1	4	
W19-20C20S0.6	19 - 20%	20	0.6	1	4	h and span location
W16-20C20S0.8	16 – 20%	20	0.8	1	16	
W15-20C20S1.3	15 -20%	20	1.3	1	13	VG interval w *f(w1)*
TW15-20C20S1.3	15 -20%	20	1.3	3	7	
T2W15-20C20S1.3	15 -20%	20	1.3	5	5	
W15-20C45S1.3	15 -20%	45	1.3	1	18	ΔZ_{VG}
TW15-20C45S1.3	15 -20%	45	1.3	3	9	ΔZ_{VG} and w
TW15-25C20S1.3	15 -25%	20	1.3	3	12	span location
W15-25C2045S1.3	15 -25%	20 and 45	1.3	1	28	mixed ΔZ_{VG}
TW15-25C2045S1.3	15 -25%	20 and 45	1.3	3	20	mixed ΔZ_{VG}
W10-15C20S1.3	*10 -15%*	*20*	*1.3*	*1*	*19*	*span location*
W10-15C20S2.0	*10 -15%*	*20*	*2.0*	*1*	*13*	*h at 10-15%R*
W05-10C20S1.3	*5 -10%*	*20*	*1.3*	*1*	*18*	*span location*

Table 5.7.2-13 Design matrix of the parametric design study of the backward wedge

5.7.3 Results for the wedge parametric design study

In this section of the thesis, the results from investigating the effect of dimensions and its locations of the wedges will be presented. The results from this parametric study suggest that for the clean blade, if the tetrahedrall elements are placed below the 15% of the blade span, it calculates a different flow topology from the results obtained from the baseline grid (Figure 5-128). There are small changes in flow topology between the baseline grid and the grid with tetra elements placed above the 15% span, but broadly a similar streamline patterns are calculated between the baseline grid and the grid with tetra elements placed above the 15% span.

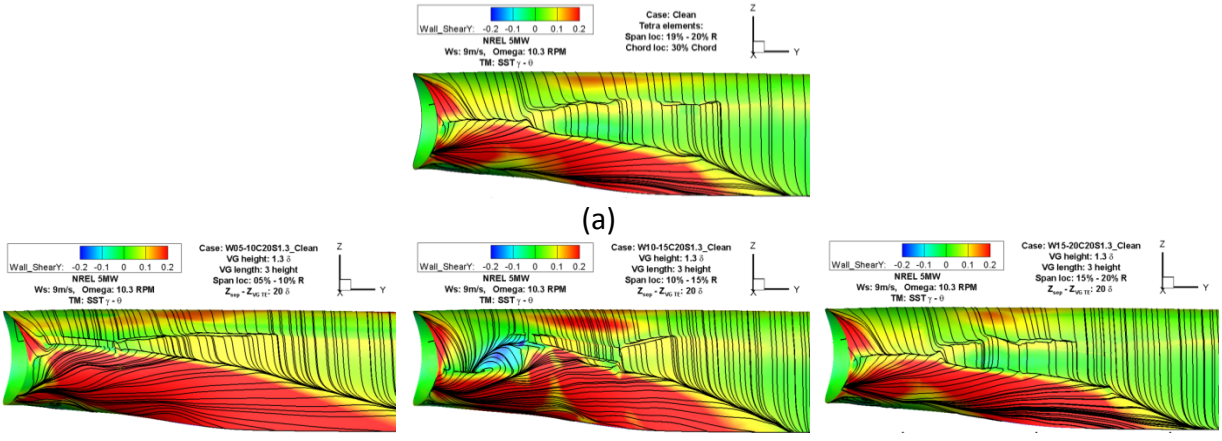

Figure 5-128 Streamline pattern of the clean blade at the hub, wind speed: 9m/s, omega: 10.3rpm, TM: SST γ – θ, (a) baseline grid, (b) Tetra location: 05-10% , case: *W05-10C20S1.3_Clean,* (c) Tetra location: 10-15% , case: *W10-15C20S1.3_Clean,* (d) Tetra location: 15-20% , case: *W15-20C20S1.3_Clean,* displayed span range: r/R=0.05 – 0.30

5.7.3.1 Effect of wedge VG spanwise location

Although there are some reservations about the accuracy of the CFD results, the broad indications from the streamline patterns suggest that the wedges only perform effectively when placed above the 15% span (r/R) of the blade (Figure 5-129). It is suspected that the wedge VGs are unable to perform effectively at the large adverse pressure gradient present at the span location below 15% blade radius.

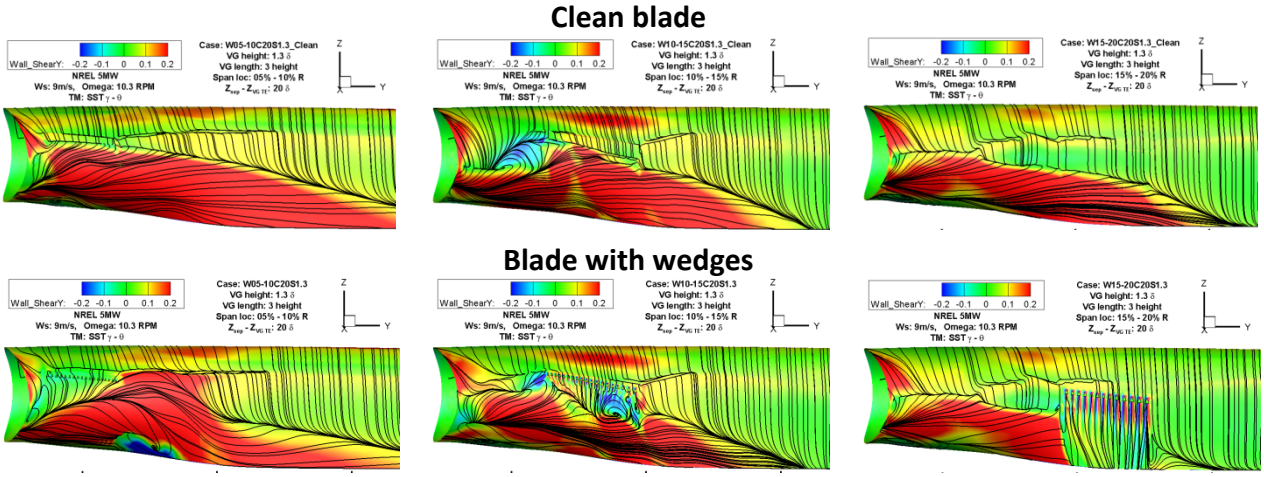

Figure 5-129 Streamline pattern at the blade hub, wind speed: 9m/s, omega: 10.3rpm, TM: SST γ – θ, (a) wedge location: 05-10% , case: *W05-10C20S1.3,* (b) wedge location: 10-15% , case: *W10-15C20S1.3,* (c) wedge location: 15-20% , case: *W15-20C20S1.3,* displayed span range: r/R=0.05 – 0.30

Based on the study conducted by Lin et al [10] for vane VGs, it was found that vane VGs are effective at the diffusion ratio $dC_P/d(x/c)$ of about 1.8 (Figure 5-130). For the NREL 5MW blade operating at its design point, the streamwise pressure gradient (dCp/d(x/c)) at r/R=0.05 was determine to be 6.5. Although Lin has not defined the largest diffusion ratios where a vane VG fails to perform effectively, based on Lin's study only 20% blade span and above of the NREL 5MW blade can be applicable for vane VGs. The CFD study of the wedge installed FFA-W3-241 airfoil (section 5.6.2.2), has shown that the wedges can perform effectively in an axial flow up to large AoA of 26^o, where a severe diffusion ratio is present (dCp/d(x/c) =15). In contrast, this CFD investigation assessing the spanwise location of the wedges on the NREL 5MW blade has shown that wedges can only perform effectively up to a diffusion ratio of 4.4 and below, which corresponds to the >15% blade span of the NREL 5MW blade (Figure 5-131). The effect of wedges in terms of increase in axial extent of the separation point is shown in Figure 5-132. This may be due to the strong cross flow (radial pressure gradient) present on the rotating NREL 5MW blade, which will be discussed later in this section.

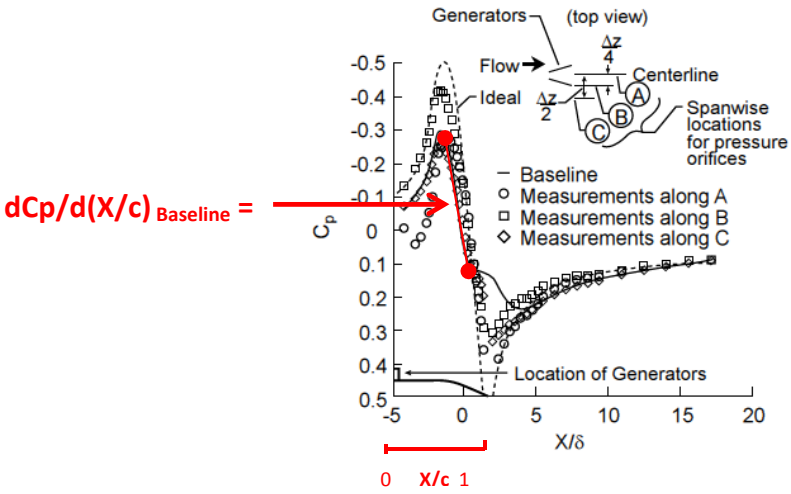

Figure 5-130 Effect of VG on streamwise pressure distribution for vane VG with h/δ= 0.8 installed on a backward facing ramp [10]

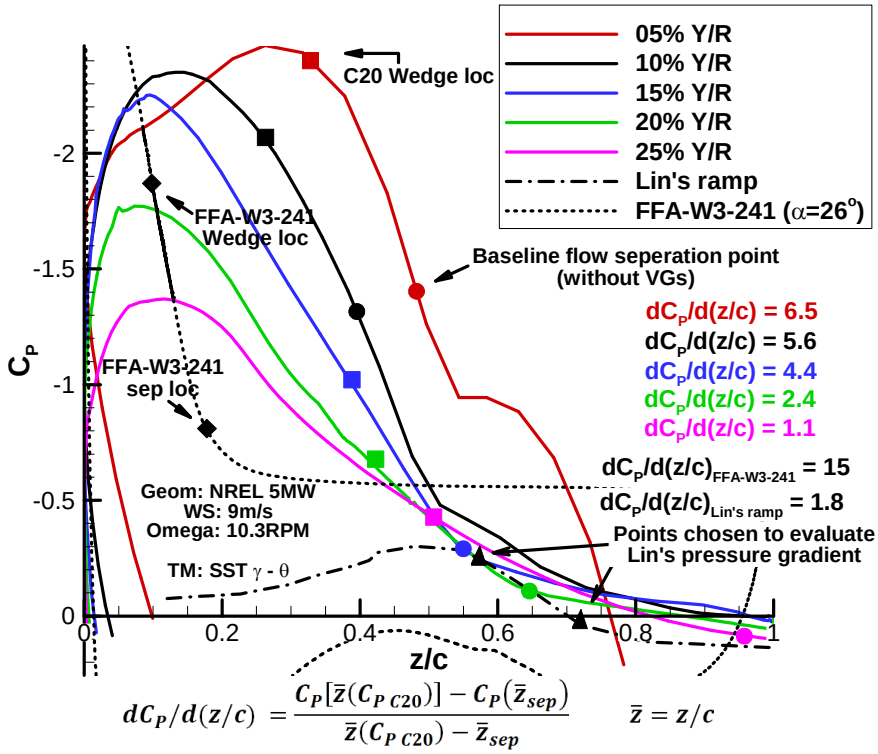

Figure 5-131 local suction side pressure coefficient as a function of chord at different span location for the clean blade, rotor: NREL 5MW, Ws: 9m/s, Omega: 10.3PRM, TM: SST γ – θ

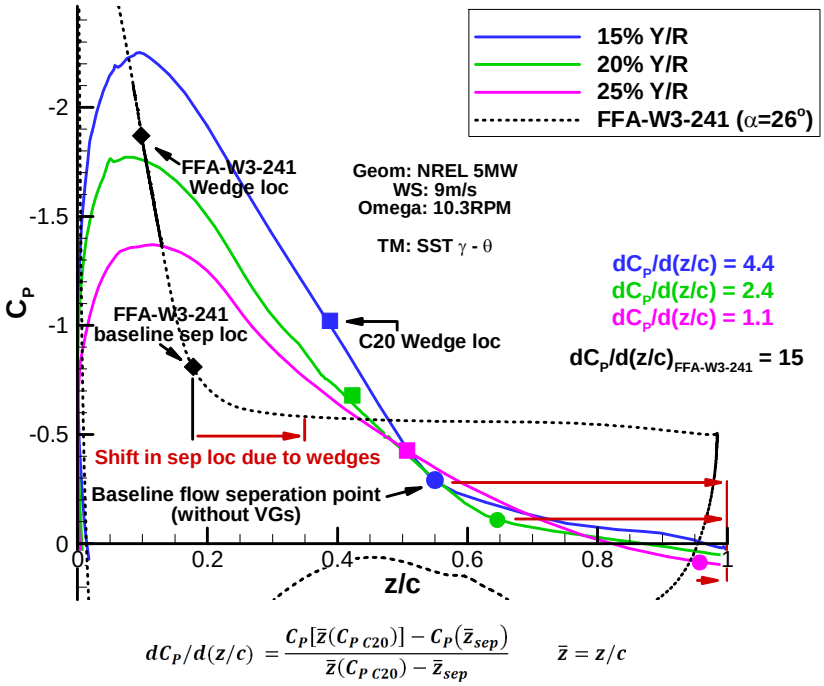

$$dC_P/d(z/c) = \frac{C_P[\bar{z}(C_{P\,C20})] - C_P(\bar{z}_{sep})}{\bar{z}(C_{P\,C20}) - \bar{z}_{sep}} \qquad \bar{z} = z/c$$

Figure 5-132 Displacement of chordwise separation location due to the backward wedge, rotor: NREL 5MW, Ws: 9m/s, Omega: 10.3PRM, TM: SST γ – θ

At the lower wind speeds the wedges are presented with a moderate diffusion ratio up to 1.4 at 5m/s, where the wedges are expected to perform effectively (Figure 5-133). However at the large wind speed of 11 m/s the adverse pressure gradient reaches up to about 5.9 at 15% blade span. This is similar to the adverse pressure gradient present at 10% span for the wind speed of 9m/s where this analysis has shown that the wedges fail to operate. Therefore it is expected that wedges placed at 15% span are not expected to perform effectively at higher wind speeds of 11m/s.

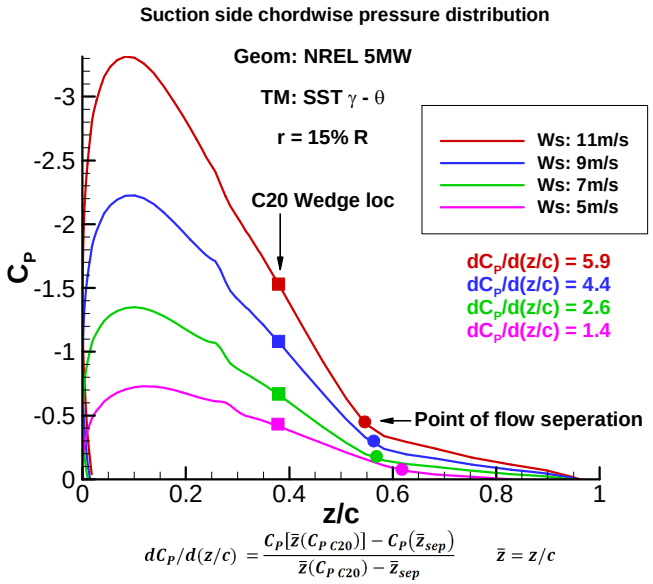

$$dC_P/d(z/c) = \frac{C_P[\bar{z}(C_{P\,C20})] - C_P(\bar{z}_{sep})}{\bar{z}(C_{P\,C20}) - \bar{z}_{sep}} \qquad \bar{z} = z/c$$

Figure 5-133 local suction side pressure coefficient as a function of chord for different wind speeds at 15% span, rotor: NREL 5MW, Ws: 9m/s, Omega: 10.3PRM, TM: SST γ – θ

Based on the pressure distributions at the 20% span within the sub rated wind speeds (Figure 5-134), the most severe pressure gradient was found to be about 2.9 at the large wind speed of 11m/s. This is less than the adverse pressure gradient that the wedges shown to perform effectively (dCp/d(x/c)=4.4), therefore it is expected that wedges placed at 20% span and above can operate effectively within the sub rated wind speed range (3 – 11m/s) of the NREL 5MW rotor.

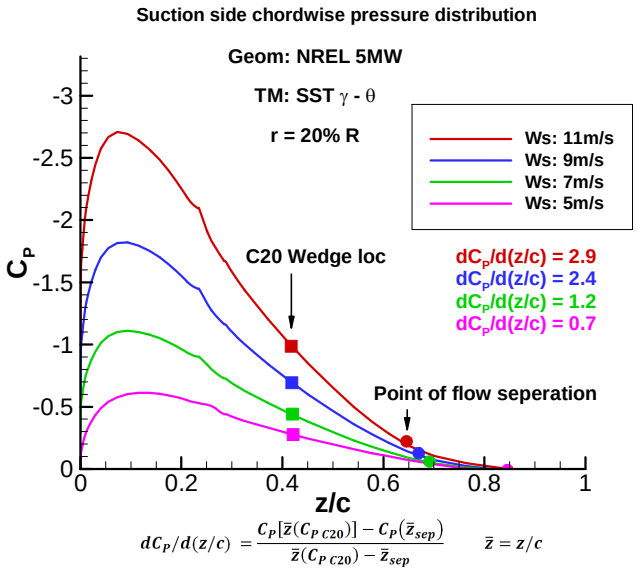

Figure 5-134 local suction side pressure coefficient as a function of chord for different wind speeds at 20% span, rotor: NREL 5MW, Ws: 9m/s, Omega: 10.3PRM, TM: SST γ – θ

The radial pressure gradient is another important factor that influences the wedges performance. However it is noted that this radial pressure gradient is also encouraged by the chord wise flow separation at the different span wise locations, therefore by using wedges to supress the chord wise flow separation reduces this radial pressure gradient i.e. radial pressure gradient is dependent on the chordwise pressure gradient. Thus the radial pressure gradients experienced by the wedges in operation are expected to be relatively lower than the clean blade. Three radial pressure distributions at the wedges locations were assessed (Figure 5-135) to determine the appropriate radial pressure gradient that the wedges can operate. The results from this exercise (Figure 5-136) indicates that the radial pressure gradients $dC_p^*/d(Y/R)$ up to 15.6 are present within the root region (r/R=0.10 to 0.15). From this CFD study it is found that the wedges only perform effectively when placed about 15% span, therefore it can be suggested that the wedges can endure a radial pressure gradients $dC_p^*/d(Y/R)$ up to about -11. At the large wind speed of 11m/s, radial pressure gradient within the 15-20% span increases to -16 (Figure 5-137), where it is expected to negatively affect the wedges performance, however this may not be true as when wedges are in operation, the radial pressure gradients are significantly reduced due to the reduced chord wise flow separations.

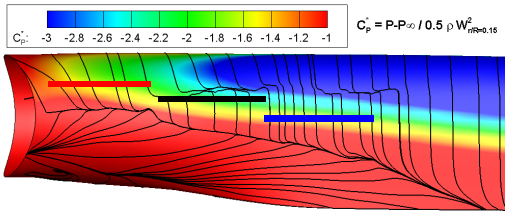

Figure 5-135 C20 Wedge locations used to assess radial coefficient pressure gradient, displayed span range: r/R=0.05 – 0.30

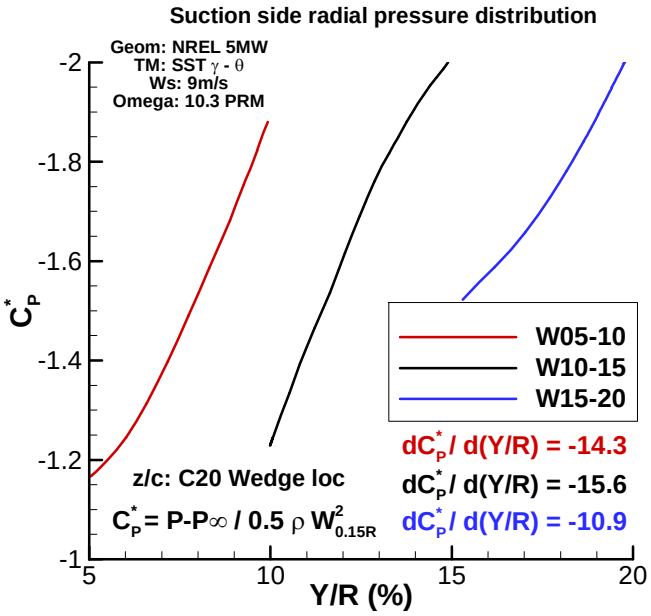

Figure 5-136 Suction side radial pressure coefficient as a function of span, rotor: NREL 5MW, Ws: 9m/s, Omega: 10.3PRM, TM: SST γ – θ

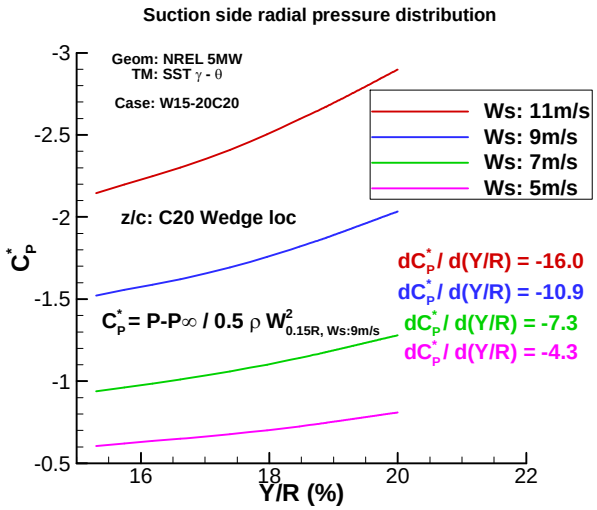

Figure 5-137 Suction side radial pressure coefficient as a function of span for different wind speeds, rotor: NREL 5MW, Ws: 9m/s, Omega: 10.3PRM, TM: SST γ – θ

Overall an increase of about 0.12% in rotor output is seen for the blade with bespoke wedges placed at 15-20% span, due to the VGs effectiveness to reduce span wise flow migration and flow separation. While the wedges placed at 05-10% span reduces the rotor power by 1.15%, and similarly when the wedges are placed at 10-15% span, the rotor

output is reduced by 1.40%. Therefore only the span location above 15% will be investigated for establishing an initial design space for the backward wedges.

5.7.3.2 Effect of VG interval spacing (w) at 15-20% span

For the wedges placed at 15-20% span and 20δ from the baseline separation the increase in interval spacing from $w/w_1=1$ to $w/w_1=3$ results in an increase in rotor power from 0.12% to 0.18%. While there is some improvement in power production, for the configuration where the wedges are placed further apart ($w=3w_1$) is only just able to reattach the flow at this design wind speed of 9m/s (Figure 5-138).

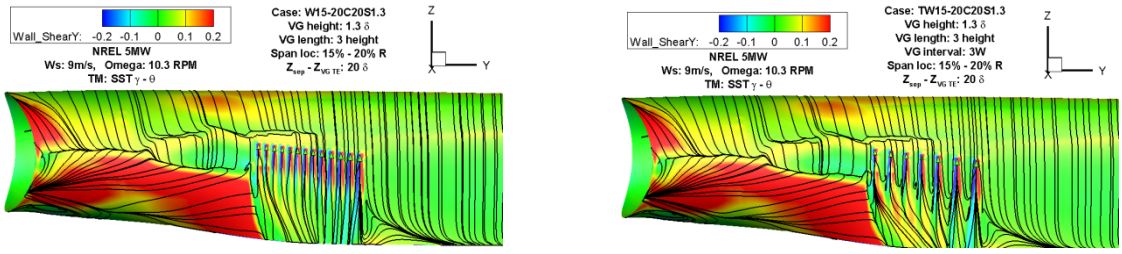

(a) **(b)**

Figure 5-138 Streamline pattern at the blade hub, , Ws: 9m/s, omega: 10.3rpm, turbulence model: SST γ – θ, wedge location: 15-20%, h/ δ: 1.3 , (a) w = w_1, (b) w= $3w_1$, case (a): *W15-20C20S1.3 - ΔPower: 0.12%,* and case (b): T*W15-20C20S2.0 - ΔPower: 0.18%,* displayed span range: r/R=0.05 – 0.30

The local aerodynamic force distribution (Figure 5-139) shows that the VGs placed at 15-20% span and 20δ from the baseline separation (Table 5.7.2-13, W15-20C20S1.3) has a small positive influence up to 4% increase in local lift production. The effect of increased VG spacing (Table 5.7.2-13, TW15-20C20S1.3) revealed that the VGs placed closer together (w= w1) helps to generate slightly better lift forces than VGs placed further apart (w= $3w_1$) i.e. change in local lift force for the W15-20C20S1.3 and TW15-20C20S1.3 are 4% and 3% respectively (Figure 5-139).

The local drag force distribution along the blade span shows that VGs placed at 15-20% span increases the drag production by up to 10%. By reducing the number of wedges from 13 to 7 or increasing the interval spacing from $w/w_1=1$ to $w/w_1=3$ the increase in local drag force relative to the clean blade can be reduced to 5%. This result suggests that the increase in rotor power is mainly due to the reduced drag incurred at 12 to 18% span by the reduced number of wedges. It was also noticed that the use of wedge VGs at this span location has a small influence up to $\pm$ 3% in the drag production at the outboard portion of the blade (r/R>0.5). This is maybe due to influence of the wedges on the outboard blades axial induction factors.

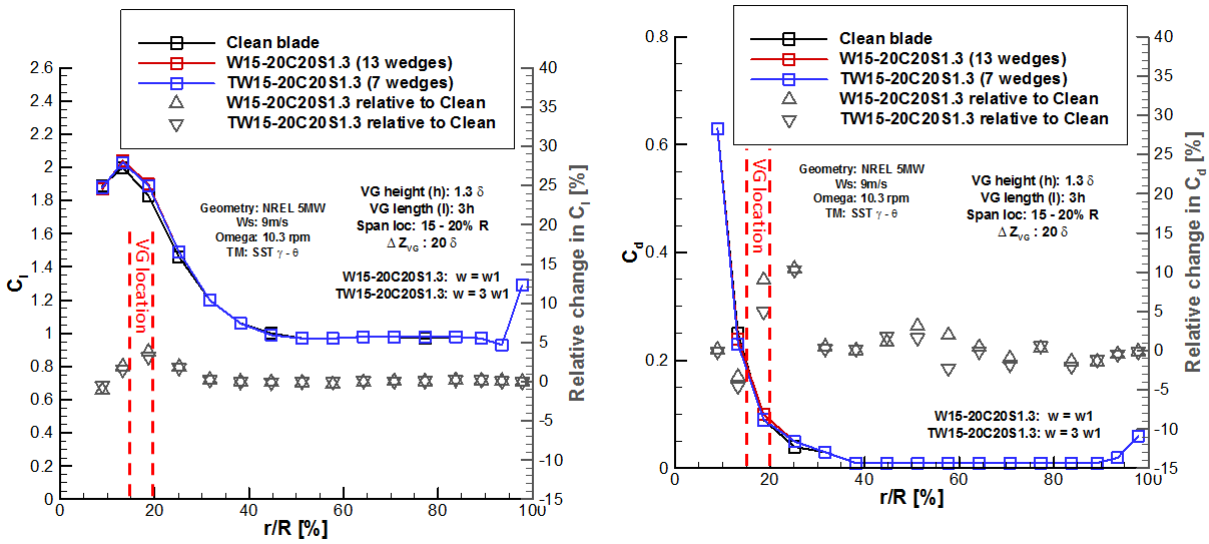

Figure 5-139 blade local lift distribution, Ws: 9m/s, omega: 10.3rpm, turbulence model: SST γ – θ, wedge location: 15-20%, h/ δ: 1.3 , w = w1 and 3w1, case: *W15-20C20S1.3 - ΔPower: 0.12%,* and case: T*W15-20C20S2.0 - ΔPower: 0.18%*

An improvement in axial induction is another interest for achieving beneficial aerodynamics for this region of the blade. Locally up to a 4.8% increase in axial induction was achieved with the wedges (Figure 5-140). The wedges with w/w_1=3 were seen to generate smaller gain in axial induction (+4.5%) than the case where the wedges placed closer together (w/w_1=1). However the wedges placed further apart (w/w_1=3) showed to improve the axial induction of the outboard sections found at 50-60% span by 0.13% where the w/w_1= 1 case shown to negatively reduce the axial induction by up to 0.3% within this span region. This exercise shows that VGs present at the 15-20% span increases local lift forces, which also seems to influence the axial induction outboard. This is maybe the cause for the changes in drag forces at the outboard blade.

The effect of further increase in interval spacing of w = 5w1 was investigated for the wedges placed at this location (15-20% span), which showed (Figure 5-141) that the effectiveness of the wedges to reduce flow separation reduces when the interval spacing is increased from 3w1 to 5w1 and the rotor power output is reduced from 0.18% to 0.13%.

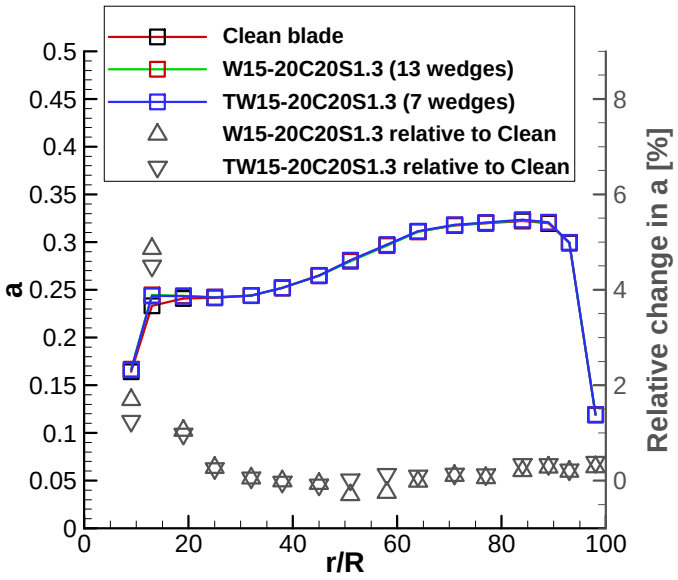

Figure 5-140 blade local axial induction distribution, Ws: 9m/s, omega: 10.3rpm, turbulence model: SST γ – θ, wedge location: 15-20%, h/ δ: 1.3, w/w_1 = 1 and 3, case: *W15-20C20S1.3 - ΔPower: 0.12%,* and case: T*W15-20C20S2.0 - ΔPower: 0.18%*

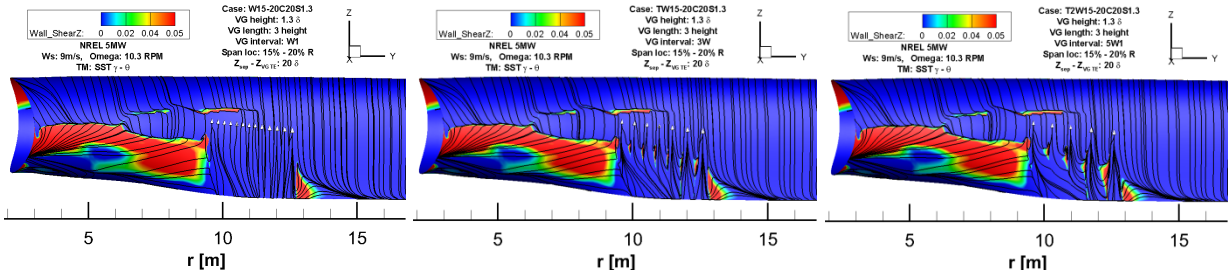

(a) (b) (c)

Figure 5-141 Streamline pattern at the blade hub, , Ws: 9m/s, omega: 10.3rpm, turbulence model: SST γ – θ, wedge location: 15-20%, h/ δ: 1.3 , (a) w= w1, (b) w= 3w1, (c) w= 5w1, case (a): *W15-20C20S1.3 - ΔPower: 0.12%,* and case (b): T*W15-20C20S2.0 - ΔPower: 0.18%,* (c): T2*W15-20C20S2.0 - ΔPower: 0.13%,* displayed span range: r/R=0.05 – 0.30

Based on this investigation it is recommend that for wedges placed at 15-20% span and 20δ from the baseline separation and w/w_1 =1 to be used, due to its effectiveness on controlling the spanwise flow migration and flow separation. An interval spacing of w/w_1 =3 is not recommended even though it achieves a greater power increase but it is expected to perform ineffectively at higher wind speeds, due to the increase in adverse pressure gradients.

5.7.3.3 Effect of chordwise location and interval spacing

The effect of chordwise location was conducted for two different span ranges, which are from 19-20% span and 15-20% span. The results for wedges placed over a small span range 19-20% showed that the both VG locations in the chord wise position are able to supress spanwise flow migration and to reduce flow separation (Figure 5-142). The wedges placed 45δ from the baseline separation are able to increase the rotor power by 0.2% while the wedges placed at Z/δ =20 achieve an increase in rotor power of only 0.08%. This suggests that the wedges should be placed at Z/δ = 45 from the baseline separation.

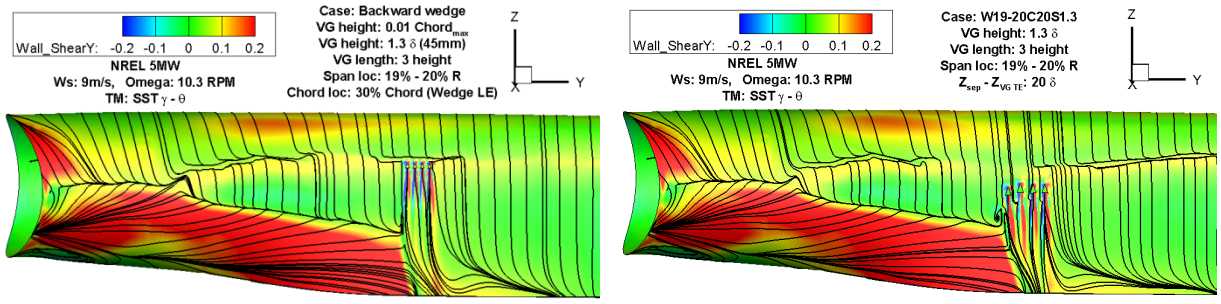

(a) (b)

Figure 5-142 Streamline pattern at the blade hub, , Ws: 9m/s, omega: 10.3rpm, TM: SST γ – θ, wedge location: 15-20%, h/ δ: 1.3 , w: w1, (a) : ΔZ_{VG} = 45δ, (b) : ΔZ_{VG} = 20δ, case (a): *W19-20C45S1.3 - ΔPower: 0.20%,* and case (b): *W19-20C20S1.3 - ΔPower: 0.08%,* displayed span range: r/R=0.05 – 0.30

The evaluation of the vortex generated by a wedge (Figure 5-143) showed that wedges placed at 45δ from the baseline separation (C45) is able to generate a greater peak circulation than the wedges placed at 20δ from the baseline separation (C20). The C45 case was able to generate up to 56% more peak circulation than the C20 case. it was noticed that the vortices generated by the C45 wedges dissipates up to 70% of its peak circulation within the first 23h downstream, while the C20 wedges dissipate up to 75% of its peak circulation within 24h downstream. This shows that the vortices generated by the wedges placed 45δ from the baseline separation has a greater strength and able to maintain most if its peak circulation for longer distance than the C20 wedges i.e. efficient vortex is generated with wedges placed 45δ from the baseline separation than 20δ.

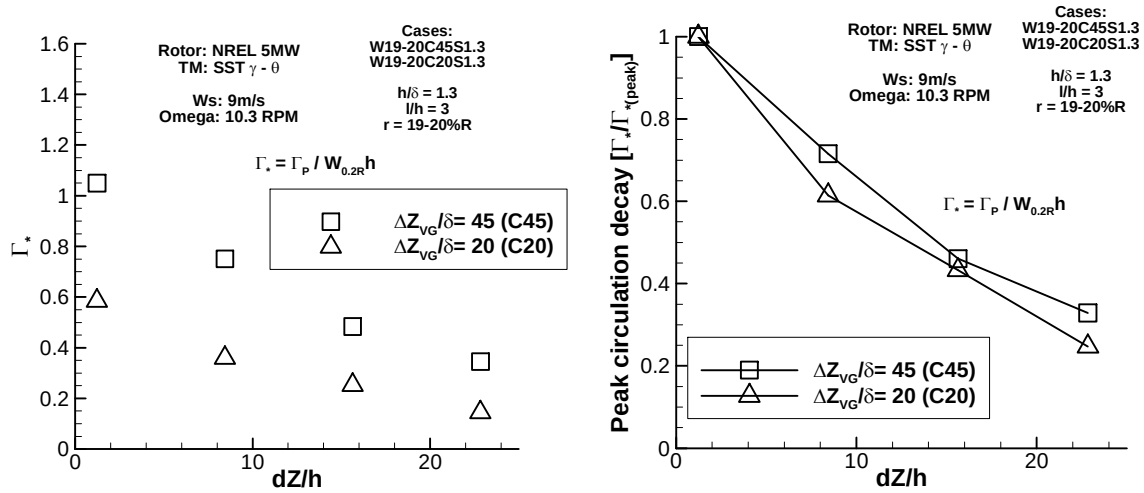

Figure 5-143 Non-dimensional stream wise circulation per wedge as a function of stream wise distance in terms of h from the wedges TE, TM: SST γ – θ, Re: 1.6 million, Geometry= NREL 5MW blade, r = 20% R, Ws: 9m/s, Omega: 10.3RPM

On account of the efficient vortex generated by the C45 wedges, they were also found to be closer to the blade surface than the vortices generated by the C20 wedges (Figure 5-144). It was noticed that the core of the vortex generated by the C45 wedges was found to elevate up to 0.9h within the first 23h downstream, while the vortex generated by the C20 wedges

were found to be about 60% further elevated from the blade surface. This assessment suggests that the full potential of the C45 wedges are experienced by the downstream boundary layer, with its higher peak circulation and an efficient decay of the circulation it performs better than the C20 wedges in terms of overall gain in rotor power.

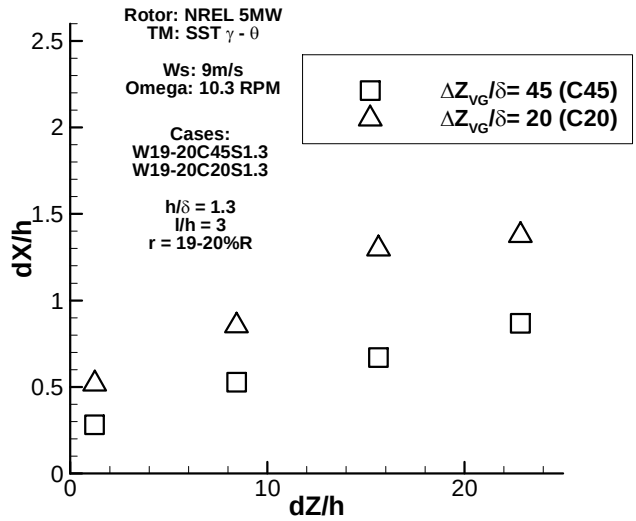

Figure 5-144 Non-dimensional location of the vortex core (peak vorticity) away from the blade surface as a function of stream wise distance from the wedge TE, TM: SST γ – θ, Geometry= NREL 5MW blade, Ws: 9m/s, Omega: 10.3RPM, X originates at the blade surface

In contrast to the wedges placed over a small span range (r/R=0.19-0.2), when an array of wedges are placed over a moderate span range such as r/R from 0.15 to 0.2 (Figure 5-145), better power output was achieved with wedges placed at Z/δ =20 (Figure 5-145) than Z/δ =45 (Table 5.7.3-14). The effectiveness of the wedges to suppress flow separation is reduced when wedges are placed over a moderate span (r/R=0.15-0.2) and Z/δ =45(Figure 5-145).

	Relative change in rotor power	
Span range (%)	ΔZ_{VG} = 45δ (C45)	ΔZ_{VG} = 20δ (C20)
19-20	+0.20%	+0.08%
15-20	+0.08%	+0.18%

Table 5.7.3-14 Changes in power output for different chord location relative to baseline separation

The wedges placed at Z/δ =20 showed an increase up to 4% in local Cl while the C45 wedges only achieve a small increase of about 1% within its local span location (Figure 5-146). However it was noticed that the C20 wedges generated larger drag forces due to their larger relative height, as the local boundary layer thickness is higher in its relative location in chord. Up to 10% increase in local drag forces relative to the clean blade were seen for the wedges placed at 20δ from the baseline separation (Figure 5-146).

The axial induction distribution has shown that the wedges placed at 45δ from the baseline separation has a better induction than the C20 case at the span location of 10%, where they achieved about 4% increase relative to the clean blade (Figure 5-147). While the C20 case only achieved about +2% at this span location. These results suggest that the C45 cases

contribute to a better aerodynamics in terms of lift to drag ratios at the blade root, which is contrary to the power output of the blade.

The benefit of the C20 wedges were seen at the outboard section of the blade where a lift to drag ratios of up to 2% are achieved within 85-90% span (Figure 5-147). This increase in lift to drag ratios at the outboard section is a greater benefit to the power output, and it is able to outweigh the large increase in drag force found at the blade root, which corresponds to about 5% reduction in lift to drag ratios. With an increase in lift forces up to 4% at the blade root and the gain in lift to drag ratios about 2% at the outboard blade allows the C20 wedges to achieve a gain in power output of 0.18% while the C45 wedges only gain about 0.1% in rotor power.

It is also noticed that for both cases, a large increase of up to 12% in drag forces was seen at the vicinity of last wedge placed in the outboard span location about 25% span (Figure 5-146), which corresponds to a large reduction of up to 9% in lift to drag ratio (Figure 5-147). This is maybe due to the counter rotating vortex from the last wedge placed at 20% span aids to separate the flow than helps to reduce it. This is effect can be reduced by using a half wedge where the counter rotating vortex is not generated, and its effects will be presented later in the thesis, where the wedges were placed up to 25% span (W15-25, section 5.7.3.5).

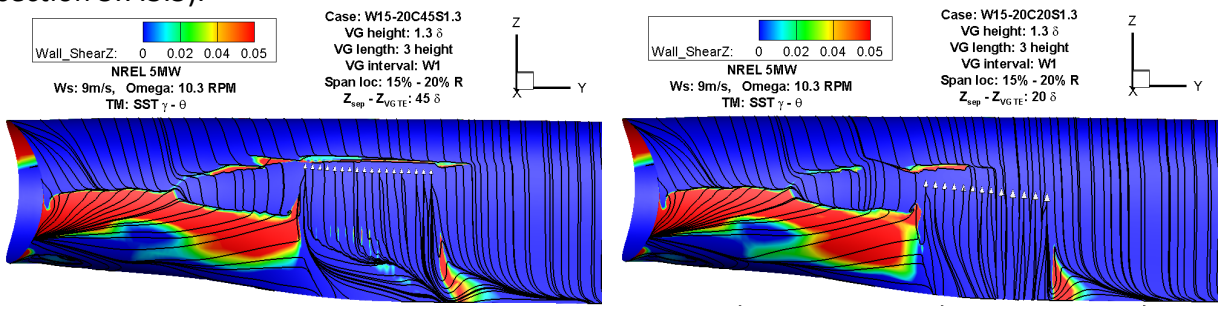

(a) (b)

Figure 5-145 Streamline pattern at the blade hub, , Ws: 9m/s, omega: 10.3rpm, turbulence model: SST γ – θ, wedge location: 15-20%, h/ δ: 1.3 , w: w1, (a) : ΔZ_{VG} = 45δ, (b) : ΔZ_{VG} = 20δ, case (a): *W15-20C45S1.3 - ΔPower: 0.08%,* and case (b): *W15-20C20S1.3 - ΔPower: 0.18%*

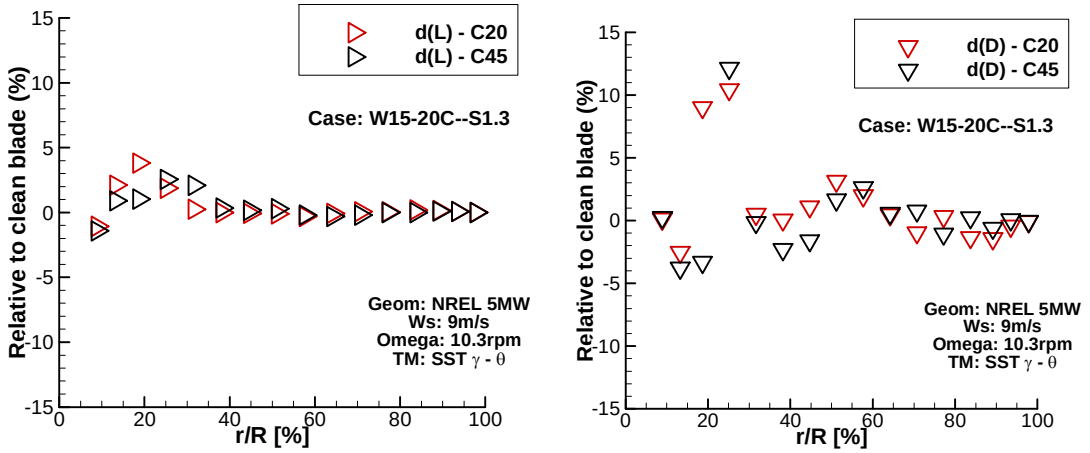

Figure 5-146 (Left) changes in blade local lift distribution as a function of blade radius, (right) changes in blade local drag distribution as a function of blade radius, Ws: 9m/s, omega: 10.3rpm, TM: SST γ – θ

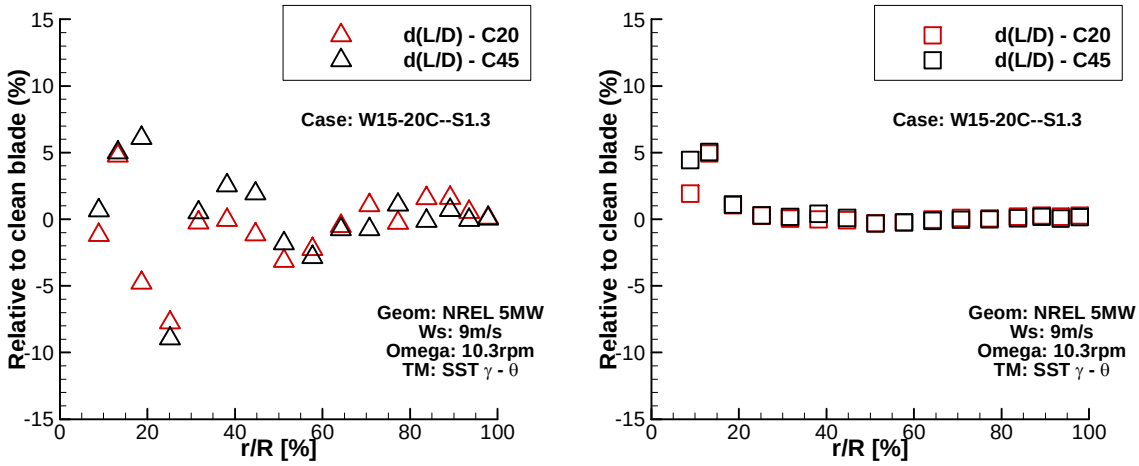

Figure 5-147 (Left) blade local lift to drag ratio distribution as a function of blade radius, (right) blade axial induction distribution as a function of blade radius, Ws: 9m/s, omega: 10.3rpm, TM: SST γ – θ

When the interval spacing of the wedges placed at r/R=0.15-0.20 and at Z/δ = 45 was increased from w/w_1=1 to 3, the rotor power is reduced from +0.08% to -0.26%. It is clear that the wedges are inefficient in reattaching the flow when w is increased to $3W_1$ and instead they generate a large flow separation (Figure 5-148). It was found that the wedges with w/w_1=3 reduces the lift production of the outboard blade by up to 1% at 60% span (Figure 5-149) and it contribution to the gain in local lift forces at its location up to 1.7% is less compared to the w=w1 wedges (+2.6%). However the severe impact is seen on the drag production of the outboard blade where the wedges with w=3w1 contribute to up to 12% increase in drag production within 45-65% span. While the w=w1 wedges helps to reduce drag by up to 4% within 15-50% of blade span.

The negative effect on drag production by the increased w for the w=3w1 wedges reduces the local lift to drag production by up to 12% in the 50-60% span (Figure 5-150). It is also seen to reduce axial induction by up to 1.4% at this span range, therefore these combined negative effects on lift to drag ratios and axial induction reduces the w=3w1 wedge installed rotor output by 0.26%.

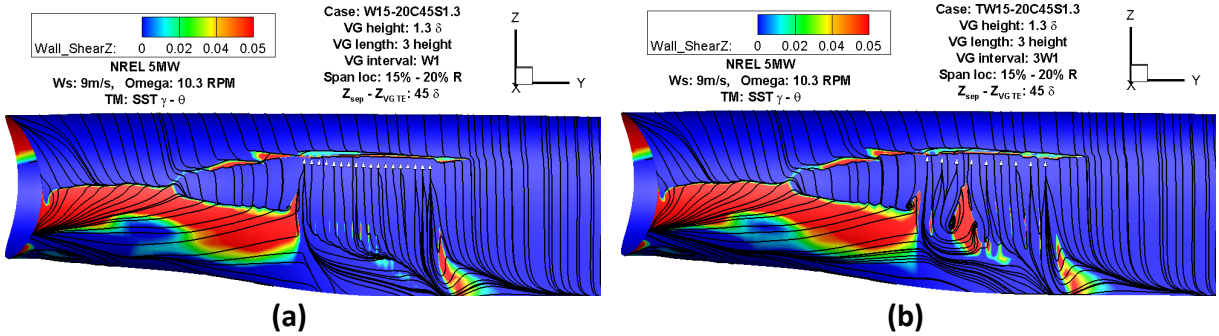

(a) **(b)**

Figure 5-148 Streamline pattern at the blade hub, , Ws: 9m/s, omega: 10.3rpm, turbulence model: SST γ – θ, wedge location: 15-20%, ΔZ_{VG} = 45δ, h/ δ: 1.3 interval spacing (a): w1, interval spacing (b): 3w1, case (a): *W15-20C45S1.3 - ΔPower: 0.18%,* and case (b): T*W15-20C45S1.3 - ΔPower: -0.26%,* displayed span range: r/R=0.05 – 0.30

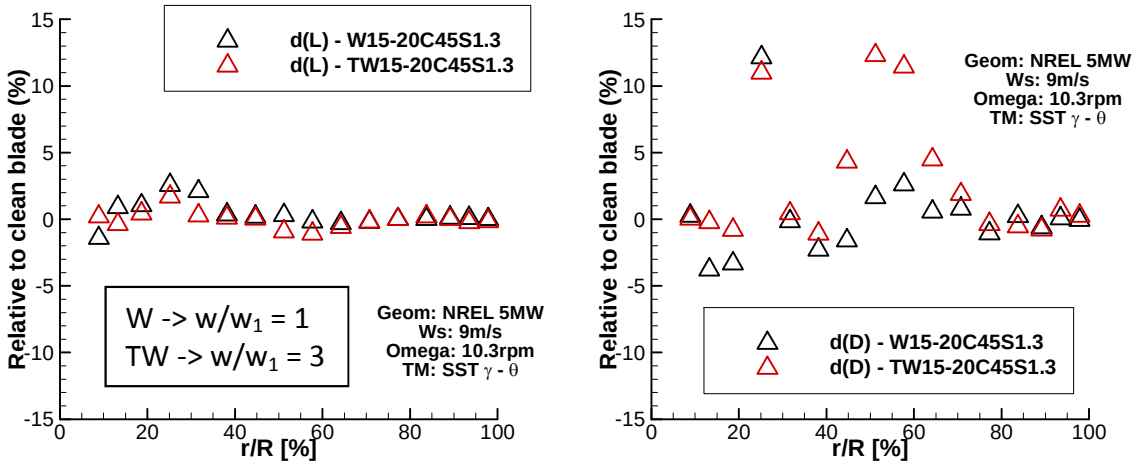

Figure 5-149 The effect of wedge lateral spacing on blade local lift distribution(Left) and the drag distribution (right) as a function of blade radius, Ws: 9m/s, omega: 10.3rpm, TM: SST γ – θ

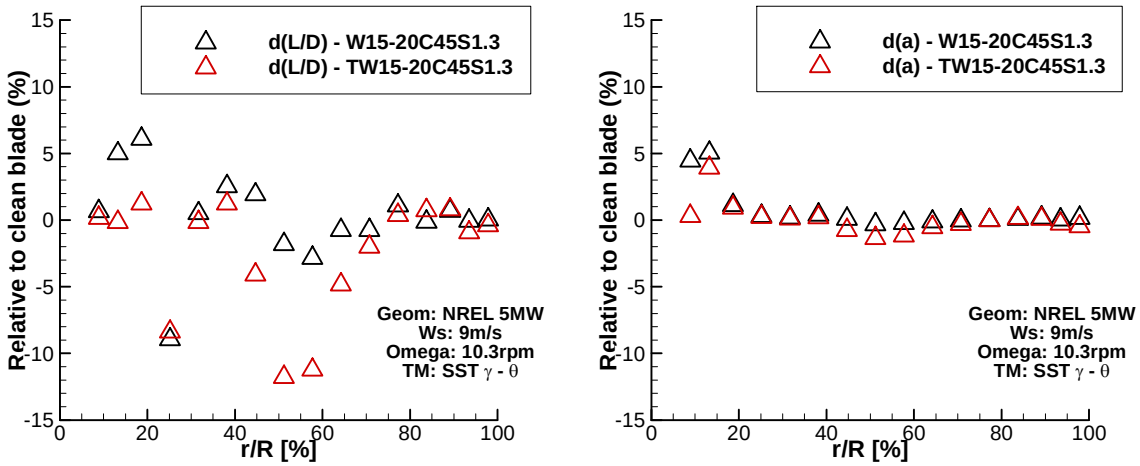

Figure 5-150 (Left) changes in blade local lift to drag ratio distribution as a function of blade radius, (right) changes in blade axial induction distribution as a function of blade radius, Ws: 9m/s, omega: 10.3rpm, TM: SST γ – θ

5.7.3.4 Effect of wedge height

The effect of wedge height was conducted using three heights relative to the local boundary layer thickness, which were h/δ =0.6, 0.8 and 1.3. This investigation was conducted for the wedges placed at r/R =0.19-0.2 and r/R=0.16-0.2. The wedges placed at Z/ δ = 20 were chosen for this investigation. The 16-20% span wedges were modelled as each VG was separately designed using the baseline separation line and the local boundary layer heights (Figure 5-151) while all the other wedge cases were performed by placed along line connecting the wedges at either end of the investigated span range to reduce complexity in modelling.

The wedges with the smallest height (h/δ =0.6) fails to improve the local aerodynamics of blade while contributing to the increase in drag due to their presence. The wedges with height of 0.8δ and 1.3δ have beneficial effects on the flow separation and the spanwise flow migration. The smallest wedge h/δ =0.6 generates a change in rotor power of -0.10% while the h/δ =0.8 and 1.3 achieve a gain in rotor power of 0.09% and 0.08%, respectively. Based

on the results from this study it is recommended as a guideline that a wedge height of h/δ = 0.8 to 1.3 should be used to gain a beneficial effect from the wedge type VGs.

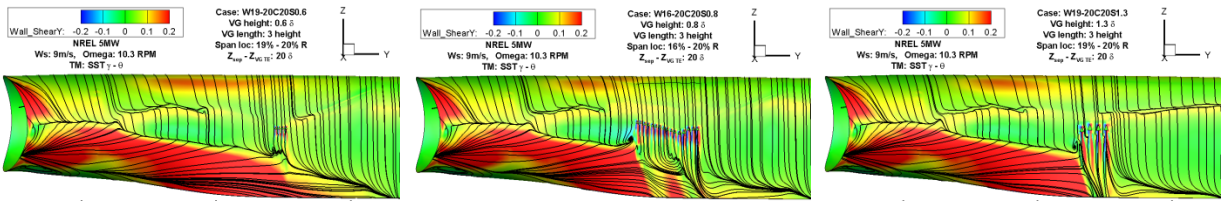

(a) (b) (c)

Figure 5-151 Streamline pattern at the blade hub, , Ws: 9m/s, omega: 10.3rpm, turbulence model: SST γ – θ, (a) h/ δ= 0.6, (b): h/ δ= 0.8, (c) h/ δ= 1.3, w: w1, case (a): *W19-20C20S0.6 - ΔPower: -0.10%,* and case (b): *W16-20C20S0.8 - ΔPower: 0.09%,* (c): *W19-20C20S1.3 - ΔPower: 0.08%,* displayed span range: r/R=0.05 – 0.30

The evaluation of the vortices generated by the wedges with different heights (Figure 5-152) showed that the h/δ = 0.8 wedges generated the strongest vortex in terms of peak circulation, while the other two heights generated about 55% of the relative peak circulation from their corresponding vortices. The wedges with h/δ = 1.3 and 0.6 generated similar vortices in terms of peak circulation and their decay within 23h downstream. It should be noted that the absolute circulation found from the h/δ = 1.3 wedges were about 10 and 60% more than the vortices generated by the h/δ = 0.8 and 0.6 respectively.

Results (Figure 5-152) also shows that the vortices generated by h/δ = 0.8 wedges decays about 80% of its peak circulation with the first 23h downstream while h/δ = 1.3 and 0.6 wedges decays about 75% and 70% of its peak circulation relatively within the first 23h downstream. The relative performance of vortex decay shows that h/δ = 0.8 generates the efficient vortex in comparison with the other heights.

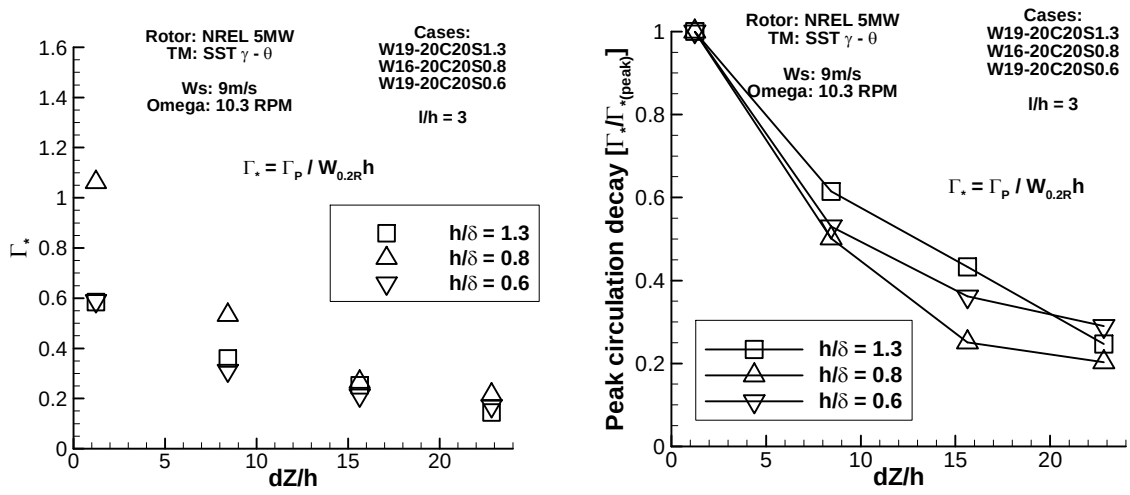

Figure 5-152 Non-dimensional stream wise circulation (left) and peak circulation decay (right) per wedge as a function of stream wise distance in terms of h from the wedges TE, TM: SST γ – θ, Geometry= NREL 5MW blade, r = 20% R, Ws: 9m/s, Omega: 10.3RPM

As anticipated the vortex generated by the h/δ = 1.3 wedges were found to be further away from the blade surface downstream than the other two smaller wedges (Figure 5-153). The relative location of the vortex core downstream away from the blade surface increases with

wedge height. It was found that the vortex core from the h/δ = 1.3 wedges reach about 1.4h away from the blade surface within the first 23h downstream, while the h/δ = 0.8 and 0.6 reaches only about 0.8h and 0.5h within this downstream distance. Based on this study it can be suggested that the core of vortices generated by a backward wedge reaches about its corresponding wedge height away from the surface only after about 20h downstream i.e. greater potential to control boundary layer within the first 20h downstream.

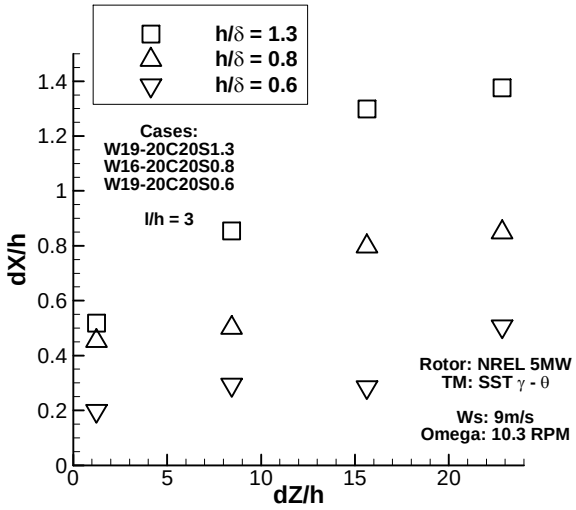

Figure 5-153 Non-dimensional location of the vortex core (peak vorticity) away from the blade surface as a function of stream wise distance from the wedge TE, TM: SST γ – θ, Geometry= NREL 5MW blade, Ws: 9m/s, Omega: 10.3RPM

5.7.3.5 Wedges extended to 25% span

The result for the wedges placed at r/R= 0.15-0.2 and Z/δ =20 with the interval spacing of w/w_1 = 3w1 showed a positive increase in power output of 0.18%. Therefore it was decided to extend this configuration to 25% of the span in an attempt to supress all of the hub separation from r/R=0.15. As expected when the wedges are extended to 25% of the blade span, most of the hub flow separation is supressed (Figure 5-154) however the benefit in aerodynamic is not fully reflected on the power output due to the increase in drag by the increased number of wedges. When the wedges are extended to 25% from 15% span the gain in rotor power is reduced to 0.16% from 0.18%.

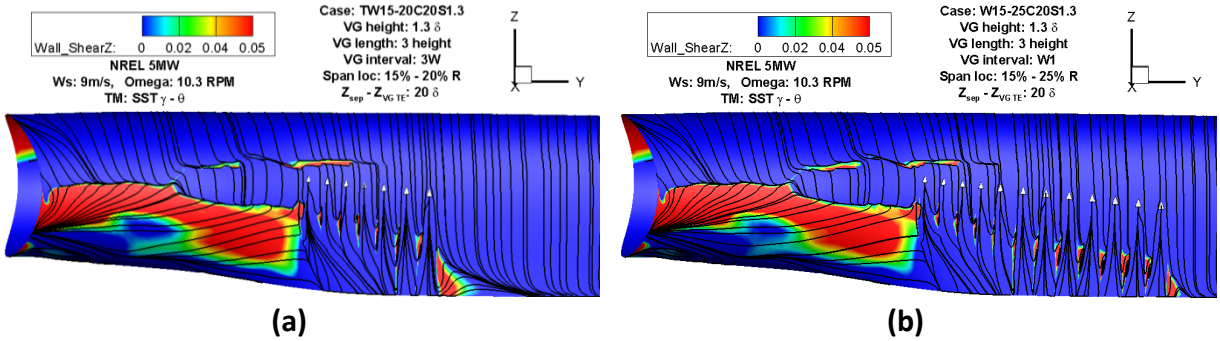

(a) **(b)**

Figure 5-154 Streamline pattern at the blade hub, , Ws: 9m/s, omega: 10.3rpm, TM: SST γ – θ, wedge location (a): 15-20%, , wedge location (b): 15-25%, ΔZ_{VG} = 20δ, h/ δ: = 1.3, w : 3w1, case (a): T*W15-20C20S1.3 - ΔPower: 0.18%,* and case (b): T*W15-20C20S1.3 - ΔPower: 0.16%,* displayed span range: r/R=0.05 – 0.30

It was seen that both cases increased lift production of the blade root (0-30% span) by up to 4% (Figure 5-155). The case with wedges extended to 25% span was able to increase the local lift production by 3% at the 25% span while the case with wedges placed only up to 20% span showed to increase local lift production by about 2% at 25% span. The significant effect due to the extension of the wedges was seen in the local drag production of the blade. When the wedges placed to cover up to 25% span from 15% it was seen that up to 22% increase in local drag production at span location of 25% (Figure 5-155). The additional 5 wedges to cover the 20-25% span showed to contribute 10% more drag production at 25% blade span. However when the wedges are extended to 25% span, this configuration was seen to reduce the local drag production at the 45-60% span range by up to 2% where the wedges placed only up to 20% increased the drag production within this span range by up to 3%.

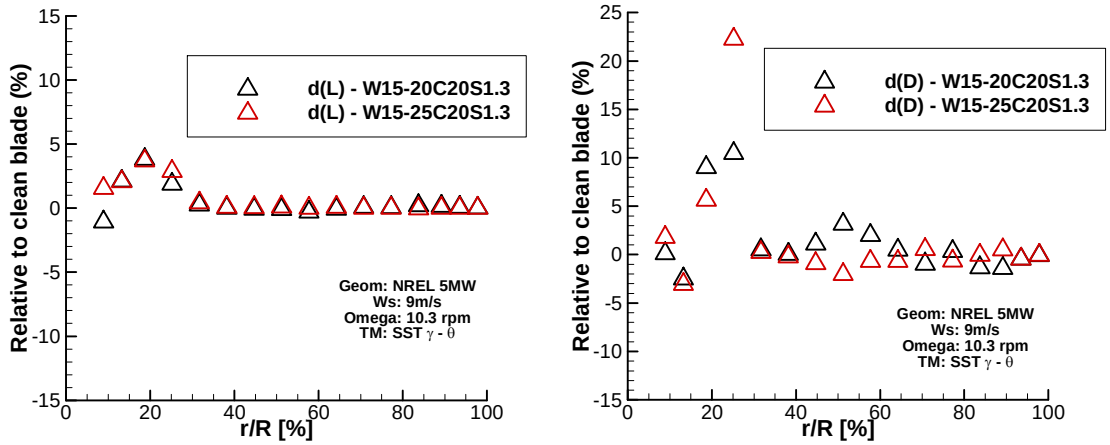

Figure 5-155 (Left) changes in blade local lift distribution as a function of blade radius, (right) changes in blade local drag distribution as a function of blade radius, Ws: 9m/s, omega: 10.3rpm, TM: SST γ – θ

When the wedges are positioned across the region of r/R from 0.15 to 0.25, slightly better lift to drag ratios at the blade root were noticed compared to the wedges placed up to only r/R= 0.2 (Figure 5-156). The large increase in drag production by the wedges placed up to r/R = 0.25 reduces the local lift to drag ratios by up to 16%, where the wedges placed only up to r/R = 0.2 reduces lift to drag ratios by 8%. The reduction in drag of about 2% at the 45 – 60% span by the wedges placed up to r/R = 0.25 showed to increase the lift to drag ratios by up to 2% within this span range.

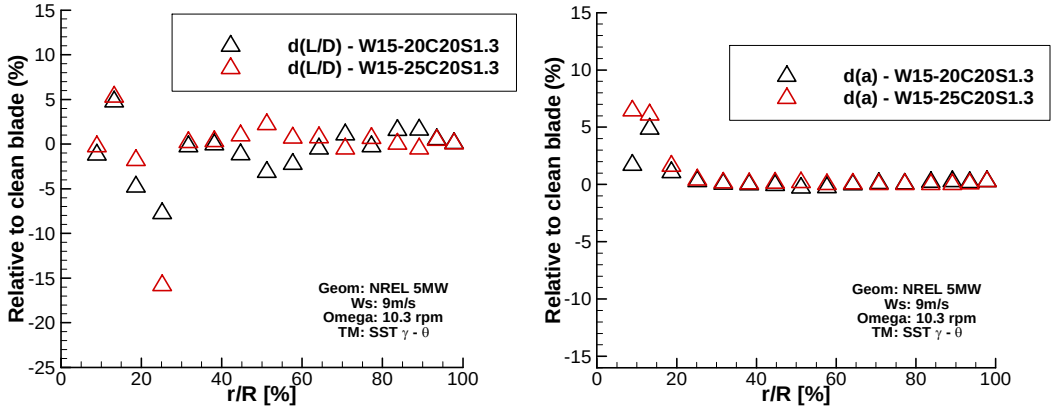

Figure 5-156 (Left) changes in blade local lift to drag ratio distribution as a function of blade radius, (right) changes in blade axial induction distribution as a function of blade radius, Ws: 9m/s, omega: 10.3rpm, TM: SST γ – θ

Both cases showed an increase the axial induction of the blade root (Figure 5-156). However the case with wedges extended to 25% span showed to gain a better axial induction within 10-20% span than the wedges extended to 20% span. The W15-25 case showed an increase up to 6% in local axial induction at the 10% blade span, while the W15-20 case only achieved an increase of up to 2%. Overall it can be seen that the large reduction in lift to drag ratio at the r/R = 0.25 limits the other benefits due to W15-25 case to be fully translated to the power output.

5.7.4 Local aerodynamic changes

Although the wedges were seen to affect the outboard aerodynamics, it is important to assess the aerodynamics proximity to the wedge location where the large influences due to the wedges are found. Therefore the local changes in aerodynamics due to the wedges were evaluated and assessed using the blade patch enclosing the wedges (Figure 5-157). The changes in local lift, drag, lift/drag and axial induction were used to conduct this study. The method of extracting blade local forces from a 3D CFD simulation of a wind turbine was developed by Riso DTU and published the method in [72]. This was implemented to determine the local changes in performance.

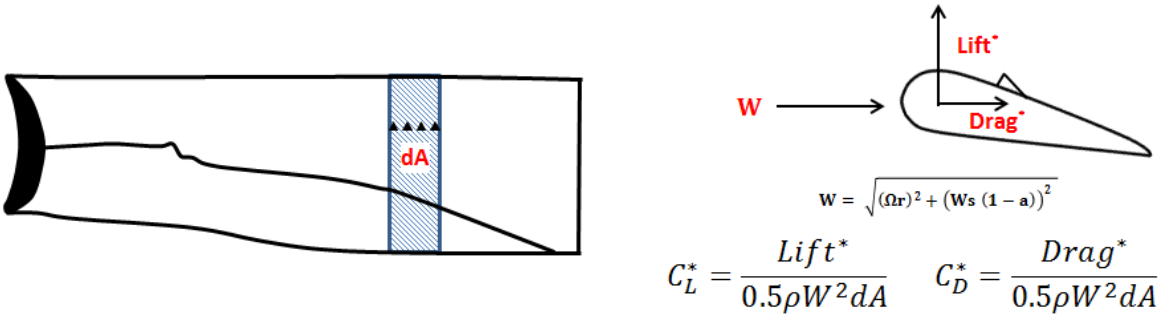

Figure 5-157 blade patch used to assess the local blade performances

Based on this exercise it was found that the backward wedges can improve the local lift coefficient by up to 4% (Figure 5-158). It is recommended that for an increase in lift production to place the wedges 20δ upstream from the baseline separation and to cover r/R = 0.15-0.25. The wedges placed at Z/δ= 20 (C20, black lines) generally showed a better increment to local lift production than the wedges placed further away from the baseline separation (C45, red lines).

Wedges placed over a small span range showed a small reduction in the local lift production of the blade patch, within 1%. The wedge height of h/δ =1.3 and 0.6 showed small influence on the lift forces up to -0.5%, while the h/δ =0.8 showed to reduce up to 1% of the local lift productions. Therefore a minimum wedge height of 1.3δ is recommended to improve the local lift performance.

Based on this result it was also found that wedges closer together in the spanwise direction increases the local lift production. Such that for the wedges placed over the span range 15-20% with the w=w1 showed to increase lift production by up to 3.3%, but when the interval spacing (w) is increased to 3w1 the gain in lift production is reduced to 2.6% and then it further reduces to 2.4% when w is increased to 5w1. According to this assessment, an interval spacing (w) of one wedge width (w/w_1=1) is recommended to increase the local lift production.

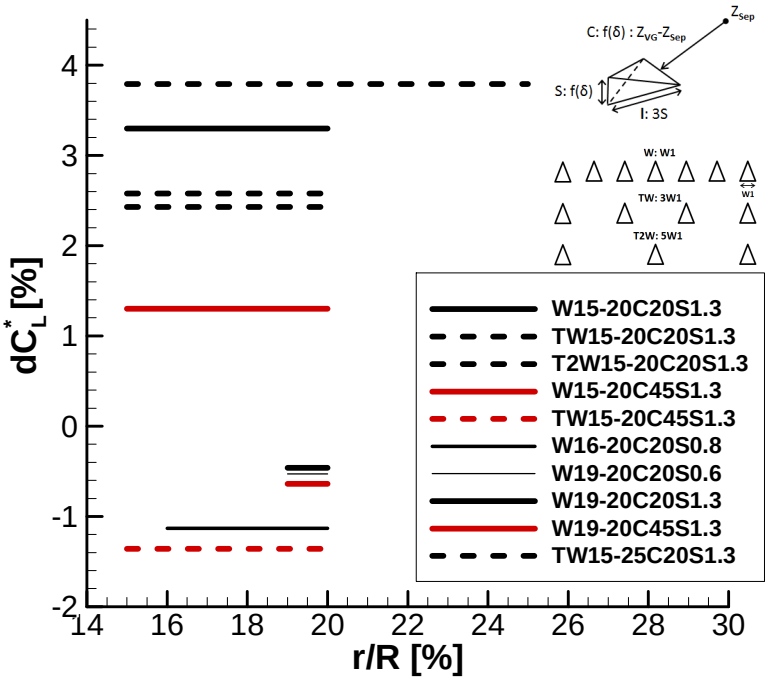

Figure 5-158 changes in local lift production due to the wedge installation, Geometry= NREL 5MW, Ws: 9m/s, omega: 10.3rpm, turbulence model: SST γ – θ

It was found that up to a 16% reduction in local drag forces are possible with the backward wedges (Figure 5-159). To use the wedges as a drag reduction device, the wedges should be placed further from the baseline separation (45δ, red lines) with interval spacing of w_1. It is recommended that the wedges should be placed over a smaller span range of 5% for better drag reduction. Based on the results for the wedges placed at 15-20% span and 20δ for the baseline separation with a h/δ =1.3, it was found that an increase in interval spacing from w/w_1=3 to 5 the changes in drag were found to be not effected, i.e. similar reduction up to 5% in local drag forces can be gained with less number of wedges (-2 wedges).

It was also noticed that wedges placed at 20δ for the baseline separation achieve better drag reduction with a w/w_1=3 than wedges placed closer together (w/w_1=1). In contrast for the wedges placed closer to the leading edge or about 45δ for the baseline separation, it is recommended that to adapt a w/w_1=1 than w/w_1=3 as a larger drag reduction is achieved with wedges placed closer together i.e. the benefits in drag reduction due to reduction in flow separation outweighs the parasitic drag due to the increased number of VGs.

The assessment of the lift to drag ratios has shown that wedges placed closer to the LE (C45, red lines) greatly improved the L/D ratios (Figure 5-160) by up to 20%, while the wedges placed closer to the TE (C20, black lines) were only able to achieve L/D ratios up to 5%. For beneficial L/D ratios a wedges height between h/δ =0.8-1.3 with interval spacing w/w_1=1 is recommended. It's also noted that due to the large increase in drag forces incurred when wedges are placed at the large span range of r/R =0.15-0.25, it was shown to reduce up to 8% reduction in lift to drag ratios. It is suggested that the wedges should be placed over a moderate span range within 5% to gain better lift to drag ratios using wedges.

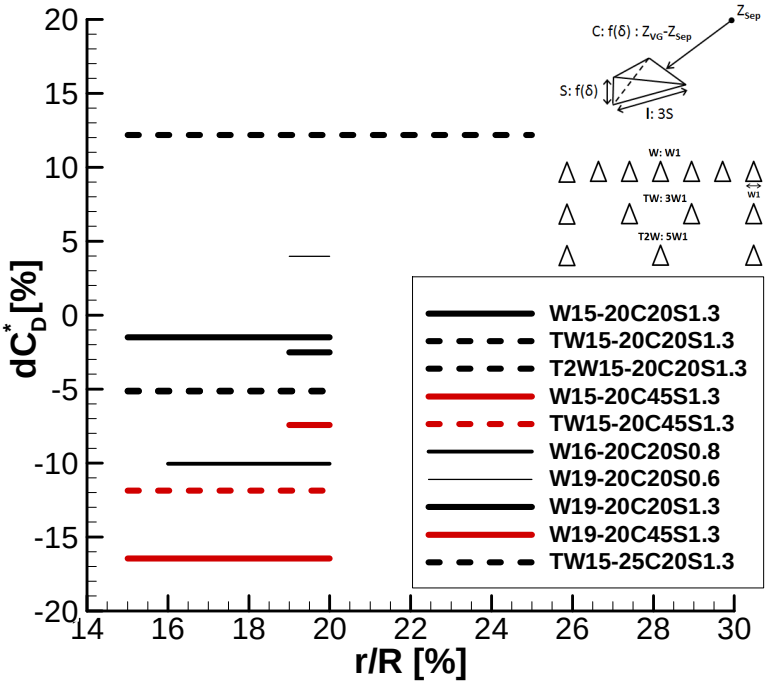

Figure 5-159 changes in local drag production due to the wedge installation, Geometry= NREL 5MW, Ws: 9m/s, omega: 10.3rpm, turbulence model: SST γ – θ

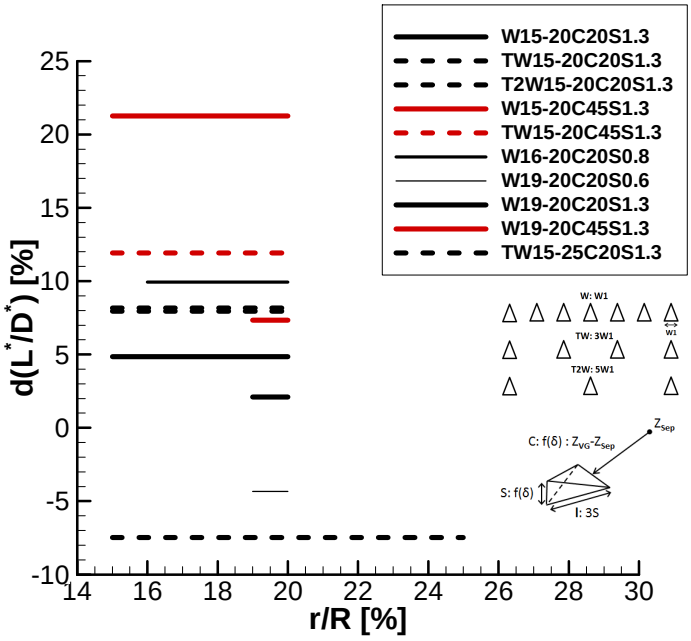

Figure 5-160 changes in local lift/drag ratio due to the wedge installation, Geometry= NREL 5MW, Ws: 9m/s, omega: 10.3rpm, turbulence model: SST γ – θ

Baseline local axial induction factor distribution over the clean NREL 5MW blade suggests that the blade is greatly underperforming specially in the hub section of the blade (10-40% span), therefore the improvements in axial induction is equally important as the improvements in lift and drag forces.

Improvements up to 2% in local axial inductions were achieved when wedges are placed over a moderate span range about 5% (Figure 5-161). Wedges placed closer to the leading edge (45δ from baseline separation) achieve better axial induction than wedges placed closer to the TE (C20). Wedges placed closer together generate better induction than wedges placed far apart, an interval spacing of w/w_1=1 is recommended to achieve a better gain in axial induction. To improve the axial induction the wedges should be placed closer to the leading edge (45δ from baseline separation) with a height of 1.3δ.

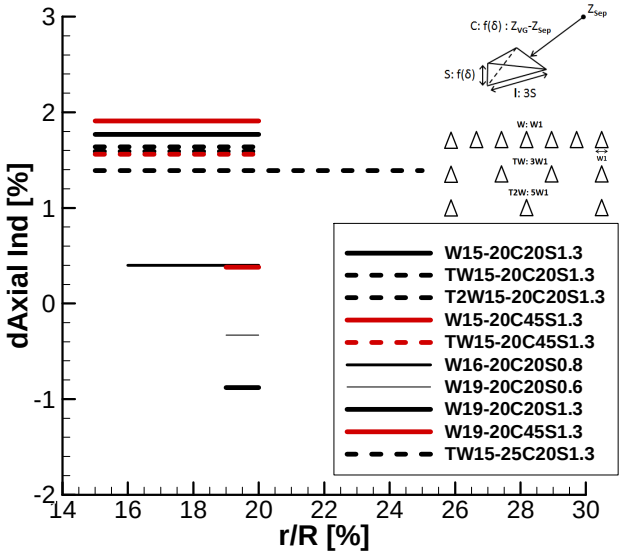

Figure 5-161 changes in local axial induction factor due to the wedge installation, Geometry= NREL 5MW, Ws: 9m/s, omega: 10.3rpm, turbulence model: SST γ – θ

5.7.5 Summary

Based on this investigation, it was found that up to 0.20% improvement in rotor power (Figure 5-162) is possible with the wedges installed over a small span range (1%). For a gain in rotor power, the wedges should be placed closer to the TE (Z/δ= 20) with a design wedge height of 1.3δ. An interval spacing of w/w_1=1 is recommended.

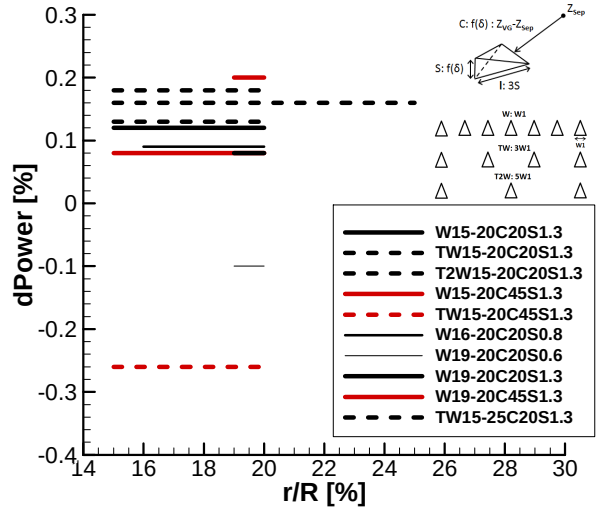

Figure 5-162 changes in rotor power due to the wedge installation, Geometry= NREL 5MW, Ws: 9m/s, omega: 10.3rpm, turbulence model: SST γ – θ

Following recommendations are made based on the results:

For better lift production:

- Place wedges to over a large span range (10%)
- Place wedges closer to the TE (C20)
- Minimum wedge height of 1.3δ is recommended
- Place wedges closer together (interval: w1)

For better axial induction:

- Place wedges to over a moderate span range (5%)
- Place wedges closer to the LE (C45)
- Design wedge height of 0.8-1.3δ is recommended
- Place wedges closer together (interval: w1)

For better drag reduction and better L/D ratio:

- Place wedges over a moderate span range (5%)
- Place wedges closer to the LE (C45)
- Design wedge height of 0.8-1.3δ is recommended
- Place wedges closer together (interval: w1)

For better power production:

- Place wedges to occupy a span range of 1% or 5%
- Place wedges closer to the TE (C20)
- Design wedge height of 1.3δ is recommended
- Adapt an interval spacing of w1 or 3w1

It was also decided that an investigation will be conducted on a mixed configuration of wedges to evaluate the performance when two configurations are combined together, in order to combine the benefits of two configurations. This case was composed of wedges placed at 20δ and 45δ from the baseline separation and covers the span location from 15-25% of the span. The wedges placed 45δ from the baseline separation were placed at outboard due to their low drag operation. The outer most wedges were replaced with a half wedges as it was expected to alleviate flow separation at that span location. The result suggests that this mixed configuration is able to reduce most of the hub separation (Figure 5-163) and up to 0.33% increase in rotor power is achievable with a combination of two configurations. This was the maximum design output seen from this investigation on wedges integrated to the NREL 5MW rotor, however further optimisation of the configuration may result in a higher output.

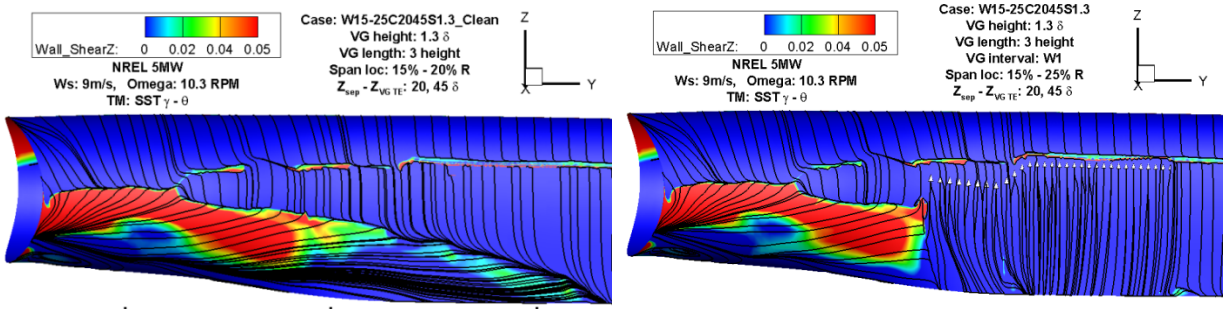

(a) **(b)**

Figure 5-163 Streamline pattern at the blade hub, , Ws: 9m/s, omega: 10.3rpm, turbulence model: SST γ – θ, wedge location: 15-20%, ΔZ_{VG} = 20δ and 45δ, height: 1.3δ interval spacing (a): w1, case (a): *W15-25C2045S1.3_Clean,* case (b): *W15-25C2045S1.3 - ΔPower: 0.33%,* displayed span range: r/R=0.05 – 0.30

5.7.6 Annualised power output of the wedge type VG

Four cases were chosen to be assessed over the sub rated wind speed range, where the performance of the wedges at the off design points, as well as the changes in annual output, were evaluated (Figure 5-164). These cases were chosen based on their relative performances at the design point wind speed (9 m/s) i.e. designs that achieved the most beneficial power production.

The first case to be investigated was the mixed configuration (W15-25C2045S1.3) which corresponds to an increase in rotor power at the design wind speed of 0.33%. The second configuration was the wedges placed further from the baseline separation (45δ), over a small span range from 19 to 20% span (W19-20C45S1.3, dPower: 0.20%). The third and the fourth cases were modelled with the wedges placed closer to the baseline separation (20δ), over a moderate span range (15- 20%) with a w/w_1: 1 and 3 respectively - (W15-20C20S1.3, TW15-20C20S1.3, dPower: 0.18%, 0.12%), which will enable the assessment of the wedge spacing over the wind speed range.

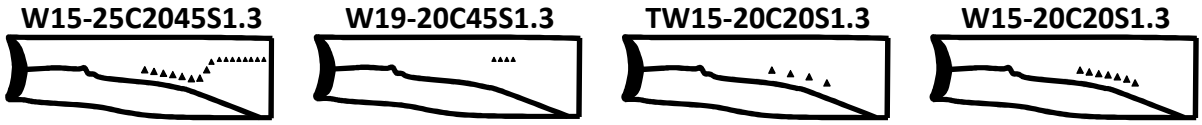

Figure 5-164 Sketches of the analysed cases

The result from this study (Table 5.7.6-15) suggest that even though the mixed configuration placed over a large span range between of 15% to 25% span is able to increase the rotor power output by 0.33% at the design wind speed, it is only able to increases the AEP by 0.05%. This is mainly because this configuration fails to improve the local aerodynamics at high wind speed. At the large wind speed of 11m/s this configuration of wedges generates large separations that severely affect the performance of the blade (Figure 5-165). When the wedges are positioned to only cover a small span range (19-20%), it was noted that the wedges are effective within all the tested wind speed range and generate an increase on AEP of 0.19%.

Changes in rotor power relative to clean blade (%)				
Wind speed (m/s)	**W15-25C2045S1.3**	**W19-20C45S1.3**	**W15-20C20S1.3**	**TW15-20C20S1.3**
5	+0.01	+0.05	+0.05	+0.13
7	+0.15	+0.13	+0.21	+0.14
9	+0.33	+0.20	+0.12	+0.18
11	-0.08	+0.94	+0.74	+0.76
AEP (%)	**+0.05**	**+0.19**	**+0.16**	**+0.16**

Table 5.7.6-15 Annual yield analysis for the wedge installed NREL 5MW

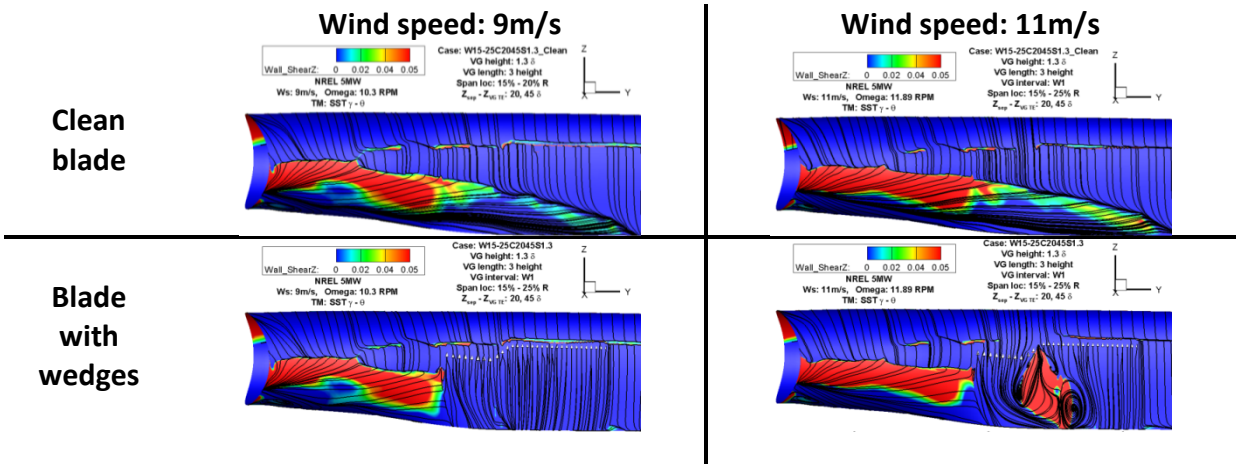

Figure 5-165 changes in flow topology at different wind speed due to the wedge installation, Geometry= NREL 5MW, Ws: 9m/s (left), 11m/s (right), omega: 10.3rpm (left), 11.8rpm (right), TM: SST γ – θ, r/R=0.05 – 0.30

The blade lift distribution showed that the mixed configuration (W15-25C2045S1.3) achieved the largest increase in lift force of up to 26% at r/R=0.10 for the lowest wind speed of 5m/s (Figure 5-166). The TW15-20C20S1.3 case showed the second best performance in terms on lift increase at the 10% blade span for the low wind speed where it achieved about 3% increase in local lift production. The worst performance was seen for the W15-20C20S1.3 case, where it showed to reduce local lift production by up to 30% at 10% blade span for the 5m/s wind speed. At 7 m/s wind speed all the tested cases generated beneficial lift increment within 4% at the blade root (10-30% span), while the influence on the outboard blade was minimal (<1%). The wedges placed over a small span range of 1% (W19-20C45S1.3) showed to have the lowest influence on the lift production below 1% within the lower wind speeds below 9m/s (Figure 5-166). Only at 7m/s it showed to reduce lift production by 2% at 10% span, while all other changes in lift was found to be below 1% at lower wind speeds.

At larger wind speed of 11m/s considerable changes in lift forces due to the wedge integration were seen at the root (10-30% span) and tip part (75-85% span) of the blade (Figure 5-166). The W15-25C2045S1.3 showed the worst performance in terms on reduction in lift forces at the blade root. Up to 8% reduction in lift forces were seen for this mixed configuration, this is mainly due to the large separated flow induced by this configuration at this high wind speed (Figure 5-165). All other three cases were able to increase the lift forces at the outboard section of the blade by up to 2%. Based on this result it can be suggested that the wedges effect on the outboard blades lift forces increase with wind speed.

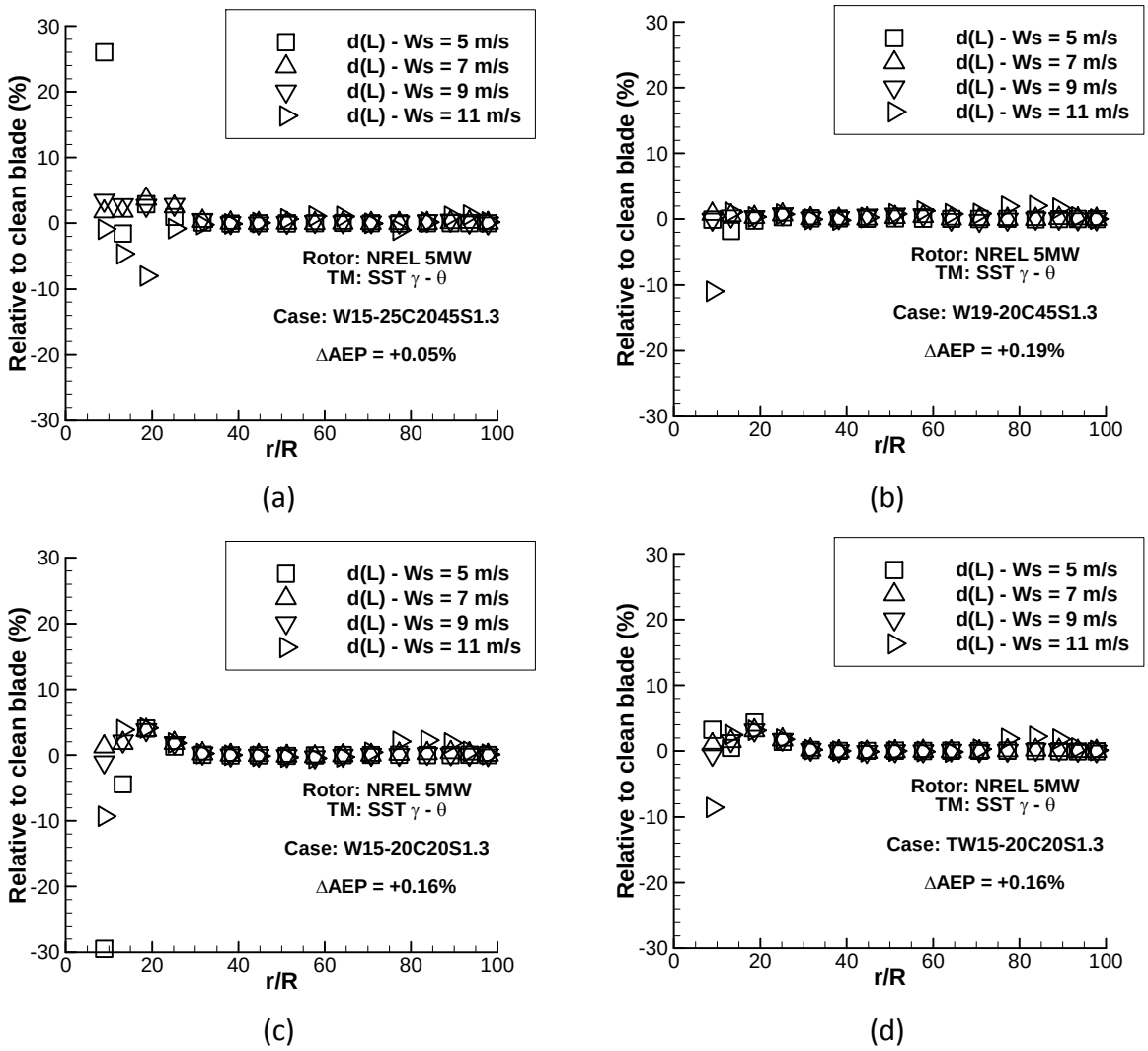

Figure 5-166 changes in blades lift forces at different wind speed due to the wedge installation, case - (a): W15-25C2045S1.3, (b): W19-20C45S1.3, (c): W15-20C20S1.3, (d): TW15-20C20S1.3

The drag distribution along the blade span for the blade with the wedges (Figure 5-167) showed that the wedges installed over a small span range perform the best in terms on their changes to the drag production of the blade. At the low wind speed of 5m/s the W15-25C2045S1.3 and the W15-20C20S1.3 case reduced drag forces by up to 10% within 10-15% of the blade span. However the mixed configuration (W15-25C2045S1.3) showed up to 25% increase drag forces of the blade root especially at the 11m/s. At 7m/s where it achieved an attached flow regime it still contributed about 22% increase in drag force at r/R=0.25. In general, all of the tested configurations increased the blade drag production at the location of the wedges (r/R=0.25).

The drag production of the outboard blade was significantly affected by the wedges at larger wind speed above 7m/s (Figure 5-167). The mixed configuration was able to achieve up to 10% reduction in local drag forces with r/R= 0.50-0.65. Larger reduction up to 15% reduction in drag forces were seen with the wedge configuration all the other there configuration at 75-90% of the blade. The case with wedges placed over a small span (W19-20C45S1.3) showed to beneficially reduce the drag production of the out board blade sections (r/R>0.40) where it is able to combine the beneficial drag reduction of the mixed

configuration and the wedges placed over a moderate span (W15-20C20S1.3, TW15-20C20S1.3) over the sub rated wind speed range. This aids the W19-20C45S1.3 configuration to achieve a better gain in annual output of 0.19% (Figure 5-167).

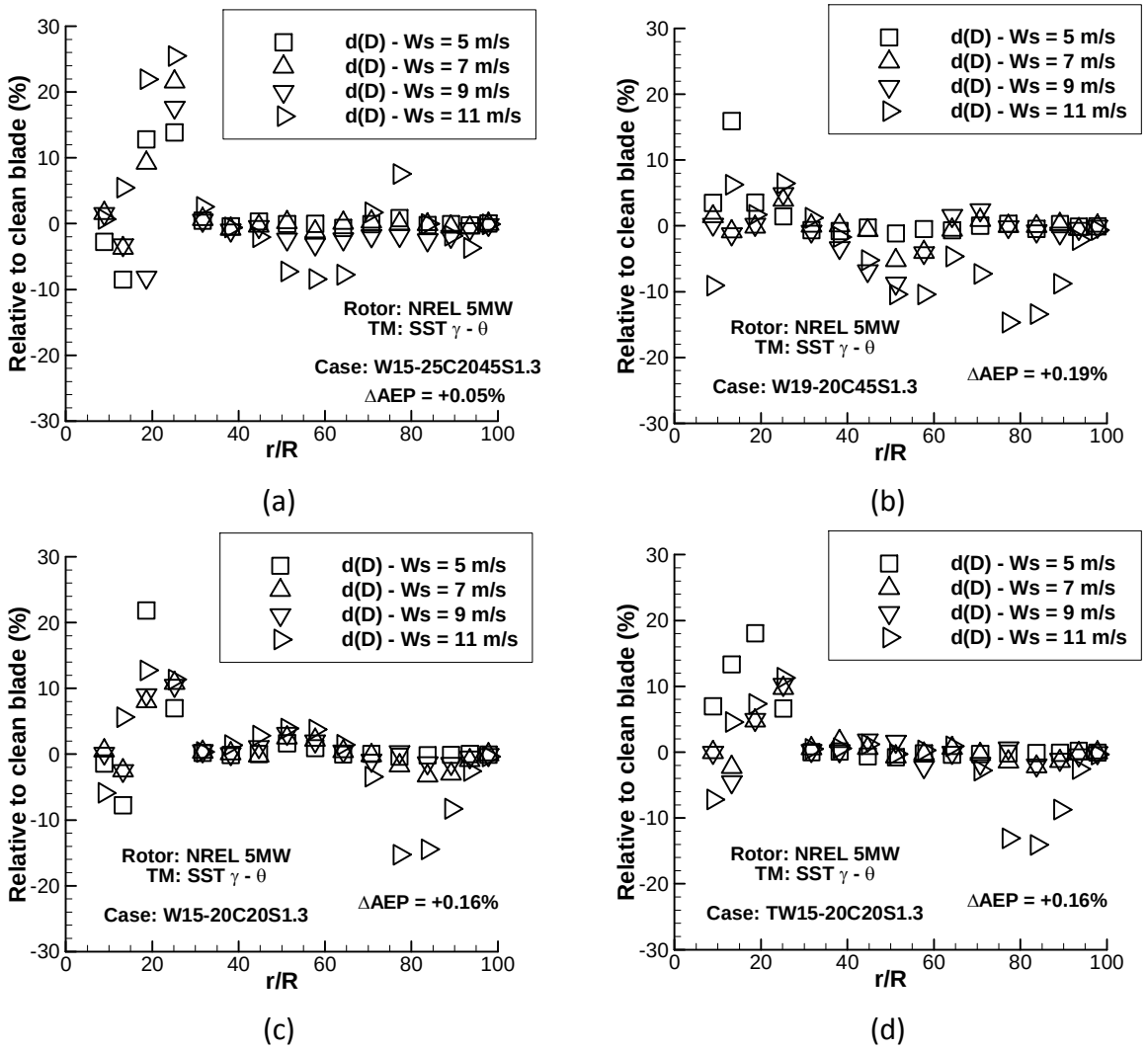

Figure 5-167 changes in blades drag forces at different wind speed due to the wedge installation, case - (a): W15-25C2045S1.3, (b): W19-20C45S1.3, (c): W15-20C20S1.3, (d): TW15-20C20S1.3

The lift to drag ratios distribution for the blade with the wedges (Figure 5-168) clearly shows the benefit of the wedges installed over a small span range (W19-20C45S1.3). In general, it was able to increase the lift to drag ratios by up to 20% of the outboard blade r/R>0.4, especially at the large wind speed of 11m/s. At the lower wind speeds it was able to increase the lift to drag ratios by 10% within r/R=0.40-0.60. However at the lowest wind speeds of 5m/s this configuration reduced the lift to drag ratios of the blade root by up to 15%. The mixed configuration (W15-25C2045S1.3) was found to show the most sensitive to the changes in lift to drag ratios of the blade root. It was able to increase the lift to drag ratios by up to 30% at 10% span for the low wind speed of 5m/s and then it was found to reduce the lift to drag ratios by up to 25% at the 20% span for the large wind speed of 11m/s.

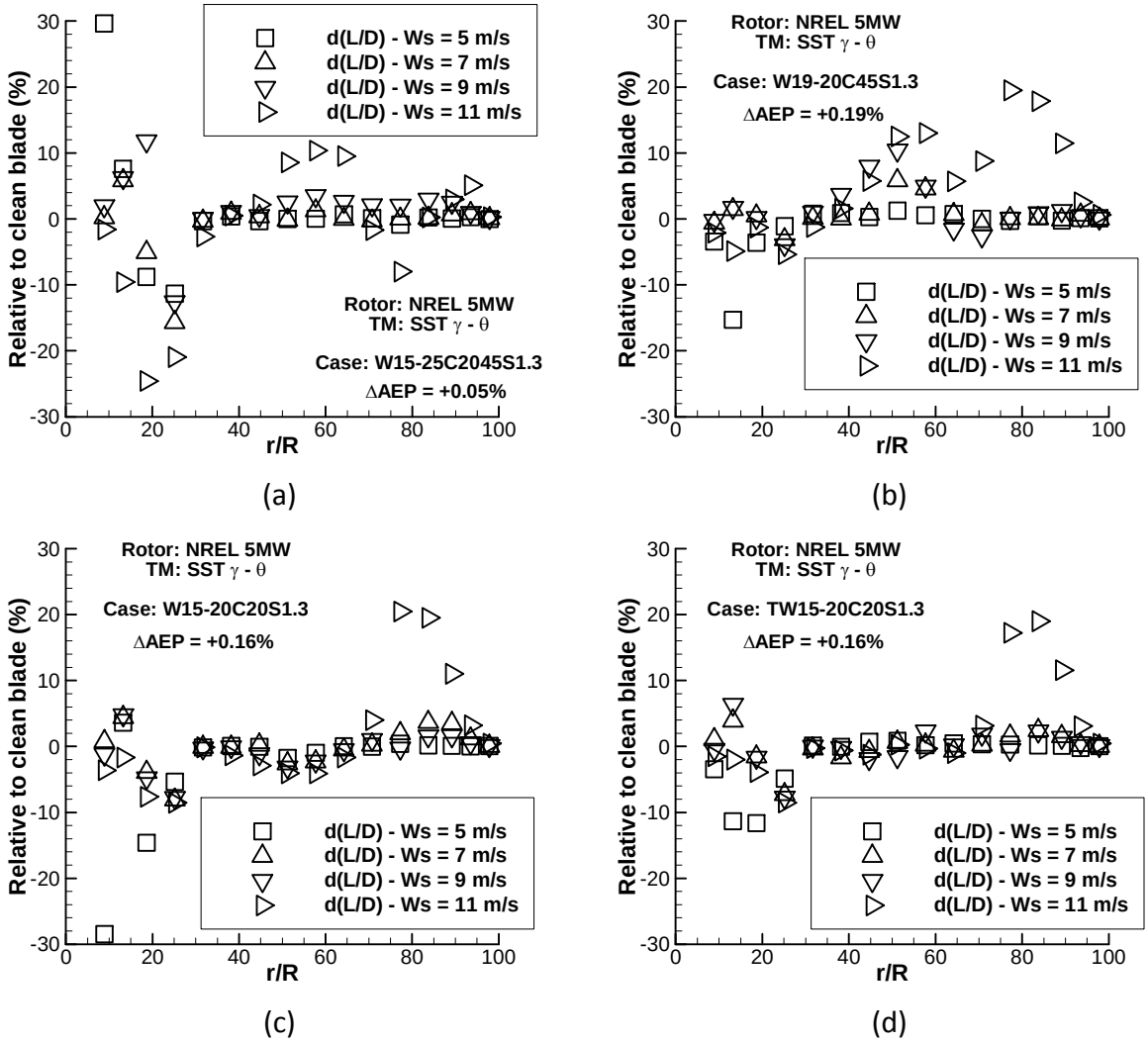

Figure 5-168 changes in blades lift to drag ratios at different wind speed due to the wedge installation, case - (a): W15-25C2045S1.3, (b): W19-20C45S1.3, (c): W15-20C20S1.3, (d): TW15-20C20S1.3

The lift to drag ratios distribution of from the NREL 5MW blade with the wedges installed over a moderate span (W15-20C20S1.3 and TW15-20C20S1.3) showed similar distributions (Figure 5-168) which is consistent with their change in AEP. The case with w=w1 (W15-20C20S1.3) showed to reduce lift to drag ratios by up to 30% at the 10% span for the low wind speed of 5m/s, where the w=3w1 (TW15-20C20S1.3) wedges reduced the lift to drag ratios by 15% at this condition. It was also seen that a better lift to drag ratios were achieved with less number of wedges that the W15-20C20S1.3 case at the location of the wedge (r/R= 0.20).

The TW15-20C20S1.3 case with an interval spacing of $w/w_1=3$ was found to reduce lift to drag ratios within 5% for the wind speeds below the 9m/s at the span location of r/R=0.2 while the W15-20C20S1.3 was found to reduce the lift to drag ratio by up to 10% at these conditions. However the interval spacing of $w/w_1=1$ (W15-20C20S1.3) wedges achieved a better lift to drag ratios at r/R=0.80-0.90 than the TW15-20C20S1.3 ($w/w_1=3$) throughout the wind speed range, this benefits seems to equal the negative aerodynamic found at the blade root and enables it to achieve the same AEP change as the TW15-20C20S1.3 case.

The axial induction factor dictates the incoming flow to the blade i.e. it controls the local angle of attack and the flow velocity. The results clear suggest that the blade with the wedges significantly effects the local axial induction of the blade root over the wind speed range (Figure 5-169). The mixed configuration (W15-25C2045S1.3) showed to increase the local axial induction by up to 15% at r/R=0.10 blade span, when it is operating at the design point wind speed. This contributed to about 0.36% increase in rotor output. However due to its poor performance in terms of flow separation found at the high wind speed of 11m/s it reduces the roots axial induction by up to 4.5%. All the other case investigated showed to beneficially increase the local axial induction of the blade throughout the wind speed range. Up to 10% increase in local axial induction was seen at the blade root for the W15-20C20S1.3 and TW15-20C20S1.3 cases.

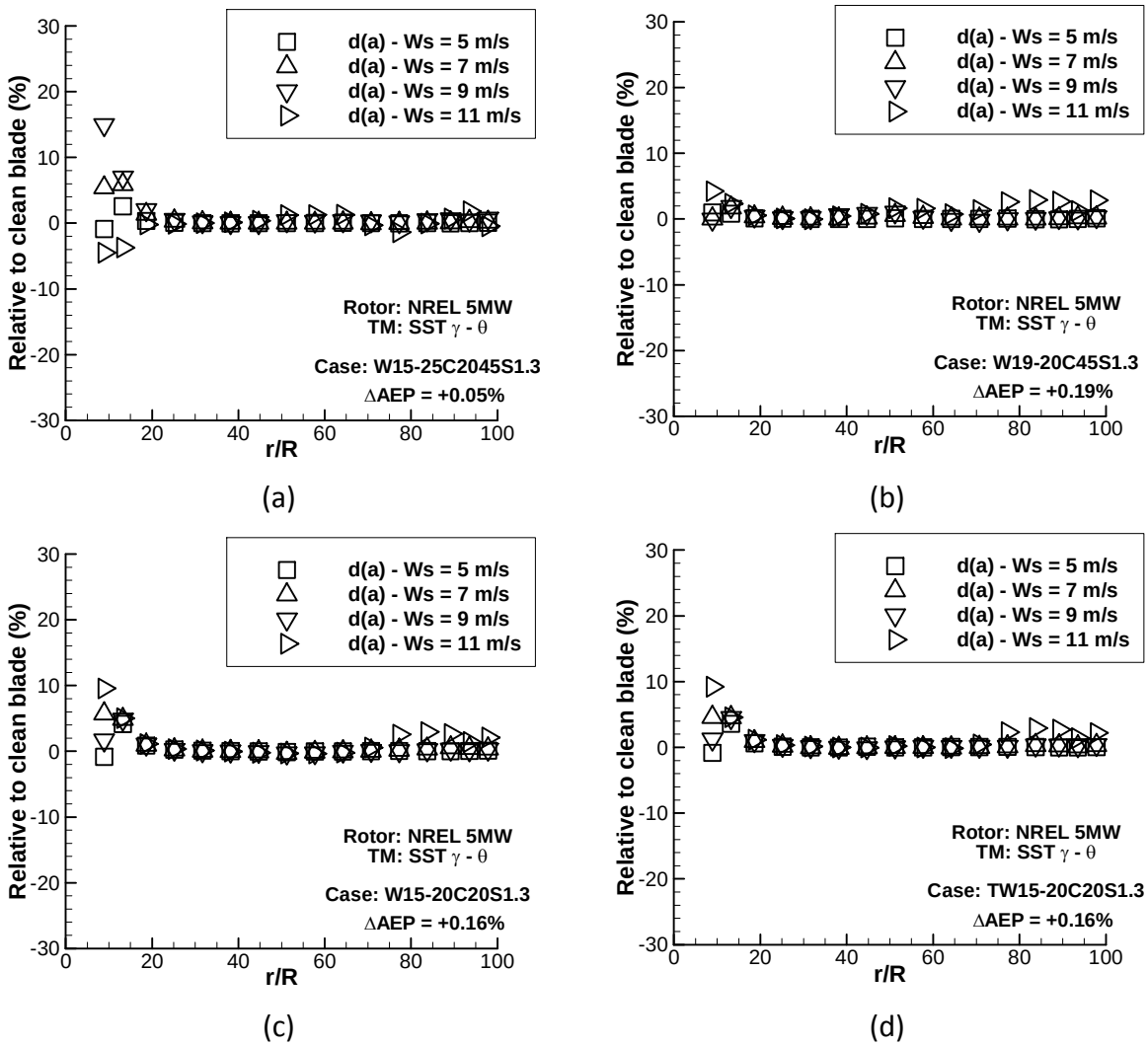

Figure 5-169 changes in blades local axial induction at different wind speed due to the wedge installation, case - (a): W15-25C2045S1.3, (b): W19-20C45S1.3, (c): W15-20C20S1.3, (d): TW15-20C20S1.3

This investigation has also shown that wedges significantly change the local axial induction outboard, which is the main cause of change in the outboard aerodynamics forces presented here. With the wedges placed over a small span range of r/R=0.19-0.2 (W19-20C45S1.3), up to 3% increase in local axial induction were seen at the blade tip r/R=0.85 for the higher wind speed of 11m/s. This corresponds to very small reduction in local relative

velocity (-0.01m/s) with about 1^{o} change in angle of attack. These reductions seem to increase the lift to drag ratios by up to 20% within this region of the blade. With a small increase in root lift to drag ratio of about 2% and the 20% at the blade tip the W19-20C45S1.3 at high wind speed of 11m/s, it is able to achieve the largest increase in AEP of 0.19%.

5.7.7 Conclusion for the wedge placed on the NREL 5MW

This extensive study to find a structurally robust VG for the baseline rotor has been successful. The backward wedge type VG which encloses a larger volume of material with an increased gluing area is identified to perform similar to a vane VGs that is conventionally used for a wind turbine. It was found that a vane VG can improve the design point rotor power by 0.23%, while the wedges achieved 0.20% increase in rotor output. The result from this study has suggested that this wedge type VGs can be used to reduce the radial flow migration and the flow separation found at the blade root. Ultimately the wedge type VGs have the potential to increase the AEP of the NREL 5MW rotor by 0.19%. This corresponds to about 467,000kWh of increase in annual yield. Based on European Wind Energy Associations (EWEA) cost per kWh [80] (7c€/kWh) the wedge installed NREL 5MW can contribute about €30,000 worth of additional energy production per annum per turbine.

5.8 Discussion and recommendation on the investigated PFC devices

This part of the thesis will discuss and summarise all the technologies presented earlier with regards to its applicability to wind turbine integration.

5.8.1 Vortex trapping devices

The 2D CFD study shows that the Fertis's suction side step does not offer any aerodynamic benefit. Based on the results, this device decreases lift and increases the drag force. The investigation has also identified uncertainty on the credibility of the experimental work by Fertis.

The CFD model for the pressure side step device has shown improvement to lift production at all the tested angles of attack. The results also show that the pressure side step modification also increases drag at all the tested angle of attack. The investigation has shown that, a simple increase in camber may provide better benefits (increased aerodynamic efficiency) than this device. The pressure side step modification showed to increase lift and drag forces by up to 10 and 80% respectively at the AoA of 5^{o}, where with a simple increase in camber by 2% showed to increase lift forces by 20% and beneficially reduce drag forces by 7%. For this reason this device is not recommended for a wind turbine application.

As anticipated, the 3D version of the Fertis's step device (extruded step), was seen to capture a vortex within the step geometry. The interesting finding was that even with this crude design, up to 40m/s radial flow were generated within the step geometry. This allows the captured vortex to perform effectively without the need for the mass removal at the core of the vortex, which was reported to be essential in the vortex capturing technique [16]. Both of the tested step designs failed to improve the power production of the baseline rotor or to produce benefits on a sectional basis.

The only vortex trapping device that can be recommend for further study is the extruded suction side step, where the large radial flow within the step geometry may also be used to drive a device such as circulation control device at the blade tip to generate positive torque production.

5.8.2 Passive ventilation

This technique that was studied to utilise the local pressure difference was the passive air jet vortex generator (PAJVG). The baseline CFD model for the PAJVG's predicts the expected trends in lift coefficients, however the model fails to predicts the reduction in drag due to PAJVGs. Initially it was decided that the increase in lift due to PAJVG can be used to reduce blade chord. Based on a simple BEM assessment of the conventional vortex generator (VG) and PAJVG, the conventional VGs provide better chord reduction without the compromise on the power output than PAJVGs. This is mainly because VGs offer better drag reduction in the increased lift conditions than the PAJVGs. The installation of a conventional VG is less difficult than PAJVG's. All of these reasons suggest that it is not recommended for a wind turbine application.

5.8.3 Corrugated leading edge

The CFD work on the corrugated leading edge wing has revealed that the baseline CFD model for this device is not adequate to replicate the measurement found at the low Reynolds number. The benefit of the corrugated leading edge was found at the post stall condition, where large drag forces are present. The experimental measurement showed that the increase in lift due to this leading edge modification is attained with the increase in drag, at the large AoAs. This behaviour is not beneficial for a wind turbine.

It should be noted that this device's effectiveness at high Reynolds number were not assessed. The time frame required to obtain an adequate CFD model to assess this technology was not permissible for this project. A low Reynolds number unsteady CFD model may help to validate the effects of this technology as it will be able to calculate the unsteady nature of the flow found at the post stall AoA.

5.8.4 Passive flow control devices for a wind turbine blade root

An initial assessment of the root strake has shown that it can help to reduce both secondary flow and hub separation. Results from the CFD simulations suggest that a root chine is capable of generating a large vortex that is able to oppose the radial flow and reduce the hub separation. The chine was found to be beneficial only at wind speeds above 7m/s. Based on an extensive parametric design study, a chine with height of 2% chord, length of 30% chord, placed at 50% chord, 20% blade span and toe angle of 20^{o} was seen as the best performing design. This design is able to increase the annual power production (AEP) of the NREL 5MW turbine by a small 0.05%. This corresponds to about €1,000/annum worth of additional energy production of the turbine. The result from the chine was compared against fences, which also helps to reduce the secondary flow. It was found that a better performance in annual power can be achieved with the fences than a root chine.

The second assessment was carried out to identify a structurally robust vortex generator, which can be used to reduce the radial flow as well as reattaching the separated flow at the blade hub. Initial studies on various VG design revealed that a backward wedge type VG is

capable of achieving similar performance of a vane VG that is conventionally used in wind turbine but due to the larger volume of material that a wedge holds, it is structurally resistant to bending or breaking. The comparative study between the vane VG and the wedge VG reveals that the vortices created by the wedges lie closer to the wall than the vane VG. Consequently wedges are expected to have the potential to be more effective in controlling boundary layer separations. It was found that wedges are able to perform effectively within adverse pressure gradient up to 5.9 when integrated to a wind turbine blade (cross flow environment). When the wedges are installed on an airfoil in an axial flow, the wedges were found to be effective up to an adverse pressure gradient of 18. Based on an extensive CFD study to assess the design space of the backward wedge, various suggestions have been established for the wedge to be used as a lift increment or a drag reduction device. For a gain in rotor power, the wedges should be placed at Z/δ =45 with a design wedge height of h/δ =1.3. An interval spacing of w/w_1=1 is recommended. It was found that up to 0.20% improvement in rotor power at the design wind speed is possible with the wedges installed over a small span range (1%), which corresponds to 0.19% increase in AEP for this device. A maximum increase of about 0.33% in design point output was noticed with a mixed configuration, however it only achieved a small increase in AEP of 0.05% as this design was detrimental at the higher wind speed of 11m/s. A further study to investigate the mixed configuration to address the flow separations caused at the higher wind speed will enable to wedges to achieve AEP increases greater than 0.19%.

5.9 Conclusion

Based on this investigation to find a PFC device for a wind turbine application, it was found that the wedge type VGs offer the most benefit in operation. The wedge type VGs can be used to increase lift or be used as a drag reduction device. It has the potential to reduce the spanwise flow migration found at the blade root while suppressing the flow separation. They are very small in size relative to a root strake, chine or a fence. Only a small number of wedges, up to 5, placed over the 19-20% of the blade span are required to improve the AEP of the NREL 5MW by 0.19%. Based on this result it was found that the wedge installed NREL 5MW can contribute about €30,000 worth of additional energy production per annum per turbine.

It is also noted that the wedges have shown to improve the power production at the lowest tested wind speed of 5m/s (dPower=0.13%), and it is hypothesised that the wedges may improve the power output at the cut-in wind speed of 3m/s, which means that the starting torque for the baseline rotor may be achieved at a lower wind speed than 3m/s. This suggests that the wedge implementation may help to start the turbine at a lower wind speeds and contribute further increases to the AEP.

6 Research conclusions and future work

The effect of incorporating a passive flow control (PFC) device for a large scale horizontal axis wind turbine has been investigated. Based on the literature survey to date it was found that there is a lack of knowledge on PFC for wind turbine. To address this, eleven potential technologies were identified and four concepts were down selected for further research. These were the vortex trapping device, passive ventilation, corrugated leading edge and the vortex generators. Based on the finding from this work, the main focus of this research was dedicated to improving the root part of the blade using a PFC device. The conclusion after a several evaluative refinements of the chosen devices, it was finally down selected to two types of vortex generators, which are recommended for a wind turbine blade integration. These technologies are found to be beneficial for the root part of the blade and they are studied as the root chine and wedges vortex generators on this thesis. All other technologies evaluated in this study were found to be either not directly applicable for a wind turbine blade or the baseline CFD model used to investigate these devices was unable to replicate the reported benefits.

Vane vortex generators are typically used in the blade root to address this large flow separation [12], however due to the thin nature of the vane VGs they are prone to breaking and coming off the blade surface. There is a lack of knowledge on application of VGs for a wind turbine in the open literature. There has been only one literature [74] found to discuss the effect of a pair of vane VGs for a wind turbine blade, based on a non-rotating wind turbine CFD simulation. In this thesis however, various type of VGs were investigated on a wind turbine airfoil and the effect of three pairs of vane VGs were quantified from a rotation modelled rotor. Additionally a wedge type VG was identified to address the structural issues with the conventional vane VGs as the wedges enclose a larger volume of material. There has been no literature to date that presents the effect of wedge VG integration for a wind turbine. The structurally robust wedge vortex generator was found to operate as efficient as a vane VGs conventionally used for a wind turbine. Up to 0.2% increase in AEP of the NREL 5MW rotor is attained, incorporating wedge VGs at the blade root, which corresponds to about €30,000 worth of additional energy production of the turbine per annum. It should be noted that the structural impact of incorporating a wedge VGs were not assessed and it was found that outboard blade loads are affected when the wedges are installed at the blade root, therefore a structural assessment of the entire blade with wedge VGs should be conducted before application of these wedges.

Novel aspects from this research are:

- The effect of incorporating a root chine for a large-scale wind turbine is quantified
- The effect of incorporating the wedge type VGs for a large-scale wind turbine is quantified
- The initial design space of the root chine and a wedge type VGs was established
- The effect of modelling boundary layer transition for a large scale rotor simulations is quantified
- The improvements to the conventional twist optimisation method typically used in the industry were identified and quantified
- Possible chord reductions and their structural impact due to VG and PAJVG integrations are quantified

The flowing area of research has been identified for future work:

1. Optimisation of mixed configuration of the wedge VG for a wind turbine blade
2. Assess the improvement in starting torque using wedges and quantity the increment in AEP due to the lower cut-in speed operation
3. Investigate the use of extruded step configuration to drive a circulation control device for the blade tip
4. Structural impact of incorporating wedge VGs at the blade root
5. The effect of weather (raining or icing) on the performance of rotor with wedge VGs
6. CFD calculation of a wind turbine blade with optimum twist determined using conventional and improved twist optimisation methods.

7 References

[1] Kisorthman V., Jason J. and Marshall B., (Last accessed: Thu Jan 27, 2011 1:36 pm), *NREL 5MW Rotor Geometry*, Available from: https://wind.nrel.gov/forum/wind/viewtopic.php?f=2&t=440, NWTC.

[2] J. Jonkman, S. Butterfield, W. Musial, and G. Scott (2009), *Definition of a 5-MW Reference Wind Turbine for Offshore System Development,* Technical Report NREL/TP-500-38060, NREL, National Renewable Energy Laboratory 1617 Cole Boulevard, Golden, Colorado.

[3] De Gregorio, F. and Fraioli, G. (2008), "Flow control on a high thickness airfoil by trapped vortex cavity", *Proc.of 14th International Symposium on Laser Application to Fluid dynamics, Lisbon*.

[4] Chow, R., and van Dam, C.P., "Inboard Stall and Separation Mitigation Techniques on Wind Turbine Rotors," 49th AIAA Aerospace Sciences Meeting, Orlando, FL, Jan. 2011.

[5] Johnson, S.J., van Dam, C.P., and Berg, D.E. Active load control techniques for wind turbines. Technical Report SAND2008-4809, Sandia National Laboratories, August 2008.

[6] Barrett, R. and Farokhi, S. (1996), "Subsonic aerodynamics and performance of a smart vortex generator system", *Journal of Aircraft,* vol. 33, no. 2, pp. 393-398.

[7] Gad-el-Hak, M. (2000), *Flow control: passive, active, and reactive flow management,* Cambridge, UK: Cambridge Univ. Press.

[8] Godard, G. and Stanislas, M. (2006), "Control of a decelerating boundary layer. Part 1: Optimization of passive vortex generators", *Aerospace Science and Technology,* vol. 10, no. 3, pp. 181-191.

[9] Johansen, J. and Sørensen, N. N. (2006), "Aerodynamic investigation of winglets on wind turbine blades using CFD", *Risø National Laboratory, Risø-R-1543(EN) report*.

[10] Lin, J. C. (2002), "Review of research on low-profile vortex generators to control boundary-layer separation", *Progress in Aerospace Sciences,* vol. 38, no. 4-5, pp. 389-420.

[11] GP Corten (2007), "Vortex Blades", *Proc. from WindPower 2007,* June 4, 2007, Los Angeles, USA.

[12] Fuglsang, P., Antoniou, I., Dahl, K. S. and Madsen, H. A. (1998), "Wind tunnel tests of the FFA-W3-241, FFA-W3-301 and NACA 63-430 airfoils", *RISO-REPORTS-RISO R*.

[13] McCullough, G. B., Nitzberg, G. E. and Kelly, J. A. (1951), "Preliminary investigation of the delay of turbulent flow separation by means of wedge-shaped bodies", NACA Research Memorandum.

[14] Kruppa, E. W. (1977), "A wind tunnel investigation of the Kasper vortex concept", *AIAA paper 115704,* pp. 77–310, Washington D.C., DOI: 10.2514/6.1977-310.

[15] Rossow, V. J. (1978), "Lift enhancement by an externally trapped vortex", *Journal of Aircraft,* vol. 15, no. 9, pp. 618-625.

[16] Rossow, V. J. (1992), "Lift enhancement by trapped vortex", *In NASA. Langley Research Center, First Annual High-Speed Research Workshop,* Part 4 p 1791-1806 (SEE N 94-33517 10-02).

[17] Fertis, D. G. (1994), "New airfoil-design concept with improved aerodynamic characteristics", *Journal of Aerospace Engineering,* vol. 7, no. 3, pp. 328-339.

[18] Lazauskas, L. and Kirke, B. (1995), "Discussion of" New Airfoil-Design Concept with Improved Aerodynamic Characteristics"", *Journal of Aerospace Engineering,* vol. 8, no. 4.

[19] Yeung, W.W.H. (2006), "Lift enhancement on unconventional airfoils", *Jurnal Mekanikal,* pp. 17-25.

[20] Khan, Z. U. and Johnston, J. P. (2000), "On vortex generating jets", *International Journal of Heat and Fluid Flow,* vol. 21, no. 5, pp. 506-511.

[21] Tensi, J., Bourgois, S., Bonnet, J., Breux, J. and Siauw, W. (2007), "Airfoil Performance Enhancement Using Fluidic Actuators", *Laboratoire d'Etudes Aérodynamiques UMR,* vol. 6609.

[22] Prince, S. A., Khodagolian, V., Singh, C. and Kokkalis, T. (2009), "Aerodynamic stall suppression on airfoil sections using passive air-jet vortex generators", *AIAA Journal,* vol. 47, no. 9, pp. 2232-2242.

[23] C P van Dam (2008), "*Research on Thick Blunt* Trailing Edge Wind Turbine *Airfoils*", *2008 Wind turbine blade workshop, Sandia National Laboratories,* Vol. nv, 2008, University of California, UC Davis, UC Davis, College of engineering, California, USA.

[24] Lim, H. -. and Lee, S. -. (2004), "Flow control of a circular cylinder with O-rings", *Fluid Dynamics Research,* vol. 35, no. 2, pp. 107-122.

[25] Watts, P. and Fish, F. E. (2001), "The Influence of Passive, Leading Edge Tubercles on Wing Performance", *Proceedings of the Twelfth International Symposium on Unmanned Untethered Submersible Technology (UUST), UUST01*.

[26] Hansen, K. L., Kelso, R. M. and Dally, B. B. (2011), "Performance variations of leading-edge tubercles for distinct airfoil profiles", *AIAA Journal,* vol. 49, no. 1, pp. 185-194.

[27] Choi, H., Jeon, W. and Kim, J. (2008), "Control of flow over a bluff body", *Annu.Rev.Fluid Mech.,* vol. 40, pp. 113-139.

[28] Achenbach, E. (1971), "Influence of surface roughness on the cross-flow around a circular cylinder", *Journal of Fluid Mechanics,* vol. 46, no. 2, pp. 321-335.

[29] Pollard, A. (1998), "Passive and active control of near-wall turbulence", *Progress in Aerospace Sciences,* vol. 33, no. 11-12, pp. 689-708.

[30] Bechert, D. W., Bruse, M., Hage, W., Van Der Hoeven, J. G. T. and Hoppe, G. (1997), "Experiments on drag-reducing surfaces and their optimization with an adjustable geometry", *Journal of Fluid Mechanics,* vol. 338, pp. 59-87.

[31] Dean, B. and Bhushan, B. (2010), "Shark-skin surfaces for fluid-drag reduction in turbulent flow: A review", *Philosophical Transactions of the Royal Society A: Mathematical, Physical and Engineering Sciences,* vol. 368, no. 1929, pp. 4775-4806.

[32] Cavanaugh, M. A., Robertson, P. and Mason, W. H. (2007), "Wind tunnel test of gurney flaps and T-strips on an NACA 23012 wing", *25th AIAA Applied Aerodynamics Conference, 2007,* Vol. 2, 25 June 2007 through 28 June 2007, Miami, FL, pp. 1060.

[33] Horner, F. and Borst, H. "Fluid dynamic lift, Horner Fluid Dynamics (1975)", *PO Box,* vol. 342, pp. 2–17.

[34] Standish, K. J. and Van Dam, C. P. (2003), "Analysis of blunt trailing edge airfoils", *ASME 2003 Wind Energy Symposium, WIND2003,* 6 January 2003 through 9 January 2003, Reno, NV, pp. 32.

[35] Baker, J. P., Mayda, E. A. and Van Dam, C. P. (2006), "Experimental and computational analysis of thick flatback wind turbine airfoils", *44th AIAA Aerospace Sciences Meeting 2006,* Vol. 4, 9 January 2006 through 12 January 2006, Reno, NV, pp. 2333.

[36] Park, H., Lee, D., Jeon, W. -., Hahn, S., Kim, J., Kim, J., Choi, J. and Choi, H. (2006), "Drag reduction in flow over a two-dimensional bluff body with a blunt trailing edge using a new passive device", *Journal of Fluid Mechanics,* vol. 563, pp. 389-414.

[37] Thiria, B., Cadot, O. and Beaudoin, J. -. (2009), "Passive drag control of a blunt trailing edge cylinder", *Journal of Fluids and Structures,* vol. 25, no. 5, pp. 766-776.

[38] Hartwich, P.M., (1992), "Porous airfoil and process"*, US Patent 5,167,387*.

[39] James F. Manwell, Jon G. McGowan and Anthony L. Rogers (2009), *Wind Energy Explained: Theory, Design and Application,* 2nd ed, John Wiley and Sons.

[40] Leishman, J. G. (2006), *Principles of helicopter aerodynamics,* Cambridge, UK: Cambridge Univ. Press.

[41] Widjanarko, S. (2010), "Internship Vestas Wind system A/S: steady blade element momentum code for wind turbine design validation tool", University of Twente.

[42] Wilson, R. E., Lissaman, P. B. S. and Walker, S. N. (1976), "Aerodynamic performance of wind turbines", *Oregon State University*.

[43] Moriarty, P. J. and Hansen, A. C. (2005), *Aerodyn theory manual*, NREL/EL-500-36881, Golden, CO: National Renewable Energy Laboratory.

[44] Hansen, M. O. L. (2008), *Aerodynamics of wind turbines,* Earthscan/James & James.

[45] Glauert, H. (1943), "Airplane Propellers, Vol. 4, Div. L in Aerodynamic Theory, edited by Durand WF", Dover ed.

[46] Buhl, M. L. and National Renewable Energy Laboratory (US) (2005), *A new empirical relationship between thrust coefficient and induction factor for the turbulent windmill state,* National Renewable Energy Laboratory.

[47] Andrew, P., (Last modified 26-November-2012; accessed 26-November-2012.), *NWTC Design Codes (WT_Perf by Andrew Platt)*, NREL, http://wind.nrel.gov/designcodes/simulators/wtperf/.

[48] Platt, A. and Buhl Jr, M. (2012), *WT_Perf User Guide for Version 3.05. 00*, Golden, CO: National Renewable Energy Laboratory.

[49] Hau, E. (2010), "Wind Turbines: Fundamentals, Technologies, Application, Economics", Springer, Berlin.

[50] Abbott, I. H. A. and Von Doenhoff, A. E. (1959), *Theory of wing sections, including a summary of airfoil data* Dover Publications, New York.

[52] H K Versteeg and W Malasekera (2007), "An introduction to computational fluid dynamics, The finite volume method", in 2nd edition ed, pp. 294.

[53] T Saad (n.d), *Turbulence modelling for beginers,* , University of Tennessee Space Institute.

[54] Yakhot V, Orszag S.A., Thangam S., Gatski T.B. and Speziale, C. G. (1992), "Development of turbulence models for shear flows by a double expansion technique", *Physics of Fluids,* vol. 4, no. 7, pp. 1510-1520.

[55] Wilcox, D. C. (1998), "Re-assessment of the scale-determining equation for advanced turbulence models", *AIAA Journal,* vol. 26, no. 11, pp. 1299-1310.

[56] Wilcox, D. C. (1998), "Turbulence Modeling for CFD", 2nd ed, Anaheim: DCW Industries, pp. 174.

[57] Menter, F. R. (1993), "Zonal Two Equation k-ω Turbulence Models for Aerodynamic Flows", *AIAA Paper 93-2906*.

[58] Menter, F., Langtry, R., Likki, S., Suzen, Y., Huang, P. and Völker, S. (2006), "A correlation-based transition model using local variables-Part I: model formulation", *Journal of Turbomachinery,* vol. 128, no. 3, pp. 413-422.

[59] Speziale, C. G., Sarkar, S. and Gatski, T. B. (1991), "Modelling the pressure–strain correlation of turbulence: an invariant dynamical systems approach", *Journal of Fluid Mechanics,* vol. 227, no. 1, pp. 245-272.

[60] Ansys, C. (2012), *Release 14.5. Ansys CFX-Solver Theory guide,* ANSYS Inc., Canonsburg, PA.

[61] Somers, D. M. (1989), "Design and experimental results for the S809 airfoil", *Airfoils, Inc. State College, PA*.

[62] Nando, T. (2011), DU Airfoil Data, [email]. Personal communication. (13/01/2011)

[63] Wolfe, W. P. and Ochs, S. S. (1997), "CFD calculations of S809 aerodynamic characteristics", Proceeding 35th AIAA Aerospace Sciences Meeting and Exhibit, Reno.

[64] P. J. Roache (1997), "Quantification of Uncertainty in Computational Fluid Dynamics", *Annu. Rev. Fluid. Mech,* vol. 29:123–6.

[65] Spalart, P. and Shur, M. (1997), "On the sensitization of turbulence models to rotation and curvature", *Aerospace Science and Technology,* vol. 1, no. 5, pp. 297-302.

[66] Sørensen, N. N. and Johansen J. "UPWIND, Aerodynamics and Aero-elasticity Rotor Aerodynamics in AtmosphericShear Flow", May 2007, Milan, Italy.

[67] H.P Horton (1968), *Laminar separation bubbles in two and three dimensional incompressible flow* (PhD thesis), Queen Mary College, United Kingdom.

[68] Langtry, R., Gola, J. and Menter, F. (2006), "Predicting 2D airfoil and 3D wind turbine rotor performance using a transition model for general CFD codes", *44th AIAA Aerospace Sciences Meeting and Exhibit,* pp. 2006.

[69] Finaish, F. and Witherspoon, S. (1998), "Aerodynamic performance of an airfoil with step-induced vortex for lift augmentation", *Journal of Aerospace Engineering,* vol. 11, no. 1, pp. 9-16.

[70] H. Johari, C. Henoch, D. Custodio and A. Levshin (2007), "Effects of Leading-Edge Protuberances on Airfoil Performance", *AIAA JOURNAL,* vol. 45, no. 11.

[71] Jacobs, E. N. and Sherman, A. (1937), *Airfoil section characteristics as affected by variations of the Reynolds number,* National Advisory Committee for Aeronautics.

[72] Johansen, J. and Sørensen, N. N. (2004), "Aerofoil characteristics from 3D CFD rotor computations", *Wind Energy,* vol. 7, no. 4, pp. 283-294.

[73] Fish, F.E. and Lauder, G.V., (2006), "Passive and active flow control by swimming fishes and mammals", Annual Review of Fluid Mechanics., vol. 38, pp. 193-224.

[74] Johansen, J., Sorensen, N., Reck, M., Hansen, M.O.L., Stuermer, A., Ramboer, J., Hirsch, C., Ekaterinaris, J., Voutsinas, S., and Perivolaris, Y., (2005), "Know-Blade task-3.3 report. Rotor blade computations with 3D vortex generators", Risø-R-1486 (EN).

[75] Sullivan, T. L. (1984), "Effect of vortex generators on the power conversion performance and structural dynamic loads of the Mod-2 wind turbine", *National Aeronautics and Space Administration Report,* vol. 1.

[76] Heinzelmann, B. S., Gollnick, B., Thamsen, P. U., Petsche, M., Christiansen, J. B., Heinzelmann, B. S. and Gollnick, B. *Investigation into boundary layer fences in the hub area of wind turbine blades,* , Technical University Berlin; REpower Systems AG; LM Glasfiber A/S.

[77] Schwetzler, D., (2008), *Engine Nacelle on a Aircraft Comprising a Vortex Generator Arrangement*, WO Patent WO/2008/151,843, Hamburg (DE).

[78] Rae, A., Galpin, S. and Fulker, J. (2002), "Investigation into scale effects on the performance of sub boundary-layer vortex generators on civil aircraft high-lift devices", *AIAA Paper,* vol. 3274, pp. 2002.

[79] Yao, C., Lin, J. C. and Allan, B. G. (2002), "Flow-field measurement of device-induced embedded streamwise vortex on a flat plate", *NASA STI/Recon Technical Report N,* vol. 3, pp. 12931.

[80] Søren , K., Poul-Erik , M. and Shimon , A. (March 2009), *The Economics of Wind Energy,* EWEA.

[81] E Ferrer and X Munduate (2007), "Wind turbine blade tip comparison using CFD", *The Science of Making Torque from Wind,* August 2007, Copenhagen (Denmark).

8 Appendix

8.1 Richardson's extrapolation

Roache [64] has proposed this approach in order to quantity the effect of mesh refinement. The method to study three different density meshes is outlined below.

There are three assumptions made for this analysis [52]:

1. No discontinuity in the flow variables
2. The convergence is monotonic
3. The numerical method is in its asymptotic range

The error in the CFD simulation can be estimated using:

$$E_U(h) = U_{exact} - U \approx Ch^p \qquad \text{Eqn 32.1.1.1}$$

Where U is the target quantity, C is a constant, h is the reference size of a control volume inside the mesh and p is the order of numerical scheme. The refinement ratio is defined as $r=h_2/h_1$. The observed order of convergence (p) is computed using the Eqn 32.1.1.2. Where the subscript 1 represent the fine mesh and 3 represents the coarse mesh.

$$p = \frac{ln\left(\frac{U_3 - U_2}{U_2 - U_1}\right)}{\ln r} \qquad \text{Eqn 32.1.1.2}$$

The relative error in the coarse mesh ($\mathcal{E}_{23}$) and the fine mesh ($\mathcal{E}_{12}$) are calculated using Eqn 32.1.1.3 and Eqn 32.1.1.4.

$$\mathcal{E}_{12} = \frac{U_2 - U_1}{U_1} \qquad \text{Eqn 32.1.1.3}$$

$$\mathcal{E}_{23} = \frac{U_3 - U_2}{U_3} \qquad \text{Eqn 32.1.1.4}$$

The extrapolated solution, when h approaches zero can be estimated using the Eqn 32.1.1.5.

$$U_0 = U_2 + \frac{(U_1 - U_2)r^p}{r^p - 1} \qquad \text{Eqn 32.1.1.5}$$

Roache has defined a grid convergence indicator GCI to quantify the numerical error in the CFD solution, which can be computed using Eqn 32.1.1.6.

$$GCI_u = \frac{F_s \mathcal{E}_U}{r^p - 1} \qquad \text{Eqn 32.1.1.6}$$

Where F_s is the safety factor, a conservative value of a safety factor of 3 is suggested for the comparison of three meshes [52]. Using the GCI of the coarse and the fine mesh, one is able to assess if the computed solution lies within the asymptotic range. For the solution to lie in the asymptotic range, the condition shown in Eqn 32.1.1.7 should be satisfied.

$$Asymptotic\ range = \frac{GCI_{coarse}}{r^P GCI_{fine}} = 1 \qquad \text{Eqn 32.1.1.7}$$

8.2 Delft validation study

8.2.1 DU93W210 domain extent sensitivity study results

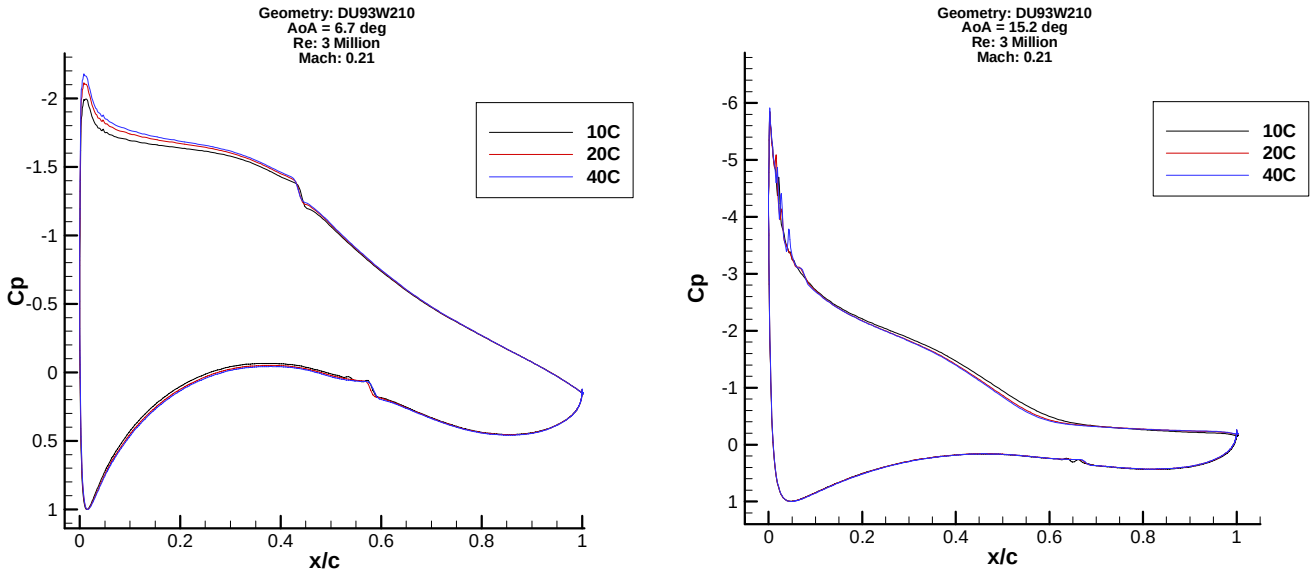

(a) (b)

Figure 8-1 Coefficient of pressure distribution as a function of chord, Geometry: DU93W210 (a): α: 6.7° and (b) α: 15.2°

Domain size (c)	C_L	C_D	C_m
10	1.229	0.019	-0.139
20	1.259	0.014	-0.139
40	1.275	0.011	-0.139
Measured	1.280	0.009	-0.134

(a)

Domain size (c)	C_L	C_D	C_m
10	1.689	0.061	-0.104
20	1.673	0.054	-0.102
40	1.681	0.050	-0.101
Measured	1.22	0.095	-0.098

(b)

Figure 8-2 Integrated force comparison for different domain extents, Geometry: DU93W210 (a): α: 6.7° and (b) α: 15.2°

8.2.2 DU93W210 mesh independence study results

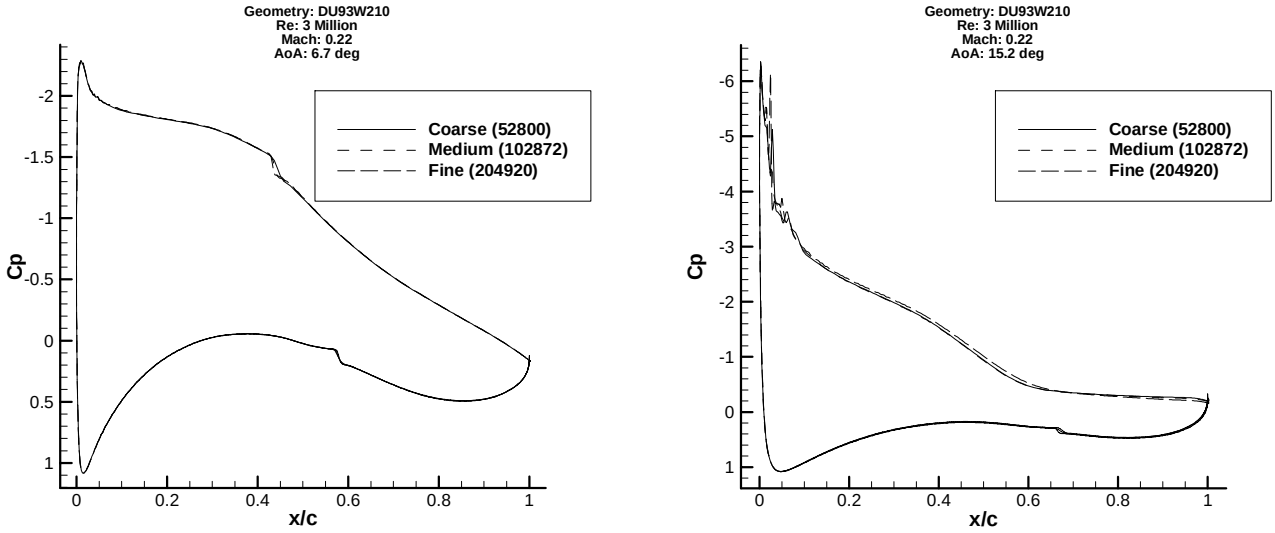

(a) (b)

Figure 8-3 Coefficient of pressure distribution as a function of chord, Geometry: DU93W210 (a): α: 6.7° and (b) α: 15.2°

	Coarse	Medium	Fine	Experimental	Extrapolated	Asymptotic range
Element size	52,800	102,872	204,920			
C_L (α = 6.7 °)	1.2579	1.2591	1.2596	1.2800	1.25983	**1.00**
C_d (α = 6.7 °)	0.0141	0.0139	0.0139	0.0092	0.01391	**0.99**
C_L (α = 15.2 °)	1.6756	1.6733	1.6712	1.2200	1.65186	**0.9986**
C_d (α = 15.2 °)	0.0545	0.0544	0.0544	0.0095	-	**-**

Table 8-1 Richardson's extrapolation analysis for DU93W210 airfoil

8.2.3 DU91W2250 airfoil validation results

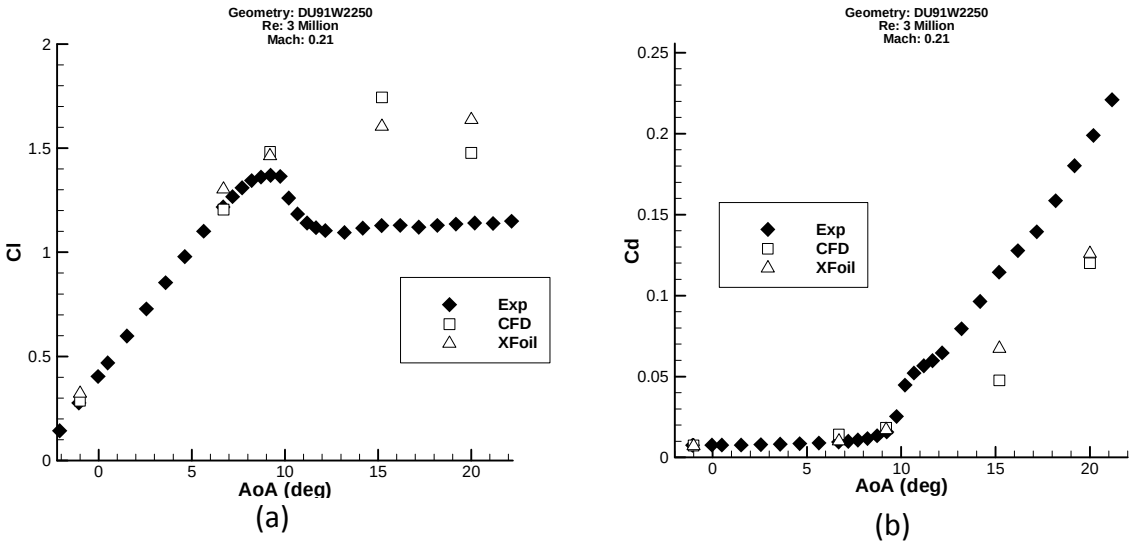

(a) (b)

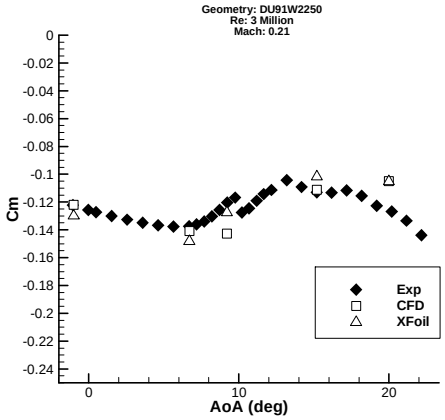

(c)

Figure 8-4 CFD results validation using measurements for the DU91W2250 airfoil – (a): Lift coefficient comparison, (b): Drag coefficient comparison, (c): Pitching moment comparison

8.2.4 DU93W210 airfoil validation results

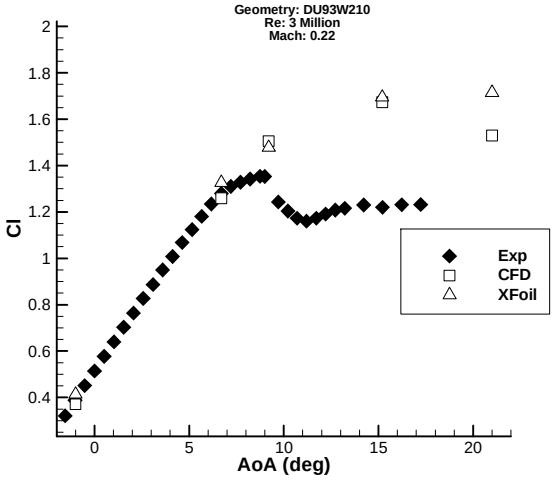

(a)

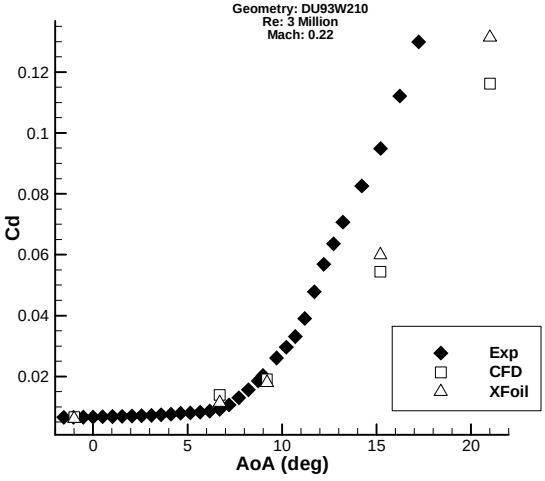

(b)

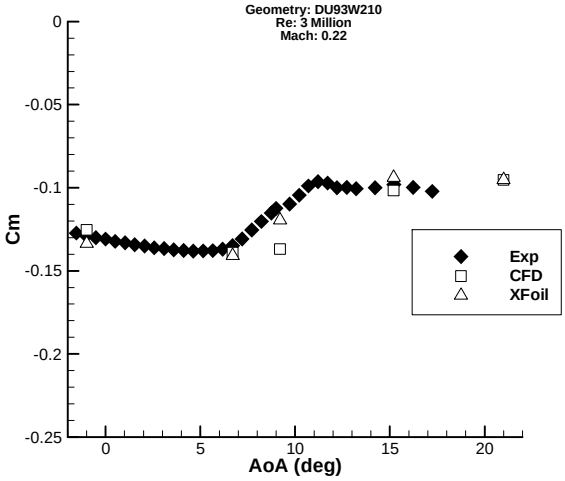

(c)

Figure 8-5 CFD results validation using measurements for the DU93W210 airfoil – (a): Lift coefficient comparison, (b): Drag coefficient comparison, (c): Pitching moment comparison

8.3 Baseline NREL 5MW rotor geometry

This section will briefly discuss the chosen baseline rotor for this study. National Renewable Energy Laboratory (NREL) has defined a conceptual turbine [2] for the purpose of academic research (NREL 5MW). This turbine has been used on numerous studies around the world [1], such as the EU UpWind research program, the IEA Wind Task 23 OC3 project, and the IEA Wind Task 30 OC4 project.

NREL has decided to use the specifications of the REpower 5M machine as the target specifications for their reference turbine. However the information regarding the properties of REpower 5M machine is not publically available. Therefore the specification of the NREL reference turbine was developed using a combination of the properties gathered from publically available studies on offshore wind turbines [2]. These include the studies conducted by DOWEC (Dutch Offshore Wind Energy Converter), WindPACT (Wind Partnerships for Advanced Component Technology) and RECOFF (Recommendations for Design of Offshore).

The NREL reference turbine (baseline rotor) has a rotor diameter of 126 meters and a hub radius of 3 meters. NREL, for their baseline rotor blade, have adapted a geometry based on a blade used in the DOWEC study (LMH64-5) [2]. One of the differences between the DOWEC LMH64-5 blade and the NREL blade is that they differ in radius. The DOWEC LMH64-5 rotor is 62.6m in radius and NREL baseline rotor blade is 61.5m. NREL have adopted this to match the blade length of the Repower 5MW rotor [2]. The available information regarding the geometry of the LMH64-5 blade is unclear. The specification of the NREL 5MW was defined in ref [2], however NREL has stated that they had no intention to include enough details to develop a CAD model or for CFD analysis [1], therefore numbers of changes were implemented to the original geometry to attain a geometry suitable for CFD analysis. The UC-Davis, the UC-San Diego and Risø DTU of Denmark have also adapted their own changes to generate a CAD model suitable for CFD analysis [1].

The implemented changes to the original NREL 5MW geometry studied in this thesis are:

1. The second cylinder at the root (bigger chord than the first one) was removed.
2. The lofting surface was only restrained through single differing profiles, i.e. only one of the repeated profiles was chosen for the surface to pass through.
3. The tip airfoil profile (NACA 64) was modified to have a blunt trailing edge, by removing the closing point of the spline.

The change in in the root geometry was considered to adapt for a visually smooth attractive blade based on the industrial experience. It was also noticed that, when a small number of airfoil profiles were restrained for the surface to pass through, the waviness in the radial direction reduced considerably. Therefore, the second change was implemented. In industry the airfoil sections are specifically designed with the consideration for a smooth surface. Lastly, the trailing edge of the tip airfoil section (NACA 64) was modified to have a blunt trailing edge as for CFD reasons it is not suitable to have the airfoil sections transition from a blunt trailing edge to a sharp trailing edge, especially for a structured mesh topology. Finally the modified blade root was defined with two cylinders and six different airfoils were used to define the rest of the blade (see Table 8.3-1).

Airfoil Name	r/R (span locations)	Chord (m)	Twist (deg) β	Pitch axis location PA/c
Cylinder	0.046	3.542	13.308	0.4988
Cylinder	0.089	3.854	13.308	0.4718
Adjusted DU_40	0.187	4.557	13.308	0.3964
Adjusted DU_35	0.317	4.458	10.162	0.3750
DU30	0.382	4.249	9.011	0.3750
DU25	0.512	3.748	6.544	0.3750
DU21	0.642	3.256	4.188	0.3750
NACA64	0.772	2.764	2.319	0.3750
NACA64	0.935	2.086	0.370	0.3750
NACA64	0.978	1.419	0.106	0.3750

Table 8.3-1 Blade definition (r = local radius in m, R = 63m, c = chord)

The pitch axis location was provided by NREL [1], which is the local distance from the leading edge of the airfoil to the pitch axis (Figure 8-6).

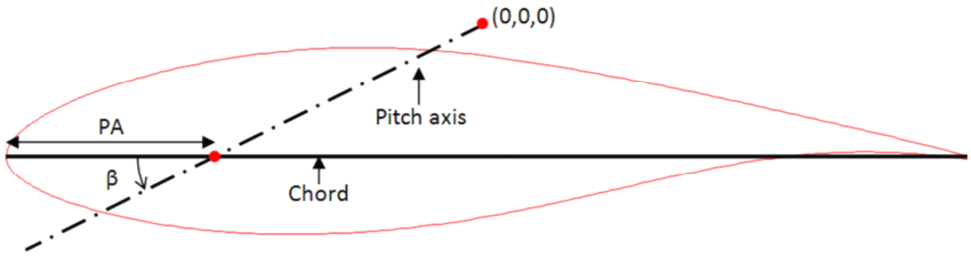

Figure 8-6 Twist and pitch axis definition

Positive twist is defined in the anticlockwise direction. The airfoil coordinates were transformed using the chord and twist (Figure 8-8). MATLAB was used to conduct the coordinate transformation.

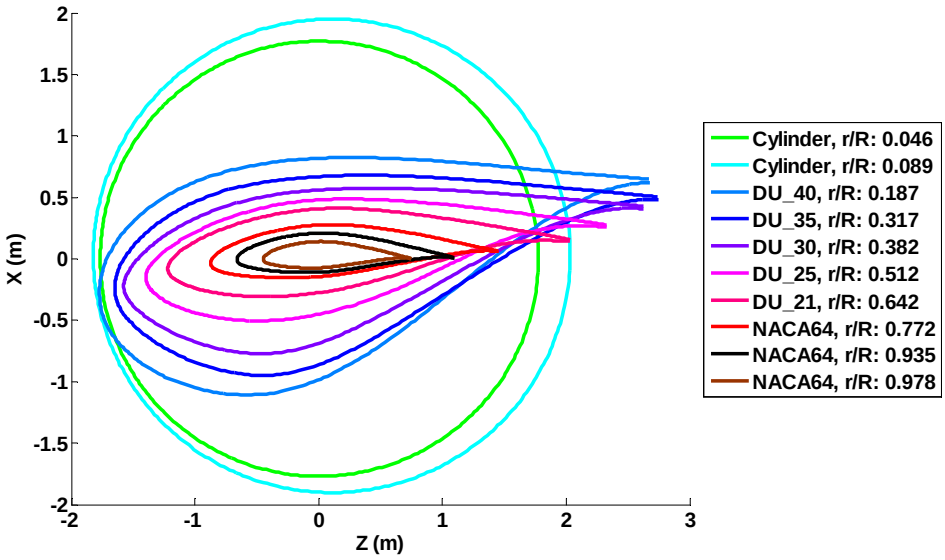

Figure 8-7 Twisted airfoil sections of the NREL 5MW rotor, (Z, X) = (0, 0): pitch axis

Using the twisted coordinates as an input for CATIA (CAD package), a wind turbine blade is generated. Generative shape design (GSD) surface was employed in CATIA to generate the surface for the blade.

The apex of the tip is chosen at the pitch axis. Usually a small positive twist is applied at the tip for noise reduction reasons. Ferrer et al [81] has also shown that a tip with its apex located on the pitch axis of the blade is beneficial, as it produces a better toque to thrust ratios. This twist is applied for the last 0.5 meters of the blade. However, for the baseline CAD model this was not implemented. Based on industrial advice a tapered trailing edge was considered for the tip geometry. This is usually adapted to reduce noise i.e. trailing edge being perpendicular to the flow, known to produce greater noise than a tapered trailing edge. For better hexahedral mesh quality the outer most tip of the blade was truncated (~ 10 cm), because the tip surface ends at a single point (Figure 8-8 and Figure 8-9). The spinner and nacelle geometries were provided by the industry.

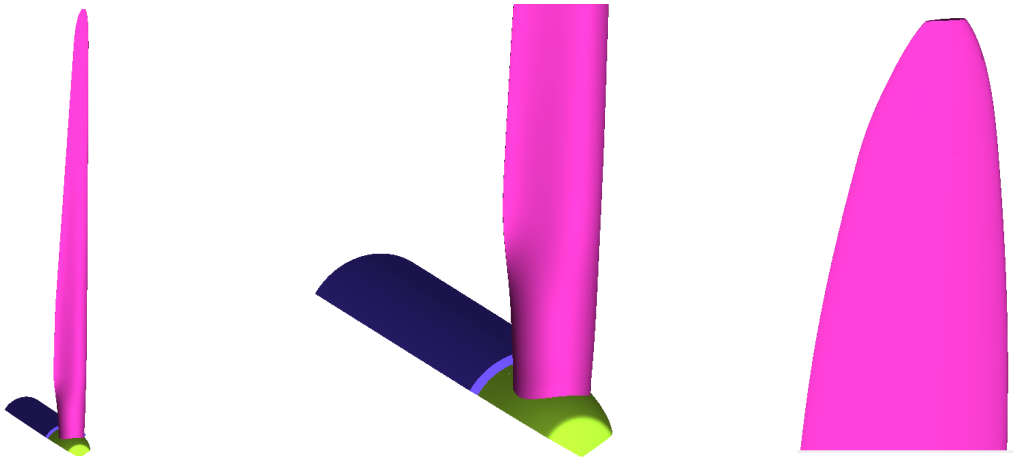

(a) (b) (c)

Figure 8-8 Final 3D CAD model (a = full blade with hub and nacelle, b = root of the blade, c = truncated tip)

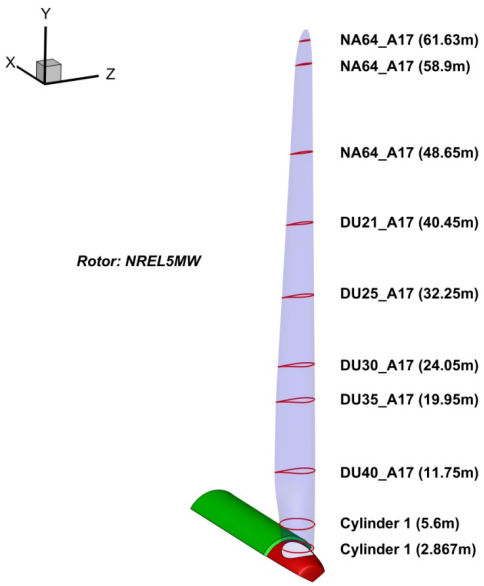

Figure 8-9 ISO view of the CU NREL 5MW rotor blade

8.4 Annual power estimation for a wind turbine

For a known turbine power and the wind speed distribution the annualised wind turbine power can be obtained using the following equation:

$$\overline{P_w} = \int_0^\infty P_w(U)p(U)dU \qquad \text{Eqn 32.1.2}$$

Where U = wind speed, $P_w(U)$ = power at the corresponding wind speed and $p(U)$is the probably density function that describes the likelihood that the corresponding wind speed will occur.

For this research the Rayleigh distribution was used to model the probability density function (Figure 8-10) and it is defined as the following equation [39]:

$$p(U) = \frac{\pi}{2}\left(\frac{U}{\overline{U}^2}\right)\exp\left[-\frac{\pi}{4}\left(\frac{U}{\overline{U}}\right)^2\right] \qquad \text{Eqn 32.1.3}$$

Where $\overline{U}$ is the mean wind speed. For this research a mean wind speed of 10 m/s was used.

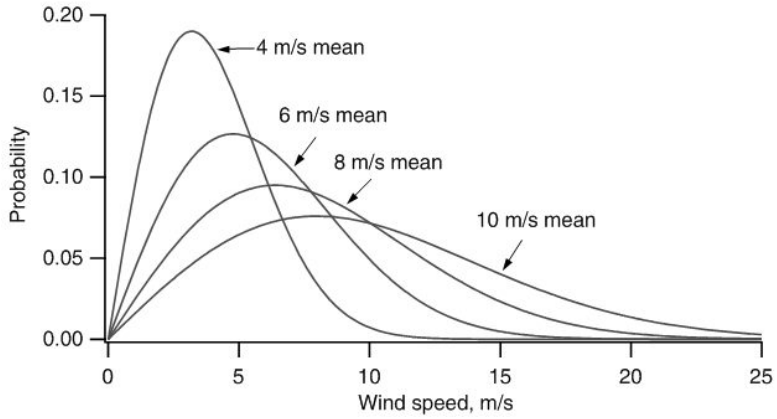

Figure 8-10 Rayleigh probability density function used for this research [39]

8.5 Minimum node requirement for 3D VG simulation

A study was conducted to determine the minimum number of nodes required in the spanwise direction and downstream direction (Figure 8-11) to calculate a solution that agree well with the solution calculated from the established grid. The established grid had 30 spanwise nodes and 90 downstream nodes.

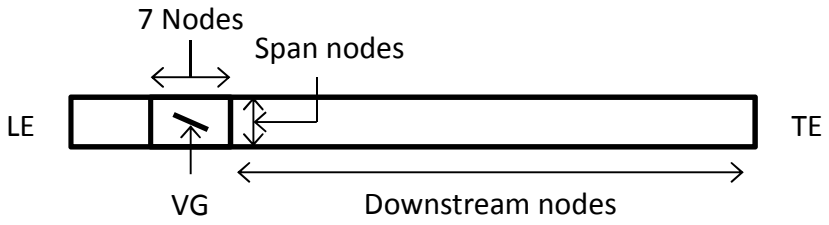

Figure 8-11 Top view of the airfoil with VG

Extensive studies were conducted with different combinations of spanwise and downstream nodes and the results were compared against the results from the baseline grid. The lift and

drag coefficient at two different AoA were used to assess the results, they were 9.9° and 14.4° respectively. The result suggests that a grid with 30 span nodes and 30 downstream nodes are adequate to resolve the VG flow that agree well with the validated grid with a small amount of increase in grid size when this configuration is implemented to a 3D grid.

Changes in lift coefficient - AoA: 9.9°

		Downstream nodes			
	X	20	30	60	120
	7		2.44%		
Span	15		0.20%		
Nodes	30	1.20%	0.16%	-0.93%	-0.83%
	60		0.42%		

(a)

Changes in lift coefficient - AoA: 14.4°

		Downstream nodes			
	X	20	30	60	120
	7		2.75%		
Span	15		3.22%		
Nodes	30	2.14%	2.75%	1.50%	1.39%
	60		2.08%		

(b

Changes in drag coefficient - AoA: 9.9°

		Downstream nodes			
	X	20	30	60	120
	7		-10.58%		
Span	15		-5.94%		
Nodes	30	-41.28%	-7.62%	-1.93%	-9.08%
	60		-11.84%		

(c)

Changes in drag coefficient - AoA: 14.4°

		Downstream nodes			
	X	20	30	60	120
	7		-6.18%		
Span	15		-9.05%		
Nodes	30	-34.63%	-9.46%	-5.27%	-13.41%
	60		-7.16%		

(d)

Table 8.2.4-2 Changes in lift and drag coefficients relative to the established grid for different combinations of spanwise and downstream nodes, a: changes in C_l at 9.9°, b: changes in C_l at 14.4°, a: changes in C_d at 9.9°, a: changes in C_d at 14.4°, Re: 1.6 million, TM: SST γ – θ